Advances in Quantum Chemistry

State of The Art of Molecular Electronic Structure Computations: Correlation Methods, Basis Sets and More

Volume 79

Volume Editors
Lorenzo Ugo Ancarani
Philip E. Hoggan

Series Editors
John R. Sabin
and Erkki J. Brändas

VOLUME SEVENTY NINE

ADVANCES IN
QUANTUM CHEMISTRY

State of The Art of Molecular Electronic Structure Computations: Correlation Methods, Basis Sets and More

VOLUME SEVENTY NINE

ADVANCES IN QUANTUM CHEMISTRY

State of The Art of Molecular Electronic Structure Computations: Correlation Methods, Basis Sets and More

Edited by

LORENZO UGO ANCARANI
Université de Lorraine, CNRS, LPCT, Metz, France

PHILIP E. HOGGAN
Institut Pascal, CNRS, Université Clermont Auvergne, Aubière Cedex, France

ACADEMIC PRESS
An imprint of Elsevier

Academic Press is an imprint of Elsevier
50 Hampshire Street, 5th Floor, Cambridge, MA 02139, United States
525 B Street, Suite 1650, San Diego, CA 92101, United States
The Boulevard, Langford Lane, Kidlington, Oxford OX5 1GB, United Kingdom
125 London Wall, London, EC2Y 5AS, United Kingdom

First edition 2019

Notices
Knowledge and best practice in this field are constantly changing. As new research and experience broaden our understanding, changes in research methods, professional practices, or medical treatment may become necessary.

Practitioners and researchers must always rely on their own experience and knowledge in evaluating and using any information, methods, compounds, or experiments described herein. In using such information or methods they should be mindful of their own safety and the safety of others, including parties for whom they have a professional responsibility.

To the fullest extent of the law, neither the Publisher nor the authors, contributors, or editors, assume any liability for any injury and/or damage to persons or property as a matter of products liability, negligence or otherwise, or from any use or operation of any methods, products, instructions, or ideas contained in the material herein.

ISBN: 978-0-12-816174-6
ISSN: 0065-3276

Publisher: Zoe Kruze
Acquisition Editor: Sam Mahfoudh
Editorial Project Manager: Shellie Bryant
Production Project Manager: Denny Mansingh
Cover Designer: Christian J. Bilbow

Typeset by SPi Global, India

Contents

This page intentionally left blank

Contributors

Luis Enrique Aguilar Suarez
Theoretical Chemistry Group, Zernike Institute for Advanced Materials, University of Groningen, Groningen, The Netherlands

José M. Alcaraz-Pelegrina
Departamento de Física, Universidad de Córdoba, Córdoba, Spain

Lorenzo Ugo Ancarani
Université de Lorraine, CNRS, LPCT, Metz, France

Vincenzo Aquilanti
Dipartimento di Chimica, Biologia e Biotecnologie, Università di Perugia, Perugia, Italy

Florian A. Bischoff
Institut für Chemie, Humboldt-Universität zu Berlin, Berlin, Germany

Enrique F. Borja
Departamento de Física, Universidad de Córdoba, Córdoba, Spain

Gabriel Breuil
Institut Charles Gerhardt—CNRS and Université de Montpellier, Montpellier, France

Michel Caffarel
Laboratoire de Chimie et Physique Quantiques, Université de Toulouse, CNRS, UPS, Toulouse, France

Johanna P. Carbone
Dipartimento di Scienze Chimiche e Farmaceutiche, Università degli Studi di Trieste, Trieste, Italy

Lan Cheng
Department of Chemistry, Krieger School of Arts and Sciences, Johns Hopkins University, Baltimore, MD, United States

Cecilia Coletti
Dipartimento di Farmacia, Università G. d'Annunzio, Chieti, Italy

Sonia Coriani
Department of Chemistry, Technical University of Denmark, Kongens Lyngby, Denmark

Thibaud Etienne
Institut Charles Gerhardt—CNRS and Université de Montpellier, Montpellier, France

Shirin Faraji
Theoretical Chemistry Group, Zernike Institute for Advanced Materials, University of Groningen, Groningen, The Netherlands

Daniel Gebremedhin
Physics Department, Florida A&M University, Tallahassee, FL, United States

Remco W.A. Havenith
Theoretical Chemistry Group, Zernike Institute for Advanced Materials; Stratingh Institute for Chemistry, University of Groningen, Groningen, The Netherlands

Philip E. Hoggan
Institut Pascal, Aubière Cedex, France

R.K. Kathir
Theoretical Chemistry Group, Zernike Institute for Advanced Materials, University of Groningen, Groningen, The Netherlands

Henrik Koch
Department of Chemistry, Norwegian University of Science and Technology, Trondheim, Norway; Scuola Normale Superiore, Pisa, Italy

Stanisław A. Kucharski
Institute of Chemistry, University of Silesia in Katowice, Katowice, Poland

Benjamin Lasorne
Institut Charles Gerhardt—CNRS and Université de Montpellier, Montpellier, France

Artur Lisoń
Institute of Chemistry, University of Silesia in Katowice, Katowice, Poland

Elise Lognon
Institut Charles Gerhardt—CNRS and Université de Montpellier, Montpellier, France

Pierre-François Loos
Laboratoire de Chimie et Physique Quantiques, Université de Toulouse, CNRS, UPS, Toulouse, France

Devin Matthews
Department of Chemistry, Southern Methodist University, Dallas, TX, United States

Alejandra M.P. Mendez
Instituto de Astronomía y Física del Espacio, Universidad de Buenos Aires – Consejo Nacional de Investigaciones Científicas y Técnicas, Buenos Aires, Argentina

Jorge E. Miraglia
Instituto de Astronomía y Física del Espacio, Universidad de Buenos Aires – Consejo Nacional de Investigaciones Científicas y Técnicas, Buenos Aires, Argentina

Darío M. Mitnik
Instituto de Astronomía y Física del Espacio, Universidad de Buenos Aires – Consejo Nacional de Investigaciones Científicas y Técnicas, Buenos Aires, Argentina

Ion Mitxelena
Kimika Fakultatea, Euskal Herriko Unibertsitatea (UPV/EHU) and Donostia International Physics Center (DIPC), Donostia, Euskadi, Spain

Milagros F. Morcillo
Departamento de Física, Universidad de Córdoba, Córdoba, Spain

Monika Musiał
Institute of Chemistry, University of Silesia in Katowice, Katowice, Poland

Rolf H. Myhre
Department of Chemistry, Norwegian University of Science and Technology, Trondheim, Norway

Egor Ospadov
Department of Chemistry, The University of Western Ontario, London, Ontario, Canada

Federico Palazzetti
Dipartimento di Chimica, Biologia e Biotecnologie, Università di Perugia, Perugia, Italy

Mario Piris
Kimika Fakultatea, Euskal Herriko Unibertsitatea (UPV/EHU) and Donostia International Physics Center (DIPC), Donostia; Basque Foundation for Science (IKERBASQUE), Bilbao, Euskadi, Spain

Sylvain Pitié
Institut Charles Gerhardt—CNRS and Université de Montpellier, Montpellier, France

Juan Martín Randazzo
Instituto Balseiro and CONICET, Río Negro, Argentina

María Belén Ruiz
Department of Theoretical Chemistry, Friedrich-Alexander-University Erlangen-Nürnberg, Erlangen, Germany

Antonio Sarsa
Departamento de Física, Universidad de Córdoba, Córdoba, Spain

Anthony Scemama
Laboratoire de Chimie et Physique Quantiques, Université de Toulouse, CNRS, UPS, Toulouse, France

Rajesh O. Sharma
Institut Pascal, Aubière Cedex, France; Physics Department, Marwadi University, Rajkot, Gujarat, India

Kaltrina Shehu
Institut Charles Gerhardt—CNRS and Université de Montpellier, Montpellier, France

Enrico Siagri
Theoretical Chemistry Group, Zernike Institute for Advanced Materials, University of Groningen, Groningen, The Netherlands

Viktor N. Staroverov
Department of Chemistry, The University of Western Ontario, London, Ontario, Canada

Jesus M. Ugalde
Kimika Fakultatea, Euskal Herriko Unibertsitatea (UPV/EHU) and Donostia International Physics Center (DIPC), Donostia, Euskadi, Spain

Charles Weatherford
Physics Department, Florida A&M University, Tallahassee, FL, United States

Brian Wilson
Physics and Life Science Directorate, Lawrence Livermore National Laboratory, Livermore, CA, United States

This page intentionally left blank

Preface

This volume of *Advances in Quantum Chemistry* comprises 15 invited expert contributions on the state of the art of molecular electronic structure computations. Related talks were given at the Molecular Electronic Structure (MES) international conference, held in Metz, France in 2018 (chaired by L.U. Ancarani, https://mesm.event.univ-lorraine.fr/). About 80 researchers, from all 5 continents, attended the meeting that comprised 30 invited and 14 contributed talks, as well as a poster session.

Financial support is gratefully acknowledged from the Université de Lorraine, CNRS Groupement de Recherche THEMS and CORREL, Q-Chem, Ville de Metz, Metz Métropole, Conseil Général de la Moselle and Région Grand Est.

We thank all local committee members and Université de Lorraine staff for making the conference run smoothly, session chairpersons, and last but not least, all participants for many lively and fruitful discussions throughout the meeting.

At a reception on 29 august 2018, for delegates of MES in Metz, Pr Clemens Roothaan's 100th birthday was celebrated. He pioneered molecular electronic structure, influencing so many of us. Sadly, he passed away on 17 June 2019.

The MES series began in 2012, the first being hosted in Çanakkale, Turkey, by Israfil Guseinov. It is with great regret that we report he passed away on February 16, 2019 (aged 85), fondly remembered by his many students.

Subsequent MES meetings were held in 2014 (Amasya, Turkey) and 2016 (Buenos Aires, Argentina).

The scientific themes covered at MES, in 2018, are reflected by the four sections presented in this volume which opens with the review by Bischoff on the Multiresolution Analysis, a useful and efficient tool to evaluate molecular properties.

Section 2 is devoted to mathematical innovations, necessary to unify the choice of basis sets (Aquilanti et al.), improve convergence rates (Randazzo and Ancarani), normalize cluster wave functions (Gebremedhin and Weatherford), and cater for the notorious electron–nuclear cusp (Loos et al.).

The first contribution presents interrelations between properties of hypergeometric orthogonal polynomials (the Jacobi ladder), discussing their use in basis sets for atomic and molecular orbitals. Next, we move on to a Sturmian approach that innovates on one example of the bases mentioned in the previous chapter, i.e., the Coulomb Sturmians, extending them to two-dimensional functions. The muffin-tin orbitals are often used in solids and leave interstices between the circular sections they make in a plane; normalizing cluster wave functions in the interstitial region within the muffin-tin approximation is the subject of the third contribution. This section closes with a chapter describing how to implement self-consistently the cusp at the nucleus for electrons in molecular orbitals.

Section 3 presents a highly accurate correlated atom (Ruiz), progress in Natural Orbital theory (Piris et al.), two different effective potential approaches (Mendez et al., Staroverov and Ospadov), and Fock-space correlated NaH (Musial et al.).

The first contribution in this section reports highly accurate atomic explicitly correlated wave functions for Boron. It is followed by a comprehensive study of progress in Natural Orbital density-oriented methods. Effective potentials are then discussed in two distinct contributions with numerical approaches. In the first contribution, the validity of effective potentials when applied to collision theory is tested for atoms and also for methane, as a molecular example. The second proposes a unified construction of Fermi, Pauli, and Exchange-Correlation potentials.

Section 4 begins with two correlated excited-state approaches (Coriani et al. and Faraji et al.), density descriptors are then presented by Etienne et al., followed by a Quantum Monte Carlo application to surface reactions (Sharma and Hoggan) and confined H atom (Sarsa et al.).

Two contributions with applications to excited-state correlated wave functions open this section: the first concerns core excitations in water, ammonia, and carbon monoxide, while the second treats singlet fission in suitable organic dimers. The next chapter deals with electron density descriptors so useful in relation to molecular structure and properties. Next, we move on to heterogeneous catalysis and use of a Quantum Monte Carlo approach to model systems (physisorption of H and H_2 on clean Pt(111)). The volume closes with a contribution on the stability of the H atom after a spatial confinement is removed.

This collection has been arranged from the most fundamental to the most applied contributions on the two themes, broadly basis sets and electron correlation, both essential for determining accurate electron densities in

atoms, molecules, and solids. Many of the properties calculated are highly sensitive to the bases and to the contribution of electron correlation, modest in energy amplitude but key to the accurate description of electronic structure.

To complete this preface, we would like to thank all the authors and also those who gave their valuable time insightfully refereeing an article for this volume. Every contribution has helped to build up a snapshot on *molecular electronic structure computations: correlation methods, basis sets and more*, with expert input.

We have taken much pleasure in editing this exciting collection and hope that it translates to a pleasurable and informative read.

Lorenzo Ugo Ancarani and Philip E. Hoggan
May 15, 2019

This page intentionally left blank

SECTION 1

Review

This page intentionally left blank

CHAPTER ONE

Computing accurate molecular properties in real space using multiresolution analysis

Florian A. Bischoff*
Institut für Chemie, Humboldt-Universität zu Berlin, Berlin, Germany
*Corresponding author: e-mail address: florian.bischoff@hu-berlin.de

Contents

Abstract

Multiresolution analysis (MRA), and specifically multiwavelets, can be used to compute properties of molecules accurately with defined error control. The truncation error induced by using only a finite mathematical basis for the quantum molecular wave function, which is a major source of inaccuracy in computations, can be controllably removed with MRA. A large variety of molecular properties can be computed, including ground-state properties and excited states, first- and second-order properties

Advances in Quantum Chemistry, Volume 79
ISSN 0065-3276
https://doi.org/10.1016/bs.aiq.2019.04.003

(dipole moments, nuclear gradients, vibrational frequencies) using density functional theory (pure and hybrid functionals) as well as correlated methods (second-order perturbation theory and Coupled-Cluster).

1. Introduction

1.1 On the computation of molecular properties

Two challenges have dominated science: finding the basic natural laws that determine everything and applying these laws to a system of interest in a complex environment. The basic theory of chemistry, quantum mechanics, is well-known since the early 20th century. Applying quantum mechanics on a chemical system is called quantum chemistry. While the laws governing the motion of a single particle are understood, the application of these laws in a complex environment such as a molecule are unsolved. Quantum chemistry thus deals with the development of approximate theories to describe the motion of particles in a molecular system and the application of these methods in chemical problem settings.[1]

Chemical structure and reactivity always involve many interacting particles but many-particle problems are not solvable analytically in general. Single-particle problems are numerically tractable, so a common theme in quantum chemistry is to reduce many-particle systems to approximate effective one-particle or few-particle systems. This reduction in complexity is called the quantum chemical model and it includes models like Hartree–Fock (HF), density functional theory (DFT), or correlated methods such as many-body perturbation theory or the Coupled-Cluster ansatz.

In addition to the approximations in the chosen model, the model's working equations cannot be solved analytically in general, so that they must be discretized in a suitable way and solved numerically. Depending on the chemical system a suitable discretization can be chosen in real space, in momentum space, or in any other representation. In molecules a set of atom-based Gaussian basis functions is typically used, in solid state chemistry plane waves form an appropriate basis.

After having chosen a model and a basis, the wave function of a chemical system can be computed. The wave function determines the energy of the system but also other properties such as dipole moments, polarizabilities, excitation energies, nuclear gradients, NMR chemical shifts, and many more. Often a derivative technique is used, i.e., the response of the molecular energy to a certain physical quantity determines the corresponding

property.[2] For instance, the dipole moment can be computed as the derivative (response) of the energy with respect to an external electric field. Even if the wave function is known computing related properties can be very expensive because the wave function is only approximate and artifacts (e.g., Pulay forces) may emerge.[3,4]

The accuracy of the computed properties critically hinges on both the model and the basis. Some properties are more sensitive to the basis set than others. Even if the energy may be essentially converged for a given quantum chemical model, these properties may not be accurately reproduced, because functions might be missing in the basis set that contribute to the property but not to the energy (e.g., diffuse functions for excited states). Furthermore there is an interplay between model and basis: the basis set requirements are in general higher for many-body methods than for effective one-particle methods.

1.2 Expanding the molecular wavefunction in a basis

1.2.1 Atoms and diatomics

In atoms and diatomic molecules separable coordinate systems may be used, enabling the computation of the wave function directly on a numerical grid. The computational load is reduced to the solution of an effective one- or two-dimensional Schrödinger equation.[5] These calculations can be very precise and may serve as benchmark calculations. The basis functions are chosen as $\chi(\vec{r}) = R(r)Y_{lm}(\theta,\phi)$, with the angular part being described by spherical harmonics $Y_{lm}(\theta, \phi)$. The radial part may be represented directly on a grid, by finite elements, by B-splines, or by any other suitable method.[5,6]

1.2.2 Atom-centered basis functions for molecules

In molecular quantum chemistry no separable coordinate system is available and the equations cannot be factorized. The approach that is typically used is called linear combination of atomic orbitals (LCAO), where a set of functions of the form $\chi(\vec{r}) = R(r)Y_{lm}(\theta,\phi)$ is placed on the atoms of the molecule, with r, θ and ϕ being spherical coordinates with a given atom as origin. As in the atomic case, the angular functions $Y_{lm}(\theta, \phi)$ are spherical harmonics, the radial part may be chosen in different ways, e.g., as Slater function, as Gaussian function,[7] or as numerical basis. Gaussian basis functions are by far the most common choice due to their computational simplicity (in particular with respect to integral evaluation[8]) and for their

fast, initial convergence to the basis limit and few Gaussians suffice to get reasonable results for molecular properties. Optimized Gaussian basis sets are available for the whole periodic table and are, in fact, the workhorse of molecular quantum chemistry.[9] However, after the fast initial convergence they tend to converge slowly to the basis set limit in particular in post-HF methods.[10] The atom-centeredness leads to the basis set superposition error (BSSE), which overbinds intermolecular complexes.[11,12] The decay of the function is too fast for representing anions or excited states properly and severe, unbalanced errors may occur. Adding diffuse functions might lead to overcompleteness and linear dependencies. In general, since the basis sets are optimized and predefined, a high degree of arbitrariness is left and hard to avoid in chemical problem settings.

1.2.3 Plane waves in the solid state

Plane waves can be seen as a grid basis in momentum space, motivated by Bloch's theorem.[13] As such they extend over the whole real space and are thus particularly suited for periodic boundary conditions in solid state calculations. Plane wave basis sets can be systematically completed without the danger of overcompleteness. The convergence is fast for one-particle methods and for many-body methods truncation schemes can be employed.[14,15] A drawback of plane waves is the inability to represent sharp features such as interelectronic or electron–nuclear cusps in the wave function but it can be alleviated by the use of sophisticated pseudopotentials.[16,17]

1.2.4 Real-space methods for high precision

Real-space grid methods have been used in quantum chemistry primarily for computing reference values for small systems, such as atoms or diatomic molecules.[18,19] Small polyatomic systems have also been investigated.[20–22] While these methods can be very precise for small (in particular low-dimensional) systems, they are expensive to apply on larger molecules because the number of grid points increases quickly. More efficient are finite element methods, where space is divided into connected polyhedral subregions or elements, with the basis functions defined only inside the elements.[23,24] In the context of density functional theory they are applicable also to large systems. A related method uses wavelets as basis functions, which have a high convergence rate with respect to the polynomial order.[25,26] Recently methods using low-rank tensor approximations have been developed that can handle the exponential increase of grid points in an efficient manner.[27]

1.2.5 Multiresolution analysis in chemistry and physics

In this review, a novel method for representing the wave function called multiresolution analysis (MRA) will be discussed. MRA is based on wavelet analysis, known from signal processing,[28] and was introduced as a basis into quantum chemistry in 2004 for HF and DFT.[29] Since 2012 MRA was also used for many-body methods, such as second-order perturbation theory (MP2) or Coupled-Cluster, which are computationally very demanding and require special numerical techniques to become tractable.[30–33] Wavelets have the advantages of adaptiveness, completeness without the danger of overcompleteness, low-scaling behavior, and guaranteed precision. On the other hand, they are more affected when the quantum chemical model is changed from effective one-particle to many-particle, which entails an increase of the dimensions from 3 to 6 or more. This behavior has been called the "curse of dimensions"[34] and it means that the effort to solve a system of size N increases exponentially as N^d with the number of dimensions d. For effective one-particle methods the dimension $d = 3$ is still feasible but for post-HF methods $d = 6$ requires special techniques as described in this work to handle the computational efforts.[30,35–37]

It will be shown that MRA is a versatile tool in quantum chemistry, it can be combined with the usual quantum chemical models (HF, DFT, and correlation methods) and it can reliably compute molecular properties. The MRA algorithms are fast in the sense that, despite having a relatively large prefactor, they show low scaling with respect to the system size and can eventually surpass the efficiency of conventional methods.[38] MRA can be used for time-dependent and time-independent molecular properties, first or higher order properties and in combination with effective one- and many-particle models.

This chapter will present the wavelet formalism as employed in MRA in Section 2, with a brief discussion of its generalization to higher dimensions. Its application in quantum chemistry will be presented in Section 3, including the translation of the commonly used LCAO matrix equations into their first-quantized counterpart and with special emphasis on the numerical implications of singularities in the working equations. Finally application examples will be given in Section 4, concluded by an outlook.

2. General wavelet formalism in higher dimensions

2.1 Wavelet formalism in one dimension

The mathematical foundations of wavelets as a basis for solving differential equations were laid out in Refs. 39–41, to which we refer for an in-depth

discussion. The basic idea is that the space **R** can be represented in a basis of repeatedly subdivided intervals (or boxes in higher dimensions), filled with polynomials of orders $0, 1, \ldots, k-1$.

An example for the expansion of an arbitrary function is the Haar scaling function corresponding to polynomial order $k = 1$.[42] A Haar scaling function, which forms the basis for the expansion, is a normalized box function. Finer scales lead to narrower boxes, with 2^n boxes on the scale n, approaching a representation with arbitrary precision with increasing number of subdivisions n. The Haar scaling function averages over the function values in a given interval. Fig. 1 shows a Slater function represented using Haar scaling functions, with increasing refinements. The poor representation with small refinements and convergence to the exact representation of the exponential (Slater) function can be clearly seen. Fig. 2 shows the Haar scaling functions for scales $n = 0, 1, 2$ with their respective translations.

Generalizing the Haar example, given a function $f(x)$ in the interval [0, 1], its representation $f^n(x)$ is given by

$$f(x) \approx f^n(x) = \sum_{i=0}^{k-1} \sum_{l=0}^{2^n-1} s_{il}^n \varphi_{il}^n(x). \tag{1}$$

If an interval other than [0, 1] is required, a suitable linear transformation may be performed. The expansion coefficients s_{il}^n and the scaling functions $\varphi_{il}^n(x)$ depend on a translational index l, a polynomial index i, and a scale index n. The coefficients s_{il}^n are computed as the inner product of the scaling function and the trial function $f(x)$

$$f(x) \approx \sum_{il} |\varphi_{il}^n\rangle \varphi_{il}^n | f, \tag{2}$$

$$s_{il}^n = \langle \varphi_{il}^n | f \rangle = \int_0^1 \varphi_{il}^n(x) f(x) \mathrm{d}x. \tag{3}$$

The scaling functions $\varphi_{il}^n(x)$ are derived from the so-called mother scaling function (or "father wavelet") $\varphi_i(x)$ by scaling and translating

$$\varphi_{il}^n(x) = 2^{n/2} \varphi_i(2^n x - l). \tag{4}$$

For the functional form of the mother scaling function $\varphi_i(x)$ several options exist, in the current work it is the Legendre polynomial $P_i(x)$,

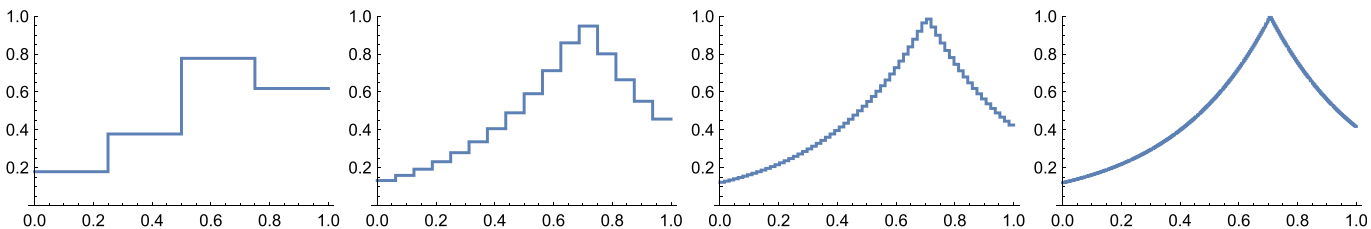

Fig. 1 Haar representation of a Slater function. From *left* to *right*: refinement scales $n = 2, 4, 6, 8$, corresponding to 4, 16, 64, and 256 intervals, respectively.

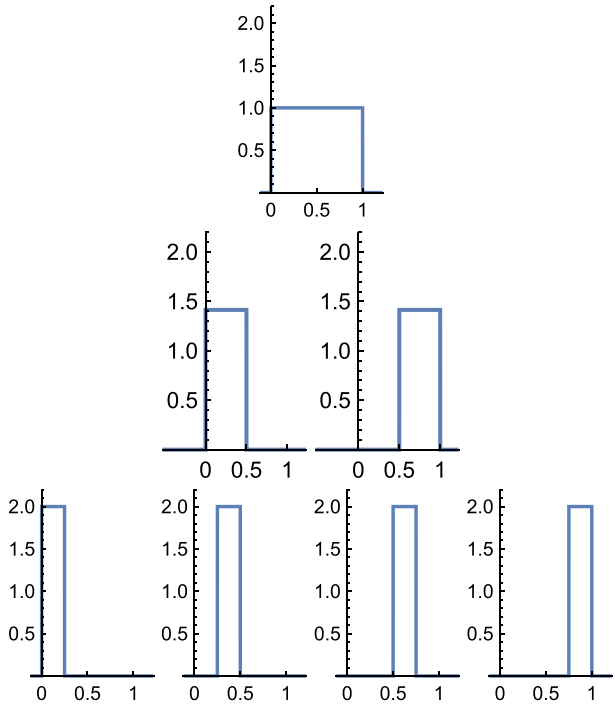

Fig. 2 From *left* to *right*: The Haar scaling function on levels (scales) $n = 0, 1, 2$ with the respective translations $l = 0$, $l = 0, 1$, and $l = 0, 1, 2, 3$.

$$\varphi_i(x) = \begin{cases} \sqrt{2i+1} P_i(2x-1), & x \in (0,1) \\ 0 & \text{otherwise} \end{cases} \tag{5}$$

but the Lagrange interpolating function is also in use[39,43]

$$\phi_i(x) = \sqrt{w_i} \sum_i^{k-1} \varphi_i(x_i) \varphi_i(x), \tag{6}$$

where w_i and x_i are quadrature weights and roots of the Gauss-Legendre quadrature, respectively.

The error of the representation depends on the regularity of the trial function. The convergence rate of the representation is[40]

$$\|f^n(x) - f(x)\| \leq 2^{-nk} \frac{2}{4^k k!} \sup_{x \in [0,1]} |f^{(k)}(x)| \tag{7}$$

Table 1 L^2 error in the wavelet representation for selected polynomial orders k and subdivisions n corresponding to the space $\mathbf{V}_n^k$.

n	k	Gaussian	Slater
2	4	5.2×10^{-5}	8.8×10^{-3}
2	6	1.9×10^{-7}	3.7×10^{-3}
2	8	1.2×10^{-8}	2.6×10^{-3}
3	4	3.3×10^{-6}	3.2×10^{-3}
3	6	3.1×10^{-9}	1.8×10^{-3}
3	8	2.2×10^{-12}	1.3×10^{-3}

where it is assumed that the function f is k times continuously differentiable in the interval: $f \in C^k[0, 1]$. In Table 1 the L^2 error is given with respect to the scaling function space $\mathbf{V}_n^k$ for a Gaussian function $\exp(-3(x-\sqrt{2}/2)^2)$ and a Slater function $\exp(-3|x-\sqrt{2}/2|)$. While the smooth Gaussian function can be represented accurately and the error decreases quickly with n or k, the error for the Slater function converges quite slowly with increasing n or k, since the function has a nondifferentiable cusp which cannot be represented accurately (see also Section 2.2).

Although the MRA representation of the Slater function in the first panel of Fig. 1 is not very faithful in a point-wise sense, it does integrate to the correct value. Furthermore, a polynomial basis of order k reproduces the first k moments correctly

$$\int_0^1 (f(x) - f^n(x))x^i \, \mathrm{d}x = 0 \quad \text{for } i = 0, 1, 2, \ldots, k-1. \tag{8}$$

This is true for both the Legendre polynomial basis as well as the interpolating polynomial basis. For each interval $l = [\mathrm{lo}, \mathrm{hi}]$ let P be the projection on the polynomials of order up to $k-1$ and Q the projection of the orthogonal complement, with $1 = P + Q$. The error in the moments expression is

$$\sum_l \int_{\mathrm{lo}}^{\mathrm{hi}} ((P+Q)(f(x)) - P(f(x)))x^i \, \mathrm{d}x = \sum_l \int_{\mathrm{lo}}^{\mathrm{hi}} Q(f(x))x^i \, \mathrm{d}x = 0, \tag{9}$$

with $f^n(x) = Pf(x)$ for a given interval l. Since P projects onto a closed subspace, the projection onto the complement Q is orthogonal to the first k moments x^k and vanishes in all intervals l.

2.2 Adaptiveness and tree structure

For an accurate representation of a function it is often sufficient to keep some sum coefficients at coarse levels and refine only locally where necessary. Fig. 3 shows a Slater function, its MRA representation and the point-wise errors on various refinement levels. The precision threshold is set to 10^{-4}, local refinement is triggered if the point-wise error exceeds this threshold. It can be seen that the shoulder to the left is well represented even on the $n = 1$ refinement level, while the representation of the cusp locally needs much higher refinements, up to $n = 8$.

The local refinement reduces the point-wise and L^2 errors but increases the number of coefficients only marginally from 12 to 18, 24, and 42 in this example, while for global, homogeneous refinement the number would increase to $2^n k = 1536$ for $n = 8$ to achieve a comparable precision.

The MRA function can be depicted as a tree, with the nodes being the subdivided intervals (boxes) holding the polynomials. Fig. 4 shows the tree structure of the MRA representation of the Slater function of Fig. 3C.

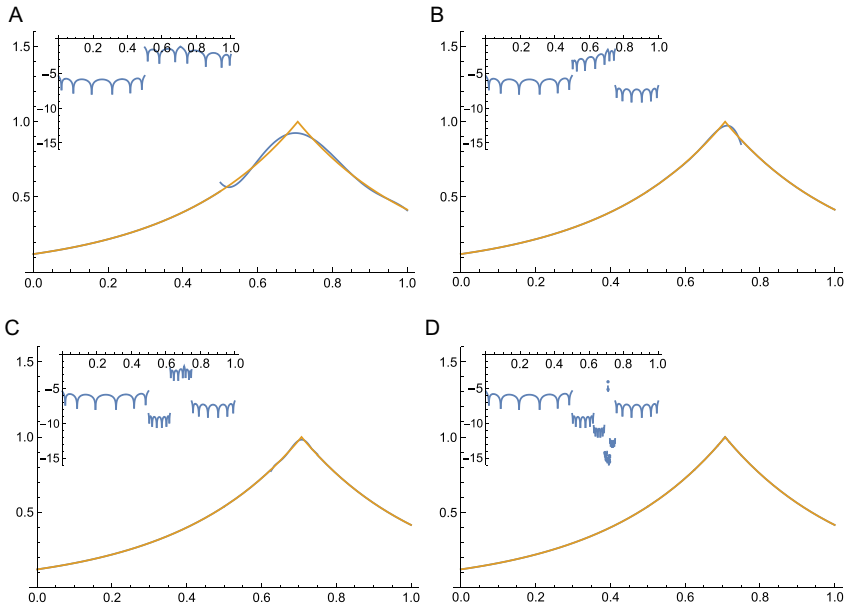

Fig. 3 Slater function and its MRA representation ($k = 6$) with various local refinement depths. The insets show the point-wise errors of the MRA representation on a logarithmic scale. (A) Max level $n = 1$, L^2 error $= 1.6 \times 10^{-2}$; (B) Max level $n = 2$, L^2 error $= 3.7 \times 10^{-3}$; (C) Max level $n = 3$, L^2 error $= 1.8 \times 10^{-3}$; (D) Max level $n = 8$, L^2 error $= 1.9 \times 10^{-6}$.

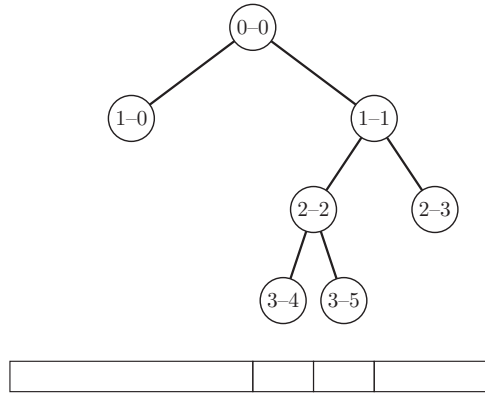

Fig. 4 Tree structure of the MRA representation of the function in Fig. 3C and corresponding intervals. The notation in the nodes is $n - l$, with n the refinement scale and l the translational index.

In the current representation the internal nodes (those with "child" nodes in higher scales) are empty, while the scaling functions are defined only in the leaf nodes (those without further children).

2.3 Wavelets and the two-scale relations

So far the MRA representation consists of the scaling functions on a given level and translation, such that the whole domain of the original function is covered. With increasing refinements the MRA scheme will represent the input function to arbitrary precision.

A formal way of expressing the completeness is to define the space $\mathbf{V}_n^k$ of the scaling functions f as[39]

$$\mathbf{V}_n^k = \{f : \text{the restriction of } f \text{ to the interval } (2^{-n}l, 2^{-n}(l+1)) \text{ is a polynomial of degree less than } k, \text{ for } l = 0, \ldots, 2^n - 1, \text{ and } f \text{ vanishes elsewhere}\}. \tag{10}$$

Note that at this point we leave the functional form of the scaling functions f open. They can be chosen first, which will determine the wavelets (see below), or certain properties of the wavelets may determine the scaling functions. The first approach is better suited for our purposes, even though the latter was used in the original papers.

The spaces $\mathbf{V}_n^k$ form a sequence converging to completeness

$$\mathbf{V}_0^k \subset \mathbf{V}_1^k \subset \mathbf{V}_2^k \subset \cdots \subset \mathbf{V}_n^k \subset \cdots . \tag{11}$$

Furthermore we can define the orthogonal complement to $\mathbf{V}_n^k$, called the wavelet space $\mathbf{W}_n^k$

$$\mathbf{V}_n^k \oplus \mathbf{W}_n^k = \mathbf{V}_{n+1}^k. \tag{12}$$

Adding the orthogonal complement $\mathbf{W}_n^k$ to a given scaling function basis $\mathbf{V}_n^k$ corresponds to subdividing the interval by two. By repeatedly subdividing the interval, any function space $\mathbf{V}_n^k$ can thus be written as

$$\mathbf{V}_n^k = \mathbf{V}_0^k \oplus \mathbf{W}_0^k \oplus \mathbf{W}_1^k \oplus \cdots \oplus \mathbf{W}_{n-1}^k, \tag{13}$$

starting from the full interval. The functions that subdivide the interval are called wavelets $\psi_{kl}^n(x)$ and they form an orthonormal basis in the wavelet space $\mathbf{W}_n^k$

$$\int_0^1 \psi_{il}^n(x)\psi_{i'l'}^{n'}(x)\mathrm{d}x = \delta_{ii'}\delta_{ll'}\delta_{nn'}. \tag{14}$$

Wavelets are constructed by scaling and translating the mother wavelet function $\psi_k(x)$, similar to the mother scaling function in Eq. (4)

$$\psi_{il}^n(x) = 2^{n/2}\psi_i(2^n x - l). \tag{15}$$

By definition, wavelets are orthogonal to the space of scaling functions, implying the first k moments vanish

$$\int_0^1 \psi_i(x)x^j\mathrm{d}x, = 0 \quad \text{for } i,j = 0,1,\ldots,k-1. \tag{16}$$

This property plays an important role in the construction of integral operators in a wavelet basis. By virtue of the vanishing moments it is guaranteed that the nonlocal integral operator becomes effectively sparse (nearly diagonal) and can therefore be applied very efficiently.

The properties of wavelets can again be best illustrated using the Haar wavelets.[42] The Haar scaling function $\varphi_{00}^0(x)$ is a constant function (i.e., $k = 1$) defined on the interval [0, 1]

$$\varphi_{00}^0(x) = \begin{cases} 1, & \text{for } 0 < x < 1 \\ 0 & \text{otherwise} \end{cases} \tag{17}$$

The corresponding wavelet function $\psi_{00}^{0}(x)$ is defined as

$$\psi_{00}^{0}(x) = \begin{cases} 1, & \text{for } 0 < x < \frac{1}{2} \\ -1 & \text{for } \frac{1}{2} < x < 1 \\ 0 & \text{otherwise} \end{cases} \tag{18}$$

Linear combination of the scaling function on level 0 and its wavelet generates the scaling functions on level 1

$$\varphi_{00}^{1}(x) = \frac{1}{\sqrt{2}}\left(\varphi_{00}^{0}(x) + \psi_{00}^{0}(x)\right) \tag{19}$$

$$\varphi_{01}^{1}(x) = \frac{1}{\sqrt{2}}\left(\varphi_{00}^{0}(x) - \psi_{00}^{0}(x)\right) \tag{20}$$

The prefactor $\frac{1}{\sqrt{2}}$ ensures that the scaling functions on level 1 are still normalized. Fig. 5 shows the scaling functions and the wavelets for the Haar basis.

Scaling functions on a scale n can be represented by the scaling function on level $n = 0$, the so-called mother scaling function and wavelets on all levels from 0 to $n - 1$. A trial function can therefore be represented either by the scaling function coefficients (or sum coefficients) s_{il}^{n} of Eq. (3), called the reconstructed state, or by the coefficients s_{k0}^{0} of the mother scaling function and the coefficients of the wavelets (or difference) coefficients d_{il}^{n}, called the compressed state. Both representations are equivalent and

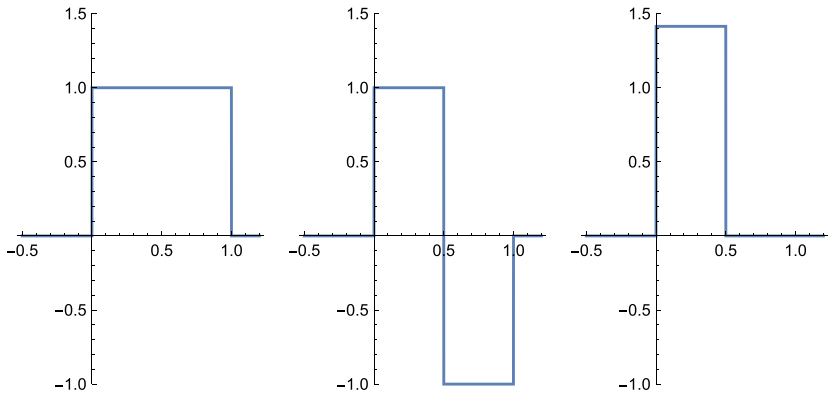

Fig. 5 From *left* to *right*: The Haar scaling function ϕ_{00}^{0}, the Haar wavelet ψ_{00}^{0}, the linear combination $\frac{1}{\sqrt{2}}\left(\phi_{00}^{0} + \psi_{00}^{0}\right)$, which is identical to the scaling function on level 1 ϕ_{00}^{1}.

can be transformed into each other losslessly by using the two-scale relations or quadrature mirror coefficients (QMF) **h** and **g**. Transforming higher scale scaling function coefficients into lower scale scaling function coefficients and wavelet coefficients (compression) reads as[39]

$$s_{il}^{n} = \sum_{j} \left(h_{ij}^{(0)} s_{j,2l}^{n+1} + h_{ij}^{(1)} s_{j,2l+1}^{n+1} \right), \tag{21}$$

$$d_{il}^{n} = \sum_{j} \left(g_{ij}^{(0)} s_{j,2l}^{n+1} + g_{ij}^{(1)} s_{j,2l+1}^{n+1} \right), \tag{22}$$

and the reverse step, transforming scaling function and wavelet coefficients into higher scale scaling function coefficients reads as

$$s_{i,2l}^{n+1} = \sum_{j} \left(h_{ji}^{(0)} s_{jl}^{n} + g_{ji}^{(0)} d_{jl}^{n} \right), \tag{23}$$

$$s_{i,2l+1}^{n+1} = \sum_{j} \left(h_{ji}^{(1)} s_{jl}^{n} + g_{ji}^{(1)} d_{jl}^{n} \right) \tag{24}$$

After compression, the tree structure of Fig. 4 has sum coefficients at the root node (level $n = 0$) and difference coefficients at all internal nodes, with all leaf nodes being empty. Extra leaf boxes can be constructed by taking the sum coefficients of the current leaf boxes, assuming vanishing difference coefficients and using the two-scale relations as for the reconstruction step.

In practical implementations the sum coefficients at level $n + 1$ are collected into a vector $\left(\mathbf{s}_{2l}^{n+1}, \mathbf{s}_{2l+1}^{n+1}\right)^{T}$, which can be converted into sum and difference coefficients $\left(\mathbf{s}_{l}^{n}, \mathbf{d}_{l}^{n}\right)^{T}$ by a matrix multiplication with the orthogonal matrix **U**

$$\mathbf{U} = \begin{pmatrix} \mathbf{h}^{(0)} & \mathbf{h}^{(1)} \\ \mathbf{g}^{(0)} & \mathbf{g}^{(1)} \end{pmatrix}, \tag{25}$$

to yield

$$\begin{pmatrix} \mathbf{s}_{l}^{n} \\ \mathbf{d}_{l}^{n} \end{pmatrix} = \begin{pmatrix} \mathbf{h}^{(0)} & \mathbf{h}^{(1)} \\ \mathbf{g}^{(0)} & \mathbf{g}^{(1)} \end{pmatrix} \begin{pmatrix} \mathbf{s}_{2l}^{n+1} \\ \mathbf{s}_{2l+1}^{n+1} \end{pmatrix}. \tag{26}$$

which is Eqs. (21) and (22) in compact form. This operation is called filtering. The reverse operation, unfiltering, is given by the transpose of **U**

$$\begin{pmatrix} \mathbf{s}_{2l}^{n+1} \\ \mathbf{s}_{2l+1}^{n+1} \end{pmatrix} = \begin{pmatrix} \mathbf{h}^{(0)} & \mathbf{h}^{(1)} \\ \mathbf{g}^{(0)} & \mathbf{g}^{(1)} \end{pmatrix}^{T} \begin{pmatrix} \mathbf{s}_{l}^{n} \\ \mathbf{d}_{l}^{n} \end{pmatrix}, \tag{27}$$

which summarizes Eqs. (23) and (24). The matrix elements of **h** and **g** depend on the polynomial order k and they are universal for a given scaling function, e.g., Legendre polynomials, or interpolating polynomials. They can be pre-computed and stored. Comparing Eqs. (19) and (20) with Eqs. (23) and (24) one can see that the filter coefficients of the Haar wavelets are given by

$$\mathbf{U} = \frac{1}{\sqrt{2}} \begin{pmatrix} 1 & 1 \\ -1 & 1 \end{pmatrix}. \tag{28}$$

An explicit derivation for higher polynomial orders is given in Ref. 39.

The representation error on an interval is given by[39]

$$||f^{n+1} - f^n||_2 = ||d_l^n||_2. \tag{29}$$

To maintain a global precision ϵ of the MRA representation, i.e.,

$$||f^{n+1} - f^n||_2 \leq \epsilon ||f^{n+1}||_2 \tag{30}$$

all nodes with wavelet coefficient norm

$$||d_l^n||_2 \leq 2^{-n/2} ||f^{n+1}|| \epsilon \tag{31}$$

may be removed from the tree. In practical calculations often the less restrictive criterion

$$||d_l^n||_2 < \epsilon \tag{32}$$

proved to yield satisfactory results for sufficiently regular functions.

2.4 Arithmetic operations in one dimension

Given an MRA representation f^n and g^n of functions f and g, respectively, several arithmetic operations are possible.

2.4.1 Inner product

The inner product is given by

$$\langle f|g\rangle = \int_0^1 \mathrm{d}x\, f(x)g(x) = \sum_i s_{i0}^0(f) s_{i0}^0(g) + \sum_{nil} d_{il}^n(f) d_{il}^n(g), \tag{33}$$

where it is understood that if the tree structures of f^n and g^n do not agree, coefficients of missing boxes are treated as zeros. Alternatively, the norm can also be computed in the reconstructed state as

$$\langle f|g\rangle = \sum_{nil} s_{il}^n(f) s_{il}^n(g), \tag{34}$$

where the tree structures must be refined to match. The L^2 norm of a single function is computed accordingly.

2.4.2 Addition

Two functions f and g can be added to yield h by adding their coefficients in compressed form

$$s^0_{i0}(h) = s^0_{i0}(f) + s^0_{i0}(g), \tag{35}$$

$$d^n_{il}(h) = d^n_{il}(f) + d^n_{il}(g). \tag{36}$$

Addition in reconstructed form is also possible, if the tree structures match

$$s^n_{il}(h) = s^n_{il}(f) + s^n_{il}(g). \tag{37}$$

2.4.3 Differentiation

Formally we project the (unknown) derivative of the function f onto the scaling function basis and perform integration by parts to get an expression which depends on the function f itself

$$\frac{\mathrm{d}}{\mathrm{d}x} f(x) \approx \sum_{nil} |\varphi^n_{il}\rangle \left\langle \varphi^n_{il} | \frac{\mathrm{d}}{\mathrm{d}x} f \right\rangle, \tag{38}$$

$$s^n_{il} = \left\langle \varphi^n_{il} | \frac{\mathrm{d}}{\mathrm{d}x} f \right\rangle = f(x)\varphi^n_{il}(x)|^{x_{l+1}}_{x_l} - \int_{x_l}^{x_{l+1}} \mathrm{d}x f(x) \frac{\mathrm{d}}{\mathrm{d}x} \varphi^n_{il}(x). \tag{39}$$

Inserting the MRA representation of f into the expression yields transition matrices $\mathbf{r}$ for the transformation of the scaling function coefficients of the trial function f to the scaling function coefficients of its derivative

$$\begin{aligned} \left\langle \varphi^n_{il} | \frac{\mathrm{d}}{\mathrm{d}x} f \right\rangle &= \sum_{i'l'} s^n_{i'l'} \left\{ \left[\varphi^n_{i'l'}(x_l)\varphi^n_{il}(x_l) - \varphi^n_{i'l'}(x_{l+1})\varphi^n_{il}(x_{l+1}) \right] \right. \\ &\quad \left. - \int_{x_l}^{x_{l+1}} \mathrm{d}x\, \varphi^n_{i'l'}(x) \frac{\mathrm{d}}{\mathrm{d}x} \varphi^n_{il}(x) \right\} \\ &= \sum_{i'l'} s^n_{i'l'} r_{i'i,l'l} \end{aligned} \tag{40}$$

The second term in curly brackets in Eq. (40) can be evaluated straightforwardly and will vanish unless $l = l'$

$$\int_{x_l}^{x_{l+1}} \mathrm{d}x \varphi^n_{i'l'}(x) \frac{\mathrm{d}}{\mathrm{d}x} \varphi^n_{il}(x) = K_{ii'} \delta_{ll'} \tag{41}$$

The first term in curly brackets in Eq. (40) requires the evaluation of the scaling functions at their boundaries. This term will introduce additional contributions to the derivative from the neighboring boxes (for details of the derivation see Ref. 39). The function values can be approximated as weighted contributions from the left and the right of the boundary, so that only three matrices r will be left, for the central box $\mathbf{r}_0$ and its left and right neighbors $\mathbf{r}_{\pm 1}$, effectively eliminating the indices l and l' in Eq. (40)

$$[\mathbf{r}_1]_{ii'} = -b\varphi_i(0)\varphi_{i'}(1), \tag{42}$$

$$[\mathbf{r}_0]_{ii'} = (1-a)\varphi_i(1)\varphi_{i'}(1) - (1-b)\varphi_i(0)\varphi_{i'}(0) - K_{ii'} \tag{43}$$

$$[\mathbf{r}_{-1}]_{ii'} = a\varphi_i(1)\varphi_{i'}(0) \tag{44}$$

The weighting parameters a and b can be chosen freely, however, if they are set to $a = b = \frac{1}{2}$, the approximation error is minimized. If both parameters are set to zero all contributions from the neighboring boxes vanish. This can be advantageous if the function f has discontinuities or cusps, because these features can cause artefactual long-range oscillations in the derivative. In general, function derivatives are numerically less stable and should be avoided if possible. Integrals and inner products of derivatives are usually stable. The algorithm for taking the derivatives of a function is to reconstruct the MRA tree, loop over all leaf boxes and apply the r matrices on the neighbor boxes. The result will be the derivative of the input function in reconstructed form.

2.4.4 Point-wise multiplication

Unlike addition, the point-wise multiplication is not closed in the fixed-k MRA formulation. Consider the functions $f(x) = x$ and $g(x) = x$, both of which will be represented exactly in MRA with polynomials $k = 2$ (i.e., constant and linear terms). The product $h(x) = f(x)g(x) = x^2$ cannot be represented exactly with $k = 2$, irrespective of the refinement level. Assuming both input functions are of the same order k, the product function will need a polynomial order of $2k - 1$.

Assuming that the result function will be represented accurately enough on the joint MRA structures of the input functions, the multiplication is performed in reconstructed form by converting the sum coefficients into function values $f(x_i)$ and $g(x_i)$ of the Gauss-Legendre quadrature points x_i, point-wise multiplication on these points, and back-transformation into sum coefficients of the result function

$$f(x_j) = \sum_i s_{il}^n(f)\varphi_{il}^n(x_j), \tag{45}$$

$$g(x_j) = \sum_i s_{il}^n(g)\varphi_{il}^n(x_j), \tag{46}$$

$$h(x_j) = f(x_j)g(x_j), \tag{47}$$

$$s_{il}^n(h) = \sum_j w_j h(x_j), \tag{48}$$

where the last line is the Gauss-Legendre quadrature of the integral of Eq. (3), with w_j being the quadrature weights. Typically the number of quadrature points is chosen to be k but any other (larger) number is also possible. If the result function is not represented accurately in the given MRA tree, local refinement may be triggered to reduce the error.

2.4.5 Integral operator application

An integral operator T can be applied on a function g as

$$f(x) = \int \mathrm{d}x\prime\, T(x - x\prime)g(x\prime). \tag{49}$$

Formally this operation can be seen as a multiplication with a two-dimensional function and followed by an inner product over one dimension. Inserting the MRA expansion for g and projecting on the scaling function basis $\phi(x)$ to compute the expansion coefficients for f yields

$$s_{il}^n(f) = \sum_{n'i'l'} \langle \phi_{il}^n(x) | T(x - x\prime) | \phi_{i'l'}^{n'}(x\prime) \rangle s_{i'l'}^{n'}(g), \tag{50}$$

where the brackets are understood to integrate over x and x'. Thus the expansion coefficients s_{il}^n of the result function f will depend on all scales n', translations l' and polynomials i' of the leaf nodes of the input function g.

Depending on the functional form of $T(x, x')$, its projection on the scaling function basis might require different refinement depths for the two dimensions. The so-called *standard form* uses a direct product given by

$$T(x, x\prime) = \sum_{il}^{n} \sum_{i'l'}^{n'} \phi_{il}^n(x) \phi_{i'l'}^{n'}(x\prime) s_{ii'll'}^{nn'}, \tag{51}$$

where n and n' may differ, leading to a coupling of different scales because of the appearance of rectangular basis intervals (boxes). In contrast, the *nonstandard form* requires $n = n'$ to be identical, leading to square boxes.

While the standard form seems more efficient because fewer boxes and thus coefficients are required, the coupling of scales leads to less efficient algorithms for the operator application.[41] Using the two-scale relations of Eqs. (23) and (24) the standard form may always be converted into the nonstandard form by additional subdivisions. In the following we will restrict the discussion to the nonstandard form.

Assume that a scale n is sufficient for the representation of the input and result functions g and f, respectively, as well as the operator T itself. The operator $T^n = P^n T P^n$ transforms the input into the result function within the precision thresholds. Using the projectors P^n and Q^n onto the scaling function and wavelet spaces $\mathbf{V}_n^k$ and $\mathbf{W}_n^k$, respectively, and using $P^n = P^{n-1} + Q^{n-1}$, we write

$$\begin{aligned} T^n &= P^n T P^n \\ &= \left(P^{n-1} + Q^{n-1}\right) T \left(P^{n-1} + Q^{n-1}\right) \\ &= P^{n-1} T P^{n-1} + Q^{n-1} T P^{n-1} + P^{n-1} T Q^{n-1} + Q^{n-1} T Q^{n-1}. \end{aligned} \tag{52}$$

Repeated insertions yield a telescopic series

$$T^n = T^0 + \sum_i^{n-1} \left(A^i + B^i + C^i\right), \tag{53}$$

with

$$A^i = Q^i T Q^i, \tag{54}$$

$$B^i = Q^i T P^i, \tag{55}$$

$$C^i = P^i T Q^i. \tag{56}$$

The operator now acts on all scales on the sum and difference coefficients of the function g. To apply the operator, the function tree of g of Fig. 4 needs to be completely filled with sum and difference coefficients. The operator acts on each function node of g and creates result function nodes on the same scale i.

The matrix elements r of the operator T are given in the scaling function basis by (see Appendix of Ref. 29)

$$r^n_{ll',ii'} = \int \mathrm{d}x \varphi^n_{i'l'}(x) T(x) \varphi^n_{il}(x), \tag{57}$$

and the matrix elements α, β, and γ of the matrices **A**, **B**, and **C**, respectively, are constructed using the two-scale relations and the matrix elements of a level below

$$\begin{pmatrix} \mathbf{r}_{ll'}^{n-1} & \boldsymbol{\gamma}_{ll'}^{n-1} \\ \boldsymbol{\beta}_{ll'}^{n-1} & \boldsymbol{\alpha}_{ll'}^{n-1} \end{pmatrix} = \begin{pmatrix} \mathbf{h}^{(0)} & \mathbf{g}^{(0)} \\ \mathbf{h}^{(1)} & \mathbf{g}^{(1)} \end{pmatrix}^T \begin{pmatrix} \boldsymbol{r}_{2l,2l'}^{n} & \boldsymbol{r}_{2l,2l'+1}^{n} \\ \boldsymbol{r}_{2l+1,2l'}^{n} & \boldsymbol{r}_{2l+1,2l'+1}^{n} \end{pmatrix} \begin{pmatrix} \mathbf{h}^{(0)} & \mathbf{g}^{(0)} \\ \mathbf{h}^{(1)} & \mathbf{g}^{(1)} \end{pmatrix} \tag{58}$$

Note that all matrix elements in this equation are understood as matrices with respect to the polynomial order k.

Using the nonstandard form for the integral kernel, the operator application consists of three steps: First, project the input function g onto its scaling function and wavelet basis on all internal nodes using the two-scale relations of Eq. (25). Second, apply on all nodes to all scales of the input function the operator tensors of the left hand side of Eq. (58), excluding $\mathbf{r}_{ll'}^{n}$ on all levels but including it at the root level $n = 0$. This yields a temporary result function $\tilde{f}$, which has sum and difference coefficients on all scales

$$\begin{pmatrix} \mathbf{s}_l^n(\tilde{f}) \\ \mathbf{d}_l^n(\tilde{f}) \end{pmatrix} = \sum_{l'} \begin{pmatrix} \boldsymbol{r}_{ll'}^{n} & \boldsymbol{\gamma}_{ll'}^{n} \\ \boldsymbol{\beta}_{ll'}^{n} & \boldsymbol{\alpha}_{ll'}^{n} \end{pmatrix} \begin{pmatrix} \mathbf{s}_{l'}^n(g) \\ \mathbf{d}_{l'}^n(g) \end{pmatrix}. \tag{59}$$

Third, sum all coefficients of $\tilde{f}$ recursively down the tree (performing the summation of Eq. (53)) to return the result function f in reconstructed form.

Fig. 6 shows the application of an operator on the input function (left) to yield the output function (right). Formally the operator application scales as l^2, i.e., quadratically with respect to the system size. However, for the most important operators, namely the Poisson and the bound-state Helmholtz operator, the matrix elements in nonstandard form of Eq. (58) are isotropic, they are translationally invariant, i.e., the matrix has a Toeplitz form with $r_{ll'} \rightarrow r_{l-l'}$, and they decay quickly away from the diagonal and can thus be screened efficiently. This grants an effective linear scaling with respect to the system size and is the key advance in MRA.

The most important operators that have to be applied are the inverse of the Poisson and the bound-state Helmholtz (BSH) equation. These equations read as

$$\nabla^2 f(x) = g(x), \tag{60}$$

$$(\nabla^2 + \kappa^2) f(x) = g(x), \tag{61}$$

respectively. The solution of the Poisson equation is needed to convert a charge density into a potential, while the BSH equation is the key step in the inversion of the Schrödinger equation (see Section 3.1). Both equations

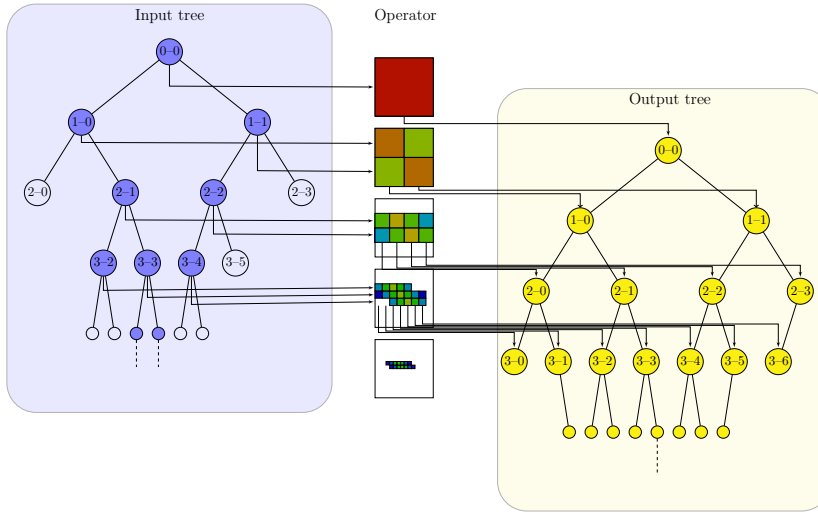

Fig. 6 Operator sparseness of the 1D convolution operator e^{-x} acting on a function $f(x) = e^{-|x-1/3|}$. The *blue tree* to the left is the input tree in nonstandard form, with the *blue vertices* indicating sum and difference coefficients, and white vertices indicating empty leaf boxes. The input boxes are passed to the operator in the center generating output boxes that are filled into the *yellow* output tree on the *right*, which is significantly widened compared to the input tree. The output tree is in a mixed form, the coefficients need to be summed down to yield a tree in the reconstructed state. The operator is color-coded, with *red* and *blue* indicating an operator norm of 10^0 and 10^{-6}, respectively. The operator boxes are strictly Toeplitz and the norms decay quickly away from the diagonal. The operator matrices are sparse due to the sparse input tree (only few rows are processed), and due to the quick decay of the operator (each input box contributes only to near neighbors). Application of the operator scales as $\mathcal{O}(N)$ with respect to the system size.

are solved by a Green's function approach, i.e., we search for the function $G(x - x')$ solving

$$f(x) = \int G(x-x\prime)g(x\prime)\mathrm{d}x\prime. \tag{62}$$

The convolution kernels for the Poisson and the BSH equations in 3D are explicitly given by

$$G(\vec{r} - \vec{r}\,') = \frac{1}{|\vec{r} - \vec{r}\,'|}, \tag{63}$$

$$G(\vec{r} - \vec{r}\,') = \frac{e^{-\mu|\vec{r} - \vec{r}\,'|}}{|\vec{r} - \vec{r}\,'|}, \tag{64}$$

with $\mu = i\kappa$. The general d-dimensional kernels of the Poisson and BSH equations are spherically symmetric and translationally invariant, they can be constructed efficiently using a sum over Gaussian functions.[44,45]

This approach allows the construction of an efficient operator application in higher dimensions since the Gaussians naturally separate. If a d-dimensional function is represented, its coefficients are given in a tensor format, e.g., the full format (see below for more details)

$$s_i \longrightarrow s_{i_1 i_2 \ldots i_d}. \tag{65}$$

The operator matrices $\boldsymbol{r}$, $\boldsymbol{\alpha}$, $\boldsymbol{\beta}$, $\boldsymbol{\gamma}$ are then $2d$-dimensional tensors

$$r_{i'i} \longrightarrow r_{i'_1 i_1 i'_2 i_2 \ldots i'_d i_d}, \tag{66}$$

and the operator application scales as k^{2d}. Using the Gaussian representation the operator tensors are linearized to

$$r_{i'_1 i_1 i'_2 i_2 \ldots i'_d i_d} \approx \sum_m^M w_m r^m_{i'_1 i_1} r^m_{i'_2 i_2} \ldots r^m_{i'_d i_d}, \tag{67}$$

and the operator application is reduced to Mdk^4, where M is the numerical rank of the operator in its sum representation.

The Poisson and the BSH kernels decay quickly and they can be applied efficiently on a trial function. Long-range, low-frequency contributions of the operator are handled by coarser scales, while the short range, high-frequency contributions are handled by the finer scales. The vanishing moments property of the wavelets of Eq. (16) also leads to a rapid decay of the operator norm (see Fig. 6). With k vanishing moments the operator matrices will decay asymptotically as $|l - m|^{-k-1}$, with l and m being translational indices of the input and output functions, respectively.[29]

2.5 Generalization to many dimensions

The wavelet formalism can be extended in a straightforward manner to few dimensions but not to many dimensions. If the dimension d is small enough, say $d \leq 3$, the one-dimensional scaling and wavelet functions are combined to a product

$$\varphi_{il}(x) \to \varphi_{i_1 l_1}(x)\varphi_{i_2 l_2}(y)\cdots = \prod_i \varphi_{i_i l_i}(x_i), \tag{68}$$

and the coefficients s_{il} and d_{il} are given as a tensor

$$s_i \longrightarrow s_{i_1 i_2 \cdots i_d}. \tag{69}$$

The wavelets and the difference coefficients (and thus the number of d-dimensional intervals, or boxes) increase as 2^d, explicitly written for $d = 2$

$$\phi(x) + \psi(x) \rightarrow \phi(x)\phi(y) + \phi(x)\psi(x) + \psi(x)\phi(y) + \psi(x)\psi(y)\ . \tag{70}$$

Both the data volume of the tensor and the number of refinement boxes (indexed with the translation index l) increase exponentially with the dimension, as k^d, and as 2^d, respectively.

If the dimension d exceeds 3 the tensor product approach quickly becomes intractable due to the increase in data volume. To keep this increase under control it is necessary to reduce both the number of boxes and of the number of coefficients in each box. The former can be achieved by making the working equations sufficiently regular so that no deep refinement level n is necessary (see Section 3.2.2), the latter by using low-rank approximations for the coefficient tensors, such as singular value decomposition (SVD), discussed in the following section.

Most of the arithmetic operations described above can be readily generalized to higher dimensions. The inner product of Eq. (33) is computed in higher dimensions by interpreting the translational and polynomial indices l and i as a multicomponent index $\vec{l}$ and $\vec{i}$

$$\langle f|g\rangle = \sum_{\vec{i}} s^0_{\vec{i}\,0}(f)\, s^0_{\vec{i}\,0}(g) + \sum_{n\,\vec{i}\,\vec{l}} d^n_{\vec{i}\,\vec{l}}(f)\, d^n_{\vec{i}\,\vec{l}}(g). \tag{71}$$

The generalization of the addition and point-wise multiplication is performed in an analogous way. The differentiation separates into the d dimensions, such that for each box all $2d$ neighboring boxes must be processed; the actual application of the differentiation operator is straightforward again. By virtue of the Gaussian representation of their kernels, the convolution operators also separate into the dimensions and the operation can be applied in a straightforward manner.

2.6 Low-rank tensor approximations

The number of coefficients in each MRA box is k^d, with k the polynomial order and d the dimension. For a $6d$ wave function and $k = 5$ with 100,000 boxes the total memory requirement is approximately 12 GByte of double precision numbers. To reduce the number of coefficients the full tensor $s_{i_1 i_2 \cdots i_d}$ may be rewritten by different approximations

$$s_{i_1 i_2 \cdots i_d} \approx \sum_{r}^{R} \sigma_r s^r_{i_1 i_2 \cdots i_{d/2}} s^r_{i_{d/2+1} \cdots i_d}, \tag{72}$$

$$s_{i_1 i_2 \cdots i_d} \approx \sum_{r}^{R} \sigma_r s^r_{i_1} s^r_{i_2} \cdots s^r_{i_d}, \tag{73}$$

$$s_{i_1 i_2 \cdots i_d} \approx \sum_{r_1, r_2, \cdots r_{d-1}}^{R_1, R_2, \ldots, R_{d-1}} s^{r_1}_{i_1} s^{r_1 r_2}_{i_2} \cdots s^{r_{d-1}}_{i_d}. \tag{74}$$

The first approximation Eq. (72) is the singular value decomposition (SVD) which can be applied to a square or rectangular matrix.[36] The construction of the SVD is stable and reasonably fast. If the rank r is truncated at a finite threshold it is guaranteed that the overall error of the SVD approximation is less than the truncation threshold. Significant savings in memory can be achieved, since the numerical rank R is typically small compared to the full rank $R = k^3$. Tensor operations, such as contractions, matrix multiplications, additions, or norm computations can be derived in this format and are fast.[30]

The second approximation Eq. (73) is called the separated representation (SR),[37] higher order SVD (HOSVD),[46] or parallel factor analysis (parafac).[47] Its construction is numerically less stable and very time-consuming. However, if such a representation is available, as it is the case for the construction of the Poisson and BSH integral operators, it is the most efficient format since it reveals most of the low-rank structure.

The third approximation Eq. (74) has been dubbed tensor train (TT),[35] it has a stable construction algorithm (namely a sequence of SVDs), and it recovers sparsity in the tensor quickly. It is in general more compact than SVD but algorithms using TT are often less efficient, therefore it is currently used in MRA only in very few operations.

There are other tensor approximations, such as the Tucker representation,[48] which are not used in this work but have been studied in the quantum chemical literature.[49] Details on the low-rank representations are beyond the scope of the present review but they are of crucial importance for the efficiency the high-dimensional algorithms in MRA.

3. Quantum chemistry in real space

3.1 The Schrödinger equation in first quantization

The Schrödinger equation of an arbitrary d-dimensional system is an eigenvalue equation containing kinetic and potential energy terms

$$(T+V)|\psi\rangle = E|\psi\rangle. \tag{75}$$

The potential V can be a physical potential, or an effective one- or many-body potential as defined in the various quantum chemical models. To solve for the wave function ψ, the equation is rearranged and inverted to

$$(T-E)|\psi\rangle = -V|\psi\rangle, \tag{76}$$

$$|\psi\rangle = -(T-E)^{-1}V|\psi\rangle. \tag{77}$$

The potential term V can assume any form, ranging from a local potential to a nonlocal exchange term in Hartree–Fock, or the fluctuation potential in correlated methods. For the solution of the inverted Schrödinger equation a guess for the wave function ψ is needed, and its solution is obtained iteratively, even if the actual quantum mechanical equations are not iterative. The efficiency of MRA now relies on the efficient application of the inverse of the kinetic operator T. The inverse is an integral operator with a Green's function kernel

$$(T-E)^{-1}f(r) = -2G_E f(r) = -2\int \mathrm{d}r' G(r-r', E)f(r') \ . \tag{78}$$

The Hamilton operator of the molecular Schrödinger equation reads as

$$\hat{H} \ = \sum_i T(i) + \sum_i V_{\mathrm{nuc}}(i) + \sum_{i<j} g_{ij} + \sum_{AB} \frac{Z_A Z_B}{r_{AB}}, \tag{79}$$

where i is the index of the ith electron and g_{ij} describes the electron–electron repulsion. This so-called first-quantized formulation is in contrast to most of the quantum chemical literature, where the Hamilton operator is given in the so-called second quantization. In this case, the Schrödinger equation is given in matrix form, discretized by the use of a finite computational basis

$$\hat{H} = \sum_{pq} h_{pq} a_p^\dagger a_q + \frac{1}{2}\sum_{pqrs} g_{pqrs} a_p^\dagger a_q^\dagger a_s a_r. \tag{80}$$

Here h_{pq} and g_{pqrs} are matrix elements of the one- and two-particle operators, respectively, and the creation and annihilation operators $a^\dagger$ and a create and annihilate electrons in the Fock space, e.g., in orbital p. The formulation of quantum chemistry in second quantization has advantages over first quantization if a finite basis is used, since working equations may be derived automatically by use of commutator relations between creation and annihilation operators,[50] and the matrix elements in a one-particle basis are easy to

translate to a linear algebra fashion to be used on a computer. In contrast to the first-quantized formulation, where the Hamilton operator is inverted by using the Green's function approach, in second quantization the Hamilton matrix is diagonalized.

3.2 Molecular energies and properties in effective one-particle methods

3.2.1 Hartree–Fock and density functional theory

In the Hartree–Fock model the molecular wave function is approximated as an antisymmetrized product Φ of one-electron functions ϕ (orbitals). The wave function is obtained as the set of orbitals that minimize the expectation value of the Hamilton operator, i.e., the energy. To minimize the energy a set of effective one-particle equations must be solved, the so-called Hartree–Fock equations.[51] The one-particle Fock operator F is defined as

$$F = T + J - K + V_{\text{nuc}} \tag{81}$$

with

$$T(\vec{r}) = -\frac{1}{2}\Delta, \tag{82}$$

$$V_{\text{nuc}}(\vec{r}) = -\sum_A \frac{Z_A}{|\vec{r} - \vec{R}_A|}, \tag{83}$$

$$J(\vec{r}) = \int \mathrm{d}\vec{r}' \frac{\sum_i |\phi_i(r')|^2}{|\vec{r} - \vec{r}'|}, \tag{84}$$

and the exchange operator K being defined by its action on a test function f as

$$K(\vec{r})f(\vec{r}) = \sum_i \phi_i(\vec{r}) \int \mathrm{d}r' \frac{\phi_i^*(\vec{r}')f(\vec{r}')}{|\vec{r} - \vec{r}'|}. \tag{85}$$

The Hartree–Fock procedure in MRA is the solution of the equations[29,52,53]

$$\phi_i(\vec{r}) = -2G_{\epsilon_i}(J - K + V_{\text{nuc}})\phi_i(\vec{r}), \tag{86}$$

with the orthonormality condition

$$\langle \phi_i | \phi_j \rangle = \delta_{ij}. \tag{87}$$

In practical implementations the Green's functions G_{ϵ_i} are applied on the corresponding orbitals $\phi_i(r)$, followed by an orthogonalization step.

A subspace solver may be used to accelerate the convergence of this iterative procedure.[54]

The scaling of Eq. (86) is quadratic with respect to the system size, because of the nonlocal exchange operator K and because of the orthogonalization step. If local orbitals are used, the scaling drops to linear because of the sparsity of the multiplication of functions in MRA, and only few matrix multiplications remain that scale quadratic. Because the dimensions of these matrices have only the size of the number of electrons (instead of the number of basis functions), these operations are very fast.

Modification of Hartree–Fock to density functional theory (DFT) is relatively straightforward. The exchange operator K of the Hartree–Fock theory in Eq. (86) is replaced with the exchange-correlation (XC) potential v_{XC} of DFT.

$$F = T + J + v_{\mathrm{XC}} + V_{\mathrm{nuc}}. \tag{88}$$

The XC potentials, and the corresponding kernels and functionals, are available from external libraries.[55] The various XC potentials require the electronic density ρ as input parameters (local density approximation, LDA), and certain classes also use the density gradients σ (generalized gradient approximation, GGA) and the kinetic energy density τ (meta-GGA):

$$\rho(\vec{r}) = \sum_i \left|\phi_i(\vec{r})\right|^2, \tag{89}$$

$$\sigma(\vec{r}) = \left(\vec{\nabla}\,\rho(\vec{r})\right) \cdot \left(\vec{\nabla}\,\rho(\vec{r})\right), \tag{90}$$

$$\tau(\vec{r}) = \frac{1}{2}\sum_i \left|\vec{\nabla}\,\phi_i(\vec{r})\right|^2. \tag{91}$$

Care has to be taken with respect to the numerical properties of the density ρ and the density gradients σ. Numerical noise in ρ might turn it negative, and the ratio of σ and ρ, which enters many XC functionals, might become ill-defined.

3.2.2 Regularization of nuclear singularities

The nuclei in a molecule are usually represented as point charges, introducing singularities into the Schrödinger equation. The singularities can make the MRA scheme fail, since the error in the MRA representations decreases slowly, the MRA representations might become very verbose, or even the quadrature might fail if quadrature points fall into the singularity. There are two basic strategies to handle the singularities: regularize the nuclear

potential, e.g., through the use of pseudopotentials or by smoothing the potential, or construct the wave function such that the singularity is canceled out analytically, as it is done in the explicitly correlated methods.[56–58]

In the context of MRA, the smoothing strategy was used first for the nuclear potential in Ref. 29

$$\frac{1}{r} \approx u(r/c)/c, \tag{92}$$

$$u(r) = \frac{\mathrm{erf}(r)}{r} + \frac{1}{3\sqrt{\pi}}\left(e^{-r^2} + 16e^{-4r^2}\right), \tag{93}$$

with $r = |\vec{r}|$. The functional form is chosen such that the expectation value of the potential is accurate, with the accuracy controlled by the regularization parameter c.

The second strategy to handle the nuclear singularity is by constructing an appropriate wave function, inspired by the explicitly correlated methods in quantum chemistry. The local energy of the Schrödinger equation

$$\frac{H\psi}{\psi} = E \tag{94}$$

is finite everywhere, therefore the infinite potential must be canceled by the only other term in the Schrödinger equation available, the kinetic energy operator acting on the wave function. To cancel the potential, the wave function ψ must have a cusp at the coalescence point, which is determined by the charge of the interacting particles and the angular symmetry of the wave function, as discussed by Kato[59]

$$\left(V - \frac{1}{2}\vec{\nabla}^2\right)\psi = f, \tag{95}$$

where f is a regular function. Kato's cusp condition may be incorporated directly into the wave function ansatz via the one-particle basis.[60,61] The same ansatz is applicable not only for the electron–nuclear singularity but also for the electron–electron singularity in correlated methods. Inclusion of a term which satisfies the cusp condition into the correlated wave function leads to the so-called explicitly correlated methods.[56,62] The regularization of the electronic singularity in MRA will be discussed in more detail in Section 3.3.2.

The ansatz for the orbitals in effective one-electron methods, such as HF or DFT is[63]

$$|\phi_i\rangle = R|F_i\rangle. \tag{96}$$

Following Seelig,[61] the regularized orbitals $|F_i\rangle$ are called "nemo," which stands for "numerical exponential molecular orbitals." The nuclear correlation factor R is valid for all orbitals. It is built up from atomic functions $S_A(r_{12})$

$$R = \prod_A S_A(r_{1A}). \tag{97}$$

The functions $S_A(r_{1A})$ depend on the distance r_{1A} of electron 1 to nucleus A, and contain the nuclear cusp condition such that the singular potential V_{nuc} is regularized and replaced by the nonsingular (albeit still discontinuous) potential U_{nuc}

$$U_{\text{nuc}} = V_{\text{nuc}} + R^{-1}[T,R] = \vec{U}_1 \cdot \vec{\nabla} + U_2, \tag{98}$$

where $\vec{U}_1$ and U_2 are local potentials, with $\vec{U}_1$ having the shape of a step function. The leading term of $S_A(r)$ is

$$S_A(r) = c(1 - Z_A r_{1A}) + \mathcal{O}(r_{1A}^2) \tag{99}$$

where c is an arbitrary number, defined by the SCF procedure. The SCF working equations are derived and their solution is discussed in Section 3.2.1, so here only the regularization is introduced briefly. The SCF working equations are rewritten as

$$(T + J - K + V_{\text{nuc}} - \epsilon_i)|\phi_i\rangle = 0 \tag{100}$$

$$R\left(T + R^{-1}[T,R] + J - R^{-1}KR + V_{\text{nuc}} - \epsilon_i\right)|F_i\rangle = 0 \tag{101}$$

yielding

$$\left(T + J - R^{-1}KR + U_{\text{nuc}} - \epsilon_i\right)|F_i\rangle = 0. \tag{102}$$

This equation has no singularities any more, and its solutions $|F_i\rangle$ accordingly have no cusps at the nuclei.

The nuclear correlation factor S_A may be chosen freely, as long as the following requirements are fulfilled[63]

1. The correlation factor must represent the nuclear cusp, and its second derivative must cancel the singular nuclear potential.
2. In a numerical calculation the correlation factor must not decay faster than the actual HF or DFT orbitals because otherwise the nemo orbitals

$|F_i\rangle$ will become numerically ill-defined. The orbitals decay as a function of the energy of the highest occupied molecular orbital, namely as $e^{-\sqrt{-2\epsilon_{\mathrm{HOMO}}}\,r}$.[64]

3. The regularized potential U_{nuc} must be nonsingular, which is most easily fulfilled if the S_A are finite everywhere since their inverse will be multiplied with their own first and second derivatives.

The actual choice of the nuclear correlation factor might therefore depend on additional requirements in the actual application. A generally reasonable choice is a Slater-type function

$$S(r_{1A}) = 1 + \frac{1}{a-1} e^{-aZ_A r_{1A}} \tag{103}$$

with the correlation length scale a (Fig. 7).

3.2.3 Time-independent properties in HF and DFT

3.2.3.1 First-order properties

Molecular properties are generally computed as derivatives of the energy expectation value with respect to an external perturbation.[2,65] Examples are the dipole moments which are computed as the derivative of the energy with respect to an external electric field, or the nuclear gradients as the derivative with respect to nuclear displacements.

Given the exact solution of the Schrödinger equation, the first derivative of the energy expectation value may be computed as follows: The Hellmann–Feynman theorem[3,66] states that the derivative of the expectation value of the energy equals the partial derivative of the Hamilton operator

$$\frac{\mathrm{d}\langle E\rangle}{\mathrm{d}X} = \left\langle \frac{\partial\psi}{\partial X}\middle|H\middle|\psi\right\rangle + \left\langle \psi\middle|\frac{\partial H}{\partial X}\middle|\psi\right\rangle + \left\langle \psi\middle|H\middle|\frac{\partial\psi}{\partial X}\right\rangle = \left\langle \psi\middle|\frac{\partial H}{\partial X}\middle|\psi\right\rangle, \tag{104}$$

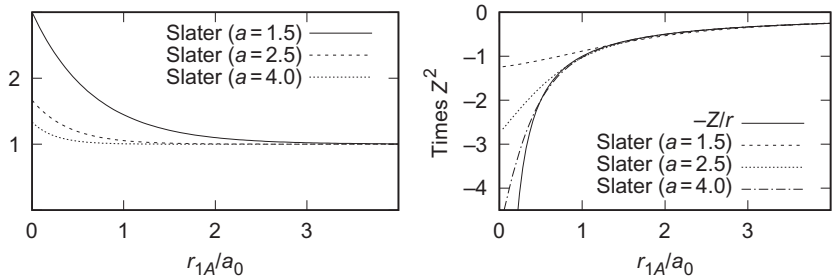

Fig. 7 *Left panel*: functional form of the Slater-type nuclear correlation factor $S(r_{1A})$ of Eq. (103) for different correlation length scales a; *right panel*: regularized nuclear potential, compared to the singular potential Z_A/r.

which holds if the wave function ψ is the exact eigenfunction of the Hamilton operator H

$$\left\langle \frac{\partial \psi}{\partial X} | H | \psi \right\rangle + \left\langle \psi | H | \frac{\partial \psi}{\partial X} \right\rangle = E \frac{\partial}{\partial X} \langle \psi | \psi \rangle = 0. \tag{105}$$

As noted by Coulson[67] the Hellmann–Feynman theorem also holds for HF or DFT wave functions, if the Brillouin theorem is fulfilled exactly, i.e., if the orbitals are exact eigenfunctions of the Fock operator. In finite basis set calculations this is in general not fulfilled, since orbitals are only eigenvectors of the Fock matrix. In contrast the Brillouin condition is met in MRA up to the requested precision.

Using the simple expression of Eq. (104) a number of first-order properties may be obtained with the derivative approach. The dipole moments $\vec{\mu}$ and nuclear gradients g_{X_A} of nucleus A with respect to direction X are

$$\vec{\mu} = \frac{\mathrm{d}\langle E \rangle}{\mathrm{d}\vec{E}} = \sum_i \langle \phi_i | \vec{r} | \phi_i \rangle, \tag{106}$$

$$g_{X_A} = \frac{\mathrm{d}\langle E \rangle}{\mathrm{d}X_A} = \sum_i \langle \phi_i | \frac{\partial V}{\partial X_A} | \phi_i \rangle, \tag{107}$$

where $\vec{E}$ is an external electric field, and X_A stands for the displacement of nucleus A in X direction. Nuclear gradients and dipole moments were implemented early on by Harrison and coworkers in Ref. 68.

3.2.3.2 Second-order properties

Second-order properties can be computed as the second derivative of the energy with respect to the required quantities. Important examples are the second nuclear derivatives for computing vibrational frequencies, i.e., the computation of the nuclear Hessian matrix, which can be obtained by differentiating Eq. (107) with respect to another nuclear displacement Y_B[69]

$$\frac{\mathrm{d}^2\langle E \rangle}{\mathrm{d}X_A \mathrm{d}Y_B} = \sum_i \langle \phi_i | H^{X_A Y_B} | \phi_i \rangle + \sum_i \langle \phi_i^{Y_B} | H^{X_A} | \phi_i \rangle + \sum_i \langle \phi_i | H^{X_A} | \phi_i^{Y_B} \rangle, \tag{108}$$

where superscripts indicate a derivative. The dipole derivatives for computing the corresponding infrared intensities are given by[69–72]

$$\frac{\mathrm{d}^2\langle E \rangle}{\mathrm{d}Q_k \mathrm{d}\vec{E}} = \frac{\mathrm{d}\langle \vec{\mu} \rangle}{\mathrm{d}Q_k} = 2 \sum_{ij} \langle \phi_i^{X_j} | \vec{r} | \phi_i \rangle L_{jk}, \tag{109}$$

where L_{jk} are the vectors of nuclear displacements j for the kth normal mode Q_k. Magnetic second-order properties have been computed by Jensen et al.,[73] specifically the magnetizability ζ and NMR shieldings σ as the response of the energy with respect to the magnetic field B and the nuclear magnetic moment M_K on nucleus K

$$\zeta = \frac{\mathrm{d}^2\langle E\rangle}{\mathrm{d}B^2} = \sum_i \langle \phi_i | H^{BB} | \phi_i \rangle + \sum_i \langle \phi_i^B | H^B | \phi_i \rangle + \sum_i \langle \phi_i | H^B | \phi_i^B \rangle, \quad (110)$$

$$\sigma_K = \frac{\mathrm{d}^2\langle E\rangle}{\mathrm{d}M_K \mathrm{d}B} = \sum_i \langle \phi_i | H^{M_K\, B} | \phi_i \rangle + \sum_i \langle \phi_i^B | H^{M_K} | \phi_i \rangle + \sum_i \langle \phi_i | H^{M_K} | \phi_i^B \rangle. \quad (111)$$

These types of calculation are often plagued by basis set incompleteness, manifesting itself in the gauge-origin problem, i.e., the unphysical dependence of the magnetizability on the arbitrarily chosen gauge origin. In LCAO this problem is handled by using gauge-invariant atomic orbitals (GIAO).

For second-order properties the response of the orbitals with respect to the external perturbation is required. Starting from the Hartree–Fock (or Kohn–Sham) equations, here in noncanonical form,

$$F|\phi_i\rangle = \sum_j \epsilon_{ij} |\phi_j\rangle \quad (112)$$

the derivative to an external perturbation X can be written as

$$F^X|\phi_i\rangle + F|\phi_i^X\rangle = \sum_j \epsilon_{ij}^X |\phi_j\rangle + \sum_j \epsilon_{ij} |\phi_j^X\rangle. \quad (113)$$

Superscript X refers to the derivatives of the respective quantities. The orbital response $|\phi_i^X\rangle$ to the external perturbation fulfills the orthogonality condition

$$\langle \phi_i^X | \phi_j \rangle + \langle \phi_i | \phi_j^X \rangle = 0, \quad (114)$$

which can be achieved in linear response theories[74] by imposing orthogonality of the orbital response to the orbitals, i.e., the response $|\phi_i^X\rangle$ must fulfill the condition

$$|\phi_i^X\rangle = Q|\phi_i^X\rangle, \quad (115)$$

where the orthogonality projector Q projects out all contributions from the occupied space spanned by $|\phi_i\rangle$

$$Q = 1 - P = 1 - \sum_i |\phi_i\rangle\langle\phi_i|. \tag{116}$$

In contrast to LCAO methods, where the response orbitals or the correlated wave function is expressed in virtual orbitals, orthogonal to the occupied space by construction, in MRA orthogonality must explicitly be enforced. The unperturbed Fock operator commutes with the orthogonality projector Q, so rearrangement of Eq. (113) leads to the equation for the orbital response $|\phi_i^X\rangle$

$$\left(\hat{T} - \epsilon_i\right)|\phi_i^X\rangle = -QF^X|\phi_i\rangle - (J - K + V_{\text{nuc}})|\phi_i^X\rangle + \sum_{j\neq i}\epsilon_{ij}|\phi_j^X\rangle. \tag{117}$$

The structure of this nonlinear equation is similar to the SCF equations and can be solved in the same manner using the bound-state Helmholtz operator G_{ϵ_i}. This general form of the coupled-perturbed Hartree–Fock (CPHF) equations, also called modified Sternheimer equation,[75] can be applied for all kinds of external perturbations.

The extension to a regularized wave function as discussed in Section 3.2.2 is straightforward if the nuclear correlation factor does not depend on the perturbation. For the case of nuclear displacements this is not true and the orbital response is expressed as

$$|\phi_i^X\rangle = R^X|F_i\rangle + R|F_i^X\rangle \tag{118}$$

The orthogonality relation of Eq. (114) is converted to

$$\langle F_i^X|R^2|F_j\rangle + \langle F_i|R^2|F_j^X\rangle = -\langle F_i|(R^2)^X|F_j\rangle, \tag{119}$$

which introduces an additional metric into the working equations.[69] For nuclear second derivatives the use of a regularized wave function is mandatory, since the operators become highly singular.

3.2.4 Time-dependent properties in HF and DFT

By analogy to the time-independent properties, time-dependent properties such as polarizabilities or excitation energies also require the response of the wave function with respect to the external perturbation. The working equations are derived starting from the equation

$$i\frac{\partial}{\partial t}\rho(t) = [F(t), \rho(t)], \tag{120}$$

where $\rho(t)$ is the time-dependent density, and $F(t)$ is the time-dependent Fock operator containing the external perturbation $f(t)$ as well as the

time-dependent density $\rho(t)$. An expansion of all quantities with respect to the order of the perturbation, some rearrangement, and elimination of the explicit time dependence yields an expression for the so-called response vector $|\mathbf{x}\rangle$.[38] The components $|x_i\rangle$ of the vector describe the response of the electrons in orbital i to the external perturbation oscillating with the frequency ω. Eq. (120) can be rearranged to yield the working equations for the response $|x_i\rangle$[38,76]

$$(T-\epsilon_i-\omega)|x_i\rangle = -Q\left(\frac{\delta F}{\delta\rho^{(0)}}\circ\tilde{\rho}\right)|\varphi_i\rangle - (J-K+V_{\text{nuc}})|x_i\rangle, \tag{121}$$

where the $\circ$ symbol denotes a convolution. This equation is structurally identical to the CPHF analog of Eq. (117), with only the perturbed Fock operator exchanged, and it can be solved in an analogous way.

The quantity

$$\frac{\delta F}{\delta\rho^{(0)}}\circ\tilde{\rho} \tag{122}$$

depends on the quantum mechanical model chosen, explicit formulas for HF and DFT are given in Refs. 38 and 77. The DFT kernels and their derivatives are available from external libraries.[55] Again, the numerical stability of the XC kernels is very important, and the treatment of densities and density gradients as described in Section 3.2.1 is mandatory.

If the excitation energy ω becomes larger than the energy of the highest occupied molecular orbitals ϵ_{HOMO}, the Green's function $G = (T-\epsilon-\omega)^{-1}$ becomes complex, reflecting the physical fact that the electron is not bound anymore. The computation of such states will always yield continuum states approaching the Fermi level. Meta-stable states above the Fermi level may be computed using a complex absorbing potential or similar approaches, although this has not been tested yet.

3.3 Molecular energies and properties in many-body methods

3.3.1 MP2 and Coupled-Cluster in first quantization

With few exceptions the Coupled-Cluster literature is formulated in second quantization which needs to be translated into first quantization when used in MRA. The Coupled-Cluster wave function defined by excitation operators into the virtual space

$$|CC\rangle = e^T|HF\rangle,$$
$$T = T_1 + T_2 + T_3 + \cdots = \sum_{ia} \tau_{ia} t_{ia} + \sum_{iajb} \tau_{iajb} t_{iajb} + \sum_{iajbkc} \tau_{iajbkc} t_{iajbkc} + \ldots, \quad (123)$$

where τ_{ia} excites an electron from orbital i to a with the corresponding amplitude t_{ia}, and similar for double and higher excitations. The real-space analog to the amplitudes t_{ia}, t_{iajb} and alike are the cluster functions τ_i and τ_{ij} which are computed explicitly in the MRA form. They can be expressed in terms of virtual orbitals (and vice versa) as

$$|\tau_i\rangle = \sum_a |\phi_a\rangle t_a^i, \qquad t_a^i = \langle \phi_a | \tau_i \rangle \quad (124)$$

$$|\tau_{ij}\rangle = \sum_{ab} |\phi_a \phi_b\rangle t_{ab}^{ij}, \qquad t_{ab}^{ij} = \langle \phi_a \phi_b | \tau_{ij} \rangle. \quad (125)$$

Since the cluster functions are not orthogonal to the occupied space by construction like the virtual orbitals, the orthogonality must be explicitly enforce through the (strong) orthogonality projector Q and $Q_{12} = Q_1 Q_2$ of Eq. (116)

$$|\tau_i\rangle = Q|\tau_i\rangle, \quad (126)$$

$$|\tau_{ij}\rangle = Q_{12}|\tau_{ij}\rangle. \quad (127)$$

The vector potential $\boldsymbol{\Omega}$ that defines the Coupled-Cluster model can also be expressed in first quantization.[32,33] It is beyond the scope of the current review to discuss all the diagrams but as an example the term D8b in the notation of Ref. 78, which reads in second and first quantization as

$$g_{cj}^{kl} t_i^c t_k^a t_l^b = Q_{12}\left(g_{\tau_i j}^{kl} | \tau_k \tau_j \rangle\right), \quad (128)$$

with the matrix element $g_{\tau_i j}^{kl} = \langle \tau_i j | g_{12} | kl \rangle$. Explicit first-quantized expressions for all diagrams of the CC2 model are given in Ref. 32. This yields for the vector potentials $\boldsymbol{\Omega}_i$ and $\boldsymbol{\Omega}_{ij}$

$$|\boldsymbol{\Omega}_i\rangle = (F - \epsilon_i)|\tau_{ij}\rangle + Q \sum_{n\prime} |S_n^i\rangle = 0, \quad (129)$$

$$|\boldsymbol{\Omega}_{ij}\rangle = \left(F_{12} - \epsilon_{ij}\right)|\tau_{ij}\rangle + Q_{12} \sum_{n\prime} |D_n^{ij}\rangle = 0, \quad (130)$$

where certain terms in the diagrammatic expansion correspond to the Fock operator term (namely S_{3a} and S_{3b} for the singles equation and

D_{2a} and D_{2b} for the doubles equation). These equations can be inverted in the usual way using Green's function to determine the cluster functions τ_i and τ_{ij}.

The MP2 model can be derived as a special case of the Coupled-Cluster formalism but also by solving the MP1 equation, which is given by

$$\left(H^{(1)} - E^{(1)}\right)|\Phi^{(0)}\rangle = -\left(H^{(0)} - E^{(0)}\right)|\psi^{(1)}\rangle. \tag{131}$$

Again, this equation can be inverted and the first-order perturbed wave function $|\psi^{(1)}\rangle$ (corresponding to the cluster function $|\tau_{ij}\rangle$) is obtained as

$$|\psi_{ij}^{(1)}\rangle = -GQ_{12}g_{12}|\phi_i\phi_j\rangle - G(J_{12} - K_{12} + V_{\text{nuc},12})|\psi_{ij}^{(1)}\rangle, \tag{132}$$

where J_{12}, K_{12}, and $V_{\text{nuc, }12}$ denote the Coulomb, exchange and nuclear potential terms for electrons 1 and 2. The final correlation energy is then given in second and first quantization as

$$E_{\text{corr}} = \sum_{iajb}\left(\langle\phi_i\phi_j|g|\phi_a\phi_b\rangle t_{ab}^{ij} + \langle\phi_i\phi_j|g|\phi_a\phi_b\rangle t_a^i t_b^j\right), \tag{133}$$

$$E_{\text{corr}} = \sum_{ij}\left(\langle\phi_i\phi_j|g|\tau_{ij}\rangle + \langle\phi_i\phi_j|g|\tau_i\tau_j\rangle\right), \tag{134}$$

where all terms are understood to be properly antisymmetrized. Since there are no virtual orbitals the canonical scaling of MP2 and Coupled-Cluster with respect to the system size is reduced by 2 orders of magnitude, e.g., for MP2 from N^5 in LCAO to N^3 in MRA, where N is some measure of the system size. However, the computational prefactor is much larger in MRA.

3.3.2 Regularization of the wave function

In effective two-particle methods, such as MP2 or Coupled-Cluster, an electron–electron cusp occurs in addition to the electron–nuclear cusp. Both the interelectronic singularity and the electron–nuclear singularity are delocalized in a three-dimensional subspace of the full six-dimensional space of the two-electron coordinates. However, the interelectronic singularity is much more severe than the nuclear singularity, since it couples the coordinates of both electrons, which is diametrical to the Cartesian MRA representation. A singularity in the working equations leads to a cusp in the wave function,[59] as was already discussed in the nemo ansatz in Section 3.2.2. Close to the coalescence point the wave function depends linearly on the interelectronic distance r_{12}. Explicitly introducing such a term into the wave

function removes the singularity from the working equations. The explicit form of the correlation factor depends on the computational model, for MP2 and CC2 it reads as

$$f_{12} = \frac{r_e}{2}\left(1 - e^{-r_{12}/r_e}\right), \tag{135}$$

which is the same correlation factor used in LCAO F12 theory.[79] The choice of the correlation length scale r_e does not change the cusp behavior, since the leading term remains the same but it affects the convergence rate to the basis set limit in LCAO calculations.

The perturbed first-order Hamilton operator in MP2 and the fluctuation potential in Coupled-Cluster contain the singular interelectronic interaction term $g_{12} = 1/r_{12}$, which can be canceled by commuting the correlation factor with the kinetic energy operator, yielding a regularized two-electron potential U_{12}[56]

$$[T, f_{12}] = -\frac{1}{r_{12}} + U_{12} \tag{136}$$

The singularity affects primarily the doubles equations. In the singles equation in Coupled-Cluster one of the coordinates of the singularity is integrated out and the singularity is thus regularized. The MP2 and CC2 working equations for the doubles cluster functions read as

$$|\tau_{ij}\rangle = -G(J - K + V_{\text{nuc}})|\tau_{ij}\rangle - GQ_{12}g_{12}|\phi_i\phi_j\rangle, \tag{137}$$

$$|\tau_{ij}\rangle = -G(J - K + V_{\text{nuc}})|\tau_{ij}\rangle - GQ^t_{12}g_{12}|t_it_j\rangle. \tag{138}$$

The ansatz for the wave function is then

$$|\tau_{ij}\rangle = |u_{ij}\rangle + Q_{12}f_{12}|\phi_i\phi_j\rangle, \tag{139}$$

$$|\tau_{ij}\rangle = |u_{ij}\rangle + Q^t_{12}f_{12}|t_it_j\rangle \tag{140}$$

for MP2 and CC2, respectively, with the regularized cluster functions $|u_{ij}\rangle$. The modified strong orthogonality projector Q^t_{12} is the most convenient form of a strong orthogonality projector in Eq. (140) but other forms are also possible, e.g., using Q_{12} directly.

Commuting the correlation factor f_{12} through the working equations yields a new set of working equations for the regularized cluster function $|u_{ij}\rangle$, similar to the original ones for the $|\tau_{ij}\rangle$ of Eqs. (137) and (138)

$$|u_{ij}\rangle = -G(J - K + V_{\text{nuc}})|u_{ij}\rangle - GQ_{12}\tilde{g}^{ij}_{12}|\phi_i\phi_j\rangle, \tag{141}$$

$$|u_{ij}\rangle = -G(J - K + V_{\text{nuc}})|u_{ij}\rangle - GQ^t_{12}\tilde{g}^{ij}_{12}|t_it_j\rangle. \tag{142}$$

The regularized Coulomb operator $\tilde{g}_{12}$ depends on the electron pair ij and is defined as

$$\tilde{g}_{12}^{ij} = f_{12}\left(F_{12} - \epsilon_{ij}\right) + U_{12} - [K_{12}, f_{12}] + \left[F_{12}, Q_{12}^t\right] f_{12}. \tag{143}$$

In the case of MP2, where the regularized Coulomb operator is applied on the reference $|\phi_i \phi_j\rangle$ and no singles cluster functions are present, the first and the last terms cancel and only the U potential and the exchange operator commutator are left (thus removing the dependence on ij)[30,32]. The regularized cluster functions $|u_{ij}\rangle$ still have cusps at the nuclear sites, these can be removed straightforwardly by using nemos.

3.3.3 Time-dependent properties in Coupled-Cluster

Accurate excitation energies can be computed using Coupled-Cluster response theory.[80] The excitation energies are given as the poles of the response function,[32] which can be computed as eigenvalues of the CC Jacobian. The excited state cluster functions $|x_i\rangle$ and $|x_{ij}\rangle$ are (strongly) orthogonal to the reference, and they can be determined by taking the functional derivative of the ground-state equations (129) and (130), yielding

$$0 = (F - \epsilon_i - \omega)|x_i\rangle + \delta|V_{\tau_i}\rangle \tag{144}$$

$$0 = \left(F_{12} - \epsilon_{ij} - \omega\right)|x_{ij}\rangle + \delta\left(Q_{12}^t g_{12}|t_i t_j\rangle\right) \tag{145}$$

The variation δ of the potential terms are computed using the chain rule for differentiation, they are given explicitly in Ref. 32. Similarly to ground-state CC2 and MP2 the equations must be completely regularized to avoid the computation of singular potentials on the grid. The regularization of the response double vector $|x_{ij}\rangle$

$$|x_{ij}\rangle = |v_{ij}\rangle + \delta Q_{12}^t|t_i t_j\rangle + Q_{12}^t f_{12}|x_i t_j\rangle + Q_{12}^t f_{12}|t_i x_j\rangle, \tag{146}$$

follows the ground-state ansatz by expanding the parentheses of Eq. (145). The regularization with respect to the nuclear-electronic cusp is straightforward.

4. Discussion

4.1 Application examples

MRA can be used for a variety of chemical applications and number of quantum chemical methods have been implemented in the MADNESS code.[52] MRA is an efficient method to compute energies and properties of large molecules with HF or DFT. The excited states of the retinal, the light

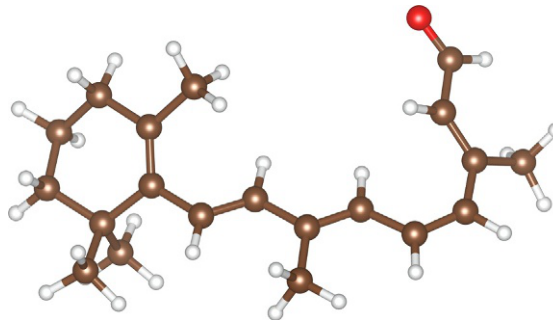

Fig. 8 11-cis-retinal (156 electrons), the light absorbing molecule in the human eye, UV/VIS spectrum computed with MRA/CIS.[38]

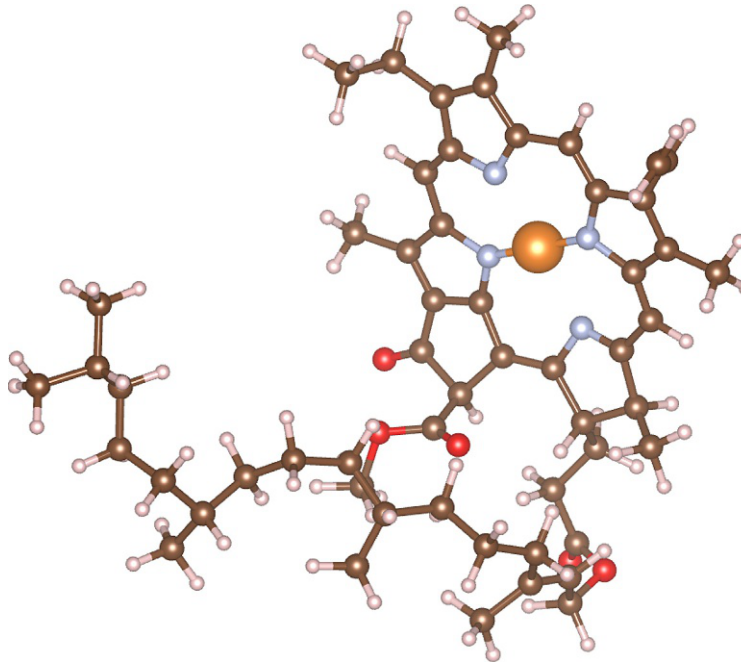

Fig. 9 Chlorophyll-a (482 electrons), structure optimized with MRA/LDA.

absorbing molecule of the rhodopsin system in the eye, can be computed using configuration interaction singles (CIS) (Fig. 8). Also ground-state calculations including structure optimizations can be performed for molecules as large as chlorophyll-a with 137 atoms and 482 electrons (Fig. 9). All these calculations are performed at the basis set limit, and they are often very hard in finite size LCAO calculations if a comparable precision is sought.

Table 2 Solvatochromatic shifts in eV of the first excited states of the water molecule in water solution computed with MRA/CIS using the polarizable continuum model.

	Vacuum			Solvated		
State	**MRA**	**aVTZ**	**daVTZ**	**MRA**	**aVTZ**	**daVTZ**
B_2	8.66	8.66	8.66	9.01	9.01	9.01
A_2	10.32	10.33	10.33	10.78	10.79	10.78
A_1	10.88	10.95	10.89	11.07	11.14	11.06
B_2	11.15	11.79	11.19	11.06	11.59	11.07

LCAO calculations were performed with the KOALA program,[82] daVTZ basis with double augmentation on oxygen only.

Table 3 Molecular properties of the water molecule.

Property	**Method**	**MRA**
Total energy (E_h)	HF	−76.066 936
	PBE	−76.388 681
	B3LYP	−74.691 437
Correlation energy (mE_h)	MP2	−298.70
	CC2	−300.82
First excitation energy (eV)	PBE	6.59
	CIS	8.66
	CC2	7.33
Dipole moment (a.u.)	B3LYP	0.73
Optimized structure	PBE	96.93 pm/104.06°
Vibrational frequencies (cm^{-1})	PBE	1595/3701/3805
Infrared intensities ($kmmol^{-1}$)	PBE	70/2/51

External libraries, such as libxc[55] or the PCMSolver library,[81] can be interfaced to the code and extend the functionality significantly. As an example, the solvatochromatic shifts of the first excitations of the water molecule are shown in Table 2 using the CIS approximation and the polarizable continuum model for solvation.

Being small enough for correlated methods, the water molecule may serve as a test case for the comparison of different methods for computing molecular properties. Table 3 shows a number of properties that can be

computed, including first- and second-order properties. The first excitation energy can be computed with CIS, CC2, and with DFT in the Tamm–Dancoff approximation (TDA). In LCAO, these methods have high demands on the basis sets, since CC2 requires higher l-quantum numbers than CIS and DFT, while DFT often predicts rather diffuse excited states. Using MRA the basis set error is strongly reduced, and all methods can be directly compared with respect to their method error without basis set artifacts, such as incompleteness or pseudoconvergence.

While first-order properties can be computed very efficiently with the Hellmann–Feynman theorem, second-order properties are computationally more demanding. Vibrational frequencies and intensities require the solution of the CPHF equations for each nuclear displacement, resulting in a higher scaling with respect to the system size compared to the ground-state calculation. Excitation energies in the CIS and TDA approximation scale linearly with respect to the number of excitations that are computed.

4.2 Precision

MRA promises numerical precision and freedom from basis set incompleteness. The thresholds can be increased to achieve numerically exact results, at the cost of computationally more expensive calculations. Note that this is not necessarily true for LCAO, where overcompleteness of the basis may prevent convergence to the basis set limit. In finite basis set calculations, the size of the basis, corresponding to the computational effort, is set by the user, defining the final precision. In MRA, the approach is inverted: the computational effort is determined by the final precision set by the user. The difference can be thought of as "defined contribution" of the former compared to "defined benefit" of the latter.

There are several important remarks concerning the precision: if extensive properties are computed, errors may accumulate. While the errors in each function can be decreased arbitrarily, by accumulation of many small contributions the total error may become greater than the threshold. This is particularly true for correlated methods, where the number of pair functions, and thus the total error, increases quadratically with system size, leading to an effective size-consistency error. The correlation energy of water is shown in Table 4. MP2 and CC2 calculations are performed with a precision threshold of $\epsilon = 10^{-3}$ and $\epsilon = 10^{-4}$ and four correlated orbitals.[32,83] The total correlation energy is not yet converged to the basis set limit for the lower precision calculations, and the error is larger than the threshold, although all 10 pair energies are well below the precision threshold.

Table 4 Correlation and excitation energies of water.

	MRA		LCAO		
Property	$\epsilon = 10^{-3}$	$\epsilon = 10^{-4}$	**aVTZ**	**aV5Z**	**Limit**
E_{corr}/mE_h (MP2)	299.32	301.93	−269.84	−294.32	301.86
excitation energy/eV (CC2)	7.34	—	7.20	7.29	7.33

The higher precision calculation meets the thresholds. In this case the error per pair function is even an order of magnitude smaller than requested.

The size-extensitivity error is an important issue in correlated calculations. However, physically electron correlation is a local phenomenon. Orbital localization makes the number of contributing pair functions per orbital constant instead of linear because of the rapid decay with increasing distance and will thus remove the size-consistency error after passing a precision threshold. This minimal precision is anticipated to occur at 0.1 mE_h error per pair function, and numerical size-consistency (up to chemical accuracy) will then be achieved. Because of the high computational costs, this point has not been passed yet, and future research will focus on this problem.

The error accumulation problem does not occur if intensive properties, e.g., excitation energies, are computed. Excitation energies are computed as eigenvalues of the CIS or CC2 equations, they do not depend on the system size, and no accumulation of small quantities occurs. Table 4 also shows the first excitation energy of the water molecule. In contrast to the correlation energy the excitation energy is converged to the basis set limit although the underlying correlated wave function is not. Excitation energies benefit greatly from the balanced description of the ground and excited state in MRA, which is hard to achieve in LCAO with (ground state) optimized basis sets where even an augmented 5Z basis set is insufficient to reproduce the basis set limit in CC2. This effect is even more pronounced for nonvalence excited states, also in effective one-particle methods such as CIS, because these states are significantly more diffuse than the ground state (see Table 2).

Furthermore, the precision of MRA depends on the regularity of the wave function and of the operators. Ground and excited states are smooth functions, containing only a nuclear cusp, and they can be represented accurately with MRA where the convergence rate depends on the differentiability of the represented function (see Eq. (7)). The orbital response to nuclear displacements, however, is highly singular and features step functions over many orders of magnitude. The corresponding perturbation

operators are first and second derivatives of the already singular nuclear potential. In such cases the precision must be significantly tightened, and the convergence of the CPHF equations might even fail, e.g., for GGA functionals, where additional derivatives of the perturbed density are required.[69]

4.3 Performance

The scaling of quantum chemical algorithms with respect to system size is typically two orders less than for LCAO methods. MP2 and CC2 scale as N^3, as opposed to N^5 encountered in the canonical LCAO case. With localized orbitals the scaling drops even further to linear or quadratic (this is also true for LCAO). Effective one-particle methods (HF and DFT) are easily competitive with LCAO. Fig. 9 shows the chlorophyll-a molecule with 482 electrons, computed with MRA/LDA on a 16 core workstation at the basis set limit. The first excited state of retinal using CIS can be computed with MRA faster and more precisely than with LCAO (Fig. 10). In contrast, the CC2 excited states are currently inaccessible for molecules with more than six atoms.

The main computational drawback for correlated methods is the massive increase of CPU and memory requirements, growing exponentially with the number of dimensions d (the "curse of dimensionality"). The number of boxes and the number of coefficients in each box increase as 2^d and k^d,

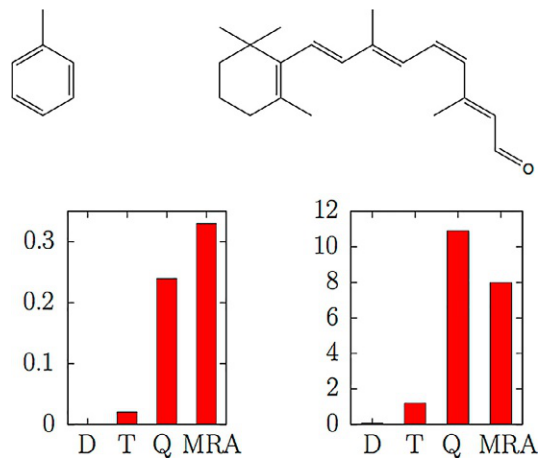

Fig. 10 CPU times in days for the computation of the first excited state of toluene and retinal. For large systems MRA is more efficient than LCAO calculations in large basis sets.

respectively, with k being the polynomial order. While for HF and DFT, where $d = 3$ is still moderate, this is not an insurmountable problem, for MP2 and CC2, where $d = 6$ is high, this becomes the computational bottleneck. Low-rank tensor approximations can reduce the number of coefficients but they require relatively complicated algorithms for simple addition of two tensors, which is an operation performed billions of times in the course of a quantum chemical calculation.

While the increase in computational requirements, in particular of memory, is massive for six dimensions as in MP2, it still is only a computational prefactor which can eventually be brought down by faster algorithms for low-rank tensors or by parallelization. For large systems the scaling with respect to system size will dominate the computational footprint, and in this respect MRA is advantageous compared to conventional methods, even for correlated methods.

4.4 Handling

MRA is a real-space method. The handling of the equations in real space is direct and does not require the translation into matrix equations. Often, there is a one-to-one correspondence of the equations on paper and their implementation in the MRA code. This allows the fast implementation of new methods, without spending too much thought on the details of the underlying MRA library or the parallel runtime.

Various types of function can be represented with equal precision, be they orbitals, densities, or potentials. Finite basis sets, often Gaussian basis functions designed for the representation of orbitals, can introduce severe imbalances between these quantities. For example, MRA represents ground and excited state functions equally well and while Gaussian basis sets often suffer from imbalances in the basis. Since MRA does not use a predefined set of basis functions but an adaptive basis it can be used for various quantum mechanical problems, not only for electronic structure. Solving the Schrödinger equation for the motion of nuclei to compute Franck–Condon factors would be another example where MRA can be used. Due to the direct translation of equations into code, MRA also qualifies for educational purposes.

5. Summary and outlook

In this review, quantum chemical methods based on multiresolution analysis (MRA) have been presented. Currently ground and excited states can be computed for HF and DFT, as well as for MP2 and CC2. First- and second-order properties, such as dipole moments, nuclear derivatives,

magnetic properties, and vibrational frequencies and intensities, are also available for HF and DFT. In all methods singularities in the working equations can be analytically removed, which is of paramount importance to make the computation of high-dimensional wave functions, as required in correlated methods, tractable.[63,83]

An important aspect of correlated methods is the use of low-rank tensor approximations, since the wavelet coefficient tensors in uncompressed form would have an insurmountable memory footprint.[30] In most operations of the six-dimensional MRA calculation an SVD of the coefficient tensor is used, and efficient algorithms for decomposition, contraction, addition, and other operations of such tensors have been developed.

While energies and molecular properties can be computed in SCF methods routinely, the computational load is much higher for correlated methods, barring MP2 and Coupled-Cluster from being used on large molecules. However, the computational scaling is lower than in the corresponding LCAO implementations and there is no fundamental reason that would prevent MRA methods from being used. With improving computer resources and more efficient algorithms, especially on the tensor representations, also correlated methods will become feasible as the computational prefactor will drop. For illustration: the first computation of the exact helium wave function took several days on 1000 nodes with 14 cores each on the Jaguar XT5 supercomputer in 2011,[30] but only 2 days on 1 node with 16 cores in 2014,[83] for the most part due to improved algorithms concerning the regularization of the wave function. Such high gains on the performance should not be expected in the future but even a speed-up of 2 or 4 will make MRA much more competitive and will allow the routine computation at least of small molecules.

The next steps will be to make MRA faster and less memory-consuming. Firstly, improved tensor representations and algorithms must be developed and implemented in order to take the heavy load from correlated calculations. Secondly, localization must be taken advantage of in all implementations. For some methods this is already the case but it must be used throughout the code. Localization will both make the calculations faster by decreasing the scaling and increase the accuracy, by reducing the number of significant pair functions (in correlated methods but also in the exchange term in Hartree–Fock). Thirdly, MRA has the potential to be a black-box method, since only the molecular geometry and an energy threshold is required for a calculation. Automated generation of input parameters, such as the polynomial order or the convergence thresholds make codes user-friendly by developer benchmarking.

MRA shows in many ways its complementary numerical properties compared to the existing LCAO paradigm. MRA provides few digits of the correct result, while LCAO provides many digits of the systematically incorrect result. As a consequence, MRA cannot take advantage of error cancelation, while LCAO is successfully doing so (depending on the actual property). MRA can compute excited states accurately with virtually no basis set incompleteness error and no imbalance in the description of ground and exited states but has to be converged very tightly for computing the nuclear Hessian without loss of precision. MRA features a low scaling with respect to system size but as of today a high computational prefactor for correlated methods.

MRA offers great potential not only as a complementary method to the existing finite basis methods. While from today's perspective it seems hard to compete with small basis set calculations for exploratory purposes, MRA is for DFT and HF already more efficient than large basis set calculations of large molecules. With improved algorithms and faster computers, MRA will become more and more competitive with respect to LCAO. Its unique numerical properties make MRA an important extension for the quantum chemical toolbox.

References

1. Dirac, P. A. M. Quantum Mechanics of Many-Electron Systems. *Proc. R. Soc. A: Math. Phys. Eng. Sci.* 1929, *123*(792), 714–733.
2. Gauss, J. Molecular Properties. In: *Modern Methods and Algorithms of Quantum Chemistry*; Grotendorst, J. Ed.; John von Neumann Institute for Computing: Julich, 2000, pp 541–592.
3. Feynman, R. P. Forces in Molecules. *Phys. Rev.* **1939**, *56*(4), 340–343.
4. Pulay, P. Ab Initio Calculation of Force Constants and Equilibrium Geometries in Polyatomic Molecules. *Mol. Phys.* **1969**, *17*(2), 197–204.
5. Froese Fischer, C. A B-Spline Hartree-Fock Program. *Comput. Phys. Commun.* **2011**, *182*(6), 1315–1326.
6. Bachau, H.; Cormier, E.; Decleva, P.; Hansen, J. E.; Martn, F. Applications of B-Splines in Atomic and Molecular Physics. *Rep. Prog. Phys.* **2001**, *64*(12), 1815–1943.
7. Boys, S. F. Electronic Wave Functions. 1. A General Method of Calculation for the Stationary States of Any Molecular System. *Proc. R. Soc. Lond. A* **1950**, *200*(1063), 542–554.
8. Obara, S.; Saika, A. Efficient Recursive Computation of Molecular Integrals Over Cartesian Gaussian Functions. *J. Chem. Phys.* **1986**, *84*(7), 3963–3974.
9. Hill, J. G. Gaussian Basis Sets for Molecular Applications. *Int. J. Quantum Chem.* **2013**, *113*(1), 21–34.
10. Halkier, A.; Helgaker, T.; Jrgensen, P.; Klopper, W.; Koch, H.; Olsen, J.; Wilson, A. K. Basis-Set Convergence in Correlated Calculations on Ne, N2, and H2O. *Chem. Phys. Lett.* **1998**, *286*(3-4), 243–252.
11. Boys, S.; Bernardi, F. The Calculation of Small Molecular Interactions by the Differences of Separate Total Energies. Some Procedures With Reduced Errors. *Mol. Phys.* **1970**, *19*(4), 553–566.

12. Van Duijneveldt, F. B.; van Duijneveldt-van de Rijdt, J. G.; van Lenthe, J. H. State of the Art in Counterpoise Theory. *Chem. Rev.* **1994**, *94*(7), 1873–1885.
13. Bloch, F. Über die quantenmechanik der elektronen in kristallgittern. *Z. Phys.* **1929**, *52*(7-8), 555–600.
14. Shepherd, J. J.; Grüneis, A.; Booth, G. H.; Kresse, G.; Alavi, A. Convergence of Many-Body Wave-Function Expansions Using a Plane-Wave Basis: From Homogeneous Electron Gas to Solid State Systems. *Phys. Rev. B* **2012**, *86*(3), 035111.
15. Booth, G. H.; Grüneis, A.; Kresse, G.; Alavi, A. Towards an Exact Description of Electronic Wavefunctions in Real Solids. *Nature* **2013**, *493*(7432), 365–370.
16. Blchl, P. E. Projector Augmented-Wave Method. *Phys. Rev. B* **1994**, *50*(24), 17953–17979.
17. Kresse, G.; Joubert, D. From Ultrasoft Pseudopotentials to the Projector Augmented-Wave Method. *Phys. Rev. B* **1999**, *59*(3), 1758–1775.
18. Flores, J. R. New Benchmarks for the Second-Order Correlation Energies of Ne and Ar Through the Finite Element MP2 Method. *Int. J. Quantum Chem.* **2008**, *108*(12), 2172–2177.
19. McCullough, E. A., Jr. Seminumerical SCF Calculations on Small Diatomic Molecules. *Chem. Phys. Lett.* **1974**, *24*(1), 55–58.
20. Pahl, F. A.; Handy, N. C. Plane Waves and Radial Polynomials: A New Mixed Basis. *Mol. Phys.* **2002**, *100*(20), 3199–3224.
21. Shiozaki, T.; Hirata, S. Grid-Based Numerical Hartree-Fock Solutions of Polyatomic Molecules. *Phys. Rev. A* **2007**, *76*(4), 040503.
22. Lehtovaara, L.; Havu, V.; Puska, M. All-Electron Density Functional Theory and Time-Dependent Density Functional Theory With High-Order Finite Elements. *J. Chem. Phys.* **2009**, *131*(5), 054103.
23. Banerjee, A. S.; Lin, L.; Hu, W.; Yang, C.; Pask, J. E. Chebyshev Polynomial Filtered Subspace Iteration in the Discontinuous Galerkin Method for Large-Scale Electronic Structure Calculations. *J. Chem. Phys.* **2016**, *145*(15), 154101.
24. Bylaska, E. J.; Holst, M.; Weare, J. H. Adaptive Finite Element Method for Solving the Exact Kohn-Sham Equation of Density Functional Theory. *J. Chem. Theory Comput.* 2009, *5*(4), 937–948.
25. Mohr, S.; Ratcliff, L.; Genovese, L.; Caliste, D.; Boulanger, P.; Goedecker, S.; Deutsch, T. Accurate and Efficient Linear Scaling DFT Calculations With Universal Applicability. *Phys. Chem. Chem. Phys.* 2015, *17*(47), 31360–31370.
26. Genovese, L.; Neelov, A.; Goedecker, S.; Deutsch, T.; Ghasemi, S. A.; Willand, A.; Caliste, D.; Zilberberg, O.; Rayson, M.; Bergman, A.; Schneider, R. Daubechies Wavelets as a Basis Set for Density Functional Pseudopotential Calculations. *J. Chem. Phys.* **2008**, *129*(1), 014109.
27. Khoromskaia, V.; Khoromskij, B. N. Mller-Plesset (MP2) Energy Correction Using Tensor Factorization of the Grid-Based Two-Electron Integrals. *Comput. Phys. Commun.* **2014**, *185*(1), 2–10.
28. Daubechies, I. *Ten Lectures on Wavelets*. Society for Industrial and Applied Mathematics: Philadelphia, 1992;p 357.
29. Harrison, R.; Fann, G.; Yanai, T.; Gan, Z.; Beylkin, G. Multiresolution Quantum Chemistry: Basic Theory and Initial Applications. *J. Chem. Phys.* **2004**, *121*(23), 11587–11598.
30. Bischoff, F. A.; Harrison, R. J.; Valeev, E. F. Computing Many-Body Wave Functions With Guaranteed Precision: The First-order Mller-Plesset Wave Function for the Ground State of Helium Atom. *J. Chem. Phys.* **2012**, *137*(10), 104103.
31. Bischoff, F. A.; Valeev, E. F. Computing Molecular Correlation Energies With Guaranteed Precision. *J. Chem. Phys.* **2013**, *139*(11), 114106.
32. Kottmann, J. S.; Bischoff, F. A. Coupled-Cluster in Real Space. 1. CC2 Ground State Energies Using Multiresolution Analysis. *J. Chem. Theory Comput.* 2017, *13*(12), 5945–5955.

33. Kottmann, J. S.; Bischoff, F. A. Coupled-Cluster in Real Space. 2. CC2 Excited States Using Multiresolution Analysis. *J. Chem. Theory Comput.* 2017, *13*(12), 5956–5965.
34. Bellman, R. E. *Adaptive Control Processes*. Princeton University Press: Princeton, 1961;p 255.
35. Oseledets, I. V. Tensor-Train Decomposition. *SIAM J. Sci. Comput.* **2011**, *33*(5), 2295–2317.
36. Golub, G. H. van Loan, C. F.. *Matrix Computations*. The Johns Hopkins University Press, 1996;p 728.
37. Beylkin, G.; Mohlenkamp, M. J. Algorithms for Numerical Analysis in High Dimensions. *SIAM J. Sci. Comput.* **2005**, *26*(6), 2133–2159.
38. Kottmann, J. S.; Hfener, S.; Bischoff, F. A. Numerically Accurate Linear Response-Properties in the Configuration-Interaction Singles (CIS) Approximation. *Phys. Chem. Chem. Phys.* 2015, *17*(47), 31453–31462.
39. Alpert, B. K.; Beylkin, G.; Gines, D.; Vozovoi, L. Adaptive Solution of Partial Differential Equations in Multiwavelet Bases. *J. Comput. Phys.* **2002**, *182*(1), 149–190.
40. Alpert, B. K. A Class of Bases in L2 for the Sparse Representation of Integral-Operators. *SIAM J. Math. Anal.* **1993**, *24*(1), 246–262.
41. Beylkin, G.; Coifman, R.; Rokhlin, V. Fast Wavelet Transforms and Numerical Algorithms I. *Commun. Pure Appl. Math.* 1991, *44*(2), 141–183.
42. Haar, A. Zur Theorie der orthogonalen Funktionensysteme. *Math. Ann.* **1910**, *69*(3), 331–371.
43. Jensen, S. R. Real-space All-electron Density Functional Theory With Multiwavelets. Ph.D. thesis, UiT The Artic University of Norway, Tromso 2014.
44. Beylkin, G.; Kurcz, C.; Monzon, L. Fast Convolution With the Free Space Helmholtz Greens Function. *J. Comput. Phys.* **2009**, *228*(8), 2770–2791.
45. Beylkin, G.; Cheruvu, V.; Perez, F. Fast Adaptive Algorithms in the Non-standard Form for Multidimensional Problems. *Appl. Comput. Harmon. Anal.* 2008, *24*(3), 354–377.
46. De Lathauwer, L.; De Lathauwer, L.; De Moor, B.; De Moor, B.; Vandewalle, J.; Vandewalle, J. A Multilinear Singular Value Decomposition. *SIAM J. Matrix Anal. Appl.* 2000, *21*(4), 1253–1278.
47. Carroll, J. D.; Chang, J.-J. Analysis of Individual Differences in Multidimensional Scaling Via an n-Way Generalization of Eckart-Young Decomposition. *Psychometrika* **1970**, *35*(3), 283–319.
48. Tucker, L. Some Mathematical Notes on Three-Mode Factor Analysis. *Psychometrika* **1966**, *31*, 279–311.
49. Khoromskij, B. N.; Khoromskaia, V.; Chinnamsetty, S. R.; Flad, H. J. Tensor Decomposition in Electronic Structure Calculations on 3D Cartesian Grids. *J. Comput. Phys.* **2009**, *228*(16), 5749–5762.
50. Hirata, S. Symbolic Algebra in Quantum Chemistry. *Theor. Chem. Acc. Theory Comput. Model.* 2006, *116*(1-3), 2–17.
51. Szabo, A.; Ostlund, N. S. *Modern Quantum Chemistry: Introduction to Advanced Electronic Structure Theory*. Dover, 1989.
52. Harrison, R. J.; Beylkin, G.; Bischoff, F. A.; Calvin, J. A.; Fann, G. I.; Fosso-Tande, J.; Galindo, D.; Hammond, J. R.; Hartman-Baker, R.; Hill, J. C.; Jia, J.; Kottmann, J. S.; Yvonne Ou, M.-J.; Pei, J.; Ratcliff, L. E.; Reuter, M. G.; Richie-Halford, A. C.; Romero, N. A.; Sekino, H.; Shelton, W. A.; Sundahl, B. E.; Thornton, W. S.; Valeev, E. F.; Vzquez-Mayagoitia, A.; Vence, N.; Yanai, T.; Yokoi, Y. MADNESS: A Multiresolution, Adaptive Numerical Environment for Scientific Simulation. *SIAM J. Sci. Comput.* **2016**, *38*(5), S123–S142.
53. Bischoff, F. A.; Valeev, E. F. Low-order Tensor Approximations for Electronic Wave Functions: Hartree-Fock Method With Guaranteed Precision. *J. Chem. Phys.* **2011**, *134*(10), 104104.

54. Harrison, R. J. Krylov Subspace Accelerated Inexact Newton Method for Linear and Nonlinear Equations. *J. Comput. Chem.* **2002**, *25*(3), 328–334.
55. Lehtola, S.; Steigemann, C.; Oliveira, M. J.; Marques, M. A. Recent Developments in LIBXC—A Comprehensive Library of Functionals for Density Functional Theory. *SoftwareX* **2018**, *7*, 1–5.
56. Kutzelnigg, W. R12-Dependent Terms in the Wave-function as Closed Sums of Partial-Wave Amplitudes for Large I. *Theor. Chim. Acta* **1985**, *68*(6), 445–469.
57. Klopper, W.; Manby, F. R.; Ten-no, S.; Valeev, E. F. R12 Methods in Explicitly Correlated Molecular Electronic Structure Theory. *Int. Rev. Phys. Chem.* **2006**, *25*(3), 427–468.
58. Kong, L.; Bischoff, F. A.; Valeev, E. F. Explicitly Correlated R12/F12 Methods for Electronic Structure. *Chem. Rev.* **2012**, *112*(1), 75–107.
59. Kato, T. On the Eigenfunctions of Many-particle Systems in Quantum Mechanics. *Commun. Pure Appl. Math.* 1957, *10*(2), 151–177.
60. Conroy, H. Molecular Schrodinger Equation. I. One-Electron Solutions. *J. Chem. Phys.* **1964**, *41*(5), 1327.
61. Seelig, F. F. Numerische Lsung der 2-und 3-dimensionalen Schrödinger-Gleichung für beliebige Molekülpotentiale durch iterative Variation numerischer Testfunktionen mit einem Digitalrechner. II. *Z. Naturforsch. A* **1966**, *21*, 1358.
62. Boys, S. F.; Handy, N. The Determination of Energies and Wavefunctions With Full Electronic Correlation. *Proc. R. Soc. Lond. A* **1969**, *310*(1500), 43–61.
63. Bischoff, F. A. Regularizing the Molecular Potential in Electronic Structure Calculations. I. SCF Methods. *J. Chem. Phys.* **2014**, *141*(18), 184105.
64. Handy, N. C.; Marron, M. T.; Silverstone, H. J. Long-Range Behavior of Hartree-Fock Orbitals. *Phys. Rev.* **1969**, *180*(1), 45–48.
65. Almlof, J.; Taylor, P. R. Molecular Properties From Perturbation Theory: A Unified Treatment of Energy Derivatives. *Int. J. Quantum Chem.* **1985**, *27*(6), 743–768.
66. Hellmann, H. Zur Rolle der kinetischen Elektronenenergie für die zwischenatomaren Krfte. *Z. Phys.* **1933**, *85*(3-4), 180–190.
67. Coulson, C. A. Brillouins Theorem and the Hellmann-Feynman Theorem for Hartree-Fock Wave Functions. *Mol. Phys.* **1971**, *20*(4), 687–694.
68. Yanai, T.; Fann, G. I.; Gan, Z.; Harrison, R. J.; Beylkin, G. Multiresolution Quantum Chemistry in Multiwavelet Bases: Analytic Derivatives for Hartree-Fock and Density Functional Theory. *J. Chem. Phys.* **2004**, *121*(7), 2866–2876.
69. Bischoff, F. A. Analytic Second Nuclear Derivatives of Hartree-Fock and DFT Using Multi-Resolution Analysis. *J. Chem. Phys.* **2017**, *146*(12), 124126.
70. Yamaguchi, Y.; Frisch, M.; Gaw, J.; Schaefer, H. F.; Binkley, J. S. Analytic Evaluation and Basis Set Dependence of Intensities of Infrared-Spectra. *J. Chem. Phys.* **1986**, *84*(4), 2262–2278.
71. Neugebauer, J.; Reiher, M.; Kind, C.; Hess, B. A. Quantum Chemical Calculation of Vibrational Spectra of Large Molecules -Raman and IR Spectra for Buckminsterfullerene. *J. Comput. Chem.* **2002**, *23*(9), 895–910.
72. Jayatilaka, D.; Maslen, P. E.; Amos, R. D.; Handy, N. C. Higher Analytic Derivatives. *Mol. Phys.* **1992**, *75*(2), 271–291.
73. Jensen, S. R.; Fl, T.; Jonsson, D.; Monstad, R. S.; Ruud, K.; Frediani, L. Magnetic Properties With Multiwavelets and DFT: The Complete Basis Set Limit Achieved. *Phys. Chem. Chem. Phys.* 2016, *18*(31), 21145–21161.
74. Andrade, X.; Botti, S.; Marques, M. A. L.; Rubio, A. Time-dependent Density Functional Theory Scheme for Efficient Calculations of Dynamic (Hyper)polarizabilities. *J. Chem. Phys.* **2007**, *126*(18), 184106.
75. Mahan, G. D. Modified Sternheimer Equation for Polarizability. *Phys. Rev. A* **1980**, *22*(5), 1780–1785.

76. Sekino, H.; Maeda, Y.; Yanai, T.; Harrison, R. J. Basis Set Limit Hartree-Fock and Density Functional Theory Response Property Evaluation by Multiresolution Multiwavelet Basis. *J. Chem. Phys.* **2008**, *129*(3), 034111.
77. Yanai, T.; Harrison, R. J.; Handy, N. C. Multiresolution Quantum Chemistry in Multiwavelet Bases: Time-Dependent Density Functional Theory With Asymptotically Corrected Potentials in Local Density and Generalized Gradient Approximations. *Mol. Phys.* **2005**, *103*(2–3), 413–424.
78. Shavitt, I.; Bartlett, R. J. *Many-body Methods in Chemistry and Physics: MBPT and Coupled-Cluster Theory*; Cambridge University Press, 2009.
79. Ten-no, S. Initiation of Explicitly Correlated Slater-type Geminal Theory. *Chem. Phys. Lett.* **2004**, *398*(1-3), 56–61.
80. Christiansen, O.; Jorgensen, P.; Httig, C. Response Functions from Fourier Component Variational Perturbation Theory Applied to a Time-averaged Quasienergy. *Int. J. Quantum Chem.* **1998**, *68*(1), 1–52.
81. Di Remigio, R.; Steindal, A. H.; Mozgawa, K.; Weijo, V.; Cao, H.; Frediani, L. PCMSolver: An Opensource Library for Solvation Modeling. *Int. J. Quantum Chem.* **2019**, *119*(1), e25685.
82. Hfener, S. Coupled-cluster Frozen-density Embedding Using Resolution of the Identity Methods. *J. Comput. Chem.* **2014**, *35*(23), 1716–1724.
83. Bischoff, F. A. Regularizing the Molecular Potential in Electronic Structure Calculations. II. Many-Body Methods. *J. Chem. Phys.* **2014**, *141*(18), 184106.

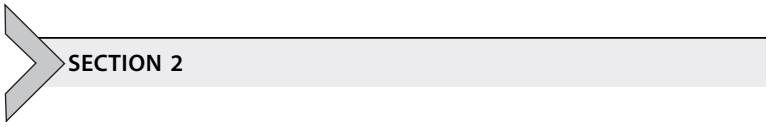

Methodology

This section is devoted to state of the art mathematical innovations, necessary to unify the choice of basis sets (Aquilanti et al.), improve wave-functions (Randazzo and Ancarani, Gebremedhin et al.) and cater for the notorious electron-nucleus cusp (Loos et al.)

This page intentionally left blank

CHAPTER TWO

Hypergeometric orthogonal polynomials as expansion basis sets for atomic and molecular orbitals: The Jacobi ladder

Cecilia Coletti[a], **Vincenzo Aquilanti**[b,*], **Federico Palazzetti**[b]
[a]Dipartimento di Farmacia, Università G. d'Annunzio, Chieti, Italy
[b]Dipartimento di Chimica, Biologia e Biotecnologie, Università di Perugia, Perugia, Italy
[1]Corresponding author: e-mail address: vincenzoaquilanti@yahoo.it

Contents

Abstract

In this survey we account for basic mathematical ingredients for dealing with quantum chemical problems. We focus on comprehensive previous work (Coletti et al., 2013, pp. 74–127, Ref. 1) documenting relationships with the Askey scheme, a classification of the orthogonal polynomials sets of hypergeometric type. A reduction of the scheme is proposed individuating nine fundamental functional sets which have their counterparts in quantum mechanics; they occur in the general Kepler–Coulomb problem: as well known basis sets for expansions of orbitals in quantum chemistry and in the treatment of specific atomic and molecular applications. A novelty of the approach, with respect to this extensively covered topic, is the establishment of this representation for Kravchuk polynomials, on the mathematical side and, correspondingly, of the spherical

Advances in Quantum Chemistry, Volume 79
ISSN 0065-3276
https://doi.org/10.1016/bs.aiq.2019.05.002

top wavefunctions on the physical side: the latter are explicitly connected with the Wigner's rotation matrix of angular momentum theory. Novel presentations of the Askey-type hierarchy of hypergeometrical orthonormal basis sets relevant in quantum mechanics and the relationships connecting them are established by powerful tools: from the mathematical viewpoint, the Askey duality and asymptotic analysis; from a physical viewpoint, the symmetry by transposition and semiclassical limits. A new three-by-three matrix visualization illustrates the set of correspondences to assist further work on the path connecting classical and quantum physics and discrete and continuous mathematics that is presented elsewhere (Coletti et al., 2019, Ref. 46). This is pictured as a bridge where Racah polynomials and harmonic oscillator wavefunctions are the corner stones, while the rotation matrix of Wigner is the keystone. Here, the path is illustrated as the steps of a stairway that we define as the Jacobi ladder, where going up and down is insightful for applications. Extension to the full Askey scheme, object of future work, is briefly noted: some reference is made to our recent progress in spherical to hyperspherical manifold representations involving the q-scheme of Askey and related orthogonal polynomials as possible orthonormal basis sets in quantum mechanics.

1. Introduction

As extensively discussed in a previous essay,[1] our investigation focusses on exploiting the connection between atomic and molecular orbitals to be used as basis sets in applied quantum chemistry and those advances in the mathematics of special functions and orthogonal polynomials, not commonly explicitly intercorrelated in the numerous expositions of the quantum theory of angular momentum.[2,3]

A survey of the mathematical ingredients that were encountered in Ref. 1, the special functions and in particular the orthogonal polynomials, is summarized in Table 1. In this list of functions, we have included those that are defined on discrete grids and others that span ranges of continuous variables. In discrete approaches, the Sturm–Liouville theory for the differential equations to which Schrödinger equations belong has its counterpart in the theory of difference equations, recurrence relationships and Jacobi (tridiagonal and symmetric) matrices. According to Favard's theorem, a recursion three-term relationship defines an orthogonal polynomial set and plays the role of a difference equation. We will encounter such relationships in the following sections.

Elsewhere[4] within the ample realm of hypergeometric and generalized hypergeometric functions, that practically covers most of solvable problems, even beyond quantum mechanics, an exploratory treatment was presented of the q-extension of the hypergeometric polynomial framework to cover

Table 1 The nine polynomial sets: Nomenclature and properties.

	Polynomial	Symbol	3 × 3 Matrix element[a]	Series[b]	*N*
I	Racah	Ra	11	R	4
II	Dual Hahn	Dh	21	R	3
III	Hahn	Ha	12	H	3
IV	Meixner	Me	13	H	2
V	Kravchuk	Kr	22	R	2
VI	Jacobi	Ja	31	C	2
VII	Charlier	Ch	32	H	1
VIII	Laguerre	La	23	C	1
IX	Hermite	He	33	C	0

[a]These labels correspond to the matrix arrangement illustrated by the graphs in Fig. 2, first column.
[b]Letter C indicates the classical series comprising the Hermite, the Laguerre, and the Jacobi polynomials ($P_n(x)$ *N*), where *N* is the number of parameters, respectively $N = 0$, 1 and 2; *n* is the order of polynomials (an integer) and *x* denote the continuous variable. For the Hahn series H: *N* is 2 for Meixner and Kravchuk, and 3 for Hahn, the variable spans a discrete grid, here quadratic.[10] The Racah series denoted by R has quadratic grids for both order and variable for the self-dual Racah polynomials; linear and quadratic grids for dual Hahn; linear grids for both order and variable for the self-dual Kravchuk polynomial.

non-Euclidean (elliptic and hyperbolic) manifolds. In other cases, e.g., spheroidal and sphero-elliptic Sturmians, explicit hypergeometric (i.e., finite series) solutions: their properties and use were covered in previous and current investigations[1,2,5,6] beyond the hypergeometric scheme.

Purpose of the present account is to put into a general perspective the theory of the basis sets for solving quantum mechanical problems, specifically those of atomic and molecular physics and of quantum chemistry, governed by the Schrödinger equation. In general, in the time-independent formulation, problems are multidimensional and tackled by expansion of products of one variable functions: the Schrödinger equation is a second order differential equation, its eigenfunctions span Hilbert spaces that can be mapped into remarkably standard manifolds. The underlying theory is a two-centuries-old theory, arising essentially through the work of Jacobi and other great mathematicians: they provided the concept of orthogonal polynomials sets. As expansion basis sets, these polynomials, when properly normalized, constitute most of the complete sets to expand, for example as far quantum chemistry is concerned, atomic orbitals, or in the case of

molecules, the orthogonal polynomials centered in different space points. We add that, when a molecular system is under the effect of fields, one has the possibility of expanding the fields themselves in the same sets of orthogonal polynomials making the calculations of all the involved integrals analytical and so presumably advantageous for computational progress.

The main mathematical ideas actually were developed also in connection with one of the pillars of theoretical physics: the quantum theory of angular momentum. The group theoretical construction leads to discrete sets of orthogonal objects, differently called vector coupling or recoupling coefficients, or, in equivalent language, 3*j*, 6*j*,…, n*j* symbols of angular momentum theory. The connection between the two areas became clear in the 1930s when the one-century old Jacobi theory of orthogonal polynomials reached its maturity.[7,8] At that point it was clear that Jacobi polynomials play a leading role and all other orthogonal polynomials, depending on a smaller number of parameters, could be arranged in a way that one could in essence solve all the problems in second order ordinary differential equations, which could be expressed through the Gaussian hypergeometric series.

The computability of these polynomials as terminating series involving a few parameters, with analytically well-defined properties, was thus completed and into play entered then: the theory of hypergeometric functions, the theory of orthogonal polynomials and the quantum theory of angular momentum. Striking interconnections were emerging since the late 1940s, when it was discovered that the Clebsch–Gordan coefficients of group representation theory and that of angular momentum essentially coincided with the set of discrete orthogonal polynomials named after Hahn. When further investigation demonstrated that the most important ingredients of the theory of angular momentum, the Racah or 6*j* coefficients, could also be expressed as orthogonal polynomials, this led to the discovery of Racah polynomials, so aptly denominated, that were going to occupy the upper level of the Askey scheme for orthogonal polynomials of discrete variables.[9] Later, the work of many investigators compacted on one side, in Russia by Nikiforov et al.[10] and, on the other, in the United States by Askey and Wilson,[11] leading to the possibility of visually arranging the knowledge at the time which is still our daily vision in the applications: the Askey scheme of hypergeometrical polynomials (a part of it is sketched in Fig. 1). Though there were other approaches, a dense compilation of formulas appeared as a report in 1998 by Koekoek and Swarttouw.[12] The book by Varshalovich and collaborators[13] summarized most of what is needed in quantum angular momentum theory, as firmly built by the school of Yutsis.[14]

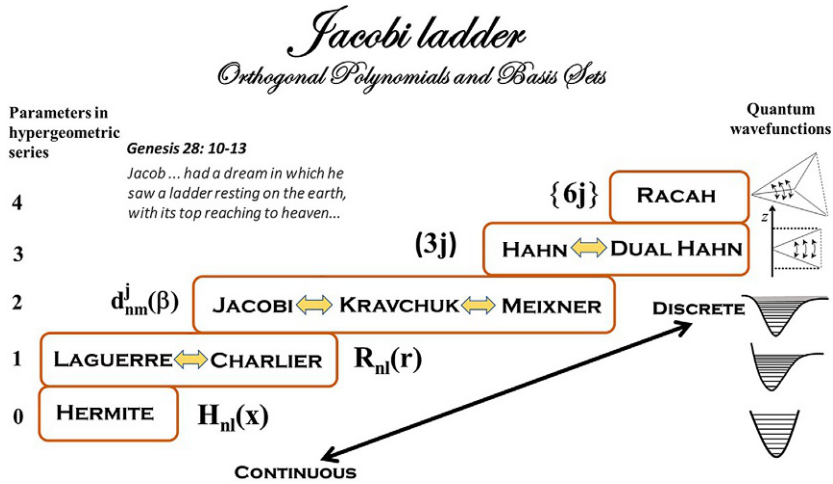

Fig. 1 A graphical summary, to be compared to the corresponding fig. 1 in Ref. 1. Important differences are the arrangement as a staircase, suggesting the biblical quotation. Details on the connections and emphasis on the central role for the Kravchuk polynomial is given in the text. The last column indicates correspondence with quantum mechanical systems.

Fig. 1 visually gives a graphical impression of the arrangement of the polynomial sets as a ladder: the level corresponds to the number of parameters in the defining hypergeometric functions,[8] those at the same level are equivalent: they are connected by duality relationships, and differ for the role played by "variable" and "degree" parameters, i.e., for the corresponding three-terms recurrence relationship and finite difference equations.

In the following section we proceed by exploring the systematic occurrence of orthogonal polynomials from the harmonic oscillator through the theory of hydrogen atom in mathematically increasing dimensions; where recent advances have involved hypergeometric approaches and specifically Sturmian basis sets in momentum and configuration spaces.

2. The nine stepping stones: Spherical and hyperspherical harmonics

The various steps in this search start from what is adequately covered by the main textbooks on the subject. The present discussion should be followed by consulting Table 1 and Fig. 2. As already noted, most textbooks

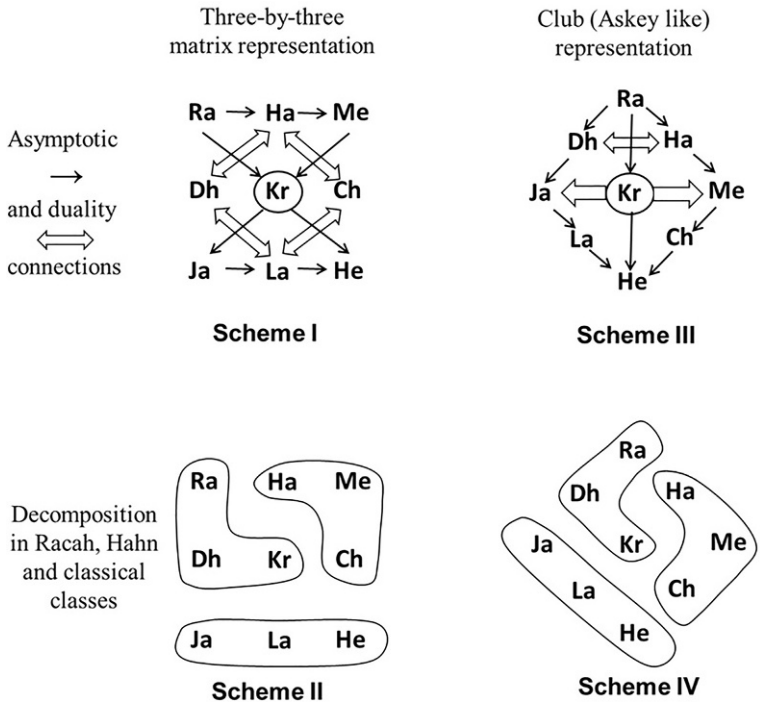

Fig. 2 The 3 × 3 matrix representation (first column) and the representation more similar to the conventional Askey scheme (second column, but with the positions of Kravchuk and Jacobi polynomials interchanged).

treat separately the various subjects that it is our purpose to connect. The developments of orthogonal polynomials of hypergeometrical type on one side and of their explicit relationships with the group theory representation[15] on the other side, eventually lead to the construction of harmonics and hyperspherical harmonics[16] that have been accounted for extensively in the Nikiforov textbook[10] and in various previous articles.[17–19]

Let us then summarize the main finding, namely, that the functions which appear in the construction are essentially those that, from a Lie group theory viewpoint, "quantize" spherical and hyperspherical manifolds. Our preceding account[1] gives the details at a state-of-the-art as we perceived it a few years ago. Functions involved in the construction of harmonics which are by definition sets of orthonormalizable functions are arranged from those that "quantize" the circle, namely $\sin(m\phi)$ or $\cos(m\phi)$, with $m = \ldots, -2, -1, 0, +1, +2, \ldots$ and ϕ spans a circle by 2π. Such functions are related to Chebyshev polynomials. When one considers spheres and

hyperspheres one gets sequences of sets of Legendre and Gegenbauer polynomials. All these are basically special cases of Jacobi polynomials obtained when some of the parameters take specific values.[1,3,20] The work developed subsequently has tried to establish explicit relationships between hyperspherical harmonics and atomic and molecular orbitals. It was soon found out that there was the possibility of building orthonormal basis sets. In addition these sets had the property of being complete, so to span the manifolds on which the functions were defined and with very important analytical properties; furthermore, they are computable in closed form. Among the main properties, they were shown to overcome some of the shortcomings (divergencies and cusps around nuclei and incorrect long range behavior) in a fully analytically motivated way, even though in earlier applications not enjoying sufficiently fast convergence properties.[21] As soon as the possibility was advanced of enjoying the fact that these sets of functions could be easily transformed into alternative forms, the search started for the best way to exploit them in a fruitful direction.[1,3,6,20,22]

Major effort was in parallel exerted on the construction of atomic hydrogenic orbitals in increasing dimensions[20] which, although not immediately important physically, were later supposed to provide orbitals to be used in many-body problems where sets of functions of increasing dimensionality might be needed. This search was accompanied by additional work on the basic solvable problem in molecular structure, that of the H_2^+ ion[23] as an example of a two-centers quantum mechanical problem, and an archetype of molecular orbitals.

Another key perspective looks for the physical application to quantum mechanical problems: the relation between configuration and momentum spaces offers a very advantageous paradigm where, through integral transforms (in this case Fourier transforms), one can exploit the peculiar requirements of specific systems to be best suited for treatment in momentum rather than in configuration space or *vice versa*.

Orthonormality and suitability of these functions as basis sets for the representation of group theory offer the further advantage that the Lie groups allow alternative reduction schemes, which, in turn, are sources of alternative basis sets interconnected by well-defined orthogonal transformations. The main striking example is an outcome of Fock's projection of the hydrogen atom onto a hypersphere in a four-dimensional space: this leads to a full classification of the hyperspherical harmonics involved as full solutions to the problem[1,3,6,22]. Additionally, as mentioned before, by Fourier transformation, one can also classify the eigenfunctions for hydrogen

atom in momentum space.[1,3,6,22] Hyperspherical harmonics, their transformations, their relationships with orthogonal polynomials of the hypergeometric type provide alternatives interconnected by orthogonal transformations, each transformation inserting or substituting labels which are associated with the order of the polynomials (a discrete number) and the number of nodes of the wavefunctions. These transformations, in the quantum mechanical application for the hydrogen atom, connect for instance the sequence n, l, m,[24,25] arising naturally via separation in polar variables, to the sequence n_1, n_2, m, obtained by the separation in parabolic variables.[20,23]

On the other hand orthogonal transformations corresponding to different reduction schemes classify the type of changes in alternative sets of separable variables: for the application of these basis sets a great flexibility is obtained in the search of those suitable for physically motivated situations (like atoms in fields or orbitals on many centers). Here the quantum numbers introduced by fully defined matrix elements permit manipulations to be exploited at the best: from a mathematical viewpoint through group theory, from a physical viewpoint through combination rules for the addition, and recoupling of angular momenta.

3. The classical series

3.1 The first angular stone: Hermite polynomials

As is well known, in early quantum mechanical applications to chemistry, hydrogen-like orbitals and their modifications, i.e., Slater type orbitals, were introduced.[26] Recently, alternatives are vigorously pursued and variants shown effective.[27–30] Quantum mechanical problems may be solved by proposing a linear combination of hydrogen-like orbitals and applying a variational approach to obtain the best coefficients that minimize the energy. This procedure may be slowly convergent and typically requires storage of large matrices and long computing diagonalization times. This led to the introduction of simpler basis sets useful to overcome these bottlenecks and the most popular was the introduction of Gaussian basis sets, in a sense a simplification of the solution of the harmonic oscillator in terms of Hermite polynomials.

This gives us the clue to focus on Hermite polynomials, $H_n(x)$, enjoying Askey Nikiforov duality to be exemplified next. As known, Hermite polynomials are the simplest hypergeometrical polynomials solving the Schrödinger equation for the harmonic oscillator and obtaining wavefunctions pertaining to the equally spaced energy levels. We encounter here a number n which

spans an infinite discrete manifold of those supported by a harmonic well. The wavefunctions are oscillatory in character as a function of a continuous variable, exhibiting a number of nodes increasing as the energy level increases. Let n define the energy and the order of the polynomials, while the characteristic points, for example the zeroes along the variable x, span discrete points on the continuous x line. The quantities n and x play a key feature in the modern view of orthogonal polynomials: they enjoy a duality and this is the simplest example which can be found in the Nikiforov work and in the Askey scheme. Hermite polynomials occupy then an important position in the orthogonal polynomials as studied by mathematicians in the XIX and early XX centuries. Askey duality was not amply considered until the middle of the XX century, although it is well known that it represents the reciprocity between configuration and momentum space, as we mentioned before and will exemplify in some detail below.

Mathematically, the important observation regarding Hermite polynomials is that they are solutions of a second order differential equation. Here x is the variable and n is the index of the eigenvalues. Well known is a reciprocal property: the Hermite polynomials, like all other orthogonal polynomials according to the inverse of Favard's theorem, are also solutions of a three-term difference equation which acts on a variable given as a discrete set. In the case of Hermite polynomials, the difference equation is defined on the grid labeled by n. Here are the two equations[12]:

1. Recurrence relation:

$$H_{n+1}(x) - 2xH_n(x) + 2nH_{n-1}(x) = 0 \tag{1}$$

2. Differential equation:

$$y''(x) - 2xy'(x) + 2ny(x) = 0, \qquad y(x) = H_n(x) \tag{2}$$

Eqs. (1) and (2) have remarkably identical coefficients: the above is the simplest manifestation of (Askey and Nikiforov) duality.

The function identity $y(x) = H_n(x)$, when multiplied by $\exp(-x^2)$ solves a one-dimensional Schrödinger equation, that can be recognized as that of the harmonic oscillator, namely that for a potential quadratic in x and eigenvalues (energies) equally spaced, ordered by the quantum number n that also counts the number of nodes.[8] These aspects exemplify a feature typical of the classical series, and therefore also of the Laguerre polynomials and Jacobi polynomials, to be considered below.

It is worth noting that the solution of Schrödinger equation in configuration space for the two-dimensional hydrogen atom in parabolic coordinates λ_1 and λ_2, i.e., the two-dimensional Sturmian basis set in parabolic coordinates, is essentially a product over two Hermite polynomials $H_{n_1}(\lambda_1) \cdot H_{n_2}(\lambda_2)$ where n_1 and n_2 are the parabolic quantum numbers (eq. (3) in Ref. 1).

3.2 Laguerre polynomials and the Bohr atom

Let us now consider the radial eigenfunctions of the hydrogen atom. When in configuration 3D space separation is carried out in polar coordinates, we encounter Laguerre polynomials, $L_n^{(\alpha)}(x)$ (note that in Fig. 1 they appear as $R_{n,l}(r)$ to emphasize their connection as the radial part of hydrogenic (or Sturmian) basis sets, see the following). Laguerre polynomials enjoy similarities and differences with Hermite polynomials.

Let us denote the variable corresponding to x as r (with respect to x, r now goes in the semidefinite range $[0, +\infty)$ to be contrasted with the $(-\infty, +\infty)$ of x). The counting of nodes, therefore the order of Laguerre polynomials, is denoted by n and the corresponding eigenvalues span a non-equidistant sequence of levels that pile up near the ionization limit, tending to be an infinite but being denser and denser as l assumes higher and higher levels. An additional parameter of Laguerre polynomials is that corresponding to the orbital quantum number l, limited to be less than n: the mathematical notation explicitly indicates that from a physical point of view we are dealing with the orbital quantum number n, being the principal quantum number.

If we consider mapping the r variable into a range going from 0 to $-\infty$ and approximate the long range potential as a harmonic one, it is physically evident that the anharmonic Coulomb potential tends to harmonic: this can be expressed by an explicit asymptotic relationship.

Similarly to the Hermite case, Laguerre polynomials enjoy a differential equation: the well known application is, as mentioned before, to the hydrogen Schrödinger second order differential equation with a Coulomb type potential. Laguerre polynomials are the radial part of the eigensolutions whereas the eigenvalues labeled by the principal quantum number of Bohr (i.e., $R_{n,l}(r) = L_{n-l-1}^{(2l+1)}(r)$, apart from a phase factor in polar coordinates) the energies of hydrogen-like atoms. Note again that in the case of parabolic Sturmians in the physical three-dimensional space (and in spaces of higher dimensions) the radial part of the wavefunction in λ_1 and λ_2 is given as a

product of Laguerre polynomials (see eqs. (12) and (39) in Ref. 1 for the d-dimensional and three-dimensional spaces, respectively).

For Laguerre polynomials, consider the three-term recursion relationship in n obeyed by $L_n(x)$[12]:

$$(n+1)L^{\alpha}_{n+1}(x) - (2n+\alpha+1-x)L^{\alpha}_{n}(x) + (n+\alpha)L^{\alpha}_{n-1}(x) = 0 \qquad (3)$$

and the second order differential equation, which is of hypergeometric type, contains one parameter more than for Hermite polynomials case[12]:

$$xy''(x) + (\alpha+1-x)y'(x) + y(x) = 0, \qquad y(x) = L^{\alpha}_{n}(x). \qquad (4)$$

Exchange of roles leads to Charlier polynomials, unrecognized in applications as those to be correctly considered in the normalization of Sturmians.

These polynomials are also related to those of anharmonic Morse-like oscillators.

3.3 Jacobi polynomials

The construction then culminates by introducing a further parameter and meets the full Gauss hypergeometric function, interpreted as an eigenvalue equation leading to Jacobi polynomials. These polynomials have thus a higher position with respect to Laguerre polynomials which can be obtained back by an asymptotic procedure. Analytical manipulation of the coefficients characterizing the Jacobi polynomials yields the most general of continuous type polynomials that allow the analytical solution of Schrödinger equation for the hydrogen atom.[1]

Since Legendre and Gegenbauer polynomial sets, as well as those of Chebyshev, are particular cases of Jacobi polynomials, they permit construction of spherical and hyperspherical harmonics. The mathematical apparatus for the expression of hydrogenic orbitals, including Sturmian orbitals,[1] is thus completed.

4. The second angular stone and the construction

4.1 Spin networks and polynomials

While these developments complete the list of basis sets of the theory of orthogonal polynomials of hypergeometric type, including the most general ones, around the middle of 19th century, important developments were propitiated by quantum mechanics, in particular thanks to angular momentum theory and due essentially to Wigner and Racah.[15] More recently the

designation "spin networks" has been adopted and popularized mainly in quantum gravity contexts.[17,25]

As noted in Section 1, Hahn started studying and putting on a firm basis the possibility that orthogonal polynomials could also be defined on discrete manifolds. Consider in Hermite polynomials the variable x that goes from $-\infty$ to $+\infty$ and the variable r in Laguerre polynomials that covers the interval from 0 to $+\infty$. If discrete variable x is allowed to be constrained to have explicitly specific values on a grid of points, polynomials are obtained obeying second order difference recursion relationships, which serve to define discrete polynomials on a uniform grid. Furthermore, other polynomials connected by Askey duality were similarly defined, where the grid on discretizing the variable was instead taken as quadratic. In the theory of hydrogen atom, the m quantum number that spans integers …, −2, −1, 0, +1, +2, … exemplifies the uniform grid; the l quantum number, whose integer values proceeds in steps of $l(l + 1)$ is instead an example of a quadratic grid.

From papers appeared in the middle of the 1940s, it was soon realized that these objects were, in terms of polynomials, the mathematical counterparts of Wigner and Racah coefficients who introduced what are known as vector coupling and recoupling coefficients or symbols (3j's, 6j's, etc.). Since these coefficients are the elements of matrices connecting alternative quantum mechanical representations of the vector coupling they are elements of orthogonal transformations. From these connections, it emerges that Askey duality when applied to Jacobi, Laguerre, or Hermite polynomials corresponds to the exchange of labeling of rows and columns of orthogonal matrices in angular momentum theory. The search then started toward generalizations and the completeness of the classification.

4.2 The Hahn and Racah series

The Clebsch–Gordan or 3j coefficients are labeled by the quadratic grid in j (explicitly in $j(j + 1)$) and by the projection quantum number m which goes from negative to positive values according to a discrete equally spaced grid. Again the physical motivation as eigenfunction of an angular momentum operator which corresponds to that of a polynomial obeying a three-term recursion relationship, clarifies the way that the Hahn and dual Hahn polynomials are related by dualization: when the matrix of vector coupling coefficients, corresponding to rows running along the allowed values of j and columns corresponding to ranges of the allowed values for the projections, dualization amounts to its matrix transposition.

We reach finally the top level of a construction (started from the harmonic oscillator, progressing by considering polynomials) which the

mathematicians worked out in analogy with the recoupling coefficients of Racah that can also be written as 6*j* Wigner coefficients.

Racah coefficients serve to connect angular momenta through two alternative schemes for coupling three angular momenta: they can be considered as matrices labeled by the intermediate values, e.g., j_{12} and j_{23}, finally to be coupled to the final sum of the three, say j_4.

It is clear that the Racah coefficients play a top role in the scheme, the highest point in the construction. They are labeled by discrete variables of the quadratic type (j_{12} and j_{23}) and obey each a difference equation, formally identical, so that the Racah coefficients are dual in j_{12} and j_{23}.

From well-defined mathematical operations that were developed in parallel and with interchanges from Racah coefficients and polynomials, one could obtain by asymptotic theory all the polynomials that have been encountered so far, whereas, from a physical viewpoint, the limit is approximately defined as semiclassical. It is then finally recognized that the procedure we have been following is mathematically a process of additional sets of discretization and, physically, a progressive sequence of quantizations. We will turn now to the next step, where we will explicitly exhibit the construction in a visual way, useful for further comments and generalizations.

5. The reduced Askey scheme, up and down the ladder

The presentation of the previous section was centered on the progress due to mathematicians of the classical theory of orthogonal polynomials along a ladder from the Hermite polynomials[9], through Laguerre polynomials, up to the Jacobi polynomials; above that level the construction proceeded mainly thanks to group theoretical development by Wigner and Racah, who formulated them by founding the quantum mechanical theory of angular momentum.

The procedure going up is that of progressive discretization, while the opposite procedure is that of an asymptotic analysis going from discrete sets to the continuum. It is known that while the first involves arbitrariness, the asymptotics or semiclassical one is definitely more robust and can be formulated in a more rigorous way. The full classification of the many sets of polynomials that now include both the continuum and discrete type is specifically the work of the Russian school of Nikiforov[10] and of the American mathematician Askey,[11,12] as mentioned in Section 1. The connection between this classification and angular momentum theory is essentially due to Nikiforov school and in subsequent work including that

by Suslov and others[10], and has been a subject under focus in our already cited previous investigations. The concern here is going to present in a compact way additional remarks on the classification of hypergeometric polynomials alongside the theory of quantum angular momentum.

5.1 The central triad

The third level of the reduced Askey scheme (Fig. 2, second column), or the antidiagonal of the matrix representation in its most reduced form (Fig. 1, first column), involves three of the nine "players" in the team, and is composed by Jacobi polynomials, their duals in the Askey scheme, the Meixner polynomials, and the central pivot of the game, the Kravchuk polynomials. It is interesting to deal in some details with these three polynomial sets because they contain *in nuce* most of the features which are common to the other elements of the scheme. First of all let us consider the hypergeometric aspects. Basically, they are given as terminating series: the three polynomials can be written explicitly as essentially the hypergeometric series ${}_2F_1$ of Gauss. As it is well known this epoch-making discovery introduced a terminating series which by specification of parameters and by limiting procedure gave most of the special functions of mathematical physics. The relationship with orthogonal polynomials arises when one of the entries of the arguments of hypergeometric function is a negative integer number, then this integer is the order of the polynomial. In particular the important Jacobi polynomials are included. The Askey duality is simply an interchange (analogous to the pair of Eq. (1) and (2) for the Hermite case) of the order of polynomials with the continuous range of variable: Meixner in 1934 introduced this set of polynomials that represented one of the main triggers leading to the definitive formulation of the scheme. Thus, we have completed, from a mathematical viewpoint, the three lower levels of the scheme.

Concerning the levels above the third, mathematicians, as mentioned before, were motivated by the physicists Wigner and Racah essential contributions in angular momentum theory for the parallel introduction of Hahn and Racah polynomials at fourth and fifth levels, respectively.

5.2 The Wigner $d^j_{mm'}(\beta)$ matrix elements

The three elements of the sets of orthogonal polynomials find their important unique realization in a key object of angular momentum theory, the Wigner d matrix, $d^j_{mm'}(\beta)$, which is related to the three sets of polynomials at the third level in the following way. The j parameter plays the role of the

order in the corresponding Jacobi polynomial, while the argument, the angle β, is in strict correlation with the variable in the Jacobi polynomial set; this variable is continuous and spans a finite range. Its dual, the Meixner polynomial set, is put into correspondence with the exchange of the role of x, β, and j quantities. The d matrix is self-dual in n, m, and dual in m'. As a matter of fact its role in angular momentum theory (see the dedicated chapter in Varshalovich[13]) proves that for given values of j and as a function of β the reduced d matrix has rows and columns labeled by m and m'; being an orthogonal matrix, its self-duality can be clearly understood as the exchange of rows and columns of the matrix.

In view of the central role in the whole construction, we summarize properties of the Wigner rotation matrix $d^j_{mm'}(\beta)$.[13] Due to relationships with the Jacobi and Meixner polynomials and then to spherical and hyperspherical harmonics this serves as exemplary of general characterizing properties of these sets of functions.

1. Three-term recursion relationship in m/m' in the matrix, as listed, e.g., by Varshalovic[13] (self-dual, note symmetry for exchange of rows and columns)

$$\frac{-m-m'\cos\beta}{\sin\beta}d^j_{m,m'}(\beta)=\frac{1}{2}\Big(\sqrt{(j+m')(j-m'+1)}d^j_{m,m'-1}(\beta) +\sqrt{(j-m')(j+m'+1)}d^j_{m,m'+1}(\beta)\Big) \tag{5}$$

2. Recursion in j, $0\le j\le\infty$ (a finite difference equation, specialized for $\alpha=\gamma=0$ from Ref. 13)

$$\cos\beta\cdot d^j_{m,m'}(\beta)=\frac{\sqrt{(j^2-m^2)(j^2-m'^2)}}{j(2j+1)}d^{j-1}_{m,m'}(\beta)+\frac{mm'}{j(j+1)}d^j_{m,m'}(\beta) +\frac{\sqrt{[(j+1)^2-m^2][(j+1)^2-m'^2]}}{(j+1)(2j+1)}d^{j+1}_{m,m'+1}(\beta) \tag{6}$$

3. Differential equation (it can be given in various forms, Gauss Hypergeometric equation for ${}_2F_1$, Edmond's equation for spherical top or equivalently to Schrödinger equation for an anharmonic Eckart oscillator)

$$-\left[\frac{1}{\sin\beta}\frac{\partial}{\partial\beta}\left(\sin\beta\frac{\partial}{\partial\beta}\right)+\frac{m^2-2mm'\cos\beta-m'^2}{\sin^2\beta}\right]d^j_{m,m'}(\beta)=j(j+1)d^j_{m,m'}(\beta) \tag{7}$$

A key reference[31] reports complete essential bibliography with graphical illustrations that we will expand in a paper in preparation. Also Ref. 32 has a good semiclassical treatment, including implication for the physics of rotations and torsions and of the geometry of intersecting cones of processing vectors along different axes of quantization.

6. Concluding and additional remarks: Continuous and discrete expansions

The celebrated Fock treatment (1935) demonstrated the use of hyperspherical harmonics as orbitals for the solution of atomic and molecular structure problems, see Ref. 1 for unique properties and computational advantages. In particular, our work over the years, partly covered in a paper[1] until 2013, has addressed not only the development of Sturmian basis sets (see also Ref. 16) which are essentially orthogonal polynomials of the classical series but also to highlight how the orbitals in the reciprocal (momentum) space are hyperspherical harmonics.[33–37] Not only they are continuous sets of hypergeometric polynomials, but also the connections between different representations (or of different systems of separable coordinates) can be all written as orthogonal polynomials of discrete type, of the Hahn and Racah series.[38–41]

In order to give the complete picture, we found it useful to generalize to the multidimensional hydrogenic Coulomb orbitals in dimensions higher than physical. Multidimensional basis sets are used as a physical resource for a variety of problems: quantum cosmology, quantum field theory, quantum information science, not to mention that the dimensional dependence of the entropic properties for the stationary states of the multidimensional quantum systems is extensively studied for quantum information (see Ref. 42 and references therein).

As extensively remarked, multidimensional Sturmian basis sets in configuration space[26,43–45] can be obtained as a product of Laguerre polynomials (one of our nine players) and a multidimensional hyperspherical harmonic, or, according to the chosen coordinate system, as the product of two Laguerre polynomials (as in parabolic coordinates) and a lower dimensional hyperspherical harmonic. These hyperspherical harmonics can, in turn, in the most general case, be written as set of Jacobi polynomials (another player in our scheme), and, in case of special values of the parameters down to Gegenbauer, or further to Legendre, polynomials, or even to

the Wigner D− matrix (e.g., occurring in the four-dimensional symmetric harmonics on the sphere S^3).

When we move to the momentum space perspective, Coulomb Sturmian basis sets can be Fourier transformed to hyperspherical harmonics (or Jacobi polynomials), for which it is easy to explicitly work out the superposition coefficients allowing the passage from one coordinate system to another (or, alternatively, from one spatial quantization scheme to a different one, i.e., to different sets of quantum numbers). Indeed, such coefficients are multidimensional integrals over a product of continuous orthogonal polynomials, which, in the most general case, correspond to discrete Racah polynomials (the upper level of our scheme), or generalized 6*j* coefficients. Again, upon simplification down to lower dimensionality, these coefficients asymptotically reduce to either Hahn (or dual Hahn) discrete polynomial sets, that are essentially Clebsch–Gordan or 3*j* coefficients, or to the Wigner *d* rotation matrices starting as our cornerstone in the conceptual scheme that we have come to describe.

A useful application of hyperspherical harmonics is the analytical representation of multidimensional functions, and their extensive use, specifically for representing potential energy surfaces is considered in Ref. 46, see in particular Refs. 47–58. Our survey of current advances in quantum chemistry, especially as far as the expansion of atomic and molecular orbitals is concerned as a function of mathematically and physically motivated basis sets, permits to focus on combined observations of relationships between this area with other related ones. In particular, from the mathematical point of view, it is expedient to present the important connections as far as concerning the widely investigated area of recent mathematics: they involve special functions and orthogonal polynomials, in turn related to the theory of representation of groups, specifically continuous groups, and therefore the Lie theory.

In this chapter, we have tried to provide a picture of our appreciation of this aspect. The presentation started with an adaptation of the current general scheme for orthogonal polynomials of hypergeometrical type as a ladder that goes from Hermite up to Racah polynomials, immediately bringing insight on further connections with the theory of angular momentum: in turn, this feature has been more and more intimately connected to the area of investigation of spin networks. Individuating the main characters of the play as nine orthogonal polynomial sets of discrete variable and arranging them as a matrix is a compact way of putting the pieces of the mosaic into a unified scheme.[17,59–70]

What we analyzed in this paper is limited to some aspects, essentially focused on the leading role of the polynomial of Kravchuk type and its equivalent in quantum mechanical language, the *d* matrix. Aspects discussed in Ref. 46 are the interconnections between the members of the set, which from a mathematical viewpoint can be considered as based on the asymptotic theory of special functions: the corresponding operations in quantum chemistry are the passage from the quantum to the classical limit through the semiclassical regime. The construction has been conceived as a stair going up from Hermite to Racah polynomials, which is essentially introducing progressively elements, corresponding to a process of successive discretization. In contrast, the opposite process, i.e., going down, is a more rigorous one because it is based on well-defined mathematical relationships: utilizing the asymptotic theory of functional analysis.

These connections between members of the sets is the object of a complementary survey[46]. Such survey also considers well known aspects, however needing compactness. For instance the explicit expression of the objects as converging terminating series, needing some care for computation, are put into reference within the theory of hypergeometric generalized series. Regarding computation, the direct sums may present calculation difficulties, often dealt with, in modern research, by using the recurrence property that all these functions, being orthogonal polynomials, obey. These recurrence relations provide a useful computational tool and are seen to be also in connection with the fact that, in the scheme, they are always associated by duality with difference equation, or, in the case of the lower steps of the ladder, with differential equations of Schrödinger type, the fundamental tool in quantum theory. The concept of special duality that involves the underlying theory is often usefully represented as a bidimensional plot, that we define as the *screen* that also will be illustrated elsewhere for the crucial member of the set, the Kravchuk polynomials.[71,72]

The centrality of the Kravchuk function was the theme of the paper and it involved a slight modification of the sequences in the Askey scheme, interchanging its position with the Jacobi polynomial. As a matter of fact, Jacobi polynomials are more centrally located if one conventionally considers the whole scheme, involving continuous orthogonal polynomials, but not discussed here. They have been so far, in our opinion, not sufficiently exploited from the viewpoint as expansion basis sets in solving quantum mechanical problems. We thus believe that this continues to be an interesting topic for further research.

On the other hand the Askey scheme has extremely important amplifications when including passage from spherical to elliptic or parabolic manifolds. The literature on q-hypergeometrical polynomials is a subject of wide interest in modern mathematics; these polynomials are less developed as tools for expansion basis sets in quantum mechanics. Some steps were undertaken recently.[4] Such theoretical progress shows perspective of advancing in the use of discrete basis sets as computational analogues for continuous function, a technique that in our work has been named the "hyperquantization" algorithm.[73–81]

Acknowledgments

The authors acknowledge the Italian Ministry for Education, University and Research, MIUR, for financial supporting through SIR 2014 "Scientific Independence for young Researchers" (RBSI14U3VF).

References

1. Coletti, C.; Calderini, D.; Aquilanti, V. D-Dimensional Kepler-Coulomb Sturmians and Hyperspherical Harmonics as Complete Orthonormal Atomic and Molecular Orbitals. *Adv. Quantum Chem.* **2013**, *67*, 73.
2. Calderini, D.; Coletti, C.; Grossi, G.; Aquilanti, V. Continuous and Discrete Algorithms in Quantum Chemistry: Polynomial Sets, Spin Networks and Sturmian Orbitals. In *Lecture Notes in Computer Science*, Murgante, B. Ed.; Springer-Verlag Publisher, 2013; Vol. 7972, pp 32–45.
3. Aquilanti, V.; Cavalli, S.; Coletti, C.; Di Domenico, D.; Grossi, G. Hyperspherical Harmonics as Sturmian Orbitals in Momentum Space: A Systematic Approach to the Few-Body Coulomb Problem. *Int. Rev. Phys. Chem.* **2001**, *20*, 673.
4. Anderson, R.; Aquilanti, V. Spherical and Hyperbolic Spin Networks: The q-extensions of Wigner-Racah 6j Coefficients and General Orthogonal Discrete Basis Sets in Applied Quantum Mechanics. In *Lecture Notes in Computer Science*, Murgante, B. Ed.; Springer-Verlag Publisher, 2017; Vol. 10408, pp 338–353.
5. Aquilanti, V.; Caligiana, A.; Cavalli, S. Hydrogenic Elliptic Orbitals, Coulomb Sturmian Sets, and Recoupling Coefficients Among Alternative Bases. *Int. J. Quantum. Chem.* **2003**, *92*, 99.
6. Aquilanti, V.; Caligiana, A.; Cavalli, S.; Coletti, C. Hydrogenic Orbitals in Momentum Space and Hyperspherical Harmonics. Elliptic Sturmian Basis Sets. *Int. J. Quantum. Chem.* **2003**, *92*, 212.
7. Abramowitz, M.; Stegun, I. *Handbook of Mathematical Functions*; Dover Publications, 1965.
8. Olver, F.; Lozier, D.; Boisvert, R.; Clark, C. *NIST Handbook of Mathematical Functions*; Cambridge University Press, 2010.
9. Aquilanti, V.; Cavalli, S.; Coletti, C. Angular and Hyperangular Momentum Recoupling, Harmonic Superposition and Racah Polynomials: A Recursive Algorithm. *Chem. Phys. Lett.* **2001**, *344*, 587.
10. Nikiforov, A.; Suslov, S.; Uvarov, V. *Classical Orthogonal Polynomials of a Discrete Variable*; Springer-Verlag, 1991.

11. Askey, R.; Wilson, J. A Set of Hypergeometric Orthogonal Polynomials. *SIAM J. Math. Anal.* **1979**, *10*, 1008–1016.
12. Koekoek, R.; Swarttouw, R. *The Askey-Scheme of Hypergeometric Orthogonal Polynomials and Its q-analogue*; TU Delft, 1998, Available via anonymous ftpsite:ftp.twi.tudelft.nl, directory:/pub/publications/tech-reports.
13. Varshalovich, D.; Moskalev, A.; Khersonskii, V. *Quantum Theory of Angular Momentum*, World Scientific, 1988.
14. Yutsis, A.; Levinson, I.; Vanagas, V. *Theory of Angular Momentum*; Israel Program for Scientific Translations, 1962.
15. Biedenharn, L.; Louck, J.; Carruthers, P. *Angular Momentum in Quantum Physics: Theory and Application (Encyclopedia of Mathematics and its Applications)*; Cambridge University Press, 1984.
16. Avery, J.; Avery, J. *Hyperspherical Harmonics and Their Physical Applications*; World Scientific, 2018.
17. Santos, R.; Arruda, M.; Bitencourt, A.; Ragni, M.; Prudente, F.; Coletti, C.; Marzuoli, A.; Aquilanti, V. Quantum Angular Momentum, Projective Geometry and the Networks of Seven and Ten Spins: Fano, Desargues and Alternative Incidence Configurations. *J. Mol. Spectr.* **2017**, *337*, 153–162.
18. Aquilanti, V.; Arruda, M.; Coletti, C.; Littlejohn, R.; Santos, R. F. Combinatorial and Geometrical Origins of Regge Symmetries: Their Manifestations from Spin-Networks to Classical Mechanisms, and Beyond. In *Lecture Notes in Computer Science*, Murgante, B. Ed.; Springer-Verlag Publisher, 2017; Vol. 10408, pp 314–327.
19. Bitencourt, A.; Ragni, M.; Littlejohn, R.; Anderson, R.; Aquilanti, V. The Screen Representation of Vector Coupling Coefficients or Wigner 3j Symbols: Exact Computation and Illustration of the Asymptotic Behavior. **2014**, *8579*, 468–481.
20. Aquilanti, V.; Cavalli, S.; Coletti, C. The D-Dimensional Hydrogen Atom: Hyperspherical Harmonics as Momentum Space Orbitals and Alternative Sturmian Basis Sets. *Chem. Phys.* **1997**, *214*, 1–13.
21. Whitten, R.; Sims, J. Three-Body Coulomb Systems Using Generalized Angular-Momentum S States. *Phys. Rev. A* **1974**, *9*, 1586.
22. Aquilanti, V.; Cavalli, S.; Coletti, C. Hyperspherical Symmetry of Hydrogenic Orbitals and Recoupling Coefficients Among Alternative Bases. *Phys. Rev. Lett.* **1998**, *80*, 3209.
23. Aquilanti, V.; Cavalli, S.; Coletti, C.; Grossi, G. Alternative Sturmian Bases and Momentum Space Orbitals: An Application to the Hydrogen Molecular Ion. *Chem. Phys.* **1996**, *209*, 405.
24. Aquilanti, V.; Coletti, C. 3*nj*-Symbols and Harmonic Superposition Coefficients: An Icosahedral Abacus. *Chem. Phys. Lett.* **2001**, *344*, 601.
25. Santos, R.; Bitencourt, A.; Ragni, M.; Prudente, F.; Coletti, C.; Marzuoli, A.; Aquilanti, V. Couplings and Recouplings of Four Angular Momenta: Alternative 9j Symbols and Spin Addition Diagrams. *J. Mol. Model.* **2017**, *23*, 147.
26. Calderini, D.; Cavalli, S.; Coletti, C.; Grossi, G.; Aquilanti, V. Hydrogenoid Orbitals Revisited: From Slater Orbitals to Coulomb Sturmians. *J. Chem. Sci.* **2012**, *124*, 187.
27. Bagci, A.; Hoggan, P. Analytical Evaluation of Relativistic Molecular Integrals. I. Auxiliary Functions. *Rend. Fis. Acc. Lincei* **2018**, *29*, 191–197.
28. Bagci, A.; Hoggan, P.; Adak, M. Analytical Evaluation of Relativistic Molecular Integrals. II: Method of Computation for Molecular Auxiliary Functions Involved. *Rend. Fis. Acc. Lincei* **2018**, *29*, 765–775.
29. Ruiz, M. Spin States of the Light Atoms. *Rend. Fis. Acc. Lincei.* **2018**, *29*, 777–786.
30. Guseinov, I.; Sahin, E.; Erturk, M. An Improvement on (α^*)-Exponential Type Orbitals for Atoms in Standard Convention. *Mol. Phys.* **2014**, *112*, 35–40.
31. Littlejohn, R.; Yu, L. Uniform Semiclassical Approximation for the Wigner 6j-Symbol in Terms of Rotation Matrices. *J. Phys. Chem. A* **2009**, *113*, 14904.

32. Braun, P.; Gewinski, P.; Haake, F.; Schomerus, H. Semiclassics of Rotation and Torsion. *Z. Phys. B* **1996**, *100*, 115–127.
33. Aquilanti, V.; Cavalli, S.; De Fazio, D.; Volpi, A. Theory of Electronically Nonadiabatic Reactions: Rotational, Coriolis, Spin-Orbit Couplings and the Hyperquantization Algorithm. *Int. J. Quantum Chem.* **2001**, *85*, 368–381.
34. Aquilanti, V.; Cavalli, S. Coordinates for Molecular Dynamics: Orthogonal Local Systems. *J. Chem. Phys.* **2002**, *85*, 1355–1361.
35. Aquilanti, V.; Cavalli, S.; Grossi, G. Hyperspherical Coordinates for Molecular Dynamics by the Method of Trees and the Mapping of Potential Energy Surfaces for Triatomic Systems. *J. Chem. Phys.* **2002**, *85*, 1362–1375.
36. Aquilanti, V.; Tonzani, S. Three-body Problem in Quantum Mechanics: Hyperspherical Elliptic Coordinates and Harmonic Basis Sets. *J. Chem. Phys.* **2004**, *120*, 4066–4073.
37. Anderson, R.; Aquilanti, V.; Cavalli, S.; Grossi, G. Stereodirected Discrete Bases in Hindered Rotor Problems: Atom-Diatom and Pendular States. *J. Phys. Chem.* **1993**, *97*, 2443–2452.
38. Aquilanti, V.; Capecchi, G. Harmonic Analysis and Discrete Polynomials from Semiclassical Angular Momentum Theory to the Hyperquantization Algorithm. *Theor. Chem. Acc.* **2000**, *104*, 182–188.
39. Aquilanti, V.; Cavalli, S.; Coletti, C.; De Fazio, D.; Grossi, G. Hyperangular Momentum: Applications to Atomic and Molecular Science. In *New Methods in Quantum Theory*, Tsipis, C., Popov, V., Herschbach, D., Eds.; Kluwer, 1996, pp 233–250.
40. Aquilanti, V.; Lombardi, A.; Littlejohn, R. Hyperspherical Harmonics for Polyatomic Systems: Basis Set for Collective Motions. *Theor. Chem. Acc.* **2004**, *111*, 400–406.
41. Aquilanti, V.; Cavalli, S.; De Fazio, D. Angular and Hyperangular Momentum Coupling Coefficients as Hahn Polynomials. *J. Phys. Chem.* **1995**, *99*, 15694–15698.
42. Puertas-Centeno, D.; Temme, N.; Toranzo, I.; Dehesa, J. Entropic Uncertainty Measures for Large Dimensional Hydrogenic Systems. *J. Math. Phys.* **2017**, *58*, 103302.
43. Aquilanti, V.; Avery, J. Generalized Potential Harmonics and Contracted Sturmians. *Chem. Phys. Lett.* **1997**, *267*, 1–8.
44. Aquilanti, V.; Avery, J. Sturmian Expansions for Quantum Mechanical Many-Body Problems, and Hyperspherical Harmonics. *Adv. Quantum Chem.* **2001**, *39*, 71–102.
45. Aquilanti, V.; Caligiana, A. Sturmian Approach to One-Electron Many-Center System: Integrals and Iteration Schemes. Chem. Phys. Lett. 366, 157–164.
46. Coletti, C.; Palazzetti, F.; Anderson, R. W.; Aquilanti, V. Hypergeometric Polynomials, Hyperharmonic Discrete and Continuous Expansions, Spin Networks: Evaluations, Interconnections, Extensions. *Lect. Notes Comput. Sci.* **2019**, *11624*, 1–17.
47. Aquilanti, V.; Grossi, G. Angular Momentum Coupling Schemes in the Quantum Mechanical Treatment of P-State Atom Collisions. *J. Chem. Phys.* **1980**, *73*, 1165–1172.
48. Palazzetti, F.; Munusamy, E.; Lombardi, A.; Grossi, G.; Aquilanti, V. Spherical and Hyperspherical Representation of Potential Energy Surfaces for Intermolecular Interactions. *Int. J. Quantum Chem.* **2011**, *111*, 318–332.
49. Lombardi, A.; Palazzetti, F.; Aquilanti, V.; Grossi, G.; Albernaz, A.; Barreto, P.; Cruz, A. Spherical and Hyperspherical Harmonics Representation of van der Waals Aggregates. *AIP Conf. Proc.* **2016**, *1790*, 020005.
50. Aquilanti, V.; Bartolomei, M.; Cappelletti, D.; Carmona-Novillo, E.; Pirani, F. The N_2-N_2 System: An Experimental Potential Energy Surface and Calculated Rotovibrational Levels of the Molecular Nitrogen Dimer. *J. Chem. Phys.* **2002**, *117*, 615.
51. Aquilanti, V.; Ascenzi, D.; Bartolomei, M.; Cappelletti, D.; Cavalli, S.; de Castro Vîtores, M.; Pirani, F. Molecular Beam Scattering of Aligned Oxygen Molecules. The Nature of the Bond in the O_2-O_2 Dimer. *J. Am. Chem. Soc.* **1999**, *121*, 10794–10802.

52. Aquilanti, V.; Bartolomei, M.; Carmona-Novillo, E.; Pirani, F. The Asymmetric Dimer N_2-O_2: Characterization of the Potential Energy Surface and Quantum Mechanical Calculation of Rotovibrational Levels. *J. Chem. Phys.* **2003**, *118*, 2214.
53. Barreto, P.; Cruz, A.; Barreto, R.; Palazzetti, F.; Albernaz, A.; Lombardi, A.; Maciel, G.; Aquilanti, V. The Spherical-Harmonics Representation for the Interaction Between Diatomic Molecules: The General Case and Applications to CO-CO and CO-HF. *J. Mol. Spectrosc.* **2017**, *337*, 163–177.
54. Barreto, P.; Ribas, V.; Palazzetti, F. Potential Energy Surface for the H_2O-H_2 System. *J. Phys. Chem. A* **2009**, *113*, 15047–15054.
55. Barreto, P.; Albernaz, A.; Capobianco, A.; Palazzetti, F.; Lombardi, A.; Grossi, G.; Aquilanti, V. Potential Energy Surfaces for Interactions of H_2O with H_2, N_2 and O_2: A Hyperspherical Harmonics Representation, and a Minimal Model for the H_2O-Rare-Gas-Atom Systems. *Comput. Theor. Chem.* **2012**, *990*, 53–61.
56. Barreto, P.; Albernaz, A.; Palazzetti, F. Potential Energy Surfaces for van der Waals Complexes of Rare Gases with H_2S and H_2S_2: Extension to Xenon Interactions and Hyperspherical Harmonics Representation. *Int. J. Quantum Chem.* **2012**, *112*, 834–847.
57. Barreto, P.; Palazzetti, F.; Grossi, G.; Lombardi, A.; Maciel, G.; Vilela, A. Range and Strength of Intermolecular Forces for van der Waals Complexes of the Type H_2X_n-Rg, with X = O, S and n = 1, 2. *Int. J. Quantum Chem.* **2010**, *110*, 777–786.
58. Barreto, P.; Vilela, A.; Lombardi, A.; Maciel, G.; Palazzetti, F.; Aquilanti, V. The Hydrogen Peroxide-Rare Gas Systems: Quantum Chemical Calculations and Hyperspherical Harmonic Representation of the Potential Energy Surface for Atom-Floppy Molecule Interactions. *J. Phys. Chem. A* **2007**, *111*, 12754–12762.
59. Anderson, R.; Aquilanti, V. The Discrete Representation Correspondence Between Quantum and Classical Spatial Distributions of Angular Momentum Vectors. *J. Chem. Phys.* **2006**, *124*, 214104.
60. Aquilanti, V.; Marinelli, D.; Marzuoli, A. Symmetric Coupling of Angular Momenta, Quadratic Algebras and Discrete Polynomials. *J. Phys. Conf. Ser.* **2014**, *482*, 012001.
61. Aquilanti, V.; Marzuoli, A. Projective Ponzano-Regge Spin Networks and Their Symmetries. *J. Phys. Conf. Ser.* **2018**, *965*, 012005.
62. Coletti, C.; Santos, R.; Arruda, M.; Bitencourt, A.; Ragni, M.; Aquilanti, V. Spin Networks and Sturmian Orbitals: Orthogonal Complete Polynomial Sets in Molecular Quantum Mechanics. *AIP Conf. Proc.* **2017**, *1906*, 030013.
63. Aquilanti, V.; Haggard, H.; Littlejohn, R.; Yu, L. Semiclassical Analysis of Wigner 3 j-symbol. *J. Phys. A.* **2007**, *40*, 5637–5674.
64. Anderson, R.; Aquilanti, V.; Ferreira, da S. C. Exact Computation and Large Angular Momentum Asymptotics of 3nj Symbols: Semiclassical Disentangling of Spin Networks. *J. Chem. Phys.* **2008**, *129*, 161101 (5 pages).
65. Aquilanti, V.; Bitencourt, A.; Ferreira, da S. C.; Marzuoli, A.; Ragni, M. Quantum and Semiclassical Spin Networks: From Atomic and Molecular Physics to Quantum Computing and Gravity. *Phys. Scr.* **2008**, *78*, 058103.
66. Aquilanti, V.; Bitencourt, A.; Ferreira, C. daS.; Marzuoli, A.; Ragni, M. Combinatorics of Angular Momentum Recoupling Theory: Spin Networks, Their Asymptotics and Applications. *Theor. Chem. Acc.* **2009**, *123*, 237.
67. Anderson, R.; Aquilanti, V.; Marzuoli, A. 3nj Morphogenesis and Semiclassical Disentangling. *J. Phys. Chem. A.* **2009**, *113*, 15106–15117.
68. Aquilanti, V.; Haggard, H.; Hedeman, A.; Jeevangee, N.; Littlejohn, R.; Yu, L. Semiclassical Mechanics of the Wigner 6j-Symbol. *J. Phys. A* **2012**, *45*, 065209.
69. Bitencourt, A.; Marzuoli, A.; Ragni, M.; Anderson, R.; Aquilanti, V. Exact and Asymptotic Computations of Elementary Spin Networks: Classification of the Quantum-Classical Boundaries. *Lect. Notes Comput. Sci.* **2012**, *7333*, 723–737.

70. Aquilanti, V.; Marinelli, D.; Marzuoli, A. Hamiltonian Dynamics of a Quantum of Space: Hidden Symmetries and Spectrum of the Volume Operator, and Discrete Orthogonal Polynomials. *J. Phys. A Math. Theor.* **2013**, 46.
71. Anderson, R.; Aquilanti, V.; Bitencourt, A.; Marinelli, D.; Ragni, M. The Screen Representation of Spin Networks: 2D Recurrence, Eigenvalue Equation for 6j Symbols, Geometric Interpretation and Hamiltonian Dynamics. *Lect. Notes Comput. Sci.* **2013**, *7972*, 46–59.
72. Bitencourt, A.; Ragni, M.; Littlejohn, R.; Anderson, R.; Aquilanti, V. The Screen Representation of Vector Coupling Coefficients or Wigner 3j Symbols: Exact Computation and Illustration of the Asymptotic Behavior. *Lect. Notes Comput. Sci.* **2014**, *8579*, 468–481.
73. Aquilanti, V.; Grossi, G. Discrete Representations by Artificial Quantization in the Quantum Mechanics of Anisotropic Interactions. *L Lett. Al Nuovo Cim.* **1985**, *42*, 157–162.
74. Aquilanti, V.; Cavalli, S.; Grossi, G. Discrete Analogs of Spherical Harmonics and Their Use in Quantum Mechanics: The Hyperquantization Algorithm. *Theor. Chim. Acta.* **1991**, *79*, 283–296.
75. Aquilanti, V.; Cavalli, S.; De Fazio, D. Hyperquantization Algorithm. I. Theory for Triatomic Systems. *J. Chem. Phys.* **1998**, *109*, 3792–3804.
76. Aquilanti, V.; Cavalli, S.; De Fazio, D.; Volpi, A.; Aguilar, A.; Giménez, X.; Lucas, J. Hyperquantization Algorithm. II. Implementation for the $F+H_2$ Reaction Dynamics Including Open-Shell and Spin-Orbit Interactions. *J. Chem. Phys.* **1998**, *109*, 3805–3818.
77. Aquilanti, V.; Cavalli, S.; De Fazio, D.; Volpi, A.; Aguilar, A.; Lucas, J. Benchmark Rate Constants by the Hyperquantization Algorithm. The $F + H_2$ Reaction for Various Potential Energy Surfaces: Features of the Entrance Channel and of the Transition State, and Low Temperature Reactivity. *Chem. Phys.* **2005**, *308*, 237–253.
78. Aquilanti, V.; Cavalli, S.; De Fazio, D.; Simoni, A.; Tscherbul, T. Direct Evaluation of the Lifetime Matrix by the Hyperquantization Algorithm: Narrow Resonances in the Reaction Dynamics and Their Splitting for Nonzero Angular Momentum. *J. Chem. Phys.* **2005**, *123*, 054314.
79. Alvarino, J.; Aquilanti, V.; Cavalli, S.; Crocchianti, S.; Laganà, A.; Martinez, T. Stereodynamics from the Stereodirected Representation of the Exact Quantum S matrix: The Li + HF = LiF + H Reaction. *J. Phys. Chem. A* **1998**, *102*, 9638–9644.
80. Aldegunde, J.; Alvari no, J.; De Fazio, D.; Cavalli, S.; Grossi, G.; Aquilanti, V. Quantum Stereodynamics of the $F+H_2$ = HF + H Reaction by the Stereodirected S-matrix Approach. *Chem. Phys.* **2004**, *301*, 251–259.
81. De Fazio, D.; Cavalli, S.; Aquilanti, V. Orthogonal Polynomials of a Discrete Variable as Expansion Basis Sets in Quantum Mechanics the Hyperquantization Algorithm. *Int. J. Quantum Chem.* **2003**, *93*, 91–111.

This page intentionally left blank

CHAPTER THREE

Two-dimensional Sturmian basis set for bound state calculations

Juan Martín Randazzo[a,*], **Lorenzo Ugo Ancarani**[b]
[a]Instituto Balseiro and CONICET, Río Negro, Argentina
[b]Université de Lorraine, CNRS, LPCT, Metz, France
*Corresponding author: e-mail address: juanm.randazzo@gmail.com

Contents

Abstract

Sturmian functions (SF) constitute a very useful spectral tool to deal with bound states or break-up problems in atomic and molecular physics. In their standard form for the three-body case, the radial part of the wave function is proposed as an expansion in products of one-dimensional generalized SF (GSF). Here, we present an alternative spectral approach. It is based on solutions of a two-dimensional Sturmian eigenvalue problem that is solved with a finite set of one-dimensional GSF. The resulting 2DSF basis set functions depend simultaneously on two interparticle distances and possess a natural reordering. Through calculations of the Helium ground and 4^1F excited states energy, we compare the efficiency of the two equivalent sets of functions. The superiority of the two-dimensional approach demonstrated here should be particularly useful to reduce computational costs for applications in the continuum regime.

1. Introduction

The ab initio treatment of bound states for atomic and molecular systems entails a high demand on computational resources which grows rapidly both with the number of particles and with the desired precision. As illustrated through many investigations spanning several decades, the chosen

Advances in Quantum Chemistry, Volume 79
ISSN 0065-3276
https://doi.org/10.1016/bs.aiq.2019.05.001

basis is of fundamental importance. The three-body Helium atom has very often been used as a testbed for numerical methods, basis sets, as well as coordinate systems (e.g., Refs. 1–8). Helium has been also systematically used as a collision target providing ideal tests of numerical methods that solve the notoriously difficult Coulomb three-body scattering problem and its cumbersome boundary conditions (e.g., Refs. 9–14); indeed, theoretical studies of single and double ionization of atoms or molecules, in particular, are usually treated considering at most two active electrons. Since scattering states need to be described on much larger spatial domains, computational demands are higher both with respect to memory size of the Hamiltonian matrix representation, and the processor time to manipulate and solve the related matrix equations. When polyatomic molecular targets are involved, another issue makes things worse: as the orientation is usually not experimentally detected, theoretical approaches need to consider large numbers of molecular orientations before averaging (e.g., Refs. 15,16, and references therein), and this automatically increases the number of required calculations. The basis choice is thus even more crucial for scattering problems.

Over the last decade, a Sturmian method based on generalized Sturmian functions (GSF)[17] has been proposed to deal with both bound and scattering problems, in particular to solve the Coulomb three-body Schrödinger equation. Within the standard recipe[18] for bound states the equation is converted into a coupled set of two-dimensional radial equations that is subsequently translated into an eigenvalue problem. The methodology is similar for scattering problems but in this case the system is linear with a unique solution (the scattering wave function) driven by some prepared state.[13,14] One very important characteristic of the GSF method is that the asymptotic conditions for bound and scattering states can be dealt with efficiently. Indeed, within the spectral method, the discrete and complete basis set of GSF (one for each radial coordinate) is built with preselected ad hoc bound or outgoing flux condition. This can be understood from the one-dimensional Sturmian eigenvalue equation

$$[T + U - E_s]s_p(r) = -\beta_p V s_p(r), \tag{1}$$

where β_p is the pth eigenvalue, T is the radial part of the total kinetic energy operator, V is an adjustable *generating* potential, U is a potential (for example the Coulomb potential) that mimics the interaction to be studied in a given application and E_s is an externally fixed energy (positive for scattering states

and negative for bound states). Except for some rare cases for which the analytical form is available,[19,20] GSF are generated numerically by solving Eq. (1) as described for example in Ref. 21. The eigensolutions $s_p(r)$ form a complete and orthogonal set, the orthogonality being with respect to the weight function $V(r)$,[19]

$$\int_0^\infty s_p(r)\,V(r)s_{p'}(r)\,dr \propto \delta_{pp'}.$$

They are ordered according to their nodal structure. While the choice of U and V is arbitrary, the generating potential V should vanish at least as fast as U at large distances.[18] Hence, when solving Eq. (1), one can impose at a given radial distance r_0 the desired asymptotic conditions through E_s and U. All Sturmian functions $s_p(r)$ will then have the same asymptotic behavior by construction (their radial extension being regulated by the range of the generating potential). When angularly coupled, these one-dimensional GSF (see Eqs. (4) and (5)) lead to a correct description in the three-body case: with outgoing behavior in the hyperspherical radial coordinate for scattering problems[13,14] and an equivalent exponential fall off decay for bound states.

With the aim of tackling ever more computationally expensive scattering problems, it is important to improve efficiency by looking for the best basis functions. One lead is to define a basis through a two-dimensional rather than a one-dimensional Sturmian equation (1). Taking two radial distances r_1 and r_2, we thus propose an eigenvalue problem of the form

$$[T_{12} + U_{12} - E_s]S_p(r_1, r_2) = -\beta_p V_{12} S_p(r_1, r_2), \tag{2}$$

where, again, β_p are the eigenvalues, T_{12} is the radial part of the total kinetic energy operator, V_{12} is an adjustable *generating* potential, U_{12} is arbitrary but should ideally include a substantial part of the potentials of the physical problem, and E_s is an externally fixed energy that governs the asymptotic behavior. The boundary conditions are set at the origin of coordinates ($r_1 = r_2 = 0$) and on the border of a square box of size r_0.

From Eq. (2) we get two-dimensional basis elements S_p ordered according to their nodal structure, with orthogonality property specified by Eq. (8). The solution to a three-body problem can then be represented in terms of the new basis that includes part of the correlation and has an appropriate asymptotic behavior associated with the total energy E_s. By solving Eq. (2) with the GSF basis, we obtain two basis sets with the same expansion capacities: the two-dimensional basis (noted 2DSF hereafter) and

the original GSF. Solving the Schrödinger equation with the 2DSF can be viewed as an adequate reordering of the GSF basis, ruled by Eq. (2).

It is the aim of this contribution to define and explore such 2DSF by comparing its performance with respect to products of one-dimensional GSF. In principle, such an optimized basis should allow us to reduce the matrix size of the calculations and thus increase as much as possible the numerical performance of the spectral method. While we expect it to be particularly valuable when dealing with scattering states involving two electrons in the continuum, here we first present and apply the novel approach to bound states.

2. Bound solutions for three-body problems

Three-body atomic and molecular bound states can be obtained by solving the Schrödinger equation in the coordinate representation. In terms of two of the three relative position coordinate vectors we have, in atomic units:

$$0 = [H - E]\Psi(\mathbf{r}_{13}, \mathbf{r}_{23}) = \left[-\frac{1}{2\mu_{13}}\nabla_{13}^2 - \frac{1}{2\mu_{23}}\nabla_{23}^2 - \frac{1}{m_3}\nabla_{13}\cdot\nabla_{23} + \tilde{U}(r_{13}, r_{23}, r_{12}) - E\right]\Psi(\mathbf{r}_{13}, \mathbf{r}_{23}), \tag{3}$$

where μ_{13} and μ_{23} are reduced masses, and the total energy E of the system and the wave function Ψ are to be determined. According to the system under study, $\tilde{U}$ can correspond to the direct sum of two-particle potentials, such as Coulomb (e.g., Refs. 1,3,4) or screened potentials (e.g., Refs. 22,23), or some molecular potential energy surface (e.g., Ref. 24). In this paper, we take the Helium atom as a benchmark to explore, and we will look for the ground and one of the excited state two electron (labeled 1 and 2) wave functions. As usually done, we consider an infinitely massive nucleus ($m_3 \to \infty$) so that we will drop the third term and suppress hereafter the index 3 from all expressions (reduced mass calculations can be done similarly). The kinetic energy operator $T_{12} = T_1 + T_2$ is then separable in r_1 and r_2; the nonseparable potential $\tilde{U} = -Z/r_1 - Z/r_2 + 1/r_{12}$ where $Z = 2$ is the sum of three Coulomb potentials, $1/r_{12}$ representing the electron–electron repulsion.

Solutions of Eq. (3) associated to fixed values of the total angular quantum numbers L and M can be written as

$$\Psi^{L,M}(\mathbf{r}_1,\mathbf{r}_2)=\sum_{l_1,l_2}\frac{R^{L,M}_{l_1,l_2}(r_1,r_2)}{r_1 r_2}\mathcal{Y}^{L,M}_{l_1,l_2}(\hat{\mathbf{r}}_1,\hat{\mathbf{r}}_2), \tag{4}$$

where $\mathcal{Y}^{L,M}_{l_1,l_2}$ are the bispherical harmonics,[8] eigenstates of the total angular momentum operator and its projection over the z axis with respective quantum numbers L and M, while $R^{L,M}_{l_1,l_2}$ are the two-dimensional radial functions (in reduced form) to be determined through some numerical method; l_1 and l_2 are the angular momenta associated to each electron. Replacing expression (4) into the Schrödinger equation (3) one finds that the functions $R^{L,M}_{l_1,l_2}$ satisfy a coupled set of differential equations for the different pairs (l_1, l_2) used in the expansion. The symmetry (antisymmetry) of the spatial wave function can be selected in order to deal with singlet (triplet) two-electron wave functions, and also preserve a well-defined parity which is a good quantum number.

Eq. (3) has been solved for the benchmark Helium system by many methods (see, e.g., Refs. 5–7,18,25–27). It is nowadays quite straightforward to obtain accurate solutions and energies for the ground and excited states, by expanding the wave function in appropriate basis sets and solving a finite eigenvalue problem. Some of the mentioned expansions correspond to very specific *ansatz* valid for ground state wave functions. Other use functions depending explicitly on all interparticle coordinates (e.g., Refs. 5–7,28), which is efficient and very accurate; the algebra, though, is not at all easy to generalize to more than three particles.[29]

A very popular and easily implemented method is the Configuration Interaction scheme. In a nutshell, it corresponds to using a one dimensional basis to represent each radial coordinate of the solution; the radial functions $R^{L,M}_{l_1,l_2}(r_1,r_2)$ are expanded in products of such one-electron basis functions. Such an approach has the advantage of being simple and flexible; it can be applied using, e.g., hydrogenlike[30] or Slater-type functions[31], GSF[17,19] or B-splines.[32] Besides, the scheme is easily extrapolated to more complex systems (atomic or molecular) involving more than three particles. In all cases, however, the computational cost increases with the basis size. The situation is aggravated when one or two electrons are in the continuum since they demand bigger basis sets per particle coordinate.

For purposes that will become clear later, it is worth looking at the radial structure of typical solutions of the pure Coulomb three-body problem (3). In Fig. 1 we illustrate, as a function of r_1 and r_2, density plots of the first partial

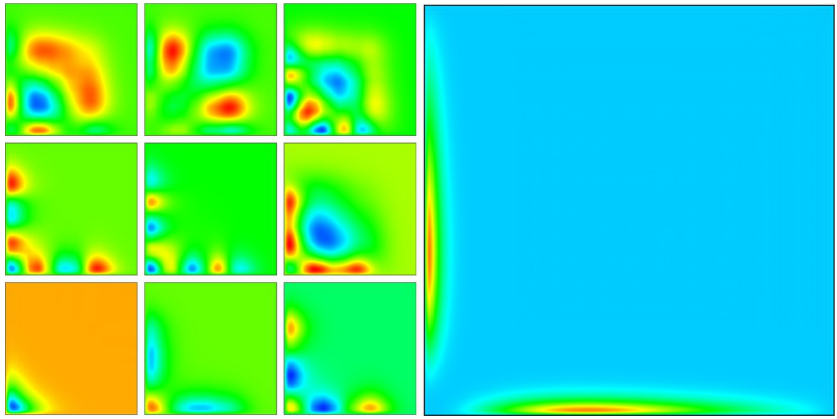

Fig. 1 *Left*: Density plots of the partial terms $R^{0,0}_{0,0}$ corresponding to the ground and some excited states of Helium obtained as "numerically exact" solutions of Eq. (3). *Right*: $R^{3,0}_{3,0}$ partial wave term of the 4^1F state.

term of the S wave, $R^{0,0}_{0,0}$, for the Helium ground and first excited states corresponding to the two-electron wave function in a radial domain of 20 a.u. per coordinate. Terms with higher l_1 and l_2 values have a similar structure but with the probability shifted to larger r_1 and r_2 values because of the centrifugal barrier effect. The figure also shows the density corresponding to the $R^{0,3}_{3,0}$ term of the 4^1F state in a radial domain of 55 a.u. per coordinate: a very asymmetrical distribution of the electron density is clearly apparent.

3. One-dimensional Sturmian functions

For a given pair (l_1,l_2) of angular momenta, the two-dimensional radial functions $R^{L,M}_{l_1,l_2}(r_1,r_2)$ in Eq. (4) can be written in terms of a double summation over products of one-dimensional Sturmian functions

$$R^{L,M}_{l_1,l_2}(r_1,r_2) = \sum_{n_1,n_2} a^{L,M}_{n_1,n_2,l_1,l_2} s_{n_1,l_1}(r_1) s_{n_2,l_2}(r_2) \tag{5}$$

where $a^{L,M}_{n_1,n_2,l_1,l_2}$ are the expansion coefficients to be determined and $s_{n,l}$ can be defined in different ways.[18,24] One particular and practical choice, widely used in the literature (see, e.g., Refs. 19, 27,33–35, and references therein), consists in taking $U(r) = V(r) = -Z/r$. The corresponding Coulomb Sturmian Functions (CSF) are solutions of the equation

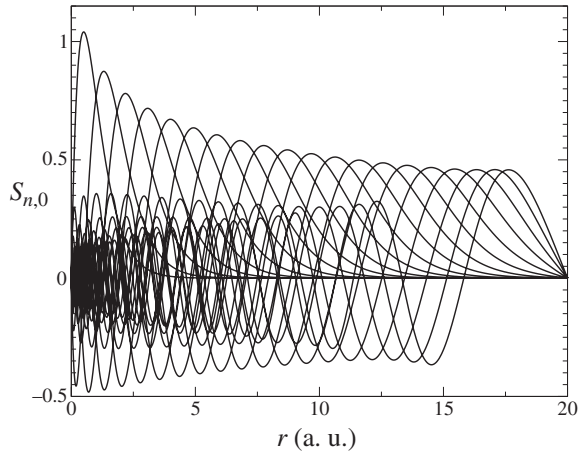

Fig. 2 One-dimensional (radial) box-based Coulomb Sturmian functions (set to 0 at $r_0 = 20$ a.u.).

$$\left[-\frac{1}{2}\frac{d^2}{dr^2} + \frac{l(l+1)}{2r^2} - \frac{Z}{r} - \tilde{E}_{1d}\right] s_{n,l}(r) = \beta_{n,l}\frac{Z}{r}s_{n,l}(r) \tag{6}$$

where the energy $\tilde{E}_{1d}$ is a fixed parameter and $\beta_{n,l}$ are the eigenvalues to be determined. The first 20 CSF, numerical solutions of Eq. (6), are shown in Fig. 2 for $l = 0$, $\tilde{E}_{1d} = -11.52$ a.u. and homogeneous conditions at $r_0 = 20$ a.u. The nodal structure clearly increases with the index n and the orthogonal set $s_{n,0}$ forms a basis within the interval $r \in [0, 20]$.

Although we do not use here the property, we emphasize that the eigensolutions $s_{n,l}$ of Eq. (6) with boundary conditions $s_{n,l}(0) = s_{n,l}(\infty) = 0$ are available in analytical form in real and also in momentum space representation. This rare situation opens up a number of possibilities. For example, it provides a tool to control accuracy of the numerical method chosen to solve Eq. (6). Also, within a Configuration Interaction scheme, CSF allow for an elegant analytical approach to treat many-electron atoms.[19] Finally, let us mention that when CSF are used as basis functions in scattering problems a number of matrix elements can be calculated analytically.

In previous contributions[18,36,37] we have reproduced published CSF calculations of three-body bound states; different angular quantum number per radial coordinate, l_1 and l_2, were used for each radial component $R^{L,M}_{l_1,l_2}$. When solving Eq. (3) with such a choice, the two radial kinetic operators—including the centrifugal barriers—are already fully absorbed

by the basis functions. In this work we adopt a different strategy that, to our knowledge, has not been taken before. We use the same value $l_1 = l_2 = 0$ for all radial functions; this is at the cost of having to deal with the centrifugal barrier matrix elements in the numerical treatment of the Hamiltonian H. This choice, however, has the important advantage of reducing the number of two-dimensional matrix elements associated with the electron–electron repulsion potential, and simultaneously simplifies the algebra of the computational codes.

A linear combination of products of these one-dimensional CSF is used, as indicated in expansion (5), to represent the solutions $R^{L,M}_{l_1,l_2}$. We show, in Fig. 3, density plots associated to simple products of one-dimensional CSF. We clearly see how the nodal structure forms a kind of *grid*; this has to be contrasted with the complex nodal structure of the one-dimensional CSF shown in Fig. 1.

For the three-body bound application below, we use N_{1d} Sturmian functions per radial coordinate for all radial functions $R^{L,M}_{l_1,l_2}$, which makes a total of $N_{2d} = N^2_{1d}$ radial basis elements. When imposing symmetrization, however, redundancies in the expansion must be avoided leading to

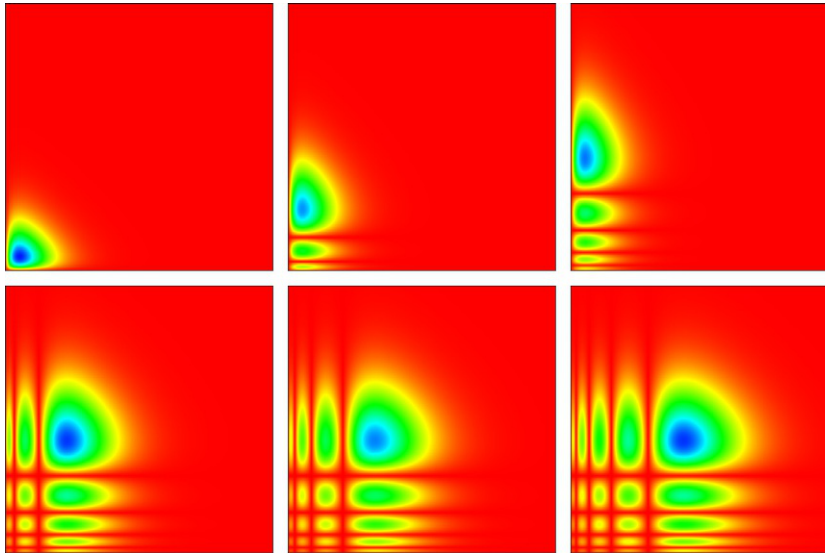

Fig. 3 Density plots of two-dimensional radial functions obtained as products of one-dimensional (radial) Coulomb Sturmian Functions, corresponding to (bottom panels) $(n_1, n_2) = (1, 1)$, (1, 3), (1, 5), and (top panels) (3, 5), (4, 5), and (5, 5).

$N_{2d} = \frac{1}{2}N_{1d}(N_{1d} \pm 1)$ for $S = \pm 1$ when $l_1 = l_2$ and N_{1d}^2 for $l_1 \neq l_2$. We also define a value for L_{max} that fixes the maximum number for the single particle angular momentum quantum number; it defines pairs of l_1 and l_2 satisfying together with L the triangle selection rule. For example, for $L = 0$ we have $l_1 = l_2 = 0, 1, \ldots, L_{max}$. Applying the Galerkin method[38] to Eq. (3) yields finally a linear generalized eigenvalue problem of size $N_{2d}(L_{max} + 1)$. For $L > 0$ we do not have a formula for the size of the system since many pairs (l_1, l_2) can be used, each corresponding in general to a different N_{2d} value. Parity is another quantity to be conserved through the appropriate selection of the (l_1,l_2) pairs included in the expansion (see, e.g., Ref. 35).

In the next section we present the two-dimensional eigenvalue problem to replace the single CSF products used in the expansions of the radial components of the three-body wave functions. Our proposal consists in defining a two-dimensional radial basis set to represent the function $R_{l_1,l_2}^{L,M}$ with a smaller number of basis elements than the one-dimensional case, *i.e.*, to reduce the value of N_{2d}.

4. Two-dimensional Sturmian functions

Similarly to CSF functions $s_{n,l}(r)$, defined as solutions of Eq. (6), we could propose a two-dimensional Sturmian basis set $S_{n,l_1,l_2}(r_1, r_2)$. Here, instead, for a given symmetry S, we define $S_n^{(S)}(r_1, r_2)$—named 2DSF hereafter—as the solutions to the equation

$$\left[-\frac{1}{2}\frac{d^2}{dr_1^2} - \frac{1}{2}\frac{d^2}{dr_2^2} - \frac{Z}{r_1} - \frac{Z}{r_2} + U(r_1, r_2) - \tilde{E}_{2d}\right] S_n^{(S)}(r_1, r_2) = \beta_n^{(S)} V(r_1, r_2) S_n^{(S)}(r_1, r_2), \tag{7}$$

where $\tilde{E}_{2d}$ is an externally fixed (energy) parameter and $\beta_n^{(S)}$ are the eigenvalues. We could include centrifugal barriers into Eq. (7) and use one set per partial wave term R_{l_1,l_2}, but we prefer to choose $l_1 = l_2 = 0$ and use the same set for all partial waves (if desired for a given application, we may add to U some approximation of the barriers). As for the one-dimensional case, there are infinite ways of defining the potentials U and V, according to the asymptotic behavior and spatial extension one wishes to represent. Besides, depending on the ultimate application of the basis (ground state, highly excited states, single, or double continuum solutions) one selects

appropriately $\tilde{E}_{2d}$. Since we are now in a two-dimensional frame, taking a positive (negative) value of $\tilde{E}_{2d}$ does not imply that both electrons possess a positive (negative) energy state behavior. For example, for $\tilde{E}_{2d} < 0$ the complete spectrum of eigenvalues $\beta_n^{(S)}$ also has a continuous part, which we are discretizing through the quadrature related to the Galerkin method.[39] It corresponds to the "physical" situation where one electron is bounded while the other is in the continuum, with a combined total negative energy. A similar situation appears in the many electron (coordinate separable) approach discussed in Ref. 19, with an energy value sum of each electron's contribution. Though interesting, such an approach was seen to suffer from lack of completeness.[40]

Solutions of the generalized eigenvalue problem given by equation (7) can be performed in the same way as for atomic orbitals[18]: through the Galerkin method. In can be easily shown that the solutions satisfy an orthonormality relation

$$\int_0^\infty dr_1 \int_0^\infty dr_2 S_{n'}^{(S)}(r_1, r_2)\, V(r_1, r_2)\, S_n^{(S)}(r_1, r_2) = \delta_{n',n} \tag{8}$$

and constitute a complete set in the whole two-dimensional radial space, with a well-defined symmetry with respect to the $r_1 \leftrightarrow r_2$ coordinate exchange.

Fig. 4 shows typical bound solutions $S_n^{(S)}(r_1, r_2)$ presenting similar structures to the helium eigenstates. The plots belonging to the upper panels correspond to the first five symmetric basis elements, while the lower ones are the sixth to tenth asymmetric ones, in order of appearance; this natural

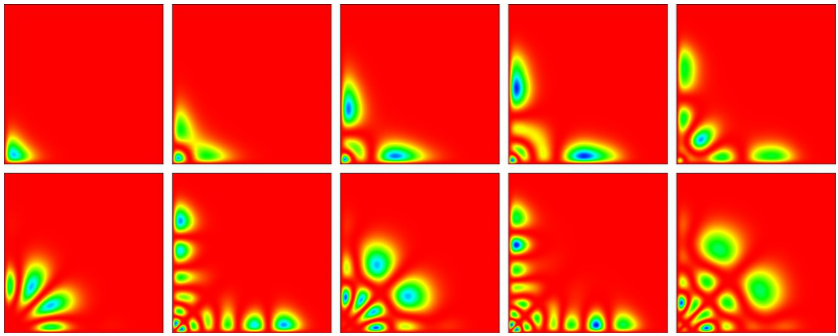

Fig. 4 Density plots of the first ten two-dimensional Sturmian eigenfunctions $S_n^{(S)}(r_1, r_2)$, solutions of the eigenvalue problem (7). Upper (lower) plots: symmetric (antisymmetric) square modulus of the two-dimensional basis elements.

order is related to the nodal structure of the 2DSF and the corresponding eigenvalue values $\beta_n^{(S)}$. In order to grasp the physical meaning of these eigenvalues, one should see the discrete set of potentials $\beta_n^{(S)} V$ all adopting a bound (or single continuum discretized through quadrature) state at the fixed energy $\tilde{E}_{2d}$. In other words, the energy $\tilde{E}_{2d}$ corresponds to the nth eigenenergy of the physical problem characterized by the potential $\beta_n^{(S)} V$, where the real value of $\beta_n^{(S)}$ decreases with n.

Similarly to the radial basis functions that have a well-defined symmetry, we must also impose symmetry on the angular basis and consequently, the total wave functions. For singlet states (which are symmetric in all space) we can combine symmetric radial functions with symmetric angular ones that correspond to eigenfunctions of the parity operator with eigenvalue $\Pi = 1$, while the product of both antisymmetric radial and angular functions correspond to parity eigenfunctions with eigenvalue $\Pi = -1$. Triplet states, on the other hand, can be written as a product of antisymmetric radial wave functions with angular symmetric ones for $\Pi = 1$ and vice versa for $\Pi = -1$. In the illustration below we consider singlet solutions corresponding to $\Pi = 1$, which can be written in the form:

$$\Psi^{L,M}(\mathbf{r}_1, \mathbf{r}_2) = \sum_{l_1, l_2, n} b^{L,M}_{l_1,l_2,n} \frac{S_n^{(1)}(r_1, r_2)}{r_1 r_2 \sqrt{2}} \left[\mathcal{Y}^{L,M}_{l_1,l_2}(\hat{\mathbf{r}}_1, \hat{\mathbf{r}}_2) + \mathcal{Y}^{L,M}_{l_1,l_2}(\hat{\mathbf{r}}_2, \hat{\mathbf{r}}_1) \right], \quad (9)$$

where the coefficients $b^{L,M}_{l_1,l_2,n}$ have to be determined through the Galerkin method as done with the 1DSF basis.

5. Results and discussion

This work considers as test cases the ground state and the excited 4^1F state of the Helium atom. We compare the two bases, 1DSF and 2DSF, by looking at the energy convergence as a function of the radial basis size. For the 1DSF representation of the ground state we choose as parameter $\tilde{E}_{1d} = -\lambda^2/2$, where $\lambda = 4.8$, according to the definition used in Ref. 27 which optimizes diagonalization for the $l_1 = l_2 = 0$ pair. We have to clarify, however, that our box-based CSF are obtained numerically by imposing homogeneous boundary conditions at $r_0 = 20$ a.u. constituting a sufficiently large domain for the He ground state (all CSF are forced to be zero at that distance, as seen in Fig. 2). Our CSF then have a behavior

similar to the analytical ones for the first basis elements ($n = 1$ up to $n \sim 14$) and a different one for the larger ones ($n \geq 15$).

We then use 20 1DSF per coordinate to solve the 2DSF equation (7) and obtain $20 \times 20 = 400$ basis elements. Employing symmetrization to the basis, we obtain 210 symmetric elements and 190 asymmetric ones, for both the 1D and 2DSF. This construction gives us two mathematical tools with the same expansion capacities; this means that, for example, in singlet states cases, we will obtain the same eigenstates and eigenenergies with the 210 elements, the difference being in the expansion coefficients. The 2DSF convergence turns out, however, to be much faster than in the 1DSF case (see results below), which means that using fewer than 210 basis elements we will obtain a better energy for the 2DSF than for the 1DSF expansion.

We have numerically explored a few possibilities for the arbitrary (symmetric) potentials $U(r_1, r_2)$ and $V(r_1, r_2)$. Their choice affects the spatial shape and extension of the resulting 2DSF basis set. The potential U should, ideally, be close to the physical problem one wishes to study, here the interelectronic Coulomb potential $1/r_{12}$. For the ground state we first use $U(r_1, r_2) = V(r_1, r_2) = r_>^{-1}$ with $r_> = \mathrm{Max}(r_1, r_2)$, and set $\tilde{E}_{2d} = -2.879028$ a.u. which corresponds to the exact energy value when only the $l = 0$ component of the $1/r_{12}$ partial wave expansion is included. The choice of this potential and $\tilde{E}_{2d}$ is motivated by the fact that it provides, as first basis element, exactly the *s*-wave solution of the ground state (the latter is then exactly obtained with just one 2DSF basis element). It turns out that, while being optimal for the $l = 0$ partial wave it makes the next partial waves converge too slowly, simply because the other 2DSF basis elements have probabilities distributions that differ from the Helium ground state. A second, better adapted, choice consists in taking the same U but a Yukawa potential $V(r_1, r_2) = r_>^{-1} e^{-\alpha r_>}$ where $\alpha = 1$ is optimized by a coarse variational procedure (this kind of adjustment is similar to that performed for one-dimensional GSF[18]); it allows us to maintain the nodal behavior of the basis elements close to the region of interest. This is the choice retained for the results presented hereafter. As the parameter $\tilde{E}_{2d}$ is concerned, we explored the domain between the $l = 0$ value and the exact He ground state energy and found a flat minimum for $\alpha = 1$.

Although showing no improvement in basis efficiency, we have also considered two other options for U that mathematically approach the electron–electron repulsion $1/r_{12}$: $(r_1 + r_2)^{-1}$ which represents the exact interaction in the Wannier region (mutual electrons angle equal π) and

$(r_1^2 + r_2^2)^{-1/2}$ which corresponds to replacing r_{12} by the hyperradius (mutual electrons angle equal $\pi/2$). Other choices of U and V, which could be possibly more efficient, will be explored in a near future.

In Table 1 we compare the minimum number of basis elements (1DSF or 2DSF) needed to obtain a given energy value, for several values of the maximum number of partial waves included.

In order to appreciate the differences between the 1DSF and 2DSF convergence we show in Fig. 5 the relative error in the energy for different

Table 1 Minimum 1DSF and 2DSF radial basis size requirements to achieve a given value (fourth column) for the Helium ground state as taken in Ref. 35, for different values of L_i ($i = 1, 2$) (the maximum angular momentum quantum numbers considered for each electron).

	***He* ground state energy requirements**		
L_i	N_{2d} 1DS	N_{2d} 2DS ($l = 0$)	Ref. 35
0	136	13	−2.87902
1	120	80	−2.90050
2	120	79	−2.90275
3	136	94	−2.90331
4	120	79	−2.90350
5	105	74	−2.90358

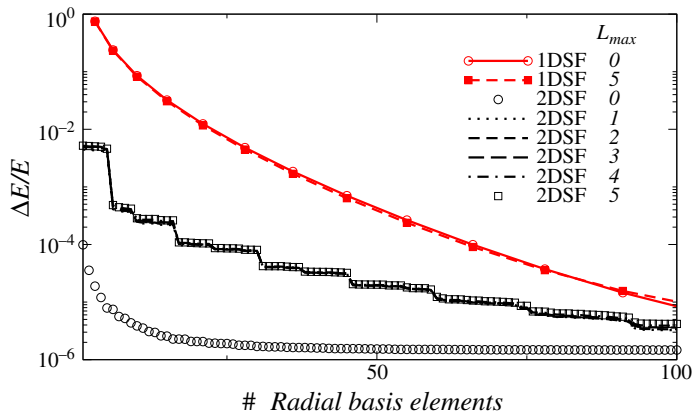

Fig. 5 Relative error of the ground state energy obtained with the 1DSF (*red*) and 2DSF (*black*) basis set as a function of the number of radial basis elements for different values of the maximum number $l = 0, \ldots, 5$ of included partial waves. The reference (exact) values are taken from Ref. 27.

partial waves, as a function of the number of radial basis elements. The behavior of the 1DSF error is practically the same for the maximum value of angular l momentum included equal to 0 and 5, the $l = 1$, 2, 3, and 4 curves (not shown) lying between them. Starting from very large errors, it progressively and steadily decreases until the maximum number of radial elements considered is reached (here we show 100). The 2DSF, on the other hand, starts with a much smaller error, corresponding to a very accurate description of the eigenstate with few basis elements. For $l = 0$ it rapidly reaches a minimum value, while the $l \neq 0$ curves behave similarly to the 1DSF case but between one and two orders of magnitude lower in the whole abscissa range. For $l = 0$ we observe a monotonous error decrease as a function of the number of basis elements, while for $l > 0$ the staggered behavior indicates there is still room for improvement in relation with the ordering of elements. The fact that the $l \neq 0$ relative error curves are higher than the $l = 0$ case is simply related to our choice, when generating the basis elements, of not including the corresponding centrifugal barriers in the eigenvalue Eq. (7). For the ground state, the $l = 0$ contribution is dominant and the more important relative error for the smaller $l \neq 0$ contributions is not a problem.

For the 4^1F excited state the procedure is similar. We use an optimized value of $\tilde{E}_{1d}$ given by $\lambda = 0.63$ and $r_0 = 55$ a.u. For this case, the spatial electron distribution is very asymmetric due to the first partial wave pair $(l_1, l_2) = (0, 3)$ domination which contributes with more than 99.9% to the state energy. The presence of the centrifugal barrier in one coordinate encourages one electron to be close to the nucleus while the other is far away, as shown in Fig. 1. This has two rather evident consequences: (i) an independent particle model description gives accurate energy values; (ii) singlet and triplet states are quasi-degenerate. For reason (i), only a few 1DSF basis elements are needed to obtain a good representation of the energy and eigenfunction. For the 2DSF expansion, this is even more dramatic; only one element would be needed if the potentials involved in the generating equation are properly chosen. To prove this, for the 4^1F excited state, we have thus added the term $l(l+1)/(2r_>^2)$ with $l = 3$, in order to include a centrifugal barrier for the outer electron only. By further setting $\tilde{E}_{1d} = -2.03125$ a.u. (close to the known exact value), the first 2D Sturmian basis element is very similar to the solution and convergence is achieved with only one radial element, while the 1DSF needs at least 91 elements to reach the value $-$ 2.0312 a.u. This situation with a domination by the first partial wave term is observed for other excited states for which convergence with

the 2DSF is seen to be very fast. The strongly asymmetric cases are the simplest to treat in comparison with situations where both electrons play a similar role, as in the ground state; it is for such cases that the electron–electron correlation plays a major role, slowing down the convergence, and providing the best ground to compare the efficiency of the two basis.

For the Helium states considered above the energies were known a priori, so that we could use their value as an input in the 2DSF equation. While an appropriate choice of $\tilde{E}_{1d}$ or $\tilde{E}_{2d}$ is desirable, the efficiency of the 1DSF or 2DSF basis sets is not so sensitive to the energy parameter value; it can nevertheless be optimized in a few iterations for the *s*-wave component, for example. Contrary to atomic or molecular bound states for which one endeavors to optimize the energy values, for break-up problems the energies are fixed by some (experimental) conditions. As an example, for double ionization processes on Helium, when both electrons are in the continuum the total energy is a known quantity that can be shared in a predefined way.[9–14] If the degree of reduction of required matrix elements, going from 1DSF to 2DSF, was the same as what we observed here for bound states, the gain in efficiency would be tremendous. The investigation of the $E > 0$ case is ongoing.

6. Summary and concluding remarks

We have introduced a novel two-dimensional Sturmian Function (2DSF) approach to deal with the coupled set of two-dimensional differential equations arising from the partial wave decomposition of the three-body Schrodinger equation. For illustration, it has been applied for energy calculations of the ground and 4^1F excited states of the Helium atom. The comparison demonstrated that one can achieve important reduction of computer resources with respect to the original 1DSF method.

The advantages of the 2DSF over the 1DSF basis can be explained by the fact that it corresponds to the solutions of a two-dimensional radial equation which may include the main characteristics of the physical system one wishes to study. Besides, the 2DSF basis set introduces a natural way of ordering the elements according to the nodal structure, a procedure which is somewhat arbitrary when considering products of 1DSF. We can say that the 2DSF equation arranges the information in an efficient way (more efficient than the 1DSF) that, when applied to atomic problems, results to be very convenient.

The present two-dimensional approach is not limited to the archetypical three-body Helium discrete states (for which there are many very accurate methods) since it can be applied to more general three-body potentials like,

for example, with three-body states of the nucleus of molecular systems in the Born Oppenheimer approximation.[24] More importantly, it could provide a great numerical benefit in scattering applications, like ionization of atoms and molecules treated in a two active electrons approach; indeed, for such problems, large number of one-dimensional basis elements are needed to achieve convergence in the corresponding three-body Coulomb continuum regime.

Acknowledgments

We acknowledge the Universidad Nacional de Cuyo (project No. 06/C480) and CONICET for funding.

References

1. Lin, C. D. Hyperspherical Coordinate Approach to Atomic and Other Coulombic Three-Body Systems. *Phys. Rep.* **1995**, *257*, 1.
2. Tanner, G.; Richter, K.; Rost, J.-M. The Theory of Two-electron Atoms: Between Ground State and Complete Fragmentation. *Rev. Mod. Phys.* **2000**, *72*, 497.
3. Baye, D. The Lagrange-mesh Method. *Phys. Rep.* **2015**, *565*, 1.
4. Edvardsson, S.; Karlsson, K.; Olin, H. corr3p-tr: A Particle Approach for the General Three-Body Problem. *Comp. Phys. Comm.* **2016**, *200*, 259.
5. Forrey, R. C. Compact Representation of Helium Wave Functions in Perimetric and Hyperspherical Coordinates. *Phys. Rev. A* **2004**, *69*, 022504.
6. Frolov, A. M. Two-stage Strategy for High-precision Variational Calculations. *Phys. Rev. A* **1998**, *57*, 2436.
7. Li, T.; Shakeshaft, R. S-wave Resonances of the Negative Positronium Ion and Stability of a System of Two Electrons and an Arbitrary Positive Charge. *Phys. Rev. A* **2005**, *71*, 052505.
8. Drake, G. W. F.; Springer, F. *Handbook of Atomic, Molecular, and Optical Physics.* New York, 2005.
9. Bray, I.; Fursa, D. V.; Kadyrov, A. S.; Stelbovics, A. T.; Kheifets, A.; Mukhamedzhanov, A. M. Electron and Photon-impact Atomic Ionisation. *Phys. Rep.* **2012**, *520*, 135.
10. McCurdy, C. W.; Baertschy, M.; Rescigno, T. N. Solving the Three-body Coulomb Breakup Problem Using Exterior Complex Scaling. *J. Phys. B* **2004**, *37*, R137.
11. Das, J. N.; Chakrabarti, K.; Paul, S. Hyperspherical Partial Wave Calculation for Double Photoionization of the Helium Atom at 20 eV Excess Energy. *J. Phys. B* **2003**, *36*, 2707.
12. Selles, P.; Malegat, L.; Kazansky, A. K. Ab Initio Calculation of the Whole Set of He Double-Photoionization Cross Sections. *Phys. Rev. A* **2002**, *65*, 032711.
13. Randazzo, J. M.; Mitnik, D. M.; Gasaneo, G.; Ancarani, L. U.; Colavecchia, F. D. Double Photoionization of Helium: A Generalized Sturmian Approach. *Eur. Phys. J. D* **2015**, *69*, 189.
14. Ambrosio, M. J.; Colavecchia, F. D.; Gasaneo, G.; Mitnik, D. M.; Ancarani, L. U. Double Ionization of Helium by Fast Electrons with the Generalized Sturmian Functions Method. *J. Phys. B* **2015**, *48*, 055204.
15. Chaluvadi, H.; Ning, C. G.; Madison, D. Theoretical Triple-differential Cross Sections of a Methane Molecule by a Proper-average Method. *Phys. Rev. A* **2014**, *89*, 062712.
16. Granados-Castro, C. M.; Ancarani, L. U. Electron Impact Ionization of the Outer Valence Orbital $1t_2$ of CH_4. *Eur. Phys. J. D* **2017**, *71*, 65.

17. Gasaneo, G.; Ancarani, L. U.; Mitnik, D. M.; Randazzo, J. M.; Frapiccini, A. L.; Colavecchia, F. D. Three-body Coulomb Problems with Generalized Sturmian Functions. *Adv. Quantum Chem.* **2013**, *67*, 153.
18. Randazzo, J. M.; Ancarani, L. U.; Gasaneo, G.; Frapiccini, A. L.; Colavecchia, F. D. Generating Optimal Sturmian Basis Functions for Atomic Problems. *Phys. Rev. A* **2010**, *81*, 042520.
19. Avery, J. S.; Avery, J. E. *Generalized Sturmians and Atomic Spectra*. World Scientific, 2006.
20. Ambrosio, M. J.; Del Punta, J. A.; Rodriguez, K. V.; Gasaneo, G.; Ancarani, L. U. Mathematical Properties of Generalized Sturmian Functions. *J. Phys. A* **2012**, *45, 015201.*
21. Mitnik, D. M.; Colavecchia, F. D.; Gasaneo, G.; Randazzo, J. M. Computational Methods for Generalized Sturmians Basis. *Comp. Phys. Comm.* **2011**, *182*, 1145.
22. Janev, R. K.; Zhang, S.; Wang, J. Review of Quantum Collision Dynamics in Debye Plasmas. *Matter Radiat. Extrem.* **2016**, *1*, 237.
23. Ancarani, L. U.; Rodriguez, K. V. Correlated Expansions of n^1S and n^3S States for Two-electron Atoms in Exponential Cosine Screened Potentials. *Phys. Rev. A* **2014**, *89, 012507.*
24. Randazzo, J. M.; Aguilar-Navarro, A. Three-body Molecular States of the LiH_2^+ System in the Born-Oppenheimer Approximation. *Int. J. Quantum Chem.* **2018**, *118*, e25611.
25. Goldman, S. P. Modified Configuration-interaction Method. *Phys. Rev. A* **1995**, *52*, 3718.
26. Goldman, S. P. Accurate Modified Configuration Interaction Calculations for Many Electron Systems Made Easy. *Phys. Rev. Lett.* **1997**, *78*, 2325.
27. Bromley, M. W. J.; Mitroy, J. Convergence of the Partial Wave Expansion of the He Ground State. *Int. J. Quantum Chem.* **2007**, *107*, 1150.
28. Bhatia, A. K.; Temkin, A. Symmetric Euler-Angle Decomposition of the Two-electron Fixed-nucleus Problem. *Rev. Mod. Phys.* **1964**, *36*, 1050.
29. Harris, F. E.; Frolov, A. M.; Smith, V. H. Exponential Variational Expansion in Relative Coordinates for Highly Accurate Bound State Calculations in Four-body Systems. *J. Chem. Phys.* **2003**, *119*, 8833.
30. Broad, J. T. Calculation of Two-photon Processes in Hydrogen with an L^2 Basis. *Phys. Rev. A* **1985**, *31*, 1494.
31. Weiss, A. W. Configuration Interaction in Simple Atomic Systems. *Phys. Rev.* **1961**, *122*, 1826.
32. Bachau, H.; Cormier, E.; Decleva, P.; Hansen, J. E.; Martín, F. Applications of B-splines in Atomic and Molecular Physics. *Rep. Prog. Phys.* **2001**, *64*, 1815.
33. Herbst, M. F.; Avery, J. E.; Dreuw, A. Quantum Chemistry with Coulomb Sturmians: Construction and Convergence of Coulomb Sturmian Basis Sets at the Hartree-Fock Level. *Phys. Rev. A* **2019**, *99*, 012512.
34. Avery, J. E.; Avery, J. S. 4-Center STO Interelectron Repulsion Integrals with Coulomb Sturmians. *Adv. Quantum Chem.* **2018**, *76*, 133.
35. Foumouo, E.; Kamta, G. L.; Edah, G.; Piraux, B. Theory of Multiphoton Single and Double Ionization of Two-electron Atomic Systems Driven by Short-wavelength Electric Fields: An Ab Initio Treatment. *Phys. Rev. A* **2006**, *74, 063409.*
36. Randazzo, J. M.; Frapiccini, A. L.; Colavecchia, F. D.; Gasaneo, G. Discrete Sets of Sturmian Functions Applied to Two-electron Atoms. *Phys. Rev. A* **2009**, *79*, 022507.
37. Frapiccini, A. L.; Randazzo, J. M.; Gasaneo, G.; Colavecchia, F. D. Sturmian Expansions for Two-electron Atomic Systems: Singly and Doubly Excited States. *Phys. Rev. A* **2010**, *82*, 042503.
38. Marchuk, G. I. *Methods of Numerical Mathematics*. Springer, 1982.
39. Randazzo, J. M.; Frapiccini, A. L.; Colavecchia, F. D.; Gasaneo, G. Discrete Sets of Many-body Sturmians. *Int. J. Quantum. Chem.* **2009**, *109*, 125.
40. Szmytkowski, R. Remarks on Completeness of Many-electron Sturmians. *J. Phys. A* **2000**, *33*, 4553.

This page intentionally left blank

CHAPTER FOUR

Normalizing cluster wavefunctions in the interstitial region within the muffin-tin approximation

Daniel Gebremedhin[a,*], **Charles Weatherford**[a], **Brian Wilson**[b]
[a]Physics Department, Florida A&M University, Tallahassee, FL, United States
[b]Physics and Life Science Directorate, Lawrence Livermore National Laboratory, Livermore, CA, United States
*Corresponding author: e-mail address: daniel1.gebremedhin@famu.edu

Contents

Abstract

In multiple-scattering methods, overlap integrals of cluster wavefunctions for an interstitial region, which lies inside the Watson sphere and outside all the enclosed ionspheres, are discussed. When the potential inside this interstitial region is taken to be constant, and hence, obeys the Helmholtz equation, the resulting solutions are known to involve Bessel functions. Normalizing the cluster wavefuntions inside this intricate region naturally leads to two-center integrals of various Bessel-type functions. In this article, all of the numerous types of integrals that might arise are exhaustively presented. Analytical expressions that are suitable for efficient computation of the overlap integrals are worked out by employing known addition theorems for the Bessel functions. These integrals require careful attention as they otherwise lead to an artificial singularity that may not cancel.

Advances in Quantum Chemistry, Volume 79
ISSN 0065-3276
https://doi.org/10.1016/bs.aiq.2019.04.005

1. Introduction

The muffin-tin approximation of the electron-moleculepotential, first suggested by Slater,[1] is "spherically symmetric within spheres surrounding the atoms, and constant outside." Later work also implemented terminating the outside region by a "Watson sphere"[2] that encloses all the spheres, outside of which the potential is once again taken to be spherically symmetric. This approximation has been implemented in various forms to tackle electronic structure calculations giving rise to enormous amount of literature. For theoretical and computational details that are pertinent to the present article one may, for example, refer to Refs. 3–9. However, there is hardly any work reported that addresses the challenges associated with the normalization of the wavefunction for this potential. Earlier studies,[5,7] partly due to lack of powerful computers, resorted to approximating the normalization of the total wavefunction using a first-order perturbation theory that takes into account small changes to the potential and total energy of the system. However, this type of approximation is not very useful, especially in the crucial early stages of a self-consistent calculation where the potential varies significantly between consecutive iterations. The main source of difficulty is the normalization integral of the interstitial region.

The interstitial region where the potential is constant, naturally admits a linear combination of spherical Bessel functions (BFs) as a solution. The contribution to the normalization from this intricate region thereby involves two-center overlap integrals over the BFs that are particularly challenging. This article discusses these overlap integrals in some detail. We shall follow closely the notation presented in the excellent paper[3] that discusses the scattered wavefunction method developed by Johnson. In the scattered wavefunction treatment of a molecule or cluster, the whole space is geometrically partitioned into three regions:

(I) *Ionic*: The region inside nonoverlapping spheres centered on the ions,
(II) *Interstitial*: The region outside the ionspheres and inside the Watson sphere which encloses the entire molecule,
(III) *Extramolecular*: The region outside the Watson sphere.

The ionspheres, which are labeled by $i, j = 0, 1, \ldots$, are of radius b_j, centered at $\mathbf{R}_j$ with local position $\mathbf{r}_j$ such that $\mathbf{r} = \mathbf{R}_j + \mathbf{r}_j$ overall. The Watson sphere, which is labeled w and is of radius b_w, encloses all the ionspheres. Ionsphere 0 and the Watson sphere are by definition concentric at the origin, and hence, $\mathbf{r} = \mathbf{r}_0 = \mathbf{r}_w$. In this paper, $r = |\mathbf{r}|$ and $\hat{r} = \mathbf{r}/r$ will represent magnitude and

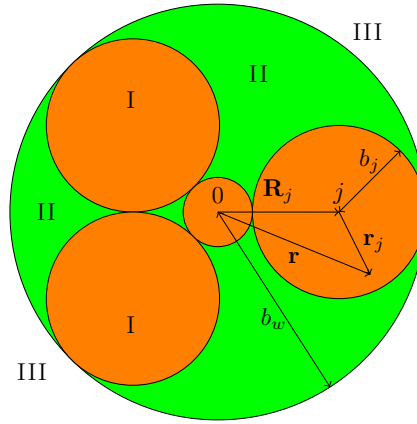

Fig. 1 Partitioning of space into (I) ionic, (II) interstitial, and (III) extramolecular regions.

unit vector, respectively. Relative positions will also be represented by $\mathbf{R}_{ji} = \mathbf{R}_i - \mathbf{R}_j$. The situation is sketched in Fig. 1.

The potential $\bar{V}_{II}$ in interstitial region II is a constant given by the volume average of the total potential on that region, which leads to the following Schrödinger equation

$$\left(-\frac{1}{2}\nabla^2 + \bar{V}_{II} - E\right)\Psi_{II}(\mathbf{r}) = -\frac{1}{2}\left(\nabla^2 + \kappa^2\right)\Psi_{II}(\mathbf{r}) = 0, \tag{1}$$

where $\kappa = \sqrt{2|E - \bar{V}_{II}|}$. Atomic units are used throughout this paper. Partitioning of the space as shown in Fig. 1 will inevitably necessitate enforcing continuity of the wavefunction across the boundaries of all the spheres. As a result, the wavefunction $\Psi_{II}(\mathbf{r})$ generally needs to be expanded in spherical BFs centered on each sphere as follows

$$\Psi_{II}(\mathbf{r}) = \sum_{j=0}\sum_{L} A_L^j K_L(\kappa, \mathbf{r}_j) + \sum_{L} A_L^w I_L(\kappa, \mathbf{r}_w), \quad E < \bar{V}_{II}, \tag{2}$$

$$\Psi_{II}(\mathbf{r}) = \sum_{j=0}\sum_{L} A_L^j N_L(\kappa, \mathbf{r}_j) + \sum_{L} A_L^w J_L(\kappa, \mathbf{r}_w), \quad E > \bar{V}_{II}. \tag{3}$$

We have used a composite index $L \equiv \{l, m\}$ and the following notation

$$\begin{aligned} I_L(\kappa, \mathbf{r}) &= i_l(\kappa r) Y_L(\hat{r}), \quad K_L(\kappa, \mathbf{r}) = k_l(\kappa r) Y_L(\hat{r}), \\ J_L(\kappa, \mathbf{r}) &= j_l(\kappa r) Y_L(\hat{r}), \quad N_L(\kappa, \mathbf{r}) = \eta_l(\kappa r) Y_L(\hat{r}), \end{aligned} \tag{4}$$

where j and η are the spherical BFs of the first and second kind whereas i and k are the spherical modified BFs of the first and second kind, respectively.[10] $Y_L(\hat{r}) \equiv Y_l^m(\hat{r})$ is a spherical harmonic (SH) function. A_L^j and A_L^w are

known expansion coefficients determined by matching the wavefunction and its radial derivative across all the spherical boundaries. Every term on the right-hand side of Eqs. (2) and (3) is a solution to Eq. (1).

Although all the equations in this article are written down for the complex SH,[11,12] they also remain valid for the less common real SH,[13,14] unless otherwise stated. Readers interested in real SH only are urged to ignore all the complex conjugation operations.

2. Addition theorems

The main topic of this article is the consideration of the overlap integrals over the intricate region II as part of the total wavefunction normalization process. Calculation of these integrals requires a translation of the spherical BFs from one center to another. The necessary additions theorems (AdTs) are discussed below. Further information about the derivation of these AdTs is given in the appendix of Ref. 3.

AdT for I and J are single range and, for the purpose of this paper, are compactly expressed as

$$J_L(\kappa,\mathbf{r}) = \sum_{L_1} \mathcal{J}_{LL_1}[J]\left(\kappa,\mathbf{R}_j\right) J_{L_1}(\kappa,\mathbf{r}_j), \tag{5}$$

$$I_L(\kappa,\mathbf{r}) = \sum_{L_1} \mathcal{I}_{LL_1}[I]\left(\kappa,\mathbf{R}_j\right) I_{L_1}(\kappa,\mathbf{r}_j), \tag{6}$$

where the summation on L_1 is a full open sum. The translation coefficient $\mathcal{J}$ is given by

$$\mathcal{J}_{LL_1}[J](\kappa,\mathbf{r}) = 4\pi \sum_{m_2} \sum_{l_2=l+l_1,-2}^{l_{2\min}} (-1)^{s/2} \langle L|L_1|L_2\rangle J_{L_2}(\kappa,\mathbf{r}), \tag{7}$$

with $s = l_1 + l_2 - l$. The above formula is written in terms of the Gaunt coefficients[11,15] of the SH which are defined as

$$\langle L_1|L_2|L_3\rangle = \int Y^*_{L_1}(\hat{r})\, Y_{L_2}(\hat{r})\, Y_{L_3}(\hat{r})\, \mathrm{d}\hat{r}. \tag{8}$$

The SHs are also known to satisfy the following orthonormality condition

$$\int Y^*_{L'}(\hat{r})\, Y_L(\hat{r})\, \mathrm{d}\hat{r} = \delta_{L'L} = \delta_{l'l}\delta_{m'm}. \tag{9}$$

The expression for $\mathcal{I}$ in Eq. (6) can be obtained from Eq. (7) by simply replacing $J \to I$ and $s = 0$.

The AdT for N, on the other hand, is a double range expression of the radial variables which can be written as the following two equivalent formulas

$$N_L(\kappa,\mathbf{r}) = \sum_{L_1} \mathcal{N}_{LL_1}[N](\kappa,\mathbf{r}_>) J_{L_1}(\kappa,\mathbf{r}_<) \tag{10}$$

$$= \sum_{L_1} \mathcal{N}_{LL_1}[J](\kappa,\mathbf{r}_<) N_{L_1}(\kappa,\mathbf{r}_>), \tag{11}$$

where the $>$ and $<$ signify the greater and lesser of r_j and R_j. For $\mathfrak{Z}$ denoting either one of J or N

$$\mathcal{N}_{LL_1}[\mathfrak{Z}](\kappa,\mathbf{r}) = 4\pi \sum_{m_2} \sum_{l_2=l+l_1,-2}^{l_{2\min}} (-1)^{s/2} \langle L_1|L|L_2\rangle \mathfrak{Z}^*_{L_2}(\kappa,\mathbf{r}), \tag{12}$$

where $s = 3l_2 + l - l_1$. Notice that this s and the one given in Eq. (7) are both even integers. Finally, the AdT for K closely resembles that of N. Namely,

$$K_L(\kappa,\mathbf{r}) = \sum_{L_1} \mathcal{K}_{LL_1}[K](\kappa,\mathbf{r}_>) I_{L_1}(\kappa,\mathbf{r}_<) \tag{13}$$

$$= (-1)^l \sum_{L_1} \mathcal{K}_{LL_1}[I](\kappa,\mathbf{r}_<) K_{L_1}(\kappa,\mathbf{r}_>), \tag{14}$$

where

$$\mathcal{K}_{LL_1}[\mathfrak{Z}](\kappa,\mathbf{r}) = 4\pi(-1)^{l_1} \sum_{m_2} \sum_{l_2=l+l_1,-2}^{l_{2\min}} \langle L_1|L|L_2\rangle \mathfrak{Z}^*_{L_2}(\kappa,\mathbf{r}), \tag{15}$$

with $\mathfrak{Z}$ now denoting either one of I or K.

In Eqs. (7), (12), and (15), the summation limit $l_{2\min} = \max(|l-l_1|,|m_2|)$ whereas the range of m_2 is different for real and complex SH functions and must be inferred from the selection rules of the Gaunt coefficients. In Eq. (8), $m_1 = m_2 + m_3$ for complex SH, while for real SH functions, according to their description given in Ref. 13, for example, m_1 takes distinct values from the set $m_1 \in \{m_2 + m_3, m_3 - m_2, m_2 - m_3, -m_3 - m_2\}$. Notice that the shown arrangement of the summations on m_2 and l_2 automatically conforms to the requirement of the selection rules of the Gaunt coefficients that the quantity $(l_1 + l_2 + l)$ be an even integer.

3. Integrals of the interstitial region

All of the overlap integrals of the interstitial region that occur upon substitution of Eq. (3) into $\int_{\Omega^{II}} |\Psi_{II}(\mathbf{r})|^2 \mathrm{d}^3 r$ will be discussed in some detail in this section. The following subsections exhaust all of the possibilities up to complex conjugation of the given overlap integrals. Analogous integrals for the bound state of Eq. (2) are not included here as they can be done easily by following the same procedure.

3.1 Watson–Watson

$$\langle wL'|wL\rangle = \int_{\Omega^{II}} \mathrm{d}^3 r J^*_{L'}(\kappa,\mathbf{r}) J_L(\kappa,\mathbf{r}). \tag{16}$$

When the interstitial region is explicitly decomposed into the interior of the Watson sphere minus the ionspheres, one obtains

$$\begin{aligned}\langle wL'|wL\rangle = &\int_{\Omega_0}^{\Omega_w} \mathrm{d}^3 r J^*_{L'}(\kappa,\mathbf{r}) J_L(\kappa,\mathbf{r}) \\ &- \sum_{i\neq 0} \int_0^{\Omega_i} \mathrm{d}^3 r_i J^*_{L'}(\kappa,\mathbf{R}_i+\mathbf{r}_i) J_L(\kappa,\mathbf{R}_i+\mathbf{r}_i).\end{aligned} \tag{17}$$

Employing Eq. (5) and orthonormality of the SH in Eq. (9) gives the following final form

$$\begin{aligned}\langle wL'|wL\rangle = &\delta_{L'L} \int_{b_0}^{b_w} j_l^2(\kappa r)\, r^2 \mathrm{d}r \\ &- \sum_{i\neq 0} \sum_{l_1=0}^{\infty} \left\{ \sum_{m_1=-l_1}^{l_1} \mathcal{J}^*_{L'L_1}[J](\kappa,\mathbf{R}_i) \mathcal{J}_{LL_1}[J](\kappa,\mathbf{R}_i) \right\} \int_0^{b_i} j_{l_1}^2(\kappa r)\, r^2 \mathrm{d}r.\end{aligned} \tag{18}$$

3.2 Watson–central ionsphere

$$\langle wL'|0L\rangle = \int_{\Omega^{II}} \mathrm{d}^3 r J^*_{L'}(\kappa,\mathbf{r}) N_L(\kappa,\mathbf{r}). \tag{19}$$

This can be written as,

$$\langle wL'|0L\rangle = \int_{\Omega_0}^{\Omega_w} \mathrm{d}^3 r J^*_{L'}(\kappa,\mathbf{r}) N_L(\kappa,\mathbf{r}) - \sum_{i\neq 0} \int_0^{\Omega_i} \mathrm{d}^3 r_i J^*_{L'}(\kappa,\mathbf{R}_i+\mathbf{r}_i) N_L(\kappa,\mathbf{R}_i+\mathbf{r}_i). \tag{20}$$

Apparently, Eq. (10) is needed since $R_i > r_i$, for $i \neq 0$. After substitution of Eq. (10) and using orthonormality of the SH the final form is

$$\langle wL'|0L\rangle = \delta_{L'L} \int_{b_0}^{b_w} j_l(\kappa r)\eta_l(\kappa r)\, r^2 \mathrm{d}r - \sum_{i\neq 0}\sum_{l_1=0}^{\infty} \left\{ \sum_{m_1=-l_1}^{l_1} \mathcal{J}^*_{L'L_1}[J](\kappa,\mathbf{R}_i)\mathcal{N}_{LL_1}[N](\kappa,\mathbf{R}_i) \right\} \int_0^{b_i} j^2_{l_1}(\kappa r)\, r^2 \mathrm{d}r. \tag{21}$$

3.3 Watson–noncentral ionsphere

$$\langle wL'|jL\rangle = \int_{\Omega^{II}} \mathrm{d}^3 r J^*_{L'}(\kappa,\mathbf{r}) N_L(\kappa,\mathbf{r}_j). \tag{22}$$

Following similar formulations as above gives

$$\langle wL'|jL\rangle = \int_{\Omega_0}^{\Omega_w} \mathrm{d}^3 r J^*_{L'}(\kappa,\mathbf{r}) N_L(\kappa,\mathbf{r}-\mathbf{R}_j) - \sum_{i\neq 0} \int_0^{\Omega_i} \mathrm{d}^3 r_i J^*_{L'}(\kappa,\mathbf{R}_i+\mathbf{r}_i) N_L(\kappa,\mathbf{r}_i+\mathbf{R}_i-\mathbf{R}_j). \tag{23}$$

Let us consider the two integrals above separately. The radial part of the first integral must be broken into two pieces and Eqs. (10) and (11) properly implemented according to the relative values of r versus R_j. The result is

$$\int_{\Omega_0}^{\Omega_w} \mathrm{d}^3 r J^*_{L'}(\kappa,\mathbf{r}) N_L(\kappa,\mathbf{r}-\mathbf{R}_j) = \mathcal{N}_{LL'}[N](\kappa,-\mathbf{R}_j) \int_{b_0}^{R_j} j^2_{l'}(\kappa r)\, r^2 \mathrm{d}r + \mathcal{N}_{LL'}[J](\kappa,-\mathbf{R}_j) \int_{R_j}^{b_w} j_{l'}(\kappa r)\eta_{l'}(\kappa r)\, r^2 \mathrm{d}r. \tag{24}$$

The second integral in Eq. (23) will depend on whether $i = j$ or not. If $i = j$, employing Eq. (5) gives

$$\int_0^{\Omega_i} \mathrm{d}^3 r_i J_{L'}^*(\kappa, \mathbf{R}_i + \mathbf{r}_i) N_L(\kappa, \mathbf{r}_i) = \mathcal{J}_{L'L}^*[J](\kappa, \mathbf{R}_j) \int_0^{b_j} j_l(\kappa r) \eta_l(\kappa r)\, r^2 \mathrm{d}r. \tag{25}$$

For the case $i \neq j$, let us use $\mathbf{R}_{ji} = \mathbf{R}_i - \mathbf{R}_j$. Since these are nonoverlapping spheres, both $R_{ji} > b_i$ and $R_{ji} > b_j$ are always true which makes Eqs. (5) and (10) relevant

$$\begin{aligned} &\int_0^{\Omega_i} \mathrm{d}^3 r_i J_{L'}^*(\kappa, \mathbf{R}_i + \mathbf{r}_i) N_L(\kappa, \mathbf{R}_{ji} + \mathbf{r}_i) \\ &= \sum_{L_1} \mathcal{J}_{L'L_1}^*[J](\kappa, \mathbf{R}_i) \mathcal{N}_{LL_1}[N](\kappa, \mathbf{R}_{ji}) \int_0^{b_i} j_{l_1}^2(\kappa r)\, r^2 \mathrm{d}r. \end{aligned} \tag{26}$$

Collecting all the terms gives

$$\begin{aligned} \langle wL' | jL \rangle = &\mathcal{N}_{LL'}[N](\kappa, -\mathbf{R}_j) \int_{b_0}^{R_j} j_{l'}^2(\kappa r)\, r^2 \mathrm{d}r \\ &+ \mathcal{N}_{LL'}[J](\kappa, -\mathbf{R}_j) \int_{R_j}^{b_w} j_{l'}(\kappa r) \eta_{l'}(\kappa r)\, r^2 \mathrm{d}r - \mathcal{J}_{L'L}^*[J](\kappa, \mathbf{R}_j) \\ &\int_0^{b_j} j_l(\kappa r) \eta_l(\kappa r)\, r^2 \mathrm{d}r \\ &- \sum_{i \neq \{0,j\}} \sum_{l_1=0}^{\infty} \left\{ \sum_{m_1=-l_1}^{l_1} \mathcal{J}_{L'L_1}^*[J](\kappa, \mathbf{R}_i) \mathcal{N}_{LL_1}[N](\kappa, \mathbf{R}_{ji}) \right\} \int_0^{b_i} j_{l_1}^2(\kappa r)\, r^2 \mathrm{d}r. \end{aligned} \tag{27}$$

3.4 Central ionsphere–central ionsphere

$$\langle 0L' | 0L \rangle = \int_{\Omega^{II}} \mathrm{d}^3 r N_{L'}^*(\kappa, \mathbf{r}) N_L(\kappa, \mathbf{r}). \tag{28}$$

As usual one can decompose the region as

$$\langle 0L' | 0L \rangle = \int_{\Omega_0}^{\Omega_w} \mathrm{d}^3 r\, N_{L'}^*(\kappa, \mathbf{r}) N_L(\kappa, \mathbf{r}) - \sum_{i \neq 0} \int_0^{\Omega_i} \mathrm{d}^3 r_i\, N_{L'}^*(\kappa, \mathbf{R}_i + \mathbf{r}_i) N_L(\kappa, \mathbf{R}_i + \mathbf{r}_i). \tag{29}$$

Since always $R_i > b_i$, a substitution will be made from Eq. (10) which leads to

$$\langle 0L'|0L\rangle = \delta_{L'L}\int_{b_0}^{b_w}\eta_l^2(\kappa r)\,r^2\mathrm{d}r - \sum_{i\neq 0}\sum_{l_1=0}^{\infty}\left\{\sum_{m_1=-l_1}^{l_1}\mathcal{N}^*_{L'L_1}[N](\kappa,\mathbf{R}_i)\mathcal{N}_{LL_1}[N](\kappa,\mathbf{R}_i)\right\}\int_0^{b_i} j^2_{l_1}(\kappa r)\,r^2\mathrm{d}r. \tag{30}$$

3.5 Central ionsphere–noncentral ionsphere

$$\langle 0L'|jL\rangle = \int_{\Omega^{II}}\mathrm{d}^3 r N^*_{L'}(\kappa,\mathbf{r})N_L(\kappa,\mathbf{r}_j). \tag{31}$$

Decomposing the region gives

$$\langle 0L'|jL\rangle = \int_{\Omega_0}^{\Omega_w}\mathrm{d}^3 r\, N^*_{L'}(\kappa,\mathbf{r})N_L(\kappa,\mathbf{r}-\mathbf{R}_j) - \sum_{i\neq 0}\int_0^{\Omega_i}\mathrm{d}^3 r_i\, N^*_{L'}(\kappa,\mathbf{R}_i+\mathbf{r}_i)N_L(\kappa,\mathbf{R}_i-\mathbf{R}_j+\mathbf{r}_i). \tag{32}$$

Following similar reasoning as in Section 3.3, the final result is

$$\langle 0L'|jL\rangle = \mathcal{N}_{LL'}[N](\kappa,-\mathbf{R}_j)\int_{b_0}^{R_j}\eta_{l'}(\kappa r)j_{l'}(\kappa r)\,r^2\mathrm{d}r + \mathcal{N}_{LL'}[J](\kappa,-\mathbf{R}_j)\int_{R_j}^{b_w}\eta^2_{l'}(\kappa r)\,r^2\mathrm{d}r - \mathcal{N}^*_{L'L}[N](\kappa,\mathbf{R}_j)\int_0^{b_j} j_l(\kappa r)\eta_l(\kappa r)\,r^2\mathrm{d}r - \sum_{i\neq\{0,j\}}\sum_{l_1=0}^{\infty}\left\{\sum_{m_1=-l_1}^{l_1}\mathcal{N}^*_{L'L_1}[N](\kappa,\mathbf{R}_i)\mathcal{N}_{LL_1}[N](\kappa,\mathbf{R}_{ji})\right\}\int_0^{b_i} j^2_{l_1}(\kappa r)\,r^2\mathrm{d}r. \tag{33}$$

3.6 Noncentral ionsphere–same noncentral ionsphere

$$\langle jL'|jL\rangle = \int_{\Omega^{II}}\mathrm{d}^3 r N^*_{L'}(\kappa,\mathbf{r}_j)N_L(\kappa,\mathbf{r}_j). \tag{34}$$

This integral is the most difficult of all. The reason is, following a similar procedure used in the above cases immediately reveals that it leads to a singular, radial integral. The only remedy will be to express it off-center, specifically on the ion j itself, as shown below

$$\langle jL'|jL\rangle = \int_{\Omega_j}^{\Omega_w[\hat{r}_j]} \mathrm{d}^3 r_j \, N^*_{L'}(\kappa, \mathbf{r}_j) N_L(\kappa, \mathbf{r}_j) - \sum_{i\neq j} \int_0^{\Omega_i} \mathrm{d}^3 r_i \, N^*_{L'}(\kappa, \mathbf{R}_i - \mathbf{R}_j + \mathbf{r}_i) N_L(\kappa, \mathbf{R}_i - \mathbf{R}_j + \mathbf{r}_i). \tag{35}$$

The complication in the first integral arises because the radius of the Watson sphere is a function of the angle of the $\mathbf{r}_j$ vector which essentially renders it be a triple integral. One may try to circumvent this by extending the upper bound of the integral to infinity and rewriting as follows

$$\begin{aligned}
&\int_{\Omega_j}^{\Omega_w[\hat{r}_j]} \mathrm{d}^3 r_j \, N^*_{L'}(\kappa, \mathbf{r}_j) N_L(\kappa, \mathbf{r}_j) \\
&= \int_{\Omega_j}^{\infty} \mathrm{d}^3 r_j \, N^*_{L'}(\kappa, \mathbf{r}_j) N_L(\kappa, \mathbf{r}_j) - \int_{\Omega_w}^{\infty} \mathrm{d}^3 r \, N^*_{L'}(\kappa, \mathbf{r} - \mathbf{R}_j) N_L(\kappa, \mathbf{r} - \mathbf{R}_j) \\
&= \delta_{L'L} \int_{b_j}^{\infty} \eta_l^2(\kappa r) \, r^2 \mathrm{d}r - \sum_{L_1} \mathcal{N}^*_{L'L_1}[J](\kappa, -\mathbf{R}_j) \mathcal{N}_{LL_1}[J](\kappa, -\mathbf{R}_j) \int_{b_w}^{\infty} \eta_{l_1}^2(\kappa r) \, r^2 \mathrm{d}r.
\end{aligned} \tag{36}$$

However, the respective boundary terms at infinity will not cancel! This point has been missed in previous work.[5] To see this more clearly, let us break the first radial integral into two and write the above equation as follows

$$\begin{aligned}
&\int_{\Omega_j}^{\Omega_w[\hat{r}_j]} \mathrm{d}^3 r_j \, N^*_{L'}(\kappa, \mathbf{r}_j) N_L(\kappa, \mathbf{r}_j) = \delta_{L'L} \int_{b_j}^{b_w} \eta_l^2(\kappa r) \, r^2 \mathrm{d}r \\
&+ \sum_{l_1} \left\{ \delta_{L'L} \, \delta_{l_1 l} - \sum_{m_1=-l_1}^{l_1} \mathcal{N}^*_{L'L_1}[J](\kappa, -\mathbf{R}_j) \mathcal{N}_{LL_1}[J](\kappa, -\mathbf{R}_j) \right\} \int_{b_w}^{\infty} \eta_{l_1}^2(\kappa r) \, r^2 \mathrm{d}r.
\end{aligned} \tag{37}$$

The quantity in curly brackets must be identically zero in order to nullify the last singular integral. However, since the direction of translation for both coefficients $\mathcal{N}$ is the same $(-\hat{R}_j)$ and also the independent summation is only over m_1, it is clear the term in curly brackets is generally nonzero.

Since it is now evident that the integral is difficult to express without singular terms, we will discuss another method of doing the integral numerically more economical than a triple integral. Let us first write

$$\int_{\Omega_j}^{\Omega_w[\hat{r}_j]} \mathrm{d}^3 r_j \, N^*_{L'}(\kappa, \mathbf{r}_j) N_L(\kappa, \mathbf{r}_j) = \int \mathrm{d}\hat{r}_j \, Y^*_{L'}(\hat{r}_j) Y_L(\hat{r}_j) \int_{b_j} \eta_{l'}(\kappa r_j) \eta_l(\kappa r_j) \, r_j^2 \mathrm{d}r_j. \tag{38}$$

Assume $\mathbf{R}_j$ is in the (global) $\hat{z}$ direction. This assumption can be made because only one ionsphere is involved and, as far as Eq. (38) is concerned, $\mathbf{R}_j$ affects only the upper limit of the radial integral. This assumption allows the integral over the azimuthal angle $\phi_j[0, 2\pi]$ to be evaluated, after which it becomes a $\delta_{m'm}$ due to the SH orthonormality. Further simplification can also be gained if the order of the ensuing double integral is reversed (by preserving the same two-dimensional integration area) as follows

$$\begin{aligned} &\int_{\Omega_j}^{\Omega_w[\hat{r}_j]} \mathrm{d}^3 r_j \, N^*_{L'}(\kappa, \mathbf{r}_j) N_L(\kappa, \mathbf{r}_j) \\ &= \delta_{m'm} \int_{b_j}^{b_w + R_j} \mathrm{d}r_j \, r_j^2 \eta_{l'}(\kappa r_j) \eta_l(\kappa r_j) \int_{-1}^{u(r_j)} \mathrm{d}x_j \, \bar{P}^m_{l'}(x_j) \bar{P}^m_l(x_j). \end{aligned} \tag{39}$$

$\bar{P}$ is a "normalized" Legendre polynomial. Specifically,

$$\bar{P}^m_l(x) = \sqrt{\frac{(2l+1)}{2} \frac{(l-m)!}{(l+m)!}} P^m_l(x), \tag{40}$$

where P is the associated Legendre polynomial.[12] The integration upper limit u is determined by imposing $\left|\mathbf{r}_j + \mathbf{R}_j\right| = b_w$. Using $\mathbf{r}_j.\mathbf{R}_j = r_j R_j x_j$, the result is

$$u(r_j) = \begin{cases} 1, & \text{if } b_j \le r_j \le b_w - R_j, \\ \left(b_w^2 - R_j^2 - r_j^2\right)/2R_j r_j, & \text{if } b_w - R_j \le r_j \le b_w + R_j, \end{cases} \tag{41}$$

which implies, $-1 \le u(r_j) \le 1$. The inner integral can thus be done analytically, as will be shown below, reducing the overall task into a single integral. To this end, let us define the inner integral and linearize as follows

$$\begin{aligned} I^m_{l_1 l_2}(x) &= \int_{-1}^{x} \bar{P}^m_{l_1}(\gamma) \bar{P}^m_{l_2}(\gamma) \, \mathrm{d}\gamma \\ &= \frac{1}{2} \sqrt{(2l_1+1)(2l_2+1)} \sum_{l=l_1+l_2,-2}^{l_{\min}} \sqrt{\frac{(l-2m)!}{(l+2m)!}} C^{l0}_{l_1 0 l_2 0} C^{l(2m)}_{l_1 m l_2 m} S^{2m}_l(x), \end{aligned} \tag{42}$$

where $l_{\min} = \max(|l_1 - l_2|, |2m|)$, C is the Clebsch–Gordan coefficient and S is a primitive of P defined as

$$S_n^m(x) = \int_{-1}^{x} P_n^m(y)\,\mathrm{d}y, \qquad -1 \le x \le 1. \tag{43}$$

Eq. (42) follows from the Clebsch–Gordan series for the SH functions.[11] It can be shown that the S polynomials satisfy the following recursion relation which is particularly favorable for expedited execution of Eq. (42)

$$\begin{aligned}(n+1)(n-m)S_n^m(x) = &-(2n-1)\left(1-x^2\right)P_{n-1}^m(x)\\ &+(n-2)(n+m-1)S_{n-2}^m(x), \quad n \ge m \wedge m \ge 0.\end{aligned} \tag{44}$$

The above recursion can be started with a proper choice of either one of the following two options

$$S_m^m(x) = 2(-1)^m \frac{(2m)!}{m!} B_{\frac{x+1}{2}}\left(\frac{m}{2}+1, \frac{m}{2}+1\right), \tag{45}$$

$$S_{m+1}^m(x) = \frac{\sqrt{1-x^2}}{m+2} P_{m+1}^{m+1}(x), \tag{46}$$

where B is the incomplete Beta function.[12] To the best of the authors' knowledge, the above three equations are given for the first time here. For the very important case of $m = 0$, an even simpler three-term recursion identity is also available[16]

$$(n+1)S_n(x) = (2n-1)xS_{n-1}(x) - (n-2)S_{n-2}(x), \quad n \ge 2, \tag{47}$$

along with $S_1(x) = (x^2 - 1)/2$ and $S_0(x) = x + 1$, where the notation $S_n(x) \equiv S_n^0(x)$ has been used. Finally, negative m values can be recovered from the following relation which carries over from a well-known property of P

$$S_n^{-m}(x) = (-1)^m \frac{(n-m)!}{(n+m)!} S_n^m(x). \tag{48}$$

The above relation is given for the sake of completeness because $I_{l_1 l_2}^{-m}(x) = I_{l_1 l_2}^m(x)$ due to the symmetry property $\bar{P}_l^{-m}(x) = (-1)^m \bar{P}_l^m(x)$. Hence, after substituting Eq. (39) into Eq. (35) and further simplification, the final form is

$$\begin{aligned}
&\langle jL'|jL\rangle \\
&= \delta_{m'm}\left[\delta_{l'l}\int_{bj}^{b_w-R_j}\eta_l^2(\kappa r)\,r^2\mathrm{d}r + \int_{b_w-R_j}^{b_w+R_j}\eta_{l'}(\kappa r)\eta_l(\kappa r)I_{l'l}^m(u(r))\,r^2\mathrm{d}r\right] \\
&-\sum_{i\neq j}\sum_{l_1=0}^{\infty}\left\{\sum_{m_1=-l_1}^{l_1}\mathcal{N}^*_{L'L_1}[N](\kappa,\mathbf{R}_{ji})\mathcal{N}_{LL_1}[N](\kappa,\mathbf{R}_{ji})\right\}\int_0^{b_i} j_{l_1}^2(\kappa r)\,r^2\mathrm{d}r,
\end{aligned} \tag{49}$$

where the argument $u(r)$ is given in Eq. (41). In the first integral, the orthonormality relation $I_{l'l}^m(1)=\delta_{l'l}$ has been used for the special case $u(r)=1$. It is now apparent that due to the presence of the I function the second radial integral above can only be done numerically. If this proves to be computationally expensive, one can optionally store it for all the required quantum numbers m, l' and l given particular values of κ and R_j. Due to the symmetry of this radial integral, it suffices to store its corresponding values for $l \geq l'$ and $0 \leq m \leq l$ only.

3.7 Noncentral ionsphere–different noncentral ionsphere

$$\langle j'L'|jL\rangle = \int_{\Omega^{II}} \mathrm{d}^3 r N^*_{L'}(\kappa,\mathbf{r}_{j'})N_L(\kappa,\mathbf{r}_j). \tag{50}$$

The region can be decomposed as

$$\begin{aligned}
\langle j'L'|jL\rangle \;&= \int_{\Omega_0}^{\Omega_w}\mathrm{d}^3 r\, N^*_{L'}(\kappa,\mathbf{r}-\mathbf{R}_{j'})N_L(\kappa,\mathbf{r}-\mathbf{R}_j) \\
&-\int_0^{\Omega_{j'}}\mathrm{d}^3 r_{j'}\, N^*_{L'}(\kappa,\mathbf{r}_{j'})N_L(\kappa,\mathbf{r}_{j'}+\mathbf{R}_{j'}-\mathbf{R}_j) \\
&-\int_0^{\Omega_j}\mathrm{d}^3 r_j\, N^*_{L'}(\kappa,\mathbf{r}_j+\mathbf{R}_j-\mathbf{R}_{j'})N_L(\kappa,\mathbf{r}_j) \\
&-\sum_{i\neq\{0,j',j\}}\int_0^{\Omega_i}\mathrm{d}^3 r_i\, N^*_{L'}(\kappa,\mathbf{r}_i+\mathbf{R}_i-\mathbf{R}_{j'})N_L(\kappa,\mathbf{r}_i+\mathbf{R}_i-\mathbf{R}_j).
\end{aligned} \tag{51}$$

Defining $R_< = \min(R_{j\prime}, R_j)$ and $R_> = \max(R_{j\prime}, R_j)$, the radial part of the first integral can be divided into three terms as follows

$$\begin{aligned}
&\int_{\Omega_0}^{\Omega_w} \mathrm{d}^3 r\, N^*_{L'}(\kappa, \mathbf{r} - \mathbf{R}_{j'}) N_L(\kappa, \mathbf{r} - \mathbf{R}_j) \\
&= \sum_{L'_1 L_1} \mathcal{N}^*_{L'L'_1}[N](\kappa, -\mathbf{R}_{j'}) \mathcal{N}_{LL_1}[N](\kappa, -\mathbf{R}_j) \int \mathrm{d}\hat{r} \int_{b_0}^{R_<} \mathrm{d}r\, r^2 J^*_{L'_1}(\kappa, \mathbf{r}) J_{L_1}(\kappa, \mathbf{r}) \\
&+ \sum_{L'_1 L_1} \mathcal{N}^*_{L'L'_1}[J](\kappa, -\mathbf{R}_<) \mathcal{N}_{LL_1}[N](\kappa, -\mathbf{R}_>) \int \mathrm{d}\hat{r} \int_{R_<}^{R_>} \mathrm{d}r\, r^2 N^*_{L'_1}(\kappa, \mathbf{r}) J_{L_1}(\kappa, \mathbf{r}) \\
&+ \sum_{L'_1 L_1} \mathcal{N}^*_{L'L'_1}[J](\kappa, -\mathbf{R}_{j'}) \mathcal{N}_{LL_1}[J](\kappa, -\mathbf{R}_j) \int \mathrm{d}\hat{r} \int_{R_>}^{b_w} \mathrm{d}r\, r^2 N^*_{L'_1}(\kappa, \mathbf{r}) N_{L_1}(\kappa, \mathbf{r}).
\end{aligned} \tag{52}$$

Hence, the final result is

$$\begin{aligned}
&\langle j'L' | jL \rangle \\
&= \sum_{l_1=0}^{\infty} \left\{ \sum_{m_1=-l_1}^{l_1} \mathcal{N}^*_{L'L_1}[N]\left(\kappa, -\mathbf{R}_{j'}\right) \mathcal{N}_{LL_1}[N]\left(\kappa, -\mathbf{R}_j\right) \right\} \int_{b_0}^{R_<} j^2_{l_1}(\kappa r)\, r^2 \mathrm{d}r \\
&+ \sum_{l_1=0}^{\infty} \left\{ \sum_{m_1=-l_1}^{l_1} \mathcal{N}^*_{L'L_1}[J](\kappa, -\mathbf{R}_<) \mathcal{N}_{LL_1}[N](\kappa, -\mathbf{R}_>) \right\} \int_{R_<}^{R_>} \eta_{l_1}(\kappa r) j_{l_1}(\kappa r)\, r^2 \mathrm{d}r \\
&+ \sum_{l_1=0}^{\infty} \left\{ \sum_{m_1=-l_1}^{l_1} \mathcal{N}^*_{L'L_1}[J]\left(\kappa, -\mathbf{R}_{j'}\right) \mathcal{N}_{LL_1}[J]\left(\kappa, -\mathbf{R}_j\right) \right\} \int_{R_>}^{b_w} \eta^2_{l_1}(\kappa r)\, r^2 \mathrm{d}r \\
&- \mathcal{N}_{LL'}[N]\left(\kappa, \mathbf{R}_{jj'}\right) \int_0^{b_{j'}} \eta_{l'}(\kappa r) j_{l'}(\kappa r)\, r^2 \mathrm{d}r - \mathcal{N}^*_{L'L}[N]\left(\kappa, \mathbf{R}_{j'j}\right) \int_0^{b_j} j_l(\kappa r) \eta_l(\kappa r)\, r^2 \mathrm{d}r \\
&- \sum_{i \neq \{0, j', j\}} \sum_{l_1=0}^{\infty} \left\{ \sum_{m_1=-l_1}^{l_1} \mathcal{N}^*_{L'L_1}[N]\left(\kappa, \mathbf{R}_{j'i}\right) \mathcal{N}_{LL_1}[N]\left(\kappa, \mathbf{R}_{ji}\right) \right\} \int_0^{b_i} j^2_{l_1}(\kappa r)\, r^2 \mathrm{d}r.
\end{aligned} \tag{53}$$

4. Conclusion

All the necessary integrals pertinent to the overlap integral of the solutions to the interstitial region have been worked out. Although only the continuum cases are discussed, the corresponding bound state integrals can be straightforwardly done. The AdTs for the bound case are already

included in this article. All of the integrals given in Section 3 have been programmed by us using real SH functions. Early numerical tests indicate that all of them exhibit good convergence and that the convergence is not very sensitive to the spatial proximity of the ionspheres. However, a direct numerical check of the integrals separately is difficult to obtain due to the complicated nature of the integrals. The only valid check comes when all of it is put together as part of a relevant theoretical method and applied to test cases of small molecules and clusters. Such an endeavor is underway and results will be reported in the future.

Appendix

Most of the necessary radial integrals are summarized here.[5] For $\mathcal{Z}$ representing the BFs i, k, j, or η, one has

$$\int [\mathcal{Z}_n(\kappa r)]^2 r^2 \mathrm{d}r = \frac{r^3}{2}\left\{[\mathcal{Z}_n(\kappa r)]^2 - \mathcal{Z}_{n-1}(\kappa r)\mathcal{Z}_{n+1}(\kappa r)\right\}. \tag{A.1}$$

The mixed integrals are

$$\int i_n(\kappa r)k_n(\kappa r)\, r^2 \mathrm{d}r = \frac{r^3}{4}[2i_n(\kappa r)k_n(\kappa r) + i_{n-1}(\kappa r)k_{n+1}(\kappa r) + i_{n+1}(\kappa r)k_{n-1}(\kappa r)], \tag{A.2}$$

$$\int j_n(\kappa r)\eta_n(\kappa r)\, r^2 \mathrm{d}r = \frac{r^3}{4}[2j_n(\kappa r)\eta_n(\kappa r) - j_{n-1}(\kappa r)\eta_{n+1}(\kappa r) - j_{n+1}(\kappa r)\eta_{n-1}(\kappa r)]. \tag{A.3}$$

All of these integrals remain valid for the $n = 0$ case with the following definitions

$$i_{-1}(x) = i_0(x) + k_0(x) = \frac{\cosh(x)}{x}, \tag{A.4}$$

$$k_{-1}(x) = k_0(x) = \frac{\mathrm{e}^{-x}}{x}, \tag{A.5}$$

$$j_{-1}(x) = -\eta_0(x) = \frac{\cos(x)}{x}, \tag{A.6}$$

$$\eta_{-1}(x) = j_0(x) = \frac{\sin(x)}{x}. \tag{A.7}$$

Acknowledgments

D.H.G. and C.A.W. were partially supported by the Department of Energy, National Nuclear Security Administration, under Award Number (s) DE-NA0003866. D.H.G. was also supported in part by Minority Serving Institutions Partnership Program, National Nuclear Security Administration and by the HED center at the Lawrence Livermore National Laboratory. D.H.G. would also like to thank Dr. Paul Grabowski and Dr. Daniel Aberg at the LLNL for their useful comments and discussions.

References

1. Slater, J. C. Wave Functions in a Periodic Potential. *Phys. Rev.* **1937**, *51*, 846–851. https://doi.org/10.1103/PhysRev.51.846.
2. Watson, R. E. Analytic Hartree-Fock Solutions for $O^{=}$. *Phys. Rev.* **1958**, *111*, 1108–1110. https://doi.org/10.1103/PhysRev.111.1108.
3. Johnson, K. H. Scattered-Wave Theory of the Chemical Bond. In Löwdin, P.-O. Ed.; Advances in Quantum Chemistry; Academic Press, 1973; Vol. 7, pp 143–185. https://doi.org/10.1016/S0065-3276(08)60561-4.
4. Connolly, J. W. D.; Sabin, J. R. Total Energy in the Multiple Scattering Formalism: Application to the Water Molecule. *J. Chem. Phys.* **1972**, *56*(11), 5529–5533. https://doi.org/10.1063/1.1677072.
5. Katsuki, S.; Klobukowski, M.; Palting, P.; Huzinaga, S. A Manual of the MSXa Program:Version II. Division of Theoretical Chemistry, Department of Chemistry, University of Alberta, 1980, pp. 54–55.
6. A. A. Bahurmuz, C. H. W. The Multi-scattering-Xn Method for Analysis of the Electronic Structure of Atomic Clusters. Whiteshell Nuclear Research Establishment: Pinawa, Manitoba, 1984.
7. Yang, C. Y. Relativistic scattered-wave theory. II. Normalization and symmetrization. *J. Chem. Phys.* **1978**, *68*(6), 2626–2629. https://doi.org/10.1063/1.436095.
8. Dill, D.; Dehmer, J. L. Electron-molecule scattering and molecular photoionization using the multiple-scattering method. *J. Chem. Phys.* **1974**, *61*(2), 692–699. 10.1063/1.1681947.
9. Sébilleau, D.; Hatada, K.; Ebert, H., Eds. Multiple Scattering Theory for Spectroscopies. In *Springer Proceedings in Physics*, vol. 204; Springer International Publishing: Cham, 2018.
10. Arfken, G. B.; Weber, H. J.; Harris, F. E. *Mathematical Methods for Physicists*, 6th ed.; Academic Press: Boston, 2005.
11. Varshalovich, D. A.; Moskalev, A. N.; Khersonskii, V. K. *Quantum Theory of Angular Momentum*. World Scientific, 1988.10.1142/0270.
12. Olver, F. W.; Lozier, D. W.; Boisvert, R. F.; Clark, C. W. *NIST Handbook of Mathematical Functions*, 1st ed.; Cambridge University Press: New York, NY, USA, 2010.
13. Homeier, H. H.; Steinborn, E. *Some properties of the coupling coefficients of real spherical harmonics and their relation to Gaunt coefficients*. *J. Mol. Struct.: THEOCHEM* **1996**, *368*, 31–37. https://doi.org/10.1016/S0166-1280(96)90531-X.
14. Blanco, M. A.; Florez, M.; Bermejo, M. Evaluation of the rotation matrices in the basis of real spherical harmonics. *J. Mol. Struct.: THEOCHEM* **1997**, *419*(1), 19–27. https://doi.org/10.1016/S0166-1280(97)00185-1.
15. Gaunt, J. A.; Fowler, R. H. IV. The triplets of helium. *Philos. Trans. R. Soc. Lond. A* **1929**, *228*(659–669), 151–196. https://doi.org/10.1098/rsta.1929.0004.
16. Gebremedhin, D.; Weatherford, C. *Numerical Integration as an Initial Value Problem*. 2018.

CHAPTER FIVE

Self-consistent electron–nucleus cusp correction for molecular orbitals

Pierre-François Loos[1], **Anthony Scemama, Michel Caffarel**
Laboratoire de Chimie et Physique Quantiques, Université de Toulouse, CNRS, UPS, Toulouse, France
[1]Corresponding author: e-mail address: loos@irsamc.ups-tlse.fr

Contents

Abstract

We describe a method for imposing the correct electron–nucleus (e-n) cusp in molecular orbitals expanded as a linear combination of (cuspless) Gaussian basis functions. Enforcing the e-n cusp in trial wave functions is an important asset in quantum Monte Carlo calculations as it significantly reduces the variance of the local energy during the Monte Carlo sampling. In the method presented here, the Gaussian basis set is augmented with a small number of Slater basis functions. Note that, unlike other e-n cusp-correction schemes, the presence of the Slater function is not limited to the vicinity of the nuclei. Both the coefficients of these cuspless Gaussian and cusp-correcting Slater basis functions may be self-consistently optimized by diagonalization of an orbital-dependent effective Fock operator. Illustrative examples are reported for atoms (H, He, and Ne) as well as for a small molecular system (BeH_2). For the simple case of the He atom, we observe that, with respect to the cuspless version, the variance is reduced by one order of magnitude by applying our cusp-corrected scheme.

Advances in Quantum Chemistry, Volume 79
ISSN 0065-3276
https://doi.org/10.1016/bs.aiq.2019.03.003

1. Introduction

In the last decade, the advent of massively parallel computational platforms and their ever-growing number of computing nodes has unveiled new horizons for studying quantum systems. It is now widely recognized that there is an imperative need to develop methods that take full advantages of these new supercomputer architectures and scale up to an arbitrary number of cores. A class of methods known to scale up nicely is stochastic approaches, and especially quantum Monte Carlo (QMC) methods which are steadily becoming the go-to computational tool for reaching high accuracy in large-scale problems (see, for example, Refs. 1–5). In practice, to make QMC feasible for large systems, it is essential to resort to accurate trial wave functions leading both to an efficient sampling of the configuration space and to low energy fluctuations. A precious guide to build up such functions is to take into account the universal features known about the exact many-electron wave function.[6–13]

In standard QMC implementations, the trial wave functions are usually defined as[14–16]

$$\Psi_{\mathrm{T}}(\boldsymbol{R}) = e^{J(\boldsymbol{R})} \sum_I c_I D_I^{\uparrow}(\boldsymbol{R}^{\uparrow})\, D_I^{\downarrow}(\boldsymbol{R}^{\downarrow}), \tag{1}$$

where D_I^{σ} and $\boldsymbol{R}^{\sigma}$ are determinants and coordinates of the spin-σ electrons, respectively. The fermionic nature of the wave function is imposed using a single- or multideterminant expansion of Slater determinants[17–22] made of Hartree–Fock (HF) or Kohn–Sham (KS) molecular orbitals (MOs)

$$\phi_i(\boldsymbol{r}) = \sum_{\mu}^{N} c_{\mu i}\, \chi_{\mu}(\boldsymbol{r}) \tag{2}$$

built as a linear combination of N Gaussian basis functions $\chi_{\mu}(\boldsymbol{r})$. $J(\boldsymbol{R})$ is called the Jastrow factor and its main purpose is to catch the bulk of the dynamic electron correlation.

At short interparticle distances, the Coulombic singularity dominates all other terms and, near the two-particle coalescence points, the behavior of the exact wave function Ψ becomes independent of other details of the system.[13] In particular, early work by Kato,[23,24] and elaborations by Pack and Brown,[25] showed that, as one electron at $\boldsymbol{r}_i$ approaches a nucleus of charge Z_A at $\boldsymbol{r}_A$, we have

$$\left.\frac{\partial\langle\Psi(\boldsymbol{R})\rangle}{\partial r_i}\right|_{r_i=r_A} = -Z_A\langle\Psi(\boldsymbol{R})\rangle|_{r_i=r_A}, \tag{3}$$

where $\langle\Psi(\boldsymbol{R})\rangle|_{r_i=r_A}$ is the spherical average of $\Psi(\boldsymbol{R})$ about $\boldsymbol{r}_i = \boldsymbol{r}_A$.

To remove divergences in the local energy at the electron–nucleus (e-n) coalescence points, cusp conditions such as (3) must be satisfied. (Note that the use of pseudopotentials also removes such divergences as routinely done in QMC calculations, but at the price of introducing systematic errors such as the pseudopotential localization error.) These divergences are especially harmful in DMC calculations, where they can lead to a large increase of the statistical variance, population-control problems, and significant biases.[15]

There are two possible ways to enforce the correct e-n cusp. One approach is to enforce the e-n cusp within the Jastrow factor in Eq. (1). This has the disadvantage of increasing the number of parameters in $J(\boldsymbol{R})$, and their interdependence can be tricky as one must optimize the large number of linear and nonlinear parameters contained in $J(\boldsymbol{R})$ via a stochastic (noisy) optimization of the energy and/or its variance. However, it is frequently done in the literature thanks to some recent progress.[26–28] Another method is to enforce the cusp within the multideterminant expansion of Eq. (1).

However, because one usually employs Gaussian basis functions[29] (as in standard quantum chemistry packages), the MOs $\phi_i(\boldsymbol{r})$ are cuspless, i.e.,

$$\left.\frac{\partial\langle\phi_i(\boldsymbol{r})\rangle}{\partial r}\right|_{r=r_A} = 0. \tag{4}$$

One solution would be to use a different set of basis functions[30] as, for instance, Slater basis functions.[31–33] However, they are known to be troublesome, mainly due to the difficulty of calculating multicentric two-electron integrals which require expensive numerical expansions or quadratures. Nevertheless, some authors[34] have explored using wave functions built with Slater basis functions[35] while imposing the right e-n cusp afterward. (Note that it is also possible to enforce the correct e-n cusp during the SCF process although it is rarely done.[36]) These types of calculations can be performed with an electronic structure package such as ADF.[37] However, as far as we know, it is hard to perform large-scale calculations with Slater basis functions and the virtual space is usually poorly described. Moreover, the available Gaussian bases are usually of better quality than Slater-based ones due to the extensive knowledge and experience gathered by quantum chemists over the last 50 years while building robust, compact and effective Gaussian basis sets.

Conventional cusp-correction methods usually replace the part of $\chi_\mu(\mathbf{r})$ or $\phi_i(\mathbf{r})$ close to the nuclei within a cusp-correction radius by a polynomial or a spline function which fulfills Kato cusp conditions and ensures a well-behaved local energy.[38–41] For atoms, one can also substitute Gaussian core orbitals by tabulated Slater-based ones.[42–44] In the same vein, Toulouse and Umrigar have fitted Slater basis functions with a large number of Gaussian functions and replaced them within the QMC calculation.[28] However, it is hardly scalable for large systems due to its lack of transferability and the ever-growing number of primitive two-electron integrals to compute.

Here, we propose to follow a different, alternative route by augmenting conventional Gaussian basis sets with cusp-correcting Slater basis functions. Mixed Gaussian-Slater basis sets have been already considered in the past with limited success due to the difficultly of computing efficiently mixed electron repulsion integrals.[45–52] However, we will show that, because of the way we introduce the cusp correction, the integrals required here are not that scary. For the sake of simplicity, we will focus on the HF formalism in the present study, although our scheme can also be applied in the KS framework.

2. Cusp-corrected orbitals

A sufficient condition to ensure that Φ fulfills the e-n cusp (3) is that each (occupied and virtual) MO $\tilde{\phi}_i(\mathbf{r})$ satisfies the e-n cusp at each nuclear position $\mathbf{r}_A$:

$$\left.\frac{\partial\langle\tilde{\phi}_i(\mathbf{r})\rangle}{\partial r}\right|_{r=r_A} = -Z_A\langle\tilde{\phi}_i(\mathbf{r})\rangle\big|_{r=r_A}. \tag{5}$$

Note that this is true only if no linear term in r is introduced within the Jastrow factor. Without loss of generality, we also assume that the basis functions have been already orthogonalized via the standard procedure,[53] i.e., $\langle\chi_\mu|\chi_\nu\rangle = \delta_{\mu\nu}$, where $\delta_{\mu\nu}$ is the Kronecker delta.[54]

Here, we enforce the correct e-n cusp by adding a cusp-correcting orbital to each MO:

$$\tilde{\phi}_i(\mathbf{r}) = \phi_i(\mathbf{r}) + \hat{P}\varphi_i(\mathbf{r}), \tag{6}$$

with

$$\varphi_i(\mathbf{r}) = \sum_A^M \tilde{c}_{Ai}\tilde{\chi}^i_A(\mathbf{r}), \tag{7}$$

where M is the number of nuclear centers and

$$\tilde{\chi}^i_A(\boldsymbol{r}) = \sqrt{\frac{\tilde{\alpha}_i^3}{\pi}} \exp\left[-\tilde{\alpha}_i |\boldsymbol{r} - \boldsymbol{r}_A|\right] \tag{8}$$

is a $1s$ Slater function centered on nucleus A with an orbital-dependent exponent $\tilde{\alpha}_i$. In Eq. (6), the projector

$$\hat{P} = \hat{I} - \sum_\mu |\chi_\mu\rangle\langle\chi_\mu| \tag{9}$$

(where $\hat{I}$ is the identity operator) ensures orthogonality between $\phi_i(\boldsymbol{r})$ and the cusp-correcting orbital $\varphi_i(\boldsymbol{r})$.

It is easy to show that ensuring the right e-n cusp yields the following linear system of equations for the coefficients c_{Ai}:

$$\sum_B \left[-\frac{\delta_{AB}}{Z_A} \partial_r \tilde{\chi}^i_A(\boldsymbol{r}_A) - \tilde{\chi}^i_A(\boldsymbol{r}_A) + \sum_\mu \tilde{S}^i_{B\mu} \chi_\mu(\boldsymbol{r}_A) \right] \tilde{c}_{Bi} = \phi_i(\boldsymbol{r}_A), \tag{10}$$

where δ_{AB} is the Kronecker delta[54] and the explicit expression of the matrix elements $\tilde{S}^i_{\mu A} = \langle \chi_\mu | \tilde{\chi}^i_A \rangle$ is given in Appendix and

$$\partial_r \tilde{\chi}^i_A(\boldsymbol{r}_A) \equiv \left. \frac{\partial \tilde{\chi}^i_A(\boldsymbol{r})}{\partial r} \right|_{r=r_A}. \tag{11}$$

Eq. (10) can be easily solved using standard linear algebra packages and provides a way to obtain a cusp-corrected orbital $\tilde{\phi}_i(\boldsymbol{r})$ from a given MO $\phi_i(\boldsymbol{r})$. For reasons that will later become apparent, we will refer to this procedure as a one-step (OS) calculation. In the next section, we are going to explain how one can optimize self-consistently the coefficients $\tilde{c}_{Ai}$.

3. Self-consistent dressing of the Fock matrix

So far, the coefficient $\tilde{c}_{Ai}$ have been set via Eq. (10). Therefore, they have not been obtained via a variational procedure as their only purpose is to enforce the e-n cusp. However, they do depend on $\phi_i(\boldsymbol{r}_A)$, hence on the MO coefficients $c_{\mu i}$. We will show below that one can optimize simultaneously the coefficients $\tilde{c}_{Ai}$ and $c_{\mu i}$ by constructing an orbital-dependent effective Fock matrix.

The key point is to assume that $\tilde{\phi}_i(\boldsymbol{r})$ is an eigenfunction of the Fock operator $\hat{f}$, as we require

$$\hat{f}\,|\tilde{\phi}_i\rangle = \tilde{\varepsilon}_i\,|\tilde{\phi}_i\rangle. \tag{12}$$

Note that, even at convergence of a conventional HF or KS calculation, the equality (12) is never fulfilled (unless the basis happens to span the exact orbital). This under-appreciated fact has been used by Deng et al. to design a measure of the quality of a MO.[55]

Next, we project out Eq. (12) over $\langle\chi_\mu|$ yielding

$$\sum_\nu F_{\mu\nu}c_{\nu i} + \sum_A \tilde{c}_{Ai}\left(\tilde{F}^i_{\mu A} - \sum_\lambda F_{\mu\lambda}\tilde{S}^i_{\lambda A}\right) = \tilde{\varepsilon}_i c_{\mu i}, \tag{13}$$

where

$$F_{\mu\nu} = \langle\chi_\mu|\hat{f}|\chi_\nu\rangle, \quad \tilde{F}^i_{\mu A} = \langle\chi_\mu|\hat{f}|\tilde{\chi}^i_A\rangle. \tag{14}$$

In the general case, because we must use basis functions with nonzero derivatives at the nucleus, finding the matrix elements $\tilde{F}^i_{\mu A}$ is challenging and costly. However, because we are interested in the e-n cusp, we have found that a satisfactory approximation is

$$\tilde{F}^i_{\mu A} - \sum_\lambda F_{\mu\lambda}\tilde{S}^i_{\lambda A} \approx \tilde{h}^i_{\mu A} - \sum_\lambda H^c_{\mu\lambda}\tilde{S}^i_{\lambda A} \tag{15}$$

where

$$H^c_{\mu\nu} = \langle\chi_\mu|\hat{h}|\chi_\nu\rangle, \quad \tilde{h}^i_{\mu A} = \langle\chi_\mu|\hat{h}|\tilde{\chi}^i_A\rangle, \tag{16}$$

and $\hat{h}$ is the core Hamiltonian. (The expression of the matrix elements $\tilde{h}^i_{\mu A}$ are given in Appendix.) Note that, in Eq. (15), it is important to use the same approximation for both terms ($\tilde{F}^i_{\mu A} \approx \tilde{h}^i_{\mu A}$ and $F_{\mu\nu} \approx H^c_{\mu\nu}$) in order to preserve the subtle balance between the two terms.

The eigenvalue problem given by Eq. (13) can be recast as

$$\sum_\nu \tilde{F}^i_{\mu\nu}c_{\nu i} = \tilde{\varepsilon}_i c_{\mu i}, \tag{17}$$

where we have "dressed" the diagonal of the Fock matrix

$$\tilde{F}^i_{\mu\nu} = \begin{cases} F_{\mu\mu} + \tilde{D}^i_\mu, & \text{if } \mu = \nu, \\ F_{\mu\nu}, & \text{otherwise,} \end{cases} \tag{18}$$

with

$$\tilde{D}^i_\mu = c^{-1}_{\mu i} \sum_A \tilde{c}_{Ai} \left(\tilde{h}^i_{\mu A} - \sum_\lambda H^c_{\mu\lambda} \tilde{S}^i_{\lambda A} \right). \tag{19}$$

The process is repeated until our convergence criterion is met, i.e., the largest absolute value of the elements of the commutator $\tilde{\boldsymbol{F}}^i \boldsymbol{P} - \boldsymbol{P}\tilde{\boldsymbol{F}}^i$ is lower than a given threshold, where $\tilde{\boldsymbol{F}}^i$ is the dressed Fock matrix [Eq. (18)] and $\boldsymbol{P}$ is the density matrix with

$$P_{\mu\nu} = \sum_i^{\text{occ}} c_{\mu i} c_{\nu i}. \tag{20}$$

In the remainder of this chapter, we will refer to this procedure as self-consistent dressing (SCD).

Similar to the Perdew–Zunger self-interaction correction,[56] the orbitals $\tilde{\phi}_i(\boldsymbol{r})$ are eigenfunctions of different Fock operators and therefore no longer necessarily orthogonal. Practically, we have found that the e-n cusp correction makes the cusp-corrected MOs $\tilde{\phi}_i$ slightly nonorthogonal. However, this is not an issue since one evaluates the energy via MC sampling which only requires the evaluation of the MOs and their first and second derivatives in QMC.

Obviously, as evidenced by Eq. (18), when $c_{\mu i}$ is small, the dressing of the Fock matrix is numerically unstable. Therefore, we have chosen not to dress the Fock matrix if $c_{\mu i}$ is smaller than a user-defined threshold τ. We have found that a value of 10^{-5} is suitable for our purposes, and we use the same value for the convergence threshold. Moreover, we have found that setting[39]

$$\tilde{\alpha}_i = \frac{\phi_i(\boldsymbol{r}_A)}{\mathring{\phi}_i(\boldsymbol{r}_A)} Z_A \tag{21}$$

(where $\mathring{\phi}_i(\boldsymbol{r})$ corresponds to the s-type components of $\phi_i(\boldsymbol{r})$ centered at $\boldsymbol{r}_A$) yields satisfactory results. In the case where $\mathring{\phi}_i(\boldsymbol{r}_A) = 0$, the MO is effectively zero at $\boldsymbol{r} = \boldsymbol{r}_A$ and, therefore, does not need to be cusp corrected. As in conventional self-consistent calculations, it is sometimes useful to switch on the convergence accelerator DIIS,[57,58] and we have done so in some cases. The general skeleton of the algorithm is given in Algorithm 1.

ALGORITHM 1 Skeleton of the e-n cusp-correction algorithm. ***c* and $\tilde{c}$ gather the coefficients $c_{\mu i}$ and $\tilde{c}_{Ai}$, respectively. τ is a user-defined threshold.**

procedure enCuspCorrection
  Do a standard HF or KS calculation
  to obtain MO coefficients $\boldsymbol{c}$ and density matrix $\boldsymbol{P}$
  ▷ *Main loop over MOs*
  for MO $i = 1, \ldots, N$ **do**
    for nuclear center $A = 1, \ldots, M$ **do**
      Compute $\phi_i(\boldsymbol{r}_A)$ and $\mathring{\phi}_i(\boldsymbol{r}_A)$
      and determine $\tilde{\alpha}_i$ via Eq. (21)
      Evaluate $\partial_r \tilde{\chi}^i_A(\boldsymbol{r}_A)$
      for nuclear center $B = 1, \ldots, M$ **do**
        Evaluate $\tilde{\chi}^i_B(\boldsymbol{r}_A)$
      end for
    end for
    Compute dressing integrals $\tilde{\boldsymbol{S}}^i$ and $\tilde{\boldsymbol{h}}^i$ (if required)
    (see Appendix)
    Compute $\tilde{c}_{Ai}$ via Eq. (10)
    if one-step calculation **go to** 34
    ▷ *Start SCF loop for ith MO*
    while $\max|\tilde{\boldsymbol{F}}^i\boldsymbol{P} - \boldsymbol{P}\tilde{\boldsymbol{F}}^i| > \tau$ **do**
      Compute Fock matrix $\boldsymbol{F}$
      for basis function $\mu = 1, \ldots N$ **do**
        if $|c_{\mu i}| > \tau$ **then**
          Dress the diagonal of the Fock matrix:
          $\tilde{F}^i_{\mu\mu} = F_{\mu\mu} + \tilde{D}^i_\mu$ (see Eq. (19))
        end if
      end for
      Diagonalize $\tilde{\boldsymbol{F}}^i$ to obtain $\boldsymbol{c}$
      Compute new density matrix $\boldsymbol{P}$
      for nuclear center $A = 1, \ldots, M$ **do**
        Update the value of $\phi_i(\boldsymbol{r}_A)$
      end for
      Update $\tilde{c}_{Ai}$ by solving Eq. (10)
    end while
    Store Gaussian coefficients $c_{\mu i}$ and
    Slater coefficients $\tilde{c}_{Ai}$ of *i*th MO
  end for
  ▷ *Return useful quantities for QMC calculation*
  return $\boldsymbol{c}$ and $\tilde{\boldsymbol{c}}$
end procedure

4. Illustrative examples

4.1 Atoms

Let us illustrate the present method with a simple example. For pedagogical purposes, we have computed the wave function of the hydrogen atom within a small Gaussian basis (decontracted STO-3G basis). In Fig. 1, we have plotted the local energy associated with this wave function as well as its OS and SCD cusp-corrected versions. The numerical results are reported in Table 1. As expected, the "cuspless" local energy (red curve) diverges for small r with a variational energy off by 4.3 millihartree compared to the exact value of $-1/2$. The OS cusp-correcting procedure which introduces a Slater basis function of unit exponent (but does not reoptimize any coefficients) cures the divergence at $r = 0$ and significantly improves (by roughly one order of magnitude) both the variational energy and the variance. Moreover, we observe that the long-range part of the wave function is also improved compared to the Gaussian basis set due to the presence of the Slater basis function which has the correct asymptotic decay. The SCD cusp-correcting procedure further improve upon the OS scheme, and we reach a variance lower than 10^{-8} after only three iterations. The values of the coefficients of the Gaussian and Slater functions reported in Table 1

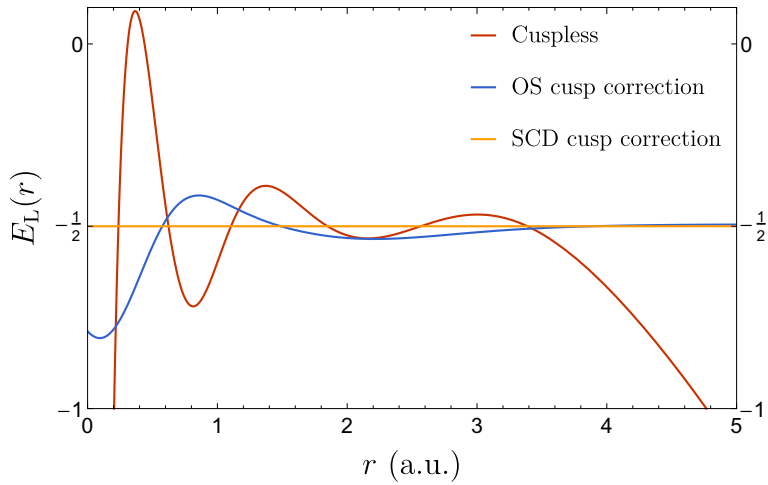

Fig. 1 Local energy $E_L(r)$ for various wave functions of the H atom. The cuspless wave function is obtained with the decontracted STO-3G Gaussian basis set (*red curve*), and the OS and SCD cusp-corrected wave functions (*blue* and *orange curves*, respectively) are obtained using $\widetilde{\alpha}_H = 1$.

Table 1 Variational energy and its variance for various wave functions of the H atom.

Basis	Cusp correction	Iteration	Energy	Variance	max $\|c\|$	$\tilde{c}$
Gaussian	—		-0.495741	2.23×10^{-1}	0.66158	0
Mixed	OS		-0.499270	4.49×10^{-2}	0.07486	1.95629
Mixed	SCD	#1	-0.499270	4.49×10^{-2}	0.07486	1.95629
		#2	-0.499970	3.07×10^{-6}	0.00254	2.00225
		#3	-0.500000	4.88×10^{-9}	0.00006	1.99691

The energy is obtained with the decontracted STO-3G Gaussian basis set. The OS and SCD cusp-corrected energies are obtained by adding a Slater basis function of unit exponent ($\tilde{\alpha}_H = 1$) to the Gaussian basis set. The energy and variance at each iteration of the SCD process is also reported. max $|c|$ is the maximum absolute value of the Gaussian basis coefficients and $\tilde{c}$ is the value of the coefficient of the Slater function.

clearly show that, as expected, the Gaussian functions are getting quickly washed away and replaced by the Slater function.

In Fig. 2, we have plotted the cuspless HF 1s core orbitals of the helium (left) and neon (right) atoms, and their cusp-corrected versions obtained with various schemes. For the He atom, we compare the cusp-corrected orbitals produced by the OS and SCD procedures. One can clearly see that the qualitative difference between the cusp-corrected orbitals is small (at least graphically). For the Ne atom, one cannot graphically distinguished between the two cusp-correcting schemes. Fig. 3 reports the local energy of the cuspless and cusp-corrected HF wave functions as an electron is moved through the nucleus of a Ne atom located at the origin. (The other electrons have been positioned randomly.) The right panel of Fig. 3 corresponds to a zoom around the origin where the local energy associated with the cuspless wave function is strongly oscillatory and ultimately diverges toward $-\infty$ as $r \to 0$. We observe that the cusp-correcting algorithm removes both the divergence of the local energy at the origin but also smooths out its erratic oscillations in the neighborhood of the origin, while remaining identical to the local energy obtained with the cuspless wave function for large r. In particular, one can see that the node (i.e., zero) of the wave function around $r = -2$ is not significantly altered by the addition of the Slater basis function (albeit not strictly identical).

Table 2 reports the energy and the corresponding variance of the He atom computed at the VMC and DMC level. The trial wave function is the HF wave function computed in the 6-31G basis with or without cusp correction. Similar to the case of the H atom discussed above, the OS and SCD schemes reduce significantly both the variational energy and the variance. The energy decreases by roughly 2.8 and 3.1 millihartree

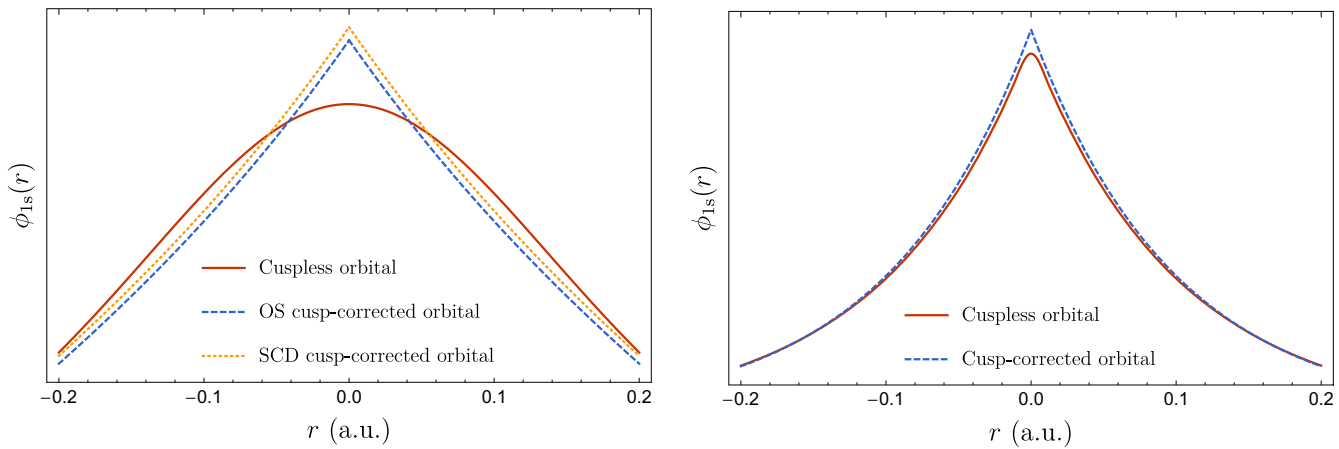

Fig. 2 Cuspless and cusp-corrected HF 1s core orbitals $\phi_{1s}(r)$ of the He (*left*) and Ne (*right*) atoms obtained with various schemes. The Gaussian basis set is Pople's 6-31G basis and the Slater basis functions have $\widetilde{\alpha}_{\mathrm{He}} = 2$ and $\widetilde{\alpha}_{\mathrm{Ne}} = 10$. For the Ne atom, the OS and SCD cusp-correction schemes yield indistinguishable curves.

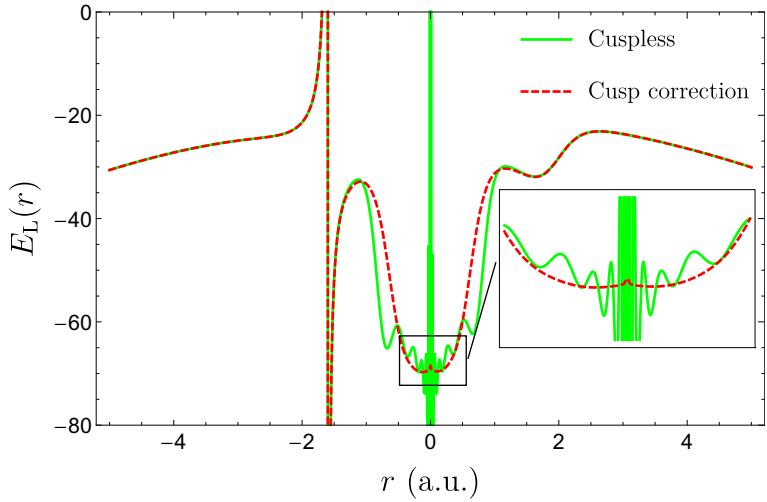

Fig. 3 Local energy $E_L(r)$ of the cuspless and cusp-corrected HF wave functions as an electron is moved through the nucleus of a Ne atom located at the origin. The other electrons have been positioned randomly. The Gaussian basis set is Pople's 6-31G basis and the Slater basis function has an exponent $\widetilde{\alpha}_{Ne} = 10$.

Table 2 Energy and corresponding variance of the He atom computed with various methods.

	Energy (a.u.)			Variance (a.u.)	
Cusp correction	**Deterministic**	**VMC**	**DMC**	**VMC**	**DMC**
—	− 2.855 160	− 2.855 12(6)	− 2.903 9(1)	3.99(3)	4.47(18)
OS		− 2.857 89(6)	− 2.903 4(3)	0.605(6)	0.498(2)
SCD		− 2.858 17(9)	− 2.903 2(2)	0.610(3)	0.498(1)

The trial wave function is the HF wave function computed in the 6-31G basis. The error bar corresponding to one standard deviation is reported in parenthesis.

(compared to the uncorrected scheme) using OS and SCD, respectively. Likewise, we observe that the variance is reduced by one order of magnitude by applying our cusp-corrected schemes, the difference between OS and SCD being negligible.

4.2 Molecules

As a molecular example, we consider the beryllium hydride molecule BeH_2 at experimental geometry. The Gaussian basis set is Pople's 6-31G basis and the Slater exponents have been obtained via Eq. (21). The two HF valence orbitals (a_g and b_{1u}) of this linear molecule are depicted in Fig. 4.

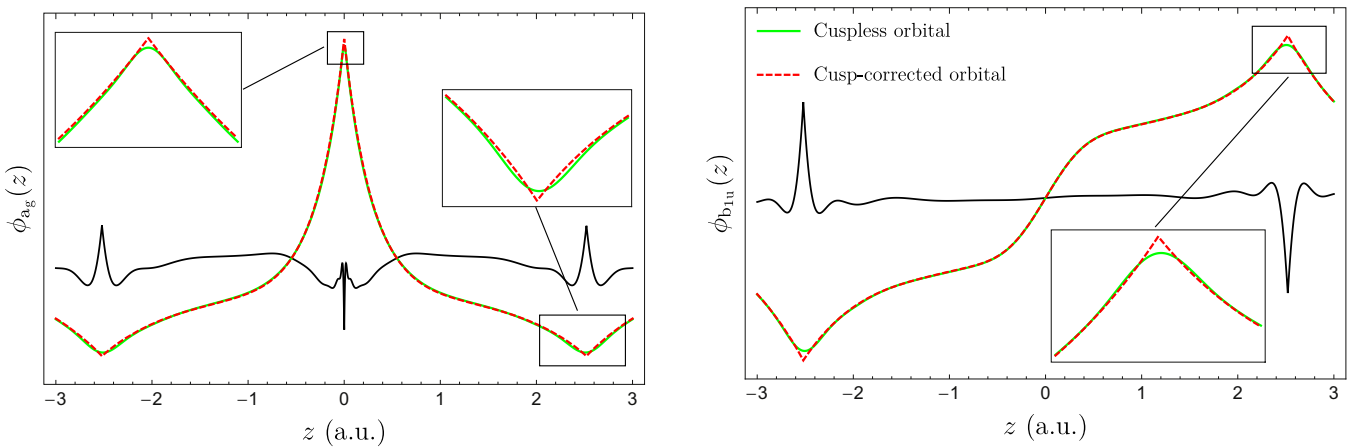

Fig. 4 Cuspless and cusp-corrected HF valence (a_g and b_{1u}) orbitals of the BeH_2 molecule obtained with the 6-31G basis set. For the a_g orbital, we have $\widetilde{\alpha}_{Be} = 3.7893$ and $\widetilde{\alpha}_{H} = 1.1199$, while for the b_{1u} orbital, $\widetilde{\alpha}_{H} = 1.2056$. The *black line* corresponds to the difference between the cuspless and cusp-corrected orbitals magnified by one order of magnitude. Note that the three nuclei lie on the z axis.

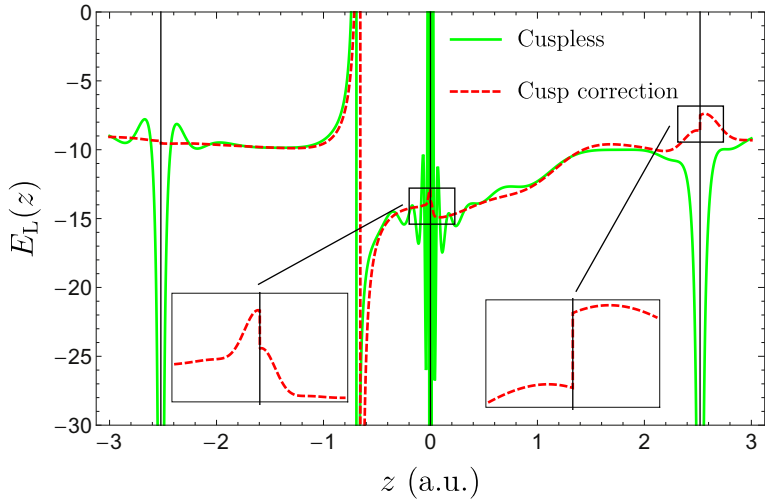

Fig. 5 Local energy $E_L(r)$ of the cuspless and cusp-corrected HF wave functions as an electron is moved through the nuclei (marked with *thin black lines*) of the BeH_2 molecule at experimental geometry. The other electrons have been positioned randomly. The Gaussian basis set is Pople's 6-31G basis and the Slater exponents have been obtained via Eq. (21). Note that the three nuclei lie on the z axis.

Note that the cusp-correcting scheme does not correct the second MO on the Be nucleus because the value of this MO is effectively zero on this center.

The corresponding local energies as an electron is moved through the nuclei (marked with thin black lines) of the BeH_2 molecule are represented in Fig. 5. (The other electrons have been positioned randomly.) Similarly to the results of the previous section, the cusp-correcting scheme removes the divergences of the local energy at the nuclei. Note, however, that a discontinuity appears in the local energy at the nuclear centers (see inset graphs of Fig. 5). It is well known that these discontinuities do not lead to any problems within QMC calculations. Note also that the node of the wave function around $z = -3/4$ is significantly shifted due to the introduction of the Slater basis function.

5. Conclusion

We have introduced a procedure to enforce the electron–nucleus (e-n) cusp by augmenting conventional (cuspless) Gaussian basis sets with cusp-correcting Slater basis functions. Two types of procedure have been presented.

In the one-step (OS) procedure, the coefficients of the Slater functions are obtained by ensuring the correct e-n cusp at each nucleus. We have also designed a self-consistent procedure to optimize simultaneously the coefficients of the Gaussian and Slater basis functions by diagonalization of an orbital-dependent effective Fock operator.

The same procedure could potentially be employed to correct the long-range part of the electronic density with obvious application within DFT. We are currently working on a similar methodology to enforce the electron–electron cusp in explicitly correlated wave functions. We hope to be able to report on this in the near future.

Appendix. Dressing integrals

Thanks to the approximation (15), we eschew the calculations of two-electron integrals and we only need to consider three types of one-electron integrals in order to dress the Fock matrix in Eq. (13): overlap, kinetic energy and nuclear attraction. (For a OS calculation, only the former is mandatory.) Their particularity is that they are "mixed" integrals as they involve one Gaussian function (with arbitrary angular momentum) and one (momentumless) Slater function.[59,60] Note that one can easily generalize the present procedure and consider a (contracted) linear combination of 1*s* Slater functions.

A.1 Overlap integrals

We must find mixed Gaussian-Slater overlap integrals of the form

$$\tilde{S}_{aB} = \langle \chi_a | \tilde{\chi}_B \rangle = \int \chi_a(\boldsymbol{r}) \tilde{\chi}_B(\boldsymbol{r}) d\boldsymbol{r}, \tag{A.1}$$

where $\tilde{\chi}_B(\boldsymbol{r})$ is given by Eq. (8) (where we have removed the superscript i for the sake of clarity) and

$$\chi_{\boldsymbol{a}}(\boldsymbol{r}) = (x - A_x)^{a_x} (y - A_y)^{a_y} (z - A_z)^{a_z} \exp\left[-\alpha |\boldsymbol{r} - \mathbf{A}|^2\right] \tag{A.2}$$

is a primitive Gaussian function of exponent α and angular momentum $\boldsymbol{a} = (a_x, a_y, a_z)$ centered in $\mathbf{A} = (A_x, A_y, A_z)$, its total angular momentum being given by $a = a_x + a_y + a_z$. Contracted integrals can be obtained by a straightforward summation of the primitive integrals weighted by their contraction coefficients.[59–61]

We shall start by reporting the expression of the fundamental integral $\tilde{S}_{\mathbf{0}B}$ (where $\mathbf{0} = (0, 0, 0)$). Higher angular momentum integrals can be obtained by differentiation with respect to the center coordinates.

Using the Gaussian representation of a Slater function

$$\exp(-\zeta r) = \frac{\zeta}{\sqrt{\pi}} \int_0^\infty \exp\left[-u^{-2} r^2 - \frac{\zeta^2 u^2}{4}\right] du, \tag{A.3}$$

we obtain

$$\begin{aligned}
\tilde{S}_{\mathbf{0}B} &= \frac{\tilde{\beta}^{5/2}}{\pi} \int_0^\infty \exp\left[-\frac{\tilde{\beta}^2 u^2}{4}\right] \left(\int \exp\left[-\alpha |\boldsymbol{r} - \mathbf{A}|^2\right] \exp\left[-u^{-2} |\boldsymbol{r} - \mathbf{B}|^2\right] d\boldsymbol{r} \right) du \\
&= \frac{\tilde{\beta}^{5/2}}{\pi} \int_0^\infty \exp\left[-\frac{\tilde{\beta}^2 u^2}{4}\right] \left(\frac{\pi}{\alpha + u^{-2}}\right)^{3/2} \exp\left[-\frac{\alpha\, u^{-2}}{\alpha + u^{-2}} \mathbf{AB}^2\right] du \\
&= \frac{\pi \tilde{\beta}^{3/2}}{2\alpha^2 |\mathbf{AB}|} \left\{ \left(\sqrt{\frac{\tilde{\beta}^2}{4\alpha}} + \sqrt{\alpha |\mathbf{AB}|} \right) \operatorname{erfc}\left(\sqrt{\frac{\tilde{\beta}^2}{4\alpha}} + \sqrt{\alpha |\mathbf{AB}|} \right) \exp\left[\frac{\tilde{\beta}^2}{4\alpha} + \tilde{\beta} |\mathbf{AB}|\right] \right. \\
&\quad \left. - \left(\sqrt{\frac{\tilde{\beta}^2}{4\alpha}} - \sqrt{\alpha |\mathbf{AB}|} \right) \operatorname{erfc}\left(\sqrt{\frac{\tilde{\beta}^2}{4\alpha}} - \sqrt{\alpha |\mathbf{AB}|} \right) \exp\left[\frac{\tilde{\beta}^2}{4\alpha} - \tilde{\beta} |\mathbf{AB}|\right] \right\},
\end{aligned} \tag{A.4}$$

where $\mathbf{AB} = \mathbf{A} - \mathbf{B}$ and $\operatorname{erfc}(x)$ is the complementary error function.[54] It is easy to show that the use of the Gaussian representation (A.3) allows us to reduce the integral to the conventional Gaussian-type function case, which has been extensively discussed in the literature.[53, 62] One only needs to perform the last integration that can be easily performed using a computer algebra system such as MATHEMATICA.[63]

A.2 Kinetic energy integrals

The same technique is applied to the kinetic energy integral

$$\tilde{T}_{aB} = -\frac{1}{2} \langle \nabla^2 \chi_a | \tilde{\chi}_B \rangle, \tag{A.5}$$

which yields

$$\begin{aligned}
\tilde{T}_{\mathbf{0}B} &= \frac{\pi \tilde{\beta}^{5/2}}{2\alpha^{3/2} |\mathbf{AB}|} \left\{ \left(1 + \frac{\tilde{\beta}^2}{4\alpha} - \sqrt{\frac{\tilde{\beta}^2}{4}} |\mathbf{AB}| \right) \operatorname{erfc}\left(\sqrt{\frac{\tilde{\beta}^2}{4\alpha}} - \sqrt{\alpha} |\mathbf{AB}| \right) \exp\left[\frac{\tilde{\beta}^2}{4\alpha} - \tilde{\beta} |\mathbf{AB}|\right] \right. \\
&\quad \left. - \left(1 + \frac{\tilde{\beta}^2}{4\alpha} + \sqrt{\frac{\tilde{\beta}^2}{4}} |\mathbf{AB}| \right) \operatorname{erfc}\left(\sqrt{\frac{\tilde{\beta}^2}{4\alpha}} + \sqrt{\alpha} |\mathbf{AB}| \right) \exp\left[\frac{\tilde{\beta}^2}{4\alpha} + \tilde{\beta} |\mathbf{AB}|\right] \right\}.
\end{aligned} \tag{A.6}$$

A.3 Nuclear attraction integrals

For the nuclear attraction integrals of the form

$$\tilde{V}_{aB} = \langle \chi_a | \, |\boldsymbol{r} - \mathbf{C}|^{-1} | \tilde{\chi}_B \rangle, \tag{A.7}$$

in addition to the Gaussian representation of the Slater function (see Eq. (A.8)), we also use the well-known Gaussian representation of the Coulomb operator:

$$\frac{1}{r} = \frac{2}{\sqrt{\pi}} \int_0^\infty \exp\left(-v^2 r^2\right) dv. \tag{A.8}$$

We obtain

$$\begin{aligned} \tilde{V}_{\mathbf{0}B} = 2\tilde{\beta}^{5/2} \int_0^\infty \frac{1}{\alpha + u^{-2}} F_0 \left[(\alpha + u^{-2}) \left| \frac{\alpha \mathbf{A} + u^{-2} \mathbf{B}}{\alpha + u^{-2}} - \mathbf{C} \right|^2 \right] \\ \exp\left[-\frac{\alpha \, u^{-2}}{\alpha + u^{-2}} |\mathbf{AB}|^2 \right] \exp\left[-\frac{\tilde{\beta}^2 u^2}{4} \right] du, \end{aligned} \tag{A.9}$$

where $F_0(t)$ is the Boys function.[64–66] To the best of our knowledge, this expression cannot be integrated further (expect in some particular cases) but it can be efficiently evaluated by numerical quadrature using the Gauss-Legendre rule. In the case of the nuclear attraction integrals, due to the form of the integrand in Eq. (A.9), we use the conventional Gaussian recurrence relations to evaluate higher angular momentum integrals. These involve the evaluation of the generalized Boys functions $F_m(t)$ which can be computed efficiently using well-established algorithms.[64–66] We refer the reader to Ref. 62 for more details.

References

1. Austin, B. M.; Zubarev, D. Y.; Lester, W. A., Jr. Quantum Monte Carlo and Related Approaches. *Chem. Rev.* **2012**, *112*, 263.
2. Dubecký, M.; Mitas, L.; Jurecka, P. Noncovalent Interactions by Quantum Monte Carlo. *Chem. Rev.* **2014**, *116*, 5188–5215.
3. Benali, A.; Shulenburger, N.; Romero, L.; Kim, J.; von Lilienfeld, O. Application of Diffusion Monte Carlo to Materials Dominated by Van Der Waals Interactions. *J. Chem. Theory Comp.* **2014**, *10*, 3417–3422.
4. Ambrosetti, A.; Alfè, D.; DiStasio, R. A., Jr; Tkatchenko, A. Hard Numbers for Large Molecules: Toward Exact Energetics for Supramolecular Systems. *J. Phys. Chem. Lett.* **2014**, *5*, 849–855.
5. Scemama, A.; Caffarel, M.; Oseret, E.; Jalby, W. QMC=Chem: A Quantum Monte Carlo Program for Large-Scale Simulations in Chemistry at the Petascale Level and Beyond. *High Performance Computing for Computational Science—VECPAR 2012*; Springer Science Business Media, 2013, pp 118–127.

6. Frankowski, K.; Pekeris, C. L. Logarithmic Terms in the Wave Functions of the Ground State of Two-Electron Atoms. *Phys. Rev.* **1984**, *146*, 46.
7. Freund, D. E.; Huxtable, B. D.; Morgan, J. D. I. I. I. Variational Calculations on the Helium Isoelectronic Sequence. *Phys. Rev. A* **1984**, *29*, 980.
8. Hattig, C.; Klopper, W.; Kohn, A.; Tew, D. P. Explicitly Correlated Electrons in Molecules. *Chem. Rev.* **2012**, *112*, 4.
9. Kong, L.; Bischo, F. A.; Valeev, E. F. Explicitly Correlated R12/F12 Methods for Electronic Structure. *Chem. Rev.* **2012**, *112*, 75.
10. Loos, P. F.; Gill, P. M. W. Two Electrons on a Hypersphere: A Quasiexactly Solvable Model. *Phys. Rev. Lett.* **2009**, *103*, 123008.
11. Loos, P. F.; Gill, P. M. W. Excited States of Spherium. *Mol. Phys.* **2010**, *108*, 2527–2532.
12. Loos, P. F.; Gill, P. M. W. Exact Wave Functions of Two-Electron Quantum Rings. *Phys. Rev. Lett.* **2012**, *108*, 083002.
13. Loos, P. F.; Bloomfield, N. J.; Gill, P. M. W. Three-Electron Coalescence Points in Two and Three Dimensions. *J. Chem. Phys.* **2015**, *143*, 181101.
14. Huang, C. J.; Umrigar, C. J.; Nightingale, M. P. Accuracy of Electronic Wave Functions in Quantum Monte Carlo: The Effect of High-Order Correlations. *J. Chem. Phys.* **1997**, *107*, 3007.
15. Drummond, N. D.; Towler, M. D.; Needs, R. J. Jastrow Correlation Factor for Atoms, Molecules, and Solids. *Phys. Rev. B* **2004**, *70*, 235119.
16. Lopez-Rios, P.; Seth, S.; Drummond, N. D.; Needs, R. J. Framework for Constructing Generic Jastrow Correlation Factors. *Phys. Rev. E* **2012**, *86*, 036703.
17. Scemama, A.; Garniron, Y.; Caffarel, M.; Loos, P. F. Deterministic Construction of Nodal Surfaces within Quantum Monte Carlo: The Case of Fes. *J. Chem. Theory Comput.* **2018**, *14*, 1395.
18. Scemama, A.; Benali, A.; Jacquemin, D.; Caffarel, M.; Loos, P. F. Excitation Energies from Diffusion Monte Carlo Using Selected Configuration Interaction Nodes. *J. Chem. Phys.* **2018**, *149*, 034108.
19. Loos, P. F.; Scemama, A.; Blondel, A.; Garniron, Y.; Caffarel, M.; Jacquemin, D. A Mountaineering Strategy to Excited States: Highly Accurate Reference Energies and Benchmarks. *J. Chem. Theory Comput.* **2018**, *14*, 4360.
20. Loos, P. F.; Boggio-Pasqua, M.; Scemama, A.; Caffarel, M.; Jacquemin, D. Reference Energies for Double Excitations. *J. Chem. Theory Comput.* **2019**, *15*, 1939, (in press).
21. Garniron, Y.; Scemama, A.; Loos, P. F.; Caffarel, M. Hybrid Stochastic-Deterministic Calculation of the Second-Order Perturbative Contribution of Multireference Perturbation Theory. *J. Chem. Phys.* **2017**, *147*, 034101.
22. Garniron, Y.; Scemama, A.; Giner, E.; Caffarel, M.; Loos, P. F. Selected Configuration Interaction Dressed by Perturbation. *J. Chem. Phys.* **2018**, *149*, 064103.
23. Kato, T. Fundamental Properties of Hamiltonian Operators of Schroedinger Type. *Trans. Am. Math. Soc.* **1951**, *70*, 195.
24. Kato, T. On the Eigenfunctions of Many-Particle Systems in Quantum Mechanics. *Commun. Pure Appl. Math.* **1957**, *10*, 151.
25. Pack, R. T.; Brown, W. B. Cusp Conditions for Molecular Wavefunctions. *J. Chem. Phys.* **1966**, *45*, 556.
26. Toulouse, J.; Umrigar, C. Optimization of Quantum Monte Carlo Wave Functions by Energy Minimization. *J. Chem. Phys.* **2007**, *126*, 084102.
27. Umrigar, C. J.; Toulouse, J.; Filippi, C.; Sorella, S.; Hennig, R. G. Alleviation of the Fermion-Sign Problem by Optimization of Many-Body Wave Functions. *Phys. Rev. Lett.* **2007**, *98*, 110201.
28. Toulouse, J.; Umrigar, C. J. Full Optimization of Jastrow-Slater Wave Functions with Application to the First-Row Atoms and Homonuclear Diatomic Molecules. *J. Chem. Phys.* **2008**, *128*, 174101.

29. Boys, S. F. Electronic Wavefunctions. I. A General Method of Calculation for Stationary States of Any Molecular System. *Proc. R. Soc. (London)* **1950**, *A200*, 542.
30. McKemmish, L. K.; Gilbert, A. T. B.; Gill, P. M. W. Mixed Ramp-Gaussian Basis Sets. *J. Chem. Theory Comput.* **2014**, *10*, 4369.
31. Slater, J. C. Atomic Shielding Constants. *Phys. Rev.* **1930**, *36*, 57.
32. Bouferguene, A.; Fares, M.; Hoggan, P. E. Stop: A Slater-Type Orbital Package for Molecular Electronic Structure Determination. *Int. J. Quantum Chem.* **1996**, *57*, 810.
33. Reinhardt, P.; Hoggan, P. E. Cusps and Derivatives for Wave-Functions Expanded in Slater Orbitals: A Density Study. *Int. J. Quantum Chem.* **2009**, *109*, 3191–3198.
34. Nemec, N.; Towler, M. D.; Needs, R. J. Benchmark All-Electron Ab Initio Quantum Monte Carlo Calculations for Small Molecules. *J. Chem. Phys.* **2010**, *132*, 03411.
35. van Lenthe, E.; Baerends, E. J. Optimized Slater-Type Basis Sets for the Elements 1-118. *J. Comput. Chem.* **2003**, *24*, 1142.
36. Galek, P. T. A.; Handy, N. C.; Cohen, A. J.; Chan, G. K. L. Hartree-Fock Orbitals Which Obey the Nuclear Cusp Condition. *Chem. Phys. Lett.* **2005**, *404*, 156.
37. te Velde, G.; Bickelhaupt, F. M.; Baerends, E. J.; Guerra, C. F.; van Gisbergen, S. J. A.; Snijders, J. G.; Ziegler, T. Chemistry with ADF. *J. Comput. Chem.* **2001**, *22*, 931.
38. Manten, S.; Lüchow, A. On the Accuracy of the Fixed-Node Diffusion Quantum Monte Carlo Method. *J. Chem. Phys.* **2001**, *115*, 5362.
39. Ma, M.; Towler, M. D.; Drummond, N. D.; Needs, R. J. Scheme for Adding Electron-Nucleus Cusps to Gaussian Orbitals. *J. Chem. Phys.* **2005**, *122*, 224322.
40. Kussmann, J.; Ochsenfeld, C. Adding Electron-Nuclear Cusps to Gaussian Basis Functions for Molecular Quantum Monte Carlo Calculations. *Phys. Rev. B* **2007**, *76*, 115115.
41. Per, M. C.; Russo, S. P.; Snook, I. K. Electron-Nucleus Cusp Correction and Forces in Quantum Monte Carlo. *J. Chem. Phys.* **2008**, *128*, 114106.
42. Bunge, C. F.; Barrientos, J. A.; Bunge-Vivier, A. Roothaan-Hartree-Fock Ground-State Atomic Wave Functions: Slater-Type Orbital Expansions and Expectation Values for Z = 2-54. *At. Data Nucl. Data Tables* **1993**, *53*, 113.
43. Caffarel, M.; Daudey, J. P.; Heully, J. L.; Ramirez-Solis, A. Towards Accurate All-Electron Quantum Monte Carlo Calculations of Transition Metal Systems: Spectroscopy of the Copper Atom. *J. Chem. Phys.* **2005**, *123*.
44. Scemama, A.; Applencourt, T.; Giner, E.; Caffarel, M. Accurate Nonrelativistic Ground-State Energies of 3D Transition Metal Atoms. *J. Chem. Phys.* **2014**, *141*, 244110.
45. Allen, L. C. Electronic Wave Functions for Polyatomic Molecules. *J. Chem. Phys.* **1959**, *31*, 736.
46. Silver, D. M. Basis Sets of Gaussian and Slater-Type Atomic Orbitals. *Chem. Phys. Lett.* **1970**, *7*, 511.
47. Silver, D. M. Energy Integrals Involving Both Slater-Type and Gaussian Atomic Orbitals. *J. Phys.* **1971**, *32*, 129–133.
48. Bacskay, G. B.; Linnett, J. W. Mixed Basis Functions in Molecular Quantum Mechanics I. Computational Methods and a Preliminary Study of the Helium Atom. *Theor. Chim. Acta* **1972**, *26*, 1.
49. Bacskay, G. B.; Linnett, J. W. Mixed Basis Functions in Molecular Quantum Mechanics II. A Study of the H2 Molecule. *Theor. Chim. Acta* **1972**, *26*, 14.
50. Bacskay, G. B.; Linnett, J. W. Mixed Basis Functions in Molecular Quantum Mechanics III. The Linear Symmetrie H3 Molecule. *Theor. Chim. Acta* **1972**, *26*, 23.
51. Bacskay, G. B. Mixed Basis Functions in Molecular Quantum Mechanics IV. The Linear, Equidistant System of Four Interacting Hydrogen Atoms. *Theor. Chem. Acc.* **1972**, *26*, 33.
52. Bugaets, O. P.; Zhogolev, D. A. On Application of Mixed Bases to Quantum-Chemical Calculations of Molecules. *Chem. Phys. Lett.* **1976**, *39*, 45.
53. Szabo, A.; Ostlund, N. S. *Modern Quantum Chemistry*. McGraw-Hill: New York, 1989.

54. Olver, F. W. J.; Lozier, D. W.; Boisvert, R. F.; Clark, C. W. *NIST Handbook of Mathematical Functions*. Cambridge University Press: New York, 2010.
55. Deng, J.; Gilbert, A. T. B.; Gill, P. M. W. Diagnostics of Molecular Orbital Quality. *Can. J. Chem.* **2010**, *88*, 754.
56. Perdew, J. P.; Zunger, A. Self-Interaction Correction to Density-Functional Approximations for Many-Electron Systems. *Phys. Rev. B* **1981**, *23*, 5048.
57. Pulay, P. Convergence Acceleration of Iterative Sequences. The Case of SCF Iteration. *Chem. Phys. Lett.* **1980**, *73*, 393.
58. Pulay, P. Improved SCF Convergence Acceleration. *J. Comput. Chem.* **1982**, *3*, 556.
59. Barca, G. M. J.; Loos, P. F.; Gill, P. M. W. Many-Electron Integrals Over Gaussian Basis Functions. I. Recurrence Relations for Three-Electron Integrals. *J. Chem. Theory Comput.* **2016**, *12*, 1725.
60. Barca, G. M. J.; Loos, P. F. Recurrence Relations for Four-Electron Integrals over Gaussian Basis Functions. *Adv. Quantum Chem.* **2018**, *76*, 147.
61. Barca, G. M. J.; Loos, P. F. Three-Electron and Four-Electron Integrals Involving Gaussian Geminals: Fundamental Integrals, Upper Bounds and Recurrence Relations. *J. Chem. Phys.* **2017**, *147*, 024103.
62. Gill, P. M. W. Molecular Integrals Over Gaussian Basis Functions. *Adv. Quantum Chem.* **1994**, *25*, 141.
63. Wolfram Research Inc. *Mathematica, Version 11.1*. Wolfram Research, Inc.: Champaign, IL, 2017
64. Gill, P. M. W.; Johnson, B. G.; Pople, J. A. Two-Electron Repulsion Integrals over Gaussian S Functions. *Int. J. Quantum Chem.* **1991**, *40*, 745.
65. Ishida, K. Ace Algorithm for the Rapid Evaluation of the Electron-Repulsion Integral over Gaussian-Type Orbitals. *Int. J. Quantum Chem.* **1996**, *59*, 209.
66. Weiss, A. K. H.; Ochsenfeld, C. A Rigorous and Optimized Strategy for the Evaluation of the Boys Function Kernel in Molecular Electronic Structure Theory. *J. Comput. Chem.* **2015**, *36*, 1390.

SECTION 3

Atomic and molecular electronic structure

This section presents a highly accurate correlated atomic wave-function (Ruiz), progress in Natural Orbital theory (Piris et al.), two different effective potential approaches (Mendez et al., Staroverov and Ospadov) and Fock-space correlated NaH (Musial et al.)

This page intentionally left blank

CHAPTER SIX

Configuration interaction study of the ^3P ground and low-lying states of the boron anion. The boron electron affinity

María Belén Ruiz*
Department of Theoretical Chemistry, Friedrich-Alexander-University Erlangen-Nürnberg, Erlangen, Germany
*Corresponding author: e-mail address: maria.belen.ruiz@fau.de

Contents

Abstract

Configuration Interaction (CI) calculations on the ground state of the B anion are carried out using a small basis set of Slater orbitals [7s6p5d4f3g]. About 1600 configurations have been selected according to their contribution to the total energy. One set of exponents is optimized for the whole expansion. Using a CI computer program with Slater orbitals from our previous publication (Ruiz and Tröger, 2018), written with the purpose of calculating the ground state of carbon atom, we have obtained an energy of −24.65090936 a.u. for the ground ^3P state of the boron anion. For the electron affinity (EA) of the boron atom we have considered a previous similar calculation on the ^2P ground state of boron atom obtaining 293.2 meV, which is comparable to other theoretical calculations and the experimental value 279.723(25) meV. The low-lying ^3P excited states of the boron anion have been determined employing a shorter wave function expansion consisting of about 1000 configurations. These states have the energies −24.57876395 a.u., −24.54146848 a.u. and −24.50013781 a.u., respectively.

Advances in Quantum Chemistry, Volume 79
ISSN 0065-3276
https://doi.org/10.1016/bs.aiq.2019.04.006

1. Introduction

The boron anion B^- is the least stable of the weakly bound anions. While H^-, C^-, O^-, F^- are stable, Li^- is weakly bound[1] and He^-, Be^- are metastable. This is probably due to the accommodation of the odd electron in the outermost orbital and to the nuclear charge screened by the doubly occupied inner shells. Commonly, the binding energy of the atomic anions is very small and comparable to the correlation energy of the system. Since for the anion the nuclear charge Z is smaller than the number of electrons, the situation is different than for the other ions of the isoelectronic sequence but in principle it does not introduce real difficulties in the computations. However, the single occupied orbital is diffuse and that has consequences in the standard one-electron basis sets. Therefore, it is commonly accepted that highly correlated wave functions are required to achieve good agreement with the experiment. The different strategies have in common the start with a powerful method like Multiconfigurational Hartree-Fock (MCHF),[2] Coupled Cluster (CC) theory[3] or Configuration Interaction (CI)[4,5] to pick up a great part of the correlation energy and a further improvement adding relativistic corrections, or those due to the Born-Oppenheimer approximation. Other methods like MCDHF[6] include relativistic corrections[7] or explicitly correlated wave functions.[8]

Among all these methods, the CI method is very important for the calculation of negative ions and electron affinities (EA) defined as the difference between the energy of the atom and the corresponding ion. CI is a systematic predictive method to calculate accurately the energy of both neutral atom and the ion, and subsequently the EA. As investigated by various authors,[6] the impact of higher correlations, relativistic effects and higher relativistic effects are very small on EA. These effects may cancel with each other when subtracting the total energies of atomic systems with the same charge. Therefore EAs obtained by CI are close to the experimental values and the CI method is a good strategy for EAs. Usually EAs are expressed in meV. The unit conversion is 1 a.u. = 27.2113961 eV.

In this work, a six-electron atomic CI computer program designed for the carbon atom is used for the B^-. This program is quite flexible and adequate to perform such calculations. Once the wave function for the ground state of carbon atom has been obtained, we have carried out the calculations with the atomic charge $Z = 5$ and selected the configurations which contribute $>10^{-9}$ a.u. to the total energy. These configurations differ

slightly from the ones employed in the case of the carbon atom, presented in our previous paper.[9] The methodology followed here is the same as in Ref. 9, and will therefore not be repeated in detail here.

In addition, using a shorter wave function and after optimization of the orbital exponents, the low-lying states of the boron anion have been calculated. No results of these states have been found in the bibliography. Data on the anions is scarce and cannot be found in either atomic data bases, or in tables of estimated energy values. Finally, the EA of the boron atom is calculated using the energy obtained here for the ^{3}P ground state of B anion and the ground state energy of the boron atom of a previous work using the same methodology.

2. Configuration interaction

The shortcomings and advantages of the CI method have been described in detail in our previous work.[9] Summarizing briefly, the method endeavors to recover rapidly a major part of the correlation energy but converges extremely slowly for obtaining highly accurate energy values. This is due to the shortcomings of the CI wave-function whose form does not fulfill the electronic cusp-condition. Therefore the CI wave function needs a huge number of Slater determinants to converge. Conversely, correlated methods that include explicitly r_{ij}, named explicit correlated methods, introduced by the pioneering work of Hylleraas in 1929,[10] converge faster to the exact solution of the Schrödinger equation. Nevertheless, in this work we employ the CI method as a first step toward Hylleraas-Configuration Interaction (Hy-CI) calculations on the ground state of the boron anion.

The CI wave function is constructed as a linear combination of N_{conf} configurations, where the coefficients C_p are determined variationally by solving the eigenvalue problem that follows from the Schrödinger equation:

$$\Psi = \sum_{i=1}^{N_{conf}} C_p \Phi_p. \tag{1}$$

The configurations Φ_p are symmetry adapted since they are eigenfunctions of the square of the angular momentum operator $\hat{L}^2$. Every configuration is then a linear combination of function terms and these ones are a linear combination of Slater determinants:

$$\Phi_p = \hat{O}(\hat{L}^2)\hat{A}\psi_p\chi. \tag{2}$$

In this work, the symmetry adapted configurations are constructed a priori, so that they are eigenfunctions of $\hat{L}^2$. The Slater determinants are constructed with the help of the anti-symmetrization operator $\hat{\mathcal{A}}$, which acts not only over the spatial orbitals but also over the spin function part.

The configurations are also eigenfunctions of the square of the spin operator $\hat{S}^2$. Here, χ is a spin eigenfunction. In the case of the ^{3}P ground state of carbon atom, a triplet state ($S=1$), we have chosen for convenience a spin eigenfunction with $M_S=0$:

$$\chi=(\alpha\beta-\beta\alpha)(\alpha\beta-\beta\alpha)(\alpha\beta+\beta\alpha). \tag{3}$$

This spin function differs only by a sign from the singlet one $S=1$ for six electrons and in this way the computer program can be used for singlet or triplet states by simply changing one sign. There are more spin eigenfunctions for $S=1$, namely, the ones with $M_S=1$ and $M_S=-1$, but they are all degenerate with respect to the energy. This means, it is indifferent which one we use and since they are orthogonal, it is sufficient to use only one of them.

As discussed in the case of the Li-atom in Ref. 11 and calculations of the Be-atom[12,13] it is also sufficient to consider only one spin-function. The spatial part of the basis-functions consists of Hartree products of Slater Type Orbitals (STOs):

$$\psi_p=\prod_{k=1}^{n_e}\phi(r_k,\theta_k,\varphi_k). \tag{4}$$

Every Slater orbital ϕ is represented by only one orbital s, p, d, f, g or i, therefore this is named the minimal basis set. The un-normalized STOs are defined:

$$\phi(r,\theta,\varphi)=r^{n-1}e^{-\alpha r}Y_l^m(\theta,\varphi) \tag{5}$$

where Y_l^m are the spherical harmonics. The Schrödinger equation to be solved is:

$$\hat{H}\Psi=E\Psi. \tag{6}$$

The atomic Hamiltonian for a fixed nucleus written in Hylleraas coordinates, see Ref. 12, for a CI wave function reduces effectively to:

$$\hat{H} = -\frac{1}{2}\sum_{i=1}^{n}\frac{\partial^2}{\partial r_i^2} - \sum_{i=1}^{n}\frac{1}{r_i}\frac{\partial}{\partial r_i} - \sum_{i=1}^{n}\frac{Z}{r_i} + \sum_{i<j}^{n}\frac{1}{r_{ij}} + \sum_{i=1}^{n}\frac{1}{r_i^2}l_i(l_i+1) \qquad (7)$$

where l_i are the angular quantum numbers of the orbitals. From the variational principle we have to solve the following matrix eigenvalue problem:

$$(\mathbf{H} - \mathbf{ES})\mathbf{C} = \mathbf{0} \qquad (8)$$

where the matrix elements of the Hamiltonian **H** and overlap **S** matrices are:

$$\begin{aligned} \mathbf{H}_{kl} &= \int \Phi_k \hat{H} \Phi_l d\tau, \\ \mathbf{S}_{kl} &= \int \Phi_k \Phi_l d\tau. \end{aligned} \qquad (9)$$

The matrix elements are sums of one- and two-electron integrals. Their expressions and calculation have been described in previous papers, see Refs. 9,11–13. The diagonalization procedure employed for the calculation of the ground state of B^- is the inverse iteration technique,[14] concretely a subroutine by Sims and Hagstrom, see Ref. 15. Using this method only one eigenvalue is obtained rapidly. For the excited states of B^- we need to calculate all eigenvalues and select and optimize the one of interest among them using the LAPACK library.

In this work we use un-normalized non-orthogonal orbitals STOs. The basis set is [7s6p5d4f3g] constructed with a single STO for every electron. In this work we make the restriction of choosing the same orbital exponent per pair of electrons.

The ground state leading configuration of the B anion is $1s^2\ 2s^2\ 2p^2$, in our nomenclature *ssspp* (i.e., s(1)s(2)s(3)s(4)p(5)p(6)). The other configurations with large contributions to the energy for the P-symmetry ($L = 1$) six-electron state are, ordered by decreasing energy contribution, *ssppd, sspppp, ssssdd, sppdd, pppppp, sssddd, ssssff, sspdf, sssgg, ssspfg, ssffpp,* and *ssggpp*. Other important configurations for the ground state of carbon atom are of the form: *ppd*, *pdf* and *pfg* and all their permutations. The permutations of these configurations were also included, see discussion in Ref. 9. In addition to these configurations, others have been tried and sorted out because of their very low energy contribution.

We systematically selected the CI configurations according to their energy contribution. This was done by calculations on blocks constructed for all possible configurations. In these blocks all excitations are included

from single, double, … up to the maximum number of excitations, in this case sextuple, whereas sextuple excited configurations seldom showed even a moderate contribution. The eigenvalue equation was diagonalized upon each addition of a configuration. In this manner, the contribution of every single configuration and of each block of a given type to the total energy was evaluated. If the energy difference was less than a chosen threshold $|E_{i-1} - E_i| < 1.10^{-9}$ a.u., the new configuration was discarded. In this manner, all configurations were checked, leading to a relatively compact CI wave function. The construction of configurations and the list of them are given in Table 1 of Ref. 9.

Table 1 Selected CI wave function expansion for the ^{3}P ground state of boron anion.

Conf.	*n*	N_{conf}	$N_{conf,tot}$	Energy (a.u.)	Virial
ssspp	3	97	97	−24.50848407	1.99996
ssspsp	3	49	146	−24.53940516	2.00010
spsssp	3	15	161	−24.54035998	1.99997
ssppss	3	3	164	−24.54168658	2.00003
spspss	3	4	168	−24.54172826	2.00002
ssssdd	3	5	173	−24.54514648	2.00025
sssdsd	3	5	178	−24.54519466	2.00022
sspppp	3	12	194	−24.56638010	2.00004
spsppp	3	24	218	−24.56859440	2.00014
ppsspp	3	28	246	−24.58884325	2.00061
ppspsp	3	4	250	−24.58948248	2.00060
ppppss	3	2	252	−24.58951245	2.00060
pppppp	3	3	255	−24.59009209	2.00061
sspdpd	3	3	258	−24.59143898	2.00074
sdsppd	3	16	274	−24.59146757	2.00075
ssddpp	3	4	278	−24.59202874	2.00077
ddsspp	3	7	285	−24.59269634	2.00087
ssppdd	3	2	287	−24.59271212	2.00087
ppssdd	3	2	289	−24.59276221	2.00087

Table 1 Selected CI wave function expansion for the ^{3}P ground state of boron anion.—cont'd

Conf.	*n*	N_{conf}	$N_{conf,tot}$	Energy (a.u.)	Virial
ppddpp	3	1	290	−24.59277819	2.00087
ddpppp	3	1	291	−24.59279493	2.00087
ssppd	3	12	303	−24.61122828	2.00193
sssdpp	3	2	305	−24.61505726	2.00223
sspdps	3	2	307	−24.61681815	2.00184
spsdps	3	3	310	−24.61705992	2.00188
spsspd	3	6	316	−24.61727618	2.00189
pdsssp	3	18	334	−24.61752166	2.00190
sspspd	3	8	342	−24.61799043	2.00177
pdspss	3	3	345	−24.61802067	2.00177
sppdss	3	2	347	−24.61810438	2.00178
sdppss	3	3	350	−24.61811594	2.00177
sdsspp	3	4	354	−24.61812413	2.00177
sdspsp	3	25	379	−24.61824554	2.00177
pdspss	3	4	383	−24.61837401	2.00177
sssddd	4	3	386	−24.61847883	2.00179
ssddsd	4	7	393	−24.61857578	2.00179
sssff	4	2	395	−24.61868593	2.00181
ssspdf	4	5	400	−24.61909233	2.00185
sspdsf	4	12	412	−24.61950653	2.00188
ssdpf	4	5	417	−24.61975352	2.00191
ssfpd	4	5	422	−24.62014007	2.00196
sspdsf	4	10	432	−24.62015962	2.00196
sspfsd	4	11	443	−24.62040930	2.00196
ssdfsp	4	7	450	−24.62082077	2.00196
sssspp	4	52	502	−24.63072600	2.00186
ssspsp	4	22	524	−24.63123634	2.00178
spsssp	4	7	531	−24.63131765	2.00179

Continued

Table 1 Selected CI wave function expansion for the ^{3}P ground state of boron anion.—cont'd

Conf.	n	N_{conf}	$N_{conf,tot}$	Energy (a.u.)	Virial
ssssdd	4	4	535	−24.63161275	2.00178
sssdsd	4	4	539	−24.63188975	2.00176
sspppp	4	15	554	−24.63249813	2.00188
spsppp	4	14	568	−24.63285279	2.00186
ppsspp	4	28	596	−24.63478458	2.00161
pppppp	4	3	599	−24.63480659	2.00161
sspdpd	4	14	613	−24.63520108	2.00156
sppdsd	4	3	616	−24.63520594	2.00156
ssddpp	4	5	621	−24.63533134	2.00154
ssppdd	4	3	624	−24.63539247	2.00154
ppssdd	4	4	628	−24.63540477	2.00154
ddsspp	4	17	645	−24.63598190	2.00158
sdsdpp	4	4	649	−24.63600196	2.00158
ssspdp	4	28	677	−24.63889963	2.00146
sssdpp	4	12	689	−24.64009023	2.00135
sspdps	4	7	696	−24.64018911	2.00133
spsdps	4	26	722	−24.64027581	2.00134
sspspd	4	8	730	−24.64036408	2.00139
sdsspp	4	8	738	−24.64038998	2.00139
sdspsp	4	15	753	−24.64046163	2.00139
spsspd	4	14	767	−24.64056098	2.00140
pdsssp	4	30	797	−24.64069580	2.00140
sppdss	4	7	804	−24.64071683	2.00140
pdspss	4	6	810	−24.64073097	2.00140
sssspp	5	69	879	−24.64271695	2.00107
ssspsp	5	71	950	−24.64406074	2.00099
spsssp	5	25	975	−24.64419029	2.00099
sssspd	5	17	992	−24.64424970	2.00099
sssdsd	5	10	1002	−24.64429613	2.00098

Table 1 Selected CI wave function expansion for the ^{3}P ground state of boron anion.—cont'd

Conf.	*n*	N_{conf}	$N_{conf,tot}$	Energy (a.u.)	Virial
ssssff	5	2	1004	−24.64434268	2.00098
sssfsf	5	3	1007	−24.64436652	2.00098
sspppp	5	9	1016	−24.64480699	2.00096
spsppp	5	5	1021	−24.64494121	2.00095
ppsspp	5	5	1026	−24.64535014	2.00093
pppppp	5	12	1038	−24.64540847	2.00092
ssppd	5	5	1043	−24.64588366	2.00087
sssdpp	5	19	1062	−24.64621151	2.00085
sspspd	5	19	1081	−24.64632752	2.00084
pdsssp	5	5	1086	−24.64633936	2.00084
pdspss	5	3	1088	−24.64634061	2.00084
sssfsf	5	1	1089	−24.64634780	2.00084
sspdpd	5	5	1104	−24.64648970	2.00082
ssddpp	5	14	1118	−24.64659836	2.00083
ssppdd	5	2	1120	−24.64660130	2.00083
ssspdf	5	4	1124	−24.64661332	2.00083
sssfdp	5	8	1132	−24.64677110	2.00082
sssdpf	5	8	1140	−24.64687864	2.00081
sssfpd	5	9	1149	−24.64692039	2.00081
sspfsd	5	6	1155	−24.64695261	2.00080
ssdpsp	5	7	1162	−24.64709080	2.00080
ssssgg	6	5	1167	−24.64709932	2.00080
sssgsg	6	1	1168	−24.64709985	2.00080
ssspfg	6	3	1171	−24.64710840	2.00080
sssgpf	6	14	1185	−24.64721094	2.00081
sdsdpp	5	5	1190	−24.64721714	2.00081
ssddsd	5	1	1191	−24.64722052	2.00081
ddsspp	5	9	1200	−24.64788184	2.00081
ddspsp	5	5	1205	−24.64788952	2.00081

Continued

Table 1 Selected CI wave function expansion for the ^{3}P ground state of boron anion.—cont'd

Conf.	*n*	N_{conf}	$N_{conf,tot}$	Energy (a.u.)	Virial
ddppss	5	1	1206	−24.64798616	2.00082
ssspp	6	38	1244	−24.64842751	2.00077
ssspsp	6	11	1255	−24.64845708	2.00077
spspss	6	2	1257	−24.64846022	2.00077
spsssp	6	5	1262	−24.64846650	2.00077
ssppss	6	1	1263	−24.64846714	2.00077
ssssdd	6	7	1269	−24.64847771	2.00077
sssdsd	6	1	1270	−24.64849334	2.00077
ssssff	6	6	1276	−24.64849892	2.00077
sssfsf	6	1	1277	−24.64849959	2.00077
ssssgg	6	1	1278	−24.64850213	2.00077
sssgsg	6	1	1279	−24.64850292	2.00077
sspppp	6	9	1288	−24.64867595	2.00077
spsppp	6	2	1291	−24.64868825	2.00077
ppsspp	6	2	1303	−24.64886678	2.00078
pppppp	6	2	1305	−24.64887293	2.00078
ssspp d	6	5	1310	−24.64888562	2.00078
sspdps	6	4	1314	−24.64893924	2.00078
spsspd	6	10	1324	−24.64895582	2.00078
sdsspp	6	4	1328	−24.64895740	2.00078
ssddpp	6	6	1334	−24.64899353	2.00078
sspdpd	6	7	1341	−24.64900380	2.00078
ddsspp	6	6	1347	−24.64924979	2.00076
ddspsp	6	3	1352	−24.64925438	2.00076
ssspdf	6	7	1356	−24.64926117	2.00075
sssfpg	6	3	1358	−24.64927258	2.00075
sssfpd	6	4	1371	−24.64935520	2.00074
ssssgg	7	1	1372	−24.64935602	2.00074

Table 1 Selected CI wave function expansion for the ^{3}P ground state of boron anion.—cont'd

Conf.	*n*	N_{conf}	$N_{conf,tot}$	Energy (a.u.)	Virial
ssspp	7	5	1385	−24.64940443	2.00075
ssssdd	7	2	1387	−24.64940591	2.00075
ssppd	7	4	1392	−24.64942797	2.00074
sspppp	7	6	1398	−24.64943602	2.00074
ppsspp	7	11	1409	−24.64952294	2.00073
sdsspp	7	3	1412	−24.64953857	2.00073
ddsspp	7	4	1416	−24.64959242	2.00073
sssdpf	7	7	1423	−24.64960725	2.00072
sssfpg	7	4	1427	−24.64964179	2.00072
sspdsf	7	1	1428	−24.64964210	2.00072
sspdps	7	4	1432	−24.64965136	2.00072
ssddpp	7	5	1436	−24.64966636	2.00072
ssffpp	7	11	1447	−24.64989477	2.00073
ssggpp	7	4	1451	−24.64989739	2.00073
sdsdpp	6	4	1455	−24.64992495	2.00073
ddspsp	6	1	1456	−24.64992651	2.00073
pppppp	3	1	1457	−24.64993177	2.00073
ssggpp	7	3	1463	−24.64997059	2.00073
sssgpf	7	5	1468	−24.65000687	2.00073
ssssff	7	5	1474	−24.65000855	2.00073
ssdfsp	7	2	1480	−24.65004730	2.00072
sspfsd	5	1	1481	−24.65005241	2.00072
ssspdf	5	9	1495	−24.65009465	2.00072
pdsssp	6	2	1497	−24.65010019	2.00072
spsspd	7	6	1504	−24.65011489	2.00072
sspspd	7	5	1520	−24.65019499	2.00072
ssppd	6	16	1538	−24.65027807	2.00069

Continued

Table 1 Selected CI wave function expansion for the ^{3}P ground state of boron anion.—cont'd

Conf.	n	N_{conf}	$N_{conf,tot}$	Energy (a.u.)	Virial
ppssdd	3	11	1545	−24.65029810	2.00069
ssddpp	6	5	1556	−24.65046440	2.00065
ddsspp	4	3	1559	−24.65046589	2.00065
sssddd	3	3	1560	−24.65046737	2.00065
sspppf	6	3	1565	−24.65049782	2.00065
sspfpp	5	1	1566	−24.65066905	2.00064
sssfpd	7	8	1574	−24.65068348	2.00064
dfsssp	7	9	1591	−24.65075860	2.00064
ddspsp	4	3	1595	−24.65077673	2.00064
fgsssp	5	5	1603	−24.65078404	2.00064
ffsspp	5	15	1622	−24.65089173	2.00067
sssddg	5	1	1623	−24.65089327	2.00067
ssdfsp	6	3	1626	−24.65089912	2.00067
ssfgsp	6	2	1628	−24.65090089	2.00067
ssffpp	6	2	1630	−24.65090924	2.00067
ssggpp	6	2	1633	−24.65090924	2.00067
ssgpgp	6	1	1634	−24.65090936	2.00067

N_{conf} is the number of symmetry adapted configurations and n is the basis set indicated by the highest principal quantum number, i.e., $n=3$ means [3s2p1d]. The orbitals exponents are $\alpha=\alpha'=4.9821441$, $\beta=\beta'=1.1401381$, $\gamma=\gamma'=0.9726643$ for all the expansion.

3. CI calculations for the B^- anion

We have used a CI computer program written for six-electron atomic systems in Fortran 95.[9] Numerical calculations have been conducted with double precision arithmetic. The program is an extension of our four- and five-electron CI programs.

In this work we start with a full-CI wave function for a basis $n=3$ (or [3s2p1d]) testing all possible configurations and retaining those that contribute $>1.10^{-9}$ a.u. (at the beginning of the calculation almost all of them). First for a relatively short expansion the orbital exponents are optimized. The method of optimization consists in parabolic fitting,

where a minimum is sought for every exponent and a new cycle is started using a smaller step-size. The optimization is considered converged when the improvement in the energy is $<1.10^{-9}$ a.u. The exponents are then kept fixed and used for the larger expansion. A set of three exponents is used (one for the K-shell, another for the electrons of the inner L-shell and another for the pair of outer electrons of the L-shell), and kept equal for all configurations. This technique accelerates computations, while still producing sufficiently accurate wave functions to determine the bound state properties. During the calculations and optimizations we use the virial theorem to control the quality of the wave function and guide the numerical optimization:

$$\sigma = -\frac{\langle V \rangle}{\langle T \rangle}. \tag{10}$$

The following step is to add all the possible configurations with $n = 4$, $n = 5$, $n = 6$ *and* $n = 7$. The resulting wave function is then very compact.

In Table 1 the truncated CI wave function expansion is shown. The configurations with larger contribution are the ground state configuration *sssspp*, the open shell configuration *ssspsp*, the *sssppd* and *sssdpp* ^{3}P configurations, followed by the configuration with inner ^{1}S excitations *ppsspp*, afterwards we find the *ssppppp*, which shows the quasi-degeneracy of the *s* and *p* orbitals of the L-shell; the configurations *ssssdd* contributed less as would be expected by the low l_i quantum numbers, and higher excitations *sspdpd, ddsspp* and *ssffpp* follow among others.

If we order the energy for the basis set *n*, we encounter the angular energy limits, assuming the wave function is saturated for these limits. The contribution to the total energy decreases with increasing *n*, see Table 2. That the $n = 7$ contribution of is still not close to zero indicates that the wave function has not fully converged. We would need to add more terms with $n = 8$ and higher.

Table 2 Angular energy limits to the energy for the ^{3}P ground state of boron anion.

n	Basis set	N_{conf}	Energy (a.u.)	Virial	−Diff. (μhartree)
$n = 3$	[3s2p1d]	383	−24.61837401	2.00177	0
$n = 4$	[4s3p2d1f]	810	−24.64073097	2.00140	22357
$n = 5$	[5s4p3d2f1g]	1206	−24.64798616	2.00082	7255
$n = 6$	[6s5p4d3f2g]	1371	−24.64935520	2.00074	1369
$n = 7$	[7s6p5d4f3g]	1634	−24.65090936	2.00067	1554

n is the basis set indicated by the highest principal quantum number. The unit 1 μhartree $= 1 \times 10^{-6}$ a. u.

Table 3 Comparison of variational upper bonds to the energy of the ^{3}P ground state of boron anion calculated by different methods.

Method	Authors	Year	Ref.	Basis set	N_{conf}	Energy (a.u.)
MCHF(CAS)	Froese Fischer et al.	1995	2	$n=7$	7891	−24.612326
MCHF(CAS)	Froese Fischer et al.	1995	2	$n=9$i	9502	−24.612465
MCHF (core pol.)	Froese Fischer et al.	1995	2	$n=7$h	28532	−24.633960
MCHF (core pol.)	Froese Fischer et al.	1995	2	$n=9$h	29274	−24.634643
CI	This work	2019		STO [7s6p5d4f3g]	1634	−24.65090936
FCI (SD)	Almora-Díaz et al.	2010	16	STO (l=20)		−24.65580432
FCI (SDTQQnSx)	Almora-Díaz et al.	2010	16	STO(l=24)	40.6 M	−24.66401395
Estimated exact	Nonrel.	1993	16			−24.664039(2)

Orbitals basis $l=24$ is [24s23p22d21f20g19h18i17k16l15m14n13o12q11r10t9u8v7w6x5y4z].[16] Abbreviations: MCHF(CAS), Multiconfiguration Hartree-Fock with complete active space; *MCHF(core pol.)*, MCHF including core polarization and core rearrangement.

We estimate that the contribution to the energy of the *h, i* and higher orbital configurations is about 1.0×10^{-3} a.u. (millihartree).

Using about 1600 selected configurations we have obtained an energy for the ^{3}P ground state of B^- −24.65090936 a.u. which compares very well with other CI and MCHF calculations. The difference in energy in our calculations may be due to the missing higher angular momentum orbitals i, h, … On the other hand, we use a smaller number of configurations than the other methods, giving value to our appropriate selection of configurations with respect to the energy contribution and a powerful optimization computational procedure, see Refs. 11–13. A comparison with the available calculations of boron anion is shown in Table 3.

4. Evaluation of the electron affinity of the boron atom

The electron affinity (EA) is defined as the energy difference between the ^{3}P ground state of the boron anion B^- and the ^{2}P ground state of the

Table 4 Electron affinity (EA) of the boron atom.

	Energy (a.u.)	Method	Basis set	N_{conf}	Ref.
Boron anion	−24.650909	CI	[7s6p5d4f3g]	1554	This work
Boron atom	−24. 640134	CI	[5s4p3d]	3957	22
EA	293.20 meV				

B atom. We have calculated the EA employing a previous calculation of the ground state of boron atom using the same methodology and computer program but a smaller basis set and smaller number of configurations and our present calculation of the boron anion, which is very accurate. This is indeed meaningful because the calculation of ions requires a larger basis than the one of the neutral atom, see discussion in Ref. 6. Nevertheless, we plan in the future to calculate the ground state of the boron atom more accurately using a larger basis set and larger number of configurations.

The calculation of the EA is presented in Table 4. As a result we have obtained 293.20 meV which is comparable with other results of the literature, see Table 5. The most accurate calculations of the EA in Table 5 correspond to very extensive strategies and include several corrections. Conversely, our EA is simply calculated as the difference between two energies. However, our EA value is slightly larger than the most accurate experimental result obtained from photodetachment 279.723(25) meV.[23] This difference may be due to the small basis $n=5$, $l=2$ used in our neutral B atom calculation. Considering f- and g-Slater orbitals, the value should be improved. In this work, relativistic effects have been neglected. These effects together with higher relativistic effects should play a small role in the calculation of the EA.

Indeed, as the nuclear charge is the same for the neutral atom and the anion, the electronic cusp effects represented by the interelectronic distance r_{12} may cancel in the inner shell[1] and the same happens with relativistic and high relativistic effects. Therefore, the CI treatment leads to a result which is competitive with experiment and more advances theories. This fact can be valuable when the EA is not as well-known as in the case of the boron atom.

5. Excited states

Finally, using a shorter wave function expansion of about 1000 configurations and $n=4$, we have optimized the exponents for the second, third and fourth eigenvalues of the energy, obtaining the up to our knowledge,

Table 5 Comparison of calculated electron affinity (EA) of the boron atom.

Author	Ref.	Year	Method	Basis set B	Basis set B^-	N(B)	N(B^-)	EA (meV)
Schaefer und Harris	4	1968	CI					250
Kendall and Dunning	5	1992	MRSD-CI					258
Wijesundera	17	1997	MC-DF					260
Li et al.	6	2012	MCDHF					260.37
Sundhold and Olsen	18	1990	MCHF					266.8(30)
Raghavachan	19	1985	MP					269
Froese Fischer et al.	2	1995	MCHF(CAS)	$n=9$i	$n=9$i	2965	9502	272.3
Froese Fischer et al.	2	1995	MCHF	$n=9$h	$n=9$h	6932	29274	277.39
Froese Fischer et al.	2	1995	Predicted					279.5(20)
Eliav et al.	7		CCSDT relativistic 4-comp.					279
Feller et al.	3		CCSD(T) + corrections					279.3(4)
Noro et al.	20	1991	MRCI(SD)					280
Gdanitz	8		r12-MR-ACPF	spdfgh				282
This work		2019	CI	$n=5$, $l=2$	$n=7$, $l=5$	3957	1554	293.20
Experimental	21	1985						277(10)
Experimental	23	1998						279.723(25)

Abbreviations: *CCSDT*, Coupled Cluster; *MC-DF*, Multiconfigurational Dirac-Fock; *MC-DHF*, Multiconfigurational Dirac–Hartree–Fock; *MP*, Möller-Plesset perturbation theory; *MRCI*, Multireference CI; *r12-MR-ACPF*, explicitly correlated Multireference Averaged Coupled-Pair Functional.

Table 6 Energy and orbital exponents for the ground and low-lying ^{3}P excited states of the boron anion.

State	Energy (a.u.)	$\alpha = \alpha'$	$\beta = \beta'$	$\gamma = \gamma'$	Virial	−Diff. (cm^{-1})
^{3}P	−24.60942625	4.9821441	1.2635381	0.8492643	1.93	0
2^3P	−24.57876395	4.8620655	1.3782524	0.5961229	1.98	6729.60
3^3P	−24.54146848	4.7613251	1.3391757	0.5344229	2.02	8185.41
4^3P	−24.50013781	4.6805287	1.3379760	0.4251931	2.06	9071.04

The number of configurations for the excited states is $N = 984$ and the basis $n = 4$.
n is the basis set indicated by the highest principal quantum number. Diff. in cm^{-1}.

the first values for the low-lying excited states of the boron anion. The calculations are presented in Table 6. We observe that the value of the orbital exponent of the outer electrons decreases when increasing the excitation, characteristic of diffuse orbitals. The states are also very close in energy. The energy conversion used in Table 6 is 1 a.u. = 219474.63068 cm^{-1}.

6. Summary and perspectives

The calculation of atomic anions does not represent any difficulty for the CI method with Slater orbitals having the possibility of optimizing the orbital exponents. In this way, the diffuse outer orbital is well described, in contrast to standard methods based in one-electron fixed basis sets. The EA of the boron atom has been extensively studied and is well-known, see also references included in Ref. 3. Nevertheless, the strategy of most methods is quite complex. Missing high correlations or truncation errors and relativistic effects does not adversely affect the results, as they are known to have a small impact in the calculation of the EA of the boron atom, mostly due to cancelation effects. The CI method offers a systematic approach to calculate accurately the EA, especially when this is not known. In any case, the present investigation can be improved by increasing the basis set of the orbitals and the number of configurations in both neutral atom and anion.

Another reason why the CI method is appropriate for the calculation of the spectra of ions is that with the CI method not only low-lying but Rydberg excited states can be obtained in a systematic way. In this work we have presented only the ^{3}P excited states, i.e., with the same symmetry as the ground state. The determination of excited states of other symmetries is very promising, since these are not known either theoretically nor experimentally.

Finally, one of the reasons for doing a CI calculation is to explore the basis set of STO orbitals and the construction of the configurations in order to perform future Hy-CI calculations.

Acknowledgments

I would like to thank here Jacob Katriel for awaking my interest on the B^- anion and James S. Sims for fruitful discussions on the atomic ions. Also I am very thankful to the Editors of this volume L. Ugo Ancarani and Philip E. Hoggan for their suggestions, which have served to improve the quality of this manuscript.

References

1. Sims, J. S. Hylleraas-Configuration Interaction Study of the ^1S Ground State of the Negative Li Ion. *J. Phys. B At. Mol. Phys.* **2017**, *50, 245003.*
2. Froese Fischer, C.; Ynnerman, A.; Gaigalas, G.; Multiconfiguration-Hartree-Fock, G. Calculations for the Electron Affinity of Boron. *Phys. Rev. A* **1995**, *51*, 4611.
3. Feller, D. Application of a Convergent, Composite Coupled Cluster Approach to Bound State, Adiabatic Electron Affinities in Atoms and Small Molecules. *J. Chem. Phys.* **2016**, *144*, 014105.
4. Schaefer, H. F.; Harris, F. E. Calculation of the Electron Affinity of Boron. *Phys. Rev.* **1968**, *170*, 108.
5. Kendall, R. A.; Dunning, T. H., Jr.; Harrison, R. J. Electron Affinities of the First-Row Atoms Revisited. Systematic Basis Sets and Wave Functions. *J. Chem. Phys.* **1992**, *96*, 6796.
6. Li, J.; Zhao, Z.; Andersson, M.; Zhang, X.; Chen, C. Theoretical Study for the Electron Affinities of Negative Ions With the MCDHF Method. *J. Phys. B At. Mol. Phys.* **2012**, *45*, 165004.
7. Eliav, E.; Ishikawa, Y.; Pyykko, P.; Kaldor, U. Electron Affinities of Boron, Aluminum, Gallium, Indium, and Thallium. *Phys. Rev. A* **1997**, *56*, 4532.
8. Gdanitz, R. J. Accurately Solving the Electronic Schrödinger Equation of Atoms and Molecules Using Explicitly Correlated (r_{12}-) Multireference Configuration Interaction. III. Electron Affinities of First-Row Atoms. *J. Chem. Phys.* **1999**, *110*, 706.
9. Ruiz, M. B.; Tröger, R. Configuration Interaction Study of the ^3P Ground State of the Carbon Atom. *Adv. Quantum Chem.* **2018**, *76*, 223.
10. Hylleraas, E. A. Neue Berechnung der Energie des Heliums im Grundzustande, sowie des tiefsten Terms von Ortho-Helium. *Z. Phys.* **1929**, *54*, 347.
11. Ruiz, M. B.; Margraf, J. T.; Frolov, A. M. Hylleraas-Configuration-Interaction Analysis of the Low-Lying States in the Three-Electron Li Atom and Be^+ Ion. *Phys. Rev. A* **2013**, *88*, 012505.
12. Ruiz, M. B.; Latorre, F.; Frolov, A. M. Singlet and Triplet Bound State Spectra in the Four-Electron Be-Like Atomic Systems. *Adv. Quantum Chem.* **2016**, *73*, 119.
13. Frolov, A. M.; Ruiz, M. B. Bound State Spectrum of the Triplet States of Be Atom. *Chem. Phys. Lett.* **2014**, *595–596*, 197.
14. Golub, G. H.; Van Loan, C. F. *Matrix Computations*; Johns Hopkins University Press: Baltimore, 2013.
15. Sims, J. S. Hylleraas-Configuration Interaction Study of the Ground State of the Negative Li Ion. *J. Phys. B Atomic Mol. Phys.* **2017**, *50*, 245003.
16. Almora-Díaz, C. X.; Bunge, C. F. Nonrelativistic CI Calculations for B+, B, and B− Ground States. *Int. J. Quantum Chem.* **2010**, *110*, 2982.

17. Wijesundera, W. P. Theoretical Study of the Negative Ions of Boron, Aluminum, Gallium, Indium, and Thallium. *Phys. Rev. A* **1997**, *55*, 1785.
18. Sundholm, D.; Olsen, J. Large MCHF Calculations on the Electron Affinity of Boron. *Chem. Phys. Lett.* **1990**, *171*, 53.
19. Raghavachan, K. Basis Set and Electron Correlation Effects on the Electron Affinities of First Row Atoms. *J. Chem. Phys.* **1985**, *82*, 4142.
20. Noro, T.; Yoshimine, M.; Sekiya, M.; Sasaki, F. Ab Initio Determination of Accurate Electron Affinities of B, C, O, and F. *Phys. Rev. Lett.* **1991**, *66*, 1157.
21. Hotop, H.; Lineberger, W. C. Binding Energies in Atomic Negative Ions: II. *J. Phys. Chem. Ref. Data* **1985**, *14*, 731.
22. Ruiz, M. B.; Rojas, M.; Chicón, G.; Otto, P. Configuration Interaction Calculations on the ^{2}P Ground State of Boron Atom and C^+ Using Slater Orbitals. *Int. J. Quantum Chem.* **2011**, *111*, 1921.
23. Scheer, M.; Bilodeau, R. C.; Haugen, H. K. Negative Ion of Boron: An Experimental Study of the ^{3}P Ground State. *Phys. Rev. Lett.* **1998**, *80*, 2562.

Further reading

24. Löwdin, P.-O. Quantum Theory of Many-Particle Systems. I. Physical Interpretations by Means of Density Matrices, Natural Spin-Orbitals, and Convergence Problems in the Method of Configurational Interaction. *Phys. Rev.* **1955**, *97*, 1474.

This page intentionally left blank

CHAPTER SEVEN

Advances in approximate natural orbital functional theory

Ion Mitxelena[a], Mario Piris[a,b,*], Jesus M. Ugalde[a]
[a]Kimika Fakultatea, Euskal Herriko Unibertsitatea (UPV/EHU) and Donostia International Physics Center (DIPC), Donostia, Euskadi, Spain
[b]Basque Foundation for Science (IKERBASQUE), Bilbao, Euskadi, Spain
*Corresponding author: e-mail address: mario.piris@ehu.eus

Contents

Abstract

The basic concepts relevant to the approximate natural orbital functional (NOF) theory are presented. We discuss in detail the reconstruction that leads to Piris NOF (PNOF) approximations focusing on the electron pairing, namely, the independent pair model PNOF5 and the inter-pair electron correlation model PNOF7. It is shown that PNOF7 is an ideal candidate to study model systems for strong correlation such as the Hubbard model and hydrogen rings. Analytic first- and second-order energy derivatives are presented for any given nuclear perturbation. Results for equilibrium geometries and harmonic vibrational frequencies corresponding to a selected set of molecules are reported.

Advances in Quantum Chemistry, Volume 79
ISSN 0065-3276
https://doi.org/10.1016/bs.aiq.2019.04.001

1. Introduction

In 1975, Gilbert[1] extended the Hohenberg–Kohn theorem to nonlocal external potentials. He showed that a nondegenerate ground-state N-particle wavefunction is a universal functional of the one-particle reduced density matrix (1RDM). This work together with those of Levy[2] and Valone[3] laid the foundations of 1RDM functional theory. Unfortunately, current computational schemes based on the exact constrained search formulations are several times more expensive than solving directly the Schrödinger equation[4]; therefore, the construction of the functional requires a practical approach.

A handy prescription relies on the fact that the ground-state energy can be cast as an exact functional of the ground-state two-particle reduced density matrix (2RDM). This approach uses the one-to-one mapping between the 2RDMs and the nondegenerate ground-state N-particle wavefunctions of a Hamiltonian with at most two-body interactions.[5] The existence theorem of the 1RDM functional implicitly establishes a one-to-one correspondence between the ground-state 1RDMs and 2RDMs, so the 1RDM functional must match the well-known 2RDM functional. Actually, we must only reconstruct the electron–electron potential energy V_{ee} in terms of the 1RDM since the noninteracting part of the electronic Hamiltonian is a one-particle operator.

So far, the exact reconstruction of V_{ee} has resulted in an unattainable goal. A convenient approach is to approximately reconstruct the 2RDM. However, this does not fully reconstruct the ground-state energy only the 2RDM. Approximating the energy is more involved because the theorems for the exact energy functionals do not apply for 2RDM reconstructions. The point is that approximate 2RDMs, in terms of the 1RDM, lead to energy functionals that still depend on the 2RDM.[6] An undesired implication of such dependence is that the functional N-representability problem arises.[7,8] That is, we have to observe the requirement that the 2RDM reconstructed in terms of 1RDM must satisfy the same N-representability conditions[9] as those imposed on unreconstructed 2RDMs. Otherwise, there might not exist an N-electron fermionic system compatible with the energy functional, therefore the energy can even drop below the exact value. In summary, we are no longer really dealing with the 1RDM functional theory but with an approximate one-particle theory, where the 2RDM continues to play a dominant, though hidden, role.

Most of the approximate functionals currently in use are not N-representable.[10] It has been generally assumed that there is no N-representability problem for approximate functionals, as it is believed that the N-representability conditions of Coleman[11] on the 1RDM are sufficient on their own. However, the N-representability constraints for acceptable 1RDM are insufficient to guarantee that the reconstructed 2RDM is N-representable and therefore the approximate functional is not N-representable either. Recently, the discovery of a systematic way to derive pure-state N-representability conditions for the 1RDM has allowed new insights[12,13] to be gained, as well as to open a new way to develop functionals.[14,15] The application of pure conditions restricts the 1RDM variational space that leads to improvements in energy but it is obvious that it does not improve the reconstruction of the approximate functional per se. A 1RDM that represents a pure state does not guarantee that an approximately reconstructed V_{ee} will be pure-state N-representable. The pure-state N-representability problem for an approximate functional is related to the N-representability of the 2RDM which determines V_{ee}.

Apart from the special case of the Hartree–Fock (HF) approximation, none of the known approximate functionals are explicitly given in terms of the 1RDM, including the venerable functional that accurately describes two-electron closed-shell systems.[16] There are energy expressions that seem to be properly expressed in terms of the 1RDM, however, these functionals violate the functional N-representability.[10] One can obtain quite reasonable results for some systems using them but there is no N-particle density matrix that supports their existence.

In most applications, the spectral decomposition of the 1RDM is used to express it in terms of the naturals orbitals (NOs) and their occupation numbers (ONs). In this representation, the energy expression is referred to as a natural orbital functional (NOF). It is worth noting that NOs are the orbitals that diagonalize the 1RDM corresponding to an approximate energy, such as those obtained from an approximate wavefunction. These energies are not invariant with respect to unitary transformations of the orbitals and the resulting functionals are only implicitly dependent on the 1RDM, through NOs and ONs. It is therefore misleading to talk about a functional of the 1RDM due to the existing dependence on the 2RDM, it is more appropriate to speak of a NOF. A detailed account of the state of the art of NOF approximations (NOFAs) can be found elsewhere.[17,18]

Most of the currently-in-use approximate NOFs are primitive functionals which involve only two-index $\mathcal{JKL}$ integrals. Recently, two more accurate expressions that include 4-index integrals have been proposed.[19–21] On the other hand, almost all NOFs are based on reasonable physical arguments.[18] The PNOFi ($i = 1$–7) family of functionals[19,22,23] rely on the reconstruction of the 2RDM subject to necessary ensemble N-representability conditions. The case of PNOF5 is quite remarkable. The latter was proposed[24] using perfect-pairing conditions in order to satisfy the sum rules for the 2RDM. Two years after, the natural geminals of PNOF5 were analyzed[25] and it was realized[26] that this NOF corresponds to the energy obtained from a wavefunction of an antisymmetrized product of strongly orthogonal geminals when the expansion of the N/2 geminals is limited to two-dimensional subspaces with fixed signs for the expansion coefficients of the corresponding geminals. Shortly afterward, this ansatz was extended to include more orbitals in the description of the electron pairs.[27] This finding demonstrated that PNOF5 is a pure-state N-representable functional.[28]

Looking closely at the constraints imposed on the ONs during the reconstruction of the PNOF5 2RDM, one realizes that the resulting ONs meet the requirements for pure-state N-representability conditions[8] to hold. Since the 1RDM's N-representability conditions are embedded in the PNOF5 reconstruction of the 2RDM, the resulting 1RDM by contraction of the so constructed 2RDM will necessarily be pure-state N-representable. Consequently, one needs to impose only ensemble N-representability constraints to the 1RDM in order to generate the variational Euler equations for the energy minimization. This is a great advantage with respect to imposing externally the 1RDM pure-state N-representability conditions as constraints on bounds of the domain of trial 1RDMs during the variational procedure, because the number of the latter increases drastically with the number of NOs.

This chapter continues with the presentation of the basic concepts and notations relevant to a NOF (Section 2). The following Section 3 is devoted to presenting the PNOF approach. The electron pairing approach for PNOF approximation is then presented in a subsection here. Section 4 is devoted to the intra-pair and inter-pair electron correlations in two model systems. Thus, we analyze the 1D Hubbard model with different numbers of sites (Section 4.1), and hydrogen chains with different ring sizes (Section 4.2). The chapter ends in Section 5 with a discussion on the geometry optimization. Analytic expressions for first- and second-order energy derivatives are obtained in Sections 5.1 and 5.2, respectively. Finally, after

discussing some computational aspects (Section 5.3), results for equilibrium geometries and harmonic vibrational frequencies corresponding to a selected set of molecules are reported in Sections 5.4 and 5.5, respectively.

2. Natural orbital functional

The electronic energy for N-electron systems is an exactly and explicitly known functional of the 1RDM (Γ) and 2RDM (D), namely,

$$E = \sum_{ik} \mathcal{H}_{ki}\Gamma_{ki} + \sum_{ijkl} \langle kl|ij\rangle D_{kl,ij}. \tag{1}$$

In Eq. (1), $\mathcal{H}_{ki}$ and $\langle kl|ij\rangle$ denote the one-electron matrix elements of the kinetic energy and external potential operators and the two-electron matrix elements of the Coulomb interaction, respectively. The spin-orbitals $|i\rangle$ constitute a complete orthonormal set of single-particle functions. The RDMs are Hermitian, positive semidefinite, and bounded. We employ the Löwdin normalization convention in which the trace of the 1RDM equals the number of electrons and the trace of the 2RDM gives the number of electron pairs in the system.

For $\hat{S}_z$ eigenstates, only density matrix blocks that conserve the number of each spin type are nonvanishing. Specifically, the 1RDM has two nonzero blocks $\Gamma^{\alpha\alpha}$ and $\Gamma^{\beta\beta}$, whereas the 2RDM has three independent nonzero blocks, $D^{\alpha\alpha}$, $D^{\alpha\beta}$, and $D^{\beta\beta}$. The parallel-spin components of the two-matrix must be antisymmetric, but $D^{\alpha\beta}$ possesses no special symmetry.[29]

The contraction relation between 1RDM and 2RDM implies that the energy functional is ultimately a functional of D. Attempts to determine the energy by minimizing $E[D]$ are formidable due to the complexity of the necessary and sufficient conditions for ensuring that the two-matrix corresponds to an N-particle density matrix.[9] Let us replace the last term in Eq. (1), which is an explicit functional of the 2RDM, by an unknown functional of the 1RDM,

$$E[\Gamma] = \sum_{ik} \mathcal{H}_{ki}\Gamma_{ki} + V_{ee}[\Gamma]. \tag{2}$$

In Eq. (2), $V_{ee}[\Gamma]$ is universal in the sense that it is independent of the external field. The existence of $E[\Gamma]$ is well-established, however, until now it has been impossible to find a practical expression of it. The obstacle lies in the construction of the functional V_{ee} capable of describing a quantum-mechanical N-electron system: the functional N-representability problem.

We have no choice but to approximate the functional $V_{ee}[\Gamma]$. In fact, most of the functionals currently in use are constructed in the representation where the 1RDM is diagonal, which leads to a NOF. Accordingly, the spectral decomposition of the 1RDM is used to approximate the electronic energy in terms of the NOs $\{|i\rangle\}$ and their ONs $\{n_i\}$, namely,

$$E = \sum_i n_i \mathcal{H}_{ii} + \sum_{ijkl} D[n_i, n_j, n_k, n_l] \langle kl|ij\rangle \tag{3}$$

where $D[n_i, n_j, n_k, n_l]$ represents the 2RDM reconstructed from the ONs. We neglect any explicit dependence of D on the NOs themselves given that the energy functional already has a strong dependence on the NOs via the one- and two-electron integrals. In this vein, it is worth noticing that our NOs are the ones that diagonalize the 1RDM of our approximate energy functional. Since the latter still depends on the 2RDM, the resulting energy will not be invariant with respect to unitary transformations of the orbitals, which prevents the existence of the corresponding extended Fockian matrix for the energy minimization by direct diagonalization.

Restriction of the ONs to the range $0 \leq n_i \leq 1$ represents a necessary and sufficient condition for ensemble N-representability of the 1RDM[11] under the normalization condition $\sum_i n_i = N$. On the other hand, the construction of an N-representable functional (3) is related to the N-representability problem of D, hence, any approximation must comply at least with tractable necessary conditions for the N-representability of the two-matrix. For simplicity, we will address only singlet states in this chapter. To avoid spin contamination effects, the spin restricted theory will be employed, in which a single set of orbitals is used for α and β spins: $\varphi_p^\alpha(\mathbf{r}) = \varphi_p^\beta(\mathbf{r}) = \varphi_p(\mathbf{r})$, and the parallel spin blocks of the RDMs are equal as well.

3. Piris natural orbital functional (PNOF)

A systematic application of N-representability conditions in the reconstruction of D has led to the PNOF series.[22] Within this reconstruction, the energy for singlet states reads as

$$E = \sum_p n_p \left(2\mathcal{H}_{pp} + \mathcal{J}_{pp}\right) + \sum_{p,q;p\neq q} \left\{ \left(n_q n_p - \Delta_{qp}\right)\left(2\mathcal{J}_{pq} - \mathcal{K}_{pq}\right) + \Pi_{qp}\mathcal{L}_{pq} \right\} \tag{4}$$

where $\mathcal{J}_{pq} = \langle pq|pq\rangle$, $\mathcal{K}_{pq} = \langle pq|qp\rangle$, and $\mathcal{L}_{pq} = \langle pp|qq\rangle$ are the usual direct, exchange and exchange-time-inversion integrals, respectively. Consequently,

the functional (4) belongs to the $\mathcal{JKL}$-only family of NOFs. Δ is a real symmetric matrix, whereas Π is a spin-independent Hermitian matrix. Appropriate forms of matrices Δ and Π lead to different implementations of the NOF known in the literature as PNOFi ($i = 1$–7).[19,22,23] The performance of these functionals is comparable to those of the most reliable quantum chemistry methods in many cases.[30]

There is no hint to determine the sign of Π_{qp} therefore, a large number of possible combinations of these signs looms up for those terms containing $\mathcal{L}_{pq}$ in Eq. (4). Making an adequate choice of the Π_{qp} signs is known as the phase dilemma.[31] In the simplest case of two electrons, an accurate NOF is known from the exact wavefunction[16] that allows the resolution of this dilemma. The knowledge of this NOF for two-electron systems is a good motivation for using electron pairs as basic units, besides being an important requirement that must be fulfilled by any NOFA.

3.1 The electron pairing approach

The electron pairing approach came to the NOF with the proposal of PNOF5.[24] So far this is the only NOF that has been obtained by top-down and bottom-up methods.[27] The existence of a generating N-particle wavefunction confirms that PNOF5 is a pure-state N-representable functional.

According to the electron pairing approach,[32] the orbital space Ω is divided into $N/2$ mutually disjoint subspaces Ω_g, so each orbital belongs only to one subspace. Consider each subspace contains one orbital g below the level $N/2$, and N_g orbitals above it, which is reflected in additional sum rules for the ONs:

$$\sum_{p\in\Omega_g} n_p = 1, \quad g = 1, 2, \ldots, N/2. \tag{5}$$

Taking into account the spin, each subspace contains only an electron pair, and the normalization condition for Γ is automatically fulfilled:

$$2\sum_{p\in\Omega} n_p = 2\sum_{g=1}^{N/2}\sum_{p\in\Omega_g} n_p = N. \tag{6}$$

Coupling each orbital g below the $N/2$ level with only one orbital above it ($N_g = 1$) leads to the perfect orbital pairing. It is important to note that orbitals satisfying the pairing conditions (5) are not required to remain fixed

throughout the orbital optimization process.[33] The simplest way to satisfy the constraints imposed on the two-particle cumulant leads to PNOF5[27]:

$$\begin{gathered}\Delta_{qp} = n_p^2\delta_{qp} + n_q n_p\left(1-\delta_{qp}\right)\delta_{q\Omega_g}\delta_{p\Omega_g} \\ \Pi_{qp} = n_p\delta_{qp} + \Pi^g_{qp}\left(1-\delta_{qp}\right)\delta_{q\Omega_g}\delta_{p\Omega_g} \\ \Pi^g_{qp} = \begin{cases} -\sqrt{n_q n_p}, & p=g \text{ or } q=g \\ +\sqrt{n_q n_p}, & p,q>N/2 \end{cases}, \quad \delta_{q\Omega_g} = \begin{cases} 1, & q\in\Omega_g \\ 0, & q\notin\Omega_g \end{cases}\end{gathered} \tag{7}$$

It is worth noting that Δ_{qp} and Π_{qp} are zero between orbitals belonging to different subspaces, therefore the 2RDM reconstruction of PNOF5 corresponds to an independent pair model. Given this functional form of the auxiliary matrices Δ and Π, the energy (4) of the PNOF5 can be conveniently written as

$$\begin{aligned} E^{pnof5} &= \sum_{g=1}^{N/2} E_g + \sum_{f\neq g}^{N/2} E_{fg} \\ E_{fg} &= \sum_{p\in\Omega_f}\sum_{q\in\Omega_g}\left[n_q n_p\left(2\mathcal{J}_{pq}-\mathcal{K}_{pq}\right)\right] \\ E_g &= \sum_{p\in\Omega_g} n_p\left(2\mathcal{H}_{pp}+\mathcal{J}_{pp}\right) + \sum_{q,p\in\Omega_g,q\neq p}\Pi^g_{qp}\mathcal{L}_{pq}. \end{aligned} \tag{8}$$

The first term of E^{pnof5} is the sum of the $N/2$ electron-pair E_g energies, whereas the second term contains the contribution to the HF mean-field of the electrons belonging to different pairs. Several performance tests have shown that PNOF5 yields remarkably accurate descriptions of systems with near-degenerate one-particle states and dissociation processes.[34] In this sense, the results obtained with PNOF5 for the electronic structure of transition metal complexes are probably the most relevant.[30]

Since the energy is not invariant with respect to a unitary transformation of the orbitals, an approximate NOF provides two complementary representations of the one-electron picture. Namely, the NO representation and the canonical orbital representation.[35] Both sets of orbitals represent unique correlated one-electron pictures of the same energy minimization problem, *ergo*, they complement each other in the analysis of the molecular electronic structure. The orbitals obtained in both representations have shown[28] that the electron pairs with opposite spins continue to be a suitable language for the chemical bond theory.

PNOF5 takes into account the important part of the electron correlation corresponding to the intra-pair interactions. However, no inter-pair electron

correlation is accounted for. To include the missing interactions, PNOF6[23] and PNOF7[19] were proposed. The latter was recently[31] improved by an adequate choice of sign factors for the inter-pair interactions, which provides a robust description of nondynamic correlation effects. Consequently, we will limit ourselves to this interacting pair model in this chapter.

Let us maintain $\Delta_{qp} = 0$ and consider nonzero the Π-elements between orbitals belonging to different subspaces. In Ref. 19, the generalization of the sign convention adopted for Π^{g}_{qp} in Eq. (7), namely $\Pi^{\Phi}_{qp} = \Phi_q \Phi_p$ with $\Phi_q = \sqrt{n_q h_q}$ if q, $p > N/2$, and $\Pi^{\Phi}_{qp} = -\Phi_q \Phi_p$ otherwise, led to a new functional denoted as PNOF7. The resulting energy is

$$E^{pnof7} = E^{pnof5} + \sum_{f \neq g}^{N/2} \sum_{p \in \Omega_f} \sum_{q \in \Omega_g} \Pi^{\Phi}_{qp} \mathcal{L}_{pq}. \tag{9}$$

It is obvious that a possible option that favors decreasing of the energy is to consider all the phase factors negative, i.e., $\Pi^{\Phi}_{qp} = -\Phi_q \Phi_p$. In Ref. 31, we analyzed several examples with strong static correlation. Comparing with accurate diagonalization calculations, our results indicated that all negative inter-pair factors is a better option. Hence, hereafter we will restrict our work to the latter.

All the results corresponding to NOFAs have been computed using the DoNOF code developed by M. Piris and co-workers.

4. Model systems

Simple correlated electron models are suitable for robust validation of approximate NOFs. In this section, we analyze the one-dimensional Hubbard model with different number of sites, and hydrogen chains with different ring sizes, in order to test the NOFs given by Eqs. (8) and (9) in strong nondynamic correlation regimes.

4.1 Hubbard model

Despite its simplicity, the Hubbard Hamiltonian captures the basic nature of the electron correlation. Motivated by the pitfalls obtained with standard electronic structure methods even in the simple two site nonsymmetric Hubbard model, we suggested using NOFAs. Recently,[36,37] we have shown that developing functionals that satisfy at least with the analytically necessary N-representability conditions of the 2RDM is essential to obtain consistent

results throughout the different correlation regions contained in the Hubbard model. In this vein, below we vary the system's size and employ exact results in order to test the usefulness of the studied NOFAs.

Let us focus on the one-dimensional Hubbard model in its simplest form, i.e.,

$$H = -t \sum_{\langle \mu, \upsilon \rangle, \sigma} \left(c^{\dagger}_{\mu,\sigma} c_{\upsilon,\sigma} + c^{\dagger}_{\upsilon,\sigma} c_{\mu,\sigma} \right) + U \sum_{\mu} n_{\mu,\alpha} n_{\mu,\beta}. \tag{10}$$

Here Greek indexes μ and υ denote sites, $\langle \mu, \upsilon \rangle$ indicates only near-neighbor hopping, $t > 0$ is the hopping parameter, $\sigma = \alpha, \beta$, $n_{\mu,\sigma} = c^{\dagger}_{\mu,\sigma} c_{\mu,\sigma}$ where $c^{\dagger}_{\mu,\sigma}\left(c_{\mu,\sigma}\right)$ corresponds to fermionic creation(annihilation) operator and U is the electron–electron interaction parameter. U/t quantifies the compromise between kinetic energy and Coulomb repulsion, so it will be employed as a dimensionless parameter to explore different correlation regimes.

Fig. 1 shows the difference in dimensionless energy values E/t with respect to exact result obtained from Full Configuration Interaction (FCI)

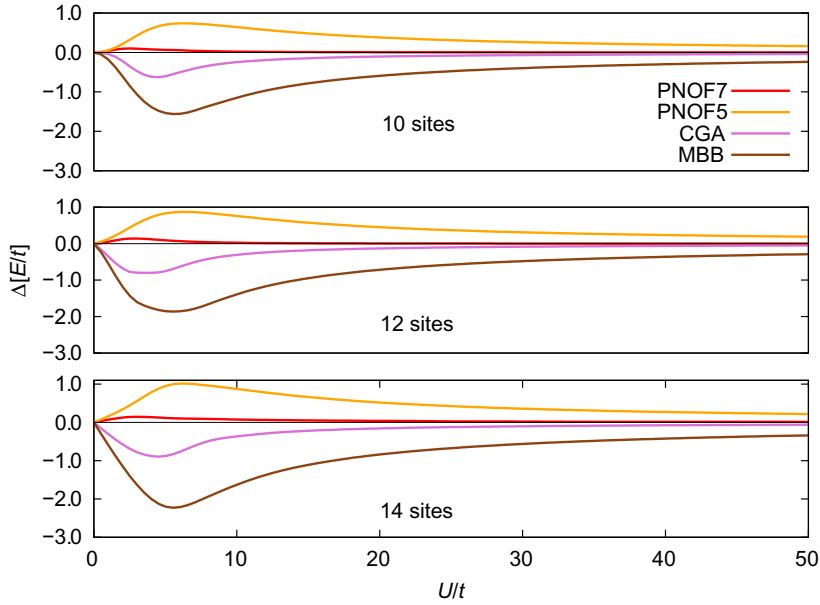

Fig. 1 Differences, as a function of U/t, in E/t values with respect to FCI obtained for the one-dimensional Hubbard model by using different NOFAs. From top to bottom, the plots correspond to the one-dimensional Hubbard model with periodic boundary conditions with 10 sites, 12 sites, and 14 sites.

calculations. Exact results are obtained from a modified version of the code developed by Knowles and Handy,[38,39] and the code DMN developed by Matito and Feixas.[40]

In contrast with many other NOFAs studied in Refs. 37 and 36 all the methods shown in Fig. 1 are able to describe the $U/t \to 0$ and $U/t \to \infty$ correlation limits. The former is well described by mean-field theories since it corresponds to weak correlation due to lacking two-electron interactions, so the tight-binging model is recovered. Conversely, correlation effects become increasingly significant as U/t gets larger, since electrons try to keep away one from each other by half-filling the sites. Although the performance of the NOFAs shown in Fig. 1 does not deteriorate significantly with the size of the system, both CGA and MBB approximations (defined elsewhere[36]) show a deficiency related to producing energies below the exact ones. Hence they are not N-representable and they cannot represent any physical quantum state. Among the results obtained by using PNOF approaches, PNOF7 outperforms the independent pair model PNOF5 whatever the number of sites and the correlation regime. A quasi-exact description of the model is obtained whenever $U/t \gg 1$, so PNOF7 describes accurately the Wigner crystallization that takes place in this regime.

4.2 Hydrogen rings

Periodic and nonperiodic hydrogen chains can be considered as the simplest examples of strong electronic correlation in low dimensions. In contrast with the Hubbard model, long-range electronic interactions are included. Besides, since more spatial dimensions are considered, this system exhibits a noticeable increase in correlation energy compared to one-dimensional systems.

Let us consider a periodic chain of hydrogen atoms and vary the number of atoms (as done in the Hubbard model with the sites) at an internuclear distance of $R_{H-H} = 2.0$ Å. In Fig. 2, we show the relative energies obtained by using PNOF5 and PNOF7 with respect to FCI, increasing the rings of hydrogen atoms from 2 to 16. We use minimal basis in all the calculations, and the PSI4 suite of programs[41] to obtain FCI energies.

According to Fig. 2, the relative errors shown by PNOF5 get larger as the size of the chain increases, so PNOF5 is not expected to give an accurate description of the electron correlation in the presence of many inter-pair interactions. In contrast, when inter-pair electron correlation is considered, the relative errors with respect to FCI do not increase with the number of

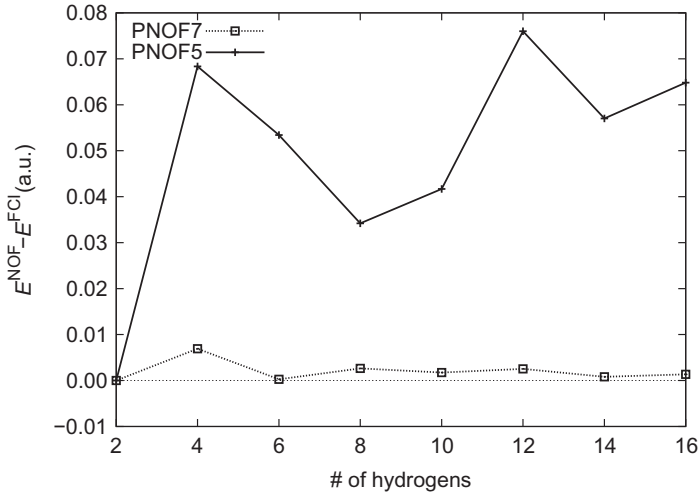

Fig. 2 Relative differences with respect to exact diagonalization energies obtained by using PNOF5 and PNOF7 for the hydrogen rings at $R_{H-H} = 2.0$ Å with varying size. Calculations are performed using minimal basis.

hydrogens. In fact, the largest error obtained by using PNOF7 is below 0.007 Hartree and it remains small and constant with increasing size of the system. According to its performance, PNOF7 captures the physics that appears in strongly correlated systems, therefore it could be used to study strongly correlated systems beyond small molecules, e.g., periodic polymers or heavy-element-containing molecules. Note that inter-pair interactions are introduced in PNOF7 meeting the particle-hole symmetry. The poor performance obtained by the independent pair model PNOF5 comparing to PNOF7 demonstrates that fully correlated methods are indeed needed to describe strongly correlated systems.

5. Geometry optimization

Geometry optimization is, together with single-point energy calculations, the most used procedure in electronic structure theory. Energy gradients are primarily employed to locate and characterize critical points on the energy surface in electronic structure theory, especially minima and saddle points, but are also essential for the study of high-resolution molecular spectroscopy, or geometry-dependent molecular properties such as electrostatic moments.[42]

5.1 Energy gradient

Analytic energy gradient expressions have been recently published for NOFAs.[43] The derivative of the total energy (in the atomic orbital (AO) representation) with respect to the coordinate x of nucleus A reads as

$$\frac{dE}{dx_A}=\sum_{\mu\nu}\Gamma_{\mu\nu}\frac{\partial\mathcal{H}_{\mu\nu}}{\partial x_A}+\sum_{\mu\nu\eta\delta}D_{\mu\eta,\nu\delta}\frac{\partial\langle\mu\eta|\nu\delta\rangle}{\partial x_A}+\frac{\partial E_{nuc}}{\partial x_A}-\sum_{\mu\nu}\lambda_{\mu\nu}\frac{\partial\mathcal{S}_{\mu\nu}}{\partial x_A} \tag{11}$$

where λ is the matrix of Lagrange multipliers,[43] E_{nuc} is the nuclear energy and $\mathcal{S}_{\mu\nu}$ represents the overlap matrix elements in the AO representation. Eq. (11) gives the general expression to obtain the energy gradients for any NOF, so that an explicit reconstruction of the 2RDM in terms of the 1RDM is the only requirement for specific approximations.

5.1.1 Separability

According to Eq. (11), the bottleneck of computing NOF gradients is due to $D_{\mu\eta,\nu\delta}$, which involves[43] a formal scaling of M^5 being M the number of functions present in the given basis set. In the following, we show that for some approximations it is possible to reduce the computational cost by summing over molecular orbital (MO) indices separately. Indeed, it is known that for the HF approximation Eq. (11) scales as M^4. When electron correlation is considered, the same technique can be used whenever the cumulant matrices are factorized. The latter is best explained with an example. To this end we use the cumulant matrix corresponding to PNOF5 (Eq. 7). First, let us focus on the transformation of the Δ matrix to the AO representation, such that the term accompanying the Coulomb integrals $\mathcal{J}_{pq}$ reads as

$$\sum_{p,q}\left(n_pn_q-\Delta_{pq}\right)C_{\mu p}C_{\nu p}C_{\eta q}C_{\delta q}=D_{\mu\nu}D_{\eta\delta}-\sum_{g=1}^{N/2}D^g_{\mu\nu}D^g_{\eta\delta} \tag{12}$$

where $D^g_{\mu\nu}=\sum_{p\epsilon\Omega_g}n_pC_{\mu p}C_{\nu p}$ and $D_{\mu\nu}=\sum_{g=1}^{N/2}D^g_{\mu\nu}$. Eq. (12) scales as $L\cdot M^4$, where L is a prefactor equal to the number of orbitals up to the $N/2$ level. The remaining cumulant part is given by the Π matrix as

$$\sum_{p,q}\Pi_{pq}C_{\mu p}C_{\nu p}C_{\eta q}C_{\delta q}=\sum_{g=1}^{N/2}\tilde{D}^g_{\mu\nu}\tilde{D}^g_{\eta\delta} \tag{13}$$

where $\tilde{D}^g_{\mu\nu}=\sum_{p\epsilon\Omega_g,p\neq g}\sqrt{n_p}C_{\mu p}C_{\nu p}-\sqrt{n_g}C_{\mu g}C_{\nu g}$. Note that Eq. (13) has the same computational cost as Eq. (12), so overall the cost corresponding to

$D_{\mu\eta,\upsilon\delta}$ is reduced considerably by using separability of MO indexes. The factorization of PNOF5 described above can be easily extended to PNOF7. To do this we have to consider the inter-pair correlation terms accompanying $\mathcal{L}_{pq}$ integrals as

$$\sum_{p,q}\Pi_{pq}C_{\mu p}C_{\upsilon p}C_{\eta q}C_{\delta q}=\sum_{g=1}^{N/2}\widetilde{D}^{g}_{\mu\upsilon}\widetilde{D}^{g}_{\eta\delta}-\left(\sum_{g}\phi^{g}_{\mu\upsilon}\right)\left(\sum_{f}\phi^{f}_{\eta\delta}\right)+\sum_{g}\phi^{g}_{\mu\upsilon}\phi^{g}_{\eta\delta} \tag{14}$$

where $\phi^{g}_{\mu\upsilon}=\sum_{p\epsilon\Omega_g}\sqrt{n_p\left(1-n_p\right)}C_{\mu p}C_{\upsilon p}$. Recall that formally the computational cost corresponding to PNOF5 and PNOF7 is the same, so a more complex functional form does not necessarily imply higher computation time.

Let us an example to illustrate the gain when computing energy gradients. As it is shown in Table 1, the computation time is significantly reduced if separability is employed for both PNOF5 and PNOF7, independently of the number of orbitals considered in the calculation (determined by M and N_g).

5.2 The Hessian

According to the derivation carried out in Ref. 44, second derivatives of the NOF energy (in the MO representation) are obtained by differentiating Eq. (11) with respect to coordinate γ of nucleus B

$$\begin{aligned}\frac{d^2E_{el}}{dx_A d\gamma_B}=&\sum_i n_i\frac{\partial^2\mathcal{H}_{ii}}{\partial x_A\partial\gamma_B}+\sum_{ijkl}D_{kl,ij}\frac{\partial^2\langle ij|kl\rangle}{\partial x_A\partial\gamma_B}\\&+2\sum_{ij}\left(U^{\gamma_B}_{ij}\lambda^{x_A}_{ij}+U^{x_A}_{ij}\lambda^{\gamma_B}_{ij}+U^{x_A\gamma_B}_{ij}\lambda_{ij}\right)+2\sum_{ijkl}U^{x_A}_{ij}U^{\gamma_B}_{kl}Y_{ijkl}\\&+\sum_m n^{\gamma_B}_m\left(\frac{\partial\mathcal{H}_{mm}}{\partial x_A}+2\sum_{ij}U^{x_A}_{ij}\frac{\partial\lambda_{ij}}{\partial n_m}+\sum_{ijkl}\frac{\partial D_{kl,ij}}{\partial n_m}\frac{\partial\langle ij|kl\rangle}{\partial x_A}\right)\end{aligned} \tag{15}$$

Table 1 Computation time (s) obtained using the cc-pVTZ basis set for the energy gradient of C_2H_4.

	Without separability	With separability
PNOF5 ($N_g=1$)	14	8
PNOF7 ($N_g=20$)	37	28

N_g determines the number of weak orbitals coupled with each strongly occupied orbital in each subspace.

$$Y_{ijkl} = n_j \delta_{jl} \mathcal{H}_{ik} + 2 \sum_{mn} D_{ln,\,jm} \langle im|kn\rangle + 4 \sum_{mn} D_{mn,\,jl} \langle ik|mn\rangle \tag{16}$$

where the derivatives of the matrix of Lagrange multipliers read as

$$\begin{aligned} \lambda_{ij}^{x_A} &= n_j \frac{\partial \mathcal{H}_{ij}}{\partial x_A} + 2 \sum_{mkl} D_{kl,\,jm} \frac{\partial \langle im|kl\rangle}{\partial x_A} \\ \frac{\partial \lambda_{ij}}{\partial n_m} &= \delta_{mj} \mathcal{H}_{ij} + 2 \sum_{rkl} \frac{\partial D_{kl,\,jr}}{\partial n_m} \langle ir|kl\rangle \end{aligned} \tag{17}$$

In Eq. (15), the first two terms contain the explicit derivatives of the core Hamiltonian and two-electron integrals, respectively. The next two terms arise from the derivatives of NO coefficients with respect to the nuclear perturbation, described by the coefficients U (see Eq. 8 in Ref. 44). $n_m^{\gamma_B}$ represents the change in ON m due to perturbation γ_B, hence the last term in Eq. (15) describes the contribution from the perturbation of the ONs. In contrast to first-order energy derivatives, the calculation of the analytic Hessian requires the knowledge of NOs and ONs at the perturbed geometry. Both magnitudes are obtained from the solution of coupled-perturbed equations, which are summarized elsewhere.[44]

5.3 Computational aspects

For any approximate NOF the evaluation of analytic energy gradients does not require resorting to linear-response theory. The gradient computation is therefore analogous to that which is performed at the HF level of theory with the corresponding savings of computational time. The bottleneck of gradient evaluation is the computation of the two-electron contribution, since 12 gradient components arise from each two-electron integral. The latter are computed on-the-fly to avoid calculating negligible contributions.

In contrast to first-order derivatives (11), coupled-perturbed equations must be solved to evaluate the Hessian expression (15), so the corresponding computational cost increases dramatically. In fact, previous calculations involving coupled-perturbed equations in NOFAs have been applied only to very small systems,[45] e.g., single atoms or molecular dimers. Second-order energy derivatives are computationally much more demanding in terms of storage capacity than the evaluation of the total electronic energy or gradients. Indeed, derivative of two-electron integrals are 45 times greater in number than usual four-index integrals.[46] In order to overcome these drawbacks, in the following we use the numerical differentiation procedure to obtain the Hessian, specifically the $6N_a$ point formula (N_a being the number of atoms).

The use of analytic gradients to compute the second derivatives has been developed efficiently before,[46] where it has been assured that an analytic evaluation of the second derivatives is not necessarily much more efficient than a numerical differentiation of analytic gradients.

5.4 Equilibrium geometries

In this section, we carry out a NOF study of the ground-state equilibrium geometries for a selected set of spin-compensated molecules in order to test PNOF5 and PNOF7 beyond the energy. This set of molecules includes the following 14 systems: HF, H_2O, NH_3, CH_4, N_2, CO, HOF, HNO, H_2CO, HNNH, H_2CCH_2, HCCH, HCN, and HNC. For comparison, we have included coupled cluster singles and doubles (CCSD)[47] and high-quality empirical equilibrium structures obtained from least-squares fits involving experimental rotational constants and theoretical vibrational corrections.[48] We use HF geometries as starting points to PNOF optimizations. All calculations are carried out using $N_g = 1$ and the correlation-consistent polarized triple-zeta (cc-pVTZ) basis set.[49]

Tables 2 and 3 show the errors in bond lengths and bond angles with respect to empirical structural data. According to the mean errors shown in these tables, PNOF5 and PNOF7 provide ground-state equilibrium structures comparable to those of the CCSD. PNOF5 underestimates some inter-atomic distances, while overestimating it in other cases, with a slight tendency to the latter as evidenced by the mean signed value $\overline{\Delta} = 0.1$ pm. PNOF5 tends to overestimate bond angles according to a mean absolute error of $\overline{\Delta} = 0.07$ degrees, in contrast with CCSD ($\overline{\Delta} = -0.09$ degrees).

PNOF7 produces larger errors than PNOF5 for the studied equilibrium geometries. Indeed, PNOF7 retrieves most of static correlation effects but it lacks inter-pair dynamic correlation that are important in equilibrium region (vide supra). Hence, we expect that including gradients corresponding to second-order Møller–Plesset perturbative (MP2) corrections in the NOF-MP2 method,[19,20] the bond distances and angles will be corrected. A work in this direction is underway.

5.5 Harmonic vibrational frequencies

Second-order energy derivatives make the calculation of harmonic vibrational frequencies commonplace. Analogous to the procedure described in Ref. 50, the Hessian is obtained by numerical differentiation of analytic gradients and immediately after it is converted to mass weighted Cartesian coordinates (MWC), i.e.

Table 2 Errors in the equilibrium bonds (in pm) at PNOF5, PNOF7, and CCSD levels of theory calculated by using the cc-pVTZ basis set with respect to empirical structural data.

Molecule	Bond	PNOF5	PNOF7	CCSD	EMP.
HF	H–F	−0.2	0.2	−0.3	91.7
H_2O	O–H	0.1	0.5	−0.2	95.8
NH_3	N–H	0.6	0.9	−0.3	101.2
CH_4	C–H	1.5	1.7	−0.1	108.6
N_2	N–N	−0.7	0.2	−0.4	109.8
CO	C–O	−1.1	−0.6	−0.3	112.8
HNO	N–O	0.0	1.7	−0.9	120.9
	H–N	−0.7	−0.5	−0.3	105.2
H_2CO	C–O	0.2	1.1	−0.5	120.5
	C–H	0.4	0.4	−0.4	110.1
HNNH	N–N	−0.1	1.3	−0.7	124.6
	N–H	0.1	0.4	−0.4	102.9
H_2CCH_2	C–C	0.9	1.9	−0.4	133.1
	C–H	1.1	1.3	−0.4	108.1
HCCH	C–C	−0.1	0.7	−0.4	120.4
	C–H	0.7	0.9	−0.4	106.1
HCN	C–N	−0.5	0.4	−0.4	115.3
	C–H	0.5	0.7	−0.6	106.5
HNC	C–N	−2.3	−0.2	−0.4	116.9
	N–H	−1.3	0.4	−0.4	99.5
HOF	O–F	3.6	8.2	−1.9	143.4
	H–O	−0.3	0.3	−0.5	96.8
$\overline{\Delta}$		0.1	1.0	−0.5	
$\overline{\Delta}_{abs}$		0.8	1.1	0.5	

$\overline{\Delta}$ and $\overline{\Delta}_{abs}$ correspond to the mean signed error and mean absolute error, respectively.

$$\left(\frac{\partial^2 E}{\partial x_A \partial y_B}\right)_{\mathrm{MWC}} = \frac{1}{m_A m_B}\frac{\partial^2 E}{\partial x_A \partial y_B}. \tag{18}$$

We obtain a set of $3N_a$ eigenvectors corresponding to normal modes, and $3N_a$ eigenvalues corresponding to the harmonic vibrational frequencies of

Table 3 Errors in the equilibrium bond angles (in degrees) at PNOF5, PNOF7, and CCSD levels of theory calculated by using the cc-pVTZ basis set with respect to empirical structural data.

Molecule	Bond angle	PNOF5	PNOF7	CCSD	EMP.
H_2O	H–O–H	0.23	−0.09	−0.47	104.51
NH_3	H–N–H	0.45	−0.92	−0.89	107.25
HOF	H–O–F	0.27	−1.35	0.43	97.94
HNO	H–N–O	−0.53	−0.67	0.00	108.27
H_2CO	H–C–O	−0.09	−0.51	0.29	121.63
HNNH	H–N–N	0.82	0.44	−0.04	106.36
H_2CCH_2	H–C–C	−0.15	0.14	0.03	121.43
$\overline{\Delta}$		0.07	−0.42	−0.09	
$\overline{\Delta}_{abs}$		0.36	0.59	0.31	

$\overline{\Delta}$ and $\overline{\Delta}_{abs}$ correspond to the mean signed error and mean absolute error, respectively.

the molecule. Unfortunately, there are six eigenvalues corresponding to overall translation and rotation that are not exactly zero at a general point of the energy surface.[51] In fact, for displacements that are not rigorously orthogonal in the $3N_a$ dimensional vector space to the gradient vector, the potential is not quadratic, so rotational and translational contaminant modes may arise. The Eckart–Sayvetz conditions are an indicator of this contamination,[52] thereby they can be employed to ensure separation of the vibrational motions via projection techniques. Thus, the Hessian is projected in order to restrict the displacements to be orthogonal to the $3N_a$ dimensional vectors corresponding to the rotations and translations of the system, i.e., displacements satisfying the Eckart–Sayvetz conditions are the only ones allowed.

We have made a comparison between harmonic vibrational frequencies obtained by using CCSD, MP2, and PNOF7, with respect to experimental fundamentals. CCSD, MP2 and experimental values are obtained from Ref. 53. Harmonic vibrational frequencies correspond to the set of molecules H_2O, NH_3, CH_4, N_2, CO, HNO, H_2CO, HNNH, H_2CCH_2, HNC, HCCH, HOF, LiH, HF, C_2H_2, H_2O_2, Li_2, LiH, HCN, F_2, CO_2, H_2, PH_3, SiH_4, H_2S, HCl, Na_2, P_2, Cl_2, NaCl, CS, SiO, ClF, and HOCl. All calculations are carried out by using the cc-pVTZ basis set[49] and the maximum N_g value allowed by the basis set.

Fig. 3 shows the distribution of the errors for the above mentioned set of molecules. According to these plots, PNOF7 shows good agreement

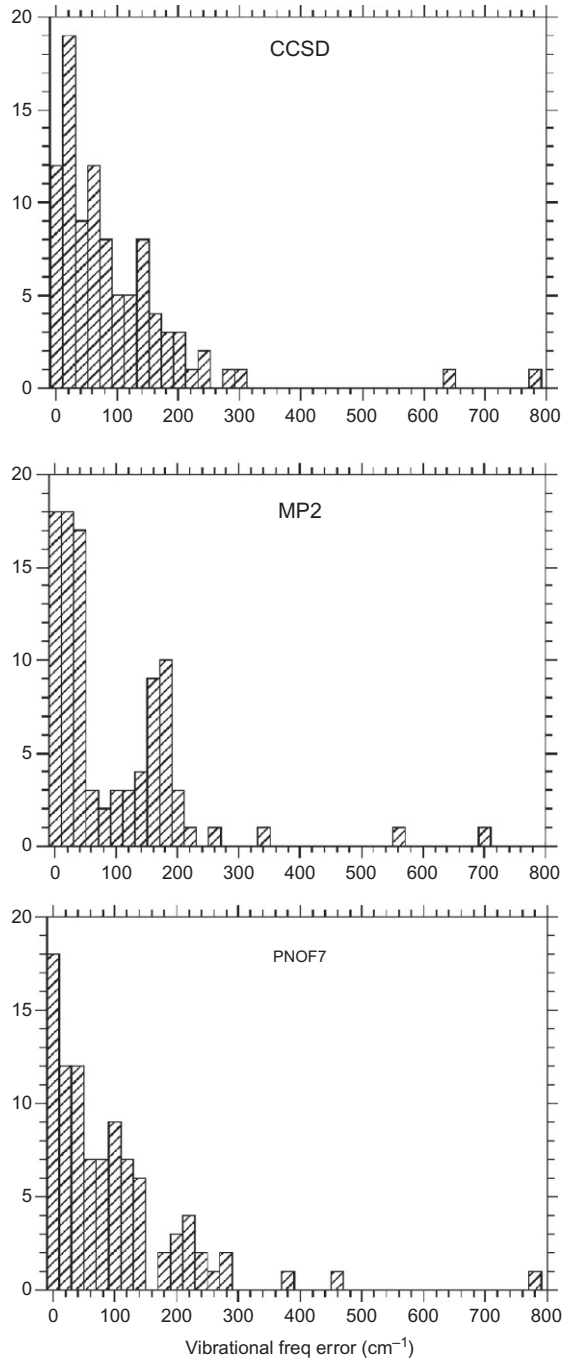

Fig. 3 Histograms with a bin of 20 cm^{-1} showing the distribution of errors with respect to experimental fundamentals obtained by using CCSD, MP2, and PNOF7 methods, with the cc-pVTZ basis set.

with CCSD and MP2. The latter has several errors between 150 and 200 cm^{-1}, whereas the distributions corresponding to both CCSD and PNOF7 show most of the results with errors below 100 cm^{-1}. Regarding the average values, there are no significance differences between the three methods: $\overline{\Delta}(PNOF7) = 104\ cm^{-1}$ over, $\overline{\Delta}(MP2) = 104\ cm^{-1}$, and $\overline{\Delta}(CCSD) = 100\,cm^{-1}$. It is worth noting that the large differences between experimental fundamental frequencies and theoretically determined harmonic vibrational frequencies are systematic, so scaling factors can be used to correct anharmonic effects in the determination of those values.[54]

6. Closing remarks

In this chapter, we have focused on electron pairing NOF approximations, namely, the independent pair model PNOF5 and the inter-pair electron correlation model PNOF7. PNOF7 has shown to be an ideal candidate to study model systems for strong correlation such as Hubbard model with different number of sites and hydrogen rings. Analytic first- and second-order-energy derivatives were presented for any given nuclear perturbation. The former does not require resorting to linear-response theory, whereas coupled-perturbed equations must be solved to attain the analytic Hessian at the perturbed geometry. Consequently, energy gradients can be computed at a computational scaling near to the HF approximation. The equilibrium geometries compare well to those obtained with CCSD. Besides, the analytic gradients have been employed to compute harmonic vibrational frequencies, which turns out to agree with MP2 and CCSD when PNOF7 is employed.

Acknowledgments

Financial support comes from Eusko Jaurlaritza (Ref. IT588-13) and Ministerio de Econom a y Competitividad (Ref. CTQ2015-67608-P). The SGI/IZO–SGIker UPV/EHU is gratefully acknowledged for generous allocation of computational resources. One of us (I.M.) is grateful to Vice-Rectory for research of the UPV/EHU for the Ph.D. grant (PIF//15/043).

References

1. Gilbert, T. L. Hohenberg-Kohn Theorem for Nonlocal External Potentials. *Phys. Rev. B* **1975**, *12*, 2111–2120.
2. Levy, M. Universal Variational Functionals of Electron Densities, First-Order Density Matrices, and Natural Spin-Orbitals and Solution of the V-Representability Problem. *Proc. Natl. Acad. Sci. USA* **1979**, *76*(12), 6062–6065. https://doi.org/10.1088/0022-3719/12/3/015.

3. Valone, S. M. Consequences of Extending 1 Matrix Energy Functionals Pure-State Representable to All Ensemble Representable 1 Matrices. *J. Chem. Phys.* **1980**, *73*(3), 1344–1349.
4. Ayers, P. W.; Liu, S. Necessary and Sufficient Conditions for the N-Representability of Density Functionals. *Phys. Rev. A* **2007**, *75*, 022514. https://doi.org/10.1103/PhysRevA.75.022514.
5. Rosina, M. Transition Amplitudes as Ground State Variational Parameters. In *Reduced Density Operators With Application to Physical and Chemical Systems*, Coleman, A. J., Erdahl, R. M., Eds.; Queens Papers in Pure and Applied Mathematics No. 11: Queens University, Kingston, Ontario, 1967; p 369.
6. Donnelly, R. A. On Fundamental Difference Between Energy Functionals Based on First- and Second-Order Density Matrices. *J. Chem. Phys.* **1979**, *71*(7), 2874–2879.
7. Ludeña, E. V.; Torres, F. J.; Costa, C. Functional N-Representability in 2-Matrix, 1-Matrix, and Density Functional Theories. *J. Mod. Phys.* **2013**, *04*, 391–400. https://doi.org/10.4236/jmp.2013.43A055.
8. Piris, M. The Role of the N-Representability in One-Particle Functional Theories. In *Many-Body Approaches at Different Scales: A Tribute to N. H. March on the Occasion of His 90th Birthday*; Angilella, G. G. N., Amovilli, C., Eds.; Springer: New York, 2018; pp 283–300. Chapter 22.
9. Mazziotti, D. A. Structure of Fermionic Density Matrices: Complete N-Representability Conditions. *Phys. Rev. Lett.* **2012**, *108*(26), 263002. https://doi.org/10.1103/PhysRevLett.108.263002.
10. Rodríguez-Mayorga, M.; Ramos-Cordoba, E.; Via-Nadal, M.; Piris, M.; Matito, E. Comprehensive Benchmarking of Density Matrix Functional Approximations. *Phys. Chem. Chem. Phys* **2017**, *19*, 24029–24041. https://doi.org/10.1039/C7CP03349D.
11. Coleman, A. J. Structure of Fermion Density Matrices. *Rev. Mod. Phys.* **1963**, *35*, 668–687.
12. Theophilou, I.; Lathiotakis, N. N.; Marques, M. A. L.; Helbig, N. Generalized Pauli constraints in Reduced Density Matrix Functional Theory. *J. Chem. Phys.* **2015**, *142*(15), 154108. https://doi.org/10.1063/1.4918346.
13. Theophilou, I.; Lathiotakis, N. N.; Helbig, N. Structure of the First Order Reduced Density Matrix in Three Electron Systems: A Generalized Pauli Constraints Assisted Study. *J. Chem. Phys.* **2018**, *148*(11), 114108. https://doi.org/10.1063/1.5020978.
14. Benavides-Riveros, C. L.; Marques, M. A. L. Static Correlated Functionals for Reduced Density Matrix Functional Theory. *Eur. Phys. J. B* **2018**, *91*, 133. https://doi.org/10.1140/epjb/e2018-90167-8.
15. Schilling, C.; Schilling, R. Diverging Exchange Force and Form of the Exact Density Matrix Functional. *Phys. Rev. Lett.* **2019**, *122*(1). https://doi.org/10.1103/PhysRevLett.122.013001013001-7.
16. Lowdin, P. O.; Shull, H. Natural Orbitals in the Quantum Theory of 2e Systems. *Phys. Rev.* **1955**, *101*(6), 1730–1739.
17. Piris, M.; Ugalde, J. M. Perspective on Natural Orbital Functional Theory. *Int. J. Quantum Chem.* **2014**, *114*(18), 1169–1175. https://doi.org/10.1002/qua.24663.
18. Pernal, K.; Giesbertz, K. J. H. Reduced Density Matrix Functional Theory (RDMFT) and Linear Response Time-Dependent RDMFT (TD-RDMFT). *Top. Curr. Chem.* **2016**, *368*, 125–184. https://doi.org/10.1007/128_2015_624.
19. Piris, M. Global Method for Electron Correlation. *Phys. Rev. Lett.* **2017**, *119*, 063002-5. https://doi.org/10.1103/PhysRevLett.119.063002.
20. Piris, M. Dynamic Electron-Correlation Energy in the Natural-Orbital-Functional Second-Order-Møller-Plesset Method From the Orbital-Invariant Perturbation Theory. *Phys. Rev. A* **2018**, *98*, 022504-6. https://doi.org/10.1103/PhysRevA.98.022504.
21. van Meer, R.; Gritsenko, O. V.; Baerends, E. J. A Non-JKL Density Matrix Functional for Intergeminal Correlation Between Closed-Shell Geminals From Analysis of Natural

Orbital Configuration Interaction Expansions. *J. Chem. Phys.* **2018**, *148*(10), 104102. https://doi.org/10.1063/1.5018671.
22. Piris, M. A Natural Orbital Functional Based on an Explicit Approach of the Two-Electron Cumulant. *Int. J. Quantum Chem.* **2013**, *113*, 620–630. https://doi.org/10.1002/qua.24020.
23. Piris, M. Interacting Pairs in Natural Orbital Functional Theory. *J. Chem. Phys.* **2014**, *141*, 044107. https://doi.org/10.1063/1.4890653.
24. Piris, M.; Lopez, X.; Ruipérez, F.; Matxain, J. M.; Ugalde, J. M. A Natural Orbital Functional for Multiconfigurational States. *J. Chem. Phys.* **2011**, *134*(16), 164102.
25. Piris, M. Bounds on the PNOF5 Natural Geminal Occupation Numbers. *Comp. Theor. Chem.* **2013**, *1003*, 123–126. https://doi.org/10.1016/j.comptc.2012.07.016.
26. Pernal, K. The Equivalence of the Piris Natural Orbital Functional 5 (PNOF5) and the Antisymmetrized Product of Strongly Orthogonal Geminal Theory. *Comp. Theor. Chem.* **2013**, *1003*, 127–129. https://doi.org/10.1016/j.comptc.2012.08.022.
27. Piris, M.; Matxain, J. M.; Lopez, X. The Intrapair Electron Correlation in Natural Orbital Functional Theory. *J. Chem. Phys.* **2013**, *139*(23), 234109-9.
28. Piris, M.; Lopez, X.; Ugalde, J. M. The Bond Order of C2 From an Strictly N-Representable Natural Orbital Energy Functional Perspective. *Chem. A Eur. J.* **2016**, *22*, 4109–4115. https://doi.org/10.1002/chem.201504491.
29. Piris, M. Natural Orbital Functional Theory. In *Reduced-Density-Matrix Mechanics: With Applications to Many-Electron Atoms and Molecules*, Mazziotti, D. A. Ed.; John Wiley and Sons: Hoboken, New Jersey, USA, 2007; pp 387–427. Chapter 14. https://doi.org/10.1002/0470106603.
30. Ruipérez, F.; Piris, M.; Ugalde, J. M.; Matxain, J. M. The Natural Orbital Functional Theory of the Bonding in Cr(2), Mo(2) and W(2). *Phys. Chem. Chem. Phys.* **2013**, *15*(6), 2055–2062.
31. Mitxelena, I.; Rodríguez-Mayorga, M.; Piris, M. Phase Dilemma in Natural Orbital Functional Theory From the N-representability Perspective. *Eur. Phys. J. B* **2018**, *91*, 109.
32. Piris, M. The Electron Pairing Approach in Natural Orbital Functional Theory. In *Theoretical and Quantum Chemistry at the Dawn of the 21st Century*, Chakraborty, T., Carbó-Dorca, R., Eds.; Apple Academic Press: New Jersey, 2018; pp 593–620. Chapter 22.
33. Piris, M.; Ugalde, J. M. Iterative Diagonalization for Orbital Optimization in Natural Orbital Functional Theory. *J. Comput. Chem.* **2009**, *30*, 2078–2086. https://doi.org/10.1002/jcc.21225.
34. Matxain, J. M.; Piris, M.; Ruipérez, F.; Lopez, X.; Ugalde, J. M. Homolytic Molecular Dissociation in Natural Orbital Functional Theory. *Phys. Chem. Chem. Phys.* **2011**, *13*(45), 20129–20135.
35. Piris, M.; Matxain, J. M.; Lopez, X.; Ugalde, J. M. The One-Electron Picture in the Piris Natural Orbital Functional 5 (PNOF5). *Theor. Chem. Acc.* **2013**, *132*, 1298.
36. Mitxelena, I.; Piris, M.; Mayorga, M. A. R. On the Performance of Natural Orbital Functional Approximations in Hubbard Model. *J. Phys. Condens. Matter* **2017**, *29*, 425602.
37. Mitxelena, I.; Piris, M.; Rodríguez-Mayorga, M. Corrigendum: "On the Performance of Natural Orbital Functional Approximations in the Hubbard Model"*J. Phys. Condens. Matter* **2018**, *30*, 089501 (J. Phys.: Condens. Matter 29 (2017) 425602).
38. Knowles, P. J.; Handy, N. C. A New Determinant-Based Full Configuration Interaction Method. *Chem. Phys. Lett.* **1984**, *111*, 315–321.
39. Knowles, P. J.; Handy, N. C. A determinant based full configuration interaction program. *Comput. Phys. Commun.* **1989**, *54*, 75. https://doi.org/10.1016/0010-4655(89)90033-7.

40. Matito, E.; Feixas, F. *DMN program*; University of Girona (Spain) and University of Szczecin (Poland), 2009.
41. Parrish, R. M.; Burns, L. A.; Smith, D. G. A.; Simmonett, A. C.; DePrince, A. E.; Hohenstein, E. G.; Bozkaya, U.; Sokolov, A. Y.; Di Remigio, R.; Richard, R. M.; Gonthier, J. F.; James, A. M.; McAlexander, H. R.; Kumar, A.; Saitow, M.; Wang, X.; Pritchard, B. P.; Verma, P.; Schaefer, H. F.; Patkowski, K.; King, R. A.; Valeev, E. F.; Evangelista, F. A.; Turney, J. M.; Crawford, T. D.; Sherrill, C. D. Psi4-1.1: An Open-Source Electronic Structure Program Emphasizing Automation, Advanced Libraries, and Interoperability. *J. Chem. Theory Comput.* **2017**, *13*(7), 3185–3197. https://doi.org/10.1021/acs.jctc.7b00174.
42. Mitxelena, I.; Piris, M. Molecular Electric Moments Calculated by Using Natural Orbital Functional Theory. *J. Chem. Phys.* **2016**, *144*, 204108. https://doi.org/10.1063/1.4951685.
43. Mitxelena, I.; Piris, M. Analytic Gradients for Natural Orbital Functional Theory. *J. Chem. Phys.* **2017**, *146*, 014102. https://doi.org/10.1063/1.4973271.
44. Mitxelena, I.; Piris, M. Analytic Second-Order Energy Derivatives in Natural Orbital Functional Theory. *J. Math. Chem.* **2018**, *56*, 1445–1455. https://doi.org/10.1007/s10910-018-0870-0.
45. van Meer, R.; Gritsenko, O. V.; Baerends, E. J. Excitation Energies With Linear Response Density Matrix Functional Theory Along the Dissociation Coordinate of an Electron-Pair Bond in N-Electron Systems. *J. Chem. Phys.* **2014**, *140*, 024101. https://doi.org/10.1063/1.4852195.
46. Bykov, D.; Petrenko, T.; Izsák, R.; Kossmann, S.; Becker, U.; Valeev, E.; Neese, F. Efficient Implementation of the Analytic Second Derivatives of Hartree-Fock and Hybrid DFT Energies: A Detailed Analysis of Different Approximations. *Mol. Phys.* **2015**, *113*, 1961–1977. https://doi.org/10.1080/00268976.2015.1025114.
47. Gauss, J.; Stanton, J. F. Analytic Gradients for the Couples-Cluster Singles, Doubles, and Triples (CCSDT) Model. *J. Chem. Phys.* **2002**, *116*, 1773–1782. https://doi.org/10.1063/1.1429244.
48. Bak, K. L.; Gauss, J.; Jørgensen, P.; Olsen, J.; Helgaker, T.; Stanton, J. F. The Accurate Determination of Molecular Equilibrium Structures. *J. Chem. Phys.* **2001**, *114*, 6548–6556. https://doi.org/10.1063/1.1357225.
49. Dunning, T. H., Jr. Gaussian Basis Sets for Use in Correlated Molecular Calculations. I. The Atoms Boron Through Neon and Hydrogen. *J. Chem. Phys.* **1989**, *90*, 1007–1023. https://doi.org/10.1063/1.456153.
50. Ochterski, J. W. *Vibrational Analysis in Gaussian the Short Answer*. 1999; pp. 1–10, help@gaussian.com.
51. Miller, W. H.; Handy, N. C.; Adams, J. E. Reaction Path Hamiltonian for Polyatomic Molecules. *J. Chem. Phys.* **1980**, *72*, 99. https://doi.org/10.1063/1.438959.
52. Szalay, V. Eckart-Sayvetz Conditions Revisited. *J. Chem. Phys.* **2014**, *140*(23), 234107. https://doi.org/10.1063/1.4883195.
53. Johnson, R. D., III. NIST Computational Chemistry Comparison and Benchmark Database, NIST Standard Reference Database Number 101, Release 19, April 2018, http://cccbdb.nist.gov/doi:10.18434/T47C7Z
54. Laury, M. L.; Carlson, M. J.; Wilson, A. K. Vibrational Frequency Scale Factors for Density Functional Theory and the Polarization Consistent Basis Sets. *J. Comput. Chem.* **2012**, *33*, 2380–2387. https://doi.org/10.1002/jcc.23073.

This page intentionally left blank

CHAPTER EIGHT

Collision processes using effective potentials

Alejandra M.P. Mendez*, Darío M. Mitnik, Jorge E. Miraglia
Instituto de Astronomía y Física del Espacio, Universidad de Buenos Aires – Consejo Nacional de Investigaciones Científicas y Técnicas, Buenos Aires, Argentina
*Corresponding author: e-mail address: alemendez@iafe.uba.ar

Contents

Abstract

We investigate the feasibility of using pseudopotentials to generate the bound and continuum orbitals needed in collisional calculations. By examination of several inelastic processes in the first Born approximation, we demonstrate the inconveniences of this approach. Instead, we advocate use of effective potentials obtained with the depurated inversion method (DIM). In this contribution, we extend this method to molecular systems. Calculations of single first-order photoionization and proton-impact ionization using the DIM show fair agreement with experimental results for both atoms and molecules.

Advances in Quantum Chemistry, Volume 79
ISSN 0065-3276
https://doi.org/10.1016/bs.aiq.2019.05.003

1. Outline

Inelastic transition calculations require the representation of the bound and continuum states involved in the collisional processes. The hypothetical existence of an effective one-electron local potential accounting for these states would allow more direct generation of the orthogonal wavefunctions for the interacting particles. This approach should include individual *nl*-orbital potentials, a feature missing from most of the standard density functional methods. The idea of replacing a many-body, nonlocal interaction by an effective one-electron equation opens up the possibility of studying extremely complex systems with high accuracy.

In this context, one promising idea emerges from the pseudopotential approximation (PPA), in which all the complexity of the wavefunctions near the core—that usually consumes a huge numerical effort—is avoided. For instance, density functional theory codes using pseudopotentials, such as the PARSEC, for example,[1,2] permit the use of an equally spaced grid involving a relatively small number of points. Otherwise, the use of realistic potentials describing the nucleus Coulomb potential requires a high density of points concentrated at the origin to describe what the pseudopotentials cast aside. Thus, if PPA was applicable in the field of collision theory, one would save an enormous amount of computational resources.

Another interesting approach is the depurated inversion method (DIM),[3–5] which allows accurate, effective potentials to be obtained by substituting the coupled multielectron equations into a Kohn–Sham-type equation. In the first step, the potential is obtained through inversion of the one-electron equation. Next, a careful optimization of the potential is carried out, eliminating poles, and imposing the appropriate boundary conditions analytically. In that way, the DIM potentials are parametrized in simple analytical expressions.

In the present work, we explore the possibility of implementing an effective potential approximation in the atomic collision theory to describe inelastic processes. In particular, we examine several collisional processes involving a single electron transition: photoionization, excitation, ionization, and electron capture. A wide variety of ab initio methods have been implemented to compute scattering cross sections for atomic targets, from the early implementations of the first Born approximation (FBA),[6,7] to more sophisticated fully quantum mechanical methods, e.g., Refs. 8–11. Whether for atoms or molecules, we shall present cross sections and compare with some

experimental data. We do not wish, here, to present a detailed comparison with existing calculations. The main purpose is to illustrate the effective use of the DIM in collision applications. To this end, several simplifications are made (1) The calculations are constrained to Hamiltonians describing only the moving projectile, the target, and the active electron; (2) The transition-matrix elements are only considered in first perturbative order. If the first-order fails, it would not make any sense to extend the calculation to higher terms of the series. For simplicity, we will restrict our calculations only to the FBA framework, which is known to give reasonable agreement with the experimental cross section in the intermediate—high projectile energy range. Moreover, within this energy range and approximation order, the Hartree–Fock orbitals are known to provide the correct high energy limit.

We examine the above mentioned inelastic processes for two atoms with a single outer electron: hydrogen and lithium. In this context, we inspect the influence of the target description in the cross sections when the PPA and DIM approaches are implemented. Furthermore, these effects have been previously studied in other perturbative approaches, i.e., the continuum distorted wave eikonal-initial-state (CDW-EIS), for various targets (for example, see Refs. 12, 13). The DIM approach is further tested in the case of many-electron atoms by comparing photoionization cross sections with experimental measurements.

On the other hand, the description of molecular systems constitutes a real challenge due to their nonspherical symmetry and multicenter character. Many ab initio and semiempirical theoretical approximations[14–16] have been developed to this end over the last century. In this work, we present an extension of the DIM method for simple molecular systems, providing a new parametric expression for the potentials. The target description is once again tested by examination of its performance in first-order collisional processes, and the methane molecule being taken as an example.

2. Theory

2.1 Pseudopotential approximation

The pseudopotential approximation consists in replacing the Coulomb potential in the many-electron system Hamiltonian with a smooth function so that the electron wavefunctions oscillating rapidly in the core region are replaced by nodeless pseudo-orbitals having the right energy and the same

outer range properties. In general, the pseudopotentials V_{PP} can be defined through a pseudocharge Z_{PP} as

$$V_{\mathrm{PP}}(r) = -\frac{Z_{\mathrm{PP}}(r)}{r}, \tag{1}$$

$$Z_{\mathrm{PP}}(r) = \begin{cases} f(r), & r \le r_c \\ 1, & r > r_c \end{cases}, \tag{2}$$

where r_c is a cutoff radius that separates the core, $r \le r_c$, from the valence region, $r > r_c$, of the target and $f(r)$ is a continuous function with a constant value at the origin. Fig. 1 illustrates a pseudopotential (solid line) and its corresponding pseudo-wavefunction for the 3*s* orbital of argon. Notice that the pseudopotential behaves as $-r^{-1}$ (dot-dash line) in the valence region, as defined in Eqs. (1) and (2). The pseudo-wavefunction agrees with the one-electron Hartree–Fock (HF) orbital (dashed line) in the outer region, losing all information about the atomic structure close to the origin.

In Section 3, we analyse the feasibility of implementing pseudopotentials in collisional processes calculations for two simple atomic targets: hydrogen and lithium. For each atom, the following pseudopotentials are examined

Name	Source	Type	Refs.
A	ABINIT	GGA	17, 18
P	PARSEC	Troullier Martins	1, 2

(3)

The hydrogen atom has only one electron, and the corresponding pseudopotential is not essential. However, the hydrogen pseudopotentials from (3) reproduce with high accuracy the main features of the wavefunctions, even for excited states.

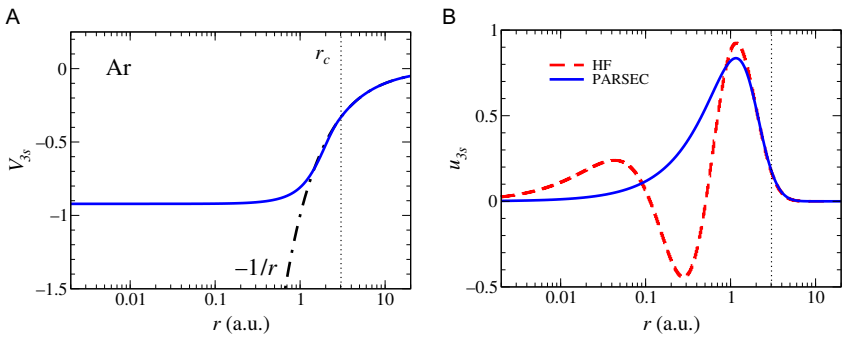

Fig. 1 (A) Pseudopotential, (B) pseudo-wavefunction and HF orbital for the 3*s* orbital of argon.

We will now proceed to examine the pseudocharges and its one-electron solutions for the lithium atom closely. First, we study the spatial and momentum representation of the pseudocharges. The momentum-space equivalent of $Z(r)$ is given by the Fourier transform

$$\tilde{Z}(k) = \frac{1}{\sqrt{2\pi}} \int_{-\infty}^{+\infty} Z(r)\, e^{-ikr}\, dr. \tag{4}$$

The pseudocharges from (3) for the 2*s* orbital of lithium are illustrated in Fig. 2. For comparison, we include the potential obtained from implementing the depurated inversion method described in Section 2.2. The pseudocharges vanish at the origin, avoiding the divergence of the Coulomb potential. However, this feature comes at a price: the pseudocharges in the spatial representation are repulsive around $r = 1$ a.u., and their momentum picture fails to represent the target for high k, showing an incorrect oscillatory behavior for values greater than $k_c = (2\pi r_c)^{-1} \sim 0.7$ a.u..

Secondly, we inspect the behavior of the bound pseudo-orbitals obtained from solving the one-electron Schrödinger equation with a pseudopotential. As usual, the bound state wavefunctions can be written as

$$\psi_{nlm}(\mathbf{r}) = \frac{u_{nl}(r)}{r} Y_l^m(\hat{r}), \tag{5}$$

where $u_{nl}(r)$ are the reduced radial wavefunctions, and $Y_l^m(\hat{r})$ are the spherical harmonics. Similarly, the Fourier transform of these functions is given by

$$\tilde{\psi}_{nlm}(\mathbf{k}) = \frac{\chi_{nl}(k)}{k} Y_l^m(\hat{k}). \tag{6}$$

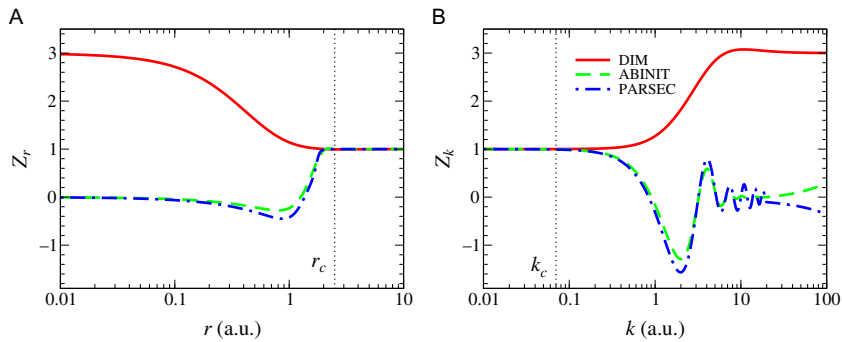

Fig. 2 Pseudo and DIM charges for the 2*s* orbital of lithium. (A) Spatial and (B) momentum representation.

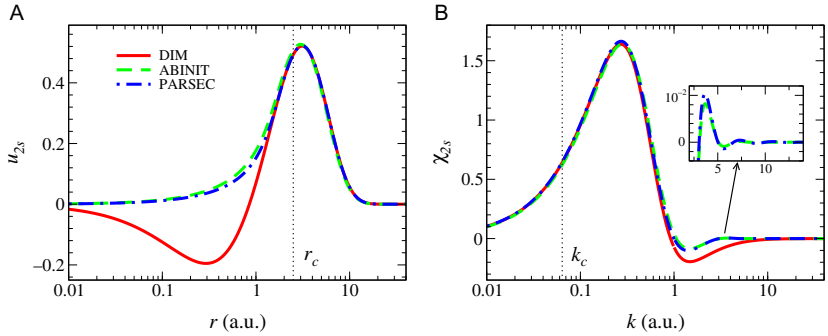

Fig. 3 Pseudo and DIM bound state wavefunction for the 2*s* orbital of lithium in (A) spatial and (B) momentum representation.

The spatial and momentum representations of the 2*s* radial pseudo-wavefunctions of lithium corresponding to the pseudocharges from (3) are displayed in Fig. 3. Although the pseudo-orbitals are very different from the DIM 2*s* wavefunction, the transformed $\chi(k)$ seems to have similar characteristics. However, a closer inspection of the tail region of these functions (see the inset of the figure) shows the existence of several nodes. We will see later that these discrepancies have significant consequences in the cross sections for most of the collisional processes examined.

Finally, the pseudopotential approach not only affects the representation of the bound orbitals but also determines the form of the continuum wavefunctions. For large *r*, the free state orbitals of an electron in the presence of a Coulomb potential can be written as

$$u_{kl}(r) \rightarrow \sin\left(kr - l\frac{\pi}{2} - \eta \ln 2kr + \sigma_l + \delta_l\right), \tag{7}$$

where k is the particle wave number, η is Sommerfeld's parameter, σ_l is the Coulomb phase shift, and δ_l is the wave phase shift with respect to the Coulomb wave.

Comparisons between the DIM (solid line) and the pseudo (dashed) continuum *ks* wavefunctions for lithium are shown in Fig. 4, close to the origin (left) and asymptotically (right). The pseudo and DIM wavefunctions behave similarly away from the nucleus. The asymptotic phase shift Δ accounts for the differences between the potentials. As the energy of the free electron increases, Δ diminishes. However, the orbitals in the core region are different even with increasing energy; the first maximum of the DIM wavefunctions is consistently smaller than of the pseudo-orbitals, which is understood since the Coulomb-type attraction of the nuclei is stronger than the pseudopotential in that region.

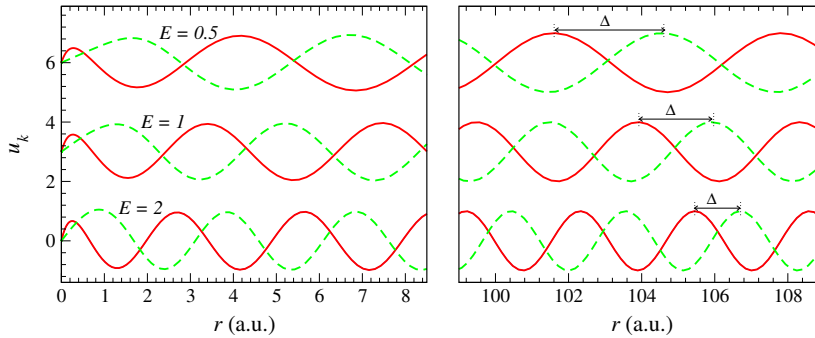

Fig. 4 Continuum *ks* wavefunctions with energies *E* near the origin (*left*) and in the asymptotic region (*right*), calculated with the DIM potential (*solid line*) and the ABINIT pseudopotential (*dashed line*).

2.2 Depurated inversion method potentials

The depurated inversion method[3–5] consists of assuming that the many-electron atom orbitals can be represented by the solution of Kohn–Sham-type equations, in which the *nl* effective potentials are given by

$$V_{nl}(r) = \frac{1}{2}\frac{1}{u_{nl}(r)}\frac{d^2u_{nl}(r)}{dr^2} - \frac{l(l+1)}{2r^2} + \varepsilon_{nl}, \tag{8}$$

where u_{nl} and ε_{nl} are the *nl* orbital wavefunctions and energies, respectively. In this work, the atomic structure is approximated with the Hartree–Fock method, which is computed with the HF codes by C. Froese Fischer[19] and the NRHF code by Johnson.[20] The computation of Eq. (8) poses various numerical problems. The nodes and asymptotic decay of the wavefunctions $u_{nl}(r)$ introduce significant numerical errors in the inversion procedure (see Ref. 5 for further details). The nodes of the orbitals produce huge unphysical poles, while the rapid asymptotic decay of the internal wavefunctions generates large divergences in the tail region of the potentials. The depuration method is implemented to tackle these unphysical features. An effective potential with a Coulomb-type shape $V_r(r) = -Z_r(r)/r$ is defined, and we enforce the correct boundary conditions fitting the inverted potential with the following analytical expression

$$Z_r(r) = \sum_{j=1}^{n} z_j e^{-\alpha_j r}(1+\beta_j r) + 1 \rightarrow \begin{cases} Z_N, & r \rightarrow 0 \\ 1, & r \rightarrow \infty \end{cases} \tag{9}$$

where $\sum z_j = Z_N - 1$ (Z_N here stands for the nuclear charge). The parameters α_j and β_j are optimized to reproduce the HF values accurately.

3. Collisional processes in atoms

The most significant advantage of the pseudopotential method is its simplicity. However, it is worth determining the validity of this approach when used for computing collisional processes. In this section, we perform a thorough examination of the pseudopotentials for hydrogen and lithium by comparing the cross sections of four inelastic processes: proton-impact excitation, proton-impact ionization, charge exchange, and photoionization. The initial and final states of the targets are obtained by solving the corresponding Schrödinger equation. For the hydrogen atom, we compare the pseudopotential results with the exact analytical solutions. Furthermore, in order to assess the applicability of the depurated inversion method, we compute the photoionization of more complex many-electron atoms and compare our findings with experimental data.

3.1 Proton-impact excitation

The proton-impact excitation of target X is defined as

$$\mathrm{H}^+ + X \rightarrow \mathrm{H}^+ + X^*. \tag{10}$$

The excitation cross section σ of the target from the initial bound state ψ_i to the excited state ψ_f may be written as

$$\sigma = \frac{\mu^2}{4\pi^2}\frac{k_f}{k_i}\int \left|T_{fi}\right|^2 d\Omega, \tag{11}$$

where μ is the reduced mass of the proton–atom system, $\mathbf{k}_i$ and $\mathbf{k}_f$ are the initial and final relative momenta, and

$$T_{fi} = \langle \psi_f | V | \psi_i \rangle \tag{12}$$

is the transition-matrix or T-matrix. If the initial and final states of the transition are described by the Hartree–Fock method, the orbitals will give the correct high energy limit in the first-order approximation (this is not the case for the charge exchange process). Hence, we will concentrate our computing efforts in the first perturbative order of the transition-matrix element through the FBA, given by

$$T_{fi}^{\mathrm{FBA}} = \tilde{V}(\mathbf{p}) F_{fi}(\mathbf{p}). \tag{13}$$

The term $F_{fi}(\mathbf{p})$ is the form factor

$$F_{fi}(\mathbf{p}) = \frac{1}{(2\pi)^{3/2}} \int \tilde{\psi}_f^*(\mathbf{k}) \tilde{\psi}_i(\mathbf{k}+\mathbf{p})\, d\mathbf{k}, \tag{14}$$

where $\mathbf{p}$ is the momentum transfer vector

$$\mathbf{p} = p_{\min}\hat{\mathbf{v}} + \boldsymbol{\eta}, \tag{15}$$

$$p_{\min} = \frac{\varepsilon_f - \varepsilon_i}{v} \rightarrow \begin{cases} \infty, & v \rightarrow 0 \\ 0, & v \rightarrow \infty \end{cases}, \tag{16}$$

$\hat{\mathbf{v}}$ is the ion velocity, $\boldsymbol{\eta}$ is the transversal momentum transfer, so that $\hat{\mathbf{v}} \cdot \boldsymbol{\eta} = 0$, whereas ε_i and ε_f are the binding energies corresponding to the initial and final states. A more comprehensive formulation of the FBA can be found, for instance, in Ref. 21.

The first Born proton-impact excitation cross sections of hydrogen and lithium from the ground states are shown in Fig. 5. The pseudopotential results for the $f_1 = 2s$, $2p$ and $f_2 = 3s$, $3p$, $3d$ final states of hydrogen agree excellently with the analytical expression. For lithium, the pseudopotential cross sections agree in a broad velocity range with the DIM calculations, except for low proton-impact velocities. This disagreement arises from the form factor. For low impact velocities, the momentum transfer vector is large (16). As discussed earlier, in this region the bound momentum orbital $\tilde{\psi}(\mathbf{k}+\mathbf{p})$ is not described adequately by the pseudopotentials. An alternative expression for the form factor can be considered by implementing the peaking approximation

$$F_{fi}(\mathbf{p}) \sim \tilde{\psi}_i(\mathbf{p})\tilde{\psi}_f^*(0) + \tilde{\psi}_f(\mathbf{p})\tilde{\psi}_i^*(0). \tag{17}$$

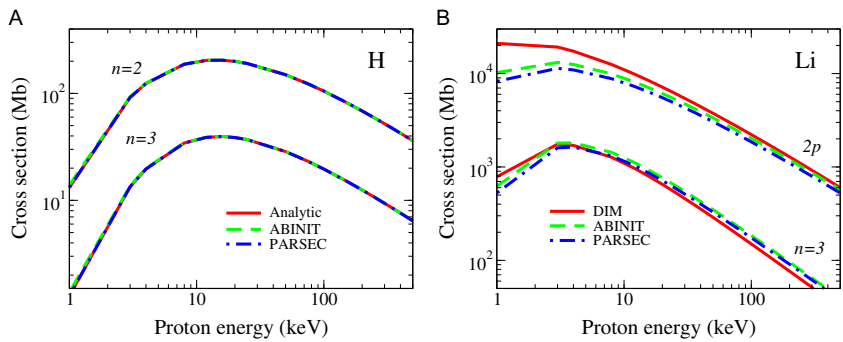

Fig. 5 Proton-impact excitation cross section from the ground state for (A) hydrogen and (B) lithium.

Therefore, in order to have the correct form factor, it is necessary to obtain an accurate description of the initial bound state at large momentum values, which is not the case for the pseudostates (see Fig. 3B) and hence their failure when used in the cross section calculation.

3.2 Proton-impact ionization

The transition matrix (12) for the proton-impact ionization of X,

$$\mathrm{H}^+ + X \rightarrow \mathrm{H}^+ + X^+ + e^-, \tag{18}$$

can also be written in terms of the first-order Born approximation. In this case, the final state ψ_f in Eq. (14) is an outgoing continuum wavefunction $\psi^-_{\mathbf{k}_f}$, while $\varepsilon_f = k_f^2/2$ is the energy of the ionized electron.

The single-differential proton-impact ionization cross sections $d\sigma/d\varepsilon_f$ of hydrogen and lithium at a proton velocity of $v_p = 1$ a.u. are shown in Fig. 6. In the case of hydrogen, the pseudopotential and analytical results agree for all the electron energy range, except at very high values. On the other hand, for lithium, the cross sections computed with pseudopotentials only agree at low energies. Once again, assuming that $\psi^-_{\mathbf{k}_f}(\mathbf{k})$ can be approximated by a plane wave, the form factor is reduced to the Fourier transform of the initial bound state

$$F_{fi}(\mathbf{p}) \sim \tilde{\psi}_i(\mathbf{p} - \mathbf{k}_f). \tag{19}$$

Then, as k_f increases, so does $p_{\min}$, and the form factor is not well represented by the pseudopotentials. The significant discrepancies shown in Fig. 6 provide another demonstration of how a wrong description of the momentum space wavefunction may produce huge errors in collisional processes calculations.

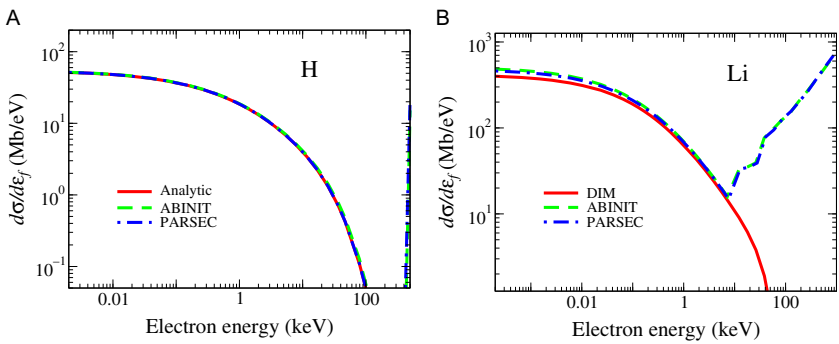

Fig. 6 Single differential proton-impact ionization cross section from the ground state of (A) hydrogen and (B) lithium at $v_p = 1$ a.u.

3.3 Proton-impact charge exchange

The proton-impact charge exchange of target X is defined as

$$\mathrm{H}^+ + X \rightarrow \mathrm{H} + X^+. \tag{20}$$

The charge transfer cross section by the collision of a proton (electron capture) is computed with the first-order Brinkman–Kramers approximation.[22] Accordingly, the matrix element is defined by

$$T_{fi}^{\mathrm{BK}} = \tilde{\psi}_f^*(\mathbf{W}_f)\left[\varepsilon_f - \frac{W_f^2}{2}\right]\tilde{\psi}_i(\mathbf{W}_i), \tag{21}$$

where $\mathbf{W}_i$ and $\mathbf{W}_f$ are the momentum transfer vectors

$$\mathbf{W}_i = W_{i0}\hat{\mathbf{v}} + \boldsymbol{\eta}, \quad W_{i0} = \frac{\nu}{2} - p_{\min} \tag{22}$$

$$\mathbf{W}_f = W_{f0}\hat{\mathbf{v}} + \boldsymbol{\eta}, \quad W_{f0} = \frac{\nu}{2} + p_{\min}, \tag{23}$$

and they satisfy the condition $\mathbf{W}_i + \mathbf{W}_f = \mathbf{v}$, and $p_{\min}$ is defined in Eq. (16).

The charge exchange cross sections of hydrogen and lithium in the ground state are illustrated in Fig. 7. The cross section of hydrogen is described with high accuracy by the pseudopotential approach for a wide range of proton velocities. However, this process constitutes a symmetrical resonance, i.e., $\varepsilon_f = \varepsilon_i$, and the agreement may be misleading. For the lithium case, the pseudopotentials fail utterly to describe the electron capture correctly at low and high velocities. For low and high v_p values, the momentum transfer vector becomes large, and therefore, the cross sections calculated with pseudopotentials disagree completely for most of the energy values.

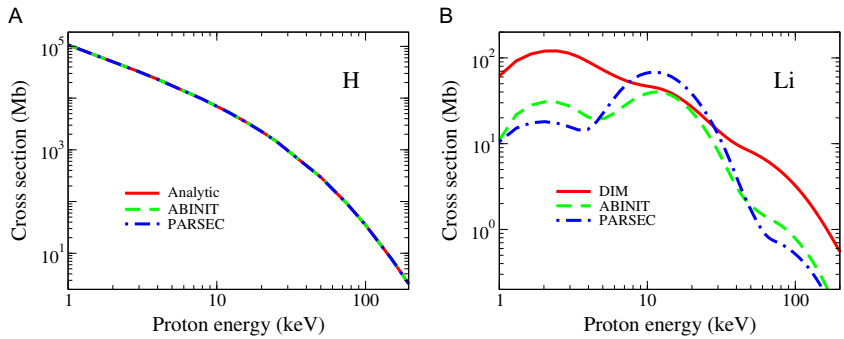

Fig. 7 Proton-impact electron capture cross section for (A) hydrogen and (B) lithium in the ground state.

3.4 Photoionization

The single photoionization is defined as

$$\hbar\omega + X \rightarrow X^+ + e. \tag{24}$$

Considering a perturbative photon field, the initial bound ψ_i and final continuum $\psi^-_{\mathbf{k}_f}$ states of the target are not significantly distorted; therefore, the relevant matrix element of the photoionization process is given by

$$T^{\mathrm{Ph}}_{\mathbf{k}} = \int \psi^-_{\mathbf{k}_f}(\mathbf{r})[-i\hat{\varepsilon}_\lambda \cdot \nabla_{\mathbf{r}}]\psi_i(\mathbf{r}), \tag{25}$$

where $\hat{\varepsilon}_\lambda$ is the polarization versor and $\mathbf{k}_f = \sqrt{2(\omega + \varepsilon_i)}$, as imposed by energy conservation.

The first-order photoionization cross sections of hydrogen and lithium are shown in Fig. 8. The pseudopotentials results for the hydrogen atom agree with the exact analytical expression results only for low photon energies, failing at larger values. These discrepancies can be understood considering the continuum wavefunction $\psi^-_{\mathbf{k}_f}(\mathbf{r})$ as a plane wave. Consequently, the matrix element $T^{\mathrm{Ph}}_{\mathbf{k}}$ is reduced to

$$T^{\mathrm{Ph}}_{\mathbf{k}} \sim -\left(\hat{\varepsilon}_\lambda \cdot \mathbf{k}_f\right)\tilde{\psi_i}\left(\mathbf{k}_f\right), \tag{26}$$

and it is determined entirely by the behavior of the bound target pseudostate in the momentum representation. For hydrogen, the pseudo-orbital from PARSEC in the Fourier space coincides with the exact analytical solution for the entire range of k, which explains the excellent agreement in the cross section results. For lithium, the pseudopotential cross sections disagree with

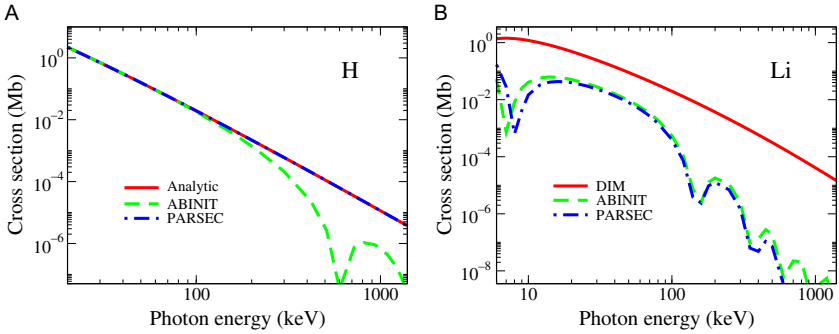

Fig. 8 Single photoionization cross section for (A) hydrogen and (B) lithium.

the DIM results for all energy values. The large oscillations in the cross sections are originated by the spurious oscillatory structure of the bound state for large k values (see inset of Fig. 3B).

3.5 DIM Photoionization of many-electron atoms

In order to assess the applicability of the depurated inversion method for atoms with a more complex structure, we compute the photoionization of many-electron targets with the DIM potentials[4] and compare our results with experimental values. The first-order photoionization cross section of nitrogen and neon are shown in Fig. 9. Experimental data from[23–26] is illustrated with hollow symbols. The DIM photoionization cross sections of these atoms agree excellently with the experimental values for low, medium and high photon energies. For neon, discrepancies start to be noticeable for low and intermediate energy. An accurate photoionization description of heavier atoms requires the inclusion of many-body effects that can be relevant, such as orbital relaxation due to the creation of a hole, collective response of inner shell electrons[27] and correlation effects.

4. Depurated inversion method for molecules

The depurated inversion method described above is extended here to determine effective potentials for molecules; methane is taken as an example. Furthermore, the molecular description of CH_4 given by DIM is tested by computing two collisional processes within the FBA.

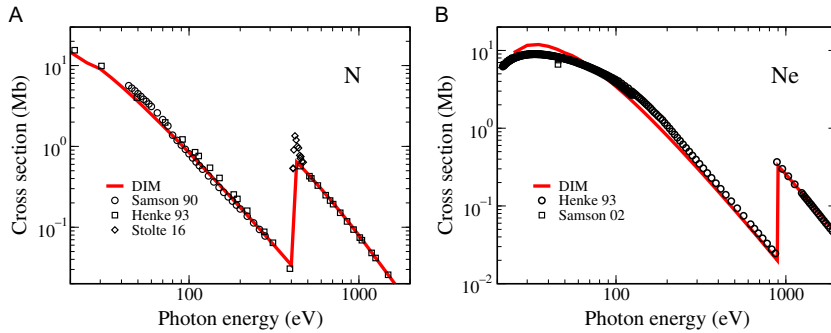

Fig. 9 Single photoionization cross section for (A) nitrogen and (B) neon.

4.1 Theory

Without loss of generality, we will present the DIM theoretical grounds for hydride compounds. The Hamiltonian of an N-electron $X\,H_n$ molecule within the Born–Oppenheimer approximation is given by

$$\mathcal{H} = -\sum_{i=1}^{N}\frac{1}{2}\nabla^2_{\mathbf{r}_i} - \sum_{i=1}^{N}\frac{Z_N}{r_i} + \sum_{i=1}^{N}V_H(r_i) + \sum_{i<j}^{N}\frac{1}{r_{ij}}, \tag{27}$$

$$V_H(r_i) = -\sum_{j=1}^{n}\frac{1}{\left|\mathbf{r}_i - \mathbf{R}_{H_j}\right|}, \tag{28}$$

where Z_N is the nuclear charge of the heavier atom, and $\mathbf{R}_{H_j}$ are the coordinates of the hydrogens respect to the X atom. The corresponding Schrödinger equation $\mathcal{H}\Psi = E\Psi$ is solved and the orbitals are expressed as in Eq. (5) considering the single-center expansion (SCE). The orbitals and energies are found by solving the Hartree–Fock equations. The computation of these equations generally relies on the use of finite basis sets for the representation of the molecular orbitals (MOs). Usually, the MOs are expressed as a linear combination of atomic orbitals (LCAO),

$$\Psi_i = \sum_j c_{ji}\phi_j, \tag{29}$$

which can be constructed with Gaussian-type orbitals (GTO) basis sets.

The inverted molecular potential expression, analogous to Eq. (8), obtained from GTO basis sets present more difficulties than the atomic case. In addition to the asymptotic divergences and the poles, large unphysical oscillations arise.[28–31] These prominent oscillations originate from undulations present in the MOs due to the finite number of the basis set. The second derivative, necessary to evaluate the inversion formula, amplifies these features.[28,31] In some cases, the oscillations are huge, e.g., near an electronegative atom like Cl. The appearance of these oscillations in the inverted potentials forces us to incorporate further actions in the depuration scheme. To illustrate this procedure, we consider the 1*s* orbital of the carbon atom. We solved the Hartree–Fock equations using the 6-311G basis set with GAMESS code[32,33] and obtained inverted potentials by implementing Eq. (8). The resulting Z_{1s}^{6-311G} charge is shown in Fig. 10A with a dot-dashed line. The charge oscillates significantly at low distances and diverges for higher r values. The same calculation was repeated using the universal Gaussian basis set (UGBS), which has a more significant amount of primitives. The corresponding inverted charge Z_{1s}^{UGBS} is exhibited in the figure

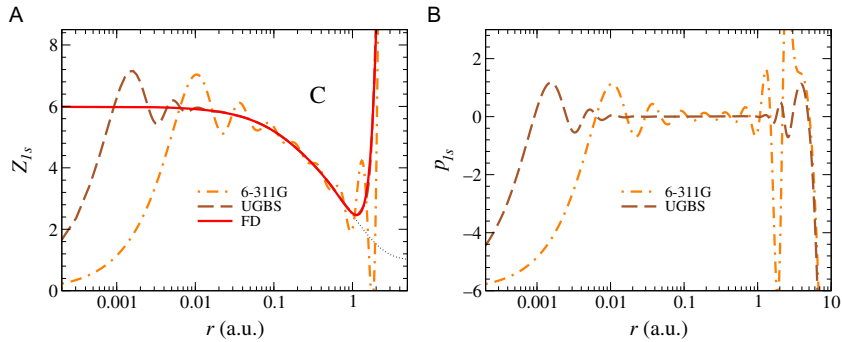

Fig. 10 (A) Effective charges for the 1*s* orbital of carbon. (B) Basis-set oscillation profiles.

with a dashed line. Although the charge still diverges around $r \approx 1$a.u., the oscillations are now circumscribed near the nucleus. Finally, the differential Hartree–Fock equations for the carbon atom were solved using the finite-differences (FD) method. The 1*s* inverted charge obtained with this procedure, Z_{nl}^{FD} (solid line) shows no oscillations since no basis sets have been used to construct the orbital; however, the charge still diverges for $r > 1$a.u., as it usually does for all HF calculations.

The oscillations pattern will vary for each basis set used in the calculations. We may define oscillation profiles as

$$p_{nl}^{\mathrm{BS}} = Z_{nl}^{\mathrm{BS}} - Z_{nl}^{\mathrm{FD}}, \tag{30}$$

where Z_{nl}^{BS} is the inverted charge of the atom using a particular basis set "BS" and Z_{nl}^{FD} is the effective charge obtained from the inversion of the finite-difference wavefunctions. In the previous example, the basis set considered for calculating the 1*s* orbital of carbon were 6-311G and UGBS. The oscillation profiles for the 1*s* orbital, using Eq. (30) for these basis sets, are shown in Fig. 10B. Since the orbital profiles for each atomic basis set are distinctive, once they are determined for the atomic case, they can be removed in further molecular calculations. An example of this procedure is given in the following section.

4.2 Example: Methane

In order to illustrate the implementation of the DIM for molecules, we considered CH_4, which is highly symmetric, and therefore, can be described with an angular averaged potential.[34] We computed the HF molecular orbitals and energies of CH_4 employing the UGBS basis sets of carbon and hydrogen, which considers angular momenta up to $L = 1$. Methane calculations with this basis set should include polarization functions

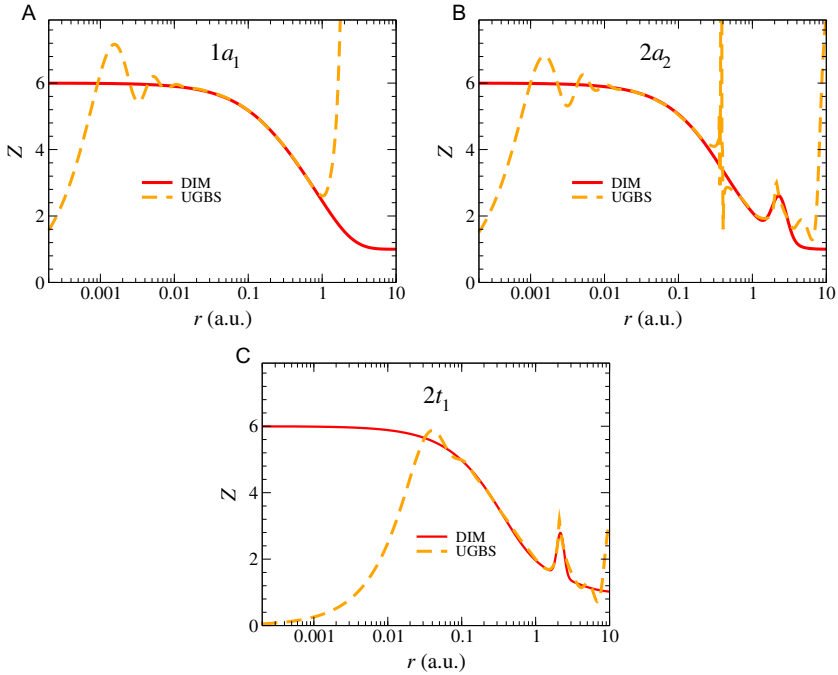

Fig. 11 (A) $1a_1$, (B) $2a_2$, and (C) $2t_1$ effective charges of CH_4; direct inversion (*dashed line*) and depurated inverted (*solid line*).

(at least d-functions) to increase the accuracy of the molecular energies.[35,36] However, to isolate the effects of the basis set, we computed the atomic oscillation profiles and the molecular orbitals on the same footing. The charges obtained by direct inversion are given in Fig. 11 with dashed lines. Since the molecular orbitals are given by LCAO of carbon and hydrogen, the oscillations of the inverted charges are a consequence of the finite basis set of these atoms. To remove the most critical oscillations, first, we must determine the oscillation profiles produced by the atomic carbon basis set. We use Eq. (30) to determine the p_{1s}^{UGBS}, p_{2s}^{UGBS}, and p_{2p}^{UGBS} profiles of carbon. Then, we remove the oscillations by subtracting the carbon p_{nl}^{UGBS} profiles from the corresponding inverted charges Z_i^{UGBS} of CH_4. The oscillations are removed for all orbitals except for the $2a_2$, which presents small oscillatory residues from the hydrogen basis set. Since the residual fluctuations are minimum and near the nucleus, we proceeded to implement the depuration scheme as described in Section 2.2. We define a new parametric DIM charge equation,

$$Z(r) = \sum_j Z_j e^{-\alpha_j r} + Z_{\mathrm{H}} e^{-(\ln r - \ln \beta)^2/(2\gamma)} + 1. \tag{31}$$

Table 1 Energies and fitting parameters for the DIM effective charges (Eq. (31)), for CH_4.

nl	E	Z	α	β	γ
$1a_1$	−11.1949	1.925280	0.641982		
		0.953120	5.571510		
		2.121600	1.500440		
$2a_2$	−0.9204	2.912200	3.149990		
		2.087800	0.771371		
		1.23640		2.329570	0.053420
$2t_1$	−0.5042	0.901953	2.895140		
		1.112030	0.388649		
		2.986017	2.931210		
		1.30182		2.169850	0.012616

In contrast to the approximation proposed for atoms (9), a second term has been added to the formula to account for the presence of the hydrogens. This expression allows us to conveniently adjust both the location and width of the screened hydrogenic potential without affecting the correct charge value at the origin. The optimized parameters for the methane molecule are given in Table 1, and the corresponding DIM charges are shown in Fig. 11, with solid lines. The orbital energies obtained with these charges are also given in the table.

4.3 Collisional processes

The orientation of the molecular targets is important for determining the cross sections of collisional processes. However, it is generally not preestablished in the experiments. Thus, the spherically averaged description of the system assumed by the DIM potential makes sense. In the following, we examine two collisional processes in the first-order approximation: proton-impact ionization and single photoionization.

Proton-impact ionization

Results for the proton-impact ionization cross section for CH_4, calculated under the first Born approximation, are given in Fig. 12. The initial bound and the final continuum states of the molecule needed for the T-matrix computation (Eq. (12)) were calculated with the DIM potentials from

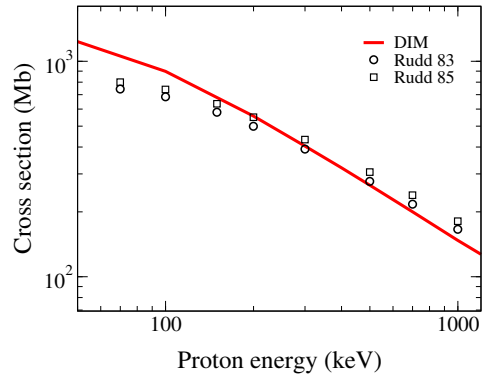

Fig. 12 Proton-impact ionization cross section for CH_4. *Solid line*: first-order DIM theoretical calculations. *Symbols*: experiments from Refs. 37 and 38.

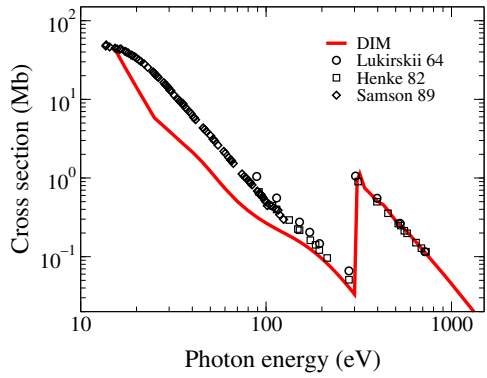

Fig. 13 Single photoionization cross section of CH_4. *Solid line*: first-order DIM theoretical calculations. *Symbols*: experiments from Refs. 39–41.

Section 4.2. The ionization cross section for high and intermediate energies shows good agreement with the experimental results. The failure at low energies is ascribed to the validity of the first Born approximation and not to our DIM approach.

Photoionization

The photoionization cross section for CH_4, calculated with the DIM potentials in a first-order approximation, is shown in Fig. 13 (solid lines). Good agreement with the experimental results (symbols) is found for high energy values and at the threshold. The curve between ∼15 and ∼300 eV shows the photoionization from the outer $n = 2$ shell, while the discontinuity

at 300 eV corresponds to the threshold of the $1a_1$ inner shell orbital. For low and intermediate photon energies, the agreement between our calculations and the experimental values from Refs. 39–41 is not that good. Phenomena such as molecular orbital relaxation, possible collective contributions, and correlation effects must be considered in further calculations. On the other hand, for the $1a_1$ inner shell photoionization, these effects are not significant, and we obtain a perfect agreement with the experimental results.

5. Concluding remarks

In this work, we explored the possibility of using pseudopotentials within the single electron model to calculate inelastic transitions. The first Born approximation was used to calculate proton-impact excitation, ionization, electron capture, and photoionization. Two simple atoms were studied, having a single electron in the outer shell. For hydrogen, we found excellent agreement for all the collisional processes, for low and intermediate energies. In the case of lithium, the only process that can be calculated with reasonable accuracy is the proton-impact excitation. We concluded that the range of validity is restrained to minimal momentum transfers. The depurated inversion method, on the other hand, accurately reproduces photoionization experimental results for many-electron atoms.

We extended the DIM for molecular systems. In this case, the inversion procedure produces huge oscillations due to the finite size of the basis sets involved in the Hartree–Fock orbital calculations. An additional step is included during the depuration scheme. In order to determine the oscillation profile for a particular basis set, we computed the inverted atomic charges in a finite-differences framework. By subtracting the charges, it is possible to isolate the oscillations corresponding to this particular basis set. We used the DIM method to determine the effective potentials for CH_4. These potentials are implemented in first-order proton-impact ionization and photoionization cross sections calculations. For both processes, we found good agreement with the experimental results. The main discrepancies can be attributed to the fact that only first-order is considered in the perturbation theory.

Acknowledgments

The authors thank the Consejo Nacional de Investigaciones Científicas y Técnicas (CONICET), Universidad de Buenos Aires (UBA) and Agencia Nacional de Promoción Científica y Tecnológica (ANPCyT) for the grants that supported this work.

References

1. PARSEC Home Page. https://parsec.ices.utexas.edu/styled-2/ (Accessed Jan 18, 2019).
2. Chelikowsky, J. R.; Troullier, N.; Saad, Y. Finite-Difference-Pseudopotential Method: Electronic Structure Calculations Without a Basis. *Phys. Rev. Lett.* **1994**, *72*(8), 1240–1243. https://doi.org/10.1103/PhysRevLett.72.1240.
3. Mendez, A. M. P. *Método de Inversión Depurada para Potenciales Locales en Átomos y Moléculas*. 2015. Tesis de Licenciatura, Universidad Nacional de Salta.
4. Mendez, A. M. P.; Mitnik, D. M.; Miraglia, J. E. Depurated Inversion Method for Orbital-Specific Exchange Potentials. *Int. J. Quantum Chem.* **2016**, *116*(24), 1882–1890. https://doi.org/10.1002/qua.25295.
5. Mendez, A. M. P.; Mitnik, D. M.; Miraglia, J. E. Local Effective Hartree-Fock Potentials Obtained by the Depurated Inversion Method. In *Nov. Electron. Struct. Theory Gen. Innov. Strongly Correl. Syst.*; Hoggan, P. E. Ed.; Advances in Quantum Chemistry.; Vol. 76, Academic Press, 2018; pp 117–132. https://doi.org/10.1016/bs.aiq.2017.07.004.
6. Bates, D. R. Theoretical Treatment of Collisions Between Atomic Systems. *Pure Appl. Phys. Elsevier* **1962**, *13*, 549–621. In At. Mol. Process.; Bates, D. R. Ed.
7. McDowell, M. R. C.; Peach, G. Ionization of Lithium by Fast Protons and Electrons. *Phys. Rev.* **1961**, *121*, 1383–1387.
8. Pindzola, M. S.; Robicheaux, F.; Loch, S. D.; Berengut, J. C.; Topcu, T.; Colgan, J.; Foster, M.; Griffin, D. C.; Ballance, C. P.; Schultz, D. R.; Minami, T.; Badnell, N. R.; Witthoeft, M. C.; Plante, D. R.; Mitnik, D. M.; Ludlow, J. A.; Kleiman, U. The Time-Dependent Close-Coupling Method for Atomic and Molecular Collision Processes. *J. Phys. B* **2007**, *40*, R39–R60.
9. Burke, P. G. *R-Matrix Theory of Atomic Collisions*; Springer-Verlag: Berlin, Heidelberg, 2011.
10. Bray, I.; Abdurakhmanov, I. B.; Bailey, J. J.; Bray, A. W.; Fursa, D. V.; Kadyrov, A. S.; Rawlins, C. M.; Savage, J. S.; Stelbovics, A. T.; Zammit, M. C. Convergent Close-Coupling Approach to Light and Heavy Projectile Scattering on Atomic and Molecular Hydrogen. *J. Phy. B* **2017**, *50*, 202001.
11. Pindzola, M. S.; Colgan, J.; Robicheaux, F.; Lee, T. G.; Ciappina, M. F.; Foster, M.; Ludlow, J. A.; Abdel-Naby, S. A. Time-Dependent Close-Coupling Calculations for Ion-Impact Ionization of Atoms and Molecules. *Adv. At. Mol. Opt. Phys.* **2016**, *65*, 291–319.
12. Kirchner, T.; Gulyás, L.; Lüdde, H. J.; Engel, E.; Dreizler, R. M. Influence of Electronic Exchange on Single and Multiple Processes in Collisions Between Bare Ions and Noble-Gas Atoms. *Phys. Rev. A* **1998**, *58*, 2063–2076.
13. Fiori, M. R.; Jalbert, G.; Bielschowsky, C. E.; Cravero, W. Ionization of Lithium by Impact of Fast Ions. *Phys. Rev. A* **2001**, *64*, 012705.
14. Szabo, A.; Ostlund, N. S. *Modern Quantum Chemistry: Introduction to Advanced Electronic Structure Theory*; Dover Publications, Inc.: Mineola, NY, 1996.
15. Helgaker, T.; JØRgensen, P.; Olsen, J. *Molecular Electronic-Structure Theory*. John Wiley & Sons, Ltd: Chichester, UK, 2000.
16. Schaefer, H. F. *Quantum Chemistry: The Development of Ab Initio Methods in Molecular Electronic Structure Theory*; Dover Publications, Inc: Mineola, NY, 2004.
17. ABINIT Home Page. https://www.abinit.org/psp-tables (Accessed Jan 18, 2019).
18. Hamann, D. R.; Schlüter, M.; Chiang, C. Norm-Conserving Pseudopotentials. *Phys. Rev. Lett.* **1979**, *43*(20), 1494–1497. https://doi.org/10.1103/PhysRevLett.43.1494.
19. Froese Fischer, C.; Brage, T.; Jönsson, P. *Computational Atomic Structure: An MCHF Approach*. Institute of Physics Publishing: Bristol, UK, 1997;p 279.
20. Johnson, W. R. *Atomic Structure Theory : Lectures on Atomic Physics*. Springer: Berlin, Heidelberg, 2007;p 312.

21. McDowell, M. R. C.; Coleman, J. P. *Introduction to the Theory of Ion-Atom Collisions*; North-Holland Publishing Company: Amsterdam, 1970.
22. *C, B. H.*. Kramers, H. A. *Physics.-Zur Theorie der Einfangung von Elektronen durch u.˜Teilchen. Proc. K. Akad. van Wet.* **1930**, *33*, 973–984. http://www.dwc.knaw.nl/DL/publications/PU00015982.pdf.
23. Henke, B. L.; Gullikson, E. M.; Davis, J. C. X-Ray Interactions: Photoabsorption, Scattering, Transmission, and Reflection at E = 50-30,000 eV, Z = 1-92. *At. Data Nucl. Data Tables* **1993**, *54*(2), 181–342. https://doi.org/10.1006/ADND.1993.1013.
24. Samson, J. A. R.; Angel, G. C. *Single- and double-photoionization cross sections of atomic nitrogen from threshold to 31 Å. Phys. Rev. A* **1990**, *42*(3), 1307–1312. https://doi.org/10.1103/PhysRevA.42.1307. https://link.aps.org/doi/10.1103/PhysRevA.42.1307.
25. Samson, J. A. R.; Stolte, W. C. Precision Measurements of the Total Photoionization Cross-Sections of He, Ne, Ar, Kr, and Xe. *J. Electron Spectros. Relat. Phenomena* **2002**, *123*(2–3), 265–276. https://doi.org/10.1016/S0368-2048(02)00026-9.
26. Stolte, W. C.; Jonauskas, V.; Lindle, D. W.; Sant'Anna, M. M.; Savin, D. W. *Inner-Shell Photoionization Studies of Neutral Atomic Nitrogen. Astrophys. J.* **2016**, *818*(2), 149. https://doi.org/10.3847/0004-637X/818/2/149. http://stacks.iop.org/0004-637X/818/i=2/a=149?key=crossref.2b86a13e417a21fe226f2d7fdc09b8c8.
27. Ederer, D. L. Photoionization of the 4d Electrons in Xenon. *Phys. Rev. Lett.* **1964**, *13*(25), 760–762. https://doi.org/10.1103/PhysRevLett.13.760.
28. Schipper, P. R. T.; Gritsenko, O. V.; Baerends, E. J. Kohn-Sham potentials corresponding to Slater and Gaussian basis set densities. *Theor. Chem. Accounts Theory, Comput. Model. (Theoretica Chim. Acta)* **1997**, *98*(1), 16–24. https://doi.org/10.1007/s002140050273.
29. Mura, M. E.; Knowles, P. J.; Reynolds, C. A. Accurate Numerical Determination of Kohn-Sham Potentials From Electronic Densities: I. Two-Electron Systems. *J. Chem. Phys.* **1997**, *106*(23), 9659–9667. https://doi.org/10.1063/1.473838.
30. Jacob, C. R. Unambiguous Optimization of Effective Potentials in Finite Basis Sets. *J. Chem. Phys.* **2011**, *135*(24), 244102. https://doi.org/10.1063/1.3670414.
31. Gaiduk, A. P.; Ryabinkin, I. G.; Staroverov, V. N. *Removal of Basis-Set Artifacts in KohnSham Potentials Recovered From Electron Densities. J. Chem. Theory Comput.* **2013**, *9*(9), 3959–3964. https://doi.org/10.1021/ct4004146. http://www.ncbi.nlm.nih.gov/pubmed/26592391.
32. Schmidt, M. W.; Baldridge, K. K.; Boatz, J. A.; Elbert, S. T.; Gordon, M. S.; Jensen, J. H.; Koseki, S.; Matsunaga, N.; Nguyen, K. A.; Su, S.; Windus, T. L.; Dupuis, M.; Montgomery, J. A. General Atomic and Molecular Electronic Structure System. *J. Comput. Chem.* **1993**, *14*(11), 1347–1363. https://doi.org/10.1002/jcc.540141112.
33. Gordon, M. S.; Schmidt, M. W. Advances in Electronic Structure Theory: GAMESS a Decade Later. In *Theory Appl. Comput. Chem.*; Dykstra, C. E., Frenking, G., Kim, K. S., Scuseria, G. E., Eds.; Elsevier: Amsterdam, 2005; pp 1167–1189. chap. 41. https://doi.org/10.1016/B978-044451719-7/50084-6.
34. Granados-Castro, C. M. Application of Generalized Sturmian Basis Functions to Molecular Systems. Ph.D. thesis, Université de Lorraine, Metz, France and Universidad Nacional del Sur, Bahía Blanca, Argentina 2016.
35. Rothenberg, S.; Schaefer, H. F. Methane as a Numerical Experiment for Polarization Basis Function Selection. *J. Chem. Phys.* **1971**, *54*, 2764–2766.
36. Hariharan, P. C.; Pople, J. A. The Effect of D-Functions on Molecular Orbital Energies for Hydrocarbons. *Chem. Phys. Lett.* **1972**, *16*, 217–219.

37. Rudd, M. E.; DuBois, R. D.; Toburen, L. H.; Ratcliffe, C. A.; Goffe, T. V. Cross Sections for Ionization of Gases by 5-4000-keV Protons and for Electron Capture by 5-150-keV Protons. *Phys. Rev. A* **1983**, *28*(6), 3244–3257. https://doi.org/10.1103/PhysRevA.28.3244.
38. Rudd, M. E.; Kim, Y. K.; Madison, D. H.; Gallagher, J. W. Electron Production in Proton Collisions: Total Cross Sections. *Rev. Mod. Phys.* **1985**, *57*(4), 965–994. https://doi.org/10.1103/RevModPhys.57.965.
39. Lukirskii, A. P.; Brytov, I. A.; Zimkina, T. M. *Optika I Spektr.* Vol. 17, 1964234. www.scopus.com.
40. Henke, B. L.; Lee, P.; Tanaka, T. J.; Shimabukuro, R. L.; Fujikawa, B. K. Low-energy X-ray Interaction Coefficients: Photoabsorption, Scattering, and Reflection: E = 1002000 eV Z = 194. *At. Data Nucl. Data Tables* **1982**, *27*(1), 1–144. https://doi.org/10.1016/0092-640X(82)90002-X.
41. Samson, J. A. R.; Haddad, G. N.; Masuoka, T.; Pareek, P. N.; Kilcoyne, D. A. L. Ionization Yields, Total Absorption, and Dissociative Photoionization Cross Sections of CH4 from 110 to 950 Å. *J. Chem. Phys.* **1989**, *90*(12), 6925–6932. https://doi.org/10.1063/1.456267.

CHAPTER NINE

Unified construction of Fermi, Pauli and exchange-correlation potentials

Viktor N. Staroverov*, Egor Ospadov
Department of Chemistry, The University of Western Ontario, London, Ontario, Canada
*Corresponding author: e-mail address: vstarove@uwo.ca

Contents

Abstract

The exchange-correlation potential of the Kohn–Sham density-functional scheme is the difference between the Fermi potential—an effective potential appearing in the one-electron Schrödinger equation for the square root of the electron density—and the Pauli potential, i.e., $v_{XC}(\mathbf{r}) = v_F(\mathbf{r}) - v_P(\mathbf{r})$. We show that, for a given external potential and electron number, knowledge of $v_F(\mathbf{r})$ alone is sufficient to generate the corresponding $v_P(\mathbf{r})$ and $v_{XC}(\mathbf{r})$. The Fermi potential itself can be computed from the system's interacting two-electron reduced density matrix or modeled directly. The unified treatment of these three potentials provides a practical method for accessing accurate functional derivatives of the exchange-correlation, Pauli kinetic, and Levy–Perdew–Sahni energy functionals without having to tackle functional differentiation and numerical challenges of other construction techniques.

Advances in Quantum Chemistry, Volume 79
ISSN 0065-3276
https://doi.org/10.1016/bs.aiq.2019.04.002

1. Motivation

Density-functional theory (DFT) of electronic structure can be put into practice in different ways such as the Kohn–Sham scheme,[1–3] the generalized Kohn–Sham method,[4] the orbital-free DFT,[5–7] the Levy–Perdew–Sahni formalism[8], and other variants.[9] All of these techniques are based on the Hohenberg–Kohn theorems[10] and have the same general setup: the total electronic energy E is treated as a functional of the electron density $\rho(\mathbf{r})$; this functional, $E[\rho]$, is partitioned in some way; minimization of $E[\rho]$ leads to an Euler–Lagrange equation whose solution produces the ground-state density $\rho(\mathbf{r})$ and hence $E[\rho]$. The partitioning is arbitrary, provided that the parts add up to $E[\rho]$. Most of these terms are defined by conveniently chosen analytic expressions but there always remains at least one term which must be approximated. Here, we will focus on two variants of DFT, namely, the Kohn–Sham scheme[1, 2] and the Levy–Perdew–Sahni[8] formalism, and limit our discussion to singlet ground-state systems.

In the Kohn–Sham scheme, the total electronic energy functional is partitioned as

$$E[\rho] = T_s[\rho] + \int \rho(\mathbf{r}) v(\mathbf{r})\, d\mathbf{r} + E_{\mathrm{H}}[\rho] + E_{\mathrm{XC}}[\rho], \tag{1}$$

where $T_s[\rho]$ is the kinetic energy of a system of noninteracting electrons having the ground-state density $\rho(\mathbf{r})$, $E_{\mathrm{H}}[\rho]$ is the Hartree electrostatic self-repulsion energy of $\rho(\mathbf{r})$, and $E_{\mathrm{XC}}[\rho]$ is the unknown exchange-correlation energy functional. The corresponding Euler–Lagrange equation is[11]

$$\left[-\frac{1}{2}\nabla^2 + v(\mathbf{r}) + v_{\mathrm{H}}(\mathbf{r}) + v_{\mathrm{XC}}(\mathbf{r})\right]\phi_i(\mathbf{r}) = \epsilon_i \phi_i(\mathbf{r}), \tag{2}$$

where the eigenfunctions $\phi_i(\mathbf{r})$ are such that $\rho(\mathbf{r}) = \sum_i^{\mathrm{occ.}} |\phi_i(\mathbf{r})|^2$,

$$v_{\mathrm{H}}(\mathbf{r}) = \frac{\delta E_{\mathrm{H}}[\rho]}{\delta \rho(\mathbf{r})} = \int \frac{\rho(\mathbf{r}')}{|\mathbf{r} - \mathbf{r}'|}\, d\mathbf{r}' \tag{3}$$

is the Hartree potential, and

$$v_{\mathrm{XC}}(\mathbf{r}) = \frac{\delta E_{\mathrm{XC}}[\rho]}{\delta \rho(\mathbf{r})} \tag{4}$$

is the exchange-correlation potential.

In the Levy–Perdew–Sahni formalism, the total energy functional is partitioned as

$$E[\rho] = T_{\mathrm{W}}[\rho] + \int \rho(\mathbf{r}) v(\mathbf{r})\, d\mathbf{r} + E_{\mathrm{H}}[\rho] + G[\rho], \tag{5}$$

where

$$T_{\mathrm{W}}[\rho] = \int \frac{|\nabla \rho(\mathbf{r})|^2}{8\rho(\mathbf{r})}\, d\mathbf{r} \tag{6}$$

is the von Weizsäcker kinetic energy and $G[\rho]$ is an unknown functional. The Euler–Lagrange equation corresponding to Eq. (5) may be cast as[8]

$$\left[-\frac{1}{2}\nabla^2 + v(\mathbf{r}) + v_{\mathrm{H}}(\mathbf{r}) + v_{\mathrm{F}}(\mathbf{r})\right]\theta(\mathbf{r}) = \mu\theta(\mathbf{r}), \tag{7}$$

where $\theta(\mathbf{r}) = \sqrt{\rho(\mathbf{r})}$, μ is the chemical potential, and

$$v_{\mathrm{F}}(\mathbf{r}) = \frac{\delta G[\rho]}{\delta \rho(\mathbf{r})} \tag{8}$$

is the Fermi potential,[12] also referred to as the "effective potential for the boson problem."[13]

The unknown functionals of the Kohn–Sham and Levy–Perdew–Sahni schemes are related by the equation

$$G[\rho] = E_{\mathrm{XC}}[\rho] + T_s[\rho] - T_{\mathrm{W}}[\rho]. \tag{9}$$

The same relation stated in terms of functional derivatives reads

$$v_{\mathrm{F}}(\mathbf{r}) = v_{\mathrm{XC}}(\mathbf{r}) + v_{\mathrm{P}}(\mathbf{r}), \tag{10}$$

where

$$v_{\mathrm{P}}(\mathbf{r}) = \frac{\delta(T_s[\rho] - T_{\mathrm{W}}[\rho])}{\delta \rho(\mathbf{r})} \tag{11}$$

is the Pauli potential.[13–18] For one- and singlet two-electron systems, where $T_{\mathrm{W}}[\rho] = T_s[\rho]$ and $v_{\mathrm{P}}(\mathbf{r}) = 0$, the Kohn–Sham and Levy–Perdew–Sahni schemes are identical.

Much insight into the workings of various density-functional schemes can be obtained by analyzing the effective multiplicative potentials arising as functional derivatives of the unknown components of the total energy

functional. In the Kohn–Sham and Levy–Perdew–Sahni schemes, these are the exchange-correlation and Fermi potentials, $v_{XC}(\mathbf{r})$ and $v_F(\mathbf{r})$, defined by Eqs. (4) and (8). These potentials are themselves functionals of $\rho(\mathbf{r})$ and therefore they encode essentially the same information as the parent functionals $E_{XC}[\rho]$ and $G[\rho]$. The Pauli potential, $v_P(\mathbf{r})$, furnishes information about the shell structure of electron densities in many-electron atoms[19] and is closely tied with the functional derivative $\delta T_s[\rho]/\delta\rho(\mathbf{r})$,[20] which is of interest in orbital-free DFT.[5–7]

Since the exact functionals $E_{XC}[\rho]$ and $G[\rho]$ are generally unknown as explicit functionals of $\rho(\mathbf{r})$, their functional derivatives can be constructed only by indirect methods. The two most common techniques used for this purpose are the Kohn–Sham inversion procedure, in which the potentials (or related quantities) are fitted to ground-state electron densities via the Kohn–Sham equations (see, e.g., Refs. 21–25 and references therein), and the optimized effective potential (OEP) method,[26–31] where one solves an integral equation for $v_{XC}(\mathbf{r})$. Unfortunately, the Kohn–Sham inversion and OEP techniques are less robust than desired for practical calculations.[24, 32] Moreover, fitting $v_{XC}(\mathbf{r})$ and $v_F(\mathbf{r})$ to finite-basis-set densities of Coulombic systems may produce results that look nothing like the potentials corresponding to the basis-set-limit densities of the same systems. For instance, exchange-correlation potentials fitted to electron densities generated in standard Gaussian basis sets diverge at large r and oscillate elsewhere.[33–35]

Here we show that it is possible to construct accurate exchange-correlation, Fermi and Pauli potentials for a given system from the system's reduced density matrices (RDM) without using numerically problematic techniques. The constituent parts of this construction procedure were developed in a series of our earlier papers.[36–47] This contribution synthesizes them into a unified method and provides new insights into the relationship between $v_F(\mathbf{r})$, $v_P(\mathbf{r})$, and $v_{XC}(\mathbf{r})$.

2. Procedure

The Fermi, Pauli, and exchange-correlation potentials are related through Eq. (10). This means that if any two out of these potentials are known, the third one is trivially determined. The point of this work is to emphasize a nonobvious fact implied by the method of Ref. 43 that the Fermi and external potentials are sufficient to calculate the associated Pauli and exchange-correlation potentials in a straightforward manner. First we will discuss how Fermi potentials can be constructed and then how to generate $v_P(\mathbf{r})$ and $v_{XC}(\mathbf{r})$ from a given $v_F(\mathbf{r})$.

2.1 Fermi potential

The Fermi potential of a given system can be constructed in more than one way, all of which would give the same result if everything were done using a complete basis set. When one employs a finite basis set at any step, complications arise. For example, one can easily invert Eq. (7) to obtain a formula for the Fermi potential corresponding, in a complete basis set, to a given ground-state density $\rho(\mathbf{r})$,

$$v_{\mathrm{F}}(\mathbf{r}) = \frac{1}{4}\frac{\nabla^2\rho(\mathbf{r})}{\rho(\mathbf{r})} - \frac{1}{8}\frac{|\nabla\rho(\mathbf{r})|^2}{\rho^2(\mathbf{r})} - v(\mathbf{r}) - v_{\mathrm{H}}(\mathbf{r}) + \mu. \tag{12}$$

The problem with this method is that when $\rho(\mathbf{r})$ is generated using a finite Gaussian basis set, the output of Eq. (12) oscillates wildly and diverges at large r[33–35,45] and may not be what one wants: a realistic finite-basis-set approximation to the Fermi potential associated with the exact (basis-set-limit) density.

Recently we showed[45] that, if one wishes to obtain Gaussian-basis-set approximations to Fermi potentials of real atoms and molecules, one needs a more sophisticated approach than Eq. (12). Our proposed solution is a different formula for $v_{\mathrm{F}}(\mathbf{r})$ that requires an interacting two-electron RDM (2-RDM). The derivation of that formula is not difficult[45] but we will not reproduce it here and will only define all of the ingredients and state the final result.

Consider a system of N interacting electrons in a singlet ground state described by a 2-RDM, $\Gamma(\mathbf{r}_1,\mathbf{r}_2;\,\mathbf{r}'_1,\mathbf{r}'_2)$, generated at some level of *ab initio* theory. Let M be the dimension of the space spanned by the one-electron basis set used. From the 2-RDM one can always derive the corresponding one-electron RDM (1-RDM)

$$\gamma(\mathbf{r}_1,\mathbf{r}'_1) = \frac{2}{N-1}\int \Gamma(\mathbf{r}_1,\mathbf{r}_2;\mathbf{r}'_1,\mathbf{r}_2)\,d\mathbf{r}_2 \tag{13}$$

and diagonalize the latter to obtain the natural orbitals $\chi_k(\mathbf{r})$ and their occupation numbers $2n_k$ ($0 \le n_k \le 1$), such that

$$\gamma(\mathbf{r},\mathbf{r}') = 2\sum_{k=1}^{M} n_k\chi_k(\mathbf{r})\chi_k^*(\mathbf{r}'). \tag{14}$$

The 1-RDM determines the electron density

$$\rho^{\mathrm{WF}}(\mathbf{r}) = 2\sum_{k=1}^{M} n_k|\chi_k(\mathbf{r})|^2 \tag{15}$$

and the Pauli kinetic energy density of the interacting electrons

$$\tau_{\mathrm{P}}^{\mathrm{WF}}(\mathbf{r}) = \tau^{\mathrm{WF}}(\mathbf{r}) - \tau_{\mathrm{W}}^{\mathrm{WF}}(\mathbf{r}), \tag{16}$$

where

$$\tau^{\mathrm{WF}}(\mathbf{r}) = \sum_{k=1}^{M} n_k |\nabla \chi_k(\mathbf{r})|^2 \tag{17}$$

and

$$\tau_{\mathrm{W}}^{\mathrm{WF}}(\mathbf{r}) = \frac{|\nabla \rho^{\mathrm{WF}}(\mathbf{r})|^2}{8\rho^{\mathrm{WF}}(\mathbf{r})}. \tag{18}$$

For practical calculations, we rewrite Eq. (16) in the form[45]

$$\tau_{\mathrm{P}}^{\mathrm{WF}}(\mathbf{r}) = \frac{2}{\rho^{\mathrm{WF}}(\mathbf{r})} \sum_{k<l}^{M} n_k n_l |\chi_k(\mathbf{r})\nabla\chi_l(\mathbf{r}) - \chi_l(\mathbf{r})\nabla\chi_k(\mathbf{r})|^2. \tag{19}$$

The 2-RDM determines the exchange-correlation hole

$$\rho_{\mathrm{XC}}(\mathbf{r}_1, \mathbf{r}_2) = \frac{2\Gamma(\mathbf{r}_1, \mathbf{r}_2; \mathbf{r}_1, \mathbf{r}_2)}{\rho(\mathbf{r}_1)} - \rho(\mathbf{r}_2) \tag{20}$$

and its "potential"

$$v_{\mathrm{XC}}^{\mathrm{hole}}(\mathbf{r}_1) = \int \frac{\rho_{\mathrm{XC}}(\mathbf{r}_1, \mathbf{r}_2)}{|\mathbf{r}_1 - \mathbf{r}_2|}\, d\mathbf{r}_2, \tag{21}$$

as well as the kernel of the generalized Fock operator

$$F(\mathbf{r}_1, \mathbf{r}_1') = \hat{h}(\mathbf{r}_1)\gamma(\mathbf{r}_1, \mathbf{r}_1') + 2\int \frac{\Gamma(\mathbf{r}_1, \mathbf{r}_2; \mathbf{r}_1', \mathbf{r}_2)}{|\mathbf{r}_1 - \mathbf{r}_2|}\, d\mathbf{r}_2, \tag{22}$$

where $\hat{h}(\mathbf{r}) = -\frac{1}{2}\nabla_{\mathbf{r}}^2 + v(\mathbf{r})$. Just like the 2-RDM, the generalized Fock operator can be diagonalized to give

$$F(\mathbf{r}, \mathbf{r}') = 2\sum_{k=1}^{M} \lambda_k f_k(\mathbf{r}) f_k^*(\mathbf{r}'), \tag{23}$$

where the factor of 2 arises from the summation over spin. The eigenfunctions $f_k(\mathbf{r})$ and eigenvalues λ_k are then assembled into the quantity

$$\overline{\epsilon}^{\mathrm{WF}}(\mathbf{r}) = \frac{2}{\rho^{\mathrm{WF}}(\mathbf{r})} \sum_{k=1}^{M} \lambda_k |f_k(\mathbf{r})|^2, \tag{24}$$

which may be interpreted as the average local ionization energy of the system.[48, 49]

With all the ingredients defined as above, the formula for the Fermi potential derived in Ref. 45 reads

$$v_{\mathrm{F}}(\mathbf{r}) = v_{\mathrm{XC}}^{\mathrm{hole}}(\mathbf{r}) - \overline{\epsilon}^{\mathrm{WF}}(\mathbf{r}) + \frac{\tau_{\mathrm{P}}^{\mathrm{WF}}(\mathbf{r})}{\rho^{\mathrm{WF}}(\mathbf{r})} + \mu, \tag{25}$$

where μ is a constant formally determined by the condition[8]

$$\lim_{r\to\infty} v_{\mathrm{F}}(\mathbf{r}) = 0, \tag{26}$$

which holds for almost all spatial directions.[50] The principal advantage of Eq. (25) over Eq. (12) is that the former, unlike the latter, assigns similar Fermi potentials to Gaussian and non-Gaussian electron densities.

The Fermi potential can also be written as a sum of $v_{\mathrm{XC}}^{\mathrm{hole}}(\mathbf{r})$, $\tau_{\mathrm{P}}^{\mathrm{WF}}(\mathbf{r})/\rho^{\mathrm{WF}}(\mathbf{r})$ and an integral over many-electron conditional amplitudes.[51] That integral can be reduced[47] to a simpler form involving the 3-RDM at most and the entire sum can then be regarded as yet another exact expression for $v_{\mathrm{F}}(\mathbf{r})$. We have not explored that approach because our Eq. (25) is simpler and already serves the purpose.

2.2 Pauli and exchange-correlation potentials from the Fermi potential

The Kohn–Sham version of DFT assumes the existence of a system of N noninteracting electrons moving in some external potential $v_s(\mathbf{r})$ such that the ground-state density of that system, $\rho^{\mathrm{KS}}(\mathbf{r})$, is equal to the ground-state density of the interacting system,

$$\rho^{\mathrm{KS}}(\mathbf{r}) = \rho^{\mathrm{WF}}(\mathbf{r}). \tag{27}$$

Referring to Eq. (2), the potential $v_s(\mathbf{r})$ is given by

$$v_s(\mathbf{r}) = v(\mathbf{r}) + v_{\mathrm{H}}(\mathbf{r}) + v_{\mathrm{XC}}(\mathbf{r}) \tag{28}$$

and the noninteracting electron density (for a singlet ground state) by

$$\rho^{\mathrm{KS}}(\mathbf{r}) = 2\sum_{i=1}^{N/2} |\phi_i(\mathbf{r})|^2, \tag{29}$$

where the summation is over the lowest-eigenvalue solutions of Eq. (2). The eigenfunctions $\phi_i(\mathbf{r})$, called the Kohn–Sham orbitals, allow one to express the Pauli kinetic energy density of the noninteracting electrons as

$$\tau_{\mathrm{P}}^{\mathrm{KS}}(\mathbf{r}) = \frac{2}{\rho^{\mathrm{KS}}(\mathbf{r})} \sum_{i<j}^{N/2} |\phi_i(\mathbf{r})\nabla\phi_j(\mathbf{r}) - \phi_j(\mathbf{r})\nabla\phi_i(\mathbf{r})|^2 \tag{30}$$

and the Kohn–Sham average local ionization energy as

$$\overline{\epsilon}^{\mathrm{KS}}(\mathbf{r}) = \frac{2}{\rho^{\mathrm{KS}}(\mathbf{r})} \sum_{i=1}^{N/2} \epsilon_i |\phi_i(\mathbf{r})|^2. \tag{31}$$

Then, as we showed in Ref. 43, the exchange-correlation potential is given by

$$v_{\mathrm{XC}}(\mathbf{r}) = v_{\mathrm{XC}}^{\mathrm{hole}}(\mathbf{r}) + \overline{\epsilon}^{\mathrm{KS}}(\mathbf{r}) - \overline{\epsilon}^{\mathrm{WF}}(\mathbf{r}) + \frac{\tau_{\mathrm{P}}^{\mathrm{WF}}(\mathbf{r})}{\rho^{\mathrm{WF}}(\mathbf{r})} - \frac{\tau_{\mathrm{P}}^{\mathrm{KS}}(\mathbf{r})}{\rho^{\mathrm{KS}}(\mathbf{r})}. \tag{32}$$

Using Eq. (25), we rewrite Eq. (32) as

$$v_{\mathrm{XC}}(\mathbf{r}) = v_{\mathrm{F}}(\mathbf{r}) + \overline{\epsilon}^{\mathrm{KS}}(\mathbf{r}) - \frac{\tau_{\mathrm{P}}^{\mathrm{KS}}(\mathbf{r})}{\rho^{\mathrm{KS}}(\mathbf{r})} - \mu. \tag{33}$$

Comparison of Eqs. (10) and (33) leads to the following expression for the Pauli potential:

$$v_{\mathrm{P}}(\mathbf{r}) = -\overline{\epsilon}^{\mathrm{KS}}(\mathbf{r}) + \frac{\tau_{\mathrm{P}}^{\mathrm{KS}}(\mathbf{r})}{\rho^{\mathrm{KS}}(\mathbf{r})} + \mu. \tag{34}$$

The right-hand side of Eq. (33) contains two types of terms: those determined by the interacting 2-RDM and those determined by the Kohn–Sham orbitals and orbital energies. The terms of the first group form the Fermi potential, while the terms of the second group constitute the Pauli potential. This natural decomposition of the exchange-correlation potential suggests the following method for computing all three potentials: first construct $v_{\mathrm{F}}(\mathbf{r})$ and then use it as a fixed part of Eq. (33) to solve iteratively the Kohn–Sham eigenvalue problem, Eq. (2). That this method can actually work is implied by our previous reports,[38, 39, 43] where we calculated exchange-correlation potentials from 2-RDMs in essentially the same manner.

2.3 Algorithm

For the sake of completeness, we describe below the proposed algorithm for the unified construction of Fermi, Pauli, and exchange-correlation potentials.

1. Construct the Fermi potential for the system of interest either by using Eq. (25) (i.e., from a 2-RDM) or by direct approximation.
2. Generate an initial guess for the Kohn–Sham orbitals and orbital energies (e.g., by solving the Kohn–Sham equations using an approximate density functional).
3. Use the current $\phi_i(\mathbf{r})$ and ϵ_i to construct $v_{\mathrm{P}}(\mathbf{r})$ by Eq. (34) and $v_{\mathrm{H}}(\mathbf{r})$ by Eq. (3) using $\rho^{\mathrm{KS}}(\mathbf{r})$.
4. Use the Fermi potential from step 1 and the Pauli potential from step 3 to construct the exchange-correlation potential as $v_{\mathrm{XC}}(\mathbf{r}) = v_{\mathrm{F}}(\mathbf{r}) - v_{\mathrm{P}}(\mathbf{r})$.
5. Solve the Kohn–Sham eigenvalue problem with the current $v_{\mathrm{H}}(\mathbf{r})$ and $v_{\mathrm{XC}}(\mathbf{r})$ to obtain a new set of $\phi_i(\mathbf{r})$ and ϵ_i. Shift the Kohn–Sham spectrum by setting the eigenvalue of the highest occupied orbital to $\epsilon_{N/2} = \mu$, as explained below.
6. If the Kohn–Sham orbitals and orbital energies are converged, then $v_{\mathrm{P}}(\mathbf{r})$ and $v_{\mathrm{XC}}(\mathbf{r})$ are also converged. In that case, stop and print the potentials. Otherwise, return to step 3 and continue.

With commutator-based direct inversion of the iterative subspace,[52] the self-consistent field (SCF) iterations of steps 3–6 can be converged as tightly as the density-functional integration grid permits. In this work, we used a saturated grid and terminated the algorithm when the Kohn–Sham density matrix elements from two consecutive iterations differed by less than 10^{-10} in the root-mean-square sense.

The potentials $v_{\mathrm{F}}(\mathbf{r})$ and $v_{\mathrm{XC}}(\mathbf{r})$ obtained by this method from a 2-RDM are supposed to recover the *ab initio* density $\rho^{\mathrm{WF}}(\mathbf{r})$ via Eqs. (2) and (7), respectively. That indeed would be the case if all of the calculations were performed in a complete basis set. In a finite basis set, the densities $|\theta(\mathbf{r})|^2$ and $\rho^{\mathrm{KS}}(\mathbf{r})$ agree with $\rho^{\mathrm{WF}}(\mathbf{r})$ only approximately with a small discrepancy that tends to zero in the basis-set limit.[43–45] The metric which we use to characterize this discrepancy is

$$\Delta_\rho = \int |\rho^{\mathrm{KS}}(\mathbf{r}) - \rho^{\mathrm{WF}}(\mathbf{r})| \, d\mathbf{r}, \tag{35}$$

where $\rho^{\mathrm{KS}}(\mathbf{r})$ is the Kohn–Sham density at convergence.

If a finite basis set is used, the Hartree potential should be constructed in step 3 using $\rho^{\mathrm{KS}}(\mathbf{r})$ rather than $\rho^{\mathrm{WF}}(\mathbf{r})$ to ensure mutual cancelation of $v_{\mathrm{H}}(\mathbf{r})$

and $v_{\mathrm{P}}(\mathbf{r})$ in the asymptotic region because the asymptotic behavior of $v_{\mathrm{XC}}(\mathbf{r})$ should be determined by that of $v_{\mathrm{F}}(\mathbf{r})$. If $v_{\mathrm{H}}(\mathbf{r})$ is constructed from $\rho^{\mathrm{WF}}(\mathbf{r})$, the procedure is unlikely to converge at all.

In order that $v_{\mathrm{F}}(\mathbf{r})$, $v_{\mathrm{P}}(\mathbf{r})$, and $v_{\mathrm{XC}}(\mathbf{r})$ vanish as they should in the $r \to \infty$ limit, the individually nonvanishing terms in Eqs. (25) and (34) must be such that

$$\lim_{r\to\infty} \overline{\epsilon}^{\mathrm{WF}}(\mathbf{r}) = \lim_{r\to\infty} \overline{\epsilon}^{\mathrm{KS}}(\mathbf{r}) = \epsilon_{N/2} = \mu, \tag{36}$$

where $\epsilon_{N/2}$ is the eigenvalue of the highest occupied Kohn–Sham orbital. The shift of the Kohn–Sham spectrum applied in step 5 constrains all of the equalities in Eq. (36) to be satisfied automatically.

There remains the question of how to calculate the chemical potential μ. When the Fermi potential is constructed from a 2-RDM, the value of μ is fixed by Eq. (26) and, theoretically, could be found as the $r \to \infty$ limit of $\overline{\epsilon}^{\mathrm{WF}}(\mathbf{r})$.[48] In practical finite-basis-set calculations, this limit is sensitive to the choice of the most diffuse basis function, so a more robust approach is needed. We take $\mu = -I$, where I is the first ionization energy obtained from the 2-RDM via the extended Koopmans theorem[53–55] using the method of Ref. 56. In particular, for Hartree–Fock (HF) wavefunctions, $I = -\epsilon^{\mathrm{HF}}_{N/2}$. If the Fermi potential is modeled by an analytic expression that obeys Eq. (26), the corresponding μ is unknown. In such cases, we satisfy Eq. (36) by setting μ to whatever value of $\epsilon_{N/2}$ comes out of the Kohn–Sham eigenvalue problem. Note that the shifting of the Kohn–Sham spectrum by μ is optional because it has no effect on the converged $\rho^{\mathrm{KS}}(\mathbf{r})$.

3. Numerical examples

The above algorithm was implemented locally in the *Gaussian* suite of programs.[57] Apart from the extension enabling the use of directly modeled Fermi potentials, this implementation is the same as that of Ref. 43.

3.1 Calculations with Fermi potentials generated from *ab initio* wavefunctions

The many-electron systems chosen to illustrate our method include the Be atom and two linear molecules (LiF and CNO^-) at their equilibrium geometries. These three systems represent most of the chemical elements of the first full row of the periodic table. The Fermi potentials were generated from

HF, complete active space (CAS) SCF and full configuration interaction (FCI) wavefunctions using the correlation-consistent polarized core-valence contracted Gaussian basis sets, cc-pCVXZ (X = D, T, Q).[58, 59] Relevant details about these systems and wavefunctions are collected in Table 1.

The small Be atom was chosen over larger alternatives to demonstrate the magnitude of differences between Fermi, Pauli, and exchange-correlation potentials generated at various *ab initio* levels. Fig. 1 shows that the Fermi potentials of Be constructed from the same type of wavefunction (in this case, HF) using different basis sets are almost indistinguishable, as are the

Table 1 Information about the wavefunctions used for generating the Fermi potentials.

System	State	Method	Basis set	E (E_h)	μ (E_h)	Δ_ρ (e)
Be	^1S	HF	cc-pCVDZ	−14.572338	−0.3091	0.0096
		HF	cc-pCVTZ	−14.572873	−0.3093	0.0112
		HF	cc-pCVQZ	−14.572968	−0.3093	0.0043
		CAS(4,6)	cc-pCVTZ	−14.630318	−0.3488	0.0052
		FCI	cc-pCVTZ	−14.662368	−0.3419	0.0052
LiF	$^1\Sigma^+$	CAS(8,8)	cc-pCVTZ	−107.125911	−0.4371	0.0161
CNO^-	$^1\Sigma^+$	CAS(16,12)	aug-cc-pCVQZ	−167.338475	−0.1592	0.0190

Internuclear distances in the molecules: $r_{LiF} = 2.96a_0$, $r_{CN} = 2.23a_0$, $r_{NO} = 2.38a_0$.

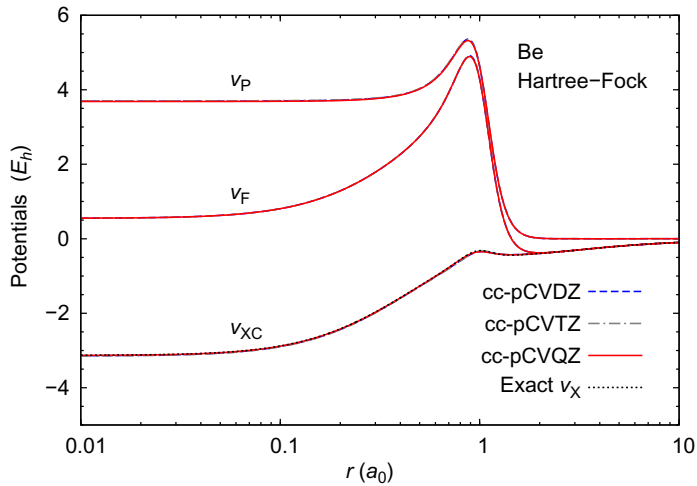

Fig. 1 Fermi, Pauli, and exchange-correlation potentials generated from HF wavefunctions of the Be atom using various basis sets. The exact exchange-only Kohn–Sham potential is from Ref. 27.

associated $v_P(\mathbf{r})$ and $v_{XC}(\mathbf{r})$ generated from those Fermi potentials. Another general result illustrated by Fig. 1 is that exchange-correlation potentials generated from atomic HF wavefunctions are excellent approximations[36, 37] to the exact exchange-only Kohn–Sham potentials obtained by numerical solution[27] of the integral OEP equation.

Fermi, Pauli, and exchange-correlation potentials generated from wavefunctions of different types show more variation depending on the fraction of the correlation energy included. For atoms such as Be, differences between potentials generated at the HF and post-HF levels of theory are relatively small (Fig. 2) but would be much larger for systems where the single-determinantal approximation is inadequate.[44, 45] Fig. 2 also shows that exchange-correlation potentials derived from correlated wavefunctions are very close to the exact numerical benchmarks.

Figs. 3 and 4 display examples of molecular Fermi, Pauli, and exchange-correlation potentials generated from correlated wavefunctions. Each of the potentials of CNO^- looks like an amalgamation of the corresponding potentials of the three constituent atoms. The Fermi and Pauli potentials of CNO^- have similar shapes and much greater magnitudes than $v_{XC}(\mathbf{r})$ near the nuclei. By contrast, the Pauli potential of LiF is flat around the Li nucleus, and both $v_F(\mathbf{r})$ and $v_P(\mathbf{r})$ remain positive in a much larger region of space than would be the case for an isolated Li atom or the Li_2 dimer. We also note that

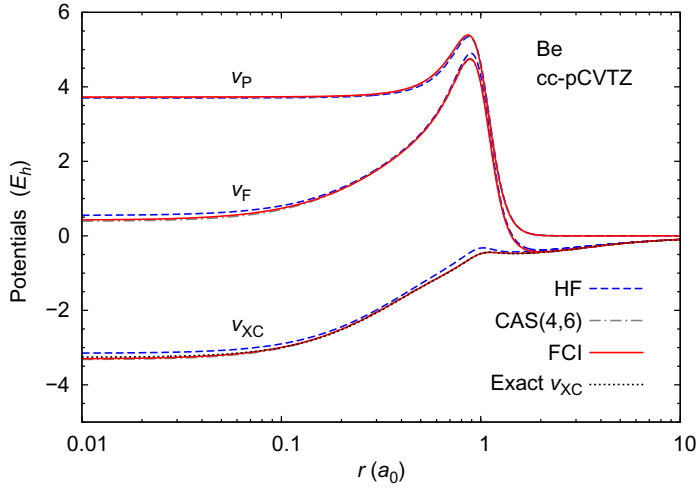

Fig. 2 Fermi, Pauli, and exchange-correlation potentials generated from various wavefunctions of the Be atom using a fixed basis set. The exact $v_{XC}(\mathbf{r})$ is from Ref. 60.

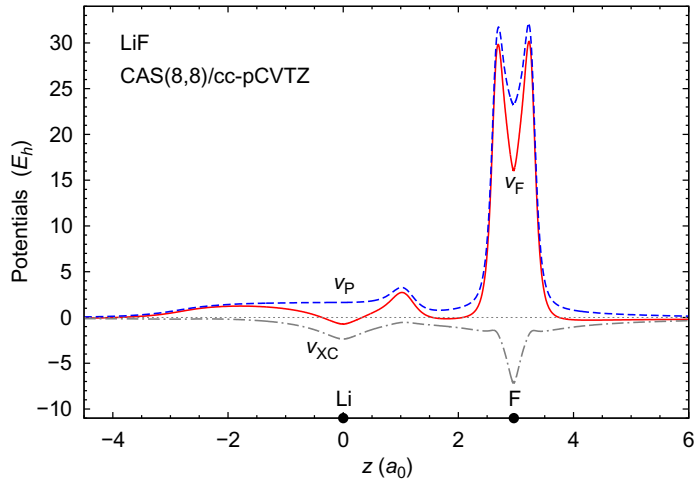

Fig. 3 Fermi, Pauli, and exchange-correlation potentials generated from a CASSCF wavefunction of the LiF molecule.

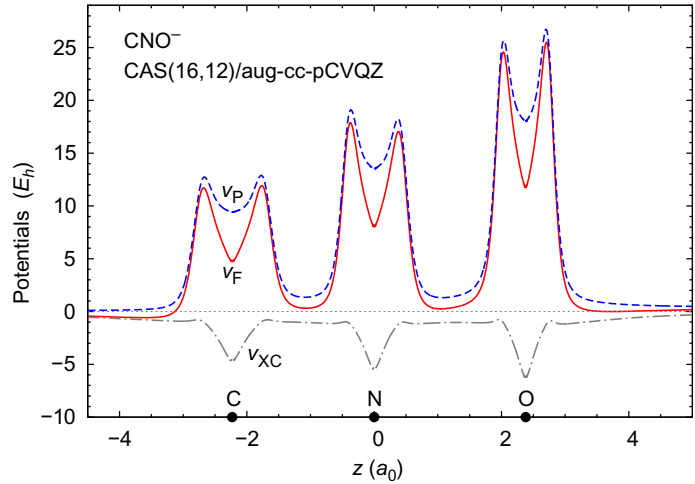

Fig. 4 Fermi, Pauli, and exchange-correlation potentials generated from a CASSCF wavefunction of the CNO^- anion.

the noninteracting electron configurations of LiF and CNO^- are $1\sigma^2\,2\sigma^2\,3\sigma^2\,4\sigma^2\,1\pi^4$ and $1\sigma^2\,2\sigma^2\,3\sigma^2\,4\sigma^2\,5\sigma^2\,6\sigma^2\,1\pi^4\,7\sigma^2\,2\pi^4$, respectively, which means that Figs. 3 and 4 show the potentials along the intersection of the nodal planes of two degenerate highest occupied Kohn–Sham orbitals.

Our approach does not allow us to obtain the total electronic energy of the system independently of the wavefunction method. One can only compute the kinetic correlation and Kohn–Sham exchange-correlation energies by combining appropriate wavefunction and Kohn–Sham quantities, as has been demonstrated elsewhere.[38, 43, 44]

3.2 Calculations with model Fermi potentials

The fixed Fermi potential used in our method for constructing Pauli and exchange-correlation potentials does not have to come from an *ab initio* wavefunction. One can also approximate $v_F(\mathbf{r})$ directly. To illustrate this strategy, we tested two simple model Fermi potentials,

$$v_F^A(\mathbf{r}) = \frac{1.60r^2 + 0.75}{0.25r^8 + 0.30} - \frac{1}{0.50 + r}, \tag{37}$$

and

$$v_F^B(\mathbf{r}) = \frac{1.20r^2 + 0.30}{0.20r^6 + 0.15} - \frac{1}{1.00 + r}, \tag{38}$$

for a four-electron system with an external potential of the Be atom. The first terms on the right-hand sides of Eqs. (37) and (38) are analogous to Finzel's analytic approximations[61] to Pauli potentials (which are positive everywhere), while the second term simulates the $-1/r$ asymptotic decay of $v_F(\mathbf{r})$. Both models were devised as deliberately imperfect fits of *ab initio* Fermi potentials of the Be atom. Of course, a model Fermi potential is unlikely to be a functional derivative.[62]

Fig. 5 shows the Pauli and exchange-correlation potentials obtained from the model Fermi potentials of Eqs. (37) and (38) using the cc-pCVTZ basis set of the Be atom. Model A gives rise to a $v_P(\mathbf{r})$ that is more positive and a $v_{XC}(\mathbf{r})$ that is more negative than the respective potentials of Fig. 2, whereas model B gives a less positive $v_P(\mathbf{r})$ and a less negative $v_{XC}(\mathbf{r})$ than in Fig. 2. Because the maxima of $v_F(\mathbf{r})$ and $v_P(\mathbf{r})$ in model B are not aligned as in model A, the $v_{XC}(\mathbf{r})$ obtained from model B has a second bump near $r = 0.7a_0$, a feature that is absent in model A. We have also experimented with model Fermi potentials of other shapes but found that the Kohn–Sham SCF iterations do not converge unless $v_F(\mathbf{r})$ is sufficiently close to the true Fermi potential of the Be atom, at least when using basis sets and density-functional integration grids designed for that system.

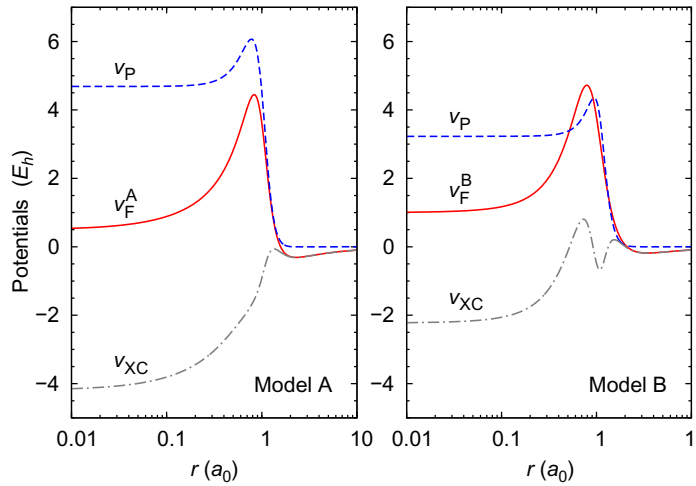

Fig. 5 Pauli and exchange-correlation potentials generated from two model Fermi potentials for a four-electron atom with $Z = 4$ using the cc-pCVTZ basis set of the Be atom.

4. Concluding remarks

We have shown that the Fermi and external potentials of a many-electron system suffice to construct the Pauli and exchange-correlation potentials. The process involves solving the Kohn–Sham equations by iteration using the expression for $v_{XC}(\mathbf{r})$ given by Eq. (33). The Fermi potential may be computed by Eq. (25) from an interacting 2-RDM or approximated directly. This unified approach reduces the problem of constructing accurate Pauli and exchange-correlation potentials to the task of constructing accurate Fermi potentials.

Calculations reported in this work and elsewhere[43–45] indicate that Fermi, Pauli, and exchange-correlation potentials derived from 2-RDMs rapidly converge with respect to the basis set, and that potentials obtained using standard Gaussian basis sets are excellent approximations to the corresponding potentials of the basis-set limit. Molecular Fermi, Pauli, and exchange-correlation potentials exhibit[42, 44] significantly more variation than atomic potentials between HF and post-HF levels of *ab initio* theory because electron correlation plays a greater role in systems with more than one atomic nucleus.

The representation of $v_{XC}(\mathbf{r})$ by the difference of Fermi and Pauli potentials, each of which has a physical meaning on its own, offers a new vantage point for analyzing exact exchange-correlation potentials. This perspective

is related to and complements the fruitful Kohn–Sham potential decomposition analysis developed by Baerends and coworkers.[51, 63] Treating $v_{XC}(\mathbf{r})$ as a combination of the Fermi and Pauli potentials may also facilitate direct approximation of exchange-correlation potentials and aid the analysis of derivative discontinuities[64] and other nonintuitive effects[65, 66] arising in the Kohn–Sham DFT.

Acknowledgments

The work was supported by the Natural Sciences and Engineering Research Council of Canada (NSERC) through a Discovery Grant (Application No. RGPIN-2015-04814) and a Discovery Accelerator Supplement (RGPAS 477791-2015).

References

1. Kohn, W.; Sham, L. J. Self-Consistent Equations Including Exchange and Correlation Effects. *Phys. Rev.* **1965**, *140*, A1133.
2. Hohenberg, P. C.; Kohn, W.; Sham, L. J. The Beginnings and Some Thoughts on the Future. *Adv. Quantum Chem.* **1990**, *21*, 7.
3. Kohn, W. Nobel Lecture: Electronic Structure of Matter—Wave Functions and Density Functionals. *Rev. Mod. Phys.* **1999**, *71*, 1253.
4. Seidl, A.; Görling, A.; Vogl, P.; Majewski, J. A.; Levy, M. Generalized Kohn–Sham Schemes and the Band-Gap Problem. *Phys. Rev. B* **1996**, *53*, 3764.
5. Wang, Y. A.; Carter, E. A. Orbital-Free Kinetic-Energy Density Functional Theory. In: *Theoretical Methods in Condensed Phase Chemistry*, Schwartz, S. D. Ed.; Kluwer Academic: Dordrecht, 2000; pp. 117–184.
6. Ludeña, E. V.; Karasiev, V. V. Kinetic Energy Functionals: History, Challenges and Prospects. In: *Reviews of Modern Quantum Chemistry: A Celebration of the Contributions of Robert G. Parr*; Sen, K. D. Ed.; Vol. 1. World Scientific: Singapore, 2002; pp. 612–665.
7. Karasiev, V. V.; Jones, R. S.; Trickey, S. B.; Harris, F. E. Recent Advances in Developing Orbital-Free Kinetic Energy Functionals. In: *New Developments in Quantum Chemistry*; Paz, J. L., Hernández, A. J., Eds.; Transworld Research Network: Trivandrum, India, 2009; pp. 25–54.
8. Levy, M.; Perdew, J. P.; Sahni, V. Exact Differential Equation for the Density and Ionization Energy of a Many-Particle System. *Phys. Rev. A* **1984**, *30*, 2745.
9. Nooijen, M. Reflections on Formal Density Functional Theory. *Adv. Quantum Chem.* **2009**, *56*, 181.
10. Hohenberg, P.; Kohn, W. Inhomogeneous Electron Gas. *Phys. Rev.* **1964**, *136*, B864.
11. Eschrig, H. *The Fundamentals of Density Functional Theory*, 2nd ed.; Edition am Gutenbergplatz: Leipzig, 2003.
12. Finzel, K.; Ayers, P. W. The Exact Fermi Potential Yielding the Hartree–Fock Electron Density from Orbital-Free Density Functional Theory. *Int. J. Quantum Chem.* **2017**, *117*, e25364.
13. Holas, A.; March, N. H. Construction of the Pauli Potential, Pauli Energy, and Effective Potential from the Electron Density. *Phys. Rev. A* **1991**, *44*, 5521.
14. March, N. H. The Local Potential Determining the Square Root of the Ground-State Electron Density of Atoms and Molecules from the Schrödinger Equation. *Phys. Lett. A* **1986**, *113*, 476.
15. Levy, M.; Ou-Yang, H. Exact Properties of the Pauli Potential for the Square Root of the Electron Density and the Kinetic Energy Functional. *Phys. Rev. A* **1988**, *38*, 625.

16. March, N. H. Concept of the Pauli Potential in Density Functional Theory. *J. Mol. Struct.: THEOCHEM* **2010**, *943*, 77.
17. Levämäki, H.; Nagy, Á.; Kokko, K.; Vitos, L. Cusp Relation for the Pauli Potential. *Phys. Rev. A* **2014**, *90*, 062515.
18. Sahni, V. *Quantal Density Functional Theory*, 2nd ed.; Springer: Berlin, 2016.
19. Ludeña, E. V.; Arroyo, D.; Salazar, E. X.; Vallejo, J. The Kinetic Energy Pauli Enhancement Factor and Its Role in Determining the Shell Structure of Atoms and Molecules. *Adv. Quantum Chem.* **2018**, *76*, 59.
20. Bartolotti, L. J.; Acharya, P. K. On the Functional Derivative of the Kinetic Energy Density Functional. *J. Chem. Phys.* **1982**, 77, 4576.
21. Wu, Q.; Yang, W. A Direct Optimization Method for Calculating Density Functionals and Exchange-Correlation Potentials from Electron Densities. *J. Chem. Phys.* **2003**, *118*, 2498.
22. Ryabinkin, I. G.; Staroverov, V. N. Determination of Kohn–Sham Effective Potentials from Electron Densities Using the Differential Virial Theorem. *J. Chem. Phys.* **2012**, *137*, 164113.
23. Finzel, K.; Ayers, P. W.; Bultinck, P. A Simple Algorithm for the Kohn-Sham Inversion Problem Applicable to General Target Densities. *Theor. Chem. Acc.* **2018**, *137*, 30.
24. Jensen, D. S.; Wasserman, A. Numerical Methods for the Inverse Problem of Density Functional Theory. *Int. J. Quantum Chem.* **2018**, *118*, e25425.
25. Schnieders, D.; Neugebauer, J. Accurate Embedding through Potential Reconstruction: A Comparison of Different Strategies. *J. Chem. Phys.* **2018**, *149*, 054103.
26. Grabo, T.; Kreibich, T.; Kurth, S. Gross, E. K. U. Orbital Functionals in Density Functional Theory: The Optimized Effective Potential Method. In: *Strong Coulomb Correlations in Electronic Structure Calculations: Beyond the Local Density Approximation*; Anisimov, V. I. Ed.; Gordon and Breach: Amsterdam, 2000; pp. 203–311.
27. Engel, E.; Dreizler, R. M. From Explicit to Implicit Density Functionals. *J. Comput. Chem.* **1999**, *20*, 31.
28. Hirata, S.; Ivanov, S.; Grabowski, I.; Bartlett, R. J.; Burke, K.; Talman, J. D. Can Optimized Effective Potentials Be Determined Uniquely? *J. Chem. Phys.* **2001**, *115*, 1635.
29. Bartlett, R. J.; Grabowski, I.; Hirata, S.; Ivanov, S. The Exchange-Correlation Potential in *ab Initio* Density Functional Theory. *J. Chem. Phys.* **2005**, *122*, 034104.
30. Bartlett, R. J.; Lotrich, V. F.; Schweigert, I. V. *Ab Initio* Density Functional Theory: The Best of Both Worlds? *J. Chem. Phys.* **2005**, *123*, 062205.
31. Kümmel, S.; Kronik, L. Orbital-Dependent Density Functionals: Theory and Applications. *Rev. Mod. Phys.* **2008**, *80*, 3.
32. Staroverov, V. N.; Scuseria, G. E.; Davidson, E. R. Optimized Effective Potentials Yielding Hartree–Fock Energies and Densities. *J. Chem. Phys.* **2006**, *124*, 141103.
33. Schipper, P. R. T.; Gritsenko, O. V.; Baerends, E. J. Kohn–Sham Potentials Corresponding to Slater and Gaussian Basis Set Densities. *Theor. Chem. Acc.* **1997**, *98*, 16.
34. Mura, M. E.; Knowles, P. J.; Reynolds, C. A. Accurate Numerical Determination of Kohn–Sham Potentials from Electronic Densities: I. Two-Electron Systems. *J. Chem. Phys.* **1997**, *106*, 9659.
35. Gaiduk, A. P.; Ryabinkin, I. G.; Staroverov, V. N. Removal of Basis-Set Artifacts in Kohn–Sham Potentials Recovered from Electron Densities. *J. Chem. Theory Comput.* **2013**, *9*, 3959.
36. Ryabinkin, I. G.; Kananenka, A. A.; Staroverov, V. N. Accurate and Efficient Approximation to the Optimized Effective Potential for Exchange. *Phys. Rev. Lett.* **2013**, *111*, 013001.
37. Kohut, S. V.; Ryabinkin, I. G.; Staroverov, V. N. Hierarchy of Model Kohn–Sham Potentials for Orbital-Dependent Functionals: A Practical Alternative to the Optimized Effective Potential Method. *J. Chem. Phys.* **2014**, *140*, 18A535.

38. Ryabinkin, I. G.; Kohut, S. V.; Staroverov, V. N. Reduction of Electronic Wavefunctions to Kohn–Sham Effective Potentials. *Phys. Rev. Lett.* **2015**, *115*, 083001.
39. Cuevas-Saavedra, R.; Ayers, P. W.; Staroverov, V. N. Kohn–Sham Exchange-Correlation Potentials from Second-Order Reduced Density Matrices. *J. Chem. Phys.* **2015**, *143*, 244116.
40. Cuevas-Saavedra, R.; Staroverov, V. N. Exact Expressions for the Kohn–Sham Exchange-Correlation Potential in Terms of Wave-Function-Based Quantities. *Mol. Phys.* **2016**, *114*, 1050.
41. Ryabinkin, I. G.; Kohut, S. V.; Cuevas-Saavedra, R.; Ayers, P. W.; Staroverov, V. N. Response to "Comment on 'Kohn–Sham Exchange-Correlation Potentials from Second-Order Reduced Density Matrices'" [J. Chem. Phys. **145**, 037101 (2016)]. *J. Chem. Phys.* **2016**, *145*, 037102.
42. Kohut, S. V.; Polgar, A. M.; Staroverov, V. N. Origin of the Step Structure of Molecular Exchange-Correlation Potentials. *Phys. Chem. Chem. Phys.* **2016**, *18*, 20938.
43. Ospadov, E.; Ryabinkin, I. G.; Staroverov, V. N. Improved Method for Generating Exchange-Correlation Potentials from Electronic Wave Functions. *J. Chem. Phys.* **2017**, *146*, 084103.
44. Ryabinkin, I. G.; Ospadov, E.; Staroverov, V. N. Exact Exchange-Correlation Potentials of Singlet Two-Electron Systems. *J. Chem. Phys.* **2017**, *147*, 164117.
45. Ospadov, E.; Staroverov, V. N. Construction of Fermi Potentials from Electronic Wave Functions. *J. Chem. Theory Comput.* **2018**, *14*, 4246.
46. Staroverov, V. N. Uniform Electron Gas Limit of an Exact Expression for the Kohn–Sham Exchange-Correlation Potential. *Theor. Chem. Acc.* **2018**, *136*, 120.
47. Staroverov, V. N. Contracted Schrödinger Equation and Kohn–Sham Effective Potentials. *Mol. Phys.* **2019**, *117*, 1.
48. Ryabinkin, I. G.; Staroverov, V. N. Average Local Ionization Energy Generalized to Correlated Wavefunctions. *J. Chem. Phys.* **2014**, *141*, 084107.
49. Kohut, S. V.; Cuevas-Saavedra, R.; Staroverov, V. N. Generalized Average Local Ionization Energy and Its Representations in Terms of Dyson and Energy Orbitals. *J. Chem. Phys.* **2016**, *145*, 074113.
50. Gori-Giorgi, P.; Baerends, E. J. Asymptotic Nodal Planes in the Electron Density and the Potential in the Effective Equation for the Square Root of the Density. *Eur. Phys. J. B* **2018**, *91*, 160.
51. Buijse, M. A.; Baerends, E. J.; Snijders, J. G. Analysis of Correlation in Terms of Exact Local Potentials: Applications to Two-Electron Systems. *Phys. Rev. A* **1989**, *40*, 4190.
52. Pulay, P. Improved SCF Convergence Acceleration. *J. Comput. Chem.* **1982**, *3*, 556.
53. Morrell, M. M.; Parr, R. G.; Levy, M. Calculation of Ionization Potentials from Density Matrices and Natural Functions, and the Long-Range Behavior of Natural Orbitals and Electron Density. *J. Chem. Phys.* **1975**, *62*, 549.
54. Smith, D. W.; Day, O. W. Extension of Koopmans' Theorem. I. Derivation. *J. Chem. Phys.* **1975**, *62*, 113.
55. Day, O. W.; Smith, D. W.; Morrison, R. C. Extension of Koopmans' Theorem. II. Accurate Ionization Energies from Correlated Wavefunctions for Closed-Shell Atoms. *J. Chem. Phys.* **1975**, *62*, 115.
56. Morrison, R. C.; Liu, G. Extended Koopmans' Theorem: Approximate Ionization Energies from MCSCF Wave Functions. *J. Comput. Chem.* **1992**, *13*, 1004.
57. Frisch, M. J.; Trucks, G. W.; Schlegel, H. B.; Scuseria, G. E.; Robb, M. A.; Cheeseman, J. R.; Scalmani, G.; Barone, V.; Petersson, G. A.; Nakatsuji, H.; Li, X.; Caricato, M.; Marenich, A. V.; Bloino, J.; Janesko, B. G.; Gomperts, R.; Mennucci, B.; Hratchian, H. P.; Ortiz, J. V.; Izmaylov, A. F.; Sonnenberg, J. L.; Williams-Young, D.; Ding, F.; Lipparini, F.; Egidi, F.; Goings, J.; Peng, B.; Petrone, A.; Henderson, T.; Ranasinghe, D.; Zakrzewski, V. G.; Gao, J.; Rega, N.;

Zheng, G.; Liang, W.; Hada, M.; Ehara, M.; Toyota, K.; Fukuda, R.; Hasegawa, J.; Ishida, M.; Nakajima, T.; Honda, Y.; Kitao, O.; Nakai, H.; Vreven, T.; Throssell, K.; Montgomery, J. A.; Jr. Peralta, J. E.; Ogliaro, F.; Bearpark, M. J.; Heyd, J. J.; Brothers, E. N.; Kudin, K. N.; Staroverov, V. N.; Keith, T. A.; Kobayashi, R.; Normand, J.; Raghavachari, K.; Rendell, A. P.; Burant, J. C.; Iyengar, S. S.; Tomasi, J.; Cossi, M.; Millam, J. M.; Klene, M.; Adamo, C.; Cammi, R.; Ochterski, J. W.; Martin, R. L.; Morokuma, K.; Farkas, O.; Foresman, J. B.; Fox, D. J. *Gaussian Development Version, Revision I.13*. Gaussian, Inc.: Wallingford, CT, 2016

58. Woon, D. E.; Dunning, Jr., T. H. Gaussian Basis Sets for Use in Correlated Molecular Calculations. V. Core-Valence Basis Sets for Boron through Neon. *J. Chem. Phys.* **1995**, *103*, 4572.
59. Schuchardt, K. L.; Didier, B. T.; Elsethagen, T.; Sun, L.; Gurumoorthi, V.; Chase, J.; Li, J.; Windus, T. L. Basis Set Exchange: A Community Database for Computational Sciences. *J. Chem. Inf. Model.* **2007**, *47*, 1045.
60. Filippi, C.; Gonze, X.; Umrigar, C. J. *Recent Developments and Applications of Modern Density Functional Theory*. Elsevier: Amsterdam, 1996; pp. 295–326.
61. Finzel, K. Approximating the Pauli Potential in Bound Coulomb Systems. *Int. J. Quantum Chem.* **2016**, *116*, 1261.
62. Gaiduk, A. P.; Staroverov, V. N. How to Tell When a Model Kohn-Sham Potential Is Not a Functional Derivative. *J. Chem. Phys.* **2009**, *131*, 044107.
63. Baerends, E. J.; Gritsenko, O. V. A Quantum Chemical View of Density Functional Theory. *J. Phys. Chem. A* **1997**, *101*, 5383.
64. Hodgson, M. J. P.; Kraisler, E.; Schild, A.; Gross, E. K. U. How Interatomic Steps in the Exact Kohn-Sham Potential Relate to Derivative Discontinuities of the Energy. *J. Phys. Chem. Lett.* **2017**, *8*, 5974.
65. Kraisler, E.; Kümmel, S. Revealing the Field-Counteracting Term in the Exact Kohn-Sham Correlation Potential. *Phys. Rev. A* **2018**, *98*, 052505.
66. Giarrusso, S.; Vuckovic, S.; Gori-Giorgi, P. Response Potential in the Strong-Interaction Limit of Density Functional Theory: Analysis and Comparison with the Coupling-Constant Average. *J. Chem. Theory Comput.* **2018**, *14*, 4151.

This page intentionally left blank

CHAPTER TEN

Potential energy curves of the NaH molecule and its cation with the Fock space coupled cluster method

Artur Lisoń, Monika Musiał*, Stanisław A. Kucharski
Institute of Chemistry, University of Silesia in Katowice, Katowice, Poland
*Corresponding author: e-mail address: musial@ich.us.edu.pl

Contents

Abstract

The Fock space coupled cluster theory provides a description of the states obtained by attachment of one ((1,0) sector) or two ((2,0) sector) electrons to the reference system. If the reference is assumed to be a doubly ionized cation then the results relate to a cation or a neutral molecule, respectively. In the current work the above scheme is applied to extensive ab initio calculations of the potential energy curves (PECs), and the spectroscopic constants of NaH and its cation for the eight lowest lying states, adopting as a reference system the doubly ionized structure, i.e., NaH^{2+}. Such a computational strategy relies on the fact that the closed shell reference (NaH^{2+}) dissociates into the closed shell fragments. This is advantageous since the restricted Hartree–Fock function can be used as the reference in the whole range of interatomic distances. This scheme offers a *first principle* size-extensive method without any model or effective potential parameters for the description of the bond breaking processes. The computed PECs and spectroscopic constants stay very close to the experimental values, with accuracy exceeding that of other theoretical approaches (in most cases) including those based on the effective core potentials.

Advances in Quantum Chemistry, Volume 79
ISSN 0065-3276
https://doi.org/10.1016/bs.aiq.2019.03.001

1. Introduction

The growing interest in studies of chemical reactions in cold or ultracold conditions creates a demand for the accurate determination of both short and long-range interatomic potentials.[1,2] Classes of chemical compound that are particularly useful in studies of collision phenomena include alkali metal diatomics and alkali hydrides. The latter molecules as well as their cations also play an important role in the processes occurring in the atmospheres of planets, dwarf stars, and the interstellar medium, hence they are intensively studied by astrophysicists.[3] In the current work, focus is on a representative example of MeH molecules (Me—alkali metal atom); the sodium hydride NaH and its cation NaH^+. In Ref. 4 we developed a particularly useful method to study the process of breaking a single bond. Here we are going to apply this method to investigate a dissociation of the NaH molecule.

Generally, dissociation of the standard single bond is still not a trivial task. The ideal situation occurs when the closed shell molecule dissociates into closed shell fragments.[4,5] In such ideal cases, the restricted Hartree–Fock (RHF) reference function can be used for the whole range of interatomic distances. However, this is not generally the case for real chemical bonds. The conditions mentioned above may nevertheless be met in cases when we dissociate a double positive ion (in our case NaH^{2+}), instead of the neutral molecule or its ion (i.e., NaH, NaH^+). This can be done if we are able to describe the molecular ion or neutral molecule on the basis of the doubly ionized reference, on condition that the applied method is able to describe the system after attachment of one or two electrons to the reference in order to describe the original structure. Thus, the EA (electron attachment) and DEA (double electron attachment) strategies avoid use of the unrestricted Hartree–Fock (UHF) reference. The latter has well-known disadvantages connected with broken symmetry problems and difficulties in reaching convergent solutions around the critical geometries. Generally, the EA calculations can be illustratively written as: $AB \xrightarrow{\text{EA}} AB^-$ which in our case takes the form: $NaH^{2+} \xrightarrow{\text{EA}} NaH^+$. The same applies to the DEA scheme: generally $AB \xrightarrow{\text{DEA}}, AB^{2-}$, in our case $NaH^{2+} \xrightarrow{\text{DEA}} NaH$

In the framework of the coupled cluster (CC) method,[6–9] we can consider EA and DEA schemes formulated within Fock space (FS) theory.[4,10,11] This technique seems particularly suitable for the bond breaking problem owing to its size-extensivity which is crucial for the correct reproduction

of the atomic excitation energies in the dissociation limit. In our previous works, these methods were applied successfully to the alkali metal molecular ions and neutral molecules.[4,12–16] Contrary to previous studies of the alkali hydride cation NaH^+ and alkali hydride molecule NaH,[17–22] mostly based on the effective potential methods, in this work we apply the size-extensive FS-CC (1,0)(≡ EA-EOM-CC—equation of motion CC[23–28]) and FS-CC (2,0)[4] methods with all electrons correlated. These are all the *first principle* electron computational schemes capable of producing potential energy curves (PECs) and spectroscopic constants for the selected states of NaH and NaH^+. These approaches introduce no auxiliary parameters with basis sets of the order of several hundred functions which is impossible using the standard scheme via full configuration interaction (FCI). The standard computational scheme used in calculations of PECs for the alkali hydride molecules (or alkali hydride ions) relies on replacement of inner-shell electrons with effective or model potentials. In this manner the computational task is reduced to the two-electron problem (or one in case of alkali hydride ions). Thanks to the rigorous FS-CCSD (2,0) method, we were able, e.g., to reach an accuracy better than 0.01 eV both for the dissociation and adiabatic excitation energies for the Li_2 molecule.[12]

In Sections 2 and 3, we give a brief overview of the computational methods applied, with computed PECs and molecular constants for the eight lowest lying states of the NaH and NaH^+ systems.

2. Synopsis of the theory

Within the coupled cluster[6–9] formalism the reference wave function Ψ is obtained by an action of the exponential e^T:

$$\Psi = e^T \Phi_0 \tag{1}$$

where T is a cluster operator being a sum of operators responsible for the single (S) and double (D) excitations at the CCSD level used in this work, and Φ_0 is the reference function, i.e., a Slater determinant constructed from the RHF orbitals. Note that by the reference system in our calculations we understand the doubly ionized structure NaH^{2+} both RHF and CCSD solutions are obtained.

A principal idea of multireference approaches[10] is to solve the eigenvalue equation for the so-called effective Hamiltonian operator, $H_{eff} = PH\Omega P$:

$$H_{eff}\Psi^0 = E\Psi^0 \tag{2}$$

defined within a model space; P—projection operator; $\mathbf{\Omega}$—valence universal wave operator ($\mathbf{\Omega} = \{e^S\}P$, S—cluster operator); $\mathbf{\Psi}^0$—model function. The model space in the FS formalism[10,11,29] is obtained as a direct sum of the particular sectors $\widetilde{\mathcal{M}}^{(i,j)}$:

$$\mathcal{M}^{(k,l)} = \bigoplus_{i,j=0}^{i=k,\, j=l} \widetilde{\mathcal{M}}^{(i,j)} \tag{3}$$

Generally, the sector $\widetilde{\mathcal{M}}^{(i,j)}$ is a configurational subspace obtained by the creation of the i particles within the m_p active virtual orbitals and j holes within the m_h active occupied orbitals. The model space is defined by giving the top sector (k, l) and the sizes of the active particle (m_p) and active hole (m_h) spaces. For the double electron attached states, i.e., (2,0) sector, we have:

$$\mathcal{M}^{(2,0)} = \bigoplus_{i=0}^{i=2} \widetilde{\mathcal{M}}^{(i,0)} \tag{4}$$

Thus, in this case the active space is defined only by the number of active particle levels, so providing the number m_p (hereafter denoted by m) is enough to define the active space. The model space is spanned by the m^2 $\mathbf{\Phi}^{\alpha\beta}$ configurations obtained by distributing the two added electrons among the m valence levels in all possible ways.

The characteristic feature of the FS approach is the hierarchical structure of the CC solutions. Hence, in order to solve the FS equations for the (k, l) sector, all solutions for lower rank sectors (i, j) with $i \leq k$ and $j \leq l$ must be known. In the current case: (0,0) and (1,0) sectors. The (0,0) sector corresponds to the above mentioned single reference solution for the reference system, i.e., the NaH^{2+} ion. The (1,0) sector is spanned by the $\mathbf{\Phi}^{\alpha}$ configurations formed by placing an additional electron in one of the m valence levels.

Energy values of double electron attached states are obtained by the diagonalization of the H_{eff} within the $\mathbf{\Phi}^{\alpha\beta}$ configurational space:

$$H_{eff}^{(2,0)} = P^{(2,0)} He^{S^{(0,0)} + S^{(1,0)} + S^{(2,0)}} P^{(2,0)} \tag{5}$$

where $P^{(2,0)}$ is defined as:

$$P^{(2,0)} = \sum_{\alpha\beta} |\mathbf{\Phi}^{\alpha\beta}\rangle\langle\mathbf{\Phi}^{\alpha\beta}| \tag{6}$$

The $S^{(0,0)}(\equiv T)$, $S^{(1,0)}$, and $S^{(2,0)}$ are cluster operators. A given superscript indicates sector. Limiting the cluster expansion to double components, the (1,0) and (2,0) sector operators are expressed as:

$$S^{(1,0)} = S_1^{(1,0)} + S_2^{(1,0)} \tag{7}$$

$$S^{(2,0)} = S_2^{(2,0)} \tag{8}$$

The $S_1^{(2,0)}$ operator does not contribute in the above equation since it cannot be defined within the DEA formalism.

It should be explained that the solutions for the $S^{(1,0)}$ sector of the Fock space CC method[10] can be obtained using the EA-EOM-CC formalism,[11,24] i.e., the EOM scheme applied to the single electron attached states.[30,31] It is well known that the eigenvalues obtained with the EA-EOM-CC scheme are identical to those of FS-CC (1,0) for the principal electron affinities.

In general, the FS-CC equations do not very readily converge, due to intruder state problems when using the standard approach, i.e., via the effective Hamiltonian formalism. The remedy for this is the intermediate Hamiltonian (IH)[30,32–34] formulation of the FS-CC method. In this formalism the iterative solving of the FS equations is replaced with a diagonalization of the IH matrix. In case of EA, i.e., (1,0) sector, the IH matrix is just $\overline{H}(\equiv e^{-T}He^{T})$.[30,31] Hence, the EA-EOM-CC is preferred in most cases for one-valence sectors. Results, in their vast majority were obtained with the EA-EOM-CCSD (S = singles, D = doubles) model but exceptionally we are also applying the more advanced model, i.e., full EA-EOM-CCSDT (T = triples). It means solving the CC equations for the reference state at the CCSDT level and then solving the EA-EOM-CC equations, assuming that the $R(k)$ operator also includes the R_3 operator.

In order to omit similar (i.e., intruder state) problems in the (2,0) sector we also applied the IH strategy described in detail in a paper devoted to the FS-CCSD (2,0) method.[4] In this case DEA-EOM-CC and FS-CC (2,0) give different eigenvalues, but the IH formalism provides identical results to the standard H_{eff} based FS method.

3. Results and discussion

All calculations are done using the ACES2[35] package supplemented with the local version of the IH-FS-CCSD (2,0) and EA-EOM-CCSDT

modules.[24] The results are collected in Figs. 1–4 and in Tables 1–3. In all single and double electron attachment calculations the orbitals are obtained by the RHF solution for the NaH^{2+} system. We used the unANO-RCC+ basis set, i.e., uncontracted ANO-RCC[36] with two additional diffuse functions for *s*, *p*, *d* shells for Na[15] and uncontracted ANO-RCC for H in NaH calculations (denoted as unANO-RCC+). The NaH^{+} results appear to be more sensitive to the hydrogen basis set, and so to get satisfactory accuracy we added diffuse functions for the *s*, *p*, *d* shells for the H atom (acronym unANO-RCC++), using an even tempered scheme. In all cases the spherical harmonic polarization functions were used with all electrons correlated. The size of the basis set for NaH is 166 (unANO-RCC+) and 205 (unANO-RCC++) in case of NaH^{+}. The active space for the FS-CCSD (2,0) part has been set to $m = 49$ in size, (i.e., 49 lowest virtual orbitals have been selected as active). An additional increase in *m* does not significantly affect the results. Note that the resulting size of the main model space is equal to 2401, i.e., that many configurations span the subspace in which the effective Hamiltonian is to be diagonalized.

In Table 1 we compare the total energies of the NaH molecule at infinite interatomic distance (last column) with the sum of energies for the Na and H atoms. Note this gives identical results, since the FS-CCSD (2,0) method is size-extensive,[10,30] which is crucial for generating correct PECs. The atomic energies are important in the current calculations since for the size-extensive methods the energies of the electronic states should converge to the atomic values at infinite distance.

The respective spectroscopic constants (obtained with help of the LEVEL-8 program of Le Roy[37]) are collected in Tables 2 and 3. The computed constants are compared with other recent theoretical and/or experimental values,[17–22,38–44] wherever the latter are available.

Table 1 Energy of the electronic states [a.u.] at the dissociation limit of the NaH molecule compared to atomic energies in the unANO-RCC+ basis set.

Config. H	H energy	Config. Na	Na energy EA-EOM-CCSD	H+Na energy	NaH energy ($R=\infty$(200 Å)) IH-FS-CCSD(2,0)
1s	−0.499984	[Ne]3s	−162.143194	−162.643178	−162.643178
1s	−0.499984	[Ne]3p	−162.066494	−162.566478	−162.566478
1s	−0.499984	[Ne]4s	−162.026623	−162.526607	−162.526607

Table 2 Spectroscopic constants of NaH for eight lowest lying electronic states obtained using the IH-FS-CCSD (2,0) method in unANO-RCC+ basis set.

Sym.	R_e [Å]	D_e [cm^{-1}]	T_e [cm^{-1}]	ω_e [cm^{-1}]	$\omega_e x_e$ [cm^{-1}]	Ref.
$X^1\Sigma^+$	1.898	15594	–	1152.4	17.8	This work
	1.883	15502	–	1171.8		Theor.[17]
	1.888	15814	–	1175.3	20.2	Theor.[18]
	1.856	15489	–			Theor.[19]
	1.889	15785	–	1176.1	21.2	Exp.[38]
	1.887	15797	–			Exp.[40]
$1^3\Sigma^+$	6.263	4	15589			This work
	6.508	3				Theor.[17]
$2^1\Sigma^+$	3.194	10002	22426	317.3	−3.3	This work
	3.171	9993	22567	320.0		Theor.[17]
	3.152	10011				Theor.[19]
	3.194			317.6		Exp.[41]
	3.193	10041	22713			Exp.[40]
$2^3\Sigma^+$	9.398	1	32426			This work
	10.58	2				Theor.[17]
$1^1\Pi$	2.779	222	32205	170.6	34.4	This work
	2.804	121	32432			Theor.[17]
	2.775	226		182	42.8	Theor.[18]
$1^3\Pi$	2.375	1174	31283	438.4	41.3	This work
	2.380	1073	31480	430.3		Theor.[17]
	2.376	1140		431	42.8	Theor.[18]
$3^1\Sigma^+$ inner	2.378	634	40544			This work
	2.403	575	44951			Theor.[19]
$3^1\Sigma^+$ outer	6.288	6512	34666	209.4	1.3	This work
	6.281	6348	34859	213.9		Theor.[17]
	6.257	6391	35164	218.3		Exp.[43]
$3^3\Sigma^+$	2.481	1236	39942	394.8	45.2	This work

Table 3 Spectroscopic constants of NaH^+ for eight lowest lying electronic states obtained using the EOM-CC methods in unANO-RCC++ basis set.

Sym.	R_e [Å]	D_e [cm^{-1}]	T_e [cm^{-1}]	ω_e [cm^{-1}]	$\omega_e x_e$ [cm^{-1}]	Ref.
$X^2\Sigma^+$	2.588	644	–	285.1	32.6	EA-EOM-CCSD
	2.581	651	–	287.7	32.8	EA-EOM-CCSDT
	2.693	458	–	266.6	37.4	Theor.[20]
	2.593	496	–	266.7		Theor.[21]
	2.645	1008	–	451.7		Theor.[22]
$2^2\Sigma^+$	4.175	3760	65368	328.4	5.8	EA-EOM-CCSD
	4.170	3737	65292	328.1	5.8	EA-EOM-CCSDT
	4.185	3621	65113	321.2	7.6	Theor.[20]
	4.159	3712	65026	345		Theor.[21]
	4.127	3726	66476	346.8		Theor.[22]
$3^2\Sigma^+$	6.702	4670	78277	195.9	2.2	EA-EOM-CCSD
	6.687	4694	78260	196.3	2.2	EA-EOM-CCSDT
	6.689	4675	78077	196.1	1.8	Theor.[20]
	6.683	4725	78071	196.0		Theor.[21]
	6.879	3291	79413	185.5		Theor.[22]
$1^2\Pi$	4.554	886	82061	176.0	6.1	EA-EOM-CCSD
	4.548	897	82058	179.0	6.6	EA-EOM-CCSDT
	4.688	716	82040	156.3	10.4	Theor.[20]
	4.572	929	81870	169.9		Theor.[21]
$4^2\Sigma^+$	Repulsive					
$5^2\Sigma^+$	10.668	649	85313	77.0	2.7	EA-EOM-CCSD
	10.699	650	85052	76.6	4.8	Theor.[20]
	10.647	653	85104	75.9		Theor.[21]
$2^2\Pi$	Repulsive					
$6^2\Sigma^+$	12.421	1713	93000	89.7	0.7	EA-EOM-CCSD
	12.573	1804	92670	88.2	1.0	Theor.[20]
	12.541	1844	92659	92.3		Theor.[21]

3.1 NaH molecule

In Fig. 1 we show the PECs for all eight states of NaH divided into three groups each correlating to a different dissociation limit: $Na(3s) + H(1s)$ ($X^1\Sigma^+$, $1^3\Sigma^+$), $Na(3p) + H(1s)$ ($2^1\Sigma^+$, $2^3\Sigma^+$, $1^1\Pi$, $1^3\Pi$), $Na(4s) + H(1s)$ ($3^1\Sigma^+$, $3^3\Sigma^+$). In the cases where p atomic levels are involved some of the molecular states are degenerate, and so the total number of state eigenfunctions amounts to 10. All of them represent bound states, but in several cases the well depth is very small (e.g., two lowest triplet Σ states). In two cases we are able to compare the computed PECs with the experimental curves extracted from Ref. 45.

In Fig. 2 we have plotted the experimental $X^1\Sigma^+$ curve. We observe it coincides very well with that of the present work. Similarly, in the same figure we present the experimental curve corresponding to the $2^1\Sigma^+$ state, superimposed on its theoretical counterpart from the current work. The experimental points are available in a limited range only, but, as we can see, the respective parts overlap each other quite well. Note that the $3^1\Sigma^+$ state displays two potential wells: one, shallow, at the $R = 2.378$ Å and the second, deeper, at $R = 6.288$ Å.

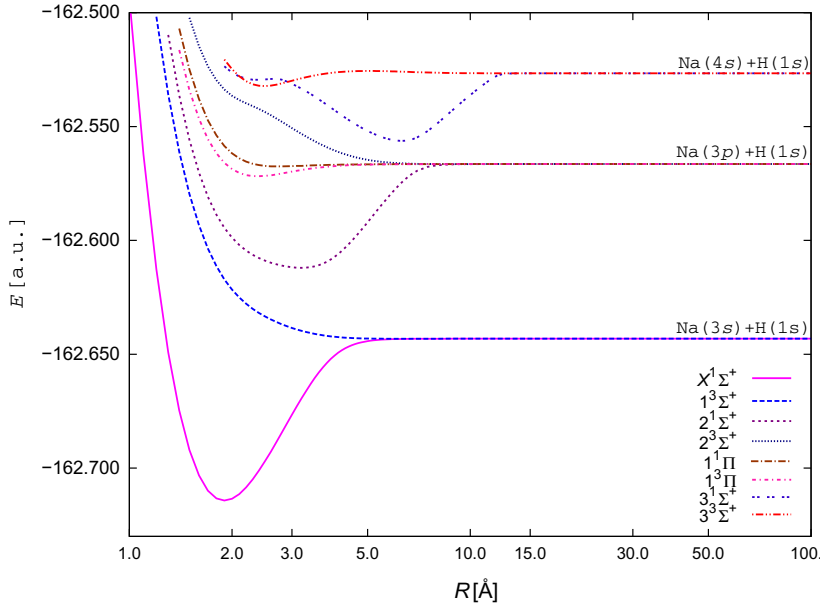

Fig. 1 Potential energy curves of the NaH molecule with the IH-FS-CCSD (2,0) method for the three lowest dissociation limits in the unANO-RCC+ basis set.

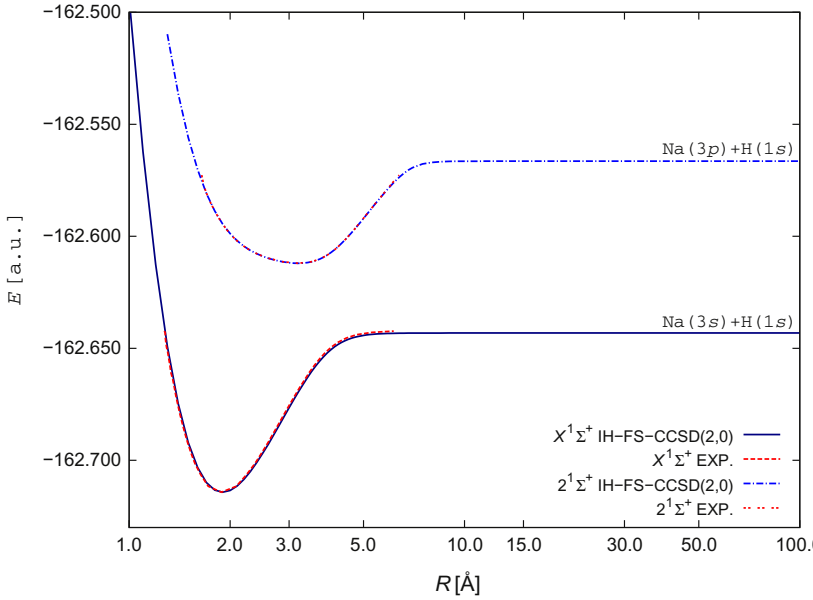

Fig. 2 Potential energy curves of the NaH molecule with the IH-FS-CCSD (2,0)/unANO-RCC+ method for the two states: - comparison with experiment.

The experimental data are only available for the singlet Σ states. The agreement with experiment of the computed molecular constants is quite satisfactory (see Table 2). For example, the deviations of theoretical dissociation energy values, D_e, from the experiment is ca. 200 cm^{-1} for the ground state, 40 cm^{-1} for the $2^1\Sigma^+$ and 120 cm^{-1} for the $3^1\Sigma^+$. The equilibrium bond length for two excited states, $2^1\Sigma^+$ and $3^1\Sigma^+$, differs from experiment by 0.001 and 0.031 Å, respectively. The experimental bond length in the second case is equal to 6.257 Å, which means that the error is below 0.5%. A reasonably good agreement is observed for the harmonic frequencies too. The computed values differ from available experimental values by 24, 0, and 9 cm^{-1} for the three states.

We can also compare our results with other theoretical studies.[17–19] In Table 2 we list the results obtained by Olson and Liu[17] with a limited CI approach, by Yang et al.[18] with the MRCI (multireference CI) approach, and by Khelifi[19] using the pseudopotential representing the inner shells and the full CI approach for two valence electrons. The most elaborate approach seems to be the MRCI scheme used in Ref. 18 applied only to three states: the ground $^1\Sigma^+$ state and the two lowest Π states. For both

excited Π states (experiment unavailable) the current results stay close to those of Ref. 18. The calculations based on the pseudopotential approach were obtained for a number of singlet Σ states out of which only the three lowest ones are studied in the current work. An interesting situation occurs for the $3^1\Sigma^+$ state for which our calculations indicate a double-well potential, while the pseudopotential-based data[18] report only one minimum corresponding to the inner well found in our work. On the other hand the results in Ref. 17 point to a single well, corresponding to the outer minimum found in the current work. It is worth noting that our computed constants concerning inner and outer wells remain very close to those reported in Refs. 18 and 17, respectively.

Test CISD calculations for the two-electron problem (all inner-shell electrons frozen). The results are not encouraging (see improvement, below). For example, the values for the equilibrium geometry for the states, $X^1\Sigma^+$, $2^1\Sigma^+$, and $3^1\Sigma^+$, differ from experiment by 0.035, 0.18, and 0.15 Å, whereas the current results are off by 0.01, 0.001, and 0.03 Å, respectively. Similar behavior is observed for the harmonic frequencies and excitation energies. This indicates that in the effective reduction of the entire electron problem to the valence one, the effective core potential is required.

3.2 NaH^+ cation

The NaH^{2+} reference has also been adopted in studies of the electronic states of the NaH^+ cation. In this case the EA-EOM-CC method (equivalent to the FS-CC-SD (1,0) approach) has been applied to recover the NaH^+ states from the di-cationic reference. For the five lowest energy states ($X^2\Sigma^+$, $2^2\Sigma^+$, $3^2\Sigma^+$, $1^2\Pi$, and $4^2\Sigma^+$), both the EA-EOM-CCSD and EA-EOM-CCSDT models were applied, while for the remaining three, $5^2\Sigma^+$, $2^2\Pi$, $6^2\Sigma^+$, only the simpler version (EA-EOM-CCSD) was used.

The PECs displayed in Fig. 3 correlate to six dissociation limits: $Na^+ + H(1s)$ ($X^2\Sigma^+$), $Na(3s) + H^+$ ($2^2\Sigma^+$), $Na^+ + H(2p)$ ($3^2\Sigma^+$, $1^2\Pi$), $Na^+ + H(2s)$ ($4^2\Sigma^+$), $Na(3p) + H^+$ ($5^2\Sigma^+$, $2^2\Pi$), and $Na(4s) + H^+$ ($6^2\Sigma^+$). Note that two of them, $Na^+ + H(2p)$ and $Na^+ + H(2s)$, for obvious reasons correspond to the same energy. The size-extensivity property of the applied computational scheme ensures the proper dissociation limits for each electronic state. Two of them, $4^2\Sigma^+$ and $2^2\Pi$, are repulsive, consistent with the results of other theoretical work.[20–22] It should be mentioned that some PECs shown in Fig. 4 are computed with the state-of-the-art EOM approach with full inclusion of the triple excitations both at the CC and EOM levels. As

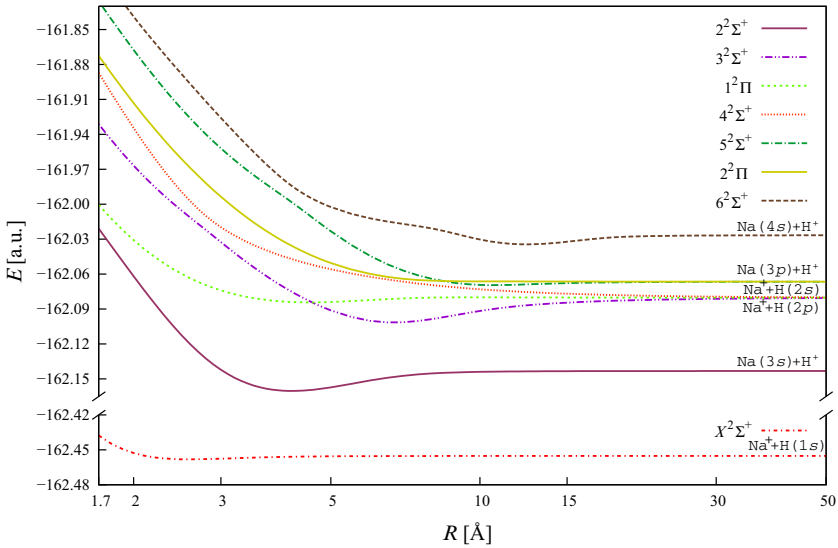

Fig. 3 Potential energy curves of the NaH^+ molecular ion with the EA-EOM-CCSD method for the six lowest dissociation limits in the unANO-RCC++ basis set.

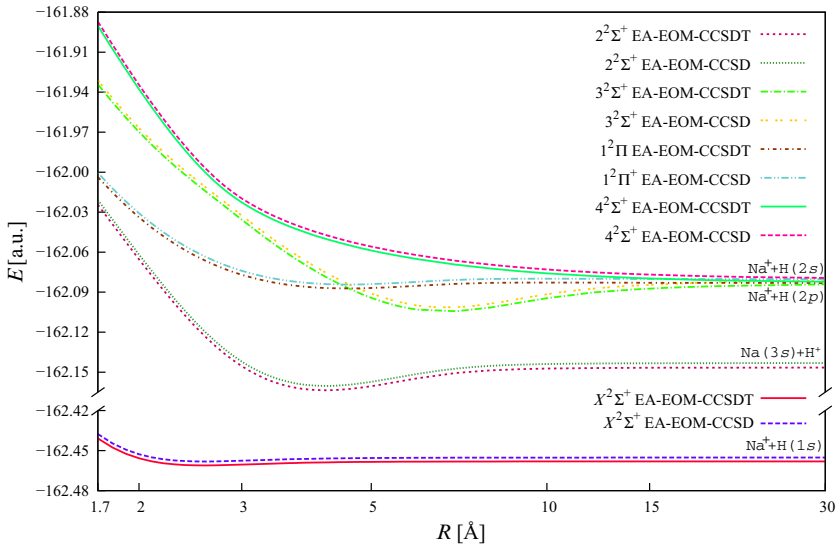

Fig. 4 Potential energy curves of the NaH^+ molecular ion with the EA-EOM-CCSD and EA-EOM-CCSDT methods for the four lowest dissociation limits in the unANO-RCC++ basis set.

observed, the two curves (CCSD and CCSDT) stay parallel in each considered state, hence qualitatively the PECs are very similar to each other at both levels of approximation.

In Table 3 we present the spectroscopic constants obtained in the current work. Since the experimental data are unavailable, we compare them with other theoretical works.[20–22] As mentioned in the introduction, the standard computational approach for cations of the alkali metals diatomics and alkali metal hydrides relies on reducing the n-electron problem to the single valence electron. That method was used in Refs. 20 and 22 whereas in Ref. 21 the MRCI scheme was applied, limited to the single and double excitations with frozen sodium 1s electrons. The inclusion of full triples allows us to estimate the role of more advanced correlation effects. Generally, the inclusion of the full triples operator reduces the optimum bond length—on average—by ca. 0.008 Å and increases the D_e value by 16 cm^{-1} with negligible effect on the harmonic and anharmonic frequencies.

Results presented here are much closer to those obtained via pseudopotential-based calculations. This can be seen for the ground state D_e values, where the difference between the current results and those based on the pseudopotential is between 150 and 200 cm^{-1} [20,22] with over 360 m^{-1} difference for the MRCI.[21] A large discrepancy occurs for the D_e values for the $3^2\Sigma^+$ state (20–30 cm^{-1} [20,22] compared to 1400 cm^{-1} [21]). Similar behavior is observed for the T_e values with the differences not exceeding 200 cm^{-1} for the pseudopotential results and over 1000 cm^{-1} for the MRCI ones.

4. Conclusions

First principle quantum chemical methods are applied in the theoretical study of the PECs and spectroscopic constants of the eight lowest lying electronic states of the NaH molecule and its cation. Computational strategy used here relies on the adoption of the NaH^{2+} dication as a reference, which dissociates into a proton and a closed shell Na^+ cation. Because of this, a convenient RHF approach could be used in the whole range of interatomic distances. At the correlated level the FS-CCSD (2,0) scheme is used which provides results pertinent to the neutral NaH molecule at each point. The adopted approach treating the dissociation process exclusively in terms of the closed shell calculations generates smooth PECs demonstrating correct size-extensive asymptotic properties. The comparison of the theoretical and experimental PECs displayed in Fig. 2 indicates the full compatibility of the theoretical and experimental data. It should be mentioned that this work

shows for the first time the double-minimum character of the $3^1\Sigma^+$ curve, whereas the previous papers report a single minimum, corresponding either to our inner or outer minima, respectively.

The electronic states of the NaH^+ cation are recovered by applying the EA-EOM-CC (equivalent to the (1,0) sector of the FS-MRCC) scheme to the NaH^{2+} reference. Two CC models were considered: standard, CCSD, and extended; CCSDT, with full inclusion of triple excitations. Resulting curves show correct asymptotic behavior and due to closed shell reference, the solutions are readily obtained, even for long interatomic distances.

The results obtained agree well with theoretical values available in the literature and with experimental data. The reported data bring a new insight into the possibility of using all electron ab initio calculations to study the nature of chemical bonds without limitation to one- or two-electron approximations.

References

1. Jones, K. M.; Tiesinga, E.; Lett, P. D.; Julienne, P. S. Ultracold Photoassociation Spectroscopy: Long-range Molecules and Atomic Scattering. *Rev. Mod. Phys.* **2006**, *78*, 483.
2. Tomza, M.; Goerz, M. H.; Musiał, M.; Moszynski, R.; Koch, C. P. Optimized Production of Ultracold Ground-State Molecules: Stabilization Employing Potentials With Ion-Pair Character and Strong Spin-Orbit Coupling. *Phys. Rev. A* **2012**, *86*, 043424.
3. Levine, J. S. *The Photochemistry of Atmospheres, Earth, the Other Planets and Comets, Ed.* New York: Academic Press, 1985.
4. Musiał, M. Multireference Fock Space Coupled Cluster Method in the Effective and Intermediate Hamiltonian Formulation for the (2,0) Sector. *J. Chem. Phys.* **2012**, *136*, 134111.
5. Musiał, M.; Kucharski, S. A.; Bartlett, R. J. Multireference Double Electron Attached Coupled Cluster Method with Full Inclusion of the Connected Triple Excitations: MR-DA-CCSDT. *J. Chem. Theory Comput.* **2011**, 7, 3088.
6. Čizek, J. On the Correlation Problem in Atomic and Molecular Systems. Calculation of Wavefunction Components in Ursell-Type Expansion Using Quantum-Field Theoretical Methods. *J. Chem. Phys.* **1966**, *45*, 4256; Paldus, J.; Čizek, J.; Shavitt, I. Correlation Problems in Atomic and Molecular Systems. IV. Extended Coupled-Pair Many-Electron Theory and Its Application to the BH_3. *Molecule, Phys. Rev. A* **1972**, *5*, 50.
7. Bartlett, R. J. Coupled-Cluster Approach to Molecular Structure and Spectra: A Step toward Predictive Quantum Chemistry. *J. Phys. Chem.* **1989**, *93*, 1697; Bartlett, R. J.; Stanton, J. F. In Lipkowitz, K. B., Boyd, D. B., Eds.; Reviews in Computational Chemistry; VCH Publishers: New York, 1994; Vol. 5; p 65.
8. Paldus, J.; Li, X. A Critical Assessment of Coupled Cluster Method in Quantum Chemistry. *Adv. Chem. Phys.* **1999**, *110*, 1.
9. Bartlett, R. J.; Musiał, M. Coupled-Cluster Theory in Quantum Chemistry. *Rev. Mod. Phys.* **2007**, *79*, 291.
10. Lyakh, D. I.; Musiał, M.; Lotrich, V.; Bartlett, R. J. Multireference Nature of Chemistry: The Coupled-Cluster View. *Chem. Rev.* **2012**, *112*, 182.

11. Musiał, M.; Bartlett, R. J. Fock Space Multireference Coupled Cluster Method With Full Inclusion of Connected Triples for Excitation Energies. *J. Chem. Phys.* **2004**, *121*, 1670.
12. Musiał, M.; Kucharski, S. A. First Principle Calculations of the Potential Energy Curves for Electronic States of the Lithium Dimer. *J. Chem. Theory Comput.* **2014**, *10*, 1200.
13. Tomza, M.; Skomorowski, W.; Musiał, M.; Gonzales-Ferez, R.; Koch, C. P.; Moszynski, R. Interatomic Potentials, Electric Properties, and Spectroscopy of the Ground and Excited States of the Rb_2 Molecule: Ab Initio Calculations and Effects of a Non-Resonant Field. *Mol. Phys.* **2013**, *111*, 1781.
14. Musiał, M.; Kowalska-Szojda, K.; Lyakh, D. I.; Bartlett, R. J. Potential Energy Curves Via Double Electron Affinity Calculations: Dissociation of Alkali Metal Dimers. *J. Chem. Phys.* **2013**, *138*, 194553.
15. Bewicz, A.; Musiał, M.; Kucharski, S. A. Potential Energy Curves of the Na_2^+ Molecular Ion From All Electron Ab Initio Relativistic Calculations. *Mol. Phys.* **2017**, *115*, 2649.
16. Skupin, P.; Musiał, M.; Kucharski, S. A. Potential Energy Curves for the Low-Lying Electronic States of K_2^+ From Ab Initio Calculations With All Electrons Correlated. *J. Phys. Chem. A* **2017**, *121*, 1480.
17. Olson, R. E.; Liu, B. Interaction Energies for Low-Lying Electronic States of NaH and NaH^-: Scattering of H^- by Alkali Atoms. *J. Chem. Phys.* **1980**, *73*, 2817.
18. Yang, C. L.; Zhang, X.; Han, K. L. Analytical Potential Energy Function and Spectroscopic Parameters for the Ground and Excited States of NaH. *J. Mol. Struc.* **2004**, *676*, 209.
19. Khelifi, N. Theoretical Study of $^1\Sigma^+$ States of Alkali Hydride Xh Molecule (X = Na, K and Rb) in Adiabatic and Nonadiabatic Representations. *J. Phys. Chem. A* **2009**, *113*, 8425.
20. Berriche, H. One-Electron Pseudopotential Study of the Alkali Hydride Cation NaH^+: Structure, Spectroscopy, Transition Dipole Moments, and Radiative Lifetimes. *Int. J. Quantum Chem.* **2013**, *113*, 1003.
21. Magnier, S. Theoretical Description of the Electronic Structure of the Alkali Hydride Cation NaH^+. *J. Phys. Chem. A* **2005**, *109*, 5411.
22. Yan, L.; Qu, Y.; Liu, C.; Wang, J.; Buenker, R. J. Ab Initio Many-Electron Study for the Low-Lying States of the Alkali Hydride Cations in the Adiabatic Representation. *J. Chem. Phys.* **2012**, *136*, 124304.
23. Nooijen, M.; Bartlett, R. J. Equation of Motion Coupled Cluster Method for Electron Attachment. *J. Chem. Phys.* **1995**, *102*, 3629.
24. Musiał, M.; Bartlett, R. J. Equation-of-Motion Coupled Cluster Method With Full Inclusion of Connected Triple Excitations for Electron-Attached States: EA-EOM-CCSDT. *J. Chem. Phys.* **2003**, *119*, 1901.
25. Krylov, A. I. Equation-of-Motion Coupled-Cluster Methods for Open-Shell and Electronically Excited Species: The Hitchhiker's Guide to Fock Space. *Annu Rev. Phys. Chem.* **2008**, *59*, 433.
26. Kamiya, M.; Hirata, S. Higher-Order Equation-of-Motion Coupled-Cluster Methods for Electron Attachment. *J. Chem. Phys.* **2007**, *126*, 134112.
27. Gour, J. R.; Piecuch, P. Efficient Formulation and Computer Implementation of the Active-Space Electron-Attached and Ionized Equation-of-Motion Coupled-Cluster Methods. *J. Chem. Phys.* **2006**, *125*, 234107.
28. Musiał, M. The Excited, Ionized and Electron Attached States Within the EOM-CC Approach With Full Inclusion of Connected Triple Excitations. *Mol. Phys.* **2010**, *108*, 2921.
29. Mukherjee, D.; Pal, S. Use of Cluster-Expansion Methods in the Open-Shell Correlation-Problem. *Adv. Quantum Chem.* **1989**, *20*, 292; Lindgren I.; Mukherjee, D. On the Connectivity Criteria in the Open-Shell Coupled-Cluster Theory for General Model Spaces. Phys. Rep. **1987**, *151*, 93; Pal, S. Fock Space Multi-reference Coupled-Cluster Method for Energies and Energy Derivatives. Mol. Phys. **2010**, *108*, 3033.

30. Meissner, L. Fock-Space Coupled-Cluster Method in the Intermediate Hamiltonian Formulation: Model With Singles and Doubles. *J. Chem. Phys.* **1998**, *108*, 9227.
31. Musiał, M.; Bartlett, R. J. Multireference Fock-Space Coupled-Cluster and Equation-of-Motion Coupled-Cluster Theories: The Detailed Interconnections. *J. Chem. Phys.* **2008**, *129*, 134105; Musiał, M.; Bartlett, R. J. Charge-Transfer Separability and Size-Extensivity in the Equation-of-Motion Coupled Cluster Method: EOM-CCx. J. Chem. Phys. **2011**, 134, 034106.
32. Musiał, M.; Meissner, L.; Kucharski, S. A.; Bartlett, R. J. Molecular Applications of Intermediate Hamiltonian Fock-Space Coupled-Cluster Method for Calculation of Excitation Energies. *J. Chem. Phys.* **2005**, *122*, 224110; Musiał, M.; Meissner, L. The Fock-Space Coupled-Cluster Method in the Calculation of Excited State Properties. *Collect. Czech. Chem. Commun.* **2005**, *70*, 811.
33. Meissner, L.; Malinowski, P. Intermediate Hamiltonian Formulation of the Valence-Universal Coupled-Cluster Method for Atoms. *Phys. Rev. A* **2000**, *61*, 062510.
34. Musiał, M.; Bartlett, R. J. Intermediate Hamiltonian Fock-Space Multireference Coupled-Cluster Method With Full Triples for Calculation of Excitation Energies. *J. Chem. Phys.* **2008**, *129*, 044101; Musiał, M. Benchmark Calculations of the Fock-Space Coupled Cluster Single, Double, Triple Excitation Method in the Intermediate Hamiltonian Formulation for Electronic Excitation Energies. *Chem. Phys. Lett.* **2008**, *457*, 267; Musiał, M.; Bartlett, R. J. Spin-Free Intermediate Hamiltonian Fock-Space Coupled-Cluster Theory With Full Inclusion of Triple Excitations for Restricted Hartree-Fock Based Triplet States. *J. Chem. Phys.* **2008**, *129*, 244111; Musiał, M.; Bartlett, R. J. Multi-reference Fock Space Coupled-Cluster Method in the Intermediate Hamiltonian Formulation for Potential Energy Surfaces. *J. Chem. Phys.* **2011**, 135, 044121.
35. ACES II program is a product of the Quantum Theory Project, University of Florida Authors: Stanton, J. F.; Gauss, J.; Watts, J. D.; Nooijen, M.; Oliphant, N.; Perera, S. A.; Szalay, P. G.; Lauderdale, W. J.; Kucharski, S. A.; Gwaltney, S. R.; Beck, S.; Balková A.; Musiał, M.; Bernholdt, D. E.; Baeck, K.-K.; Sekino, H.; Rozyczko, P.; Huber, C.; Bartlett, R. J.; Integral Packages Included are VMOL (Almlöf, J.; Taylor, P.); VPROPS (Taylor, P. R.); A modified version of ABACUS integral derivative package (Helgaker, T. U.; Jensen, H. J. Aa.; Olsen, J.; Jørgensen, P.; Taylor, P.R.).
36. Roos, B. O.; Veryazov, V.; Widmark, P. O. Relativistic Atomic Natural Orbital Type Basis Sets for the Alkaline and Alkaline-Earth Atoms Applied to the Ground-State Potentials for the Corresponding Dimer. *Theor. Chem. Acc.* **2004**, *111*, 345.
37. Roy, R. J. L.*LEVEL 8.0: A Computer Program for Solving the Radial Schrödinger Equation for Bound and Quasibound Levels*. See http://leroy.uwaterloo.ca/programs/.
38. Giroud, M.; Nedelec, O. Spectroscopy of the NaH, NaD, KH, and KD $X^1\Sigma^+$ Ground State by Laser Excited Fluorescence in a High Frequency Discharge. *J. Chem. Phys.* **1980**, *73*, 4151.
39. Huang, H. Y.; Lu, T. L.; Whang, T. J.; Chang, Y. Y.; Tsai, C. C. Dissociation Energy of the Ground State of NaH. *J. Phys. Chem.* **2010**, *133*, 044301.
40. Walji, S. D.; Sentjens, K. M.; Le Roy, R. J. Dissociation Energies and Potential Energy Functions for the Ground $X^1\Sigma^+$ and Avoided-Crossing $A^1\Sigma^+$ States of NaH. *J. Phys. Chem.* **2015**, *142*, 044305.
41. Orth, F. B.; Stwalley, W. C.; Yang, S. C.; Hsieh, Y. K. New Spectroscopic Analyses and Potential Energy Curves for the $X^1\Sigma^+$ and $A^1\Sigma^+$ States of NaH. *J. Mol. Spectrosc.* **1980**, *79*, 314.
42. Stwalley, W. C.; Zemke, W. T.; Yang, S. C. Spectroscopy and Structure of Alkali Hydride Diatomic Molecules and Their Ions. *J. Phys. Chem. Ref. Data No. 1* **1991**, *20*, 153.

43. Huang, H. Y.; Chang, Y. Y.; Liao, M. H.; Wua, K. L.; Lu, T. L.; Chang, Y. Y.; Tsai, C. C.; Whang, T. J. Characterization of the Outer Well of NaH $C^1\Sigma^+$ State by Fluorescence Depletion Spectroscopy. *Chem. Phys. Lett.* **2010**, *493*, 53.
44. Stwalley, W. C.; Zemke, W. T.; Yang, S. C. Spectroscopy and Structure of Alkali Hydride Diatomic Molecules and Their Ions. *J. Phys. Chem. Ref. Data No. 1* **1991**, *20*, 153.
45. Maki, A. G.; Olson, W. B. Infrared Spectrum of Sodium Hydride. *J. Chem. Phys.* **1989**, *90*, 6887; Orth, F. B.; Stwalley, W. C.; Yang, S. C.; Hsieh, Y. K. New Spectroscopic Analyses and Potential Energy Curves for the $X^1\Sigma^+$ and $A^1\Sigma^+$ States of NaH. J. Mol. Spectrosc. **1980**, 79, 314.

This page intentionally left blank

SECTION 4

Excited states and other applications

This section begins with two correlated excited state approaches (Coriani et al. and Faraji et al.), density descriptors are then presented by Etienne et al., followed by a Quantum Monte Carlo application to surface reactions (Sharma and Hoggan) and a study of the H atom, released from confinement (Sarsa et al.)

This page intentionally left blank

CHAPTER ELEVEN

An analysis of the performance of coupled cluster methods for K-edge core excitations and ionizations using standard basis sets

Johanna P. Carbone[a], Lan Cheng[b], Rolf H. Myhre[c], Devin Matthews[d], Henrik Koch[c,e], Sonia Coriani[f,*]

[a]Dipartimento di Scienze Chimiche e Farmaceutiche, Università degli Studi di Trieste, Trieste, Italy
[b]Department of Chemistry, Krieger School of Arts and Sciences, Johns Hopkins University, Baltimore, MD, United States
[c]Department of Chemistry, Norwegian University of Science and Technology, Trondheim, Norway
[d]Department of Chemistry, Southern Methodist University, Dallas, TX, United States
[e]Scuola Normale Superiore, Pisa, Italy
[f]Department of Chemistry, Technical University of Denmark, Kongens Lyngby, Denmark
*Corresponding author: e-mail address: soco@kemi.dtu.dk

Contents

Abstract

An extensive analysis has been carried out of the performance of standard families of basis sets with the hierarchy of coupled cluster methods CC2, CCSD, CC3, and CCSDT in computing selected Oxygen, Carbon, and Nitrogen K-edge (vertical) core excitation and ionization energies within a core-valence separated scheme in the molecules water, ammonia, and carbon monoxide. Complete basis set limits for the excitation energies have been estimated via different basis set extrapolation schemes. The importance of scalar relativistic effects has been established within the spin-free exact two-component theory in its one-electron variant (SFX2C-1e).

Advances in Quantum Chemistry, Volume 79
ISSN 0065-3276
https://doi.org/10.1016/bs.aiq.2019.05.005

1. Introduction

Core-level spectroscopy, including techniques such as near-edge absorption fine structure and X-ray photoelectron spectroscopies, is widely used in various areas of contemporary research, such as in surface science, organic electronics, and medical biological research.[1] It is considered a powerful tool to gain insight into the electronic structure of molecular species. The recent improvements of the synchrotron radiation sources and the emergence of the free-electron laser have further broadened the range of phenomena and systems that can be studied by core-level spectroscopy, see e.g., Refs. 1–9.

An essential requirement for a successful application of core-level techniques is the availability of reliable computational methods that allow for a proper interpretation of the resulting spectra. Several quantum chemical approaches exist for the calculation of core-excited/ionized states. While referring to Ref. 10 for a recent review, we mention here as examples the symmetry-adapted cluster configuration interaction (SAC-CI),[11] the GW approximation (self-energy approximated by Green-function G and screened Coulomb W) to the Bethe–Salpeter equation,[12,13] the static-exchange (STEX) approach,[14] and the restricted and unrestricted algebraic diagrammatic construction scheme (ADC)[15–18] up to third order exploiting the core–valence separation (CVS)[19] approximation. Large systems are often treated with time-dependent density functional theory (TD-DFT),[20–26] but the results are plagued by the self-interaction error and the arbitrary dependence on the choice of the exchange-correlation functional. Indeed, unless short-range corrected hybrid functionals are used,[27] core-excited states calculated by TD-DFT with conventional functionals often reproduce experimental spectra qualitatively well, but the self-interaction error and the small gap between occupied and unoccupied electronic levels inherent in the TD-DFT formalism lead to underestimation of core-excited states. Therefore absolute core excitation energies obtained by conventional TD-DFT are typically corrected by shifting them tens of eVs in order to agree with experiment. Among the time-independent DFT-based approaches for core excitations, we mention the recently proposed, and remarkably accurate, variational orthogonality constrained density functional theory method of Evangelista and coworkers,[28,29] see also the work of Glushkov, Assfeld and coworkers on orthogonality constrained/local Hartree–Hock Self-Consistent-Field.[30–33]

Over the last decade, we have made a significant effort to extend the applicability of the coupled cluster linear response (CC-LR)[34,35] and equation-of-motion coupled cluster (EOM-CC)[36–38] formalisms to the

computation of core-level spectroscopies.[6,39–50] The CC ansatz is known to provide a systematic hierarchy of models with increasing accuracy, allowing for the prediction of molecular properties and spectra with controlled accuracy within the hierarchy.[35,51,52]

With the introduction in 2015 of CVS and restricted-excitation-window schemes within CC-LR and EOM-CC,[43,44,53] the use of CC methods for the determination of core-absorption spectra and core ionization energies has become as straightforward as it is for UV–vis excitations. Since the computational determination of spectroscopic observables related to the interaction of the sample with X-ray radiation displays strong dependence on the level of theory and size of the basis sets, a systematic approach becomes particularly attractive. An important component to this end is a rigorous assessment of the basis set requirements and the relative accuracy of the various CC approximations, when computing core spectra using the different members of the CC(-LR) hierarchy. This study is meant as a contribution in this direction, in the spirit of a similar study conducted within the ADC formalism.[18]

2. Methodology and computational details

Calculations of core excitation energies, oscillator strengths (in length gauge) and ionization energies (IE) have been performed for the hierarchy of CC methods: coupled cluster singles and approximate doubles (CC2), coupled cluster singles and doubles (CCSD), coupled cluster singles, doubles and approximate triples (CC3), and coupled cluster singles, doubles and triples (CCSDT). All methods are extensively described in the literature, see e.g., Refs. 54–60, and we refrain therefore from repeating their derivation here. We limit ourselves to draw the reader's attention to Ref. 43 for the description of how the core-valence separation scheme used here has been implemented within CC-LR/CC-EOM, to Ref. 61 for a new, more efficient, implementation of CC3, and to Refs. 62 and 63 for efficient implementation of the CCSDT method. Scalar-relativistic effects have been taken into account in CCSDT using the spin-free exact two-component theory in its one-electron variant (SFX2C-1e).[64–66]

All calculations up to CC3 have been run with a development version of the Dalton code,[67] whereas the CFOUR[68] code was used for the CCSDT core excitation and ionization energies, respectively. Accurate experimental equilibrium geometries were adopted for all three systems: R_e (CO) = 1.12832 Å for CO; R_e (NH) = 1.011 Å and $\alpha_{\mathrm{HNH}} = 106.7°$ for ammonia; R_e (OH) = 0.9570 Å and $\alpha_{\mathrm{HOH}} = 104.5°$ for water.

3. Results and discussion

3.1 Excitation energies

We start our discussion with a detailed comparison of the computed excitation energy values using the different basis sets across the CC hierarchy and with respect to the experimentally derived values. To this end, we plot in Figs. 1–4 the trends within each basis set family and method for the considered excitation energies. We will focus our discussion primarily on core excitations that are individually resolved in the experimental spectra: the $1s \rightarrow 3s$ (a_1) and $1s \rightarrow 3p$ (b_2) transitions in water, the $1s \rightarrow \pi^*$ transition for both C and O of CO, and the first three core excitations in NH_3. The third intense peak in the X-ray absorption spectrum of H_2O is known to originate from the overlap of core transition into a_1 and b_1 states and will be commented upon in Section 3.3. The full set of numerical values of the core excitation energies is available on arXiv.[69]

Within each series of correlation consistent (cc) basis sets (regular, single augmented and double augmented), we observe an almost monotonically decreasing trend (toward the experimental value) while increasing the basis set cardinal number.

In the cc-pVDZ basis, the excitation energies are always overestimated, by 2–5 eV depending on the case, with respect to both the other members of the series and the experimental values. By further increasing the cardinal number, the differences within each series reduce to tenths or hundredths of an eV. In other words, any Dunning set of $X \geq 3$ is reasonably accurate, and the results are significantly improved by inclusion of the first level of augmentation. Double augmentation has moderate effects for the chosen core excitations.

For the $1s \rightarrow 3s(a_1)$ in water, for instance, the differences between the CCSD results obtained for $X = 2$ (DZ) and $X = 3$ (TZ) in the series cc-pVXZ are always of the order of 3 eV, and slightly lower than 2 eV for the cc-pCVXZ series, progressively reducing to tenths and hundredths of an eV when increasing X. With reference to the experimental value for the same excitation, the basis sets with $X = 2$ overestimate the edge by ca. 3.5–4.5 eV (depending on the basis); for $X \geq 3$, the deviation is reduced to ca. 1.0–1.2 eV for the (x-aug-)cc-pVXZ sets, and to ca. 1.5–1.7 eV for the (singly and doubly augmented) cc-pCVXZ sets.

The trend observed for the first excitation is roughly the same also for the second one. However, for the third and fourth core excitations of water (third peak in the experimental spectrum), as well as any higher lying excitations

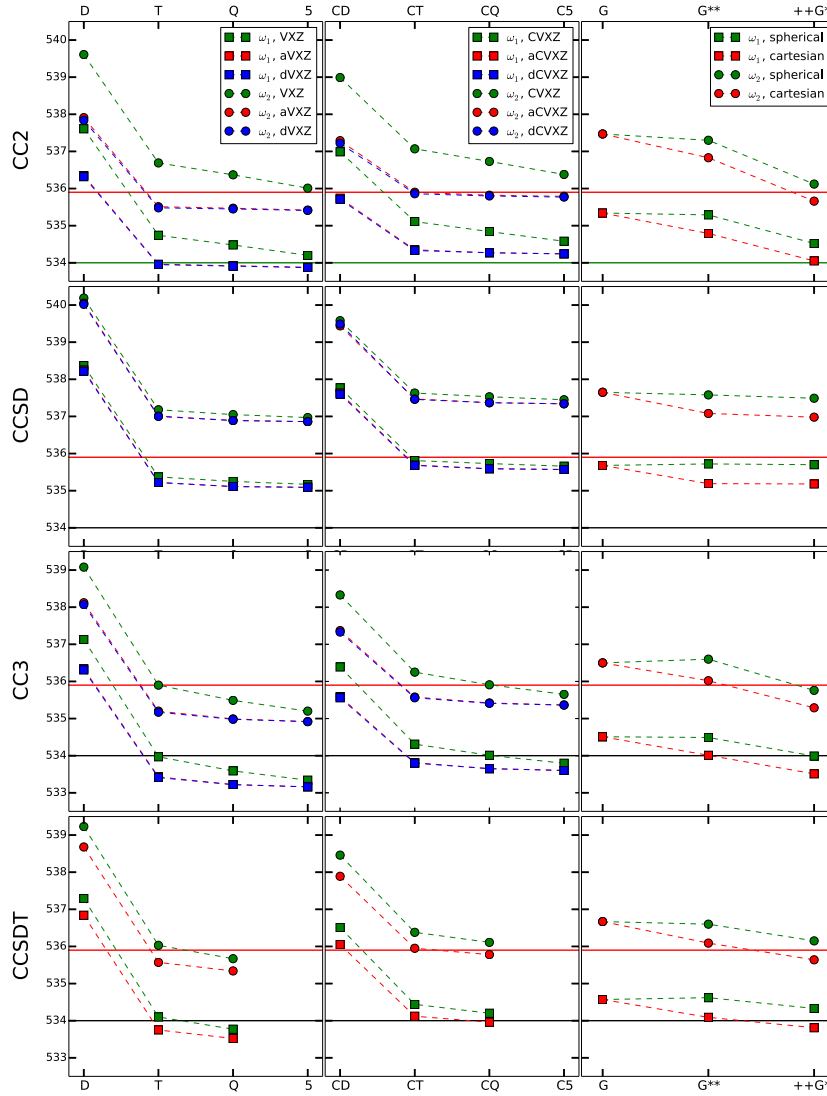

Fig. 1 H_2O, Oxygen K-edge. Basis set convergence of the first two vertical core excitation energies with different CC methods and basis sets. The horizontal green line indicates the experimental ω_1 value and the red line the experimental ω_2 value.

of more diffuse/Rydberg character than those considered here, it becomes of paramount importance to include additional diffuse functions.[39,47,50]

Among the Pople basis sets, the 6-311++G** set emerges as remarkably accurate in basically all cases (states and methods) despite its moderate size, as

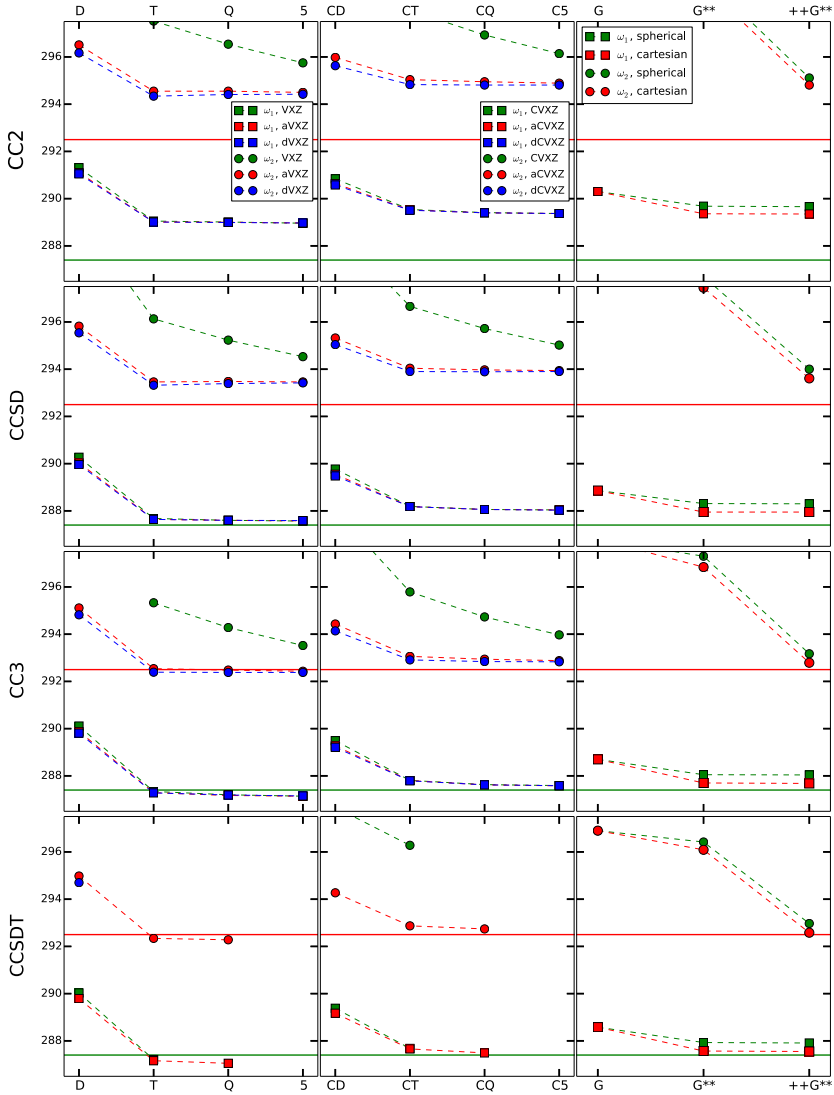

Fig. 2 CO, Carbon K-edge. Basis set convergence of the first two vertical core excitation energies with different CC methods and basis sets. The horizontal green line indicates the experimental ω_1 value and the red line indicates the experimental ω_2 value.

also previously observed for the ADC family of methods.[17] Use of Cartesian *d* functions is to be slightly preferred.

The CCSD model systematically overestimates all core excitation energies (roughly of the same amount for all excitations), allowing for a "rigid–shift" correction. The CC2 core excitation energies tend to be smaller than the CCSD ones, and they can be both red-shifted and blue-shifted compared

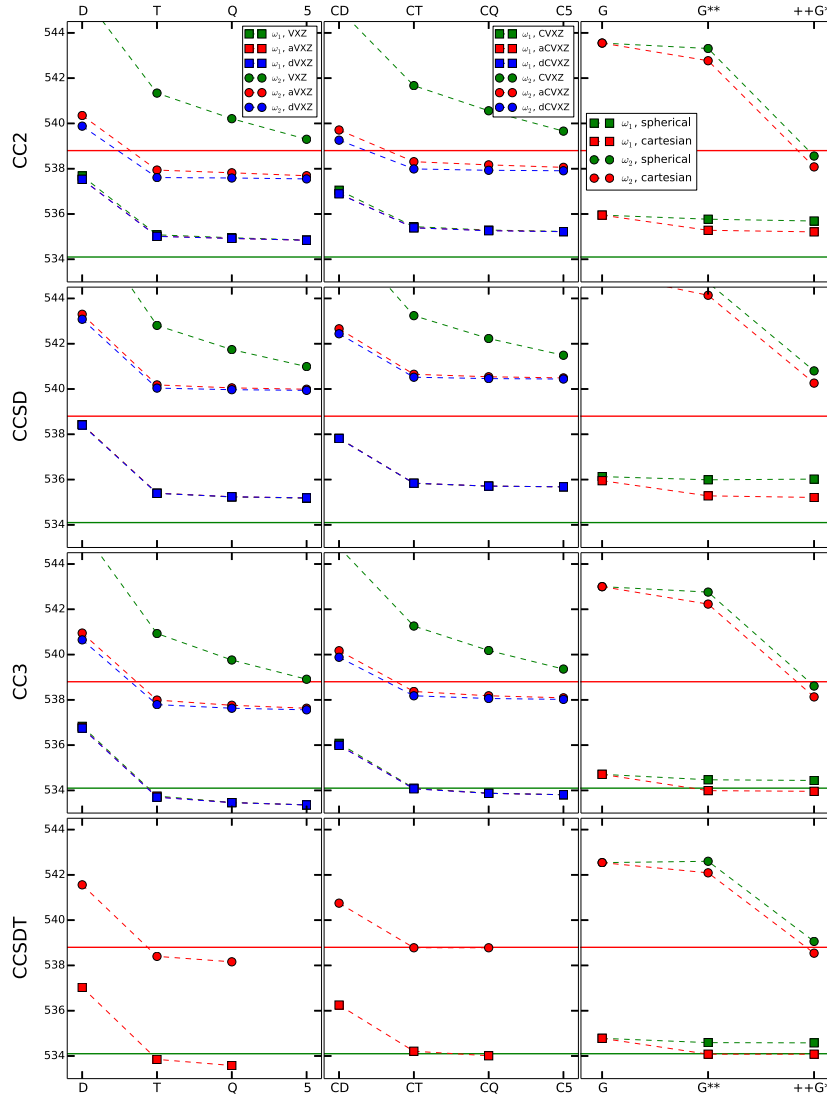

Fig. 3 CO, Oxygen K-edge. Basis set convergence of the first two vertical core excitation energies with different CC methods and basis sets. The horizontal green line indicates the experimental ω_1 value and the red line indicates the experimental ω_2 value.

to their experimental counterparts. For the first excitation, they are, at first sight, also closer to the experimental value, but the peak separation is underestimated. As we will see in Section 3.3, this, together with the results for intensities, actually results in a poor comparison of the CC2 spectral profile with the experimental one, at least for the three systems considered here.

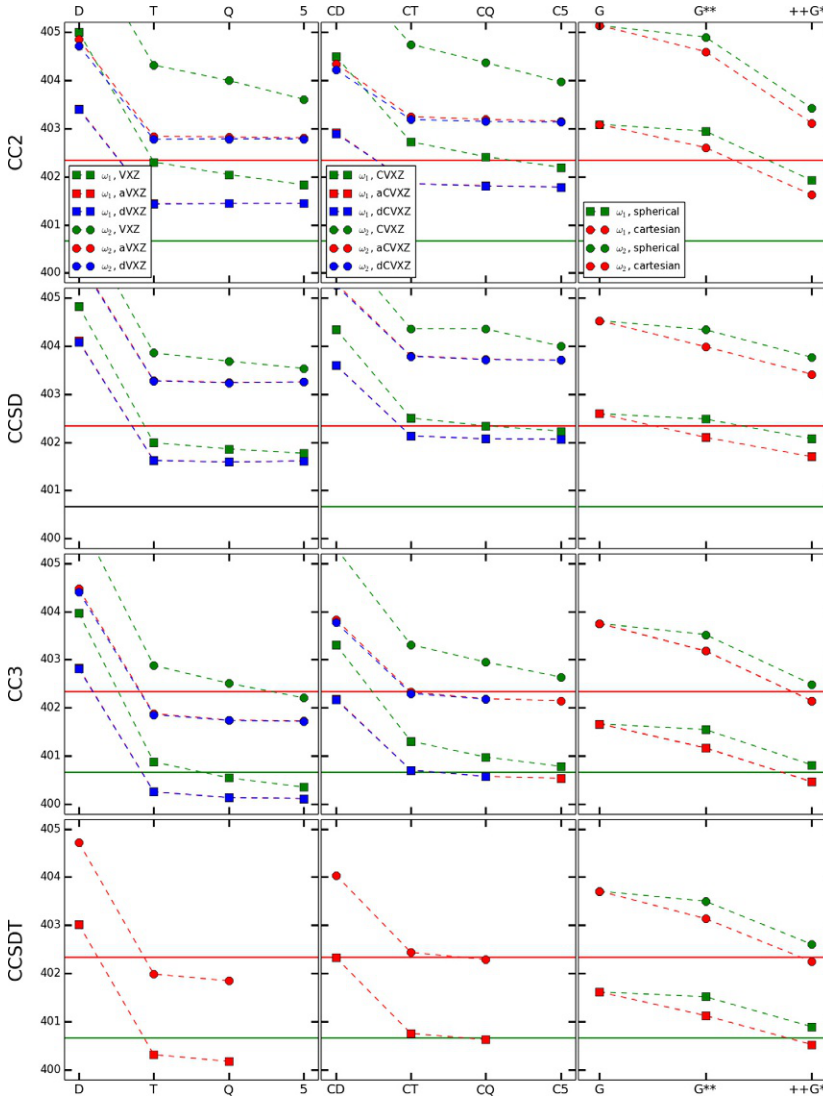

Fig. 4 NH_3, Nitrogen K-edge. Basis set convergence of the first two vertical core excitation energies with different CC methods and basis sets. The horizontal green line indicates the experimental ω_1 value and the red line indicates the experimental ω_2 value.

3.2 Extrapolation toward the complete basis set (CBS) limits

As observed in Section 3.1, the results in the cc basis sets show a monotonically decreasing behavior when increasing the cardinal number. The cc basis sets are known to yield a systematic convergence toward the complete basis set limit for the correlation energy of the ground state, as well as for other

molecular properties, and various extrapolation formulae have been proposed in the literature. Some of these formulae tend to overestimate the limit, and others to underestimate it. Inspired by the analysis performed by Wenzel et al. for the ADC hierarchies,[17] we have considered whether two popular extrapolations formulae, namely the X^{-3} formula[70] and the exponential formula,[71]

$$E_X = E_{CBS} + AX^{-3}; \quad (1)$$

$$E_X = E_{CBS} + Ae^{-(X-1)} + Be^{-(X-1)^2} \quad (2)$$

can be applied to obtain an estimate of the CBS values of the core excitation energies considered in this study. In Eqs. (1) and (2), E_{CBS} is the resulting estimated energy of the CBS limit, and E_X is the calculated energy using the basis set with cardinal number X.

The two formulae have been applied in different ways in the literature for different properties. One can fit directly the results of each basis set series, imposing the functional forms in Eqs. (1) and (2). Alternatively, one can derive the CBS limits via either a two-point strategy (on the X^{-3} formula) or three point strategy (on the exponential formula), using the energy values relative to the two (three) highest values of the cardinal numbers: X = Q, 5 for the two-point extrapolation, and X = T, Q, 5 for the three point extrapolation. In the following, we have considered both strategies.

Notice that in standard basis set extrapolation schemes,[70,71] the exponential and X^{-3} formulae apply to Hartree–Fock and correlation energies, respectively. Since a separation of the excitation energies into HF and correlation contributions is not straightforward, we apply the formulae directly to the computed excitation energies. It is also important to bear in mind that these extrapolation formulae are not rigorous expressions for the basis set dependence of energies, but serve as an estimate of the trend.

In Fig. 5 we show the results obtained for one selected basis set family, the aug-cc-pCVXZ one, for all four CC methods in the case of the water molecule. The trends observed for CO (both edges) and NH_3 are completely analogous and can be found in the document on the arXiv.[69] The CBS values obtained directly from the two points X^{-3} or three points exponential procedures are basically identical, and only marginally different from those obtained by fitting with the exponential regression over the entire series. This difference is slightly larger than what was observed by Wenzel et al.[17] for the ADC methods.

By fitting the results with a X^{-3} formula, on the other hand, we could not reproduce the behavior of the excitation energies.

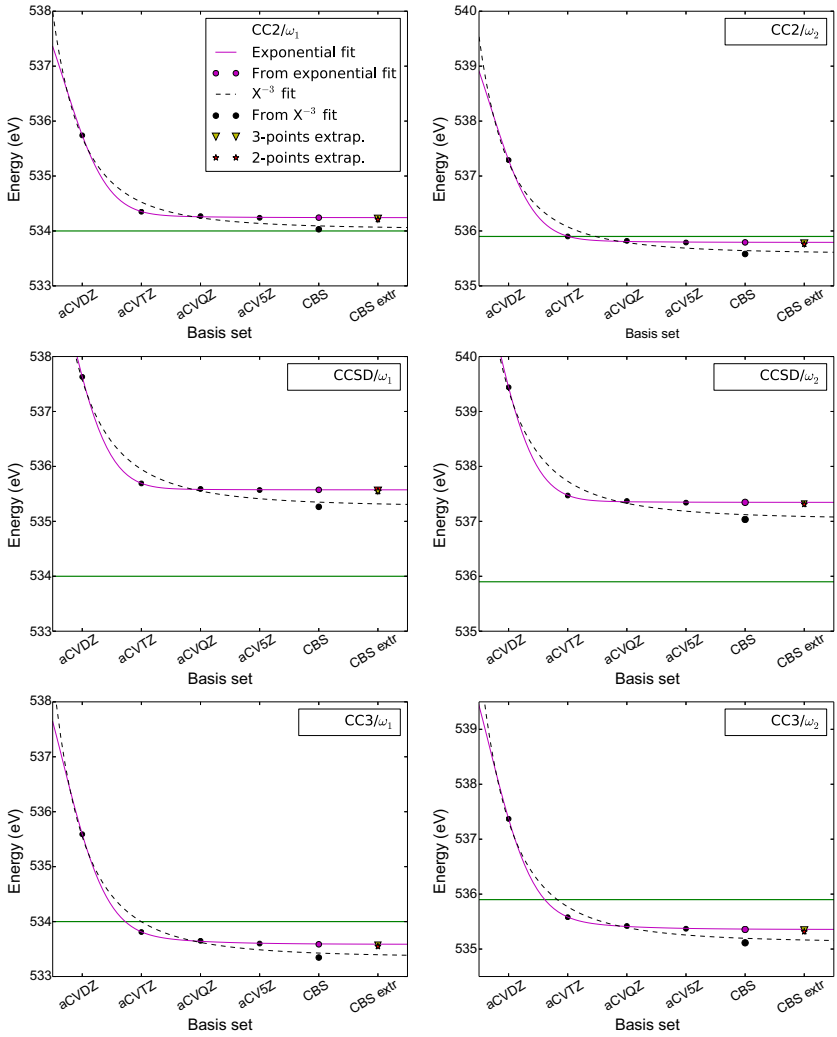

Fig. 5 H_2O, Oxygen K-edge. Extrapolated complete basis set (CBS) limits for the first two core excitations with different CC methods and the aug-cc-pCVXZ series. *Upper panels*: CC2; *Middle panels*: CCSD; *Bottom panels*: CC3. The horizontal green lines correspond to the experimentally estimated core energies.

3.3 Spectral bands

For comparison and assignment of the experimental spectra, the intensities of the absorption bands are required, and they are here obtained from the computed oscillator strengths. The full set of oscillator strengths obtained for the different basis sets at the CC2 and CCSD levels are available on the arXiv.

Spectral simulations based on oscillator strengths for the molecules H_2O and NH_3 computed in the cc-pCVXZ, aug-cc-pCVXZ, and d-aug-cc-pCVXZ bases are shown in Figs. 6 and 7. They were obtained using a Lorentzian broadening function with a half-width-half-maximum of 0.01 a.u.

For the first two transitions of water, the CCSD oscillator strengths are practically the same as soon as one set of augmenting functions is added, and little affected by variation of the cardinal number, the largest differences in

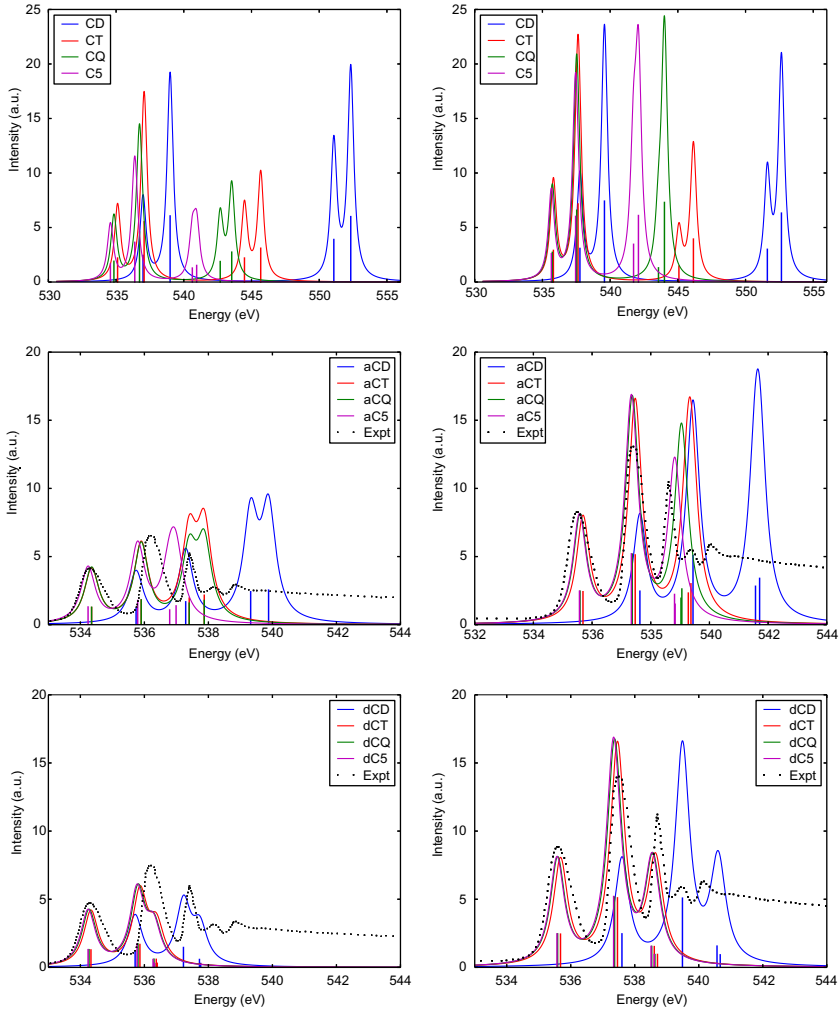

Fig. 6 H_2O, Oxygen K-edge. CC2 (*left panels*) and CCSD (*right panels*) spectral profiles with the x-aug-CVXZ basis sets. The augmented bases results are compared with the experimental spectrum,[72] which has been shifted and rescaled to roughly overlap with the first computed band (X = T, Q, 5).

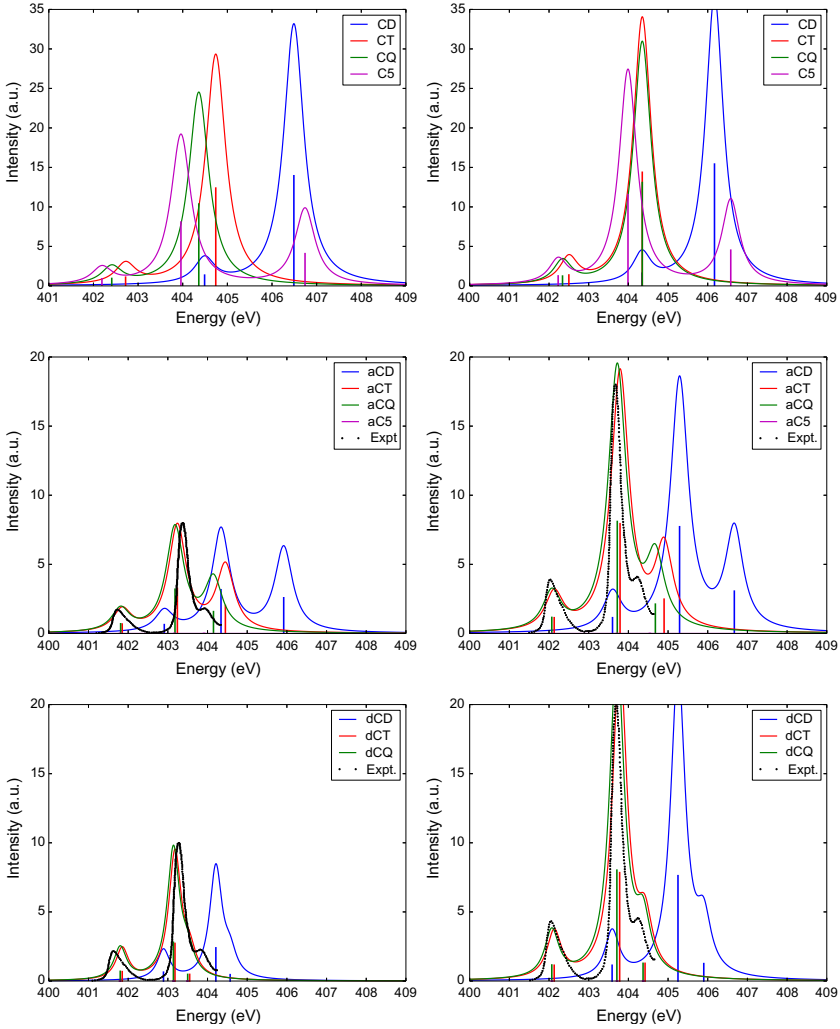

Fig. 7 NH_3, Nitrogen K-edge. Spectral profiles (first 3 bands) at the CC2 (*left*) and CCSD (*right*) level in the cc-pCVXZ, aug-cc-pCVXZ, and d-aug-cc-pCVXZ basis sets. The augmented bases results are compared with the experimental spectrum,[72] which has been shifted and rescaled to roughly overlap with the first computed band (X > D).

the spectra being due to variations in the position of the peaks. The situation is quite different for the third peak, which results from the combination of two excitations and has Rydberg character: many basis sets are insufficiently diffuse to yield an accurate description of the oscillator strengths, which are strongly overestimated. Inspection of the symmetry of the excited states also reveals that the third and fourth excited states contributing to the third spectral band

switch position energetically in the different basis sets. An efficient strategy to have a good representation of the third band on H_2O is to include Rydberg type functions, as done in Ref. 39. The CC2 oscillator strengths are more erratic, showing a relative intensity of the peaks at large variance compared to the experimental one, even in the larger basis sets. The CC2 spectra at the O K-edge of H_2O are "compressed," due to the underestimation of the separation between the bands, as it can be appreciated in Fig. 6.

For carbon in CO both the CCSD and the CC2 intensity of the first transition grows slightly within each series as the cardinal number increases. The intensity of the second transition is roughly constant, while large variations are observed for the intensities of the third peak, in particular at CC2 level. For oxygen, the intense peak has similarly almost constant intensity for all bases at CCSD level, while in the CC2 case some variations are recorded around an average value lower than the CCSD value. The intensities of the second and third peak are extremely low for both methods, and in the CC2 case sometimes even lower than the limit of detection.

Finally, in the case of ammonia (see Fig. 7), at both levels relatively large variations in intensity are observed for the second state (the most intense transition) for the bases lacking diffuse functions, and almost constant values for the other Dunning series. The intensities of the first state are roughly constant with the exception of in the smallest bases, which yield slightly overestimated values. Regarding the third state, the intensity decreases in the singly augmented sets and is almost constant for the doubly augmented ones, an indication of the greater sensitivity of this state to the presence of diffuse functions. The best agreement with the experimental profile is found for the d-aug-cc-pCVQZ basis set (we did not compute the aug-cc-pCV5Z and d-aug-cc-pCV5Z oscillator strengths). At CC2 level, there is in general a greater variation in the intensity, which is significantly smaller than in the CCSD case. Also at the N K-edge of NH_3, the peak separation is underestimated, yielding "squeezed" spectral profiles, compared to both CCSD and experiment.

3.4 Ionization energies

Tables 1 and 2 contain the results of the core ionization energies for different basis sets in the CC hierarchy up to CCSDT.

Inspection of the results clearly reveals, also for the IE, the inaccuracy of the double zeta basis sets for the core IE: for all three edges (C, N, and O) and at all CC levels the X = D basis sets overestimate the IEs by in between 1 and 3 eV. The largest improvement is observed for X = T, whereas going

Table 1 Core ionization energies of water and ammonia using different standard basis sets and the hierarchy of CC methods CC2, CCSD, CC3, and CCSDT.

	H_2O				NH_3			
Basis set	**CC2**	**CCSD**	**CC3**	**CCSDT**	**CC2**	**CCSD**	**CC3**	**CCSDT**
VDZ	539.15	543.31	541.21	541.77	406.58	408.66	407.15	407.45
VTZ	537.56	540.67	538.54	539.04	404.65	406.30	404.69	404.90
VQZ	537.57	540.77	538.33	538.94	404.69	406.40	404.60	—
V5Z	537.55	540.85	538.25	—	404.70	406.49	404.59	—
CVDZ	539.15	542.70	540.46	540.97	406.07	408.16	406.50	406.76
CVTZ	537.92	541.14	538.90	539.40	405.05	406.82	405.12	405.33
CVQZ	537.91	541.26	538.76	—	405.04	406.89	405.04	—
CV5Z	537.90	541.35	538.70	—	405.04	406.95	—	—
aVDZ	539.88	544.08	541.31	542.31	406.59	409.01	407.24	407.71
aVTZ	537.61	541.00	538.49	539.23	404.70	406.51	404.72	405.02
aVQZ	537.59	540.91	538.31	539.02	404.71	406.49	404.61	404.89
aV5Z	537.56	540.89	538.24	—	404.71	406.52	—	—
aCVDZ	539.27	543.45	540.56	541.51	406.09	408.52	406.60	407.02
aCVTZ	537.98	541.47	538.87	539.61	405.10	407.03	405.17	405.47
aCVQZ	537.93	541.40	538.73	539.46	405.06	406.98	405.05	405.34
aCV5Z	537.91	541.38	538.69	—	405.05	406.97	—	—
6-311G	538.16	541.07	539.15	—	405.19	406.77	405.32	—
6-311G**	537.99	540.92	539.01	—	405.02	406.61	405.15	—
6-311++G**	538.09	541.46	538.97	—	405.09	406.92	405.19	—

Experimental values are 539.78 eV for H_2O and 405.6 eV for NH_3.[72]

beyond triple-ζ has either moderate or negligible effect, and so also does the inclusion of single augmentation.

Moving along the CC hierarchy, we note that the CCSD IEs are significantly larger (1.5–4 eV) than the CC2 ones for both O and N, whereas for the C K-edge they are just slightly smaller (a few tenths of eV). Inclusion of triple excitations at the approximate CC3 lowers the IEs by ≈2.5–2.8 eV for O, by ≈1.6–1.9 eV for N, and ≈1.0 eV for C. Inclusion of the full treatment of triples by CCSDT, on the other hand, increases the CC3 results by a constant amount (independent of the basis set) of ≈0.7 eV for the

Table 2 Carbon monoxide.

	Carbon				Oxygen			
Basis set	**CC2**	**CCSD**	**CC3**	**CCSDT**	**CC2**	**CCSD**	**CC3**	**CCSDT**
VDZ	299.02	299.32	298.53	298.49	542.01	546.59	543.89	544.72
VTZ	297.17	296.98	295.99	295.88	539.92	543.71	541.19	541.83
VQZ	297.26	297.08	295.98	295.88	539.92	543.68	541.66	541.66
V5Z	297.27	297.12	—	—	539.89	543.67	—	—
CVDZ	298.46	298.81	297.80	297.73	541.40	545.97	543.14	543.91
CVTZ	297.64	297.54	296.48	296.38	540.28	544.18	541.55	542.19
CVQZ	297.65	297.59	296.44	296.34	540.25	544.18	—	—
CV5Z	297.66	297.61	—	—	540.24	544.18	—	—
aVDZ	299.04	299.34	298.49	298.46	542.16	546.83	543.98	543.93
aVTZ	297.20	297.04	296.00	295.90	539.96	543.79	541.18	541.86
aVQZ	297.28	297.11	295.999	295.90	539.94	543.71	541.02	541.68
aV5Z	297.29	297.14	—	—	539.90	543.69	—	—
aCVDZ	298.50	298.84	297.80	297.76	541.54	546.20	543.22	544.12
aCVTZ	297.68	297.62	296.53	296.43	540.32	544.27	541.57	542.25
aCVQZ	297.66	297.61	296.44	296.36	540.27	544.21	541.44	542.12
aCV5Z	297.66	297.62	—	—	540.25	544.19	—	—

Core ionization energies of oxygen and carbon using different standard basis sets and the hierarchy of CC methods CC2, CCSD, CC3, and CCSDT. Experimental values are 296.2 eV for C and 542.5 eV for O.[72]

O edge, ≈0.3 eV for the N edge; the C-edge IEs, on the other hand, are further reduced by 0.1 eV.

Comparing with the experimental results, we observe that in the case of Carbon both CC2 and CCSD overestimate the IE; CC3 and CCSDT either overestimate or underestimate the IE, depending on the basis set, by a few tenths of eV.

The core IEs of the two types of Oxygen K-edge (H_2O and CO) are significantly underestimated (ca 2 eV) at the CC2 level, and overestimated (1.5–2 eV) at the CCSD level. For X ≥ T, the CC3 results are 1.0–1.5 eV lower than experiment. The CCSDT results in the largest core-valence set are about −0.3 eV from experiment (and relativistic effects are +0.3 eV).

The N-edge IE is underestimated by 0.5–1.0 eV at the CC2 level, and overestimated by 1.0–1.5 eV at the CCSD level. The CC3 estimates are

very similar to the CC2 ones, and around −0.5 eV off in the core-valence bases. The agreement with experiment is further improved by full inclusion of triple excitations: in the aug-cc-pVQZ basis the CCSDT IE is −0.26 eV lower than the experimental IE.

The importance of scalar relativistic effects is illustrated in Table 3. As previously observed,[39,46,48] the relativistic effect is core-specific and practically

Table 3 Comparison of relativistic and nonrelativistic results for the IEs (eV).

	Nonrel	SFX2C-1e	ΔRel	Nonrel	SFX2C-1e	ΔRel
		O(H_2O)			N(NH_3)	
CCSD/aVTZ	541.03	541.39	0.36	406.51	406.73	0.22
CCSD/aVQZ	540.91	541.30	0.39	406.50	406.71	0.21
CCSD/aV5Z	540.90	541.28	0.38	406.52	406.73	0.21
CCSD/aCVTZ	541.48	541.86	0.38	407.03	407.24	0.21
CCSD/aCVQZ	541.40	541.79	0.39	406.99	407.20	0.21
CCSD/aCV5Z	541.38	541.77	0.39	406.98	407.19	0.21
CCSDT/aVTZ	539.23	539.61	0.38	405.02	405.23	0.21
CCSDT/aVQZ	539.02	539.40	0.38	404.89	405.10	0.21
CCSDT/aCVTZ	539.61	540.00	0.39	405.47	405.68	0.21
CCSDT/aCVQZ	539.46	539.85	0.39	405.34	405.55	0.21
		O(CO)			C(CO)	
CCSD/aVTZ	543.79	544.17	0.38	297.04	297.14	0.10
CCSD/aVQZ	543.71	544.10	0.39	297.11	297.21	0.10
CCSD/aV5Z	543.69	544.07	0.38	297.14	297.24	0.10
CCSD/aCVTZ	544.27	544.65	0.38	297.62	297.72	0.10
CCSD/aCVQZ	544.21	544.59	0.38	297.61	297.71	0.10
CCSD/aCV5Z	544.19	544.57	0.38	297.62	297.72	0.10
CCSDT/aVTZ	541.86	542.25	0.39	295.90	295.99	0.09
CCSDT/aVQZ	541.68	542.06	0.38	295.90	295.99	0.09
CCSDT/aCVTZ	542.25	542.63	0.38	296.43	296.53	0.10
CCSDT/aCVQZ	542.12	542.50	0.38	296.36	296.46	0.10

the same independent of the chosen method and basis set. The effect is to increase the IEs in all cases, which can be ascribed to the contraction, and thereby stabilization, of the core orbitals.

4. Concluding remarks

We have carried out a coupled cluster investigation of the performance of the standard hierarchy CC2-CCSD-CC3-CCSDT in connection with conventional Dunning correlation consistent and Pople basis sets to yield accurate vertical core excitation energies (and strengths) and core ionization energies for N, C, and O K-edges in the prototypical molecules H_2O, CO, and NH_3. Complete basis set limit values have been derived.

The use of singly augmented triple-zeta basis sets is sufficiently accurate for the low-energy core excitations, which are of limited or no Rydberg character. The Pople set 6-311++G** set provides results of quality almost comparable as the aug-cc-pVTZ set, but at lower computational cost.

Acknowledgments

S.C. acknowledges financial support from the AIAS-COFUND program (Grant Agreement No. 609033) and from the Independent Research Fund Denmark, DFF-Forskningsprojekt2 (Grant No. 7014-00258B). H.K. acknowledges financial support from the FP7-PEOPLE-2013-IOF funding scheme (Project No. 625321) and a visiting professorship grant at DTU Chemistry from the Otto Mønsted Foundation. R.H.M. acknowledges computer time from NOTUR through Project No. nn2962k. The COST Actions No. MP1306 "Modern Tools for Spectroscopy on Advanced Materials (EUSPEC)," CM1204 "XUV/X-ray light and fast ions for ultrafast chemistry (XLIC)," and CM1405 "MOLIM—Molecules in Motion" are also acknowledged.

References

1. Bergmann, U.; Yachandra, V.; Yano, J. *X-Ray Free Electron Lasers: Applications in Materials, Chemistry and Biology. Energy and Environment Series, no. 18*; Royal Society of Chemistry, 2017.
2. Van Kuiken, B. E.; Huse, N.; Cho, H.; Strader, M. L.; Lynch, M. S.; Schoenlein, R. W.; Khalil, M. Probing the Electronic Structure of a Photoexcited Solar Cell Dye With Transient X-Ray Absorption Spectroscopy. *J. Phys. Chem. Lett.* **2012**, *3*, 1695–1700.
3. Piancastelli, M. N.; Simon, M.; Ueda, K. Present Trends and Future Perspectives for Atomic and Molecular Physics at the New X-Ray Light Sources. *J. Electron Spectrosc. Relat. Phenom.* **2010**, *181*(1), 98–110.
4. Milne, C. J.; Penfold, T. J.; Chergui, M. Recent Experimental and Theoretical Developments in Time-Resolved X-Ray Spectroscopies. *Coord. Chem. Revi.* **2014**, *277–278*, 44–68.
5. van Bokhoven, J. A.; Lamberti, C. *X-Ray Absorption and X-ray Emission Spectroscopy; Theory and Applications*; Wiley & Sons, 2016.

6. Wolf, T. J. A.; Myhre, R. H.; Cryan, J. P.; Coriani, S.; Squibb, R. J.; Battistoni, A.; Berrah, N.; Bostedt, C.; Bucksbaum, P.; Coslovich, G.; Feifel, R.; Gaffney, K. J.; Grilj, J.; Martinez, T. J.; Miyabe, S.; Moeller, S. P.; Mucke, M.; Natan, A.; Obaid, R.; Osipov, T.; Plekan, O.; Wang, S.; Koch, H.; Gühr, M. Probing Ultrafast $\pi\pi^*/n\pi^*$ Internal Conversion in Organic Chromophores Via K-Edge Resonant Absorption. *Nat. Commun.* **2017**, *8*(29), 1–7.
7. Chergui, M.; Collet, E. Photoinduced Structural Dynamics of Molecular Systems Mapped by Time-Resolved X-ray Methods. *Chem. Rev.* **2017**, *117*(16), 11025–11065.
8. Lin, F.; Liu, Y.; Yu, X.; Cheng, L.; Singer, A.; Shpyrko, O. G.; Xin, H. L.; Tamura, N.; Tian, C.; Weng, T. C.; Yang, X. Q.; Meng, Y. S.; Nordlund, D.; Yang, W.; Doeff, M. M. Synchrotron X-ray Analytical Techniques for Studying Materials Electrochemistry in Rechargeable Batteries. *Chem. Rev.* **2017**, *117*(21), 13123–13186.
9. Kraus, P. M.; Zürch, M.; Cushing, S. K.; Neumark, D. M.; Leone, S. R. The Ultrafast X-ray Spectroscopic Revolution in Chemical Dynamics. *Nat. Rev. Chem.* **2018**, *2*, 82–94.
10. Norman, P.; Dreuw, A. Simulating X-ray Spectroscopies and Calculating Core-Excited States of Molecules. *Chem. Rev.* **2018**, *118*, 7208–7248.
11. Kuramoto, K.; Ehara, M.; Nakatsuji, H. Theoretical Fine Spectroscopy With Symmetry Adapted Cluster-Configuration Interaction General-R Method: First-Row K-Shell Ionizations and Their Satellites. *J. Chem. Phys.* **2005**, *122*, 014304.
12. Vinson, J.; Rehr, J. J.; Kas, J. J.; Shirley, E. L. Bethe-Salpeter Equation Calculations of Core Excitation Spectra. *Phys. Rev. B: Condens. Matter Mater. Phys.* **2011**, *83*, 115106.
13. Gilmore, K.; Vinson, J.; Shirley, E. L.; Prendergast, D.; Pemmaraju, C. D.; Kas, J. J.; Vila, F. D.; Rehr, J. J. Efficient Implementation of Core-Excitation Bethe-Salpeter Equation Calculations. *Comput. Phys. Commun.* **2015**, *197*, 109–117.
14. Ågren, H.; Carravetta, V.; Vahtras, O.; Pettersson, M. L. G. Direct SCF Direct Static-Exchange Calculations of Electronic Spectra. *Theor. Chem. Acc.* **1997**, *97*, 14–40.
15. Schirmer, J. Beyond the Random-Phase Approximation: A New Approximation Scheme for the Polarization Propagator. *Phys. Rev. A* **1982**, *26*, 2395–2416.
16. Dreuw, A.; Wormit, M. The Algebraic Diagrammatic Construction Scheme for the Polarization Propagator for the Calculation of Excited States. *WIREs Comput. Mol. Sci.* **2015**, *5*, 82–95.
17. Wenzel, J.; Wormit, M.; Dreuw, A. Calculating Core-Level Excitations and X-Ray Absorption Spectra of Medium-Sized Closed-Shell Molecules With the Algebraic-Diagrammatic Construction Scheme for the Polarization Propagator. *J. Comput. Chem.* **2014**, *35*, 1900.
18. Wenzel, J.; Holzer, A.; Wormit, M.; Dreuw, A. Analysis and Comparison of CVS-ADC Approaches up to Third Order for the Calculation of Core-Excited States. *J. Chem. Phys.* **2015**, *142*, 214104.
19. Cederbaum, L. S.; Domcke, W.; Schirmer, J. Many-Body Theory of Core Holes. *Phys. Rev. A: At. Mol. Opt. Phys.* **1980**, *22*, 206–222.
20. Stener, M.; Fronzoni, G.; de Simone, M. Time Dependent Density Functional Theory of Core Electrons Excitations. *Chem. Phys. Lett.* **2003**, *15*, 115.
21. Ekström, U.; Norman, P.; Carravetta, V.; Ågren, H. polarization Propagator for X-ray Spectra. *Phys. Rev. Lett.* **2006**, *97*, 143001.
22. Ekström, U.; Norman, P. X-ray Absorption Spectra From the Resonant-Convergent First-Order Polarization Propagator Approach. *Phys. Rev. A* **2006**, *74*, 042722.
23. Tu, G.; Rinkevicius, Z.; Vahtras, O.; Ågren, H.; Ekström, U.; Norman, P.; Carravetta, V. Self-Interaction-Corrected Time-Dependent Density-Functional-Theory Calculations of X-ray-Absorption Spectra. *Phys. Rev. A* **2007**, *76*, 022506.

24. Liang, W.; Fischer, S. A.; Frisch, M. J.; Li, X. Energy-Specific Linear Response TDHF/TDDFT for Calculating High-Energy Excited States. *J. Chem. Theory Comput.* **2011**, *7*(11), 3540–3547.
25. Besley, N. A.; Asmuruf, F. A. Time-Dependent Density Functional Theory Calculations of the Spectroscopy of Core Electrons. *Phys. Chem. Chem. Phys.* **2010**, *12*, 12024.
26. Lestrange, P. J.; Nguyen, P. D.; Li, X. Calibration of Energy-Specific TDDFT for Modeling K-edge XAS Spectra of Light Elements. *J. Chem. Theory Comput.* **2015**, *11*(7), 2994–2999.
27. Besley, N. A.; Gilbert, A. T.; Gill, P. M. Self-Consistent-Field Calculations of Core Excited States. *J. Chem. Phys.* **2009**, *130*(12), 124308.
28. Derricotte, W. D.; Evangelista, F. A. Simulation of X-Ray Absorption Spectra With Orthogonality Constrained Density Functional Theory. *Phys. Chem. Chem. Phys.* **2015**, *17*(22), 14360–14374.
29. Evangelista, F. A.; Shushkov, P.; Tully, J. C. Orthogonality Constrained Density Functional Theory for Electronic Excited States. *J. Phys. Chem. A* **2013**, *117*, 7378–7392.
30. Glushkov, V. N.; Assfeld, X. Orthogonality-Constrained Hartree-Fock and Perturbation Theory for High-Spin Open-Shell Excited States. *Theor. Chem. Accounts* **2015**, *135*(1), 3.
31. Glushkov, V. N.; Assfeld, X. Electronic Transition Dipole Moments From Orthogonality Constrained Hartree-Fock Wavefunctions. *J. Phys. B: At. Mol. Opt. Phys.* **2017**, *50*(12), 125101.
32. Ferré, N.; Assfeld, X. Application of the Local Self-Consistent-Field Method to Core-Ionized and Core-Excited Molecules, Polymers, and Proteins: True Orthogonality Between Ground and Excited States. *J. Chem. Phys.* **2002**, *117*, 4119–4125.
33. Glushkov, V. N.; Assfeld, X. On Orthogonality Constrained Multiple Core-Hole States and Optimized Effective Potential Method. *J. Comp. Chem.* **2012**, *33*, 2058–2066.
34. Koch, H.; Jørgensen, P. Coupled Cluster Response Functions. *J. Chem. Phys.* **1990**, *93*, 3333–3344.
35. Christiansen, O.; Jørgensen, P.; Hättig, C. Response Functions from Fourier Component Variational Perturbation Theory Applied to a Time-Averaged Quasienergy. *Int. J. Quantum Chem.* **1998**, *98*, 1.
36. Stanton, J. F.; Bartlett, R. J. The Equation of Motion Coupled-Cluster Method. A Systematic Biorthogonal Approach to Molecular Excitation Energies, Transition Probabilities, and Excited State Properties. *J. Chem. Phys* **1993**, *98*(9), 7029–7039.
37. Bartlett, R. J. Coupled-Cluster Theory and Its Equation-of-Motion Extensions. *WIREs Comput. Mol. Sci.* **2012**, *2*(1), 126–138.
38. Krylov, A. I. Equation-of-Motion Coupled-Cluster Methods for Open-Shell and Electronically Excited Species: The Hitchhiker's Guide to Fock Space. *Ann. Rev. Phys. Chem.* **2008**, *59*(1), 433–462.
39. Coriani, S.; Christiansen, O.; Fransson, T.; Norman, P. Coupled-Cluster Response Theory for Near-Edge X-Ray-Absorption Fine Structure of Atoms and Molecules. *Phys. Rev. A* **2012**, *85*, 022507.
40. Coriani, S.; Fransson, T.; Christiansen, O.; Norman, P. Asymmetric-Lanczos-Chain-Driven Implementation of Electronic Resonance Convergent Coupled-Cluster Linear Response Theory. *J. Chem. Theory Comput.* **2012**, *8*, 1616.
41. Fransson, T.; Coriani, S.; Christiansen, O.; Norman, P. Carbon X-ray Absorption Spectra of Fluoroethenes and Acetone: A Study at the Coupled Cluster, Density Functional, and Static-Exchange Levels of Theory. *J. Chem. Phys.* **2013**, *138*, 124311.
42. List, N. H.; Coriani, S.; Kongsted, J.; Christiansen, O. Lanczos-Driven Coupled-Cluster Damped Linear Response Theory for Molecules in Polarizable Environments. *J. Chem. Phys.* **2014**, *141*, 244107.

43. Coriani, S.; Koch, H. Communication: X-ray Absorption Spectra and Core-Ionization Potentials Within a Core-Valence Separated Coupled Cluster Framework. *J. Chem. Phys.* **2015**, *143*, 181103.
44. Coriani, S.; Koch, H. Erratum: "Communication: X-Ray Absorption Spectra and Core-Ionization Potentials Within a Core-Valence Separated Coupled Cluster Framework" [J. Chem. Phys. 143, 181103 (2015)]. *J. Chem. Phys.* **2016**, *145*(14), 149901.
45. Myhre, R. H.; Coriani, S.; Koch, H. Near-Edge X-ray Absorption Fine Structure Within Multilevel Coupled Cluster Theory. *J. Chem. Theory Comput.* **2016**, *12*(6), 2633–2643.
46. Myhre, R. H.; Wolf, T. J. A.; Cheng, L.; Nandi, S.; Coriani, S.; Gühr, M.; Koch, H. A Theoretical and Experimental Benchmark Study of Core-Excited States in Nitrogen. *J. Chem. Phys.* **2018**, *148*(6), 064106.
47. Vidal, M. L.; Feng, X.; Epifanovsky, E.; Krylov, A. I.; Coriani, S. A New and Efficient Equation-of-motion Coupled-Cluster Framework for Core-Excited and Core-Ionized States. *J. Chem. Theory Comput.* **2019**, *15*(5), 3117–3133.
48. Liu, J.; Matthews, D.; Coriani, S.; Cheng, L. Benchmark Calculations of K-Edge Ionization Energies for First-Row Elements Using Scalar-Relativistic Core-Valence-Separated Equation-of-Motion Coupled-Cluster Methods. *J. Chem. Theory and Comput.* **2019**, *15*, 1642–1651.
49. Faber, R.; Coriani, S. Resonant Inelastic X-Ray Scattering and Nonesonant X-Ray Emission Spectra From Coupled-Cluster (Damped) Response Theory. *J. Chem. Theory Comput.* **2019**, *15*, 520–528.
50. Frati, F.; de Groot, F.; Cerezo, J.; Santoro, F.; Cheng, L.; Faber, R.; Coriani, S. Coupled Cluster Study of the X-ray Absorption Spectra of Formaldehyde Derivatives at the Oxygen, Carbon, and Fluorine K-Edges. *J. Chem. Phys.* **2019**, *151*, 064107.
51. Helgaker, T.; Coriani, S.; Jørgensen, P.; Kristensen, K.; Olsen, J.; Ruud, K. Recent Advances in Wave Function-Based Methods of Molecular-Property Calculations. *Chem. Rev.* **2012**, *112*, 543–631.
52. Helgaker, T.; Jørgensen, P.; Olsen, J. *Molecular Electronic Structure Theory*; Wiley, 2004.
53. Peng, B.; Lestrange, P. J.; Goings, J. J.; Caricato, M.; Li, X. Energy-Specific Equation-of-Motion Coupled-Cluster Methods for High-Energy Excited States: Application to K-Edge X-Ray Absorption Spectroscopy. *J. Chem. Theory Comput.* **2015**, *11*, 4146.
54. Christiansen, O.; Koch, H.; Jørgensen, P. The Second-Order Approximate Coupled Cluster Singles and Doubles Model CC2. *Chem. Phys. Lett.* **1995**, *243*, 409.
55. Purvis, G. D.; Bartlett, R. J. A Full Coupled-Cluster Singles and Doubles Model: The Inclusion of Disconnected Triples. *J. Chem. Phys.* **1982**, *76*, 1910.
56. Koch, H.; Sánchez de Merás, A.; Helgaker, T.; Christiansen, O. The Integral-Direct Coupled Cluster Singles and Doubles Model. *J. Chem. Phys.* **1996**, *104*, 4157.
57. Christiansen, O.; Koch, H.; Halkier, A.; Jørgensen, P.; Helgaker, T.; Sánchez de Merás, A. Large-Scale Calculations of Excitation Energies in Coupled Cluster Theory: The Singlet Excited States of Benzene. *J. Chem. Phys.* **1996**, *105*, 6921.
58. Koch, H.; Christiansen, O.; Jørgensen, P.; de Merás, A. S.; Helgaker, T. The CC3 Model: An Iterative Coupled Cluster Approach Including Connected Triples. *J. Chem. Phys.* **1997**, *106*, 1808.
59. Christiansen, O.; Koch, H.; Jørgensen, P. Response Functions in the CC3 Iterative Triple Excitation Model. *J. Chem. Phys.* **1995**, *103*(17), 7429–7441.
60. Kucharski, S. A.; Włoch, M.; Musiał, M.; Bartlett, R. J. Coupled-Cluster Theory for Excited Electronic States: The Full Equation-of-Motion Coupled-Cluster Single, Double, and Triple Excitation Method. *J. Chem. Phys.* **2001**, *115*(18), 8263–8266.
61. Myhre, R. H.; Koch, H. The Multi-Level CC3 Coupled Cluster Model. *J. Chem. Phys.* **2016**, *145*, 044111.

62. Matthews, D. A.; Stanton, J. F. Non-Orthogonal Spin-Adaptation of Coupled Cluster Methods: A New Implementation of Methods Including Quadruple Excitations. *J. Chem. Phys.* **2015**, *142*(6), 064108.
63. Baraban, J. H.; Matthews, D. A.; Stanton, J. F. Communication: An Accurate Calculation of the S_1 C_2H_2 Cis-Trans Isomerization Barrier Height. *J. Chem. Phys.* **2016**, *144*(11), 111102.
64. Dyall, K. G. Interfacing Relativistic and Nonrelativistic Methods. I. Normalized Elimination of the Small Component in the Modified Dirac Equation. *J. Chem. Phys.* **1997**, *106*(23), 9618–9626.
65. Liu, W.; Peng, D. Exact Two-Component Hamiltonians Revisited. *J. Chem. Phys.* **2009**, *131*(3), 031104.
66. Cheng, L.; Gauss, J. Analytic Energy Gradients for the Spin-Free Exact Two-Component Theory Using an Exact Block Diagonalization for the One-Electron Dirac Hamiltonian. *J. Chem. Phys.* **2011**, *135*(8), 084114.
67. Aidas, K.; Angeli, C.; Bak, K. L.; Bakken, V.; Bast, R.; Boman, L.; Christiansen, O.; Cimiraglia, R.; Coriani, S.; Dahle, P.; Dalskov, E. K.; Ekström, U.; Enevoldsen, T.; Eriksen, J. J.; Ettenhuber, P.; Fernández, B.; Ferrighi, L.; Fliegl, H.; Frediani, L.; Hald, K.; Halkier, A.; Hättig, C.; Heiberg, H.; Helgaker, T.; Hennum, A. C.; Hettema, H.; Hjertenæs, E.; Høst, S.; Høyvik, I. M.; Iozzi, M. F.; Jansik, B.; Jensen, H. J. A.; Jonsson, D.; Jørgensen, P.; Kauczor, J.; Kirpekar, S.; Kjærgaard, T.; Klopper, W.; Knecht, S.; Kobayashi, R.; Koch, H.; Kongsted, J.; Krapp, A.; Kristensen, K.; Ligabue, A.; Lutnæs, O. B.; Melo, J. I.; Mikkelsen, K. V.; Myhre, R. H.; Neiss, C.; Nielsen, C. B.; Norman, P.; Olsen, J.; Olsen, J. M. H.; Osted, A.; Packer, M. J.; Pawlowski, F.; Pedersen, T. B.; Provasi, P. F.; Reine, S.; Rinkevicius, Z.; Ruden, T. A.; Ruud, K.; Rybkin, V. V.; Salek, P.; Samson, C. C. M.; de Merás, A. S.; Saue, T.; Sauer, S. P. A.; Schimmelpfennig, B.; Sneskov, K.; Steindal, A. H.; Sylvester-Hvid, K. O.; Taylor, P. R.; Teale, A. M.; Tellgren, E. I.; Tew, D. P.; Thorvaldsen, A. J.; Thøgersen, L.; Vahtras, O.; Watson, M. A.; Wilson, D. J. D.; Ziolkowski, M.; Ågren, H. The Dalton Quantum Chemistry Program System. *WIREs Comput. Mol. Sci.* **2014**, *4*, 269.
68. Stanton, J. F.; Gauss, J.; Harding, M. E.; Szalay, P. G.; Auer, A. A.; Bartlett, R. J.; Benedikt, U.; Berger, C.; Bernholdt, D. E.; Bomble, Y. J.; Cheng, L.; Christiansen, O.; Heckert, M.; Heun, O.; Huber, C.; Jagau, T. C.; Jonsson, D.; Jusélius, J.; Klein, K.; Lauderdale, W. J.; Lipparini, F.; Matthews, D. A.; Metzroth, T.; Mück, L. A.; O'Neill, D. P.; Price, D. R.; Prochnow, E.; Puzzarini, C.; Ruud, K.; Schiffmann, F.; Schwalbach, W.; Simmons, C.; Stopkowicz, S.; Tajti, A.; Vázquez, J.; Wang, F.; Watts, J. D.; Almlöf, J.; Taylor, P. R.; Taylor, P. R.; Helgaker, T.; Jensen, H. J. A.; Jørgensen, P.; Olsen, J.; Mitin, A. V.; van Wüllen, C. *CFOUR, Coupled-Cluster Techniques for Computational Chemistry*; 2015 http://www.cfour.de/.
69. Carbone, J. P.; Cheng, L.; Myhre, R. H.; Matthews, D.; Koch, H.; Coriani, S. *An Analysis of the Performance of Coupled Cluster Methods for K-Edge Core Excitations and Ionizations Using Standard Basis Sets*. 2019, arXiv:1908.03635 [physics.chem-ph].
70. Helgaker, T.; Klopper, W.; Koch, H.; Noga, J. Basis-Set Convergence of Correlated Calculations on Water. *J. Chem. Phys.* **1997**, *106*, 9639.
71. Peterson, K. A.; Woon, D. E.; Dunning, T. H. Benchmark Calculations With Correlated Molecular Wave Functions. IV. The Classical Barrier Height of the $H+H_2 \rightarrow H_2+H$ Reaction. *J. Chem. Phys.* **1994**, *100*(10), 7410–7415.
72. Schirmer, J.; Trofimov, A. B.; Randall, K. J.; Feldhaus, J.; Bradshaw, A. M.; Ma, Y.; Chen, C. T.; Sette, F. *K*-Shell Excitation of the Water, Ammonia and Methane Molecules Using High-Resolution Photoabsorption Spectroscopy. *Phys. Rev. A* **1993**, *47*, 1136.

This page intentionally left blank

CHAPTER TWELVE

Determination of electronic couplings in the singlet fission process using a nonorthogonal configuration interaction approach

Luis Enrique Aguilar Suarez[a], R.K. Kathir[a], Enrico Siagri[a], Remco W.A. Havenith[a,b], Shirin Faraji[a,*]

[a]Theoretical Chemistry Group, Zernike Institute for Advanced Materials, University of Groningen, Groningen, The Netherlands
[b]Stratingh Institute for Chemistry, University of Groningen, Groningen, The Netherlands
*Corresponding author: e-mail address: s.s.faraji@rug.nl

Contents

Abstract

Singlet fission has been explored as an alternative mechanism to enhance the performance of solar cells. In this work, we use a nonorthogonal configuration interaction approach to study the singlet fission process in solid 2-methylene-2H-indene, an identified potential singlet fission molecule. Results of the electronic coupling calculations in pairs of molecules show that this molecule is suitable for the efficient formation of the ^1TT state (≈40 meV). We report, for the first time, a comparison of the nonorthogonal configuration interaction approach with two other theoretical methodologies: restricted active space with two spin flips and the *ab initio* Frenkel–Davydov exciton model.

Advances in Quantum Chemistry, Volume 79
ISSN 0065-3276
https://doi.org/10.1016/bs.aiq.2019.05.004

1. Introduction

Singlet fission (SF) is a multiexciton generation phenomenon that occurs in organic molecules and in which the first singlet excited state of a molecule splits into two triplets in an overall spin-allowed process by forming the so-called ^1TT state (Fig. 1).[1,2] Since SF may give rise to the generation of four charge carriers per absorbed photon, this multiexciton generation process has been explored as an alternative scheme to enhance the efficiency of current solar cells and overcome the so-called Shockley–Queisser limit.[3,4] Nevertheless, the number of molecules known experimentally to exhibit this process is limited. Furthermore the mechanistic details of the process are not yet well-understood and are the subject of an active area of research.[5–10] The lack of materials and poor understanding of the process have limited the technological development of SF-enhanced solar cells. Finding proper materials and obtaining a deeper comprehension of how SF occurs in organic solids may lead to its further implementation in solar cell technology[11].

In order for SF to be an efficient process, the following criteria must be fulfilled[1,12]: (1) SF has to occur faster than any other competing process (e.g., radiative decay or intersystem crossing); (2) the process should preferably be isoergic or slightly exoergic (although endoergic SF has been observed in tetracene[13–15]) which means fulfilling the energetic requirement

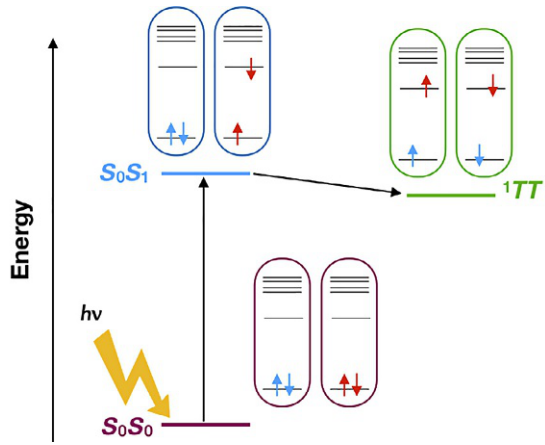

Fig. 1 Schematic representation of singlet fission. Upon absorption of a photon, a singlet excited molecule (S_1) transfers part of its energy to a neighbor to form two triplets (^1TT) that are coupled into a singlet.

$E(S_1) \geq 2E(T_1)$; and (3) the T_2 state in the molecule should be higher in energy than S_1, and at least twice the energy of T_1 to avoid triplet–triplet annihilation. Additionally, some properties are desired from these materials, such as high stability under continuous radiation, low cost associated to their production for practical applications and long-lived triplets to ensure that the charge carriers can be harvested. Theoretical simulations can assist the design of SF-enhanced solar cells and be used to optimize the SF process in organic solids that fulfill the above mentioned requirements.[16,17] The mechanism underlying SF is still unclear;[18,19] the schematic representation in Fig. 1 is generally accepted but the understanding of how the ^1TT state is formed from the singlet excited state is still a matter for debate. Different mechanisms have been proposed: one in which the ^1TT state is formed directly from the singlet excited state via a two-electron transfer (blue arrow in Fig. 2) or a transition in which the charge transfer (CT) states act as intermediates (red arrows in Fig. 2). Alternatively, if the CT states are too high in energy, a "mediated" mechanism (green arrows in Fig. 2) can occur in which CT configurations appear in the wave functions of the initial and final states facilitating the process. Therefore, studying the influence of the CT states in the mechanism of SF is essential. Additionally, vibrations and molecular motions have been suggested as playing active roles in SF.[20–23]

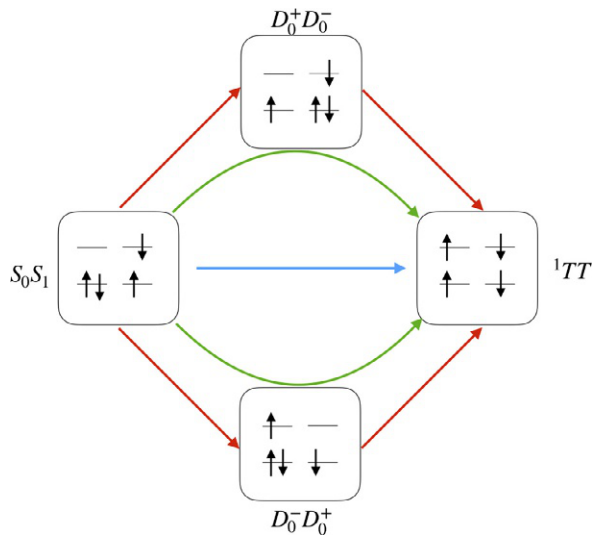

Fig. 2 Direct (*blue arrow*), intermediate (*red arrows*), and mediated (*green arrows*) mechanisms between the different states (singlet excited, S_0S_1; charge transfer, $D_0^+D_0^-/D_0^-D_0^+$; and multiexciton state, ^1TT) in singlet fission.

In order to study SF, a rate constant (k_E) associated with the process can be approximated by means of the Fermi's golden rule[24]:

$$k_E \approx \frac{2\pi}{\hbar} |V_{\mu\nu}|^2 \rho(E) \tag{1}$$

where $V_{\mu\nu}$ represents the electronic coupling between two (diabatic) states, μ and ν, and $\rho(E)$ denotes the density of states per unit of energy E. Different ways to evaluate the electronic coupling exist,[16,25] and in this work, we use a nonorthogonal configuration interaction (NOCI) approach;[26–29] advantages of this method are that it is conceptually simple and yet considers orbital relaxation effects as well as (static) electron correlation. In cases where the orbitals of the excited states differ significantly (e.g., for CT states), lengthy CI expansions can be avoided using the NOCI approach and if the states of interest have multireference character, NOCI is expected to outperform methods based on single reference wave functions. With the NOCI approach, a solid is described in terms of molecular states. Therefore we calculate, for different electronic states of each molecule in an ensemble, molecular wave functions that are subsequently combined into basis functions which describe a particular combination of molecular states. The final wave function for the ensemble is then written as an expansion of these many-electron basis functions (MEBFs). The NOCI approach is attractive for the description of SF since the wave function is constructed with MEBFs that describe all the states involved and, moreover, the interaction between the photo excited state and the multiexciton state can be directly calculated. The molecular wave functions can be chosen to be complete active space self-consistent field (CASSCF) wave functions in which both the orbitals and CI coefficients are fully optimized. Each molecular wave function is optimized with its own set of orbitals and represents a specific electronic state I of molecule A (Ψ_A^I), such as the ground state ($\Psi_A^{S_0}$), the lowest singlet excited state ($\Psi_A^{S_1}$), the lowest triplet state (Ψ_A^T), the cationic ground state ($\Psi_A^{D_0^+}$), and the anionic ground state ($\Psi_A^{D_0^-}$). The MEBFs ($|\Phi_\mu\rangle$) are then constructed as spin-adapted antisymmetrized products of the molecular wave functions:

$$|\Phi_\mu\rangle = \sum_\sigma \kappa_\sigma \hat{A} \prod_A^N |\Psi_A^I\rangle_\sigma \tag{2}$$

where N is the number of molecules in the ensemble, κ_σ are the corresponding spin-coupling coefficients, and the summation over σ indicates that several antisymmetrized products of molecular wave functions with different M_s eigenvalues are combined such that the resulting MEBFs are spin eigenfunctions. In practice, for example for a pair of molecules, a MEBF is generated from the molecular CASSCF wave functions as:

$$\begin{aligned}\hat{A}\left(\sum_i C_i^A \Delta_i^A\right)\left(\sum_j C_j^B \Delta_j^B\right) &= \sum_{ij} C_i^A C_j^B \hat{A}|\phi_\mu^A \ldots \| \phi_\nu^B \ldots| \\ &= \sum_{ij} C_i^A C_j^B |\phi_\mu^A \ldots \phi_\nu^B \ldots|.\end{aligned} \tag{3}$$

In this notation, C_i and C_j denote the CI coefficients of the molecular CASSCF wave functions, Δ is a Slater determinant, and ϕ indicates the occupied spin orbitals in the Slater determinant for molecules A and B. In principle, the number of molecules included in the ensemble is not limited. However, our preliminary investigation following the protocol outlined in Ref. 26, for a pair of molecules taken from the structure reported in Ref. 26, resulted in an electronic coupling between the photo excited and the multiexciton state of 9 meV, compared to 12 meV reported for a cluster of three molecules; this indicates that the size of the ensemble only marginally affects the electronic coupling. Therefore, in this work we focus on the study of pairs of molecules.

In a pair of molecules named as A and B, several MEBFs can be constructed, e.g., one MEBF describing both molecules in their ground state ($|\Phi_{S_0S_0}\rangle$); two MEBFs in which one of the molecules is in the lowest singlet excited state ($|\Phi_{S_0S_1}\rangle$ and $|\Phi_{S_1S_0}\rangle$); one MEBF representing the two triplets coupled into a singlet ($|\Phi_{^1TT}\rangle$); and two MEBFs describing the charge transfer states ($|\Phi_{D_0^+D_0^-}\rangle$ and $|\Phi_{D_0^-D_0^+}\rangle$). The three spin singlet MEBFs constructed from the molecular wave functions with $S = 0$ are formed as:

$$|\Phi_{S_0S_0}\rangle = \hat{A}|\Psi_A^{S_0}\Psi_B^{S_0}\rangle \tag{4a}$$

$$|\Phi_{S_0S_1}\rangle = \hat{A}|\Psi_A^{S_0}\Psi_B^{S_1}\rangle \tag{4b}$$

$$|\Phi_{S_1S_0}\rangle = \hat{A}|\Psi_A^{S_1}\Psi_B^{S_0}\rangle \tag{4c}$$

whereas the MEBFs constructed from the molecular wave functions with $S > 0$ (i.e., Ψ^T, $\Psi^{D_0^+}$, and $\Psi^{D_0^-}$) are expressed as linear combinations of the antisymmetrized products of those molecular functions, in such a way that the total M_s and S are equal to 0[30]:

$$|\Phi_{^1TT}\rangle = \frac{1}{\sqrt{3}}\hat{A}\left|\left(\Psi_A^T\right)_{M_s=+1}\left(\Psi_B^T\right)_{M_s=-1}\right\rangle + \frac{1}{\sqrt{3}}\hat{A}\left|\left(\Psi_A^T\right)_{M_s=-1}\left(\Psi_B^T\right)_{M_s=+1}\right\rangle - \frac{1}{\sqrt{3}}\hat{A}\left|\left(\Psi_A^T\right)_{M_s=0}\left(\Psi_B^T\right)_{M_s=0}\right\rangle \tag{5a}$$

$$\left|\Phi_{D_0^+D_0^-}\right\rangle = \frac{1}{\sqrt{2}}\hat{A}\left|\left(\Psi_A^{D_0^+}\right)_{M_s=+1/2}\left(\Psi_B^{D_0^-}\right)_{M_s=-1/2}\right\rangle - \frac{1}{\sqrt{2}}\hat{A}\left|\left(\Psi_A^{D_0^+}\right)_{M_s=-1/2}\left(\Psi_B^{D_0^-}\right)_{M_s=+1/2}\right\rangle \tag{5b}$$

$$\left|\Phi_{D_0^-D_0^+}\right\rangle = \frac{1}{\sqrt{2}}\hat{A}\left|\left(\Psi_A^{D_0^-}\right)_{M_s=+1/2}\left(\Psi_B^{D_0^+}\right)_{M_s=-1/2}\right\rangle - \frac{1}{\sqrt{2}}\hat{A}\left|\left(\Psi_A^{D_0^-}\right)_{M_s=-1/2}\left(\Psi_B^{D_0^+}\right)_{M_s=+1/2}\right\rangle. \tag{5c}$$

Then, the total NOCI wave function (Ψ_{NOCI}) describing the ensemble is expressed as a linear combination of the different MEBFs:

$$\Psi_{\mathrm{NOCI}} = \sum_{\mu} C_\mu |\Phi_\mu\rangle \tag{6}$$

in which the coefficients C_μ are determined using variational theory and can be related to a weight for each MEBF that indicates the importance of a particular combination of molecular electronic states in the description of an electronic state of the ensemble. To perform such a calculation the Hamiltonian $\langle\Phi_\mu|\hat{H}|\Phi_\nu\rangle$ and overlap $\langle\Phi_\mu|\Phi_\nu\rangle$ matrix elements are needed. The MEBFs are mutually nonorthogonal, since they are constructed from independent and fully optimized molecular wave functions. Note that each $|\Phi_\mu\rangle$ consists of multiple determinants and therefore for the calculation of $\langle\Phi_\mu|\hat{H}|\Phi_\nu\rangle$ a large number of Hamiltonian matrix elements over determinant pairs has to be evaluated; this becomes the main computational challenge. The Hamiltonian and overlap matrix elements can be then used to calculate the electronic coupling, according to[26]

$$V_{\mu\nu} = \frac{\langle\Phi_\mu|\hat{H}|\Phi_\nu\rangle - \frac{\left(\langle\Phi_\mu|\hat{H}|\Phi_\mu\rangle + \langle\Phi_\nu|\hat{H}|\Phi_\nu\rangle\right)}{2}\cdot\langle\Phi_\mu|\Phi_\nu\rangle}{1-\langle\Phi_\mu|\Phi_\nu\rangle^2} \tag{7}$$

where Φ_μ and Φ_ν denote the initial and final (diabatic) states of interest, respectively, which in the case of SF correspond to the photo excited states and the two coupled triplets. The Hamiltonian in Eq. (7) is the Hamiltonian for the ensemble within the Born–Oppenheimer approximation. Please note that the MEBFs are denoted as $|\Phi\rangle$ whereas the electronic states are denoted by Φ.

The chapter is structured as follows: in Section 3.1, we compare the NOCI method with two other methodologies, restricted active space with two spin flips (RAS-2SF)[31–33] and the *ab initio* Frenkel–Davydov exciton model (AIFDEM)[34–36] for a tetracene dimer. Then in Section 3.2, we identify a potential SF molecule from a group of candidates and, finally, in Section 3.3 we perform a comparison of the NOCI, RAS-2SF and AIFDEM methods applied to the identified molecule. Our conclusions are given in Section 4.

2. Computational details

The identification of suitable SF molecules requires the evaluation of excitation energies. T_1, S_1, and T_2 (vertical) excitation energies for a set of candidates (Fig. S2) were calculated with various methodologies: (1) time-dependent density functional theory (TD-DFT);[37] (2) scaled-opposite-spin configuration interaction singles with a perturbative account of double excitations (SOS-CIS(D));[38] (3) CASSCF with correction to the energy using second-order perturbation theory (CASSCF/CASPT2),[39]; and (4) the second-order algebraic diagrammatic construction scheme[40] (ADC(2)) of the polarization propagator. TD-DFT, SOS-CIS(D), and ADC(2) calculations were performed using Q-Chem 5.0,[41] whereas the CASSCF/CASPT2 calculations with the MOLCAS 8.0[42] code. The active spaces selected for each of the molecules are specified in Table S1. Unless otherwise stated, the basis set used is cc-pVDZ.

A crystal structure of the potential SF molecule is proposed, and all the relevant geometries of the identified pairs of molecules are given in Supplementary Materials in the online version at https://10.1016/bs.aiq.2019.05.004. Additionally, the molecules in the identified pairs in the optimized crystal structure were replaced by an optimized molecule at the ωB97X-D/cc-pVDZ level of theory, by arranging them as in the respective crystal structure distance and angle. Electronic couplings were

calculated for the pairs of molecules obtained by the periodic DFT calculations and for the pairs in which the molecules were replaced, in order to study the influence of different structural arrangements in the electronic couplings.

Molecular wave functions of the CASSCF-type with an active space of four electrons in four orbitals (CASSCF(4,4)) describing the S_0, S_1, T_1, D_0^+, and D_0^- states for the different molecules in each pair were calculated using the GAMESS-UK package.[43] MEBFs representing the following electronic states of the pairs of molecules were generated: $|\Phi_{S_0S_0}\rangle$, $|\Phi_{S_1S_0}\rangle$, $|\Phi_{S_0S_1}\rangle$, $|\Phi_{^1TT}\rangle$, $|\Phi_{D_0^+D_0^-}\rangle$ and $|\Phi_{D_0^-D_0^+}\rangle$. Two diabatic states, $\Phi_{S_{[1]}}$ and $\Phi_{S_{[2]}}$, were constructed from a 2 × 2 NOCI calculation in the basis of the $|\Phi_{S_0S_1}\rangle$ and $|\Phi_{S_1S_0}\rangle$ MEBFs, whereas the diabatic state $\Phi_{^1TT}$ corresponds to the $|\Phi_{^1TT}\rangle$ MEBF. The influence of the charge transfer states is explored by adding the corresponding MEBFs to the $\Phi_{S_{[1]}}$ and $\Phi_{S_{[2]}}$ states (resulting in 4 × 4 NOCI calculations) and to the $\Phi_{^1TT}$ (resulting in a 3 × 3 NOCI calculation). To investigate the importance of each MEBF in the diabatic $\Phi_{S_{[1]}}$, $\Phi_{S_{[2]}}$, and $\Phi_{^1TT}$ states, the weights (ω_i) of the MEBFs were calculated using the Gallup and Norbeck scheme,[44] $\omega_i = |C_i|^2/(S^{-1})_{ii}$, where C_i corresponds to the CI coefficient of the ith MEBF and $(S^{-1})_{ii}$ denotes the iith element of the inverse of the overlap matrix in the MEBF basis. The NOCI methodology has been implemented in the package GronOR.[45] The calculation of the Hamiltonian matrix elements is performed by means of the factorized cofactor method which is described in Ref. 46.

For the RAS-2SF and AIFDEM methodologies we follow the protocols as outlined in Refs. 47 and 36, respectively. The RAS-2SF calculations for the dimer arrangements were performed with an active space of four electrons in four orbitals (RAS(4,4)-2SF) using a high-spin quintet as the initial reference.[33] The resulting dimer wave functions ($|\Phi\rangle$) are then described in terms of different configurations: local excited ($|\Psi_{LE}\rangle$), multiexcitonic ($|\Psi_{^1TT}\rangle$), and charge transfer states or charge-resonance ($|\Psi_{CT}\rangle$);

$$|\Phi\rangle = C^{LE}|\Psi_{LE}\rangle + C^{^1TT}|\Psi_{^1TT}\rangle + C^{CT}|\Psi_{CT}\rangle \tag{8}$$

where C^{LE}, $C^{^1TT}$, and C^{CT} are the corresponding amplitudes of the LE, CT, and ^1TT configurations. The importance of each configuration in the different states is described by the corresponding weights (ω_i), calculated as the square of their amplitudes ($\omega_{LE} = |C^{LE}|^2, \omega_{^1TT} = |C^{^1TT}|^2$, and $\omega_{CT} = |C^{CT}|^2$). Based on these weights, $\Phi_{S_{[1]}}$ and $\Phi_{S_{[2]}}$ states are assigned to those wave functions with large ω_{LE}, whereas the $\Phi_{^1TT}$ corresponds to the one

with large $\omega_{^1TT}$. Then, the norm of the one-particle transition density matrix ($||\gamma||^2$) is used to estimate the couplings between singlet excited and ^1TT states.[48]

The nonorthogonal AIFDEM methodology follows, in principle, the same protocol as the NOCI approach. For each pair of molecules, molecular wave functions are generated and then, MEBFs describing the electronic states of the ensemble are constructed as direct products of those molecular wave functions. In AIFDEM, Hartree–Fock wave functions are used for the description of the S_0, D_0^+, and D_0^- states and CIS wave functions for the S_1 and T_1 states.[34] As in NOCI, six different MEBFs were generated: $|\Phi_{S_0S_0}\rangle$, $|\Phi_{S_1S_0}\rangle$, $|\Phi_{S_0S_1}\rangle$, $|\Phi_{^1TT}\rangle$, $|\Phi_{D_0^+D_0^-}\rangle$, and $|\Phi_{D_0^-D_0^+}\rangle$. Then, the total wave function of the ensemble is expanded as a linear combination of the MEBFs, and the CI coefficients (C_μ in Eq. (6)) are determined using variational theory. The resulting CIS and Hartree–Fock energies were corrected, as outlined in the protocol in Ref. 36, by shifting the diagonal elements of the Hamiltonian matrix in the orthogonalized[49] basis to match reference values calculated for an optimized molecule at the ωB97X-D/cc-pVDZ level of theory. The $\langle\Phi_{S_0S_1}|\hat{H}|\Phi_{S_0S_1}\rangle$ and $\langle\Phi_{S_1S_0}|\hat{H}|\Phi_{S_1S_0}\rangle$ elements were shifted to match the vertical S_1 excitation energy, whereas the $\langle\Phi_{^1TT}|\hat{H}|\Phi_{^1TT}\rangle$ element was shifted to twice the T_1 excitation energy. It has been shown in a benchmark study that among various popular functionals, the ωB97X-D functional gives the best description of excited state properties when compared to high-level wave function methods.[50–52] The $\Phi_{D_0^+D_0^-}$ and $\Phi_{D_0^-D_0^+}$ energy reference values were approximated as the sum of three terms: ionization potential (IP), electron affinity (EA), and the Coulombic attraction (CA). IP and EA were calculated from the energies of the neutral, cationic, and anionic form of a molecule at the ωB97X-D/cc-pVDZ level of theory, whereas the CA was determined as the electrostatic attraction between the centers of mass of the molecules in the corresponding cationic and anionic ground states. The weights of each MEBF were calculated similarly to the NOCI approach. The RAS-2SF and AIFDEM calculations were carried out using Q-Chem 5.0.[41]

3. Results and discussion

3.1 Comparing NOCI, RAS-2SF, and AIFDEM for tetracene

A pair of tetracene molecules, an extensively studied singlet fission molecule,[53,54] has been used to compare the NOCI approach with RAS-2SF and AIFDEM before studying unexplored systems. Fig. 3 shows the

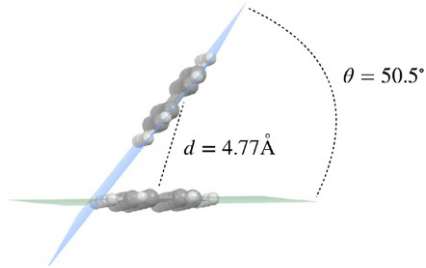

Fig. 3 Tetracene dimer arrangement; d = centers of masses distance, θ = angle between the molecular planes.

Table 1 State energies (in eV) of the different electronic states for a pair of tetracene molecules.

Method	$\Phi_{^1TT}$	$\Phi_{S_{[1]}}$	$\Phi_{S_{[2]}}$	$\Phi_{D_0^+D_0^-}$	$\Phi_{D_0^-D_0^+}$
NOCI:CASSCF(4,4)	3.96	4.30	4.41	4.71	5.42
NOCI:CASCI[26]	4.12	4.45	4.49	4.94	5.03
RAS(4,4)-2SF	3.52	4.11		5.00	
AIFDEM	3.20(4.39)	3.20(3.78)	3.26(3.86)	3.50(3.42)	3.52(4.13)
Experimental	2.54[55]	2.62[56]	2.62[56]	2.90[57]	2.90[57]

For AIFDEM, the unshifted values are reported in parenthesis. The calculated $\Phi_{S_{[2]}}$ state with RAS-2SF is dominated by the $|\Phi_{S_1S_1}\rangle$ configuration and is not included.

orientation of the tetracenes in the tetracene dimer arrangement. The methods are compared in three aspects: (1) the calculated state energies in order to determine whether the charge transfer states act as real or virtual intermediate states, (2) the calculated weights of the different MEBFs in order to determine if the methods can predict similar character for the electronic states, and (3) we compare the calculated electronic couplings. The calculated state energies and the individual contributions for the tetracene dimer arrangement are shown in Tables 1 and 2, respectively. The energies in Table 1 were calculated in the gas-phase, whereas the reported experimental values correspond to determinations in solution[55,56] for S_1 and T_1 and in the crystal structure for the CT states[57].

3.1.1 Excited state energies

The energies calculated with the NOCI approach are reported in Table 1. For the sake of computational cost, we have restricted the active space of the molecular wave functions to four electrons in four orbitals (denoted NOCI:

Table 2 Comparison of the individual weights of MEBFs obtained for a pair of tetracene molecules.

State	$\Phi_{^1TT}$			$\Phi_{S_{[1]}}$			$\Phi_{S_{[2]}}$		
Configuration	**NOCI**	**RAS-2SF**	**AIFDEM**	**NOCI**	**RAS-2SF**	**AIFDEM**	**NOCI**	**RAS-2SF**	**AIFDEM**
$\lvert\Phi_{S_0S_0}\rangle$	0.000	0.001	0.000	0.001	0.017	0.002	0.000		0.000
$\lvert\Phi_{S_0S_1}\rangle$	0.000	0.001	0.005	**0.999**	**0.642**	**0.929**	0.000		0.009
$\lvert\Phi_{S_1S_0}\rangle$	0.001	0.001	0.027	0.000	0.063	0.016	**0.978**		**0.867**
$\lvert\Phi_{^1TT}\rangle$	**0.999**	**0.935**	**0.894**	0.000	0.001	0.009	0.020		0.007
$\lvert\Phi_{D_0^+D_0^-}\rangle$	0.000	0.008	0.014	0.000	0.023	0.038	0.001		0.112
$\lvert\Phi_{D_0^-D_0^+}\rangle$	0.000	0.054	0.060	0.000	0.003	0.006	0.000		0.005

The main contributions are highlighted as bold numbers. The calculated $\Phi_{S_{[2]}}$ state with RAS-2SF is dominated by the $\lvert\Phi_{S_1S_1}\rangle$ configuration and is not included.

CASSCF(4,4)). The NOCI energies are overestimated when compared to the experimental values. The energies might be improved by adding the remaining π- and π^*-like orbitals to the active space. RAS-2SF also overestimates the energies of the electronic states because of an incomplete account of dynamic correlation,[58] and as in the NOCI approach, the energies are expected to improve by increasing the active space. The energies calculated with AIFDEM have been corrected as explained in Section 2; these energy values are also overestimated. The overestimation of the energies for the three methods might be due to the fact that the calculations are performed without the environment effects, neither the solvent nor the surrounding crystal structure. Despite this overestimation, the results suggest that the CT states are too high in energy to be accessed but perhaps act as virtual states promoting a mediated mechanism. The calculated state energies in this work are compared with previously reported values[26] in which a NOCI calculation was performed for a cluster of three tetracene molecules (values denoted as NOCI: CASCI in Table 1). Unlike here, where we generate proper spin-adapted, antisymmetrized products of molecular wave functions as the MEBFs, in that work MEBFs were approximated by CASCI wave functions: the orbital sets resulting from molecular CASSCF(4,4) wave functions were projected on the basis of the trimer, followed by orthogonalization and a CASCI(12,12) calculation. This procedure results in MEBFs, contaminated with small contributions of (unwanted) CT states. Differences between the results in state energies and electronic couplings in this work and Ref. 26 can be attributed to differences in the geometry of the ensemble (Ref. 26 used a B3LYP/6-21G optimized geometry and here the pair of molecules was taken from Supplementary Materials in the online version at https://10.1016/bs.aiq.2019.05.004 of Ref. 36 from a plane-wave DFT optimized structure).

3.1.2 Weights of MEBFs

The weights of the individual contributions of the different MEBFs to the $\Phi_{^1TT}$, $\Phi_{S_{[1]}}$, and $\Phi_{S_{[2]}}$ states are listed in Table 2. The dominant contributions to the electronic states are highlighted as bold numbers; the $\Phi_{^1TT}$ state corresponds mainly to the $|\Phi_{^1TT}\rangle$ MEBF for the three methodologies. The AIFDEM predicts a contribution from the $|\Phi_{D_0^- D_0^+}\rangle$ state that is not observed in the NOCI approach. In order to shed more light on the origin of this discrepancy, we have applied the same shift to NOCI. The NOCI results (Tables S2 and S3) predict also a contribution from $|\Phi_{D_0^+ D_0^-}\rangle$ and $|\Phi_{D_0^- D_0^+}\rangle$ after applying the shift. From the shiftings applied to NOCI and AIFDEM,

we have observed two opposite trends; in the case of NOCI, the CT states become more important (higher weights) since the CT energies are lowered, whereas in the case of AIFDEM, the CT weights decrease since the CT states are shifted to the reference value which is higher (see Tables S2 and S3 for shifted and unshifted NOCI and AIFDEM individual weights of MEBFs). For the $\Phi_{S_{[1]}}$ and $\Phi_{S_{[2]}}$ states, the main contributions obtained with NOCI and AIFDEM correspond to the $|\Phi_{S_0S_1}\rangle$ and $|\Phi_{S_1S_0}\rangle$ MEBFs, respectively. For the $\Phi_{S_{[1]}}$ state, the configuration $|\Phi_{S_1S_1}\rangle$ was found to have a large weight in the RAS-2SF calculations, however, this particular configuration is not of interest for the SF process. The calculated $\Phi_{S_{[2]}}$ state with RAS-2SF is dominated by the $|\Phi_{S_1S_1}\rangle$ configuration and it is not included for comparison. In fact, differences in calculated weights with NOCI and AIFDEM and those obtained with RAS-2SF are attributed to the fact that additional configurations, such as $|\Phi_{S_1S_1}\rangle$, are considered in RAS-2SF. In sum, the methods show similar contributions of the different electronic states, despite the differences in the numerical values.

3.1.3 Electronic couplings

Electronic couplings between $\Phi_{S_{[1]}}$ and $\Phi_{S_{[2]}}$ with the $\Phi_{^1TT}$ states calculated with the NOCI approach for the tetracene pair are reported in Table 3. In the primed wave functions, the CT states were allowed to mix with the wave functions of the singlet excited and ^1TT states. The results indicate that the electronic coupling is enhanced from 2.2 to 37.6 meV when the CT states are allowed to mix; this enhancement is in line with a previous NOCI study of a cluster of three tetracene molecules.[26] A similar trend is observed in the electronic couplings that we calculated with AIFDEM; the values are enhanced when the CT configurations are included in the calculation (see Table S4). The increase in the coupling can be then attributed to the mixing in of the CT states with both photo excited states and the multiexcitonic state.

Table 3 Electronic couplings (in meV) between the (diabatic) states $\Phi_{S[1]}$ and $\Phi_{S[2]}$ with $\Phi_{^1TT}$ for the tetracene pair.

States	$\Phi_{S_{[1]}}$	$\Phi_{S_{[2]}}$	$\Phi'_{S_{[1]}}$	$\Phi'_{S_{[2]}}$
$\Phi_{^1TT}$	4.0	2.2	2.2	58.9
$\Phi'_{^1TT}$	7.9	19.6	4.0	37.6

In the primed wave functions the CT states were included in the NOCI calculation.

3.1.4 Comparison

All three methods show a similar qualitative trend for the tetracene dimer; they predict that the CT states are too high in energy to be accessed. However, the discrepancies between numerical values are evident. The three methods overestimate the state energies when compared with the experimental values. The NOCI and AIFDEM approaches are conceptually similar. (Static) electron correlation and (local) orbital relaxation effects can be included in the NOCI approach but our current implementation in the GronOR package is able to treat only small clusters of small molecules. The current AIFDEM implementation is able to handle large clusters and molecules. Additionally, analytical gradients and nonadiabatic couplings are available for the AIFDEM method[36] but not implemented in GronOR so far. Electronic couplings can be directly calculated for NOCI and AIFDEM but for RAS-2SF it is only possible to estimate the coupling based on $||\gamma||^2$ values.

3.2 Identification of a SF molecule based on excitation energies

In this chapter, a group of SF candidates has been selected (Fig. S2). (Vertical) excitation energies of the T_1, S_1, and T_2 states calculated with different levels of electronic structure theories are reported in Table S5 together with E_{stt}, which is defined as $E_{stt} = E(S_1) - 2E(T_1)$. SF should be, in principle, an isoergic process which means that E_{stt} must be ideally close to zero. Nevertheless, experimental values (Table S5) suggest that the process also occurs if it is slightly endo or exoergic. Therefore, for potential SF molecules E_{stt} should lie roughly in the -0.1 to 0.1 eV range. From the results in Table S5, the isobenzofulvene derivative 2-methylene-2H-indene (named as M2I for the upcoming discussion) is selected for further evaluation as a promising SF molecule.

3.3 Comparing NOCI, RAS-2SF, and AIFDEM for 2-methylene-2H-indene

3.3.1 Pairs of molecules

In the optimized crystal structure of M2I, four different pairs of molecules were identified (Fig. 4A). Two of them show a π-like stacking (slip-stacked) and have been named I-A and I-C, whereas the other two correspond to structural arrangements that differ in the angle between the molecular planes of the molecules, and they are denoted for the upcoming discussion I-B ($\theta = 131°$) and I-D ($\theta = 49°$) (Fig. 4B and Fig. S3 for further information).

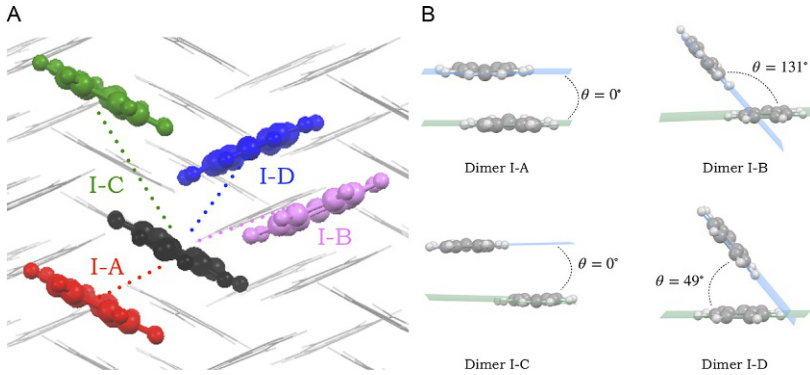

Fig. 4 (A) Identified pairs of molecules of M2I; from a central molecule (*black*) the I-A (*red*), I-B (*pink*), I-C (*green*), and I-D (*blue*) conformations are depicted. (B) The angle between the molecular planes in each pair is depicted. Crystal structure optimized at the PBE/6-31G(d,p) level of theory.

3.3.2 Excited state analysis

The first singlet excited and lowest triplet states of M2I correspond mainly to a single excitation with $\pi \rightarrow \pi^*$ character as can be seen from the frontier orbitals depicted in Fig. S4. The biradicaloid character of M2I has been reported,[59] but a CASSCF(10,10) calculation on the ground state shows 1.83 and 0.20 as the natural orbital occupation numbers for the HOMO and LUMO, respectively, suggesting a closed shell character for the molecule.

3.3.3 Excited state energies

The energies of the $\Phi_{^1TT}$, $\Phi_{S_{[1]}}$, $\Phi_{S_{[2]}}$, $\Phi_{D_0^+D_0^-}$, and $\Phi_{D_0^-D_0^+}$ states for the four pairs of molecules are shown in Table 4. The RAS-2SF energies are lower than those obtained with the NOCI approach and the shifted energies in AIFDEM. A close look at the hole and particle contributions in the RAS active space reveals that the HOMO-1 should have been included as an active orbital; the underestimation of the excitation energies in this case suggests that RAS-2SF is suitable for the description of molecules in which it is sufficient to consider the frontier orbitals in the active space, e.g., tetracene. State energies are improved by including the required orbitals in the active space (see RAS(8,6)-2SF and RAS(8,8)-2SF calculations in Table S6). For I-B and I-D, the $\Phi_{S_{[2]}}$ state is dominated by the $|\Psi_{S_1S_1}\rangle$ configuration which suggests a double excitation character. Therefore, these states were not included in the comparison. The NOCI energies of the $\Phi_{S_{[1]}}$ and $\Phi_{S_{[2]}}$ states

Table 4 State energies (in eV) for the different electronic states for the four pairs of molecules of M2I.

Pair	Method	$\Phi_{^1TT}$	$\Phi_{S_{[1]}}$	$\Phi_{S_{[2]}}$	$\Phi_{D_0^+D_0^-}$	$\Phi_{D_0^-D_0^+}$
I-A	NOCI	2.15	2.47	2.49	4.27	4.32
	RAS(4,4)-2SF	1.33	1.97	2.08	3.29	3.32
	AIFDEM	2.29(3.38)	2.43(3.53)	2.50(4.05)	5.03(2.68)	5.13(2.99)
I-B	NOCI	2.12	2.41	2.42	4.69	5.07
	RAS(4,4)-2SF	1.28	1.96		4.05	
	AIFDEM	2.33(2.95)	2.39(3.02)	2.53(3.17)	5.00(2.78)	5.11(3.11)
I-C	NOCI	2.12	2.41	2.42	4.69	5.07
	RAS(4,4)-2SF	1.27	1.96	1.98	4.11	4.25
	AIFDEM	2.34(2.72)	2.41(3.02)	2.47(3.07)	5.00(2.92)	5.12(2.94)
I-D	NOCI	2.11	2.39	2.42	4.36	4.92
	RAS(4,4)-2SF	1.26	1.97		3.64	
	AIFDEM	2.33(2.97)	2.43(3.01)	2.46(3.19)	5.00(2.40)	5.12(2.90)

For AIFDEM, the unshifted values are shown in parenthesis. $\Phi_{S_{[2]}}$ states calculated with RAS-2SF are dominated by the $|\Phi_{S_1S_1}\rangle$ configuration and are not included.

are close to the $\Phi_{^1TT}$ energy deviating by only ~0.3 meV, showing that the system almost fulfills the requirement $E_{stt} = 0$. The NOCI $\Phi_{D_0^+D_0^-}$ and $\Phi_{D_0^-D_0^+}$ energies are 2.0 eV or more above the $\Phi_{S_{[1]}}$ and $\Phi_{S_{[2]}}$ energies indicating that these states are too high in energy to be accessed but might act as virtual states mediating the SF process; the same trend holds for RAS-2SF and AIFDEM CT state energies.

3.3.4 Weights of MEBFs

Table 5 shows a comparison between the weights of the MEBFs to the $\Phi_{^1TT}$, $\Phi_{S_{[1]}}$, and $\Phi_{S_{[2]}}$ states in the pairs of molecules. The dominant contributions, highlighted as bold numbers, show that for the four pairs of molecules the $\Phi_{^1TT}$ states have almost pure $|\Phi_{^1TT}\rangle$ character, whereas $\Phi_{S_{[1]}}$ and $\Phi_{S_{[2]}}$ are described mainly by the singlet excited MEBFs; the weights suggest that the excitation is localized on one of the two molecules for all the cases. A similar trend is observed with the RAS-2SF and AIFDEM methodologies, although in RAS-2SF the $|C|^2$ values are lower than those calculated with

Table 5 Comparison of the individual weights of MEBFs in the four pair arrangements of M2I.

	$\Phi_{^1TT}$			$\Phi_{S_{[1]}}$			$\Phi_{S_{[2]}}$		
Configuration	**NOCI**	**RAS-2SF**	**AIFDEM**	**NOCI**	**RAS-2SF**	**AIFDEM**	**NOCI**	**RAS-2SF**	**AIFDEM**
				Pair I-A					
$\lvert\Phi_{S_0S_0}\rangle$	0.001	0.001	0.000	0.000	0.066	0.014	0.000	0.000	0.007
$\lvert\Phi_{S_0S_1}\rangle$	0.014	0.013	0.041	**0.982**	**0.665**	**0.889**	0.000	0.000	0.000
$\lvert\Phi_{S_1S_0}\rangle$	0.000	0.013	0.059	0.000	0.000	0.000	**0.999**	**0.828**	**0.929**
$\lvert\Phi_{^1TT}\rangle$	**0.985**	**0.885**	**0.539**	0.018	0.060	0.000	0.000	0.000	0.000
$\lvert\Phi_{D_0^+D_0^-}\rangle$	0.000	0.037	0.000	0.000	0.019	0.096	0.000	0.008	0.063
$\lvert\Phi_{D_0^-D_0^+}\rangle$	0.000	0.037	0.360	0.000	0.019	0.000	0.000	0.008	0.000
				Pair I-B					
$\lvert\Phi_{S_0S_0}\rangle$	0.000	0.000	0.000	0.000	0.009	0.001	0.000		0.004
$\lvert\Phi_{S_0S_1}\rangle$	0.000	0.000	0.001	**1.000**	**0.675**	**0.995**	0.000		0.003
$\lvert\Phi_{S_1S_0}\rangle$	0.000	0.000	0.000	0.000	0.000	0.003	**1.000**		**0.991**
$\lvert\Phi_{^1TT}\rangle$	**1.000**	**1.000**	**0.999**	0.000	0.000	0.000	0.000		0.000
$\lvert\Phi_{D_0^+D_0^-}\rangle$	0.000	0.000	0.000	0.000	0.000	0.001	0.000		0.002
$\lvert\Phi_{D_0^-D_0^+}\rangle$	0.000	0.000	0.000	0.000	0.000	0.000	0.000		0.000

Continued

Table 5 Comparison of the individual weights of MEBFs in the four pair arrangements of M2I.—cont'd

	$\Phi_{^1TT}$			$\Phi_{S_{[1]}}$			$\Phi_{S_{[2]}}$		
Configuration	**NOCI**	**RAS-2SF**	**AIFDEM**	**NOCI**	**RAS-2SF**	**AIFDEM**	**NOCI**	**RAS-2SF**	**AIFDEM**
					Pair I-C				
$\lvert\Phi_{S_0S_0}\rangle$	0.000	0.000	0.000	0.000	0.000	0.001	0.000	0.015	0.001
$\lvert\Phi_{S_0S_1}\rangle$	0.000	0.000	0.000	**1.000**	**0.853**	**0.996**	0.000	0.000	0.003
$\lvert\Phi_{S_1S_0}\rangle$	0.000	0.000	0.000	0.000	0.000	0.003	**1.000**	**0.822**	**0.996**
$\lvert\Phi_{^1TT}\rangle$	**1.000**	**1.000**	**1.000**	0.000	0.000	0.000	0.000	0.000	0.000
$\lvert\Phi_{D_0^+D_0^-}\rangle$	0.000	0.000	0.000	0.000	0.000	0.000	0.000	0.000	0.000
$\lvert\Phi_{D_0^-D_0^+}\rangle$	0.000	0.000	0.000	0.000	0.000	0.000	0.000	0.000	0.000
					Pair I-D				
$\lvert\Phi_{S_0S_0}\rangle$	0.000	0.000	0.000	0.000	0.226	0.001	0.000		0.001
$\lvert\Phi_{S_0S_1}\rangle$	0.000	0.000	0.000	**1.000**	**0.572**	**0.999**	0.000		0.000
$\lvert\Phi_{S_1S_0}\rangle$	0.000	0.000	0.000	0.000	0.000	0.000	**1.000**		**0.999**
$\lvert\Phi_{^1TT}\rangle$	**1.000**	**0.996**	**0.998**	0.000	0.000	0.000	0.000		0.000
$\lvert\Phi_{D_0^+D_0^-}\rangle$	0.000	0.003	0.001	0.000	0.004	0.000	0.000		0.000
$\lvert\Phi_{D_0^-D_0^+}\rangle$	0.000	0.001	0.001	0.000	0.002	0.000	0.000		0.000

The main contributions are highlighted as bold numbers. $\Phi_{[2]}$ states calculated with RAS-2SF are dominated by the $\lvert\Phi_{S_1S_1}\rangle$ configuration and are not included.

NOCI and AIFDEM since additional configurations, such as double excitations ($|\Phi_{S_1S_1}\rangle$), contribute. NOCI shows that the states in I-B, I-C, and I-D retain mostly a pure character, which is also observed in the individual contributions calculated with RAS-2SF and AIFDEM. However, the contributions for the $\Phi_{^1TT}$ state in dimer I-A are different between the methods; the weights from the NOCI calculation predict that $\Phi_{^1TT}$ has mainly a contribution from the $|\Phi_{^1TT}\rangle$ MEBF with a small contribution from $|\Phi_{S_0S_1}\rangle$, whereas RAS-2SF and the weights obtained with AIFDEM predict a contribution from the CT states. After applying the same shift to NOCI, contributions from the CT states are also observed (see Table S8). When we shift NOCI and AIFDEM (see Tables S8 and S9), we observed the same trends in the weights as in tetracene.

3.3.5 Electronic couplings

In Table 6, electronic couplings are reported for the four pairs of molecules between the $\Phi_{S_{[1]}}$ and $\Phi_{S_{[2]}}$ states with the $\Phi_{^1TT}$ state. The largest coupling values are observed in I-A, whereas the lower values are obtained for I-B and I-C. For I-A, the inclusion of the CT states to the $\Phi_{S_{[1]}}$ state enhances the electronic coupling from 21.4 to 42.2 meV. The electronic coupling is also enhanced if the CT states are allowed to interact only with the $\Phi_{^1TT}$ state. For the $\Phi_{S_{[2]}}$ state, no significant enhancement is observed. The most plausible determination of the electronic coupling in I-A corresponds to that

Table 6 Electronic couplings (in meV) between the (diabatic) states $\Phi_{S[1]}$ and $\Phi_{S[2]}$ with $\Phi_{^1TT}$ for the dimer arrangements of M2I.

Pair	States	$\Phi_{S_{[1]}}$	$\Phi_{S_{[2]}}$	$\Phi'_{S_{[1]}}$	$\Phi'_{S_{[2]}}$
I-A	$\Phi_{^1TT}$	21.4	0.4	42.2	0.4
I-B		0.2	0.1	0.2	0.2
I-C		0.0	0.3	0.0	0.4
I-D		0.6	0.6	0.4	1.3
I-A	$\Phi'_{^1TT}$	38.0	1.1	39.8	0.4
I-B		0.2	0.3	0.2	0.2
I-C		0.0	0.4	0.0	0.4
I-D		0.1	1.2	0.3	1.3

In the primed wave functions the CT states were included in the NOCI calculation.

in which the CT states are allowed to mix with both the $\Phi_{S_{[1]}}$ and $\Phi_{^1TT}$ states, with a value of 39.8 meV. The magnitude of the electronic coupling suggests that the formation of the ^1TT state could occur efficiently. We performed the same analysis for the four pairs of molecules in which the molecules were replaced by optimized molecules (Tables S10–S12). Originally, the pairs of molecules from the periodic DFT optimization were slightly bent, and after the replacement they became planar. Although the quantitative results changed, the same observations as discussed above (regarding the excitation energies of the states, the individual contributions of the MEBFs and the electronic couplings) are observed; the highest electronic coupling is found for I-A and the lowest for I-B and I-C. It is apparent that the electronic couplings strongly depend on the orientation of the molecules in the cluster.

Table 7 shows the configurational analysis of the RAS-2SF wave functions of the pairs of molecules showing their local excited (LE), multiexcitonic (ME) and CT character, and the $||\gamma||^2$ values between the $\Phi_{^1TT}$ with $\Phi_{S_{[1]}}$ and $\Phi_{S_{[2]}}$ states are also listed. The $||\gamma||^2$ values indicate that the transition is most probable to occur when the molecules are disposed as in arrangement I-A (0.25 and 0.30), for I-D also a transition is expected to occur (0.09), whereas for I-B and I-C no transition would be observed. The $||\gamma||^2$ values obtained with the RAS(8,6)-2SF and RAS(8,8)-2SF calculations (see Tables S13 and S14) show the same trend. The differences in

Table 7 Configuration analysis of the RAS-2SF wave functions for the pair arrangements of M2I using localized obitals within the DMO-LCFMO framework.

Pair	State	LE	ME	CT	$\|\|\gamma\|\|^2$	Pair	State	LE	ME	CT	$\|\|\gamma\|\|^2$
I-A	$\Phi_{^1TT}$	0.03	0.89	0.07		I-B	$\Phi_{^1TT}$	0.00	1.00	0.00	
	$\Phi_{S_{[1]}}$	0.83	0.15	0.02	0.25		$\Phi_{S_{[1]}}$	0.67	0.32	0.00	0.01
	$\Phi_{S_{[2]}}$	0.66	0.23	0.04	0.30		$\Phi_{S_{[2]}}$				
I-C	$\Phi_{^1TT}$	0.00	1.00	0.00		I-D	$\Phi_{^1TT}$	0.00	0.99	0.00	
	$\Phi_{S_{[1]}}$	0.85	0.15	0.00	0.02		$\Phi_{S_{[1]}}$	0.57	0.20	0.01	0.09
	$\Phi_{S_{[2]}}$	0.82	0.16	0.00	0.02		$\Phi_{S_{[2]}}$				

The values of $||\gamma||^2$ between the $\Phi_{^1TT}$ and each of the local excited states $\Phi_{S_{[1]}}$ and $\Phi_{S_{[2]}}$ are shown. $\Phi_{S_{[2]}}$ states calculated with RAS-2SF are dominated by the $|\Phi_{S_1 S_1}\rangle$ configuration, and are not included for comparison.

the $||\gamma||^2$ values can be associated to the degree of contribution of the CT states to the singlet excited and ^1TT states. CT contributions are predicted for I-A and I-D whereas they are negligible for I-B and I-C. Remarkably, the electronic couplings calculated with NOCI and AIFDEM (Table S15) follow the qualitative behavior predicted by the RAS-2SF method, in which the highest values are observed for I-A; this implies that if the molecules are disposed as in this conformation in the crystal structure, the SF process might occur efficiently.

4. Conclusions

We report a comparison of the NOCI approach with two theoretical approaches, RAS-2SF and AIFDEM used for the study of SF, and we propose 2-methylene-2H-indene as a potential SF molecule. The comparison of the methods indicate that for tetracene, NOCI, RAS-2SF, and AIFDEM overestimate the energies of the states when compared with the experimental values. Despite this overestimation, our results suggest that the CT states act as virtual states in the SF process. The three methods agree on the character of the excited states, however, more configurations were found to be important in the RAS-2SF calculations, which were not included in the NOCI and AIFDEM calculations. The major difference between the NOCI and AIFDEM approaches, despite being conceptually similar, are that electron correlation and orbital relaxation effects can be included in the NOCI approach, but currently only small clusters of small molecules can be treated, whereas the AIFDEM approach can handle large clusters and molecules. Calculated electronic couplings for four pairs of the 2-methylene-2H-indene with the NOCI and AIFDEM approaches, and $||\gamma||^2$ values calculated with RAS-2SF show that the formation of the ^1TT state could occur efficiently in the crystal when the molecules are oriented as in conformation I-A. NOCI and AIFDEM overestimate the state energies, whereas RAS-2SF underestimates them; however, the three methods predict similar character for the relevant electronic states. The CT state energies are too high to be accessible, and a mediated mechanism is proposed for the SF process in 2-methylene-2H-indene. Finally, the methodologies are able to distinguish between configurations with low and high SF probabilities. A further comparison beyond these two systems has to be done in order to establish and generalize the predictive power of the methodologies.

Acknowledgments

This research used resources of the Oak Ridge Leadership Computing Facility located at Oak Ridge National Laboratory, which was supported by the Office of Science of the Department of Energy under Contract No. DEAC05-00OR22725. We acknowledge Dr. David Casanova (Spain) and Prof. Dr. Anna Krylov (USA) for valuable discussions, Prof. Dr. Coen de Graaf (Spain), Prof. Dr. Ria Broer (The Netherlands), and Dr. Tjerk P. Straatsma (USA) for their contributions to GronOR and The Netherlands Organisation for Scientific research (NWO) for the visitor travel grant (040-11-672) provided to Prof. Krylov for visiting The Netherlands.

References

1. Smith, M. B.; Michl, J. Singlet Fission. *Chem. Rev.* **2010**, *110*(11), 6891–6936.
2. Lee, J.; Jadhav, P.; Reusswig, P. D.; Yost, S. R.; Thompson, N. J.; Congreve, D. N.; Hontz, E.; van Voorhis, T.; Baldo, M. A. Singlet Exciton Fission Photovoltaics. *Acc. Chem. Res.* **2013**, *46*(6), 1300–1311.
3. Rao, A.; Friend, R. H. Harnessing Singlet Exciton Fission to Break the Shockley-Queisser Limit. *Nat. Mater.* **2017**, *2*, 17063.
4. Nozik, A. J.; Ellingson, R. J.; Micic, O. I.; Blackburn, J. L.; Yu, P.; Murphy, J. E.; Beard, M. C.; Rumbles, G. In *Twenty-Seventh DOE Solar Photochemistry Research Conference*; Warrenton, Virginia, 2004, p 63.
5. Hetzer, C.; Guldi, D. M.; Tykwinski, R. R. Pentacene Dimers as a Critical Tool for the Investigation of Intramolecular Singlet Fission. *Chem. Eur. J.* **2018**, *24*, 8245–8257.
6. Smith, M. B.; Michl, J. Recent Advances in Singlet Fission. *Annu. Rev. Phys. Chem.* **2013**, *64*, 361–386.
7. Johnson, J. C.; Nozik, A. J.; Michl, J. The Role of Chromophore Coupling in Singlet Fission. *Acc. Chem. Res.* **2013**, *46*(6), 1290–1299.
8. Gish, M. K.; Pace, N. A.; Rumbles, G.; Johnson, J. C. Emerging Design Principles for Enhanced Solar Energy Utilization with Singlet Fission. *J. Phys. Chem. C* **2019**, *123*, 3923–3934.
9. Ito, S.; Nagami, T.; Nakano, M. Molecular Design for Efficient Singlet Fission. *J. Photochem. Photobiol. C* **2018**, *34*, 85–120.
10. Japahuge, A.; Zeng, T. Theoretical Studies of Singlet Fission: Searching for Materials and Exploring Mechanisms. *ChemPlusChem* **2018**, *83*, 146–182.
11. Xia, J.; Sanders, S. N.; Cheng, W.; Low, J. Z.; Liu, J.; Campos, L. M.; Sun, T. Singlet Fission: Progress and Prospects in Solar Cells. *Adv. Mater.* **2017**, *29*(20), 1601652.
12. Paci, I.; Johnson, J. C.; Chen, X.; Rana, G.; Popovia, D.; David, D. E.; Nozik, A. J.; Ratner, M. A.; Michl, J. Singlet Fission for Dye-Sensitized Solar Cells: Can a Suitable Sensitizer Be Found?*J. Am. Chem. Soc.* **2006**, *128*(51), 16546–16553.
13. Geacintov, N.; Pope, M.; Vogel, F. Effect of Magnetic Field on the Fluorescence of Tetracene Crystals: Exciton Fission. *Phys. Rev. Lett.* **1969**, *22*(12), 593–596.
14. Groff, R. P.; Avakian, P.; Merrifield, R. E. Coexistence of Exciton Fission and Fusion in Tetracene Crystals. *Phys. Rev. B* **1970**, *1*(2), 815–817.
15. Burdett, J. J.; Müller, A. M.; Gosztola, D.; Bardeen, C. J. Excited State Dynamics in Solid and Monomeric Tetracene: The Roles of Superradiance and Exciton Fission. *J. Chem. Phys.* **2010**, *133*, 144506.
16. Casanova, D. Theoretical Modeling of Singlet Fission. *Chem. Rev.* **2018**, *118*(15), 7164–7207.
17. Grotjahn, R.; Maier, T. M.; Michl, J.; Kaupp, M. Development of a TDDFT-Based Protocol with Local Hybrid Functionals for the Screening of Potential Singlet Fission Chromophores. *J. Chem. Theory Comput.* **2017**, *13*, 4984–4996.

18. Mirjani, F.; Renaud, N.; Gorczak, N.; Grozema, F. C. Theoretical Investigation of Singlet Fission in Molecular Dimers: The Role of Charge Transfer States and Quantum Interference. *J. Phys. Chem. C* **2014**, *118*, 14192–14199.
19. Havlas, Z.; Michl, J. Guidance for Mutual Disposition of Chromophores for Singlet Fission. *Isr. J. Chem.* **2016**, *56*, 96–106.
20. Elfers, N.; Lyskov, I.; Spiegel, J. D.; Marian, C. M. Singlet Fission in Quinoidal Oligothiophenes. *J. Phys. Chem. C* **2016**, *120*, 13901–13910.
21. Zimmerman, P. M.; Bell, F.; Casanova, D.; Head-Gordon, M. Mechanism for Singlet Fission in Pentacene and Tetracene: From Single Exciton to Two Triplets. *J. Am. Chem. Soc.* **2011**, *133*, 19944–19952.
22. Zimmerman, P. M.; Musgrave, C. B.; Head-Gordon, M. A Correlated Electron View of Singlet Fission. *Acc. Chem. Res.* **2013**, *46*(6), 1339–1347.
23. Morrison, A. F.; Herbert, J. M. Analytic Derivative Couplings and First-Principles Exciton/Phonon Coupling Constants for an Ab Initio Frenkel-Davydov Exciton Model: Theory, Implementation, and Application to Compute Triplet Exciton Mobility Parameters for Crystalline Tetracene. *J. Chem. Phys.* **2017**, *146*, 224110.
24. Yang, C.-H.; Hsu, C.-P. First-Principle Characterization for Singlet Fission Couplings. *J. Phys. Chem. Lett.* **2015**, *6*, 1925–1929.
25. Buchanan, E. A.; Havlas, Z.; Michl, J. Singlet Fission: Optimization of Chromophore Dimer Geometry. *Adv. Quantum Chem.* **2017**, *75*, 175–227.
26. Havenith, R. W. A.; de Gier, H. D.; Broer, R. Explorative Computational Study of the Singlet Fission Process. *Mol. Phys.* **2012**, *110*(19-20), 2445–2454.
27. Wibowo, M.; Broer, R.; Havenith, R. W. A. A Rigorous Nonorthogonal Configuration Interaction Approach for the Calculation of Electronic Couplings Between Diabatic States Applied to Singlet Fission. *Comput. Theor. Chem.* **2017**, *1116*, 190–194.
28. Straatsma, T. P.; Broer, R.; Faraji, S.; Havenith, R. W. A. Chapter Three—GronOR Nonorthogonal Configuration Interaction Calculations at Exascale. In Dixon, D. A., Ed; *Annual Reports in Computational Chemistry*; Elsevier, 2018; Vol. 14, pp 77–91.
29. Broer, R. Localized Orbitals and Broken Symmetry in Molecules. Theory and Applications to the Chromate Ion and Para-benzoquinone (Ph.D. thesis). University of Groningen 1981.
30. Piland, G.; Burdett, J.; Dillon, R.; Bardeen, C. Singlet Fission: From Coherences to Kinetics. *J. Phys. Chem. Lett.* **2014**, *5*, 2312–2319.
31. Casanova, D.; Head-Gordon, M. Restricted Active Space Spin-Flip Configuration Interaction Approach: Theory, Implementation and Examples. *Phys. Chem. Chem. Phys.* **2009**, *11*, 9779–9790.
32. Casanova, D. Efficient Implementation of Restricted Active Space Configuration Interaction with the Hole and Particle Approximation. *J. Comp. Chem.* **2013**, *34*, 720–730.
33. Matsika, S.; Feng, X.; Luzanov, A. V.; Krylov, A. I. What We Can Learn from the Norms of One-Particle Density Matrices, and What We Can't: Some Results for Interstate Properties in Model Singlet Fission Systems. *J. Phys. Chem. A* **2014**, *118*, 11943–11955.
34. Morrison, A. F.; You, Z.-Q.; Herbert, J. M. Ab Initio Implementation of the Frenkel-Davydov Exciton Model: A Naturally Parallelizable Approach to Computing Collective Excitations in Crystals and Aggregates. *J. Chem. Theory Comput.* **2014**, *10*(12), 5366–5376.
35. Herbert, J. M.; Zhang, X.; Morrison, A. F.; Liu, J. Beyond Time-Dependent Density Functional Theory Using Only Single Excitations: Methods for Computational Studies of Excited States in Complex Systems. *Acc. Chem. Res.* **2016**, *49*(5), 931–941.
36. Morrison, A. F.; Herbert, J. M. Evidence for Singlet Fission Driven by Vibronic Coherence in Crystalline Tetracene. *Phys. Chem. Lett.* **2017**, *8*(7), 1442–1448.

37. Ullrich, C. A. *Time-Dependent Density-Functional Theory: Concepts and Applications*; Oxford University Press, 2012.
38. Rhee, Y. M.; Head-Gordon, M. Scaled Second-Order Perturbation Corrections to Configuration Interaction Singles: Efficient and Reliable Excitation Energy Methods. *J. Phys. Chem. A* **2007**, *111*, 5314–5326.
39. Andersson, K.; Roos, B. O. Multiconfigurational second-order perturbation theory. *In Modern Electronic Structure Theory. World Scientific* **1995**, 55–109.
40. Dreuw, A.; Wormit, M. The Algebraic Diagrammatic Construction Scheme for the Polarization Propagator for the Calculation of Excited States. *Comput. Mol. Sci.* **2015**, *5*, 82–95.
41. Shao, Y.; Gan, Z.; Epifanovsky, E.; Gilbert, A. T.; Wormit, M.; Kussmann, J.; Lange, A. W.; Behn, A.; Deng, J.; Feng, X.; Ghosh, D.; Goldey, M.; Horn, P. R.; Jacobson, L. D.; Kaliman, I.; Khaliullin, R. Z.; Kuś, T.; Landau, A.; Liu, J.; Proynov, E. I.; Rhee, Y. M.; Richard, R. M.; Rohrdanz, M. A.; Steele, R. P.; Sundstrom, E. J.; Woodcock, H. L., III.; Zimmerman, P. M.; Zuev, D.; Albrecht, B.; Alguire, E.; Austin, B.; Beran, G. J. O.; Bernard, Y. A.; Berquist, E.; Brandhorst, K.; Bravaya, K. B.; Brown, S. T.; Casanova, D.; Chang, C.-M.; Chen, Y.; Chien, S. H.; Closser, K. D.; Crittenden, D. L.; Diedenhofen, M.; DiStasio, R. A., Jr.; Do, H.; Dutoi, A. D.; Edgar, R. G.; Fatehi, S.; Fusti-Molnar, L.; Ghysels, A.; Golubeva-Zadorozhnaya, A.; Gomes, J.; Hanson-Heine, M. W.; Harbach, P. H.; Hauser, A. W.; Hohenstein, E. G.; Holden, Z. C.; Jagau, T.-C.; Ji, H.; Kaduk, B.; Khistyaev, K.; Kim, J.; Kim, J.; King, R. A.; Klunzinger, P.; Kosenkov, D.; Kowalczyk, T.; Krauter, C. M.; Lao, K. U.; Laurent, A. D.; Lawler, K. V.; Levchenko, S. V.; Lin, C. Y.; Liu, F.; Livshits, E.; Lochan, R. C.; Luenser, A.; Manohar, P.; Manzer, S. F.; Mao, S.-P.; Mardirossian, N.; Marenich, A. V.; Maurer, S. A.; Mayhall, N. J.; Neuscamman, E.; Oana, C. M.; Olivares-Amaya, R.; O'Neill, D. P.; Parkhill, J. A.; Perrine, T. M.; Peverati, R.; Prociuk, A.; Rehn, D. R.; Rosta, E.; Russ, N. J.; Sharada, S. M.; Sharma, S.; Small, D. W.; Sodt, A.; Stein, T.; Stück, D.; Su, Y.-C.; Thom, A. J.; Tsuchimochi, T.; Vanovschi, V.; Vogt, L.; Vydrov, O.; Wang, T.; Watson, M. A.; Wenzel, J.; White, A.; Williams, C. F.; Yang, J.; Yeganeh, S.; Yost, S. R.; You, Z.-Q.; Zhang, I. Y.; Zhang, X.; Zhao, Y.; Brooks, B. R.; Chan, G. K.; Chipman, D. M.; Cramer, C. J.; Goddard, W. A., I.I.I.; Gordon, M. S.; Hehre, W. J.; Klamt, A.; Schaefer, H. F., III.; Schmidt, M. W.; Sherrill, C. D.; Truhlar, D. G.; Warshel, A.; Xu, X.; Aspuru-Guzik, A.; Baer, R.; Bell, A. T.; Besley, N. A.; Chai, J.-D.; Dreuw, A.; Dunietz, B. D.; Furlani, T. R.; Gwaltney, S. R.; Hsu, C.-P.; Jung, Y.; Kong, J.; Lambrecht, D. S.; Liang, W.; Ochsenfeld, C.; Rassolov, V. A.; Slipchenko, L. V.; Subotnik, J. E.; Voorhis, T. V.; Herbert, J. M.; Krylov, A. I.; Gill, P. M.; Head-Gordon, M. Advances in Molecular Quantum Chemistry Contained in the Q-Chem 4 Program Package. *Mol. Phys.* **2015**, *113*, 184–215.
42. Aquilante, F.; Autschbach, J.; Carlson, R. K.; Chibotaru, L. F.; Delcey, M. G.; De Vico, L.; Galván, Fdez., I.; Ferré, N.; Frutos, L. M.; Gagliardi, L.; Garavelli, M.; Giussani, A.; Hoyer, C. E.; Li Manni, G.; Lischka, H.; Ma, D.; Malmqvist, P. Å.; Müller, T.; Nenov, A.; Olivucci, M.; Pedersen, T. B.; Peng, D.; Plasser, F.; Pritchard, B.; Reiher, M.; Rivalta, I.; Schapiro, I.; Segarra-Martí, J.; Stenrup, M.; Truhlar, D. G.; Ungur, L.; Valentini, A.; Vancoillie, S.; Veryazov, V.; Vysotskiy, V. P.; Weingart, O.; Zapata, F.; Lindh, R. Molcas 8: New Capabilities for Multiconfigurational Quantum Chemical Calculations Across the Periodic Table. *J. Comp. Chem.* **2016**, *37*, 506–541.
43. Guest, M. F.; Bush, I. J.; van Dam, H.; Sherwood, P.; Thomas, J.; van Lenthe, J.; Havenith, R. W. A.; Kendrick, J. The GAMESS-UK Electronic Structure Package: Algorithms, Developments and Applications. *Mol. Phys.* **2005**, *103*(6–8), 719–747.

44. Gallup, G. A.; Norbeck, J. M. Population Analyses of Valence-bond Wavefunctions and BeH_2. *Chem. Phys. Lett.* **1973**, *21*, 495–500.
45. Kathir, R. K.; de Graaf, C.; Broer, R.; Havenith, R. W. A. *Gamess-UK-GronOR Interface*; University of Groningen, 2018.
46. van Montfort J. T., Photo-electron spectroscopy: Theoretical aspects and calculations, Ph.D. thesis, University of Groningen, 1980.
47. Feng, X.; Luzanov, A. V.; Krylov, A. I. Fission of Entangled Spins: An Electronic Structure Perspective. *J. Phys. Chem. Lett.* **2013**, *4*, 3845–3852.
48. Farag, M. H.; Krylov, A. I. Singlet Fission in Perylenediimide Dimers. *J. Phys. Chem. C* **2018**, *122*, 25753–25763.
49. Löwdin, P.-O. On the Nonorthogonality Problem. *Adv. Quantum Chem.* **1970**, *5*, 185–199.
50. Engels, B.; Engel, V. The Dimer-approach to Characterize Optoelectronic Properties of and Exciton Trapping and Diffusion in Organic Semiconductor Aggregates and Crystals. *Phys. Chem. Chem. Phys.* **2017**, *19*, 12604–12619.
51. Walter, C.; Krämer, V.; Engels, B. On the Applicability of Time-dependent Density Functional Theory (TDDFT) and Semiempirical Methods to the Computation of Excited-state Potential Energy Surfaces of Perylene-based Dye-aggregates. *Int. J. Quant. Chem.* **2017**, *117* (e25337).
52. Mewes, S. A.; Plasser, F.; Krylov, A. I.; Dreuw, A. Benchmarking Excited-state Calculations Using Exciton Properties. *J. Chem. Theory Comput* **2018**, *14*, 710–725.
53. Burdett, J. J.; Bardeen, C. J. The Dynamics of Singlet Fission in Crystalline Tetracene and Covalent Analogs. *Acc. Chem. Res.* **2013**, *46*(6), 1312–1320.
54. Izadnia, S.; Schönleber, D. W.; Eisfeld, A.; Ruf, A.; Laforge, A. C.; Stienkemeier, F. Singlet Fission in Weakly Interacting Acene Molecules. *J. Phys. Chem. Lett.* **2017**, *8*, 2068–2073.
55. McGlynn, S. P.; Padhye, M. R.; Kasha, M. Lowest Triplet Levels of the Polyacenes. *J. Chem. Phys.* **1955**, *23*(593), 593–594.
56. Klevens, H. B.; Platt, J. R. Spectral Resemblances of Cata-Condensed Hydrocarbons. *J. Chem. Phys.* **1949**, *17*(5), 470–481.
57. Pope, M.; Burgos, J.; Giachino, J. Charge-Transfer Exciton State and Energy Levels in Tetracene Crystal. *J. Chem. Phys.* **1965**, *43*, 3367.
58. Feng, X.; Casanova, D.; Krylov, A. I. Intra- and Intermolecular Singlet Fission in Covalently Linked Dimers. *J. Phys. Chem. C* **2016**, *120*, 19070–19077.
59. Minami, T.; Ito, S.; Nakano, M. Fundamental of Diradical-Character-Based Molecular Design for Singlet Fission. *J. Phys. Chem. Lett.* **2013**, *4*, 2133–2137.

This page intentionally left blank

CHAPTER THIRTEEN

Diagnosis of two evaluation paths to density-based descriptors of molecular electronic transitions

Gabriel Breuil, Kaltrina Shehu, Elise Lognon, Sylvain Pitié, Benjamin Lasorne, Thibaud Etienne*

Institut Charles Gerhardt—CNRS and Université de Montpellier, Montpellier, France
*Corresponding author: e-mail address: thibaud.etienne@umontpellier.fr

Contents

Abstract

In this chapter we discuss the reliability of two computational methods (numerical integration on Cartesian grids and population analysis) used for evaluating scalar quantities related to the nature of electronic transitions. These descriptors are integrals of charge density functions built from the detachment and attachment density matrices projected onto the Euclidean space using a finite basis of orbitals. While the numerical integration on Cartesian grids is easily considered to be converged for medium-sized density grids, the population analysis approximation to the numerical integration values is diagnosed using 8 tests performed on 59 molecules with a combination of 15 Gaussian basis sets and 6 exchange-correlation functionals.

Advances in Quantum Chemistry, Volume 79
ISSN 0065-3276
https://doi.org/10.1016/bs.aiq.2019.04.004

1. Introduction

The possibility of analyzing the charge-transfer character of electronic transitions of complex molecular systems has been of interest for decades, and still attracts considerable attention in the excited-state electronic structure community.[1–40]

In this context, a variety of quantities have been designed in order to unveil the nature of electronic transitions with scalars that provide—through a simple number—specific information related to the light-induced electronic structure reorganization.[1, 12,20–23,28–36,39,41–47] An example of information that one might wish to seek when considering a molecular system undergoing a photoinduced intramolecular charge transfer is the locality of this charge transfer, i.e., the extent to which the electronic cloud has been perturbed and polarized.[20–22,34,46] In addition to such probing of the charge transfer locality one can evaluate the extent to which the photogenerated hole and particle contribute to the net charge displacement occurring during an electronic transition.[22,34,46] These two pieces of information are contained in two separate quantities, named ϕ_S and φ, respectively.

Three different implementations were mentioned for evaluating these density-based descriptors.[22] Two of them were based on the population analysis[48] of the so-called detachment and attachment one-body reduced density matrices.[2] The third one was the direct numerical integration of the related one-body charge density functions using Cartesian grids. When first published,[22] the population analysis approximations to our density-based descriptors were compared to the numerical integration method as a reference solely for organic push-pull molecules using a single level of theory, for the sake of demonstrating its hypothetical usefulness, given that its implementation allows an extremely fast evaluation of the ϕ_S and φ descriptors.

In this contribution we wish to extend this diagnosis to a much wider test set made up of various types of molecules and providing a rigorous and extensive diagnosis of the population analysis as an evaluation tool for our density-based descriptors. For this sake, we will use and combine in this chapter multiple diagnosis criteria for choosing the population analysis to perform. We will also discuss preliminary basis transformations that can be applied before performing the population analysis. These principles will be involved in the critical discussion of the reliability of this evaluation path, which might be discarded in certain situations. With this we hope to provide

the reader and user the possibility to rationalize their choice among the different possible formulations of the descriptors.

This report is organized as follows: we will first recall how one can use the detachment and attachment one-body densities for computing quantities describing the electronic structure reorganization of a molecule. The matrix-algebraic approximation to these quantities will then be given, before the detailed diagnosis strategy of this chapter is fully described in a dedicated section. Subsequently, the results of this diagnosis are introduced and discussed, before we conclude with the recommended best practices the authors suggest for evaluating the descriptors, with regard to the choice of the relevant evaluation method to use according to the system of interest. With this in hand, and taking into account certain restrictions related to the systems themselves one should be able to consider the values of the descriptors for a self-diagnosis of their own reliability.

2. Theoretical introduction

In this contribution, we will bring a few modifications to the nomenclature used until now in Refs. 20–23,34, 46. These amendments are fully detailed in Appendix with explanations about the reason why they were used then, and will no longer be employed.

A brief reminder on the one-particle reduced density matrix (1-RDM) and one-body charge density (1-CD) functions can also be found in Appendix.

2.1 The target density-based descriptors

The descriptors reported in this publication are directly derived from the detachment (n_d) and attachment (n_a) 1-CDs, i.e., respectively, the hole and particle characterizing electronic transition in a one-hole/one-particle picture of it. Their derivation is briefly recalled in an appendix to be found via the link to Appendix. We have, for any real x in the [0, 1] interval,

$$\begin{aligned}\vartheta &= \int_{\mathbb{R}^3} d\mathbf{r}\; n_d(\mathbf{r}) = \mathrm{tr}\left(\mathbf{S}^x\mathbf{D}\mathbf{S}^{1-x}\right) \\ &= \int_{\mathbb{R}^3} d\mathbf{r}\; n_a(\mathbf{r}) = \mathrm{tr}\left(\mathbf{S}^x\mathbf{A}\mathbf{S}^{1-x}\right)\end{aligned} \tag{1}$$

where "**A**" and "**D**" denote the attachment and detachment density matrices in the atomic space and should not be confused with electron

"Acceptor" and "Donor." The **S** matrix contains the spatial overlap integrals between atomic basis functions.

This ϑ represents the quantity of charge that has been involved in the electronic transition. It is this integral of the hole (detachment) and particle (attachment) density that will be used as a normalization factor for the quantities defined below.

We can now write two functions involving the detachment/attachment densities

$$n_\Delta(\mathbf{r}) = n_a(\mathbf{r}) - n_d(\mathbf{r}) \in \mathbb{R} \tag{2}$$

and

$$\eta(\mathbf{r}) = \sqrt{n_d(\mathbf{r}) n_a(\mathbf{r})} \in \mathbb{R}^+ \tag{3}$$

where $n_\Delta(\mathbf{r})$, the difference density, is also equal to the difference between the electron density of the excited (n_n) and ground (n_0) states

$$n_\Delta(\mathbf{r}) = n_n(\mathbf{r}) - n_0(\mathbf{r}). \tag{4}$$

From these two functions one can write the detachment/attachment overlap integral[20]

$$\phi_S := \vartheta^{-1} \int_{\mathbb{R}^3} d\mathbf{r} \sqrt{n_d(\mathbf{r}) n_a(\mathbf{r})} \equiv 2\vartheta^{-1} G[\eta] \in [0, 1] \tag{5}$$

where we define the G rule as

$$G[f] = \frac{1}{2} \int_{\mathbb{R}^3} d\mathbf{r} \, |f(\mathbf{r})| \tag{6}$$

The detailed construction and use of G is given in Appendix.

From the difference density, one can derive the unnormalized[21] charge-transfer descriptor

$$\chi := G[n_\Delta] \tag{7}$$

and its normalization[22]

$$\vartheta \geq \chi \Rightarrow \exists! \, \varphi = \vartheta^{-1} \chi \in [0, 1]. \tag{8}$$

φ measures the fraction of detachment/attachment density contributing to the net transferred charge. The normalization condition $\vartheta \geq \chi$ was obtained by construction in Ref. 22, where ϕ_S and φ were combined into the normalized, general ψ descriptor

$$\psi := (\pi/2)^{-1} \arctan\left(\frac{\phi_S}{\varphi}\right) \in [0, 1] \tag{9}$$

jointly describing the range of a charge separation and the amount of charge transferred during an electronic transition.

2.2 Alternative approach: The population analysis

Since it is not possible to solve analytically the ϕ_S and φ integrals reported above, only approximate values can be obtained. In this chapter we extend the matrix-algebraic procedure proposed in Ref. 22, where numerical integrations on Cartesian grids usually used for computing the density-based descriptors ϕ_S and φ were approximated by performing a detachment/attachment population analysis. These two methods were loosely called direct- and Hilbert-space derivations in Ref. 22, the latter being employed because one-body orbital wave function integrals were part of the derivation procedure.

If the atomic functions are centered on atoms, a known procedure is to approximate the atomic population, i.e., the partial charge that an atom bears for a given electronic distribution, through a Mulliken population analysis by multiplying a density matrix with the basis set overlap matrix **S** and to consider the *k*th diagonal entry of this product of matrices as the contribution of the *k*th atomic orbital to the electronic population of the system. The actual approximation then consisted in considering the fact that the basis of atomic functions was local, with the Gaussian basis functions grossly covering a given region of space, so that manipulating (in particular, subtracting or multiplying) the diagonal entries of the matrix product of the atomic-space detachment and attachment density matrices with **S** was an approximation to the manipulation of elementary fractions of a charge density in a given region of space. Another possible approximation reported in Ref. 22 is the Löwdin detachment/attachment population analysis, where the density matrices are contracted to the left and to the right by the square root of **S** to orthogonalize the basis set while conserving its local character as much as possible. In fact, any combination of exponents for the left and right multiplication can arbitrarily be used, as long as the sum of the exponents is equal to unity, in order to satisfy Eq. (1). The justification has been discussed in the reminder on density matrices and charge densities and allowed us to generalize the population analysis to any x value in Appendix.

Though the choice of the x exponent seems quite arbitrary, it was demonstrated in Appendix that only a Löwdin-like population analysis produces

atomic populations that do not have a tendency of being negative or greater than the maximum allowed occupancy, which would be unphysical. Therefore, though the generalized matrix-algebraic definition of the approximate density-based descriptors can be given as in Appendix for any value of x, from now on we will solely use the Löwdin-like scheme (denoted by the "ℓ" symbol). The only exception to this is the evaluation of ϑ: According to Eq. (1), since the integral of the detachment/attachment 1-CD functions is unequivocally equal to the trace of the product of $\mathbf{S}$ with the corresponding density matrix, the ϑ quantity is computed without approximation as the trace of the detachment/attachment density matrices multiplied by $\mathbf{S}$, i.e., using $x = 0$ in Eq. (1) for sparing the effort of diagonalizing $\mathbf{S}$.

The population analysis approximations to ϕ_S, χ and φ using Löwdin's scheme are given as[22]

$$\begin{aligned}\phi_S^{\ell} &= \vartheta^{-1}\sum_{\mu=1}^{K}\sqrt{\left(\mathbf{S}^{1/2}\mathbf{D}\mathbf{S}^{1/2}\right)_{\mu\mu}\left(\mathbf{S}^{1/2}\mathbf{A}\mathbf{S}^{1/2}\right)_{\mu\mu}} \\ &:= F[\mathbf{D},\mathbf{A},\mathbf{S}]\end{aligned} \tag{10}$$

and

$$\varphi^{\ell} = \vartheta^{-1}\underbrace{H[\mathbf{S}^{1/2}\mathbf{\Delta}\mathbf{S}^{1/2}]}_{\chi^{\ell}} \tag{11}$$

where the H rule relates any real $K \times K$ matrix to a scalar by summing the absolute value of the diagonal entries of that matrix:

$$2H[\mathbf{Q}] = \sum_{\mu=1}^{K}\left|(\mathbf{Q})_{\mu\mu}\right|. \tag{12}$$

As for the G rule, the details related to the construction and use of H are given in Appendix.

The limitations of the approximation made by using symmetrically orthogonalized[49] orbitals populations as if we were mapping these charges to point charges in space when computing our descriptors are diagnosed and discussed in this report for the F and H rules only. This is due to the fact that the population analysis approximation to the ψ descriptor involves no further approximation than those made using F and H.

Note finally that in Ref. 23, we have designed quantities relating the pseudo orbital relaxation performed using a post-linear response treatment of the difference-density matrix. In Appendix we provide their expression together with their population analysis formulation, which solely involves the H rules, allowing us to extend the conclusions of our current diagnosis to these quantities.

3. Diagnosis strategy

Our diagnosis strategy is summarized in Table 1. All the calculations reported in this chapter were performed *in vacuo*, using the Gaussian16 (revision A03) package.[50] A set of 59 metal-free molecules of variable size (from diatomics to complex molecular systems) was used in order to perform our diagnosis. The Cartesian grids were generated using the Cubegen utility from Gaussian16, and the analyses (numerical integration (NI) of the Cartesian grids, and population analyses (PA)) were performed using a homemade code, to be released soon.

In order to determine to what extent both methods are consistent, different variables have been chosen for comparing NI and PA values: the system size, the charge transfer (CT) nature, the basis set (BS) size and nature, and the type of exchange-correlation (xc) functional used in time-dependent density functional theory.

Table 1 Summary of the eight detachment/attachment PA diagnosis strategies.

Diagnosis	Molecule	System size	CT nature	BS	xc-functional
d_1	nIII, nV-X, nVI-c	√	√	√	×
d_2	nV-X	×	√	√	×
d_3	N_2, CO, HCl, H_2CO	×	×	×	√
d_4	Acenes	√	×	√	√
d_5		×	×	√	×
d_6	PP	×	√	×	×
d_7		×	×	√	×
d_8		×	(√)	×	√

Molecules for d_1 and d_2 are taken from Ref. 20; molecules for d_3 to d_5 are taken from Ref. 41; and PP is taken from Ref. 23. The sketches of the molecules are reported in Figure S1 of Appendix.

Through this study, the influence of the Cartesian grid density of points has been evaluated by comparing medium (6 points/bohr for each direction) grids to fine (12 points/bohr for each direction) ones.

Our first molecular test-set (S1) is taken directly from Ref. 20 and is constituted by a series of conjugated molecules with nitro (-NO_2) acceptor and dimethylamino (-NMe_2) donor terminal groups, separated by a variable number (ranging from one to five) of bridge subunits. The level of theory used here for our computations is exactly the one from the reference cited above.

One of the spacers is an oligo-ethylene for the nIII group of molecules. The oligo-ethylene might separate two donor groups for what we will call the nIII-NMe_2-NMe_2 series here, or two nitro groups (nIII-NO_2-NO_2), or one of each (nIII-NMe_2-NO_2).

If the donor and the acceptor are separated by a variable number of phenyl moieties, we have the nVI-c series.

Finally, in the nV-X series, the dimethylamino and nitro groups are connected through an heterocyclic oligomer (with five-member rings containing one oxygen, sulfur, or selenium) or through oligo-pyrroles.

The equilibrium geometries of the molecules belonging to the S1 set of molecules were obtained using the PBE0/6-311G(d,p) level of theory. Vibrational frequencies have been calculated to verify that the optimized geometries are actual minima. The excited-state calculations were done at the PBE0/6-311++G(2d,p) level of theory.

The specific interest of this set lies in the possibility of investigating electronic transitions of different natures through a series, with molecules of different size. Hence the calculations use basis sets of different size, so that the only stable variable is the xc-functional through the diagnosis. When switching the heteroatom in the nV-X series from oxygen to sulfur or selenium, one can also see how an increase of the number of electrons and basis functions for molecules of comparable size influences the precision of the PA-approximation. This will be our first diagnosis, denoted d_1 in the results section, as well as in Table 1.

In addition to this, excited-state calculations were performed on the nV-X series using a small (6-31G) and intermediate (6-31+G(d,p)) BS in order to check the BS convergence for the PA values at a given geometry for this type of push-pull molecule (d_2).

The second test-set (S2) originates from Ref. 41 and will be investigated using the same level theory as in the original paper, unless otherwise stated. In particular, we will investigate the diatomic (N_2, CO, and HCl) and formaldehyde molecules from S2 in order to diagnose the reliability of F and H

rules for very small molecules (d_3). From S2 we will also focus on the acenes. This is a series of $n + 1$ fused benzene rings, with n ranging from one to five, as we know that for such molecules the photogenerated hole and the particle will exhibit a substantial spatial overlap, no matter the number of subunits. This diagnosis will allow us to know whether, for such an extreme case of transition nature, there might be an influence of system size on the accuracy of the PA-approximation (d_4). Note that we also performed excited-state calculations on the acene series using the B3LYP/6-31G and B3LYP/6-311++G(2d,p) levels of theory in order to assess the basis set convergence on the reference and approximated descriptor values (d_5).

The last system that was used for this report is the pyridinium phenolate (PP) that was already investigated in Ref. 23. We used a rigid scan of the central dihedral angle, scanning the angle from zero to ninety degrees with a one-degree step, in order to monitor the evolution of the nature of the donor-acceptor intramolecular charge transfer. Such an approach allowed us to investigate a system of fixed size, at a given level of theory, with tunable CT character, for a one-variable diagnosis (d_6) on a medium-sized molecular system. This study was also repeated including a variation of the level of theory by performing this 91-point scan for a combination of 15 split-valence Pople basis sets[51, 52] and 6 xc-functionals (the hybrid B3LYP,[53] PBE0,[54] and M06-2X,[55] the long-range corrected CAM-B3LYP[56] and LC-ωHPBE[57] and the range-separated, dispersion-corrected ωB97X-D[58]) so that we could select some geometries and evaluate the separate influence of the basis set size (and nature), as well as the type (hybrid/range-separated hybrid) of xc-functional (d_7 and d_8). Configuration Interaction with single excitations (CIS[59]) and Time-Dependent Hartree–Fock (TDHF[59]) calculations were also performed on PP, combined to the fifteen Pople BSs mentioned above.

The sketch of the molecules investigated in this report is given in Figure S1 of Supplementary Information.

4. Results

Due to our practical use of the descriptors, we report hereafter their values to two decimal places and, when comparing two evaluation paths, we will consider consistency between the two methods achieved when the results are consistent within two decimal places. Moreover, as in Ref. 22 we will consider a tolerance for the absolute deviation of ± 0.05 arbitrary units for the descriptors as the maximum allowed deviation between two methods.

4.1 Influence of the NI grid density of points

When studying the whole set of molecular systems for this report, we quasi-systematically used both density of points grid-definitions (6 and 12 points/bohr in each direction) for the sake of comparison. According to our convergence/consistency criterion defined above, we noticed that the results on the descriptors are strictly converged for medium-density grids (6 points/bohr in each direction) and can be considered exact for the level of theory used. This means that the users who wish to compute our descriptors can reliably spare themselves the cost of producing fine grids eight times denser than the medium-density one.

We attract the attention of the reader to the fact that when the numerical integration is performed, one has always to carefully check whether the integral of the detachment and attachment densities are strictly equal. We report in SI (see Tables S29–S34) our data for the nIII group of molecules and show that for the nIII-NMe_2-NMe_2 series and one excited state of the nIII-NMe_2-NO_2 series the standard grid sizes lead to a significant fraction of charge lost in the attachment. The integrals obtained with finer grids are also provided in order to prove that the fraction of charge lost comes from the grid size instead of the grid density of points. In order to overcome such an issue the user should increase the grid size with the same density of points to get the right detachment/attachment integral. In this regard one can use the exact value of the trace of **DS** and **AS** to diagnose the size and quality of the integration grid, as was done in Tables S29, S31, and S33.

4.2 The *F* and *H* rules

Again, when considering the total set of data that we report in Appendix for the 59 molecules we observed that according to our accuracy/consistency criterion, when the PA-derived ϕ_S values were found to be reliable, so were the φ values. This was true though they were not obtained from the exact same rule. Therefore, from now on in this section we solely will discuss the ϕ_S and ϕ_S^{ℓ} values for the sake of brevity, though the data in the tables and in the Appendix will also contain the φ and ψ diagnosis.

4.3 The oligo-acenes series

As expected, when studying the oligo-acenes series with our density-based descriptors, we noticed that for the three xc-functionals used, i.e., PBE, B3LYP, and CAM-B3LYP, in the d_4 diagnosis (see Table 1), the electronic cloud remains almost unperturbed by the electronic transitions, leading to

Table 2 Descriptors values and their PA-approximated deviations, $\Delta(q) = q(\text{NI}) - q(\text{PA})$, obtained for the three first excited states of the oligo-acenes series with the B3LYP/cc-pVTZ level of theory (part of d_4).

n	E-S	ϕ_S	$\Delta(\phi_S)$	φ	$\Delta(\varphi)$	ψ	$\Delta(\psi)$
1	1	0.92	−0.06	0.26	0.13	0.82	−0.09
	2	0.98	0.00	0.15	0.00	0.90	0.00
	3	0.88	−0.07	0.32	0.11	0.78	−0.08
2	1	0.90	0.08	0.29	0.17	0.80	−0.12
	2	0.98	−0.01	0.15	0.02	0.90	−0.01
	3	0.91	−0.06	0.27	0.09	0.81	−0.07
3	1	0.90	−0.09	0.27	0.10	0.81	−0.12
	2	0.97	−0.01	0.15	0.03	0.90	−0.02
	3	0.90	−0.06	0.30	0.07	0.79	−0.05
4	1	0.90	0.10	0.27	0.18	0.81	−0.13
	2	0.89	−0.05	0.30	0.05	0.79	−0.04
	3	0.97	−0.01	0.15	0.03	0.90	−0.02
5	1	0.90	−0.09	0.26	0.17	0.82	−0.12
	2	0.90	−0.06	0.33	0.06	0.78	−0.05
	3	0.89	−0.05	0.35	0.09	0.76	−0.07

ϕ_S values systematically greater than 0.9, which is quite an extreme case of hole/particle overlap. This statement holds irrespective of the size of the molecule and of the BS (diagnosis d_5), or of the xc-functional used. Results in Table 2 and in Tables S1–S5 show that in such an extreme case the reliability of the PA to approximate the value of ϕ_S cannot be firmly established. Indeed, we saw among the results both exact NI/PA matching and deviations beyond our tolerance criterion, which means that for such extreme situations the use of the PA-approximation ϕ_S^{ℓ} is strongly discouraged. These conclusions also hold for the poly-acetylene series from the same S2 set of molecules (see Tables S38–S40).

4.4 Influence of the size of the system

When the nV-X and nVI-c sets of molecular systems are concerned, we globally observe that the molecular composition influences the nature of

Table 3 Hole/particle overlap integral values and their PA-approximated deviations, $\Delta(X) = \phi_S(X) - \phi_S^{\ell}(X)$, calculated for the different molecules from the nV-X molecular test-set (part of d_1).

n	E-S	ϕ_S(NH)	Δ(NH)	ϕ_S(O)	Δ(O)	ϕ_S(S)	Δ(S)	ϕ_S(Se)	Δ(Se)
1	1	0.69	0.02	0.68	0.03	0.70	0.03	0.72	0.04
	2	0.48	0.36	0.48	0.36	0.48	0.39	0.48	0.38
	3	0.34	0.14	0.52	0.40	0.51	0.41	0.54	0.03
2	1	0.57	0.01	0.60	0.03	0.58	0.02	0.68	0.02
	2	0.49	0.42	0.48	0.35	0.76	0.25	0.52	0.25
	3	0.40	0.03	0.71	0.04	0.72	0.00	0.60	0.12
3	1	0.48	0.01	0.53	0.02	0.51	0.02	0.62	0.02
	2	0.73	−0.01	0.78	−0.02	0.75	−0.01	0.79	−0.01
	3	0.63	0.01	0.69	0.00	0.70	−0.01	0.74	−0.01
4	1	0.39	0.00	0.47	0.02	0.52	0.01	0.57	0.01
	2	0.60	0.00	0.77	−0.02	0.75	−0.02	0.78	−0.01
	3	0.71	−0.03	0.66	0.00	0.70	−0.01	0.74	−0.01
5	1	0.34	0.01	0.42	0.01	0.47	0.00	0.53	0.00
	2	0.52	0.00	0.75	−0.02	0.73	−0.02	0.76	−0.02
	3	0.71	−0.04	0.65	−0.01	0.68	−0.02	0.72	−0.02

Those values were obtained using PBE0/6-311++G(2d,p) excited-state calculations, based on PBE0/6-311G(d,p) geometries.

the CT. We have also noticed when performing diagnosis d_1 that the ϕ_S^{ℓ} approximation can become problematic both for small systems and for electronic transitions characterized by a small ϕ_S^{ℓ}. However, this difficulty is neither inevitable nor commonplace.

For the nV-X (see Table 3 and Tables S27, S36, S44, and S46) and nVI-c (see Table S27 and S28, S35–S37, and S44–S47) series we observe that for medium- to large-sized systems ($n > 3$) the ϕ_S^{ℓ} descriptor reproduces very accurately the ϕ_S value. Conversely, for small systems ($n = 1, 2$) the PA-approximation is no longer reliable for ϕ_S values less than or equal to 0.52. This was also observed for the oligo-peptides of the S2 set of molecules (see Tables S6–S8, S12–S14, and S48–S50). Note that in the S2 set of molecules the geometrical origin of the NI-PA deviation also applies for higher ϕ_S values, for example when the CO, N_2, HCl, and H_2CO molecules

(see Tables S9–S11 and S18–S26), which are too small for considering the ϕ_S^ℓ approximation as reliable, are concerned (diagnosis d_3).

Diagnosis d_2 (see Tables S27 and S28, S36 and S37, and S44–S47) allowed us to conclude that the BS convergence was rapidly achieved for the ϕ_S value with medium-sized BS. When comparing the converged ϕ_S values to their PA-approximated values, we have noticed that the accuracy of the PA-approximation was independent from the BS size. In other words, if the level of theory contains a BS of intermediate or large size, increasing the size of the BS did not improve the accuracy of the PA, as was already observed in diagnosis d_5. Following the same idea, we notice in Table 3 that replacing oxygen by sulfur or selenium might alter the ϕ_S value but not the accuracy of its PA-approximation, although in such substitutions we considerably modify the number of basis functions centered on the heteroatom positions before the symmetric orthogonalization.

4.5 Study of medium-sized molecules

The accurate ϕ_S^ℓ results for the S2-belonging dimethylaminobenzonitrile (DMABN) and N-phenylpyrrole molecules (see Tables S15–S17 and S41–S43) should be considered with care. Indeed, we have seen when investigating the PP molecule that tuning the CT character of electronic transitions for a given molecule has an impact on the reliability of the PA-approximation (diagnosis d_6).

The PP molecule excited states, when computed at the B3LYP/6-311++G(2d,p) level of theory, show an avoided crossing between the first and second singlet excited states and a conical intersection between the second and third excited states. This behavior is very well reproduced by both the ϕ_S and ϕ_S^ℓ computation (see the left part of Fig. 1), which leads us to state that one should not systematically discard ϕ_S^ℓ results for the only reason that it may be characterized by a sizeable gradient. However, one sees in Fig. 1 that when the ϕ_S^ℓ value drops below 0.4 the values might or might not be reliable. For instance the first electronic transition at this level of theory is quite well described by ϕ_S^ℓ when tuning down the twist angle from 90 to ca. 55 degrees while the trends completely differ afterwards, i.e., when ϕ_S^ℓ is dropping below 0.4. Significant divergences also occur for the second and third excited state as long as ϕ_S^ℓ is maintained below 0.4, while non-negligible but tolerable deviations are observed when ϕ_S^ℓ is lying between 0.4 and 0.5 for the second excited state.

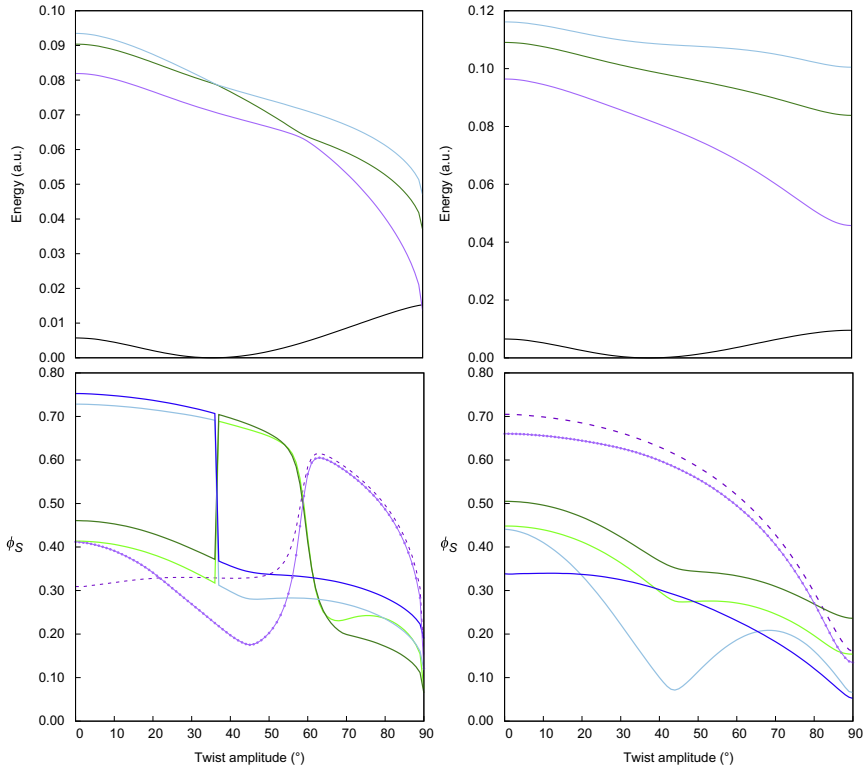

Fig. 1 (*Top*) Energy landscapes for the PP molecule along the scan of its central dihedral (twist) angle. The *black line* is the ground-state energy, the *purple* one is the first singlet excited-state energy, the *green* one is the second singlet excited-state energy, and the *blue* one is the third singlet excited-state energy. The *left part* is obtained using the B3LYP/6-311++G(2d,p) level of theory, and the *right part* is obtained using the CAM-B3LYP level of theory. (*Bottom*) Comparison of the ϕ_S and ϕ_S^{ℓ} values, with the same color code and levels of theory as the top part of the figure.*Deep blue* and *green colors* are for the NI values of the second and third excited states, the *dashed line* represents the NI values for the first singlet excited state, and the *dotted line* represents the PA values for the first singlet excited state.

While there is neither avoided crossings nor conical intersections in the PP excited-state energy landscape for the first three excited states when computed at the CAM-B3LYP/6-311++G(2d,p) level of theory, the observations reported for the B3LYP xc-functional strictly apply to the CAM-B3LYP computations (see the right part of Fig. 1). Finally, the results in Table 4 show that at given geometries, since the xc-functional influences the CT character, it indirectly influences the

Table 4 Descriptors values for the first excited state of PP obtained with B3LYP and CAM-B3LYP xc-functionals and 6 BSs out of the 15 investigated in this contribution. Two dihedral angles have been chosen (0 and 80 degrees).

Angle 0 degree

		B3LYP		CAM-B3LYP		B3LYP		CAM-B3LYP		B3LYP		CAM-B3LYP	
BS	***K***	ϕ_S	ϕ_S^ℓ	ϕ_S	ϕ_S^ℓ	φ	φ^ℓ	φ	φ^ℓ	ψ	ψ^ℓ	ψ	ψ^ℓ
3-21G	135	0.33	0.43	0.74	0.71	0.86	0.82	0.60	0.63	0.23	0.31	0.57	0.54
6-31G	135	0.32	0.42	0.73	0.69	0.86	0.83	0.62	0.65	0.23	0.30	0.55	0.52
6-31+G	187	0.31	0.41	0.70	0.66	0.87	0.83	0.63	0.66	0.22	0.30	0.53	0.50
6-31G(d)	213	0.31	0.42	0.73	0.69	0.86	0.83	0.61	0.65	0.22	0.30	0.56	0.52
6-311+G(d)	313	0.31	0.40	0.71	0.66	0.87	0.84	0.63	0.66	0.22	0.29	0.54	0.50
6-311++G(2d,p)	414	0.31	0.41	0.70	0.66	0.87	0.83	0.63	0.66	0.22	0.29	0.53	0.50

Angle 80 degrees

		B3LYP		CAM-B3LYP		B3LYP		CAM-B3LYP		B3LYP		CAM-B3LYP	
BS	***K***	ϕ_S	ϕ_S^ℓ	ϕ_S	ϕ_S^ℓ	φ	φ^ℓ	φ	φ^ℓ	ψ	ψ^ℓ	ψ	ψ^ℓ
3-21G	135	0.53	0.54	0.37	0.34	0.81	0.82	0.90	0.93	0.37	0.37	0.25	0.22
6-31G	135	0.55	0.55	0.33	0.30	0.81	0.82	0.92	0.94	0.38	0.38	0.22	0.20
6-31+G	187	0.50	0.51	0.30	0.26	0.84	0.85	0.93	0.95	0.35	0.34	0.20	0.17
6-31G(d)	213	0.54	0.54	0.33	0.30	0.81	0.83	0.92	0.94	0.37	0.37	0.22	0.20
6-311+G(d)	313	0.49	0.50	0.30	0.26	0.84	0.86	0.93	0.95	0.34	0.33	0.20	0.17
6-311++G(2d,p)	414	0.49	0.50	0.30	0.27	0.84	0.85	0.93	0.94	0.34	0.33	0.20	0.18

accuracy of the PA-approximation. Indeed, while the xc-functional does not explicitly play any role in the definition of the F rule, since we established that the ϕ_S^ℓ approximation reliability was CT nature-dependent, overtuning the hole/particle overlap down by changing the xc-functional at certain geometries might result in ϕ_S values that cannot be approximated by Löwdin's symmetrically orthogonalized orbitals population analysis. Note however that when turning to diagnosis d_8 the conclusions related to the CAM-B3LYP computation of PP excited states are transferrable to the other two range-separated xc-functionals, LC-ωHPBE and ωB97X-D (as well as the CIS and TDHF results). On the other hand the B3LYP results also hold for the other hybrid xc-functional PBE0 while M06-2X reproduces the analysis of range-separated hybrid xc-functionals, which is a feature already reported in Ref. 60. All the data for the six xc-functionals and the data related to the CIS and TDHF excited-state computations can be found in Tables S50–S170 and Figures S3–S378. B3LYP and CAM-B3LYP data are also reported in Table 4 where two PP twist angles, 80 and 0 degrees, have been selected, as they allow us to highlight the particular behavior of B3LYP for this molecule with a low dihedral angle.

Finally, as reported in Table 4 for six basis sets and in SI for the nine others that were used in this investigation (d_7), again, once the convergence on the basis set is achieved for the ϕ_S value, the accuracy of the ϕ_S^ℓ approximation is stable. This allows us to conclude that if the BS used is reliable for the excited-state computation, its size will not influence the accuracy of the ϕ_S^ℓ approximation.

5. Discussion

Our approximation here is to consider the Löwdin symmetrically orthogonalized orbitals as being centered in one point and multiplying or subtracting diagonal entries of $\mathbf{S}^{1/2}\mathbf{D}\mathbf{S}^{1/2}$ and $\mathbf{S}^{1/2}\mathbf{A}\mathbf{S}^{1/2}$ as if we were manipulating point charges with precise locations (centered on the atomic positions), so that Löwdin's symmetric orthogonalization tails are ignored in such a model. However, as we saw, there are few cases in which our approximation is limited.

In a diatomic molecule for example: if the atomic orbitals are indeed centered on atomic positions, the orthogonalization tail for the transformation of the orbital centered on the first atom, will be centered on the position of

the second one (see figure in chapter 3 of Ref. 61). More generally, Löwdin's symmetrically orthogonalized orbitals have orthogonalization tails centered on the position of other atoms and can no longer be considered as strictly centered on one position, unlike the original atomic orbitals.

Therefore, for small molecular systems, the presence of these orthogonalization tails introduces a bias into the picture of the electronic distribution given by the population analysis we wish to use. Since the number of atoms is reduced, among the atomic orbitals there is a high percentage of them that is likely to possess a significant overlap. In such a case, the orthogonalization tails are distributed over a few atoms in a close region of space, so the deviation from our "local population" model (i.e., ignoring the orthogonalization tails), introduces a bias of significant relative importance in the population analysis.

The bias can also be significant for very high values of ϕ_S^ℓ (greater than 0.90), since in that case there are numerous contributions from many pairs of atomic orbitals that are to be considered. In such a case, the number and importance of the orthogonalization tails that are ignored in the model increases. More generally there is a collective effect observed from the sum of the individual small contributions to the deviation from the exact integral value.

For low values of ϕ_S^ℓ (less than 0.5) the problem is quite different: Such low values for the hole/particle Löwdin population overlap means that only a few diagonal product amplitudes are nonnegligible. Since these contributions are summed, introducing a bias on the value of a few number of entries of small amplitude can introduce a strong deviation on the total outcome of the evaluation of F. This bias is assumed to be particularly substantial for molecular Rydberg states, since in principle those should lead to extremely low values of ϕ_S.

6. Conclusion

We reported the study of two computational methods for evaluating two types of integral related to the nature of molecular electronic transitions. The first type of integral is the spatial overlap between two density functions, while the second type separately sums the positive and negative entries of a difference-density function. The first integral evaluation method tested is the projection of the one-body reduced density matrices corresponding to the density functions onto the Euclidean space using Cartesian grids

and discrete summations. The second evaluation path is the population analysis of the related density matrices in the basis of symmetrically orthogonalized orbitals. The diagnosis is related to two rules (*F* and *H*) mapping the orbital space to a scalar quantity.

Our first conclusion concerns the first integral evaluation method: we observed that the precision of the results of our numerical integrations on Cartesian grids is converged for medium-density grids with six points per bohr for the three directions of space. We also reported that the degree to which a trace of some relevant matrices can be evaluated exactly and allows the quality of the grid to be diagnosed.

Regarding the diagnosis of the population analysis, we first noticed that the behavior of the *F* and *H* rules was very similar and decided to focus the analysis on the *F* rule leading to the PA-approximation (ϕ_S^ℓ) to the hole/particle spatial overlap integral ϕ_S.

We then deduced from an extensive diagnosis of the *F* rule that its accuracy depends on the size of the target molecular systems, and on the nature of the electronic transitions considered. Basically, the PA-approximation to ϕ_S is limited to medium- and large-sized molecular systems. In addition to that, ϕ_S^ℓ values below 0.5 (for small and medium-sized molecules) and above 0.9 for any type of molecule should not be trusted, so that numerical integrations should be performed in such occurrences.

We also noticed that large ϕ_S^ℓ gradients are not necessarily corresponding to large errors in the population analysis, and that globally the accuracy of the PA-approximation is independent from the size of the basis set used, apart for very small basis sets that in any case would not be used for the accurate computation of excited-state properties in general.

Appendix

A comment on the nomenclature used in the literature and here, a brief reminder on density matrices and density functions and the derivation of the detachment/attachment density matrices, are given in the arXiv repository 1902.05840, and is available using the "pdf" link in the Download section. In the same text, one can find a comment related to the construction of the *G* and *H* rules, and the generalization of the orbitals population analysis, as well as the demonstration leading to the conclusion that only a Löwdin-like scheme ensures physical orbital populations. Finally, the relaxed picture of a transition, and the related descriptors, are

discussed there, before concluding with some comments on the use of the *G* and *H* rules in the context of previous papers, and in the present one. Tables S1–S170, and Figures S1–S378, are also available at the same address (arxiv.org/abs/1902.05840) in the Supplementary_Information.pdf file downloadable in the 'Ancillary files' section.

References

1. Luzanov, A. V.; Pedash, V. F. Interpretation of Excited States Using Charge-Transfer Numbers. *Theor. Exp. Chem.* **1980**, *15*, 338–341.
2. Head-Gordon, M.; Grana, A. M.; Maurice, D.; White, C. A. Analysis of Electronic Transitions as the Difference of Electron Attachment and Detachment Densities. *J. Phys. Chem.* **1995**, *99*, 14261–14270.
3. Furche, F. On the Density Matrix Based Approach to Time-Dependent Density Functional Response Theory. *J. Chem. Phys.* **2001**, *114*, 5982–5992.
4. Tretiak, S.; Mukamel, S. Density Matrix Analysis and Simulation of Electronic Excitations in Conjugated and Aggregated Molecules. *Chem. Rev.* **2002**, *102*, 3171–3212.
5. Martin, R. L. Natural Transition Orbitals. *J. Chem. Phys.* **2003**, *118*, 4775–4777.
6. Batista, E. R.; Martin, R. L. *Encyclopedia of Computational Chemistry*. American Cancer Society, 2004.
7. Tretiak, S.; Igumenshchev, K.; Chernyak, V. Exciton Sizes of Conducting Polymers Predicted by Time-Dependent Density Functional Theory. *Phys. Rev. B* **2005**, *71*, 033201.
8. Dreuw, A.; Head-Gordon, M. Single-Reference Ab Initio Methods for the Calculation of Excited States of Large Molecules. *Chem. Rev.* **2005**, *105*, 4009–4037.
9. Mayer, I. Using Singular Value Decomposition for a Compact Presentation and Improved Interpretation of the CIS Wave Functions. *Chem. Phys. Lett.* **2007**, *437*, 284–286.
10. Surján, P. R. Natural Orbitals in CIS and Singular-Value Decomposition. *Chem. Phys. Lett.* **2007**, *439*, 393–394.
11. Wu, C.; Malinin, S. V.; Tretiak, S.; Chernyak, V. Y. Exciton Scattering Approach for Branched Conjugated Molecules and Complexes. I. Formalism. *J. Chem. Phys.* **2008**, *129*, 174111.
12. Luzanov, A. V.; Zhikol, O. A. Electron Invariants and Excited State Structural Analysis for Electronic Transitions Within CIS, RPA, and TDDFT Models. *Int. J. Quantum Chem.* **2009**, *110*, 902–924.
13. Li, Y.; Ullrich, C. A. Time-Dependent Transition Density Matrix. *Chem. Phys.* **2011**, *391*, 157–163.
14. Plasser, F.; Lischka, H. Analysis of Excitonic and Charge Transfer Interactions from Quantum Chemical Calculations. *J. Chem. Theory Comput.* **2012**, *8*, 2777–2789.
15. Plasser, F.; Wormit, M.; Dreuw, A. New Tools for the Systematic Analysis and Visualization of Electronic Excitations. I. Formalism. *J. Chem. Phys.* **2014**, *141*, 024106.
16. Plasser, F.; Bäppler, S. A.; Wormit, M.; Dreuw, A. New Tools for the Systematic Analysis and Visualization of Electronic Excitations. II. Applications. *J. Chem. Phys.* **2014**, *141*, 024107.
17. Bäppler, S. A.; Plasser, F.; Wormit, M.; Dreuw, A. Exciton Analysis of Many-Body Wave Functions: Bridging the Gap Between the Quasiparticle and Molecular Orbital Pictures. *Phys. Rev. A* **2014**, *90*, 052521.
18. Ronca, E.; Pastore, M.; Belpassi, L.; Angelis, F. D.; Angeli, C.; Cimiraglia, R.; Tarantelli, F. Charge-Displacement Analysis for Excited States. *J. Chem. Phys.* **2014**, *140*.

19. Ronca, E.; Angeli, C.; Belpassi, L.; De Angelis, F.; Tarantelli, F.; Pastore, M. Density Relaxation in Time-Dependent Density Functional Theory: Combining Relaxed Density Natural Orbitals and Multireference Perturbation Theories for an Improved Description of Excited States. *J. Chem. Theory Comput.* **2014**, *10*, 4014–4024.
20. Etienne, T.; Assfeld, X.; Monari, A. Toward a Quantitative Assessment of Electronic Transitions Charge-Transfer Character. *J. Chem. Theory Comput.* **2014**, *10*, 3896–3905.
21. Etienne, T.; Assfeld, X.; Monari, A. New Insight Into the Topology of Excited States through Detachment/Attachment Density Matrices-Based Centroids of Charge. *J. Chem. Theory Comput.* **2014**, *10*, 3906–3914.
22. Etienne, T. Probing the Locality of Excited States with Linear Algebra. *J. Chem. Theory Comput.* **2015**, *11*, 1692–1699.
23. Pastore, M.; Assfeld, X.; Mosconi, E.; Monari, A.; Etienne, T. Unveiling the Nature of Post-Linear Response Z-Vector Method for Time-Dependent Density Functional Theory. *J. Chem. Phys.* **2017**, *147*, 024108.
24. Pluhar, E. A.; Ullrich, C. A. Visualizing Electronic Excitations With the Particle-Hole Map: Orbital Localization and Metric Space Analysis. *Eur. Phys. J. B* **2018**, *91*, 137.
25. Mewes, S. A.; Plasser, F.; Dreuw, A. Communication: Exciton Analysis in Time-Dependent Density Functional Theory: How Functionals Shape Excited-State Characters. *J. Chem. Phys.* **2015**, *143*, 171101.
26. Li, Y.; Ullrich, C. A. The ParticleHole Map: A Computational Tool To Visualize Electronic Excitations. *J. Chem. Theory Comput.* **2015**, *11*, 5838–5852.
27. Etienne, T. Transition Matrices and Orbitals From Reduced Density Matrix Theory. *J. Chem. Phys.* **2015**, *142*, 244103.
28. Plasser, F.; Thomitzni, B.; Bäppler, S. A.; Wenzel, J.; Rehn, D. R.; Wormit, M.; Dreuw, A. Statistical Analysis of Electronic Excitation Processes: Spatial Location, Compactness, Charge Transfer, and Electron-Hole Correlation. *J. Comput. Chem.* **2015**, *36*, 1609–1620.
29. Poidevin, C.; Lepetit, C.; Ben Amor, N.; Chauvin, R. Truncated Transition Densities for the Analysis of the (Nonlinear) Optical Properties of Carbo-Chromophores. *J. Chem. Theory Comput* **2016**, *12*, 3727–3740.
30. Wenzel, J.; Dreuw, A. Physical Properties, Exciton Analysis, and Visualization of Core-Excited States: An Intermediate State Representation Approach. *J. Chem. Theory Comput.* **2016**, *12*, 1314–1330.
31. Plasser, F. Entanglement Entropy of Electronic Excitations. *J. Chem. Phys.* **2016**, *144*, 194107.
32. Savarese, M.; Guido, C. A.; Brémond, E.; Ciofini, I.; Adamo, C. Metrics for Molecular Electronic Excitations: A Comparison Between Orbital- and Density-Based Descriptors. *J. Phys. Chem. A* **2017**, *121*, 7543–7549.
33. Plasser, F.; Mewes, S. A.; Dreuw, A.; González, L. Detailed Wave Function Analysis for Multireference Methods: Implementation in the Molcas Program Package and Applications to Tetracene. *J. Chem. Theory Comput* **2017**, *13*, 5343–5353.
34. Etienne, T. Theoretical Insights Into the Topology of Molecular Excitons From Single-Reference Excited States Calculation Methods. In Pyshkin, S. L. Ed.; Excitons; IntechOpen, 2017. https://doi.org/10.5772/intechopen.70688.
35. Mai, S.; Plasser, F.; Dorn, J.; Fumanal, M.; Daniel, C.; González, L. Quantitative Wave Function Analysis for Excited States of Transition Metal Complexes. *Coord. Chem. Rev.* **2018**, *361*, 74–97.
36. Mewes, S. A.; Plasser, F.; Krylov, A.; Dreuw, A. Benchmarking Excited-State Calculations Using Exciton Properties. *J. Chem. Theory Comput* **2018**, *14*, 710–725.
37. Skomorowski, W.; Krylov, A. I. Real and Imaginary Excitons: Making Sense of Resonance Wave Functions by Using Reduced State and Transition Density Matrices. *J. Phys. Chem. Lett.* **2018**, *9*, 4101–4108.

38. Park, Y. C.; Perera, A.; Bartlett, R. J. Low Scaling EOM-CCSD and EOM-MBPT(2) Method With Natural Transition Orbitals. *J. Chem. Phys.* **2018**, *149*, 184103.
39. Barca, G. M. J.; Gilbert, A. T. B.; Gill, P. M. W. Excitation Number: Characterizing Multiply Excited States. *J. Chem. Theory Comput.* **2018**, *14*, 9–13.
40. Etienne, T. A Comprehensive, Self-Contained Derivation of the One-Body Density Matrices From Single-Reference Excited States Calculation Methods Using the Equation-of-Motion formalism. *arXiv:1811.08849 [physics]* **2018**, ArXiv: 1811.08849.
41. Peach, M. J. G.; Benfield, P.; Helgaker, T.; Tozer, D. J. Excitation Energies in Density Functional Theory: An Evaluation and a Diagnostic Test. *J. Chem. Phys.* **2008**, *128*. 044118-044118-8.
42. Le Bahers, T.; Adamo, C.; Ciofini, I. A Qualitative Index of Spatial Extent in Charge-Transfer Excitations. *J. Chem. Theory Comput.* **2011**, 7, 2498–2506.
43. García, G.; Adamo, C.; Ciofini, I. Evaluating Push-Pull Dye Efficiency Using TD-DFT and Charge Transfer Indices. *Phys. Chem. Chem. Phys.* **2013**, *15*, 20210–20219.
44. Guido, C. A.; Cortona, P.; Mennucci, B.; Adamo, C. On the Metric of Charge Transfer Molecular Excitations: A Simple Chemical Descriptor. *J. Chem. Theory Comput.* **2013**, *9*, 3118–3126.
45. Guido, C.; Cortona, P.; Adamo, C. Effective electron displacements: A tool for time-dependent density functional theory computational spectroscopy. *J. Chem. Phys.* **2014**, *140*, 104101.
46. Etienne, T.; Pastore, M. Charge Separation: From the Topology of Molecular Electronic Transitions to the Dye/Semiconductor Interfacial Energetics and Kinetics. *arXiv:1811.10526 [physics]* **2018**, ArXiv: 1811.10526.
47. Campetella, M.; Perfetto, A.; Ciofini, I. Quantifying Partial Hole-Particle Distance at the Excited State: A Revised Version of the DCT Index. *Chem. Phys. Lett.* **2019**, *714*, 81–86.
48. Bachrach, S. M. *Reviews in Computational Chemistry*. John Wiley & Sons, Ltd, 2007; pp 171–228.
49. Löwdin, P. On the Non-Orthogonality Problem Connected With the Use of Atomic Wave Functions in the Theory of Molecules and Crystals. *J. Chem. Phys.* **1950**, *18*, 365–375.
50. Frisch, M. J. *Gaussian16 Revision A.03*. Gaussian Inc: Wallingford CT, 2016.
51. Ditchfield, R.; Hehre, W. J.; Pople, J. A. Self-Consistent Molecular-Orbital Methods. IX. An Extended Gaussian Type Basis for Molecular Orbital Studies of Organic Molecules. *J. Chem. Phys.* **1971**, *54*, 724–728.
52. Frisch, M. J.; Pople, J. A.; Binkley, J. S. Self-consistent Molecular-Orbital Methods 25. Supplementary Functions for Gaussian Basis Sets. *J. Chem. Phys.* **1984**, *80*, 3265–3269.
53. Becke, A. D. Density-Functional Thermochemistry. III. The Role of Exact Exchange. *J. Chem. Phys.* **1993**, *98*, 5648–5652.
54. Adamo, C.; Barone, V. Toward Reliable Density Functional Methods Without Adjustable Parameters: The PBE0 Model. *J. Chem. Phys.* **1999**, *110*, 6158–6170.
55. Zhao, Y.; Truhlar, D. The M06 Suite of Density Functionals for Main Group Thermochemistry, Thermochemical Kinetics, Noncovalent Interactions, Excited States, and Transition Elements: Two New Functionals and Systematic Testing of Four M06-Class Functionals and 12 Other Functionals. *Theor. Chem. Account* **2008**, *120*, 215–241.
56. Yanai, T.; Tew, D. P.; Handy, N. C. A New Hybrid Exchange–correlation Functional Using the Coulomb-Attenuating Method (CAM-B3LYP). *Chem. Phys. Lett.* **2004**, *393*, 51–57.

57. Vydrov, O. A.; Heyd, J.; Krukau, A. V.; Scuseria, G. E. Importance of Short-Range Versus Long-Range Hartree-Fock Exchange for the Performance of Hybrid Density Functionals. *J. Chem. Phys.* **2006**, *125*. 074106-074106-9.
58. Chai, J.-D.; Head-Gordon, M. Long-Range Corrected Hybrid Density Functionals With Damped Atom-atom Dispersion Corrections. *Phys. Chem. Chem. Phys.* **2008**, *10*, 6615–6620.
59. Hirata, S.; Head-Gordon, M.; Bartlett, R. J. Configuration Interaction Singles, Time-Dependent Hartree–Fock, and Time-Dependent Density Functional Theory for the Electronic Excited States of Extended Systems. *J. Chem. Phys.* **1999**, *111*, 10774–10786.
60. Etienne, T.; Gattuso, H.; Michaux, C.; Monari, A.; Assfeld, X.; Perpète, E. A. Fluorene-Imidazole Dyes Excited States From First-Principles Calculations—Topological Insights. *Theor. Chem. Acc* **2016**, *135*, 1–11.
61. Mayer, I. *Simple Theorems, Proofs, and Derivations in Quantum Chemistry; Mathematical and Computational Chemistry*. Springer US, 2003.

CHAPTER FOURTEEN

Physisorption energy of H and H_2 on clean Pt(111) as a useful surface energy reference in Quantum Monte Carlo calculation

Rajesh O. Sharma[a,b], **Philip E. Hoggan**[a,*]
[a]Institut Pascal, Aubière Cedex, France
[b]Physics Department, Marwadi University, Rajkot, Gujarat, India
*Corresponding author: e-mail address: pehoggan@yahoo.com

Contents

Abstract

First-principles approaches to key points on reaction paths at metal surfaces are now required to deliver chemical accuracy compared to reliable experiment. By this we mean that such calculated values as the activation barrier should be available to within 1 kcal/mol of empirical values. Such accuracy excludes *ab initio* DFT.

Quantum Monte Carlo (QMC) is a promising (albeit lengthy) first-principles method to achieve this goal and we are now beyond the dawn of QMC benchmarks for metal catalyst systems, since hydrogen dissociation on the copper Cu(111) face was studied with quite adequate accuracy in two improving QMC studies and compared to molecular beam measurements (Doblhoff-Dier et al., 2017[4]; Hoggan, 2015[3]).

The present work determines physisorption energies for hydrogen (the atoms and molecules) on platinum, i.e., Pt(111). Such systems are used as asymptotes to determine reaction barriers. The reference is a clean Pt(111) surface and isolated hydrogen atom or molecule.

Pt and Cu require the use of pseudo-potentials in these large calculations and we show that those of Pt are less problematic than the Cu case, notably for QMC work.

Previous work gave the activation barrier to hydrogen dissociation on Pt(111) using the bridging geometry. The method used is state-of-the-art (*ab initio*) QMC. It gives the barrier to better than chemical accuracy. Specific reaction parameter (SRP-DFT)

Advances in Quantum Chemistry, Volume 79
ISSN 0065-3276
https://doi.org/10.1016/bs.aiq.2019.04.007

calculations agree. They are fitted to measurement (accurate molecular beam results) (Nour Ghassemi et al., 2017). SRP-DFT can thus be considered empirical.

The QMC approach evaluates the hydrogen dissociation barrier on Pt(111) as 5.4 kcal/mol with standard error below 1 kcal/mol (The SRP-DFT barrier is 6.2 kcal/mol).

This is encouraging for establishing less well-known benchmark values of industrial reaction barriers on Pt(111).

1. Introduction

Stochastic approaches to the time-dependent Schrödinger equation are currently attracting significant rapidly growing interest. Such an approach is the Quantum Monte Carlo (QMC) method, which is applied here. Errors can be made small, given time. The procedure scales well on highly parallel computers.

QMC has become quite well-established for application to molecules. One example is the Scemama et al. all-electron (434 electron) QMC energy difference calculation between the β-strand and α-helix conformations of amyloid peptide A β related to Alzheimer's disease.[1]

Solids and heterogeneous systems are less studied by QMC, because of error linked to finite-size and fixed-nodes (phase). However, in recent years major methodological progress has been made and periodic systems (or heterogeneous systems that can be made periodic) are well-provided for by software, such as the CASINO code that we have developed after the principal authors provided a tested starting point. Applications to, e.g., metal surfaces and, *a fortiori* their catalytic properties, are still a work-in-progress. Our multiconfigurational molecular "active-site" approach embedded in a periodic solid surface is described in the Ref. 2. It uses orbitals for the molecule, the whole system is expanded in plane-waves for QMC input.

Certain metal surfaces catalyze hydrogen dissociation. In our previous work, transition-state (TS) geometry was compared to that of the reacting molecules at a distance of over 6 Å from the surface. This was done firstly to avoid breaking the surface 2D symmetry by comparing the adsorbed TS to separate molecules and clean surface, secondly because it models catalytic reactions more closely and, last but not least, because comparing the same molecules in these two distinct geometries reduces fixed-node error (see below). However, it is convenient to refer to clean surface energy. Also, even at long range, there is some physical interaction between molecules and the surface. The work described here aims to study physisorption of very

simple systems and compare the errors committed by using long-range molecule-surface asymptotes as compared to the clean surface reference.

Our recent benchmark studies for hydrogen dissociation at a Cu(111) surface, compare specific reaction parameter (SRP) density functional theory (DFT) and state-of-the art Quantum Monte Carlo. Reliable molecular beam reaction barrier measurements are used.[3,4]

The QMC benchmark assumes a planar Cu(111) surface, which is an approximation.[5]

The SRP-DFT fixes a parameter experimentally, to combine two Perdew group functionals (PBE and PW91), in so doing their defects for barrier heights are much-reduced.

To limit the QMC fixed-node error (see below), the same atoms were compared in two geometries. The higher-energy "transition-state" structure, determined by QMC geometry optimization as a maximum along the reaction path is compared to an "asymptotic geometry." In the latter, atoms, or more generally molecules in their equilibrium geometry, i.e., experimental H_2, from Hertzberg, are placed 6.5 Å from the solid surface, an estimated long-range limit of weak interactions. We used this as asymptotic geometry for Cu(111) and Pt(111) surfaces.

In the present work, this asymptotic geometry is compared for the hydrogen molecule and also the atom to the separate clean surface and molecule or atom. Analytical isolated H atom energy has well-known values and the hydrogen molecule energy can also be determined to arbitrary numerical accuracy.

This study therefore shows how referring to the clean surface influences the errors due to differences in the trial wave-function, in particular its nodal changes between the clean surface and the physisorped asymptote with, e.g., a physisorped hydrogen molecule. Quantitative evaluation of interactions between physically adsorbed species and Pt(111) is given here. This interaction is generally so small as to fall within standard error of the clean Pt(111) slab calculation in QMC. Nevertheless, it is useful to compare the clean surface and isolated reactant reference to that with all atoms involved in a reaction, initially physisorped beyond the range for binding strongly to Pt.

Here, clean Pt(111) and isolated H_2 are tested for reliability as a reference for hydrogen dissociation on platinum. As stated above, the equilibrium molecule at asymptotic geometry was used in previous work on H_2 dissociation at Pt(111). The system tested is Pt(111), for bridging hydrogen dissociation with a low activation barrier. It is given by QMC to within chemical accuracy of experiment.[6]

In QMC calculations, the Pt(111) case is more favorable than copper, since the metal can be described by trial wave-functions with variance an order of magnitude less than in the copper case, which is adversely affected by the presence of a full 3d shell. The Pt pseudo-potentials used in this study are stringently analyzed and used to determine atomic spectra.

This study aims to explain industrial catalyst mechanism. Catalysts often use Pt(111) for selective reactions triggered by bond-breaking. This surface also catalyzes bond dissociation in hydrogen. Unfortunately, Pt(111) does not yet benefit from accurate molecular beam results for the reaction. A recent DFT study[7] shows that there are several coordinations of the hydrogen molecule, leading to two main categories of transition-state; "on-top" and "bridging" geometries: they are mono and bidentate, respectively, for Pt atoms. The "on-top" molecule is perpendicular to the surface plane. The reaction then appears to be almost barrier free. The "bridging" geometry spans a surface Pt–Pt pair, parallel to the surface.

The Quantum Monte Carlo approach used here is *ab initio* (unlike the SRP-DFT method) but subject to the fixed-node approximation and time-consuming. It could be used for fitting a DFT functional. Rapid DFT calculations would then allow potential energy surfaces to be explored, fixed at a few points calculated by the present QMC approach.

The methods used in this work were developed in Refs. 3, 4, 8, 8a, and 9 that describe them fully.

QMC benchmarks the accurately measured and significantly higher barrier for hydrogen dissociation on Cu(111) to within some 1.5 kcal/mol.[4] The barrier on Cu(111) has been given by accurate molecular beam experiments at 0.63 eV or 14.5 kcal/mol. The H_2 molecule dissociation on Pt(111) has a low experimental barrier which depends strongly on the molecular orientation and active site and ranges from some 0.06 to 0.420 eV. The higher barriers are for trigonal sites on the surface with minimal rearrangements and no defects.[7]

For a H_2 molecule parallel to the surface, the lowest experimental barrier is 0.27 eV.

Evaluating the bridging hydrogen dissociation barrier on Pt(111) is therefore likely to pose a stiff challenge to QMC. Our previous work shows hydrogen dissociation QMC barriers are reliable on Pt(111) for "bridge" orientations (standard error under 0.043 eV or 0.99 kcal/mol of *chemical accuracy*, i.e., within 1 kcal/mol). The DMC bridge activation barrier height is obtained as 0.23 eV. Experiment gives 0.27 c.f. 0.23 ± 0.043 eV.[6]

This work investigates any differences found regarding the reference to a clean surface and isolated molecule, as opposed to the physisorped molecule asymptote (equilibrium geometry at long range from the surface). Best practices are thus suggested to calculate these heterogeneous systems in QMC.

Wave-function nodes are modified between the (2D) clean surface and asymptotes.

This is manifest in the desorption of open-shell radicals (like the H-atom).

The closed-shell H_2 breaks translational symmetry. This 2 by 2 k-point grid trial wave-function doubles x and y of the real-space cell. This unfolded cell then contains 64 Pt atoms and 4 H_2 molecules (i.e., having a coverage-layer symmetry artefact). These extra wave-function nodes affect the fixed-node approximation result in QMC, to give small energy differences for physisorption.

2. Methods, best practices: QMC for solid surfaces

Our Slater determinant is built of ground-state Kohn–Sham orbitals obtained using the Perdew, Burke, Ernzerhof (PBE) functional (and ABINIT code) for periodic slabs with a suitable pseudo-potential for all atoms in a plane-wave basis.

The Pt slab surface is (111) with 2 atoms along $[\bar{1}10]$ and 2 along $[01\bar{1}]$ (see Fig. 1) in equilateral triangles. The 4 layers of this cell are stacked ABAB, B-atoms under centers of A triangles. The bulk lattice-parameter is $a = 3.912$ Å. The top 3 layers are relaxed to reproduce experimentally observed spacing. Layers 3 and 4 are exactly a bulk $\frac{a}{\sqrt{3}}$ apart.

Either a single H-atom (therefore one unpaired spin H.) is positioned vertically 6.5 Å above (one of the four) surface Pt atoms, or a H_2 molecule

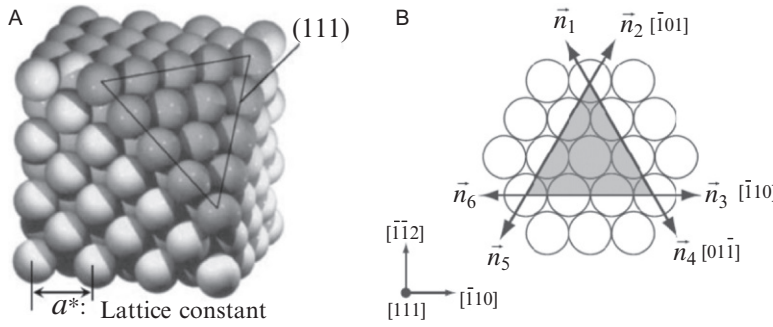

Fig. 1 Pt slab: 2 × 2 atoms in a (111) surface, 4 ABAB layers cut from the FCC lattice.[10] (A) Face centered cubic structure with (111) face exposed. (B) Packing in (111) face.

symmetrically bridging two adjacent Pt atoms along, e.g., $[\bar{1}10]$ (H_2 parallel to the surface and 6.5 Å above it).

Pt with a Troullier–Martins (TM)-PP leaves 10 valence electrons per atom (160 per cell) plus 1 or 2, for the H-atom or molecule, respectively.

For the $Z = 60$ Pt pseudo-potential, with 18 valence electrons per Pt, there are 288 electrons per super-cell. Since the plane-waves are generated on a 2 2 1 k-point grid, the total numbers of electrons input to QMC correspond to four real-space cells, giving (for physisorped atomic H) $4 * 161 = 644$ (for the TM-PP) and thus $4 * 289 = 1156$ (for the $Z = 60$ PP).

The plane-waves basis is expanded in B-splines to ensure favorable scaling with system size (computer time, t proportional to n^3 for n-electrons).[10a]

A generic Jastrow factor (gJastrow) is premultiplied into the Slater-determinants (from Kohn–Sham spin-orbitals in the present work). This must account for all possible interactions of electrons with different spin. The product is the Slater–Jastrow wave-function. It is used to evaluate the local energy:

$$E_{local} = \frac{H\psi}{\psi}$$

A Monte Carlo algorithm solves the requisite integrals stochastically, to give the local energy for a distribution of particle positions (configurations). From these, we obtain an expectation value (average) subject to the variation principle.

The set of configurations or "walkers" represents particle density in real space. The number of configurations used here was 4 per core, i.e., 16384 for a 4096 core calculation. These were checked for bias (they could be visualized as a "normal" distribution). Low variance is a criterion of reliability of the configuration distribution. By extension, a low-variance wave-function is often sought by optimization. Finer (gJastrow) optimization is preferably carried out (for minimal variance) with respect to ground-state energy estimated as this local energy.

The best (i.e., minimum) result is obtained by the step termed Variational Monte Carlo (VMC). After a fairly brief equilibration, VMC is used to optimize the unknown parameters in the Jastrow factor, to reduce wave-function variance and, above all, VMC is used for energy minimization.

The Jastrow factor spin-dependence for electron pairs ($\alpha(i)\beta(j) \neq \alpha(i)\alpha(j)$, *or* $= \alpha(i)\alpha(j)$) is chosen from the physics of combining atoms to form polyatomic systems. In this case, radical H atoms are physisorped,

remaining open shell whereas the molecule is closed shell, whether isolated or physisorped. The metal slab may have a complete set of spin interactions.

The Jastrow optimization must be done carefully in all cases. The most flexible parameter-set structure in CASINO uses the Common Algebraic Specification Language (CASL).

It is generally best practice to variationally optimize first with respect to mean absolute deviation from median energy (madmin). Then, more fine tuning can be applied with energy minimization using VMC to optimize free parameters in the Jastrow factors expressed as polynomials in the instantaneous inter-particle separations (with range fixed by madmin).

Once this gJastrow is optimal the VMC step is run once more, to generate the requisite configurations per core to initialize the Diffusion Monte Carlo (DMC) step, then the major time-consuming phase of QMC begins. DMC samples the exact wave-function as follows:

(i) The time-dependent Schrödinger equation is transformed into a diffusion equation by replacing the time-variable "*t*" by (pure-imaginary) "*it*."

(ii) This imaginary time is treated as "time" (often labeled τ) and increased in small steps. Equilibration may be quite long so a fairly large increment of 0.01 au was used for this phase.

The set of configurations are subject to diffusion and drift and represent the asymmetric density formed by the trial and updated wave-function product ($\Psi_T * \Psi_0$).

Since an arbitrary wave-function of the system can be expanded in eigenfunctions of its Hamiltonian and we seek that with lowest energy (eigenvalue of the exact ground-state Ψ_0), the others present in the approximate trial wave-function Ψ_T, fade out exponentially with the advance in time-variable τ by small steps.

In the data collection phase, τ should thus be vanishingly small. Often, in practice, it is sufficient to chose 0.005 au, as was done in this work. Time-step bias is controlled by halving it, rerunning and, if necessary showing the extrapolation to zero changes no observable value of interest. See Ref. 11 and references therein.

2.1 Soft pseudo-potentials and correlation for Pt atoms

The atomic cores are represented by pseudo-potentials. They correspond to atomic orbitals that are radially node-less up to a given radius.

This approximation is required for the calculations to take accessible computer time. These pseudo-potentials are relativistically correct, which is a definite prerequisite. The Pt atom here has a relativistic $Z = 60$ core defined by pseudo-potentials designed by the Stuttgart group; Ref. 8 and references therein.

The atomic spectra are accurately reproduced by spin-polarized guiding wave-functions in the DMC tests carried out as a prelude to this work.

Each of the platinum group metals (Ni, Pd, and Pt) has a different atomic electronic ground-state configuration. The vast majority of correlation energy is accounted for by the region immediately surrounding atoms, even when few electrons are treated explicitly, i.e., for large core pseudo-potentials. This suggests the relevance of both spin-orbit coupling and the nonlinear core correction (NLCC)[12] in pseudo-potentials as well as a configuration interaction (CI) of 3 states. Troullier–Martins PP for Pt leaves 10-valence electrons. Their electronic configurations for these three states are: [$5d^9$ $6s^1$] (ground state), [$5d^8$ $6s^2$], and [$5d^{10}$].

This CI is based on the ground-state electronic configurations of Ni, Pd, Pt. The Ni ground state is $3d^8$ $4s^2$ (compared to copper Cu $3d^{10}$ $4s^1$), Pd $4d^{10}$, and Pt $5d^9$ $6s^1$.

The pseudo-potential is expanded in spherical harmonics, with one l-value as local channel. These values are usually $l = 0, 1, 2, 3$. The local l selected corresponds to vacant valence states. The default is the maximum, $l = 3$. However, in this work, $l = 1$ reduces nonlocal effects.

Previous studies have shown that the nonlocality approximation is poorly satisfied for Cu (especially with the $l = 0$ local channel but also with other choices).[9] Tests have shown that this is a minor problem for Pt, particularly with the $l = 1$ local-channel choice. The other channels up to $l = 3$ require high-order nonlocal integration.

Resolution of the electronic spectrum for the Pt atom shows accurate excitation energies for spin-polarized cases, in particular for the transition between the ground-state Pt $5d^9$ $6s^1$ ($^3D_3$) and Pt $4d^{10}$ ($^1S_0$).

All results are in atomic units/primitive cell [Hartree (Ha)/cell] unless otherwise stated.

The ABINIT pseudo-potential is the Fritz-Haber Institute (FHI) Troullier–Martins PP.

This PP leaves 10 valence electrons and gives:

Ground state at −26.0113195 Ha

Excited state at −25.9833442 Ha (large-CI value −25.9851687 Ha, from Ref. 13; a 6% gap error).

Transition: 0.762 eV (error 0.0496 eV)

Using the Stuttgart PP (60 electron core *vide infra*) gives 0.76 eV (exact to 0.25 %).

The other excited states are resolved quite adequately.

Fixed-node error arises because this QMC implementation uses a product of input wave-function and its update to represent "density" and even the accurate diffusion step (DMC) where configurations are updated to represent this density will have the same nodes. A significant portion of the fixed-node error is due to atomic cores. It is minimized by subtracting energies corresponding to structures with the same number of metal atoms.[13a] This feature is also observed when comparing clean metal surfaces and gaseous reactant with an atom or gas molecule physisorped at the metal surface, as a precursor for the reacting system. This fine energy resolution has been tested successfully in the cases of hydrogen radicals as well as the H_2 molecule physisorped on Pt(111).

Note that nonlocality in the pseudo-potential requires a specific algorithm to cater for the requisite integral and render DMC variational. It is referred to as the Casula T-move scheme.[14] Tests below show that use of this algorithm stabilizes the results and renders them more accurate even for the relatively well-behaved pseudo-potentials with $Z = 60$, for Pt.

3. Results for hydrogen atoms and molecules on Pt(111)

Test of H-atom adsorption without recourse to Casula T-moves, gives (in Ha/primitive cell):

(with $l = 1$ as pseudo-potential local channel)

Clean Pt(111) surface: $-$ 409.1354 $\pm$ 0.002

Surface with a H atom: $-$ 409.6360 $\pm$ 0.003

Difference: $-$ 0.5006 $\pm$ 0.0036. The exact isolated ground-state energy of H is -0.5 by definition. A very modest stabilization estimated at 0.0004 Ha may be deducted (from our estimate) giving -0.5002.

Solid Pt model slabs expose the compact (111) face. They are detailed in Ref. 6. Fig. 1 shows this model. Slabs are 4 layers thick and most studies use a 2 by 2 mesh.

The $l = 0$ local channel is the worst-case scenario. The work continued with $l = 1$ as local channel and Casula T-moves, which also gives the accurate atomic spectra for Pt.

The clean surface averages −408.428 Ha and that with physisorped H_2 −409.687 Ha.

Resolution of the H_2 energy thus requires twist-averaging and a physisorption term, as the free molecule can be obtained with exact total energy at −1.1758 Ha.

Note that the optimized VMC values, using energy minimization, give brute differences close to the exact value: clean Pt(111) at −407.56 and −408.73 Ha with physisorped H_2. The difference is 1.17 Ha. It is essentially exact (see Table 1). The standard error for this test is close to 0.01 Ha. This suggests a defect in the pseudo-potential that becomes apparent when the more accurate DMC method is applied. DMC implementations converge quadratically and may be subvariational beforehand.

Subvariational DMC values are amplified by nonlocal pseudo-potentials and we use the variational Casula T-move scheme when this is seen. This has been well-documented for copper in our previous work.[9] It causes difficulties for physisorption of hydrogen. By using T-moves and varying the local channel of the pseudo-potential more stable statistics ensued. One of the harmonics of order l is chosen to be local, generally the highest present, i.e., $l = 3$, however, $l = 1$ reduces nonlocality error here. This accounts for part of the defect in resolving the H_2 physisorption. The remainder cancels by comparing the same molecules, with bond-length near the equilibrium value (for isolated hydrogen molecules or even the physisorped system). T-moves bring the estimate of hydrogen molecule total energy from a twist-averaged (over 20 offset grids) is improved, value of −1.1510 to −1.1721 Ha (0.0037 Ha lower). This difference is the contribution to systematic error of nonlocality in the pseudo-potential.

This PP leads to a 2.5 % error in the total energy of H_2, which is not as drastic as some 3d dimer binding energy errors.[9] Subtracting the same atoms gives the binding energy that corresponds to −1.1760 Ha (standard error is: 0.0002). This low error in the subtraction is indicative of the nodes being systematically in error in the trial wave-function of each system.[13a] Subtraction improves the fixed-node error by about 95% in this case (see Table 2).

Table 1 Total energy without T-moves in atomic units.

Structure	VMC E_{tot}	DMC $l = 1$	DMC $l = 2$	DMC $l = 0$
Clean Pt(111) 2 × 2 mesh	−407.56	−408.536	−408.475	−408.602
Hydrogen molecule (phys.)	−408.73	−409.687	−409.664	−409.706
Hydrogen molecule E (tot)	−1.17	−1.15	−1.189	−1.104

Table 2 Total energy (H_2 as difference of Pt(111) with and without it) uses T-moves in atomic units.

Structure	VMC E_{tot} c	DMC $l = 3$ c	DMC atom cons.	DMC gas
Hydrogen molecule E (tot)	−1.17	−1.1721	−1.1760	−1.1758485
Standard error	0.0005	0.00003	0.00002	0

Columns denoted c are the clean Pt(111) compared with the separate hydrogen molecule. Total molecular energy is obtained by subtracting the clean Pt(111) energy from the physisorped system. The column labeled DMC atom cons. is obtained by subtracting the asymptotic H-atoms on Pt(111) from the physisorped case. All are corrected for physisorption energy determined by QMC. The DMC gas column is the isolated hydrogen molecule DMC.

4. Perspectives and conclusions

The present study shows that calculations involving the clean Pt(111) surface are consistent with those using asymptotic physisorped geometries. The "same atom" systems are, nevertheless, more accurate. This phenomenon is ascribed to a cancelation of the majority of fixed-node error, when the nodes should be comparable.

This is not the case when a clean surface is involved, because of intrinsically 2-D surface states, having specific nodal structure.

Surface 2D symmetry is broken once an atom is adsorbed. The comparison of systems with the same atoms further renders the nodes comparable, although not identical because of the consequences of geometry changes. The formation and dissociation of bonds are certain to influence nodal structure. These processes are strongly multireference (MR) in nature, so the trial wave-function needs to reflect this. Setting up local active sites with molecular MRCI wave-functions is now possible. Their use and the effect on fixed-node error will be the subject of future work.

Some authors have already shown the advantages of a valence bond CI with breathing orbitals for C–H bond dissociation in acetylene using QMC.[15] We will investigate related strategies.

This work completes preparation for elementary reaction step studies in contact with Pt(111) and, subsequently, the rate-limiting step of catalytic processes can be identified.

Acknowledgments

The authors thank the President A. Mahul and staff of the Regional Computation facility (CRRI) on Clermont University Campus for generous allocations of computer resources. R.O.S. thanks them for arranging remote login. P.E.H. thanks Pablo Lopez-Rios for helpful discussions.

References

1. Scemama, A.; Caffarel, M.; Oseret, E.; Jalby, W. Quantum Monte Carlo for Large Chemical Systems: Implementing Efficient Strategies for Petascale Platforms and Beyond. *J. Comput. Chem.* **2013**, *34*, 938–951.
2. Hoggan, P. E.; Bensitel, M.; Lavalley, J. C. A New Method of Calculating Interactions Between Adsorbates and Metal Oxide Surfaces: Application to the Study of CO_2 Insertion in Hydroxyl or Methoxy Groups on Al_2O_3 and TiO_2. *J. Mol. Struct.* **1994**, *320*, 49–56.
3. Hoggan, P. E. Quantum Monte Carlo Activation Barrier for Hydrogen Dissociation on Copper to Unprecedented Accuracy. *ArXiv Mat. Cond* **2015**, .
4. Doblhoff-Dier, K.; Meyer, J.; Hoggan, P. E.; Kroes, G.-J. Quantum Monte Carlo calculations on a Benchmark Molecule—Metal Surface Reaction: H2 + Cu(111). *J. Chem. Theory Comput.* **2017**, *13*, 3208–3219.
5. Ben Hadj Hamouda, A.; Absi, N.; Hoggan, P. E.; Pimpinelli, A. Growth Instabilities and Adsorbed Impurities: A Case Study. *Phys. Rev. B* **2008**, 77, 245430.
6. Hoggan, P. E. Quantum Monte Carlo Calculations for Industrial Catalysts: Reaction Barrier to H_2 Dissociation on Pt(111). *Adv. Quantum Chem.* **2018**, *76*, 273–280.
7. Nour Ghassemi, E.; Wijzenbroek, M.; Somers, M. F.; Kroes, G. J. Chemically Accurate Simulation of Dissociative Chemisorption of D2 on Pt(111). *Chem. Phys. Lett.* **2017**, *683*, 329–335.
8. Absi, N.; Hoggan, P. E. Quantum Monte Carlo Investigation of Two Catalytic Reaction Paths for Hydrogen Synthesis on Pt(111). In: *Recent Progress in Quantum Monte Carlo, ACS Symposium Series*. 2016; p. 7788, 1234, Ch. 5.

8a. Hoggan, P. E.; Bouferguene, A. Relative Advantages of Quantum Monte Carlo Simulation for Changing Electron Correlation: CO Reactions on Copper and Platinum Catalysts. *Adv. Quantum Chem.* **2014**, *68*, 89–103.

9. Doblhoff-Dier, K.; Meyer, J.; Hoggan, P. E.; Kroes, G.-J.; Wagner, L. K. Diffusion Monte Carlo for Accurate Dissociation Energies of 3d Transition Metal Containing Molecules. *J. Chem. Theory Comput.* **2016**, *12*, 2583–2597.
10. Kong, L.-Y.; Gao, Y.-J.; Deng, Q.-Q.; Luo, Z.-R.; Lu, Y.-J. A Study of Strain-Driven Nucleation and Extension of Deformed Grain: Phase Field Crystal and Continuum Modeling. *Materials* **2018**, *11*, 1805.

10a. Pozzo, M.; Alfè, D. Hydrogen Dissociation on Mg(0001) Studied Via Quantum Monte Carlo Calculations. *Phys. Rev. B* **2008**, *78*, 245313.

11. Zen, A.; Sorella, S.; Gillan, M. J.; Michaelides, A.; Alfè, D. Boosting the Accuracy and Speed of Quantum Monte Carlo: Size Consistency and Time Step. *Phys. Rev. B* **2016**, *93*, 241118(R).
12. Louie, S. G.; Froyen, S.; Cohen, M. L. Nonlinear Ionic Pseudopotentials in Spin-Density-Functional Calculations. *Phys. Rev. B* **1982**, *26*, 1738–1742.
13. Ray, S. S.; Chaudhuri, R. K.; Chattopadhyay, S. *Viewing the Ground and Excited Electronic Structures of Platinum and Its Ion Through the Window of Relativistic Coupled Cluster Method*. *J. Chem. Phys.* **2017**, *146*. https://doi.org/10.1063/1.4973706.

13a. Needs, R. J.; Towler, M. D.; Drummond, N. D.; Lopez-Rios, P. Continuum Variational and Diffusion Quantum Monte Carlo Calculations. *J. Phys. Condens. Matter* **2010**, *22*, 023201. www.tcm.phy.cam.ac.uk/mdt26/casino2.html (Casino website).

14. Casula, M. Beyond the Locality Approximation in the Standard Diffusion Monte Carlo Method. *Phys. Rev. B* **2006**, *74*, 161102 R.
15. Domin, D.; Brada, B.; Lester, W. A. Breathing Orbital Valence Bond Method in Diffusion Monte Carlo: C-H Bond Dissociation of Acetylene. *J. Phys. Chem. A* **2008**, *112*, 8964–8969.

CHAPTER FIFTEEN

Stability after confinement of the H atom

Milagros F. Morcillo, Enrique F. Borja, José M. Alcaraz-Pelegrina, Antonio Sarsa*

Departamento de Física, Universidad de Córdoba, Córdoba, Spain
*Corresponding author: e-mail address: fa1sarua@uco.es

Contents

Abstract

The stability of a spherically confined atomic system when confinement is removed is studied. We consider *s*, *p*, *d*, and *f* states of the Hydrogen atom confined by a finite barrier. The stability is characterized in terms of the ionization probability of the atom when confinement is removed. The ionization probability presents different sharply peaked, non-symmetric maxima as a function of the confinement radius that can be explained in terms of tunneling and retunneling of the confined bound states. The spatial structure of the confined bound state plays a key role in the stability of the atom. Different measures arising from information theory, such as information entropy, disequilibrium indices, and complexity measures, have been calculated to characterize quantitatively the structure of the confined state. A direct relationship between the complexity of a confined state and its stability when it is released from confinement has been found.

1. Introduction

The experimental achievement of inserting atoms and molecules in molecular nanocontainers[1–3] has increased the interest in these complexes. Different applications of these structures have been proposed for energy transport and storage[4] or in medicine.[5,6] Spatial confinement leads to a modification of the properties of enclosed species as, for example, the energy

Advances in Quantum Chemistry, Volume 79
ISSN 0065-3276
https://doi.org/10.1016/bs.aiq.2019.03.002

levels. Absorption and emission properties can be modified by the confinement, see e.g.,[7] so encapsulated atoms present interesting applications because they open the possibility of designing materials with selected optical properties.[8]

The bound state properties of encapsulated atoms and molecules have been widely studied in the literature, see e.g., the reviews.[9–12] However, the knowledge of stability after confinement is much more scarce.[13,14] This aspect is important because many of the above mentioned applications are based, first, on inserting the atom or molecule of interest into a molecular cavity, and second, on extracting it for its future use. This requires that the atom remains stable when confinement is removed, which is not necessarily the case because spatial confinement changes the energy of the encapsulated atom with respect to its value when no confinement is present. This leads to a probability of ionization or dissociation of the atom or molecule when it is extracted from the cage.

In this work we address the problem of the stability of an atom when it is released from confinement. The ionization probability is calculated for different initial states and confining sizes. We consider a penetrable repulsive spherically symmetric model for confinement which contains relevant physical features of spatial confinement.[15,16] We study the excited states of the Hydrogen atom, for which a very accurate analysis can be carried out and it provides the basis for the understanding of this process for more complex systems. The sudden approximation is employed for calculating the time evolution of the atomic state when it is released from confinement. The results have been analyzed in terms of energy and confined orbitals shell structure that plays a key role in the stability of the atom when it is released from confinement. The structure of the charge distribution is characterized in terms of quantitative measures of the complexity of the electronic density. The complexity is related to the information content, uncertainty or delocalization of the electronic charge distribution. In Quantum Chemistry, several definitions of complexity have been applied to analyze different properties and processes related to structure studies and reactivity.[17] Atomic units are used throughout this work.

2. Methodology

We start from a confined atom in a stationary state, Ψ^{c}_{nlm},

$$H^{c}\,\Psi^{c}_{nlm}(\vec{r}) = E^{c}_{nl}\,\Psi^{c}_{nlm}(\vec{r}) \tag{1}$$

where H^c is the Hamiltonian of the confined Hydrogen atom

$$H^c = -\frac{1}{2}\nabla^2 - \frac{1}{r} + v_c(r), \tag{2}$$

and $v_c(r)$ is the confining potential

$$v_c(r) = \begin{cases} v_0 & \text{if} \quad r_0 \le r \le r_0 + \Delta \\ 0 & \text{otherwise,} \end{cases} \tag{3}$$

with r_0 the inner radius, v_0, the height, and Δ, the width of the barrier. Here, we use $v_0 = 2.5$ and $\Delta = 5$, as in Ref. 16. The wave function of the confined state can be written as

$$\Psi^c_{nlm}(\vec{r}) = \frac{u^c_{nl}(r)}{r} Y_{lm}(\Omega). \tag{4}$$

When the atom is extracted from the confining cavity, the Hamiltonian reduces to that of the free Hydrogen atom. The wave function of the atom when it is released from confinement can be expanded in terms of the stationary states of the free Hydrogen atom

$$\Psi^f_{lm}(\vec{r}\,, t) = \sum_{n'=0}^{\infty} C^{nl}_{n'} e^{-iE_{n'}\,t} \Psi_{n'lm}(\vec{r}) + \int_0^{\infty} dE\, C^{nl}(E) e^{-iE\,t} \Psi_{Elm}(\vec{r}). \tag{5}$$

Note that, due to the spherical symmetry of the confining potential, l and m do not change when confinement is removed.

If we assume that one can neglect the time to extract the atom from the confining cavity, then

$$C^{nl}_{n'} = \int_0^{\infty} dr\; u_{n'l}(r)\, u^c_{nl}(r), \quad C^{nl}(E) = \int_0^{\infty} dr\; u_{El}(r)\, u^c_{nl}(r), \tag{6}$$

where $u_{n'l}(r)$ and $u_{El}(r)$ are the reduced radial functions of the bound and ionized hydrogen states, respectively. The bound states are normalized to one and the states of the continuum spectrum are normalized in the energy scale. When confinement is removed, $|C^{nl}_{n'}|^2$ gives the probability that the electron lies in the $\{n'lm\}$ bound state of the free atom, and $|C^{nl}(E)|^2 dE$ is the probability that the electron is ejected with energy between E and $E + dE$. The total ionization probability is calculated as

$$P_I = \int_0^{\infty} dE\, |C^{nl}(E)|^2, \tag{7}$$

and the probability that the atom is not ionized as

$$P_{\mathrm{B}} = \sum_{n'=0}^{\infty} |C_{n'}^{nl}|^2 = 1 - P_{\mathrm{I}}. \tag{8}$$

The reduced radial functions are computed here by using the analytic continuation method.[18–20] This technique is based on a polynomial expansion of the solution around each one of the tabular points. The interaction potential is also expanded in a power series around these points. The linear coefficients of the solution at each point are obtained through a three term recursion relation. By using step sizes of 10^{-3} and polynomials of range 20, very accurate solutions of the radial Schrödinger equation are obtained. The calculation of the integrals giving the C coefficients, Eq. (6), can be done analytically by using the piecewise polynomial representation of the reduced radial function.

Quantitative analysis of complexity is based on measure indices which provide different information about the confined system. These indices can be written as the product of two terms, one related to the disequilibrium from the most probable state and the other to the information content of the system. In particular, we consider complexity measures proposed by López-Ruiz et al.[21] (LMC) in its shape complexity form,[22] and the Fisher-Shannon complexity[23] (FS). Information, delocalization, and complexity indices have been employed to quantitatively study the importance of the shape and structure of the electronic charge distribution of different properties[17] and effects as for example relativistic[24] and confinement effects.[25,26]

The shape form of the LMC index in position space is defined as

$$C_r^s = D_r H_r, \tag{9}$$

where D_r is the disequilibrium function given by the density expectation value

$$D_r = \int d\vec{r}\ \ \rho^2(r), \tag{10}$$

with $\rho(r)$ the spherically averaged electron density distribution normalized to unity. D_r is related to the distance from the most probable state, the equilibrium, which within this framework is the uniform density.

H_r is a measure of the information of the state and it is defined as

$$H_r = e^{S_r} \tag{11}$$

where S_r is the Shannon information entropy

$$S_r = -\int d\vec{r} \quad \rho(r)\ln\rho(r). \tag{12}$$

On the other hand, the FS index is, in position space,

$$P_r = I_r \frac{1}{2\pi e} H_r^{\frac{2}{3}}, \tag{13}$$

with the Fisher information measure, I_r, as

$$I_r = \int d\vec{r} \; \frac{|\vec{\nabla}\rho(r)|^2}{\rho(r)}. \tag{14}$$

This is another measure for the distance from the most probable state.

3. Results and discussion

In Fig. 1, we plot the energy of the confined $2p$ to $5p$ states as a function of r_0. It is negative and presents a sawtooth structure. Each np orbital energy has $n-1$ local maxima whose positions coincide with the positions of the local minima of the $(n+1)p$ orbital energy.

The physical origin of these kinks lies in the behavior of the orbitals around some critical values of the confinement radius r_0. This is studied

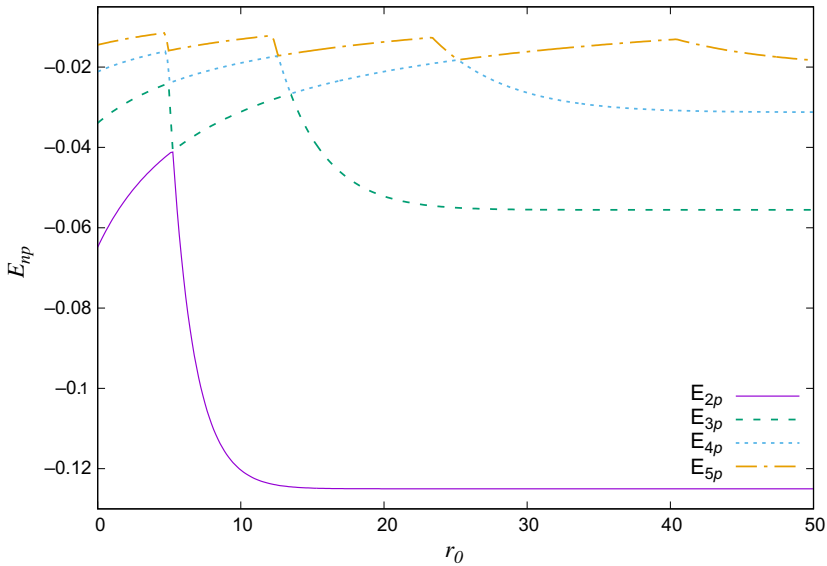

Fig. 1 Energy of the confined $2p$ to $5p$ states as a function of the confinement size, r_0.

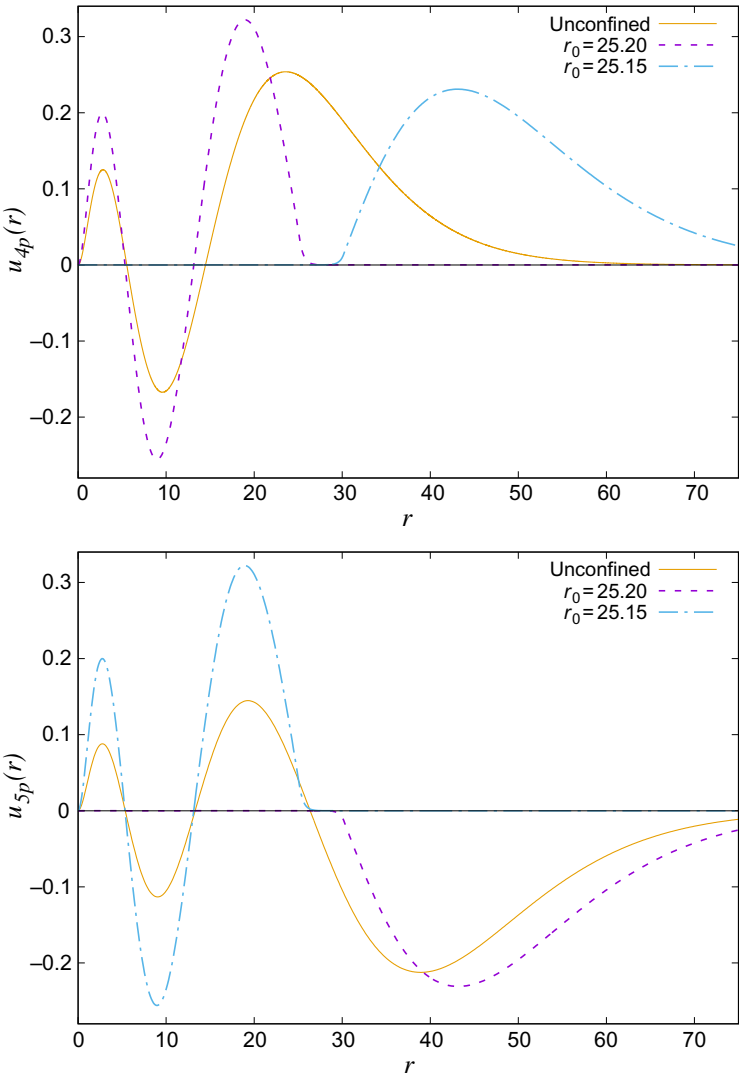

Fig. 2 *Upper panel*: Reduced radial functions, $u(r)$, of the confined 4*p* state for confinement sizes of $r_0 = 25.15$ and $r_0 = 25.2$. The unconfined radial orbital is also shown. *Lower panel*: The same for the 5*p* state.

in Fig. 2, where we plot in the upper panel, the 4*p* orbital obtained for $r_0 = 25.15$ and $r_0 = 25.20$. The unconfined orbital, i.e., without the penetrable barrier, is also plotted for the sake of comparison.

For $r_0 = 25.20$ the 4*p* state is within the confinement region. A small decrease of the confinement size, $r_0 = 25.15$, leads to an abrupt change in

the structure of the orbital, which becomes negligible inside the cavity. The nodes of the 4*p* orbital for $r_0 = 25.15$ are not visible within the scale of the figure. The orbital has tunneled out when the confinement radius has been reduced. Although the charge distribution is very different in both situations, the energy of the 4*p* orbital is very similar. In fact, the orbital energy is continuous as a function of the cavity size, as it can be seen in Fig. 1. The behavior of the 5*p* orbital, see the lower panel of Fig. 2, is the opposite to that of the 4*p* orbital. For $r_0 = 25.20$ it lies outside the confinement region while for $r_0 = 25.15$ it is within the confinement region. The 4*p* orbital leaves the cavity when the 5*p* orbital tunnels in. The energy of both orbitals for that particular r_0 value is very similar and corresponds to a local maximum and a local minimum of the 4*p* and 5*p* orbital energies respectively. The behavior of the orbital energy as a function of r_0 is related to the phenomena of the avoided crossing: neighboring levels with the same symmetry repel each other when they become close and do not cross. This behavior has been also obtained for *d*, *f*, … confined orbitals here studied and it was previously found for the *s* orbitals[14] and for *S* states of the confined He atom in a spherical potential well.[27]

The energy of the *nl* orbital as a function of r_0 presents a sawtooth structure with $n - l$ local maxima, as shown in Fig. 3 for the orbitals of the *N* shell of the Hydrogen atom. If one starts the analysis from the unconfined situation, $r_0 \to \infty$, when smaller r_0 values are considered, the states that tunnel out

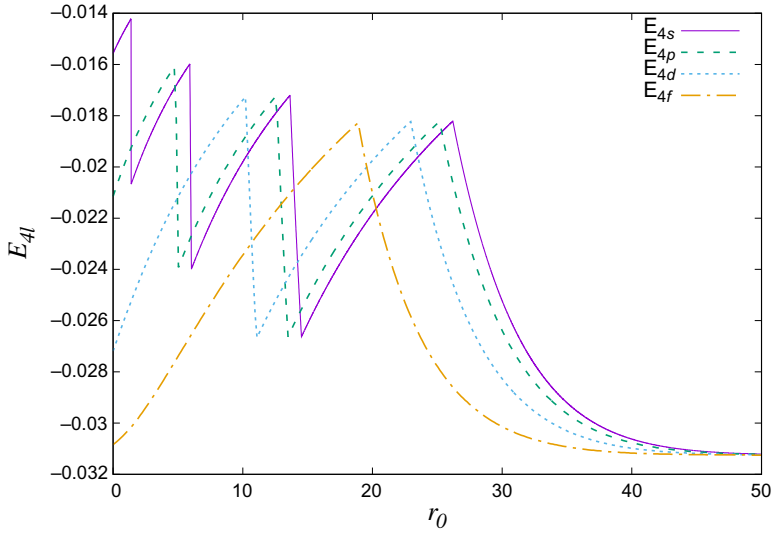

Fig. 3 Energy of the confined 4*s* to 4*f* orbitals as a function of r_0.

first are those whose orbital quantum number is smaller. The local maxima of the 4*s* orbital appear for lager r_0, followed by the local maxima of the 4*p*, 4*d*, and 4*f* states. The reason is that their spatial extension is larger and they are affected by confinement at bigger values of r_0.

The behavior of the confined orbitals with the cavity size has an effect on the ionization probability when the atom is released from confinement. In previous studies,[13] we have obtained that the ionization probability does not depend directly on the energy of the confined state as one could think beforehand. The spatial structure of the radial function of the confined orbital, and in particular the location and extension of the electronic shells, governs the ionization probability.

In Fig. 4 we plot the ionization probabilities for the 2*p* to 5*p* states as a function of r_0. An oscillatory behavior with several sharply peaked, non-symmetric maxima are found for those r_0 values where the states tunnel. When the state is within the confinement region, the ionization probability increases as r_0 decreases, while an oscillatory behavior is observed when the state is outside the confinement region. The ionization probability presents a counterintuitive behavior when the state tunnels. A steep rise in the ionization probability is observed when the orbital enters into the confinement region. The quantitative value energy of the orbital is practically unchanged when the orbital tunnels in, and it is a local maximum of the energy as a function of r_0. The ionization probability is governed by the structure of the charge distribution.

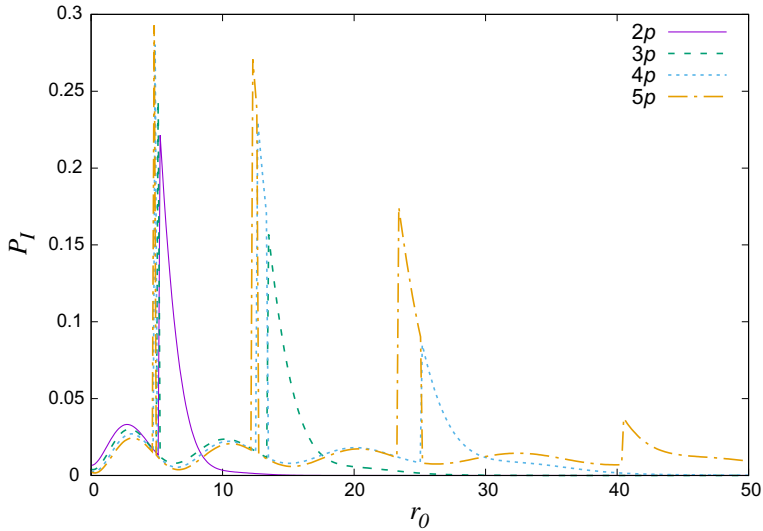

Fig. 4 Ionization probability of the 2*p* to 5*p* orbitals as a function of r_0.

Information theoretical tools are employed to study quantitatively the structure of the confined orbitals. The complexity indices here employed, Eqs. (9) and (13), include both the delocalization and the information content of the charge density. For the sake of space we only report here results for the N shell, which are representative for the rest of cases.

In Fig. 5, we plot the disequilibrium function, D_r, Eq. (10), and the Fisher information measure, I_r, Eq. (14), for the 4s to 4f orbitals as a function of r_0.

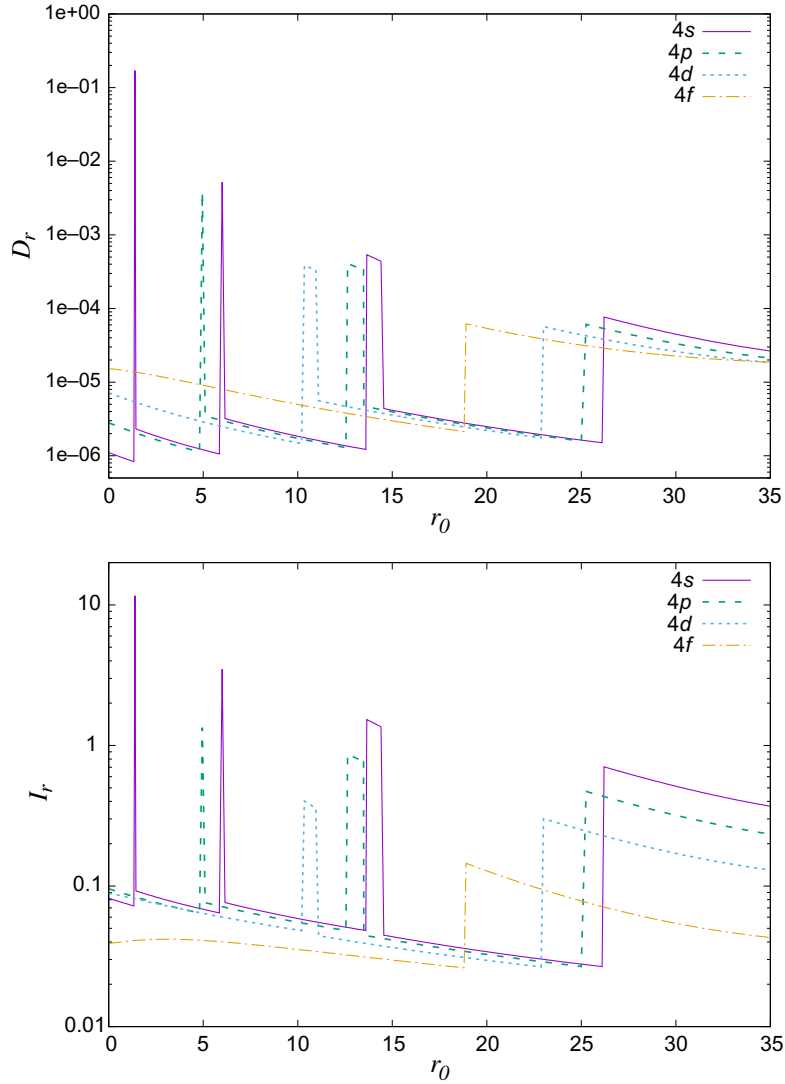

Fig. 5 *Upper panel*: Disequilibrium, D_r, in log scale for the 4s to 4f states as a function of r_0. *Lower panel*: The same for the Fisher information index, I_r.

Both indices present a similar pattern characterized by maxima in the regions where states are confined inside the barrier. This is due to the compression of the electronic charge toward the nucleus which leads to both, a more compact density and a larger curvature of the radial functions. On the other hand, these indices practically vanish when the states tunnel out because their spatial extension is larger, the curvature decreases and the density is more uniform inducing a minimum disequilibrium.

In Fig. 6, we plot the exponential Shannon entropy, H_r, Eq. (11), as a function of the confinement size. This index provides a measure of the information of the state. Unlike disequilibrium indices, if states are confined between the origin and the wall, their uncertainty in position drops and small H_r is obtained. The opposite holds when orbitals lie mostly outside the barrier, the uncertainty in the position is higher and the value of the information index is larger.

Complexity indices contain both, disequilibrium, and information measures simultaneously. Both indices present opposite behaviors when the charge is localized inside or outside the confinement region. The complexity indices here studied are governed by the disequilibrium as shown in Fig. 7, where we plot the LMC shape complexity measure, C_r^s, Eq. (9), and the FS index, P_r, Eq. (13), as a function of r_0. When the states are inside the cage, the larger value of disequilibrium index compensates for the lower information

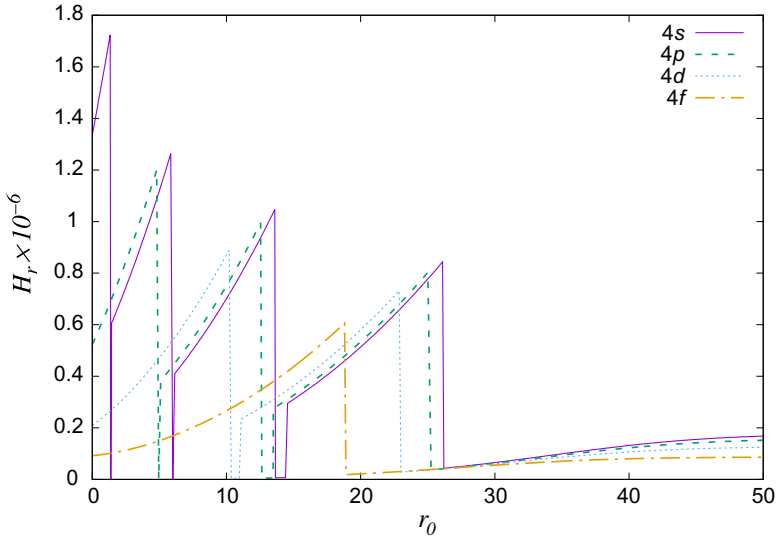

Fig. 6 Exponential Shannon information entropy, H_r, for the 4*s* to 4*f* states as a function of r_0.

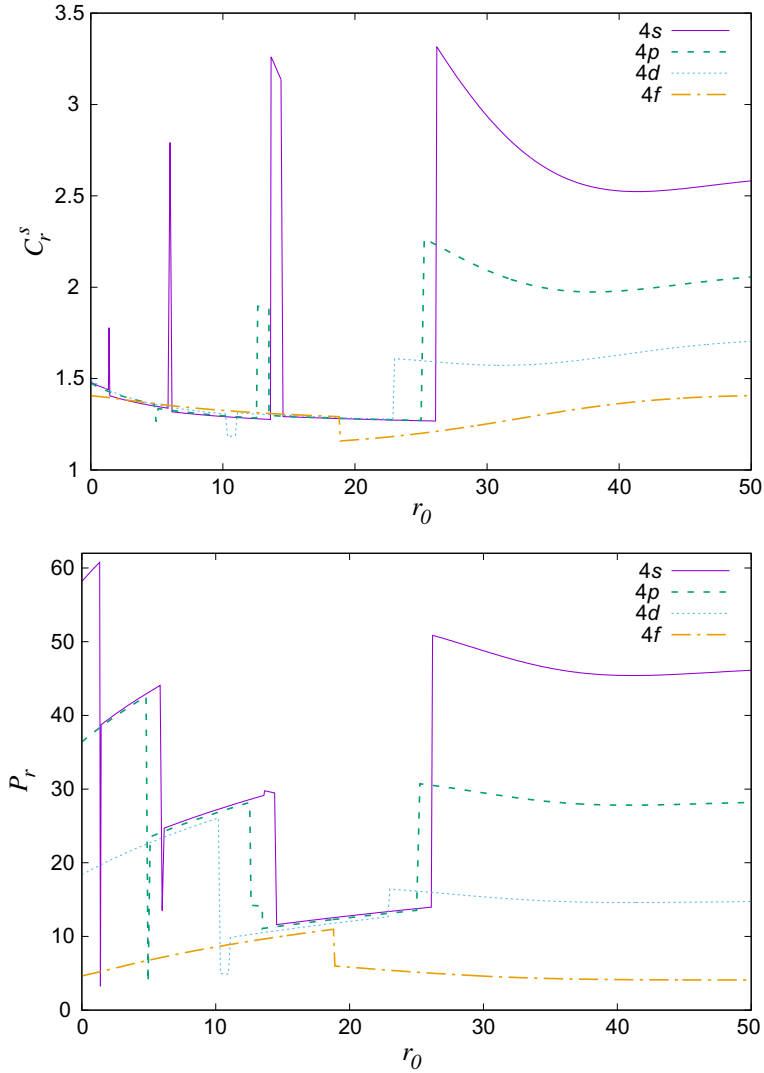

Fig. 7 *Upper panel*: Shape LMC complexity index, C_r^s, for the 4*s* to 4*f* states as a function of r_0. *Lower panel*: FS complexity index, P_r, for the same orbitals as a function of r_0.

content. Outside the confinement region, although the information index is large, the low values of the disequilibrium lead to a smaller complexity of the state. As a result the complexity indices are sensitive to the structure of the orbitals and present the same structure as the ionization probability. The states are more complex when they are localized inside the confinement region and the complexity grows as the confinement volume is reduced.

When the state jumps out of the confinement region a sharp drop in the complexity is observed. In the light of these results, complexity indices and other information theory measures characterize avoided level crossing, tunneling of confined states, and the stability of the atom when confinement is removed.

4. Conclusions

The stability of a Hydrogen atom when confinement is removed is studied in terms of the ionization probability of the confined states. A penetrable spherical barrier is used as a model for confinement. The confined atom is initially in a stationary state and the time needed to extract the atom is assumed to be small. The ionization probability of each *nl* state as a function of the confinement size presents an oscillatory behavior with $n - l$ sharply peaked, nonsymmetric maxima. This behavior has been explained in terms of successive tunneling and retunneling processes through the barrier at different inner radii. This is also reflected in the energy and its sawtooth structure, where the maxima are located at the same radii as those of the ionization probability.

The shape LMC and the FS complexity measures have also been calculated. Confinement effects on these indices have been studied. The value of the disequilibrium governs the behavior of the complexity of the confined state. The larger value of the disequilibrium indices of the states when the charge is localized within the confinement barrier overcomes the lower information content of the state. Our calculations show that complexity is a measure of the stability of the confined atom when it is released from confinement: the larger the complexity the smaller its stability. The complexity, as well as the ionization probability, is greatly reduced when the electronic charge distribution of the confined state lies mostly outside the confinement region. This particular charge distribution appears when the confined bound state has tunneled out the penetrable confining barrier.

Acknowledgments

This work was partially supported by the Spanish Dirección General de Investigación Científica y Técnica (DGICYT) and FEDER under contract FIS2015-69941-C2-2-P and the Junta de Andalucía under grant FQM378. M.F.M. acknowledges partial support by a Ph.D fellowship from the Spanish Ministerio de Ciencia, Innovación y Universidades under grant FPU16/05950.

References

1. Komatsu, K.; Murata, M.; Murata, Y. Encapsulation of Molecular Hydrogen in Fullerene C_{60} by Organic Synthesis. *Science* **2005**, *307*, 238.
2. Horsewill, A. J.; Panesar, K. S.; Rols, S.; Johnson, M. R.; Murata, Y.; Komatsu, K.; Mamone, S.; Danquigny, A.; Cuda, F.; Maltsev, S.; Grossel, M. C.; Carravetta, M.; Levitt, M. H. Quantum Translator-Rotator: Inelastic Neutron Scattering of Dihydrogen Molecules Trapped Inside Anisotropic Fullerene Cages. *Phy. Rev. Lett.* **2009**, *102*, 013001.
3. Krachmalnicoff, A.; Bounds, R.; Mamone, S.; Alom, S.; Concistre, M.; Meier, B.; Kouril, K.; Light, M. E.; Johnson, M. R.; Rols, S.; Horsewill, A. J.; Shugai, A.; Nagel, U.; Room, T.; Carravetta, M.; Levitt, M. H.; Whitby, R. J. The Dipolar Endofullerene HF@C60. *Nat. Chem.* **2016**, *8*, 953.
4. Ayub, K. Transportation of Hydrogen Atom and Molecule Through $X_{12}Y_{12}$ Nanocages. *Int. J. Hydrogen Energy* **2017**, *42*, 11439.
5. Cagle, D. W.; Kennel, S. J.; Mirzadeh, S.; Alford, J. M.; Wilson, L. J. In Vivo Studies of Fullerene-Based Materials Using Endohedral Metallofullerene Radiotracers. *Proc. Natl. Acad. Sci.* **1999**, *96*, 5182–5187.
6. Li, T.; Dorn, H. C. Biomedical Applications of Metalencapsulated Fullerene Nanoparticles. *Small* **2017**, *13*, 1603152.
7. Cabrera-Trujillo, R. Sum Rules and the Role of Pressure on the Excitation Spectrum of a Confined Hydrogen Atom by a Spherical Cavity. *J. Phys. B At. Mol. Opt. Phys.* 2017, *50*, 155006.
8. Anaya, M.; Rubino, A.; Rojas, T. C.; Galisteo-López, J. F.; Calvo, M. E.; Míguez, H. Strong Quantum Confinement and Fast Photoemission Activation in $CH_3NH_3PbI_3$ Perovskite Nanocrystals Grown Within Periodically Mesostructured Films. *Adv. Opt. Mater.* **2017**, *5*, 1601087.
9. Jaskolski, W. Confined Many-Electron Systems. *Phys. Rep.* **1996**, *271*, 1.
10. Sabin, J.; Brändas, E.; Cruz, S., Eds.; Theory. Oxford, UK, 2009; Vol. 57–58, pp 1–34.
11. Sen, K. D. *Electronic Structure of Quantum Confined Atoms and Molecules*. Springer-Verlag: Switzerland, 2014.
12. Ley-Koo, E. Recent Progress in Confined Atoms and Molecules: Superintegrability and Symmetry Breakings. *Rev. Mex. Fis.* **2018**, *64*, 326–363.
13. Morcillo, M. F.; Alcaraz-Pelegrina, J. M.; Sarsa, A. Ionization Probability of the Hydrogen Atom Suddenly Released From Confinement. *Int. J. Quantum Chem.* **2018**, *118*, e25563.
14. Morcillo, M. F.; Alcaraz-Pelegrina, J. M.; Sarsa, A. Ionisation and Excitation Probabilities of a Hydrogen Atom Suddenly Released From Penetrable Confinement. *Mol. Phys.* **2019**, 1–8. https://doi.org/10.1080/00268976.2018.1547429.
15. Connerade, J. P.; Dolmatov, V. K.; Lakshmi, P. A. The Filling of Shells in Compressed Atoms. *J. Phys. B At. Mol. Opt. Phys.* **2000**, *33*, 251–264.
16. Dolmatov, V. K.; King, J. L. Atomic Swelling Upon Compression. *J. Phys. B At. Mol. Opt. Phys.* **2012**, *45*, 225003-1–225003-5.
17. Sen, K. D. *Statistical Complexity, Applications in Electronic Structure*. Springer: London, 2011.
18. Holubec, A.; Stauffer, A. D. Efficient Solution of Differential Equations by Analytic Continuation. *J. Phys. A Math. Theor.* **1985**, *18*, 2141.
19. Hodgson, R. J. W. Precise Shooting Methods for the Schrodinger Equation. *J. Phys. A Math. Theor.* **1988**, *21*, 679.
20. Buendía, E.; Gálvez, F. J.; Puertas, A. Study of the Singular Anharmonic Potentials by Means of the Analytic Continuation Method. *J. Phys. A Math. Theor.* **1995**, *28*, 6731.

21. López-Ruiz, R.; Mancini, H. L.; Calbet, X. A Statistical Measure of Complexity. *Phys. Lett. A* **1995**, *209*, 321–326.
22. Catalán, R. G.; Garay, J.; López-Ruiz, R. Features of the Extension of a Statistical Measure of Complexity to Continuous Eystems. *Phys. Rev. E* **2002**, *66*, 011102.
23. Angulo, J. C.; Antolín, J.; Sen, K. D. Fisher-Shannon plane and statistical complexity of atoms. *Phys. Lett. A* **2008**, *372*, 670–674.
24. Maldonado, P.; Sarsa, A.; Buendía, E.; Gálvez, F. J. Relativistic Effects on Complexity Indexes in Atoms in Position and Momentum Spaces. *Phys. Lett. A* **2010**, *374*, 3847.
25. Rodríguez-Bautista, M.; Vargas, R.; Aquino, N.; Garza, J. Electron-Density Delocalization in Many-Electron Atoms Confined by Penetrable Walls: A Hartree-Fock Study. *Int. J. Quantum Chem.* **2018**, *143*, e25571.
26. Nascimento, W. S.; Prudente, F. V. Shannon Entropy: A Study of Confined Hydrogenic-Like Ions. *Chem. Phys. Lett.* **2018**, *691*, 401–407.
27. Mitnik, D. M.; Randazzo, J.; Gasaneo, G. Endohedrally Confined Helium: Study of Mirror Collapses. *Phys. Rev. A* **2008**, *78*, 062501.

Index

Note: Page numbers followed by "*f*" indicate figures, "*t*" indicate tables, and "*b*" indicate boxes.

D

E

F

N

O

P

Q

This page intentionally left blank

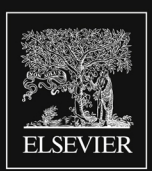

ACADEMIC PRESS

An imprint of Elsevier
elsevier.com/books-and-journals